

FRACTURE TOUGHNESS
AND
FATIGUE RESISTANCE
OF A
RANGE OF SINTERED STEELS

BY
DULAL CHANDRA GHOSH
B.TECH.(HONS.), M.Sc.

A THESIS SUBMITTED TO THE
UNIVERSITY OF ASTON IN BIRMINGHAM
FOR THE DEGREE OF
DOCTOR OF PHILOSOPHY.

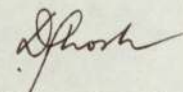
DECEMBER, 1976

SYNOPSIS

A range of notched, sintered maraging and diluted maraging steel compacts have been fatigue tested in three point bending with two levels of notch root radii. The number of cycles to produce a detectable fatigue crack correlated well with an empirical parameter of the form $(\Delta K / \rho^{0.3})$, thereby minimising the banding effect, possibly characteristic in these sintered steels. Decreased fatigue resistance have been observed with increased sintered density above a critical porosity level. Comparatively higher crack growth rate have been found in the highly diluted maraging steel compacts due to the presence of soft ferrite in the matrix, which largely superceded the crack blunting effect due to porosities. The micromechanism of fracture was of ductile dimple type in every case.

In the sintered materials tested so far, including some sintered specimens of the Ancoloy SA (Hoganas) variety, the increase in toughness value with the increased yield stress seemed to be the basic trend - a trend which would carry them into competition with the high-strength wrought steels.

I certify that to the best of my knowledge, no part of the work described in this thesis was done in collaboration unless specifically mentioned, and that the work has not been submitted for any other award.



D.C. Ghosh,
Dec., 1976.

CONTENTS

SYNOPSIS	I
1. INTRODUCTION	1
2. LITERATURE REVIEWS	6
3. LITERATURE REVIEW PART I (a) - MARAGING STEELS	6
3.1. Introduction	6
3.2. Some Basic Characteristics	6
3.3. Main Types of Maraging Steels	8
3.4. Heat Treatment and Properties	9
3.5. The Structure of Maraging Steels	10
3.5.1. The Matrix	10
3.5.2. Effects of Alloying Elements	11
3.5.3. Physical Metallurgy and Hardening	15
Mechanisms of Maraging Steels	
4. LITERATURE REVIEW PART I(b)	19
4.1. Ancoloy SA.	19
5. LITERATURE REVIEW PART II - GENERAL PRINCIPLES OF SINTERING	20
5.1. Introduction	20
5.2. Sintering Mechanism	21
5.3. The Stages of Sintering	22
5.4. Possible Mechanisms of Material Transport	23
5.5. Sintering of Multicomponent Systems	25
5.6. Liquid Phase Sintering	26
5.7. The Homogenisation Behaviour of Maraging Steel Powder and Iron Powder Mixes	28
6. LITERATURE REVIEW PART III	31

6.1.	Relation Between Young's Modulus and Porosity	31
7.	LITERATURE REVIEW PART IV - THE MECHANICS OF FRACTURE	32
7.1.	Introduction to Fracture Mechanics	32
7.2.	Criteria for Fracture	34
7.3.	The Effect of Yielding	38
7.4.	Micromechanisms of Initiation and Growth of Fatigue Cracks	41
7.4.1.	Introduction	41
7.4.2.	Mechanism of Crack Initiation	41
7.4.3.	Accepted Model of Mechanism for Initiation	42
7.4.4.	Mechanisms of Fatigue Crack Growth	43
7.5.	Fatigue Crack Initiation	49
7.5.1.	Introduction	49
7.5.2.	Review of Criteria for Correlating Fatigue Crack Initiation Data in Notched Specimens	50
7.5.2.1.	Stress-Strain Concentration Approach	50
7.5.2.2.	Fracture Mechanics Approach	52
7.6.	Fatigue Crack Propagation Laws	54
7.6.1.	Introduction	54
7.6.2.	Crack Propagation Laws	55
8.	EXPERIMENTAL DETAILS	62
8.1.	Objectives with An Outline of Experimental Work	62
8.2.	Powder Materials	62
8.3.	Specimen Preparation - Compaction, Calibration	66
8.4.	Test Specimens	67
8.5.	Treatment of Specimens	68
8.6.	Plane Strain Fracture Toughness Testing	69

8.7.	Calculation of KQ	71
8.8.	Crack Growth Measurement	71
8.9.	Potential Drop Calibration	75
8.10.	Method of Crack Growth Rate Calculation	78
8.11.	Fatigue Crack Initiation	79
8.12.	Constant Load Fatigue Tests	81
8.13.	Mechanical Testing	81
8.14.	Physical Examinations	82
8.14.1.	Metallographic Specimens	82
8.14.2.	Scanning Electron Microfractography	82
8.14.3.	Electron Microprobe Analysis and Electron Microscopy	83
8.14.4.	Quantitative Image Analysis	84
9.	RESULTS	85
9.1.	Mechanical Properties etc	85
9.2.	Pore Distribution	86
9.3.	Initiation Results	87
9.4.	Crack Growth Results	88
9.5.	Metallographic Observations	90
9.6.	Fractographic Observations	93
10.	DISCUSSIONS	95
10.1.	Importance of Titanium in Maraging Steels	97
10.2.	Crack Initiation Results	100
10.3.	Crack Growth Rate	110
10.4.	Fractographic and other observations	116
11.	CONCLUSIONS	120
12.	RECOMMENDATIONS FOR FUTURE WORK	121
13.	ACKNOWLEDGEMENTS	122
14.	BIBLIOGRAPHY	123

15. APPENDIX I

136

16. APPENDIX II

138

1. INTRODUCTION

The most common cause of failure in modern machineries and components is due to fatigue, and disasters have been reported to result from a failure to anticipate its occurrence. A component whose service conditions are known, may be designed to have either a finite or an infinite fatigue life, depending on the economics of operating high strength-to-weight structures or using too great a mass of material at a low level of stress. A number of contemporary structures require, however, the utmost in materials utilisation, in terms of stiffness-to-weight or strength-to-weight ratios, and these requirements have led to several imaginative innovations in materials engineering. One of these innovations has been the development of composite materials, such as the diffusion-hardened metals and pre-alloyed sintered compacts, which are introducing or about to introduce new and interesting combinations of mechanical properties.

In another direction, the techniques of fracture safe design has evolved around the discipline of Linear Elastic Fracture Mechanics (L.E.F.M). This approach introduced the concept that the relevant property of a material is the force required to extend a crack through a structural member, and this crack extension force parameter can be used to rank materials in some order of fracture resistance.

Linear Fracture design approaches a structural problem in a pragmatic fashion, attempting to answer the following questions: For a given design stress, what is the largest crack which can be tolerated without failure (or vice-versa)? The fantasies of perfect materials and infallible fabrication are swept away, and the designer considers, instead, the resolving power of the best inspection he is willing to provide for a particular application, and this is true for statically loaded as well as cyclically loaded structures.

There is a profusion of data on fatigue behaviour of homogeneous continuum metals and alloys, and these data are more or less readily amenable to be processed and analysed by applying the concept of L.E.F.M. However, despite the rapidly increasing application of sintered metal parts over the past thirty-five years, little attention has been paid to their toughness and fatigue behaviour. Sintered materials are, by definition and nature, heterogeneous materials. So, a persistent question is concerned with the applicability of the concepts and results developed for homogeneous material models to heterogeneous materials. A partial answer to this question has been provided by previous experience of the present author et al.,⁽¹⁾ with Fe - C, Fe - Cu and Fe - C - Cu compacts. One should also bear in mind that the early use and much recent use of sintered parts has been in situations in which the parts have been subjected to little or no mechanical stress. However, during the past several years sintered alloys have been developed which are now chosen for applications involving stressing. In fact, sintered components are giving satisfactory service under conditions of repeated stressing as bearings, synchroniser hubs and baulk rings in motor-car gear boxes, connecting rods, gears in hydraulic pumps, valve rocker brackets in internal combustion engines, sliding clutches in bicycle three-speed hub gears, sewing machine components⁽²⁾, etc.

The distinguishing feature of the majority of sintered materials is their porosity, and it is this that exercises the primary influence on fatigue. Some engineers believe that the inherent porosity of sintered materials produces a multitude of stress raisers, but according to Talmage⁽³⁾, this is probably influential only at very high stress level, providing the pores are small. Such small porosity is relatively easy to produce in a 90% - dense sintered part, and its uniformity

and consistency can be very high in comparison to castings, forgings, and even wrought metal. In practice, castings have always been plagued with surface and sub-surface porosity due to gas effects, and erratic molten metal-flow. Forgings and wrought metals have inclusions, and porosity which often appear at the surface and can be concentrated in some areas to make the condition worse. Forgings also have oxides in the surface caused by the hammering of oxidised billets.

In fatigue, it is recognised that one of the most influential factors is the quality of the surface finish. Sintered steel is excellent in this regard. The ease with which a very high quality of finish can be produced is well-known, particularly with parts that are as dense as 90%. This ability, it is believed, can produce a better fatigue-life picture than that now found in production of parts made of conventional material.

If a higher order of fatigue strength is desired, there is available a rather simple and comparatively inexpensive patented method of improving it considerably⁽³⁾. This involves the shot peening of a porous sintered surface to close the pores and then re-sintering to bond the closure surface⁽⁴⁾. This has proved very successful in the production of some sintered parts, e.g. roller chain bushings used in cars.

Another factor that is important in this comparison with conventional materials, is the fact that a normal sintered-metal part has none of the disparities found in castings due to liquid-metal flow or differences in rates of freezing. Also, it has the same properties in the transverse as in the longitudinal direction. This is a major strength reducer in forgings where the transverse properties can be 50% lower. Moreover, mass production of simple sintered components to close tolerances at competitive cost is already a reality in automotive industry.

Maraging steels made a commanding appearance in the metallurgical scene in the early sixties as one of those super-alloys, with the interesting combination of high strength and toughness values^(2,5,10-16). In subsequent years, an abundance of data have been extracted on their crack propagation characteristics and fracture toughness, weldability etc.,^(6-9, 17, 18), and as a consequence, these steels have already found applications in aircraft landing gears, aircraft arrester hooks, space vehicle cases, gimbal bearings, hydrofoil struts, torque transmission shafts, bolts, dies for cold forging, extrusion press rams, etc.⁽¹⁹⁾. However, as stated before, there is a general lack of data on fatigue behaviour of sintered materials, and sintered maraging steels are no exception.

In the present study, the fracture toughness and fatigue behaviour of a representative maraging steel produced from pre-alloyed powders, have been investigated. Properties of sintered maraging steel compacts made from elemental powders have been found by Snape and Veltry^(12A) to be inferior to those made from pre-alloyed powders. Based on the experiences of Fischer⁽¹³⁾ and Yates and Hamaker⁽¹¹⁾, a composition of 0.03 C max, 17.50 to 18.50 Ni, 7 to 8 Co, 4.5 to 5.5 Mo, 0.4 to 0.6 Ti, 0.01 P max, 0.10 Si max, 0.1 Mn max, 0.01 S max, 0.10 Al, 0.01 Zr and 0.003 B had been selected and subsequently diluted with 25% and 50% iron powder, grade ASC.100.29 ("Hoganas"), to yield two more varieties of sintered powder compacts. Besides these, another variety of powder compact made from pre-alloyed powders with the patent name of Ancoloy SA ("Hoganas") and containing 1.50 Cu, 0.50 Mo, 1.75 Ni, 0.01 C, 0.16 SiO₂, 95.98 Fe, had been tested after sintering and heat treatment. A low titanium variety of maraging steel compacts had also been tested for toughness, crack initiation and propagation studies.

The present investigation is primarily aimed at assessing toughness, crack initiation and propagation characteristics of the range of sintered materials mentioned earlier, using the concept of Fracture Mechanics.

Often engineers and designers are reluctant to use sintered materials despite their advantages in certain situations. Therefore it seems highly desirable that their attention should be drawn to the potential of sintered materials and that data about their properties and behaviour, including fatigue, should be available to them. Only when they become aware of the potential will sintered materials be exploited most effectively and be presented as viable materials to compete with high strength steels and other materials.

2. LITERATURE REVIEWS

In order to limit this review to sensible proportions, only the literature directly relevant to the present study has been included, and only interesting aspects on some related topics has been touched upon.

3. LITERATURE REVIEW PART I (a) - MARAGING STEEL

3.1. Introduction

Because of the high strength and toughness combinations achievable in the maraging steels by age - hardening of their iron-nickel martensitic microstructures, these materials have come under intensive study in recent years, specially by aerospace designers and missile system engineers⁽²⁰⁾. This is particularly true of the important iron-based 18% Ni, Co and Mo alloys, additionally hardened with Ti and Al. But, in spite of the rapidly increasing volume of data on these alloys, there is still no satisfactory understanding of the basic physical metallurgy of these complex precipitation - hardened martensitic alloys. Indeed the basic hardening mechanisms involved are still open to much question. For example, though synergistic effects of Co-Mo interactions have been suggested by Decker et al.⁽²¹⁾, no clearly defined mechanism for this has yet been demonstrated⁽²⁰⁾.

3.2 Some basic characteristics

Several basic characteristics of maraging steels are directly related to the characteristics of the iron-rich end of the iron-nickel phase diagram. Actually two diagrams must be considered. The first

is the equilibrium diagram, Fig. 1, as given by Owen and Liu⁽²²⁾. The essential point to be noted is that at lower temperatures, the equilibrium phases for alloys containing 3-30% Ni are ferrite and austenite.

The austenite-martensite transformation characteristics in iron-nickel alloy have been studied by several investigators^(23,24) and are shown in the metastable equilibrium diagram of Jones and Pumphrey⁽²³⁾, Fig. 2. In practice, if an alloy containing, say, 18% Ni is cooled, from the austenite field, the austenite will not decompose into the equilibrium austenite and ferrite compositions, even if held for very long times in the two-phase region. Instead, with further cooling, the austenite transforms to martensite that has a b.c.c. crystal structure.

If the martensite is reheated, one of two things may happen. If the alloy is brought to a temperature below the A_s temperature (i.e. the start of the $\alpha \rightarrow \gamma$ transformation shown in Fig. 2), the martensite will decompose into the equilibrium austenite and ferrite compositions i.e. the martensite reverts to the equilibrium structures given by Fig. 1. The rate of this reversion reaction depends upon the temperature, and fortunately for maraging steels, the rate at temperatures of the order of 485°C (900°F) is slow enough for considerable precipitation hardening to be achieved before the reversion reaction predominates.

If, on the other hand, the alloy is heated above the A_s temperature the martensite transforms by a shear reaction back to an austenite of the same composition. Fig. 2 indicates only that alloys containing up to 33% Ni transform martensitically.

The martensites at 18% Ni and above, form by diffusionless shear as in conventional steels, but the nature of transformation and

product contrast sharply with that of conventional carbon steels in that:

(a) Section-size effects are small due to an insensitivity of the martensite reaction to cooling rate and the lack of higher temperature-diffusion controlled austenite decomposition to carbide phases. Thus rapid quenching is not required and hardenability is no problem.

(b) The transformation can proceed both athermally and isothermally.

(c) The martensite structure exhibits no tetragonality; but rather, is body-centred cubic.

(d) Tempering does not occur upon reheating of the martensite. As in (c) and (d) above, this is due to absence of carbon. Finally, the hysteresis of the transformation seen in Fig. 2 allows considerable reheating of the martensite for ageing (in the presence of alloying additions) before reversion to austenite occurs. This step is designated as maraging⁽¹⁰⁾.

It is desired to further strengthen this iron-nickel martensite to a level of engineering interest, but with a minimum loss of toughness. In the 18% Ni maraging steel selected, the hardening is achieved mainly by Co, Mo and Ti.

3.3 Main types of maraging steels

Three main types of maraging steel currently exist and are specified by their nickel contents. These are the 20% and 25% Ni maraging steels, which still persist despite their inherently complicated treatments, and the 18% Ni variety. The 18% Ni maraging steel is the most popular and is subdivided according to the attainable yield strengths which vary due to slight differences in composition

and treatment. The three common grades are designated as 18 Ni (200) (250) and (300), the figures in brackets referring to the yield strengths in Ksi. A very comprehensive review of all these steels along with their physical and mechanical properties is given by Decker et al ⁽¹⁰⁾. The essential difference between the 18% Ni grades and the higher nickel types is the absence of Co and Mo in the latter and consequently these attain strengths only equivalent to those of the 18% Ni (250) grade. Detailed discussion of higher %Ni types of maraging steel is beyond the scope of this review.

3.4 Heat Treatment and Properties

Basically maraging steels require a solution treatment which serves to dissolve the precipitate phase elements into the matrix and to render the matrix martensitic on cooling. This is the most suitable conditions for working operations as it is relatively soft and ductile. To harden the steel, the precipitates must be formed by an ageing treatment i.e. by holding at an elevated temperature which is sufficient to accelerate the precipitation process without causing any reversion of the martensite back to austenite.

The standard heat treatment of the 18% Ni maraging steel is annealing for an hour per inch of thickness at 815°C (1500°F), followed by air cooling to room temperature, and then ageing at 485°C (905°F) for 3 hours. Higher annealing temperatures produce coarse grain sizes which reduce strength and ductility. That the choice of annealing temperature can markedly affect the final properties of the steel ⁽¹²⁾ is illustrated in Fig. 3, which clearly shows the optimum annealing temperature to be 815°C. Based on this figure, an ageing temperature of 485°C. (905°F). has been selected not entirely for optimum properties, but to approach such properties in a reasonable ageing time.

It is also interesting to observe from the figure that the hardness rises rapidly e.g. from 400 to 450 D.P.N. within the first ten minutes of ageing at 485°C . Softening at this ageing temperature does not occur until over 200 hours. The softening has been shown to be due mainly to reversion to austenite rather than over ageing of this precipitate. Increasing the ageing temperature causes the peak hardness to occur at shorter times.

Ageing between 470°C (880°F) and 500°C (930°F) results in yield strengths of 1929 MN/m^2 (280 Ksi) to 1964 MN/m^2 (285 Ksi) and tensile strengths of 1998 MN/m^2 (290 Ksi) to 2033 MN/m^2 (295 Ksi) combined with 12% elongation and 55% reduction in area. For such strength levels, this ductility is very high, Fig. 4.

The M_s and M_f temperatures for the 18% Ni maraging steel are 160°C and 100°C respectively so that on air cooling to room temperature, the structure is fully martensitic. However, raising the percentage of Nickel lowers the M_s and causes austenite to be retained at room temperature. Ni lowers M_s by 40°C for every additional 1%.

3.5 The Structure of Maraging Steels

3.5.1. The Matrix

The matrix of maraging steel is ductile B.C.C. martensite formed by a diffusionless shear reaction. The phase diagram shows that the equilibrium phase of these iron-nickel alloys is either alpha or alpha + gamma. In practice, slow cooling results in the formation of martensites in all but those alloys containing less than 10% Ni which can form alpha and those alloys containing more than 33% which remain austenitic. The type of martensites formed in the 10-25% Ni alloys is termed "massive"⁽¹⁶⁾. The composition limits are not exact

and vary not only with cooling rate, but also the annealing temperature and interstitial content ⁽²⁵⁾. There is evidence that after ageing, a massive martensitic matrix gives better toughness than a twinned martensite encountered in maraging steels containing more than 25% Ni. The structure of massive martensites consists of a series of elongated laths or platelets with wavy interfaces and containing a high density of dislocations. According to Patterson and Wayman ⁽²⁶⁾, the dislocations in structures of this kind tend to lie in $[111]$ directions. The platelets lie in parallel groups separated from neighbouring groups by low angle boundaries. Typically, three such groups may lie within the boundary of an old austenite grain which will itself be a high angle boundary. The masses are made up of parallel shear plates and individual shear plates are not resolvable by etching. The martensite plate orientation relationships follow the Kurdjumov-Sachs rule i.e.

$$\begin{aligned} (111)_{\gamma} &\parallel (011)_{\alpha} \\ [\bar{1}\bar{1}0]_{\gamma} &\parallel [\bar{1}\bar{1}1]_{\alpha} \end{aligned}$$

It can be seen that the coincidence of the slip planes and direction of the parent and product lattices allows simple slip to form one from the other without any twinning, somewhat similar to the reaction which occur in very low carbon steels ⁽²⁷⁾.

3.5.2. Effects of Alloying Elements

Many different substitutional alloying elements can produce age-hardening in Fe-Ni martensites. The degree of hardening, however, may vary appreciably with changes in the Ni content or with variations in the ageing kinetics or the reversion reaction. In addition, there can be rather strong interactions between particular combinations of elements, such as that between Co and Mo. Qualitatively, though one

can classify the alloying additions roughly as follows: elements that produce "strong" age hardening (Ti); "moderate" hardeners (Al, Mo, Mn, Si); and "weak" hardeners (Co, Zr).

The higher strengths in the 18% Ni maraging steels are achieved mainly by increasing the Ti content. For each 0.1% Ti, the yield strength is increased by 68.9 MN/m² (10 Ksi). The NTS/TS ratio decreases in air melts containing more than 0.4% Ti. This drop-off is very sharp for maraging at 485°C (905°F) dropping to a NTS/TS ratio of 1 at 0.6 to 0.7% Ti. A Ti content of 0.7% was found to be the upper limit by Decker et al ⁽¹⁰⁾, to preserve the excellent air melting characteristics of these alloys, Fig. 5. Above this level, dross and films develop.

Ti also causes segregation and the fact that Ti lowers the M_s temp. by 40°C per 1% addition means that excessive amounts of Ti may result in bands of retained austenite ⁽²⁸⁾. Ti also neutralises residual carbon and nitrogen by removing them from solution in the martensite.

Mo is a less powerful hardener, increasing strength by only 14 MN/m² (~2Ksi) for 0.1% addition. Mo (up to 5.4%) in Fe-Ni alloys had been claimed to increase toughness by preventing segregation or precipitation at the grain boundaries thereby lowering the propensity to failure through grain boundary cracking ⁽⁵⁾. However, Banerjee and Hauser ⁽²⁰⁾ dispute this claim. They did find grain boundary precipitation in Mo containing Fe-Ni alloys. In previous studies by Floreen and Speich ⁽⁵⁾, these precipitates might have been missed because of etching specificity. Banerjee and Hauser, in their turn, however, could not put forward any alternative explanation for the toughening by Mo.

Perhaps the most interesting strengthening effect in maraging steels is that due to the combination of Co and Mo. Decker et al. ⁽¹⁰⁾ found that the hardening when these two elements were present together was much greater than the sum of the strength increments produced when they were added individually. Although this effect was not observed by Banerjee and Hauser ⁽²⁰⁾, the data of at least three other investigators ^(5, 29, 30) show this general trend.

As pointed out before, moderate age-hardening results from Mo additions. In fig.6 are shown the effects of Mo and Mo+7% Co on maraged hardness. A strong additional effect from the presence of Co can be seen. Fig.7 reveals the synergistic effect (defined as 'the co-operative action of discrete agencies such that the total effect is greater than the sum of the two effects taken independently' ⁽²⁰⁾) of Co with Mo on maraging steel between 427°C (800°F) and 485°C (905°F). Maraged hardness increased linearly as the product, Co times Mo, increased between the limits of 1.7 Co., 1.8 Mo to 7 Co, 5.4 Mo. It is possible by increasing this product to obtain alloys that show only a change from Rockwell C-25, in the absence of both Co and Mo, to Rockwell C-30 in the annealed martensitic condition, but then exhibit very strong maraging to give hardness above Rockwell C-50.

With this balance of strong maraging effect and weak solid solution hardening, a tough martensite matrix is maintained even with high strength. This appears to be the key to the remarkable toughness of the Ni-Co-Mo steels.

In the Mo-containing alloys, the strength increases by 517 MN/m² (75 Ksi) by the Co addition, though Co itself supplies only a relatively small, roughly additive strengthening contribution. The addition of Co results in a finer dispersion of precipitates in the Mo-bearing Fe-Ni alloys; since Co has not been found by Floreen ⁽¹⁶⁾

to be present to any extent in the Mo precipitates, he considered that Co might have lowered the solubility of Mo in the matrix and this increased the amount of Mo precipitate. Miller and Mitchell⁽³¹⁾ also came to this conclusion. It is considered that a Mo-based precipitate is nucleated on dislocations within the martensite plates and that this precipitate will be most affected by Co addition. Co may also lower the solubility of Mo in the matrix so that an improved distribution of the precipitate and an increased volume fraction of the precipitate could be formed for a given Mo content. Strengthening due to Co addition increases in a continuous fashion and it is thought that hardening at the 18% Ni-8% Co level may be due to a low degree of long-range ordering, Co is also considered to lower the resistance of the matrix to the passage of dislocations and to lower the interaction energy between dislocations and interstitial atoms⁽³²⁾. According to Banerjee and Hauser⁽²⁰⁾, the matrix strengthening by Co addition is due to lowering of stacking fault energy (SFE) of the matrix. The lowered SFE discourages cross slip and retards cell growth. Thus, the average dislocation density is increased, which provides more numerous nucleation sites for precipitation. The resulting increased barrier to dislocation movement causes the observed increased hardness.

In the 18% Ni maraging steels, Mn and Si should be kept below 0.1% and C should be 0.03% (maximum), otherwise ductility and notched tensile strength will be markedly reduced.

As only a small amount of Mn is available for sulphide formation, a maximum S content of 0.01% is specified. P content should also be kept below 0.01%.

Because of the need for low Si and Mn contents to ensure adequate deoxidation and desulphurisation, Al and Ca are added. B and Zr additions are used to suppress harmful grain boundary precipitation, thereby improving toughness and stress corrosion⁽³²⁾.

3.5.3. Physical Metallurgy and Hardening Mechanisms of Maraging Steel

The primary attribute of maraging steels is their excellent combination of strength and toughness. This seems to be especially true of the 18% Ni grades, which in general have a toughness superior to that of the other grades at higher strength levels.

In the case of strengthening mechanisms, the yield strengths of unaged maraging steels are typically $\sim 700 \text{ MN/m}^2$. After maraging, the increase in yield strengths of the various 18% Ni steels range from 700 MN/m^2 to 1400 MN/m^2 . The precipitation strengthening of this magnitude can be accounted for quite reasonably by an Orwan relationship, e.g.

$$\sigma = \sigma_0 + \frac{\alpha G b}{\lambda} \quad \dots (1)$$

where σ is the total strength, σ_0 the matrix strength, α is a constant, G the shear modulus, b the Burgers vector, and λ the interparticle spacing. After maraging, the values of λ are of the order of 300-500 angstroms, and the corresponding strength increments are ~ 700 - 1400 MN/m^2 . Thus an Orwan-type hardening involving dislocation motion between the precipitate particles can account for the strengths observed (33,34).

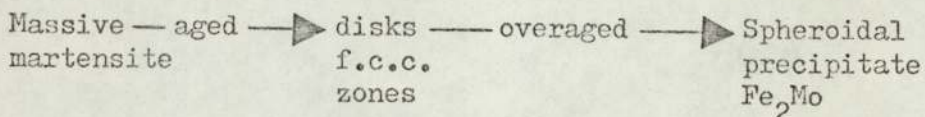
On the other hand, Detert^(35, 36) has suggested that hardening could be controlled by the stress necessary to shear through the precipitate particles. Reisdorf and Baker⁽³⁴⁾ have observed however, that the structure of the 18% Ni (250) steel showed tangles of dislocation around the precipitate particles, and also instances of dislocations bowing between the particles.

The reasons for the superior toughness of the 18% Ni maraging steels are not clear. It has often been noted that the elimination of C and other deleterious impurities should be beneficial. Also the relatively uniform precipitate distribution achieved by age-hardening in a massive martensite matrix would be helpful.

The particular mechanism, which operates contributing to hardening, depends upon the nature, size and density of the precipitate distribution. Much work has been done towards identifying the composition and structure of these precipitates. Floreen (16) has reviewed the results of 22 efforts to analyse the precipitate phases which are by no means in agreement. A general trend, however, suggests that Mo precipitates out as Ni_3Mo under normal ageing conditions. This is a metastable phase, being replaced, on overageing, by Fe_2Mo or a sigma phase. Ti generally appears to form Ni_3Ti but this is generally difficult to identify in the presence of Ni_3Mo , and so a complex $Ni_3(Mo,Ti)$ may actually exist (27). Other elements are found to be present in these precipitates but Co is the exception, appearing to remain entirely in solution. Most workers (5,16,20,34,37) consider Mo to be the primary hardening element and Ti as the secondary hardener.

Much of the controversy arises out of the need to overage precipitates in order to extract them for analysis and the existence of Fe_2Mo and austenite in the matrix are undoubtedly due to this. Miller and Mitchell (31) quote Fe_2Mo in preference to Ni_3Mo as the primary hardening precipitate. They consider that in maraging steels, in the overaged condition, the Fe_2Mo precipitate is spheroidal, but in the fully aged condition, the precipitate is disk shaped, having a f.c.c. structure. This suggests that the hardening mechanism of

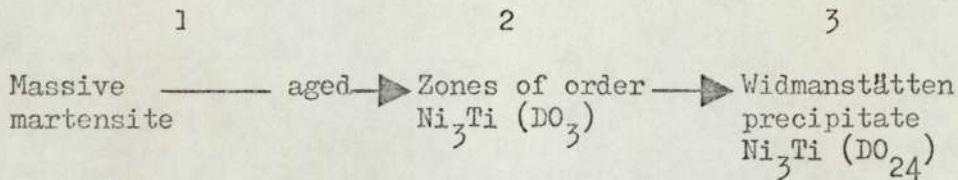
Mo may be summarised as:



By this mechanism, there is a gradual increase in the packing density of the atoms and by examination of interplanar spacing, it may be assumed that the {110} ferrite planes are parallel to the {100} planes of the f.c.c. zones which, in turn, are parallel to the {112} Fe₂Mo planes. Floreen⁽¹⁶⁾ describes Ni₃Mo as H.C.P. structured and rod or ribbon shaped which forms coherently and whose growth is limited in that form by increased coherency stresses and these may lead to the nucleation of the equilibrium precipitate.

The addition of Ti to 18% Ni maraging steels results in the formation, in the overaged condition, of a lath-like Widmanstätten precipitate formed with its long axis parallel to the <111> direction of the matrix, and having the composition and structure of Ni₃Ti. However, in the condition of maximum hardness, although a Widmanstätten precipitate is present in thin foils as observed by Miller and Mitchell⁽³¹⁾ and can be associated with streaking of the thin foil diffraction patterns, a fine spheroidal precipitate is also present in an amount much too plentiful to result from the viewing of laths end-on. Miller and Mitchell⁽³¹⁾ found faint spots in the {100} matrix reflection positions, but these cannot result from either streaking caused by the precipitate, or double diffraction, but are an indication of ordering. It seems probable that ordering may occur as a pre-precipitation reaction, involving the spheroidal zones. This ordering could possibly be based on the NiTi, B₂ structure or more likely on a metastable Ni₃Ti, DO₃, structure. Co, which also forms ordered b.c.c. compounds with Fe, could possibly stabilize formation of these ordered zones at peak hardness even though, in the final equilibrium precipitate,

Co is not present in detectable amounts. Thus the hardening mechanism of Ti may be suggested as:



where peak hardness occurs between 2 and 3.

Although ordering by Co addition would be a convenient explanation, and strength has been found to increase with Co content without its presence in the precipitate form, and even without Mo present in the alloy, the ordering theory has not been widely accepted and no evidence has been put forward to support it ⁽¹⁶⁾, because in the ordered Fe-Ni-Co alloys, it is difficult to obtain direct structural evidence by X-Ray or electron diffraction techniques. Miller and Mitchell ⁽³¹⁾ suggest that the peak hardness due to the Co-Mo interaction would be reached slightly later than that due to the Ti precipitate.

The ultra high strength with good ductility, which characterizes the 18%Ni maraging steel is probably due to the combination of the ferrite/austenite transformation with the conventional precipitation hardening mechanisms. Thus, a larger quantity of precipitate can be dissolved in the austenite at a fairly low solution temperature, a grain-refining process occurring at the same time as the solution of the precipitate and the massive martensite transformation which occurs during cooling results in a matrix with a high dislocation density ideal for precipitation hardening.

4. LITERATURE REVIEW PART I (b)4.1 Ancoloy SA

Ancoloy SA^(37A) is an iron powder containing Cu, Ni and Mo. Mixed with graphite, it is especially intended for parts to be heat treated. After hardening and tempering, a high ultimate tensile strength in combination with a certain ductility is achieved. The alloying elements facilitate the hardening, and very consistent hardness without any soft spots is achieved.

Ancoloy SA is manufactured from sponge iron and the individual particles, therefore, have a spongy irregular shape contributing to a high green strength of the compacted component. The individual particles mainly consist of unaffected pure iron (ferrite) to which the finely divided alloying elements are diffusion bonded. Therefore, Ancoloy SA has a very high compressibility. The risk of segregation of the alloying elements in the mixture is eliminated. As the alloying elements are added in a very finely divided form, they diffuse rapidly into the iron particles during sintering. Thus, the additions are well utilized. The addition of Cu and Ni are so balanced that a very small dimensional change takes place during sintering and heat treatment. The Mo added raises the hardenability considerably, and consequently, the material becomes less sensitive to minor changes of hardening variables. All three of the alloying additives have less affinity to oxygen than iron. Therefore, when sintering ancloy S.A. the same atmosphere can be used as for the sintering of normal iron powder with low H₂-loss. If close tolerances with regard to the amount of combined carbon in the sintered part are desired, the carbon potential of the sintering atmosphere has to be thoroughly controlled or closed sintering boxes should be used.

5. LITERATURE REVIEW PART II - GENERAL PRINCIPLES OF SINTERING

5.1 Introduction

The term "sintering" is commonly used to refer to the annealing treatment by which powders are consolidated into coherent and/or dense polycrystalline aggregates. The technological importance of this process hardly needs emphasizing. It is one of the most important and versatile methods of integration of materials in metallurgy and ceramics. Fast development of the art of powder technology in modern times necessitated better scientific understanding of the processes involved in sintering, the central problem of powder technology.

To be generally valid, however, a definition of sintering must satisfy the following essential factors:

- (a) A liquid phase is present only to the extent that it leaves a solid skeleton behind.
- (b) A decrease in free enthalpy of the system, which represents the driving force of the sintering process, results from:
 - (i) Diminution in the specific surface area due to initiation and/or growth of contacts (necks).
 - (ii) Decrease in pore volume and/or the surface area of the pores.
 - (iii) Elimination of non-equilibrium states in the lattice.
 - (iv) Important properties approximate to those of the compact, porosity free material.

On these bases, Thummler and Thomma⁽³⁸⁾ have proposed the following definitions:

'By sintering is understood the heat treatment of a system of individual particles or of a porous body, with or without the

application of external pressure, in which some or all of the properties of the system are changed with the reduction of the free enthalpy in the direction of the porosity-free system. In this connection, at least enough solid phases remain to ensure shape stability.'

It is clear that sintering of powders involves two broad phenomena: (a) adhesion or welding of surfaces together and (b) change in shape of the particles to permit more and more of adhesion. Without (a) there is no sintering at all, and without (b), there cannot be any densification.

5.2 Sintering Mechanism

It is not possible to deal with all the aspects of this complex field in this survey, so only the main factors of influence will be considered.

The tendency of a system to assume its state of lowest free energy is the driving force for sintering. At high temperature, the powder compact approximates to the stable state, with the co-operation of all the transport mechanisms concerned. The excess free energy exists in the compact in the form of surface energy of all interfaces, including grain boundaries, and as excess lattice energy in the form of vacancies, dislocations and internal stresses.

The surface energy remains more or less constant during compaction, as it is an intrinsic property of the powder. What is dependent upon the compacting operation to a greater extent, however, is the lattice, or internal energy factor, and the number of metal-to-metal contacts. The former increases due to the formation of dislocation vacancies, and internal stresses, and the latter increases with compacting pressure. The high free energy level of the compact

leads to the sintering reactions which occur at high temperatures.

5.3. The stages of Sintering

There are three distinct interconnected stages of sintering:

(a) The early stage of neck growth. In this stage, neck growth proceeds according to an exponential time law, and the powder particles remain as individual, since it is still not possible for strong grain growth to take place beyond the original particle. The tensile stresses resulting from surface tension maintain the grain boundaries between two adjacent particles in the plane of contact. However, the occasional formation of new grains is possible. The midpoints of the particles approach only slightly corresponding to a small contraction, but a marked decrease in surface activity takes place.

(b) The stage of densification and grain growth. When the x/a ratio, Fig. 8, exceeds a certain value after intensified neck growth, the separate particles begin to lose their identity. Most of the shrinkage takes place at this stage, where a coherent network of pores is formed, and grain growth continues. This is somewhat overlapping start of third stage sintering. As channels are lost, the geometric form of the pore network becomes simplified (40). Instead of a complete network, the disconnected parts degenerate into trees, with systems of branches that connect to nothing else. The tips of the branches may be absorbed into the parent limb, or they may be cut off to become isolated pores, Fig. 9.

(c) The final stage with closed pore spaces. At this stage, the "genus" or connectivity of the pore network becomes zero, with very small tendency to densify further. This is because the isolated pore shapes tend to become spheroidised. The third stage

is finally characterized by a reduction in the number of these isolated spheroidised pores.

5.4 Possible Mechanisms of Material Transport

Table 1 enumerates all the conceivable mechanisms of material transport that can occur in sintering processes⁽³⁸⁾.

TABLE 1

Possible elementary processes (transport mechanisms) during sintering

A	Without material transport	Adhesion	
B	With material transport (Movement of atoms over increased distances)	Surface diffusion Lattice diffusion via vacancies Lattice diffusion via interstitials Grain boundary diffusion Vaporisation and re-condensation	Movements of individual lattice structural components
		Plastic flow Grain-boundary Slip	Movements of lattice regions
C	With material transport (movement of atoms over very small distances)	Recovery or recrystallisation	

Although adhesion occurs in every type of particle contact, it is not likely to constitute the dominating mechanism except in impact sintering.⁽⁴¹⁾

The transport mechanisms listed in Table IB might be supplemented by viscous flow associated with self diffusion co-efficients. This is the same as 'diffusion creep' according to the Nabarro-Herring mechanism⁽⁴²⁾, where an 'oriented' diffusion is activated by external stresses.

It is extremely probable that surface diffusion occurs in all sintering processes. The rounding off of the internal and external surfaces and pores is produced by surface diffusion which requires the least activation energy of all types of diffusion.

Lattice diffusion by a vacancy mechanism is the most important. Vacancy gradients exist between the undistorted lattice and both curved surfaces and pore edges, between surfaces having different curvatures and between the distorted and undistorted lattice. Vacancy sources can be small pores or concave surfaces, while vacancy sinks can be larger pores, convex surfaces, and grain boundaries. This process can lead to densification.

Interstitial diffusion has not been studied in much detail. In cases where it might have a strong influence, for example, on neck growth, phase separation must always occur.

Vaporisation and recondensation have been observed to be the predominant mechanism in some cases, mainly in metallic oxides where the vapour pressure is high. Flow processes are no longer thought to be of major importance, but have enabled the mechanisms of hot pressing to be understood.

The relative importance of the above mechanisms depend solely upon the system concerned. Kuczynski⁽⁴³⁾ has carried out an

experimental approach to the determination of these mechanisms by using wire-wire and wire-bar models. Herring⁽⁴²⁾ formulated his 'scaling laws' from these model data and suggested experiments in which a group of particles of the same material with different radii a_1 and a_2 with $a_1 = \lambda a_2$ are sintered until their necks bear the relationship $x_1 = \lambda x_2$ Fig. 8. The times required to reach this neck radius relationship would be t_1 and t_2 with $t_1 = H t_2$, where H is Herring's Scaling factor. The relationships between H and λ would then determine the mechanism, with $H = \lambda^3$ for volume diffusion, $H = \lambda^4$ for surface diffusion etc.⁽³⁹⁾ The time law of neck growth can thus give an indication of the predominant sintering mechanism⁽⁴⁴⁾.

5.5. Sintering of multicomponent systems

In the case of mutual solubility of the systems, it is necessary to differentiate between:

- (a) Sintering homogeneous solid solutions (with a concentration gradient)
- (b) Sintering with simultaneous homogenisation
- (c) Sintering with the decomposition of solid solutions

"
Thummler studied the systems Fe-Sn, Fe-Mo, Fe-Ni and Cu-Sn with up to ~ 2 at.% of the second metal in homogeneous solid solution. He found the sintering behaviour to be closely related to the physical, and thermodynamic properties of the solid solutions. Strong promoting or inhibiting effects can be observed due to the different partial diffusion co-efficients of the constituents. New vacancies are continually formed and if they coagulate to form new pores, they have an inhibiting action, by producing the Kirkendall effect (preferential penetration of one phase into the other). The formation of a new phase (reaction sintering) is associated with expansion

phenomena in many cases. The result of the different atom mobilities is that a large amount of diffusion porosity is formed and along with the inherent brittleness of many phases, this can lead to premature failure of some compacts.

5.6. Liquid Phase Sintering

This field occupies a special position attributable to the different mechanisms such as:

- (a) The ease of diffusion in melts
- (b) The possibilities of re-ordering of the phase remaining solid in the melt, and
- (c) Rapid dissolution and re-precipitation

These play a major part in solid/liquid systems compared to the predominance of diffusion in the solid state.

Based on phenomenological observations, Kingery⁽⁴⁵⁾ considered three distinguishable stages:

1. Rearrangement of the particles of the residual solid phase by viscous flow in the liquid phase. In this case, wetting of the solid by the liquid is the important factor, not solubility.
2. Dissolution and re-precipitation. At least limited solubility is necessary and densification is slower because transport is dependent upon solution and diffusion in the melt. Small grains with strongly convex curvatures disappear while larger ones assume a more regular shape. The driving force is the enhanced chemical potential in the contact zones due to higher compressive stresses. This leads to dissolution in these regions and precipitation in regions of lower stress. In case of complete wetting (angle of contact $\approx 0^\circ$), the grains remain separated by films of liquid.
3. Coalescence. In the case of incomplete wetting

(angle of contact $<90^\circ$), the solid grains are partly in contact without the interposition of the melt, and processes such as those formed with solid phase sintering can occur, and become rate-determining.

A non-wetting liquid phase (contact Angle $>90^\circ$) is ineffective or inhibiting and usually exudes partially from the sintered compact in the form of droplets.

In the case of Fe-Cu, the liquid metal dissolves into the iron matrix giving a growth component in addition to shrinkage upon sintering. This enables closer tolerances to be achieved, and so is of some technological advantage.

5.7 THE HOMOGENISATION BEHAVIOUR OF MARAGING STEEL POWDER AND IRON POWDER MIXES.

The homogenisation behaviour of maraging steel and pure iron powder mixes can be understood by considering the geometry of the compacted mass, which may be idealised to spherical particles of the minor constituent (i.e. 25% pure iron powder in case of M_2 series) embedded in a continuous matrix of the major constituent (i.e. maraging steel powder in the rest of M_2 series). This situation is shown in Fig. 9A. The idealised geometry can be referred to as the concentric-sphere model wherein each minor constituent particle has associated with a shell of matrix. (182)

The homogenisation behaviour of powder compacts that approximate the idealised, concentric-sphere geometry may be compared to the behaviour of ordinary diffusion couples. The principal differences between the concentric sphere model and diffusion couples are the diffusion geometry (spherical Vs. planar) and the fact that diffusion distances in couples are usually small compared to the size of the couples, whereas, in the concentric-sphere model, the diffusion is to be considered over the entire sphere-shell composite. The similarities between the concentric-sphere model and diffusion couples include:

- (a) the general form of the concentration-distance profiles,
- (b) the applicability of Fick's laws of diffusion,
- (c) the development of Kirkendall effect
- (d) the validity of the approximation that equilibrium compositions are present at interfaces between phases in the multi-phase system.

To delve deeper into these aspects of homogenisation is beyond the scope of the present work. Only those points of some

significance and applicable to the present work will be dwelt ^{with} here.

The progress of homogenisation in the idealised, concentric-sphere model, and concentration-distance profiles for the microstructures can be shown schematically in Fig. 9B . The shaded areas represent the areas of inter-diffusion.

From this, it appears that, for M_2 groups of compacts, Fig. 9B (a,b) after sintering and heat-treatment, ferritic areas are embedded in a martensitic matrix, with interparticle and intraparticle porosities randomly distributed throughout the compacted mass, and equilibrium compositions being present at interfaces between the phases in the martensite-ferrite system. The pockets of ferritic zones might act as buffer between the surrounding martensites, and thus reduce volume contraction, as experienced by the maraging steel compacts of M_1 group, while sintering.

For M_3 group of compacts which consist of a compacted mass of maraging steel Powder diluted with 50% pure iron powder, the idealised geometry can be referred to as a concentric-sphere model wherein each constituent particle (iron particle or pre-alloyed maraging steel particle) has associated with it a shell of the matrix, which is more or less equally dominated by either of the constituent particles. Fig. 9B(c,d) . The shaded areas, as usual represent the areas of inter-diffusion. In this group of compacts, the continuity of martensites is broken, after sintering and heat-treatment by the presence of an equal amount of ferrite, more or less evenly distributed throughout the compacted mass.

The variations that may exist between the idealised, concentric-sphere model and actual powder compacts are primarily geometric. The interparticle porosity, non-uniform distribution of particles, particle size distributions of the minor constituent, and

non-spherical minor constituent shape can cause variations in homogenisation behaviour from that predicted from the idealised model. In addition to these geometry effects, interparticle and intraparticle porosity can give rise to enhanced mass transport through the compact. These effects would, therefore, result in variations between homogenisation behaviour predicted by volume interdiffusion models and experimentally-determined behaviour.

Since the variation of concentration with distance is the principal structural feature to be studied in homogenisation, microprobe scans across the microstructure provide a direct measurement of the degree of heterogeneity. In Fig. 67 is shown a typical distribution of the elements in the sintered compacts studied. As stated in section 9.5, the distribution of Ti, Co and Mo is not uniform, and the abrupt fluctuations in the distribution curve for Ti, Al, are due to the presence of some complex titanium or aluminium precipitates.

The structure of sintered materials is inhomogeneous, at least over short distances, as a result of irregularities in the particle stacking, etc, and over greater distances in compacted structures. If a sample containing several hundred particles is analysed, small scale inhomogeneities are averaged out. Any long range variation in the topological properties can, in principle, be detected by analysing samples at various locations in the sinter body, but it is a time consuming undertaking which has not been attempted for the present work.

6. LITERATURE REVIEW PART III6.1. Relation between Young's Modulus and Porosity

The elastic modulus E_N of sintered steels and iron-based alloys is influenced mainly by the void content in the material and is relatively insensitive to changes in composition. The elasticity ratio E_N/E has been related to the porosity (ϵ) by McAdam⁽⁴⁶⁾ by the expression:

$$E_N = E(1 - \epsilon)^{3/4} \times 10^6 \text{ psi.} \quad (2)$$

where E_N = elastic modulus of sintered steels and iron-base alloys
 E = elastic modulus of steel
 ϵ = fractional porosity.

This limits the elasticity of these alloys to a range $0-29 \times 10^6$ psi, corresponding to porosities of 100% and 0 respectively.

The plot of E_N Vs. fractional porosity for a series of porous iron-base compacts is shown in Fig. 10. The elasticity of all porous compacts is lowered by increasing the porosity. The decrease is progressively more rapid for products with more than 20% void and is independent of the dimensions of the particles.

7. LITERATURE REVIEW PART IV — THE MECHANICS OF FRACTURE7.1. Introduction to Fracture Mechanics

An overwhelming amount of research on brittle fracture in engineering structures has shown that numerous factors (e.g. service, temperature, material toughness, design, residual stresses, fatigue, etc.) can contribute to brittle fracture. However, the recent development of Linear Elastic Fracture Mechanics (L.E.F.M.) has shown that three primary factors control the susceptibility of a structure to brittle fracture. These are:

(1) Material Toughness (K_{Ic} , K_{IC}),

Material toughness can be defined as the resistance to crack propagation in the presence of a notch and can be described in terms of the static critical stress-intensity factor under conditions of plane stress or plane strain. In addition to metallurgical factors such as composition and heat-treatment, the notch toughness of a structure also depends on the application temperature, loading rate, and constraint (state-of-stress) ahead of the notch.

(2) Flaw Size (a).

Brittle fractures initiate from flaws or discontinuities of various kinds. These discontinuities can vary from extremely small cracks to much larger weld or fatigue cracks. Complex structures are not fabricated without discontinuities (porosity, lack of fusion, mis-match, etc), although good fabrications practice and inspections can minimize the original size and number of flaws. Even though only 'small' flaws may be present initially, static loading can cause them to enlarge, possibly to a critical size.

(3) Stress Level (σ)

Tensile stresses (nominal, residual or both) are necessary for brittle fracture to occur. The stresses in many complex structures are difficult to analyse because of the complexity of possible dynamic loading, and because of the stress concentrations present throughout a structure that increase the local stress levels, as well as the residual stresses.

All three of these basic factors are inter-related in brittle fractures in structures. All other factors such as temperature, loading rate, residual stresses, etc., merely affect the above three primary factors.

Engineers have known these facts for many years and have reduced the susceptibility of structures to brittle fractures by applying these concepts qualitatively, and in recent years, the engineers are endeavouring to specify design guidelines to evaluate the relative performance and economic trade-offs between design, fabrication and materials in quantitative manner.

The fundamental principle of Fracture Mechanics is that the stress field ahead of a sharp crack can be characterized in terms of a single parameter K , the stress intensity factor, having units of $\text{MN/m}^{3/2}$ ($\text{Ksi} \sqrt{\text{in.}}$). This single parameter, K , is related to both the stress level (σ) and flaw size (a). When the particular combination of σ and a (represented by K) reaches a critical value of K , called K_c , unstable crack growth occurs.

By knowing the critical value of K_I at failure (K_c, K_{IC}) for a given structure of a particular thickness and at a specific temperature and loading rate, the designer can determine flaw sizes that can be tolerated in structural members for a given design stress level. Conversely, he can determine the design stress level that can be

safely used for a flaw size that may be present in a structure.

This general relationship between material toughness (K_c), nominal stress (σ) and flaw size (a) is shown schematically in Fig.11. If a particular combination of stress and flaw size in a structure (K_I) reaches the K_c value, fracture can occur. Thus, there are many combinations of stress and flaw size (e.g. σ_f and a_f) that may cause fracture in a structure having a particular value of K_c at a particular service temperature, loading rate and plate thickness. Conversely, there are many combinations of stress and flaw size (e.g. σ_o and a_o) that will not cause failure of a particular structure i.e. below the K_c line.

The preceding L.E.F.M. analysis pertains to conditions at fracture. For most structural members, the tolerable flaw sizes are much larger than any initial undetected flaws. However, for structures subjected to fatigue loading, these initial cracks can grow throughout the life of the structure. L.E.F.M. provides a means to analyse the subcritical crack growth behaviour of structures under fatigue loading using the same conditions as at fracture. L.E.F.M. philosophy assumes the existence of small flaw or flaws of certain geometry in structures after fabrication and that this flaw can either cause brittle fracture or grow by fatigue to the critical size. To ensure that the structure does not fail by fracture, the calculated critical crack size, a_{cr} , at design load, must be sufficiently large, and the number of cycles of loading required to grow a small crack to a critical crack must be greater than the design life of the structure⁽⁴⁷⁾.

7.2 Criteria for Fracture

The first notable contribution to fracture was due to Griffith⁽⁴⁸⁾, who proposed an energy criterion for the extension of

such a crack. This involved a balance between the elastic strain energy released and the surface energy created due to an incremental increase in its length. Thus at equilibrium, the stress was given by

$$\sigma_f = \left(\frac{2E\gamma}{\pi a} \right)^{\frac{1}{2}} \dots\dots\dots (2A)$$

where a = half crack length
 E = Young's modulus and
 γ = Surface energy

The Griffiths equation is valid only for a completely brittle solid; for metals where crack extension is accompanied by plastic flow, the increase in surface energy considered in Griffith's equation is several orders of magnitude less than the energy expended in plastic deformation. So, Griffith's criterion was subsequently modified by Irwin⁽⁴⁹⁾ and Orowan⁽⁵⁰⁾ to account for the predominantly plastic work that is involved in most metal fractures under normal conditions, and energy of plastic deformations or crack extension force G replaced the surface energy, as the controlling factor in brittle fracture. Thus the applied stress required to propagate an elliptical crack of length $2a$ within a large plate under conditions of plane stress is given by

$$\sigma_f = \left(\frac{G_c E}{\pi a} \right)^{\frac{1}{2}} \dots\dots\dots (3)$$

where E is the Young's modulus and G_c represents the total work consumed in producing unit area of new crack surface and known as 'critical strain-energy release rate', the suffix c denoting its value at instability. Further rationalisation of this criteria by Irwin⁽⁴⁹⁾ realised the parameter K_c , defined as the 'critical stress intensification factor' or the 'Fracture toughness parameter' and is regarded as a basic material property and the basis of Fracture Mechanics concept, and which enables direct comparison between materials.

In contrast to Inglis⁽⁵¹⁾ work, where he considered the stress concentration at a crack tip, Irwin considers the stress distribution at the close vicinity of the tip and thus plasticity effects can be appreciated. For conditions of plane stress, K_c and G_c are related by:

$$K_c = (G_c E)^{\frac{1}{2}} \dots \dots \dots (4)$$

and for plane strain

$$K_c = \left[\frac{G_c E}{1-\nu^2} \right]^{\frac{1}{2}} \dots \dots \dots (5)$$

where ν is the Poisson's ratio.

From equations (3) and (4), it is evident that

$$K_c \propto \sigma_f (a)^{\frac{1}{2}},$$

which satisfies Griffith's analysis and is normally used in the form

$$K_c = Y \cdot \sigma_f (a)^{\frac{1}{2}} \dots \dots \dots (6)$$

where Y is called the compliance function and depends on crack length and specimen or component geometry and has been evaluated for many situations using boundary collocation techniques^(52,53) and experimental compliance calibration^(54,55). Through the use of this geometrical factor, the data generated from the laboratory tests can be used in real situations.

Subsequent to the development for monotonic loading, L.E.F.M. found its application to fatigue as well. Substituting the σ term in the equation (6) by $\Delta\sigma$, σ_{\min} , σ_{\max} and σ_{mean} , the corresponding stress intensity terms can be obtained. In fact, many research workers⁽⁵⁶⁾ have related fatigue crack growth rates in a variety of materials to stress intensity factors by means of simple equations. The L.E.F.M. approach is now widely used to evaluate the resistance of materials to fatigue crack propagation.

Three basic modes of crack surface displacement⁽⁵⁷⁾ have been isolated, shown in Fig. 12. These are:

(I) The tensile opening mode. The crack surfaces move directly apart; analogous to an edge dislocation.

(II) The edge sliding mode. The crack surfaces move normal to the crack front and remain in the crack plane, also analogous to an edge dislocation.

(III) The shear mode. The crack surfaces move parallel to the crack front and remain in the crack plane; analogous to a screw dislocation⁽⁵⁹⁾.

K_I denotes the stress intensification level for the tensile opening mode, and at the level of instability becomes K_{IC} . Irwin's analysis of the stress field at the tip of a crack for mode I crack surface displacement in a homogeneous elastic solid can be specified by Westergaard's⁽⁶⁰⁾ stress field equation for cracks:

$$\begin{aligned}\sigma_x &= \frac{K_I}{\sqrt{2\pi r}} \cos \frac{\theta}{2} \left(1 - \sin \frac{\theta}{2} \sin \frac{3\theta}{2}\right) \\ \sigma_y &= \frac{K_I}{\sqrt{2\pi r}} \cos \frac{\theta}{2} \left(1 + \sin \frac{\theta}{2} \sin \frac{3\theta}{2}\right) \quad (7)\end{aligned}$$

$$\tau_{xy} = \frac{K_I}{\sqrt{2\pi r}} \cos \frac{\theta}{2} \sin \frac{\theta}{2} \cos \frac{3\theta}{2}$$

$$\sigma_z = \nu (\sigma_x + \sigma_y) \quad (\text{Plane Strain})$$

$$\tau_{xz} = \tau_{yz} = 0, \quad \sigma_z = 0 \quad (\text{Generalised Plane Stress})$$

$$u = \frac{K_I}{G} \left(\frac{r}{2\pi}\right)^{\frac{1}{2}} \cos \frac{\theta}{2} \left(1 - 2\nu + \sin^2 \frac{\theta}{2}\right)$$

$$v = \frac{K_I}{G} \left(\frac{r}{2\pi}\right)^{\frac{1}{2}} \sin \frac{\theta}{2} \left(2 - 2\nu - \cos^2 \frac{\theta}{2}\right)$$

$$w = 0$$

where (r, θ) denotes the polar co-ordinates of a point in the stress field taking the crack tip as origin; u, v, w are displacements in the x, y, z directions; G is the shear modulus, ν is the Poisson's ratio, and which indicate that identical stress fields are obtained for identical K_I values. The co-ordinate system is shown in fig. 13. Elastic stresses are inversely proportional to the square root of the distance from the crack tip, and become infinite at the crack tip.

7.3 The Effect of Yielding

An uncracked metal plate loaded in uniaxial tension is in a state of plane stress. The insertion of a crack does not affect the plate remote from the crack tip, which remains in plane stress, but the highly stressed material near the crack tip is prevented from contracting in the thickness direction by the material further away from the crack, and is, therefore, in a state of plane strain. In the interior of the plate, there is a transverse stress⁽⁶¹⁾ of the form.

$$\sigma_z = \nu (\sigma_x + \sigma_y) \quad \dots \quad (8)$$

where ν is the Poisson's ratio, Fig. 14. All the plate surfaces, however, will still be in a state of plane stress.

In a metal, the yield stress is exceeded near the crack tip and a plastic zone develops; the approximate extent of this plastic zone can be estimated by substituting a yield criterion into the stress field equation. If the plastic zone is small compared with the plate thickness, transverse yielding is restricted and conditions near the crack tip approximate to plane strain through most of the plate thickness. In Fracture Mechanics, this localized plane strain situation is called plane strain, Fig. 15 and 16, and exists in most metals, provided the thickness is at least

$$2.5 \left(\frac{K_{IC}}{\sigma_y} \right)^2$$

where σ_y is the yield stress (usually taken as the 0.2% proof stress). A large plastic zone means that σ_z is not fully developed through the specimen thickness; when the plastic zone size becomes comparable with the thickness, yielding can take place on 45° planes, Fig. 17, and the stress state near the crack tip changes to plane stress. This happens when the thickness $\ll 2.5 \left(\frac{K_{IC}}{\sigma_y} \right)^2$ and in Fracture Mechanics is referred to as plane stress.

The actual size and shape of plastic zone, Fig. 18, depends on the plastic flow properties of the material, but it is proportional to $(K_{IC}/\sigma_y)^2$. The relaxation of stress, caused by yielding inside the plastic zone means that to maintain equilibrium, the stresses outside the plastic zone must increase slightly. The plastic zone, thus, increases the effective length of the crack. This effective increase, called r_y (a symbol for nominal plastic zone radius) is given approximately by Irwin⁽⁴⁹⁾ as

$$r_y = \frac{1}{2\pi} \left(\frac{K_{IC}}{\sigma_y} \right)^2, \text{ for plane stress } \dots\dots (9)$$

$$r_y = \frac{1}{6\pi} \left(\frac{K_{IC}}{\sigma_y} \right)^2, \text{ for plane strain } \dots\dots (10)$$

These corrections are only applicable when the plastic zone is small compared with specimen dimensions in the plane of the plate, and are, therefore, within the region where the stresses are reasonably accurately described by the stress intensity factor⁽⁶³⁾. If the plastic zone becomes too large, which happens when the net section stress exceeds about $0.8 \sigma_y$ ⁽⁶⁴⁾, the L.E.F.M. is no longer applicable. It is not always possible to define the net section stress unambiguously and other criteria may be adopted⁽⁶⁵⁾, for example, the crack length is at least $2.5 \left(\frac{K_{IC}}{\sigma_y} \right)^2$.

It is interesting to note that Paris⁽⁶⁶⁾ and Rice⁽⁶⁷⁾ independently stated that the equations (9) and (10) do not apply to fatigue situations. Due to extreme stress concentration at the crack tip, plasticity is always present in the material. When the load is reversed as in the case of fatigue, plasticity occurs at the crack tip in the reversed sense. The new plastic zone starts to form within the old plastic zone from the maximum load.

Since to cause plasticity in the reversed direction, the yield stress should be doubled, the new fatigue plastic zone size is approximated by

$$r_y = \frac{\Delta K^2}{2\pi(2\sigma_{ys})^2} = \frac{1}{8\pi} \left(\frac{\Delta K}{\sigma_{ys}} \right)^2 \quad \text{for Plane stress}$$

$$\text{and } r_y = \frac{\Delta K^2}{2\pi(\sqrt{3}2\sigma_{ys})^2} = \frac{1}{24\pi} \left(\frac{\Delta K}{\sigma_{ys}} \right)^2 \quad \text{for Plane strain} \quad (11)$$

For fatigue cycling with a stress amplitude of ΔP , the cyclic plastic zone depends on ΔP only and is independent of the maximum stress provided that no crack closure occurs during compressive part of the load cycle. The formation of the cyclic plastic zone within the maximum plastic zone is shown schematically in Fig. 19.

The value of K_c is normally a minimum under plane strain conditions as shown in Fig. 16; it becomes a material property denoted as K_{IC} , in the same sense as the 0.2% proof stress. The existence of K_{IC} as a material property is the main justification for the application of Linear Elastic Fracture Mechanics to brittle fracture problems.

When a specimen containing a crack is loaded, the crack tip opens without extension of the crack. This movement is called the crack opening displacement (COD) and is associated with the development of plastic zone. Its critical value δ_c , when the crack starts

to grow, is roughly constant⁽⁶⁸⁾, and approximately equals G_c / σ_y ; δ_c is used as a measure of toughness for low strength steels and has the advantage that it still has meaning at, and beyond general yield.

7.4 Micromechanisms of Initiation and Growth of Fatigue Cracks

7.4.1. Introduction

The early work of relating initiation sites and topography of fracture surfaces to their causes and basic mechanisms was severely restricted by the inherent limitations of optical microscopy. The recent application of electron microscopy with its far larger depth of field and higher resolving power has, to a great extent, overcome the limitations imposed by optical microscopy in the study of fracture surfaces. With the help of this technique, usually referred to as electron micro-fractography (using scanning and transmission electron microscopes), at high magnification, more details are visible, and need to be categorized and described if the fractographs are to be related to the micromechanisms of crack initiation and propagation.

Fatigue is a complex phenomenon, involving microscopic flow processes and macroscopic crack extension, to final fracture. Forsyth⁽⁷⁰⁾ divided fatigue cracking into three stages - initiation, Stage I or slip band growth (crystallographic) and Stage II growth on planes normal to the maximum tensile stress (non-crystallographic).

7.4.2. Mechanism of Crack Initiation

It was first noted by Ewing and Humphrey⁽⁷¹⁾ that the process of crack initiation in un-notched specimens takes place at slip bands. During further investigation of these slip bands in fatigued specimens, Forsyth⁽⁷²⁾ observed that metal was extruded

from the slip bands ('extrusions'), and at the same time, fine crevices, generally termed 'intrusions' were formed within the bands. These intrusions developed into cracks and crack initiation was loosely defined as the formation of a 'viable' crack from a slip band intrusion. While little attention has been paid to the number of cycles taken to initiate cracks in un-notched specimens, it has been shown that crack initiation occupies the majority of the life in high cycle fatigue^{(73), (74)}.

It is well established that surface conditions greatly influence the fatigue life, rough surfaces giving shorter lives than smooth surfaces and this is attributed to the presence of favourable sites for the early formation of slip bands at stress concentrations such as surface scratches. Several mechanisms for the formation of extrusions and intrusions have been proposed, and have been summarized by Kennedy⁽⁷⁵⁾ and Lynch⁽⁷⁶⁾, Fig. 20. These mechanisms, although differing in details, postulate reversed slip mechanisms on planes of maximum resolved shear stress. While there have been many investigations concerned with the effect of notches on fatigue life, crack initiations in notched or pre-cracked specimens has been almost entirely neglected, it being generally assumed that crack initiation takes place immediately at sharp cracks, and after a small proportion of the fatigue life from blunt notches. Exceptions to this are the investigations of Weibull⁽⁷⁷⁾ and Hoepfner⁽⁷⁸⁾ who showed that crack initiation could occupy a significant proportion of the fatigue life of notched specimens.

7.4.3. Accepted Model of Mechanism for Initiation

While specific dislocation mechanisms have been proposed to account for extrusion and intrusion during fatigue^(79, 80, 81, 82),

Cottrell⁽⁸³⁾ proposed that extrusions would result when soft material in slip bands was squeezed out plastically during the compressive phase of the fatigue cycle and not sucked back during the tensile phase, Fig. 20. In many materials, cyclic stressing may locally remove strengthening components⁽⁷⁶⁾ within persistent-slip bands (PSB's), where extrusion/intrusion commonly occurs, and PSB's should then be softer than their surrounding matrix. In age-hardened Al alloys, PSB's are thin layers of material, usually $\sim 0.1 \mu\text{m}$ thick, in which re-resolution or overaging of precipitates has occurred^(84, 85, 86). In these alloys, fatigue initially produces narrow discrete bands of high dislocation density; these bands form along "quench bands", which usually contain only a slightly lower than normal density of precipitates and are already present before fatigue⁽⁸⁷⁾. Re-resolution of precipitates within these bands of high dislocation density, probably involving dislocation enhanced diffusion, enables the dislocations within the bands to re-arrange into a fine sub-grain structure. In cold-worked Al, fatigue can induce localised recrystallisation along slip bands⁽⁷⁰⁾. In other alloy systems, the same mechanisms of crack initiation may be seen to operate.

7.4.4. Mechanisms of Fatigue Crack Growth

Stage I fatigue crack growth, Fig. 21, is characterized by propagation of the crack on a plane oriented at approximately 45° to the stress axis and by crystallographic fracture facets changing direction slightly⁽⁸⁹⁾ with orientation at grain boundaries, and it is considered by Forsyth⁽⁷⁰⁾ to be an extension of the reversed slip process responsible for crack initiation. According to the model of mechanisms of crack initiation⁽⁷⁶⁾, Stage I cracks initiating from intrusions, propagate along PSB's (and grain boundaries) and

their crack-tip regions often consist of series of holes (tunnels), extending to different depths into PSB's which subsequently link up, Fig 20. This mode of growth can continue for an appreciable proportion of the life in un-notched specimens, particularly under torsional loading, but persists only through a few grains in notched specimens after which Stage II takes over.

In Stage II, plane of crack propagation is at 90° to the stress axis and it is generally characterized by certain microscopic features, known as fatigue striations on the fracture surface. These fatigue striations first wrongly observed by Zappfe and Worden⁽⁹⁰⁾ as some micro-cellular structure in metals, are characteristic to fatigue crack growth only, running more or less parallel to the crack front, Fig. 22. Crussard⁽⁹¹⁾ suggested that each striation represented the crack growth by ten load cycles. Tests employing single programme loading, however, showed that each striation was produced by a single cycle^(92, 93), an observation confirmed by many workers and providing the basis for subsequent quantitative work. The converse of this statement i.e. 'that every load cycle produces one striation' is not necessarily valid, since the crack-tip stress resulting from some cycles may be too small to produce an increment of crack length, especially in programme or block loading⁽⁹⁴⁾. In many alloys, for example, aluminium alloys and 3% silicon iron⁽⁹⁵⁾ striations are well defined, but they are less clearly visible in ferritic and bainitic structures and their presence in tempered martensitic structures has not been conclusively demonstrated. The regularity of striations is also distorted by the presence of large volume fractions of second phase particles as in spheroidised 1% carbon steel⁽⁹⁶⁾.

The presence of numerous well-defined striations on a fracture surface unambiguously defines that failure was by fatigue. Their absence does not preclude the possibility of fatigue fracture. Invisibility of striations on a fracture produced by cyclic load may arise from:

(a) Their spacing being too small to be resolved by the observational technique used. The smallest inter-striation spacing reported is a $\sim 200 \text{ \AA}$ (97).

(b) Insufficient ductility at the crack tip to produce a ripple by plastic deformation large enough to be subsequently observed.

(c) The operation of a fatigue fracture mode that does not produce striations.

(d) Their obliteration by damage subsequent to fracture (97).

The striations that are formed at very low crack growth rates ($< 5 \times 10^{-6}$ in./cycle or 127 nm/c) are difficult to resolve and often cannot be distinguished from the network of slip lines and slip-bands associated with plastic deformation at, and near the fracture surface. Under these circumstances, measurement of striation spacing is difficult, if not impossible (98).

The main mechanisms for Stage II crack growth and the striation formation can be listed as:

- (i) Plastic blunting process of crack growth
- (ii) Cyclic slip and movement of dislocations
- (iii) By shear and decohesions.
- (iv) Microvoid coalescence and growth.

All the models relate to damage by cycling at the vicinity of the crack tip, differing only in the way in which the damage occurs.

In his plastic blunting process, Laird⁽⁸⁸⁾ assumes that a small double notch exists at the crack tip from prior damage. As a tensile load is applied, the double notch at the crack tip serves to concentrate slip band along planes at 45° to the plane of the crack and to maintain a square geometry of the tip. When the specimen is deformed to the maximum tensile strain, the stress concentration effect of the crack is lessened, and the crack tip blunts to a semi-circular shape due to the broadening of the slip bands at the tip. Upon application of compressive load, reversed slip occurs, and the new crack surface created in tension is forced into the plane of the crack and partly folded by buckling of the very front of the crack tip into another notch. The process then repeats and crack growth occurs, Fig. 23. Depending on the inclusions, grain boundaries etc., slip zones may not remain symmetric. Moreover, variation of the position of slip planes with respect to the stress axis for different orientation of the cycles at the crack tip may cause asymmetry of the notch tip⁽⁹⁹⁾. Subsequent loading may induce plastic blunting in the most advanced part of the crack. Thus, in effect, crack growth occurs, according to Laird⁽⁸⁸⁾, during the increasing part of the load cycle only, but Schijve⁽¹⁰⁰⁾ believes that crack tip sharpening occurs during unloading, as depicted in Fig. 24.

Basically alternate blunting and re-sharpening of the crack tip give rise to striation formations, Fig. 23,24. Forsyth et al⁽¹⁰¹⁾ have distinguished between two types of fatigue fracture striation: Type A or 'ductile' striations, each consisting of a light and dark band, lying on irregular non-crystallographic plateau, e.g. Al-Zn-Mg alloy. Type B or 'brittle' striation lying on fan-shaped crystallographic facets, as on $\{100\}$ facets in corrosion-fatigue tested Al-Zn-Mg alloy and hydrogen-charged iron⁽⁹⁴⁾ Fig. 25. These facets often

exhibit 'river markings' and the striations show limited ductility. The spacing of both types of striation increases with the stress at the crack tip; their curvature is away from the origin of failure and large local variations in spacing and orientation have been observed in immediately adjacent areas of fractures in specimens cycled at constant load; the plateaux or facets on which striations lie are usually at different levels joined by regions of ductile tearing^(97,103,104). Both types of striation have been reported on grain boundaries⁽¹⁰⁵⁾. The spacing of fatigue striations does not correlate well with macroscopic crack growth rates⁽¹⁰⁶⁾, especially at higher crack growth rate, Fig. 26. The macroscopic crack growth rate is the sum of the normal fatigue process causing striations and the dimple fracture component caused by tensile tearing.

According to Laird⁽¹⁰⁸⁾ and Schijve⁽¹⁰⁹⁾, the Stage II crack propagation is an extension of Stage I crack propagation. On cycling, dislocation movement occurs on one or two sets of crystallographic planes at 45° to the crack plane, Fig. 27. Depending on the stress condition, crack tip may act as source or sink. Thus the crack extension occurs in each cycle as a consequence of a 'sliding off' mechanism⁽⁹⁹⁾. According to Broek⁽¹¹⁰⁾, striation depth could be larger on one fracture surface than on its mating part, depending on the orientation of the slip planes.

According to Pelloux⁽¹¹¹⁾, deformation at the crack tip may be caused either by alternate shears or simultaneous shear on two shear bands. If shear starts on one plane and strain hardening occurs, it could be easier to shear on the other plane, and this process may alternate.

If the material is non-hardening, or the hardening is saturated, crack blunting will take place by simultaneous shear. Due to high strain at the crack tip, void nucleation and growth may occur by further blunting and re-sharpening of the crack tip. On the other hand, Tomkins⁽¹¹²⁾ considers that the shear decohesion along the inner edges of both the flaw bands occurs during the tensile part of the fatigue cycle. During compression, the reversed slip occurs, and the crack closes without significant re-cohesion of the newly cracked surface. Due to this process, Fig. 28, according to Tomkins, the familiar ripple patterns on the fatigue fracture surface can form and this mechanism is also active in Stage I crack growth, but only on one plane.

Second phase particles can nucleate voids and cracks can extend by growth and coalescence of these voids. Pelloux⁽¹¹³⁾ proposed that the effects of second phase particles on crack growth rate depends on the ratio of fatigue plastic zone size, r_p , to the interparticle spacing S . He suggested that when

- (a) $r_p < 10S$, crack growth rate depends on the matrix properties;
- (b) $r_p \approx S$, crack growth is a result of propagation through the matrix and second phase particles;
- (c) $10 r_p \geq S$, crack growth is mainly a result of crack extension through and around second phase particles⁽¹¹⁴⁾. Broek⁽¹¹⁰⁾ shows that at low ΔK , fracture occurs around second phase particles, but at high ΔK , voids form due to loss of coherency of the second phase particles with the matrix. However, Grosskreutz and Shaw⁽¹¹⁵⁾ have shown that at low values of ΔK , second phase particles effectively hold up propagation and act as crack arresters, which is the opposite of the relationship proposed by Pelloux⁽¹¹³⁾. A mechanism of void formation and coalescence by second phase particles has been proposed

by Forsyth and Ryder⁽¹¹⁶⁾. In this mechanism, the high hydrostatic stresses ahead of the crack tip cause voids to form probably at some discontinuity in the matrix. e.g. a brittle particle. These voids eventually link up by thinning of the unfractured bridges under biaxial stresses, resulting in crack extension, Fig. 29. Therefore, it can be expected that plane stress situations would be more favourable to void coalescence than plane strain condition, although void coalescence has been observed to occur under plane strain conditions. El Soudani and Pelloux⁽¹¹⁷⁾ noted that the extent of void coalescence could be reduced by decreasing the volume fraction of inclusions in the matrix.

7.5. FATIGUE CRACK INITIATION

7.5.1. Introduction

Much of the data relating to the resistance of materials to fatigue failure has been obtained using smooth specimens. The data thus generated are of limited use, because engineering components almost invariably contain stress concentrators due either to design, in the form of section changes, notches, keyways etc., or to fabrication difficulties in the form of defects such as laps, microporosity etc. In these circumstances, the choice of a safe design criterion depends on the working conditions of each individual component. If the stresses are low, then the defects may be assumed to be sharp cracks, and from a knowledge of the fatigue crack propagation rate, the time taken for the crack to reach a critical size, and hence the safe working life of the component, may be calculated. In these cases the application of fracture mechanics concepts has been found very successful. However, if the stresses are high, fatigue crack

propagation rate is rapid, and it becomes necessary to design against the initiation of cracking at the stress concentrators.

7.5.2. Review of Criteria for Correlating Fatigue Crack initiation data in notched specimens.

7.5.2.1. Stress-Strain Concentration Approach

The theoretical stress concentration factor, K_t applies only when the material at the notch root remains elastic. Neuber⁽¹¹⁸⁾ analysed a specific notch geometry and loading and derived a rule which applies when the material at the notch root deforms non-linearly. Recent work has shown that this rule adequately describes the more general case of plastic action in notched axial specimen^(119, 120). According to Neuber, the theoretical stress concentration factor K_t is equal to the geometric mean of the actual stress and strain concentration factors i.e.

$$K_t = (K_\sigma \cdot K_\epsilon)^{\frac{1}{2}}, \text{ Neuber's Rule } \dots\dots\dots (12)$$

Topper et al.⁽¹²⁰⁾ used the Neuber's rule to take into account plastic deformation at the notch root. This rule was derived for shear strained prismatical bodies containing deep longitudinal notches.

In applying Neuber's Rule to the notched fatigue problem, K_t is replaced by K_f , 'fatigue concentration factor', and K_σ , K_ϵ are written in terms of the nominal stress and strain ranges Δs and Δe i.e.

$$K_f = \left(\frac{\Delta \sigma}{\Delta S} \cdot \frac{\Delta \epsilon}{\Delta e} \right)^{\frac{1}{2}} \dots\dots\dots (13)$$

where $\Delta \sigma$ and $\Delta \epsilon$ are local stress and strain ranges at the notch root.

Rearranging and multiplying both sides by Young's modulus, E , we can write:

$$K_f (\Delta S \Delta \epsilon E)^{\frac{1}{2}} = (\Delta \sigma \Delta \epsilon E)^{\frac{1}{2}} \dots \dots \dots (14)$$

and if the nominal stress and strain are limited to the elastic region,

$$K_f \Delta S = (\Delta \sigma \Delta \epsilon E)^{\frac{1}{2}} \dots \dots \dots (15)$$

The expression (14) is useful and important because it shows that a function of nominal stress and strain $(\Delta S \Delta \epsilon E)^{\frac{1}{2}}$ need only be multiplied by an experimentally determined constant concentration factor to obtain the value of $(\Delta \sigma \Delta \epsilon E)^{\frac{1}{2}}$ at the notch root⁽¹²⁰⁾.

The special case where ΔS is elastic but $\Delta \sigma$ and $\Delta \epsilon$ are inelastic, is important, because it covers most problems of engineering interest. At even longer lives, and lower values of ΔS , the notch root remains essentially elastic and equation (14) reduces to the familiar form

$$K_f \Delta S = \Delta \sigma \dots \dots \dots (16)$$

This equation is frequently used at shorter lives when the material near the notch behaves inelastically.

The relationship in equation (14) can be interpreted as furnishing indexes of equal fatigue damage in notched and unnotched specimens, or in other words, a notched specimen and a smooth specimen will form detectable cracks after the same number of cycles, provided $K_f (\Delta S \Delta \epsilon E)^{\frac{1}{2}}$ for the notched specimen is equal to $(\Delta \sigma \Delta \epsilon E)^{\frac{1}{2}}$ for the smooth specimen. Thus, if a master curve of $(\Delta \sigma \Delta \epsilon E)^{\frac{1}{2}}$ versus crack initiation (or life, as an approximation, provided the specimens are small) is obtained for smooth specimens, the life of a notched specimen can be obtained from the value of $K_f \Delta S$ on the $(\Delta \sigma \Delta \epsilon E)^{\frac{1}{2}}$ axis. This correlation has been checked experimentally and reasonable agreement has been found between the predicted and observed notch behaviour^(121, 122).

A limitation of this method is that it only applies to constant amplitude, completely reversed (i.e. the stress ratio, $R = \frac{\sigma_{\max}}{\sigma_{\min}} = -1$) strain controlled loading. However, while direct correlation between smooth and notched specimens is only possible for $R = -1$, examination of equation (15) indicates that for other R values crack initiation data for different notches can be correlated using the parameter $K_f \Delta S$.

7.5.2.2. Fracture Mechanics approach

Several workers^(123, 124) have related the number of cycles, N_i , to initiate growth of a crack to the stress intensity range, ΔK , by an equation of the form

$$N_i = A (\Delta K)^{-n} \dots \dots \dots (17)$$

where A and n are constants for a given material in a given condition. Since fracture mechanics analysis applies strictly to sharp cracks, then, for defects with blunt tips some sort of adjustment to ΔK is required. Jack and Price⁽¹²³⁾ measured initiation at notches in mild steel and found that for sharp notches of root radius $\rho \leq 0.25$ mm., N_i was independent of root radius, and equation (17) applied.

Above the critical notch root radius, N_i is a function of root radius, written in the form $\Delta K / \rho^{1/2}$. Thus the effective stress intensity factor (K_{eff}) for a blunt notch is related to that for a sharp notch or crack by:

$$K_{eff} = K \left(\frac{\rho_0}{\rho'} \right)^{1/2} \dots \dots \dots (18)$$

where ρ_0 is the critical value of ρ and equal to 0.25mm. for mild steel⁽¹²³⁾,

ρ' is the effective root radius and

$$\rho' = \rho \quad \text{when} \quad \rho \geq \rho_0$$

$$\rho' = \rho_0 \quad \text{when} \quad \rho \leq \rho_0$$

Pearson⁽¹²⁵⁾ was unable to determine whether a critical root radius existed for a high strength aluminium alloy and he suggested that, if it did exist, it must be less than the 0.254 mm obtained by Jack⁽¹²⁶⁾ for mild steels. Pearson also described his initiation results in terms of the parameter $\Delta K/\rho^{1/2}$. Scatter was found to be fairly extreme. This could possibly be attributed to his criteria for initiation, which he defined as the load cycle when a 0.127 mm crack was first observed. Forman's⁽¹²⁸⁾ initiation data plotted in terms of the parameter $\Delta K/\rho^{1/2}$ also resulted in some scatter⁽¹²⁷⁾. Here again, an explanation can be found by properly defining the initiation event.

According to Forman⁽¹²⁸⁾, crack initiation, analogous to crack growth rate, should be a function of the relative stress intensity parameter, $\frac{\Delta K}{K_c}$, where K_c is the fracture toughness. For blunt notches, he replaced K_c by an apparent fracture toughness K_a , which is corrected for the finite root radius. K_a is defined as the product of K_c and the ratio of the size of the plastic zone r at the tip of the blunt notch to the size of the plastic zone w at the tip of the sharp crack; thus

$$K_a = K_c \cdot \frac{r}{w} \dots\dots\dots (19)$$

Values of $\frac{r}{w}$ were calculated using the equation derived by Creager and Paris⁽¹²⁹⁾ for the stresses at the tip of blunt notches.

Various initiation criteria cannot be tested accurately by experiment but crack growth law can be accurately measured by experiment. According to Forman⁽¹²⁸⁾, a satisfactory approach for predicting cycles to initiation of an 'engineering size' crack is to use crack propagation theory in which it is assumed that crack growth begins with the first load cycle. Forman correlated his initiation data extracted from sheet specimens of 7075-T6 aluminium alloy with $\frac{\Delta K}{K_a}$.

For his data, N_i was for the initiation of an average crack length of 0.254 mm. He also showed that data obtained by Manson⁽¹³⁰⁾ for 2014-T6 aluminium alloy could be correlated with $\frac{\Delta K}{K_a}$. For this data, crack initiation was defined as the load cycle when a 0.063 mm. crack was first observed.

It is apparent that several methods have been employed for correlating fatigue crack initiation behaviour at notches. Each method appears to correlate specific sets of data. An explanation lies in the fact that, in order to know that initiation has taken place, some crack growth must occur, since detection of a fatigue crack is the sole criteria of initiation. Thus the experimental value of N_i , is in general,

$$N_i \text{ measured}_{(N_i)} = N_i \text{ true}_{(N_o)} + N \text{ propagation}_{N(a)} \dots\dots\dots (20)$$

The criteria of initiation may be very sensitive and then the $N(a)$ contribution to N_i is small, or vice versa⁽¹³¹⁾.

Both from a fundamental and a design point of view, it is important to know how N_i varies as the initiation criteria is varied from the presence of a large fatigue 'nucleus' to a very small 'nucleus'. This study of the very early stages of propagation is necessary in order to judge how conservative a particular criteria of nucleation is⁽¹³¹⁾.

7.6 Fatigue Crack Propagation Laws

7.6.1. Introduction

In recent years, considerable effort has been focussed on the crack propagation phase of fatigue failures in an attempt to develop useful design rules. Analytical solutions have stemmed from several distinct disciplines of engineering science and to review all

such models, a broad classification of crack propagation laws has been necessary.

The various approaches can be divided into those involving dislocation theories, those based on the mechanics of fracture and dimensional consideration, and those founded on empirical studies of cyclic material behaviour and damage accumulation.

7.6.2. Crack Propagation Laws

The first continuum model for fatigue crack propagation was presented by Head ⁽¹³²⁾ in 1953, in the following form:

$$\frac{da}{dN} = \frac{C \Delta\sigma^3 a^3/2}{(\sigma_{ys} - \Delta\sigma) r_y^{1/2}} \dots\dots\dots (21)$$

where C is a material constant

$\Delta\sigma$ is the stress range

σ_{ys} is the yield strength

a is the crack length and

r_y is the plastic zone size at the crack tip,

and is assumed to be constant.

Frost and Dugdale ⁽¹³³⁾ showed on the basis of experimental results that plastic zone size is proportional to crack length.

Further they concluded that the crack propagation rate is linearly dependent on the crack length which in turn is proportional to $\Delta\sigma^3$.

Thus they proposed the following model.

$$\frac{da}{dN} = A \Delta\sigma^3 a \dots\dots\dots (22)$$

where A is a constant.

Liu ⁽¹³⁴⁾ modified the above equation, in subsequent work, to

$$\frac{da}{dN} = A \Delta\sigma^2 a \dots\dots\dots (23)$$

Frost and Dugdale⁽¹³³⁾, and later, Frost⁽¹³⁵⁾, examined the effect of mean stress on the rate of crack propagations in several materials, including an annealed mild steel, cold rolled mild steel and 18/8 austenitic steel, and a crack growth relationship of the form:

$$\frac{da}{dN} = (P + Q \sigma_m) \Delta\sigma^3 a \dots\dots\dots (24)$$

was proposed, where P, Q are constants and σ_m is the mean stress.

Tomkins and Biggs⁽¹³⁶⁾ deduced a mechanism of fracture in terms of plastic deformation at the crack tip and this formed the basis of Tomkin's theory⁽¹³⁷⁾. Essentially, he calculated the crack tip decohesion which would occur as a result of the plastic strain at the crack tip and equated this to da/dN . The result was a relationship similar to that obtained experimentally by Frost⁽¹³⁵⁾, equation 24. It was

$$\frac{da}{dN} = A \Delta\sigma^3 \sigma_m a \dots\dots\dots (25)$$

Equation (24) would be the same as equation (25) if $P = 0$ as was found for aluminium alloys.

According to Paris and Erdogan⁽¹³⁸⁾, the laws of Head, equation (21), Frost and Dugdale, equation (22) and Liu equation (23), can all be approximated by the form

$$\frac{da}{dN} = \frac{\Delta\sigma^m a^n}{C} \dots\dots\dots (26)$$

where C is a constant and $n = \frac{m}{2}$

Paris⁽⁶⁶⁾ adopted an energy approach to crack propagation. This was based on the assumption that the rate of change of elastic energy during fracture equals the rate of absorption of energy as plastic deformation. Assuming that all the plastic work is absorbed at the crack tip, the work is proportional to the area of the plastic zone per unit thickness, which in turn, is proportional to K^4 . He

went on to suggest that, in fatigue, the alternating plastic zone⁽⁶⁷⁾, based on ΔK , is relevant, so that the crack propagation relationship is

$$\frac{da}{dN} = C (\Delta K)^m \dots\dots\dots (27)$$

Thus Paris' theory predicts a value of $m = 4$, in equation (27) and no influence of mean stress on fatigue crack propagation.

According to Liu's⁽¹³⁴⁾ analysis, the value of $m = 2$. He argued that this value holds good for results with maximum stress levels. Since the elastic strain energy released is a function of maximum stress, the maximum stress should give reasonable correlation. Liu admitted that the value of m will have to be modified if σ_{max} is not the same.

Although a good fit for a variety of experimental data has been observed with Paris type equation, it has been well established that m can have values ranging from 2 to 6^(139, 140).

Forman et al.⁽¹⁴¹⁾ noted that Paris's equation was not a good fit for higher load ratios and crack growth rates. They attributed this to the onset of fast fracture as K_{max} approached K_c , the fracture toughness of the material. Forman et al.⁽¹⁴¹⁾ suggested that the approach to K_c could be incorporated in the crack propagation relationship by adopting the criterion

$$\lim_{K_{max} \rightarrow K_c} \frac{da}{dN} = \infty$$

Putting $K_{max} = \Delta K / (1-R)$, where R is the stress ratio (K_{min}/K_{max}), this may be expressed as

$$\lim_{\Delta K \rightarrow (1-R) K_c} \frac{da}{dN} = \infty$$

So, the crack propagation relationship suggested to include this condition can be written as:

$$\frac{da}{dN} = \frac{C (\Delta K)^m}{(1-R) K_c - \Delta K} \dots\dots\dots (28)$$

This equation fitted nicely Broek and Schijves⁽¹⁴²⁾ results, and also those obtained by Illg and McEvilly⁽¹⁴³⁾ for $R = -1$. Later Hudson and Scardina⁽¹⁴⁴⁾ also used equation (28) and found that it fitted their data for $R > 0$, those for $R \leq 0$ being fitted by the simpler equation (27), if the compressive part of a cycle was ignored.

Crooker and Lange⁽¹⁴⁴⁾ were less successful in unifying their data for steel when they applied Forman's equation. It should be noted that, since K_c is geometry and environment dependent, it cannot be regarded as a material constant. The value used in equation (28) would be appropriate to the test specimen geometry. This places a serious limitation on the use of the equation in practical situations.

Pearson⁽¹⁴⁵⁾ investigated the effect of mean stress using thick (12.7mm) bend specimens, in which plane strain conditions are maintained until failure. This contrasts with the tests using thin specimens in which the fracture mode would be plane stress when final failure occurred. Hence, using equation (28) with K_c replaced by its plane strain value K_{IC} , and further modifying the equation to bias the effect of stress ratio towards high values of ΔK , Pearson obtained

$$\frac{da}{dN} = \frac{C (\Delta K)^m}{[(1-R) K_{IC} - \Delta K]^{\frac{1}{2}}} \dots\dots\dots (29)$$

to secure better fit with his data.

This equation (29) still complies with the criterion that $\frac{da}{dN} = \infty$ when $K_{max} = K_{IC}$. Pearson's equation was also successful in correlating Broek and Schijves data⁽¹⁴²⁾, as well as Maddox's⁽¹⁴⁶⁾ data at $R = 0$ and $+0.5$.

An indication of how the two equations (28 and 29 predict the influence of mean stress over a range of ΔK values, for high and low toughness materials, may be provided graphically as follows.

First, the predicted magnifications (M) in $\frac{da}{dN}$ for given values of R , K_{IC} and ΔK , have been redefined relative to the values for $R = 0$, and are given by

$$M_F = \frac{1}{(1-R)K_{IC} - \Delta K} \div \frac{1}{K_{IC} - \Delta K} = \frac{K_{IC} - \Delta K}{(1-R)K_{IC} - \Delta K} \dots\dots\dots (30A)$$

$$M_P = \frac{1}{[(1-R)K_{IC} - \Delta K]^{\frac{1}{2}}} \div \frac{1}{(K_{IC} - \Delta K)^{\frac{1}{2}}} = \left[\frac{K_{IC} - \Delta K}{(1-R)K_{IC} - \Delta K} \right]^{\frac{1}{2}} \quad (30B)$$

where suffix F refers to Forman's and suffix P refers to Pearson's equation (146). Secondly, the magnification factors have been plotted against ΔK for various stress ratios and two arbitrary K_{IC} values in Figs. 30 and 31. It will be seen from Fig. 30 (high toughness) that Forman's equation predicts the greatest influence of stress ratio, although the two factors do not differ widely for low values of R and ΔK . Thus, the effect of R on plots of $\log (da/dN)$ vs. $\log \Delta K$ would be to shift the curves along the $\log (da/dN)$ axis to give approximately parallel curves, as found in the results obtained by Broek and Schijve (142). Clearly, either expression would be suitable for correlating such data over a wide range of R and ΔK values. In contrast, the factors for a low toughness material, Fig. 31, differ widely over the whole range of ΔK and R values, especially at high values, Forman's equation giving the highest values. The data obtained by Pearson for low toughness materials were consistent with his equation, while Forman's equation (28) was not suitable.

A fuller attempt to take account of the material properties, has been made by Heald et al.⁽¹⁴⁷⁾. Basing their equation on one given by Weertman⁽¹⁴⁸⁾, they proposed the following modified equation

$$\frac{da}{dN} = A \left[\frac{\Delta K^4}{\sigma_c^2 (K_c^2 - K_{max}^2)} \right]^n \dots\dots\dots (31)$$

where A is a constant, n lies between 0.5 to 1 and Kc is the fracture toughness of the component. Besides predicting an effect of Kmax, where K max approaches Kc, this expression describes an effect of microstructure, principally through the parameter Kc. Heald et al.⁽¹⁴⁷⁾ showed that the fatigue crack growth results obtained from heat-treating a 1.0 percent carbon steel to different micro-structures were in good agreement with the equation (31).

Roberts and Erdogan⁽¹⁴⁹⁾ analysed the results of Broek and Schijve⁽¹⁴²⁾ on 2024-T6 aluminium sheet specimens in tension and some of their own results on 2024-T₃ in bending and showed that the dependency of crack growth rate on mean stress and ΔK can be satisfactorily represented by an equation of the form

$$\frac{da}{dN} = B (K_{max})^m (\Delta K)^n \dots\dots\dots (32)$$

where B is constant. The values of m and n were both found to be 2.

Klensil and Lukas⁽¹⁵⁰⁾ reviewed evidence suggesting the existence of a threshold value of ΔK below which cracks will not propagate, and modified the Paris's equation to take ΔK_{th} into account i.e.

$$\frac{da}{dN} = C (\Delta K_a^n - \Delta K_{th}^n) \dots\dots\dots (33)$$

where ΔK_{th} is related to ΔK_a by the equation

$$\Delta K_{th} = \Delta K_{thb}^{1-\alpha} \cdot \Delta K_a^\alpha \dots\dots\dots (34)$$

where ΔK_{th} = threshold stress intensity following the stress intensity of ΔK_a

ΔK_{thb} = basic threshold value of stress intensity factor

independent of the strength of the material.

α = material constant dependent on strength

Cooke and Beavers⁽¹⁵¹⁾ have also found evidence of threshold stress intensities in five medium carbon steels and concluded that ΔK_{th} depends on load ratio R . Prior loading could also be responsible for the existence of threshold ΔK values as found by Donahue et al⁽¹⁵²⁾ and Klensil and Lukas⁽¹⁵⁰⁾.

Finally, to provide an equation which predicts fatigue crack propagation from very small values of ΔK to impending unstable failure, a combination of equations (31 and 33) have been suggested by Richards and Lindley⁽¹⁵³⁾ in the form

$$\frac{da}{dN} = A' \left[\frac{(\Delta K - \Delta K_0)^4}{\sigma_c^2 (K_c^2 - K_{max}^2)} \right]^n \dots \dots \dots (35)$$

where ΔK_0 is the threshold stress intensity value and A' is a constant. The equation (35) represents an attempt to extend the prediction of fatigue crack propagation rates to extreme cyclic stress intensity regimes.

The complete relationship between fatigue crack growth rate and stress intensity factor, schematically plotted on logarithmic co-ordinates has been shown to be sigmoidal, consisting of three regions, Fig. 32. While most of the crack propagation laws is applicable to the linear middle portion of the sigmoidal curve, the rest of the curve is sensibly covered by incorporating the threshold stress intensity factor (ΔK_{th}) at very low values of ΔK and K_c term for very high values of ΔK close to catastrophic failure.

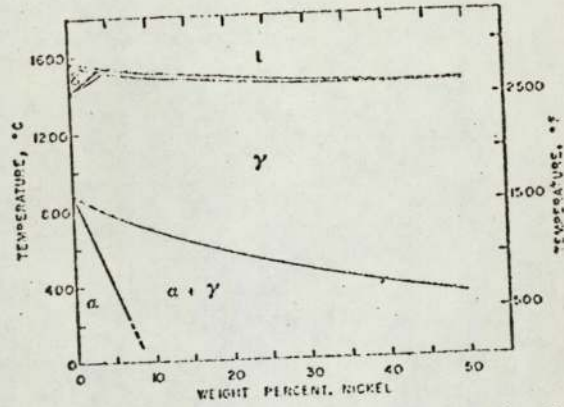


Fig.1. Iron-rich portion of the iron-nickel equilibrium diagram.
 (After Ref:22) [Courtesy Iron Steel Inst.]

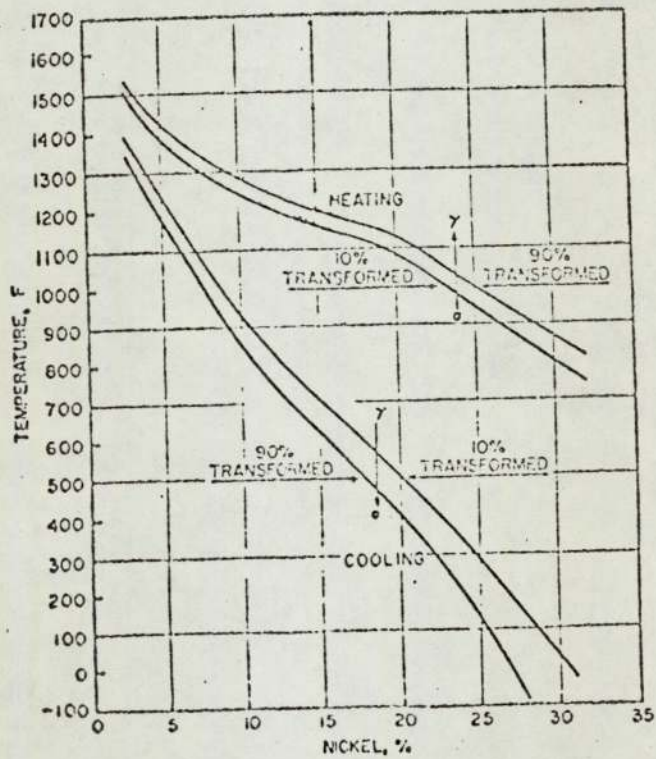


Fig.2. The Fe-Ni transformation diagram
 (After Ref:10)

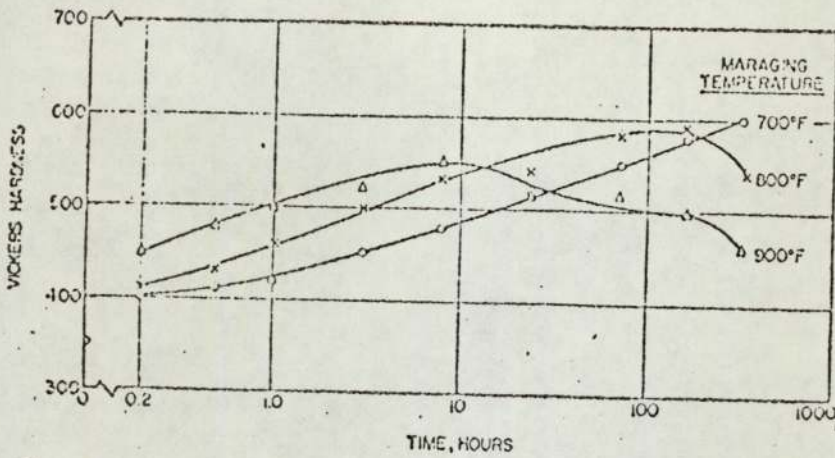


Fig. 3. Effect of maraging on hardness of 18% Ni steel. Initially annealed at 1500°F.
(After Ref: 12)

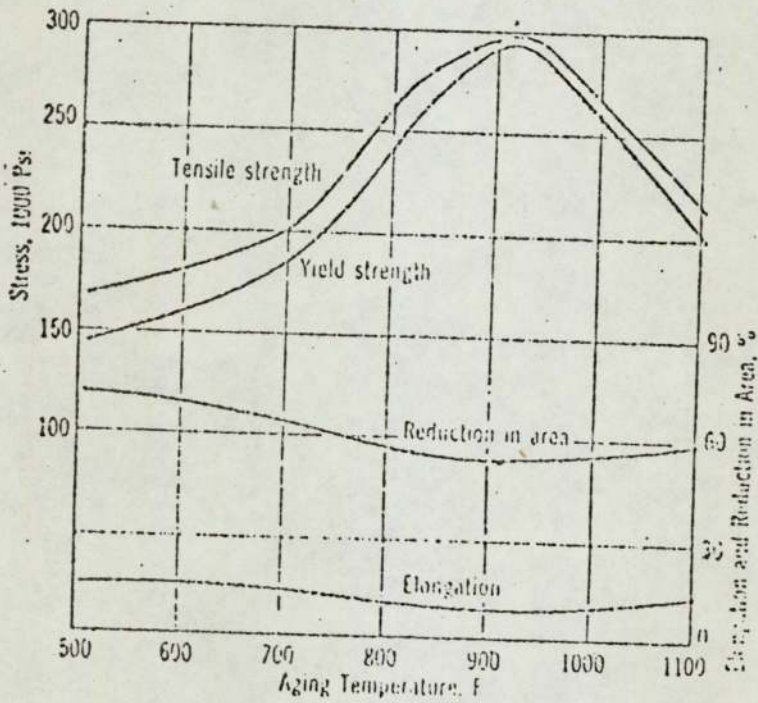


Fig. 4. Effect of Ageing Temp. on mechanical properties of a 18% Ni Maraging steel
(After Ref: 11)

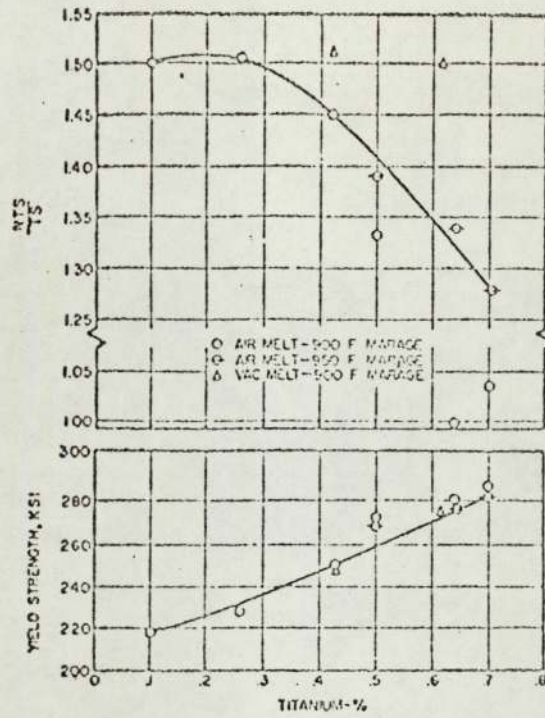


Fig. 5. Effect of titanium on yield strength and NTS/TS of 18.5 Ni, 7 to 7.5 Co, 6 Mo-Fe alloys 30 lb melts. Annealed 1 hr at 1500 F, maraged.

(After Ref: 10)

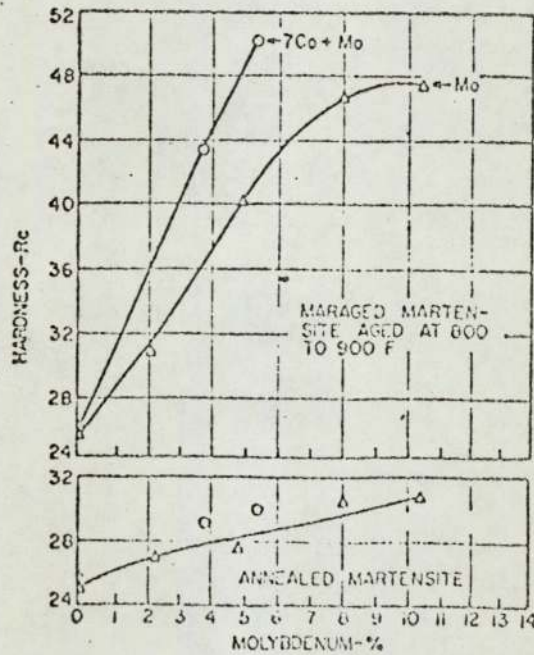


Fig. 6. Effect of molybdenum and molybdenum + 7% Co on maximum hardness of 18.5 to 20.1 Ni-Fe alloys. Solution annealed 1 hr at 1600 F, air cooled; maraged

(After Ref: 10)

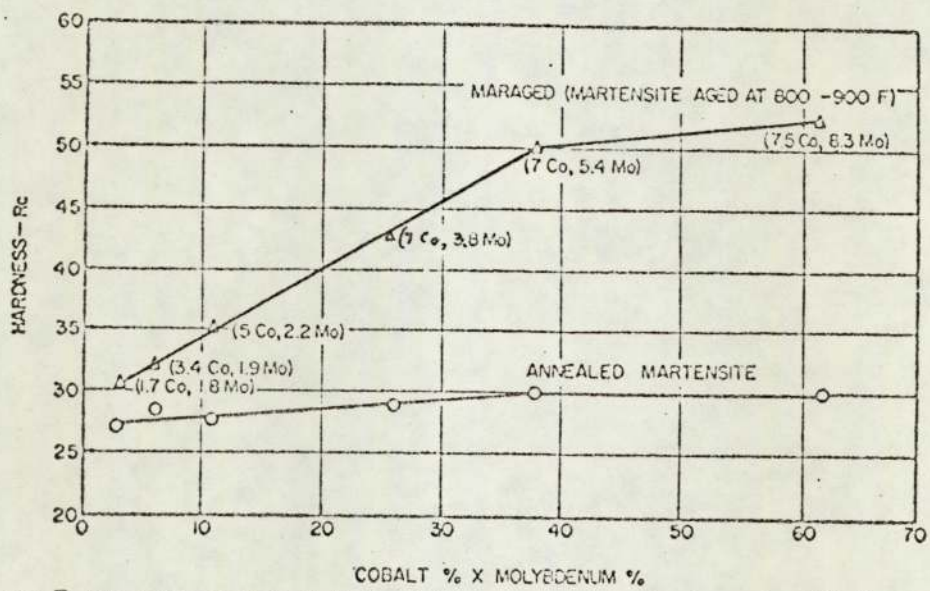


Fig. 7. Effect of product of cobalt X molybdenum on maximum hardness of 18.5 to 20.1 Ni-Fe alloys. Solution annealed 1 hr at 1600 F, air cooled; maraged 3 to 10 hr at 800 to 900 F.
(After Ref:10)

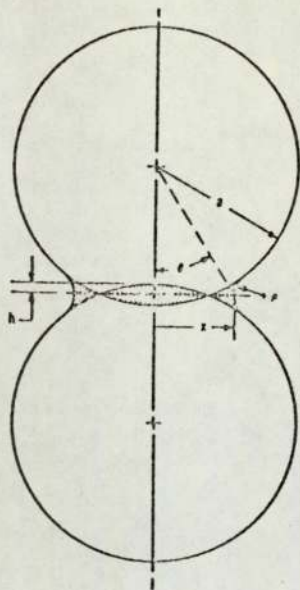


Fig.8. Two Sphere Model with interpenetration.
(After Ref:39)

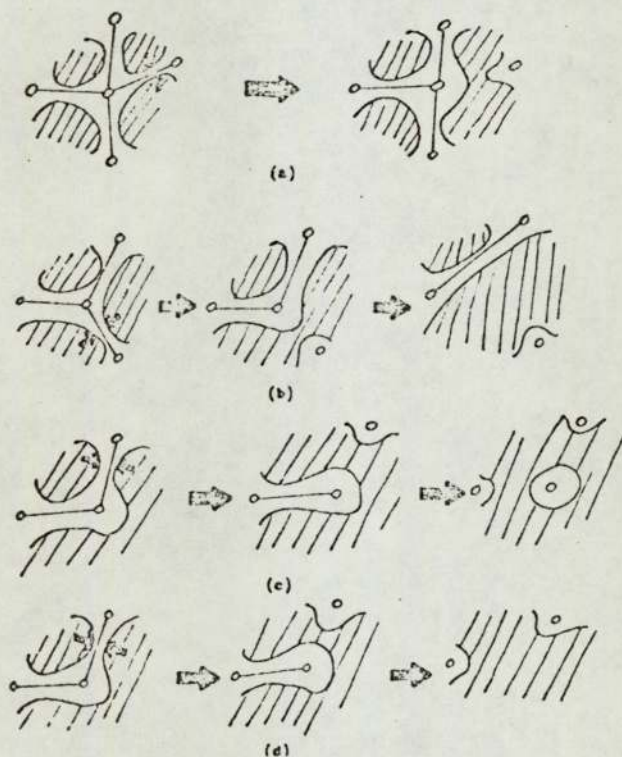
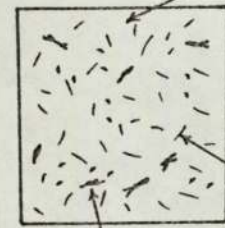


Fig.9. Whether a given pore is isolated (c) or adsorbed (d) into the main network depends upon the competition between shrinkage and surface rounding mechanisms, as well as upon the shape of the last connecting channel.
(After Rhines and DeHoff (40))

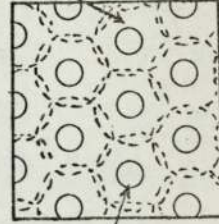
COMPACT

IDEALIZED
GEOMETRY

Continuous mass of particles of
the major constituent



Interparticle
Porosity



Particles of
the minor constituent

Fig.9A. Schematic representation of a Sintered Compact along with the Idealized Geometry of the Concentric-Sphere Model.

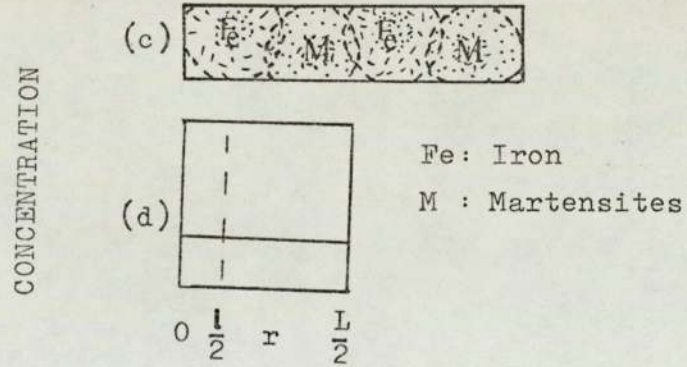
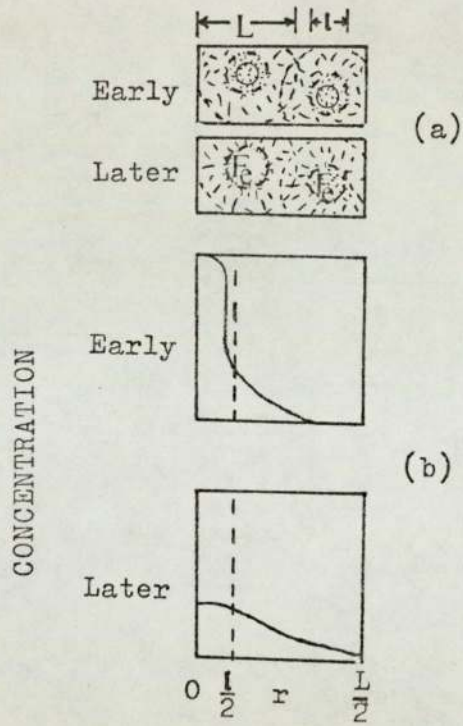


Fig.9B. Schematic representation of the Homogenisation Process for Martensite-Iron System in terms of the Microstructural Changes and Composition-Distance Profile.

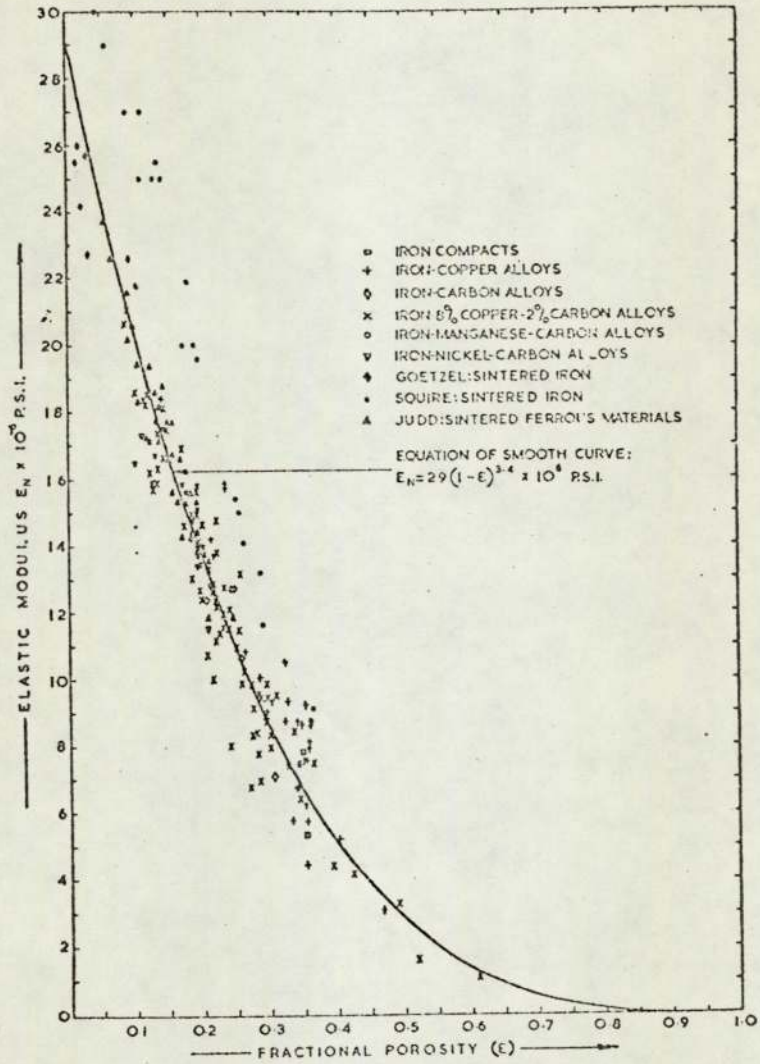


Fig. 10. Relation between elastic modulus and fractional porosity of iron-base alloy compacts.

(After McAdam (46))

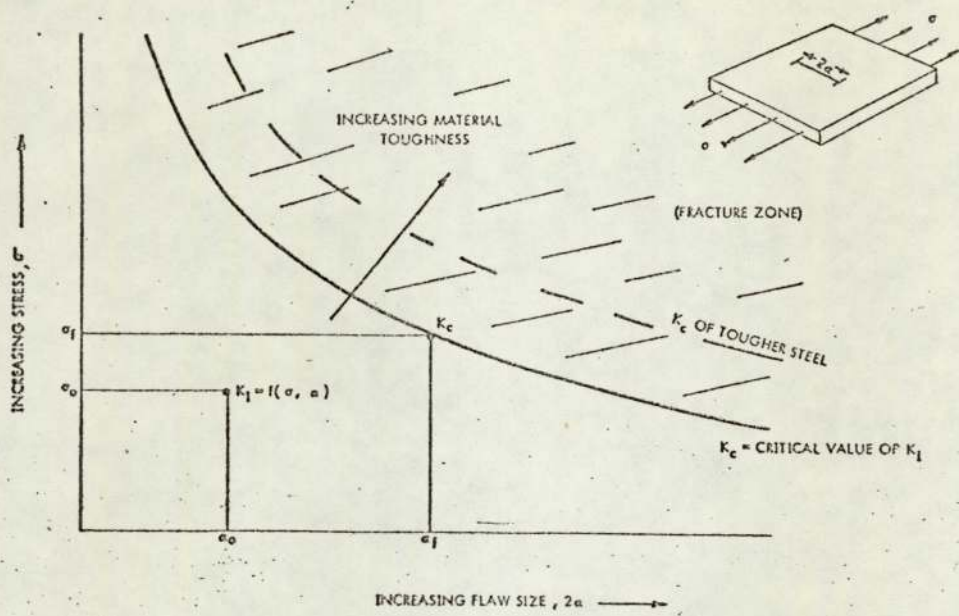


Fig.11. Schematic relation between stress, flaw size, and material toughness. (After Rolfe (47))

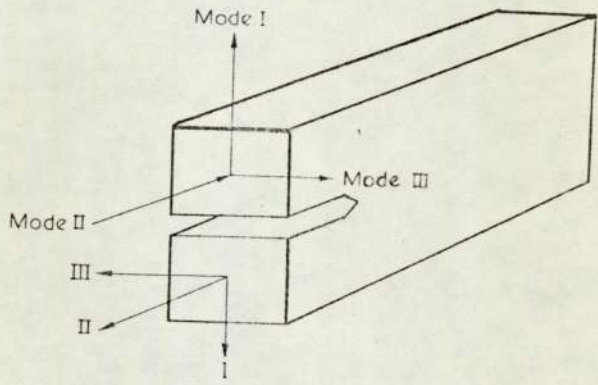


Fig.12. Diagram showing directions of Mode I, II and III cracking. It is possible to crack a body with shear loadings in Modes II or III. (After Ref:58)

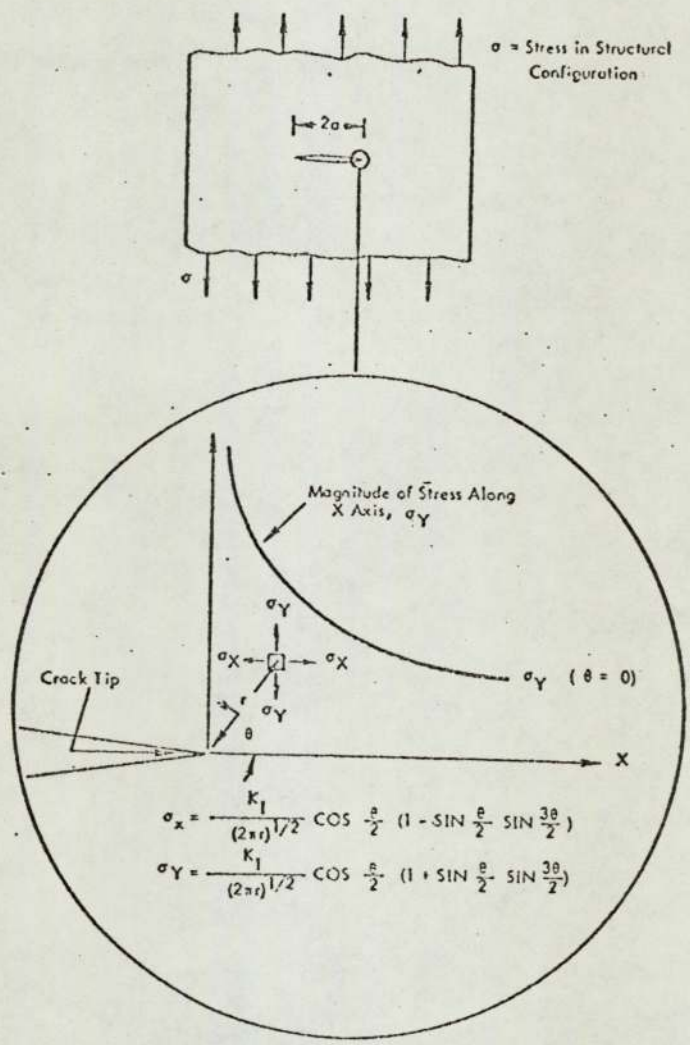


Fig.13. Elastic-stress-field distribution ahead of a crack.
(After Ref:47)

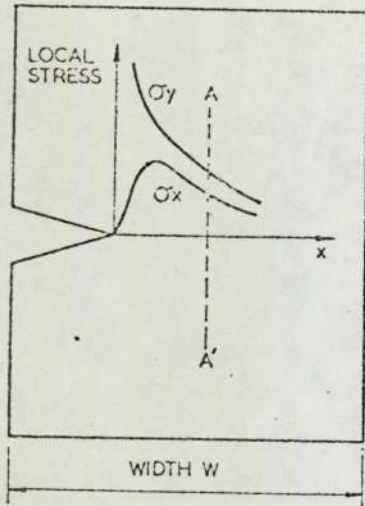


Fig.(a). Variation of σ_y and σ_x across width. Elastic condition.

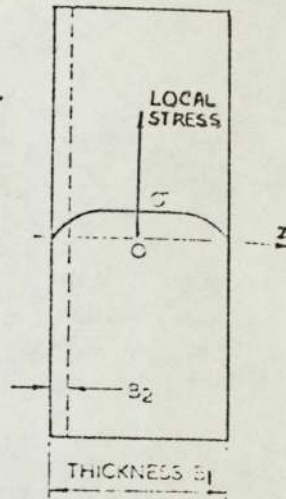


Fig.(b) Section at AA', $\sigma_z = \nu(\sigma_y + \sigma_x)$. Variation of σ_z through the thickness at section AA'. Elastic condition.

Fig. 14. Development of Constraint Stresses through width and thickness of a notched plate. (After Ref:61)

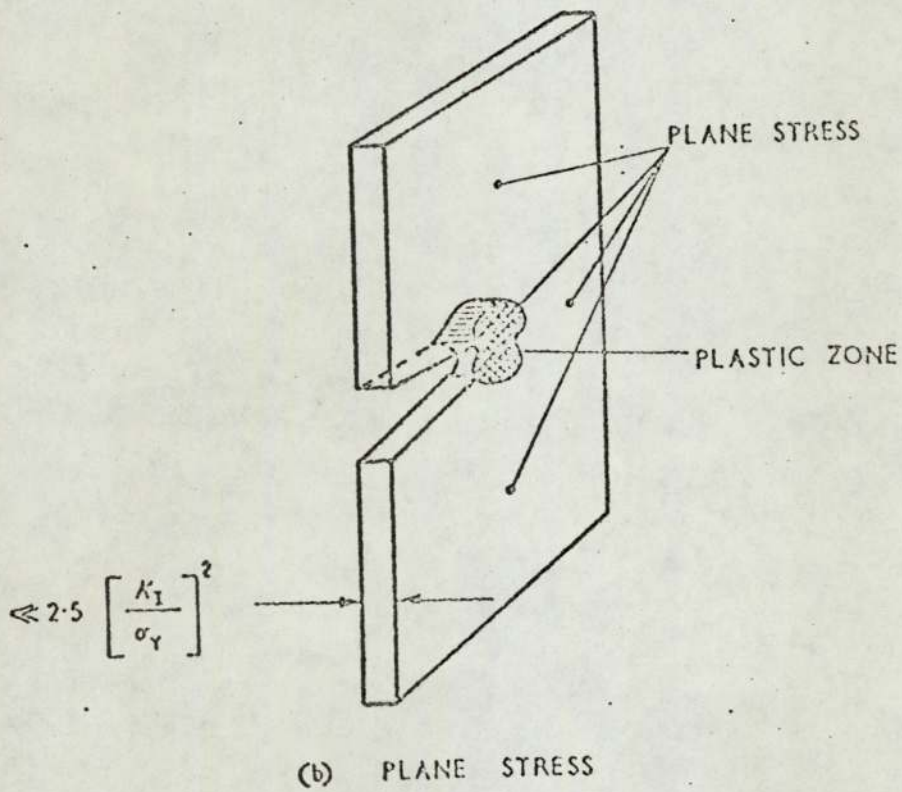
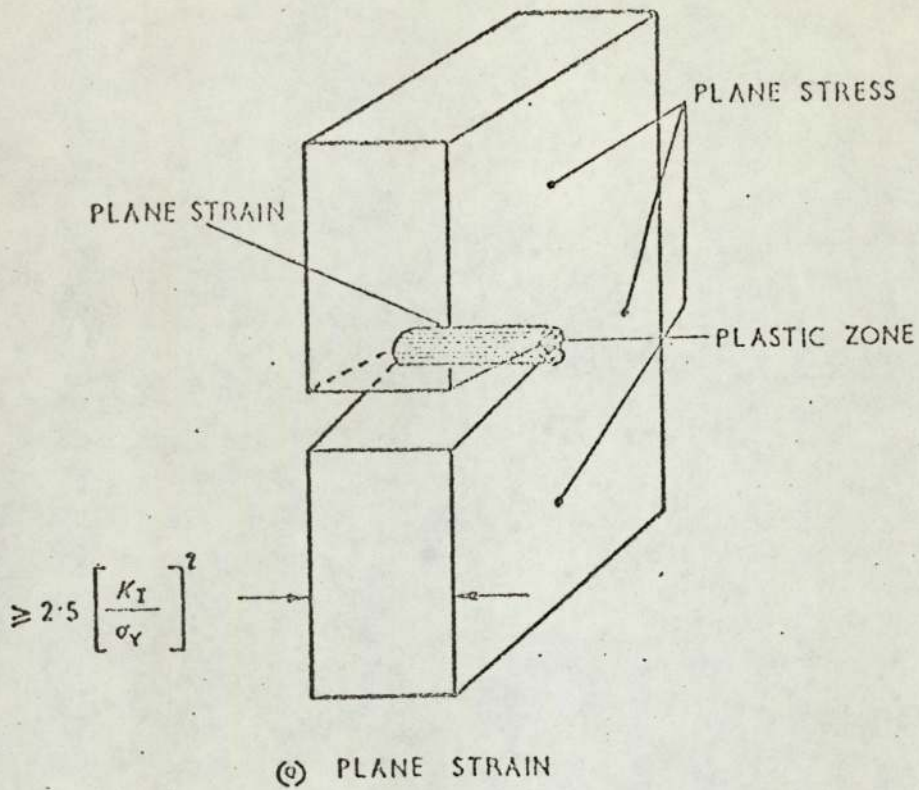


FIG.15. NOMENCLATURE FOR THE STATE OF STRESS IN A CRACKED PLATE (After Ref:59)

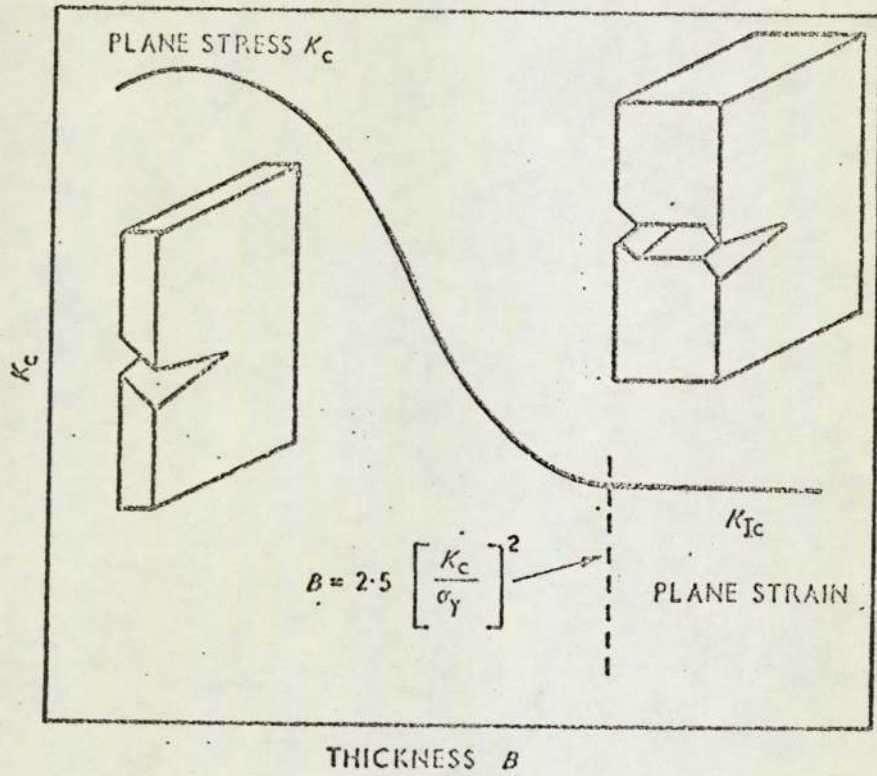
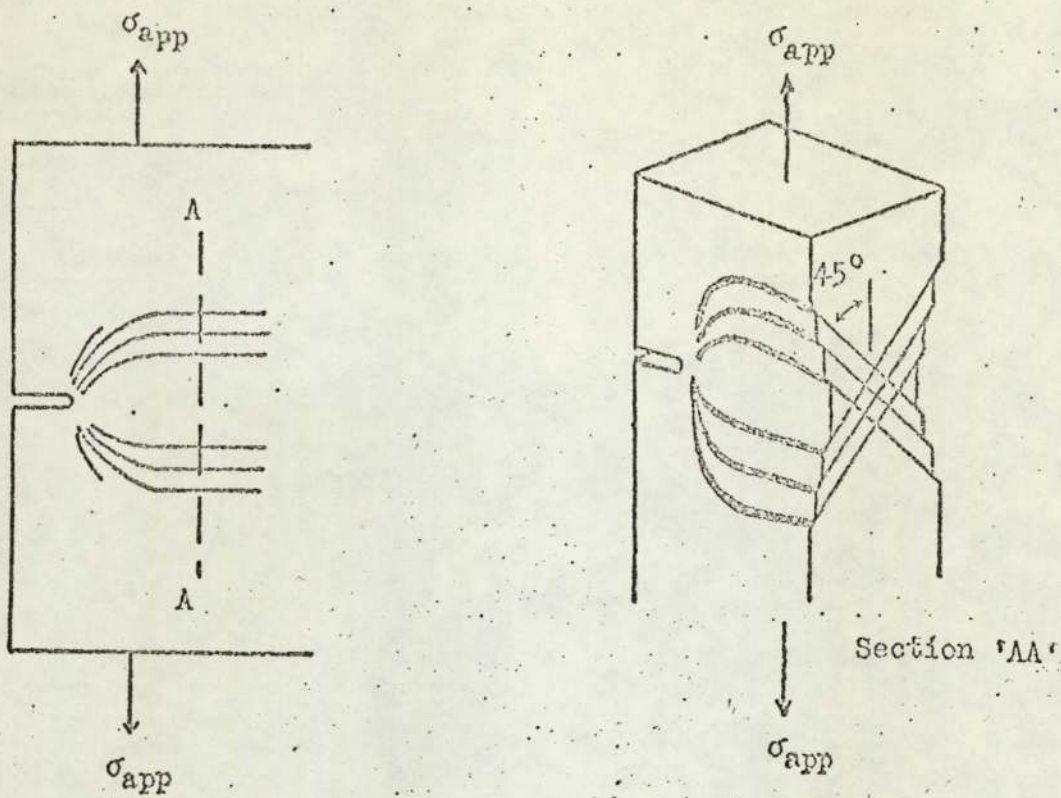
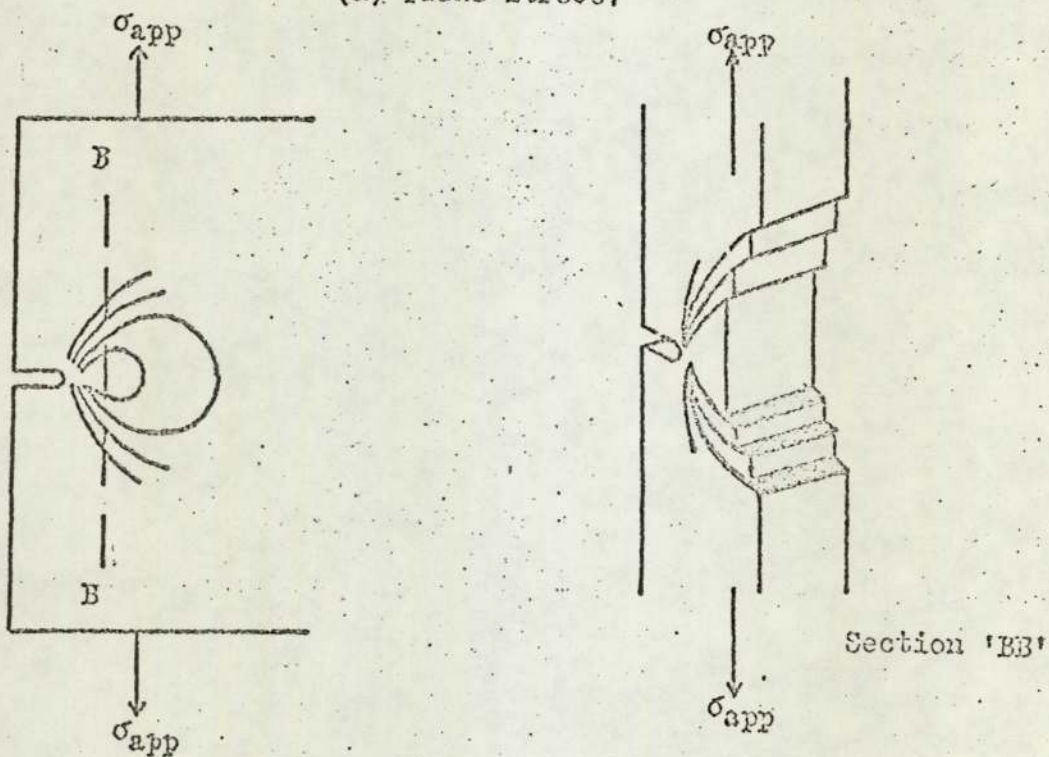


FIG.16. RELATIONSHIP BETWEEN THICKNESS AND K_c
 (After Pook (59))



(a) Plane Stress.



(b) Plane Strain.

Fig.17. Yield Zones through the Cross Section of a Cracked Plate in Plane Stress and Plane Strain. (After Ref:62)

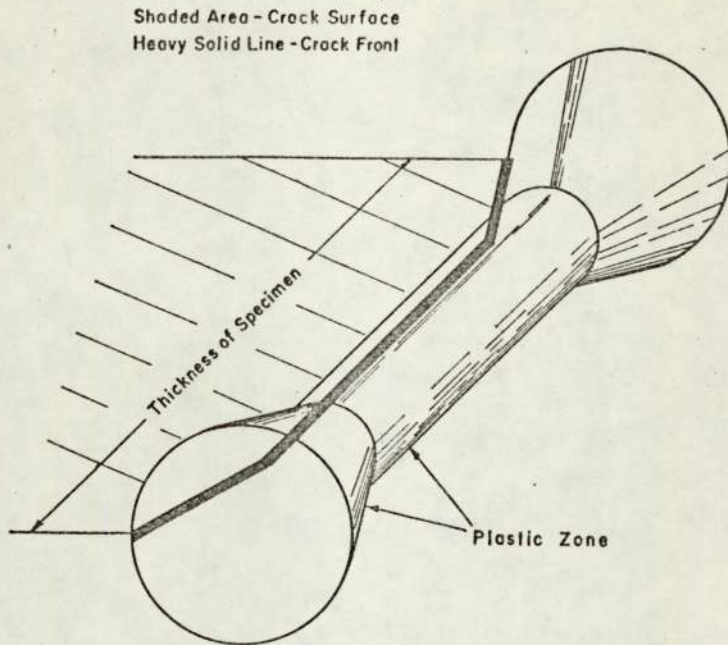


FIG. 18. Three-Dimensional Schematic Diagram of the Crack Surface, the Crack Front and the Plastic Zone.
(After Ref:60)

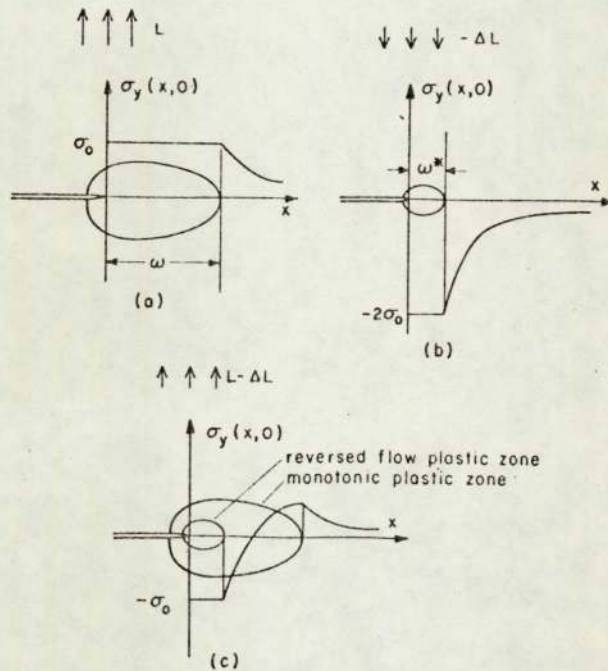


FIG. 19. Plastic superposition for unloading. Adding (b) for load $-\Delta L$ with a doubled yield stress to (a) gives the solution (c) resulting after unloading from L to $L-\Delta L$. Reloading, $L-\Delta L$ to L , restores (a).

(After Rice (67))

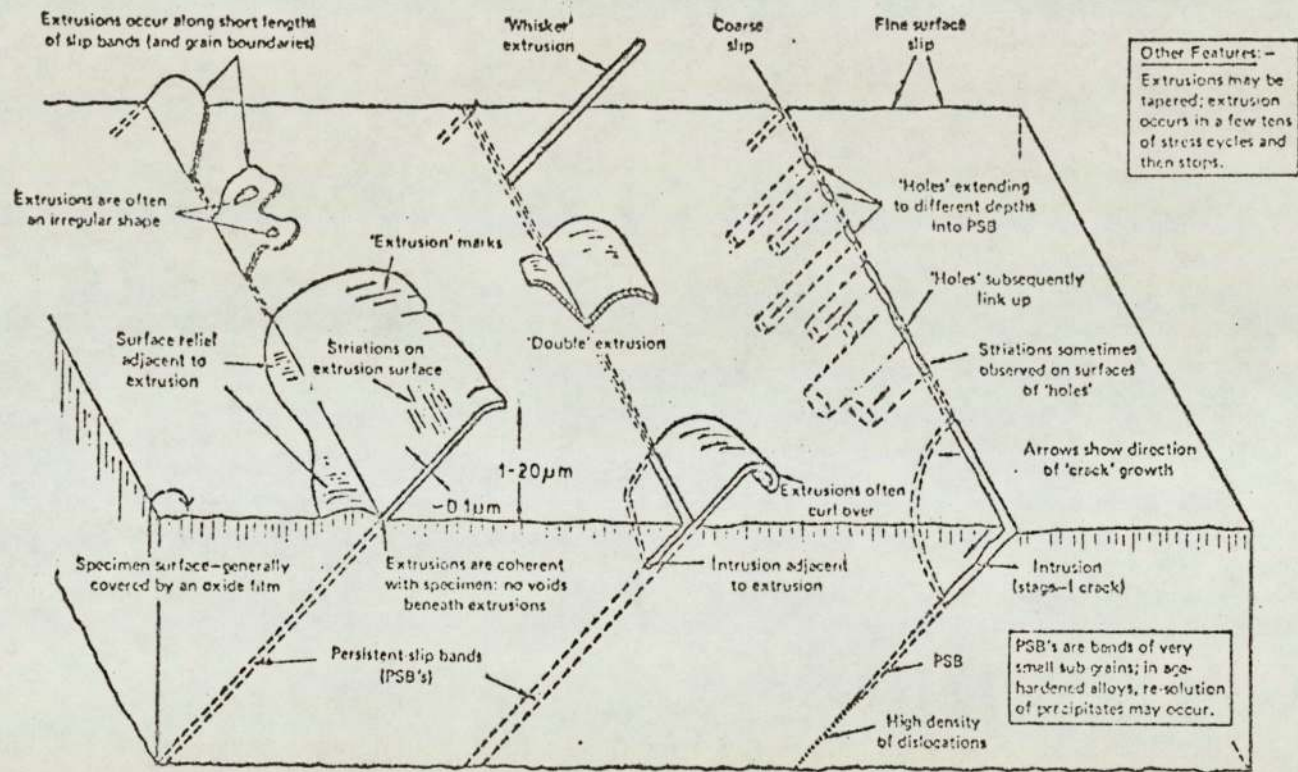


Fig.20. Diagrammatic summary of important features of slip-band extrusion and intrusion. Specific details depend on material, stress, environment, etc.

(After Lynch (76))

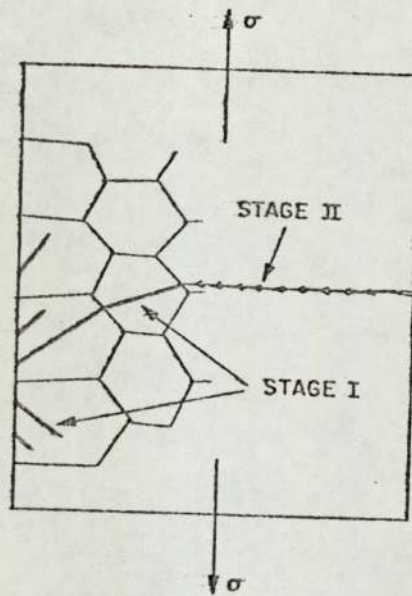


FIG. 21 Schematic representation of the two stages of crack propagation.
(After Ref:88)

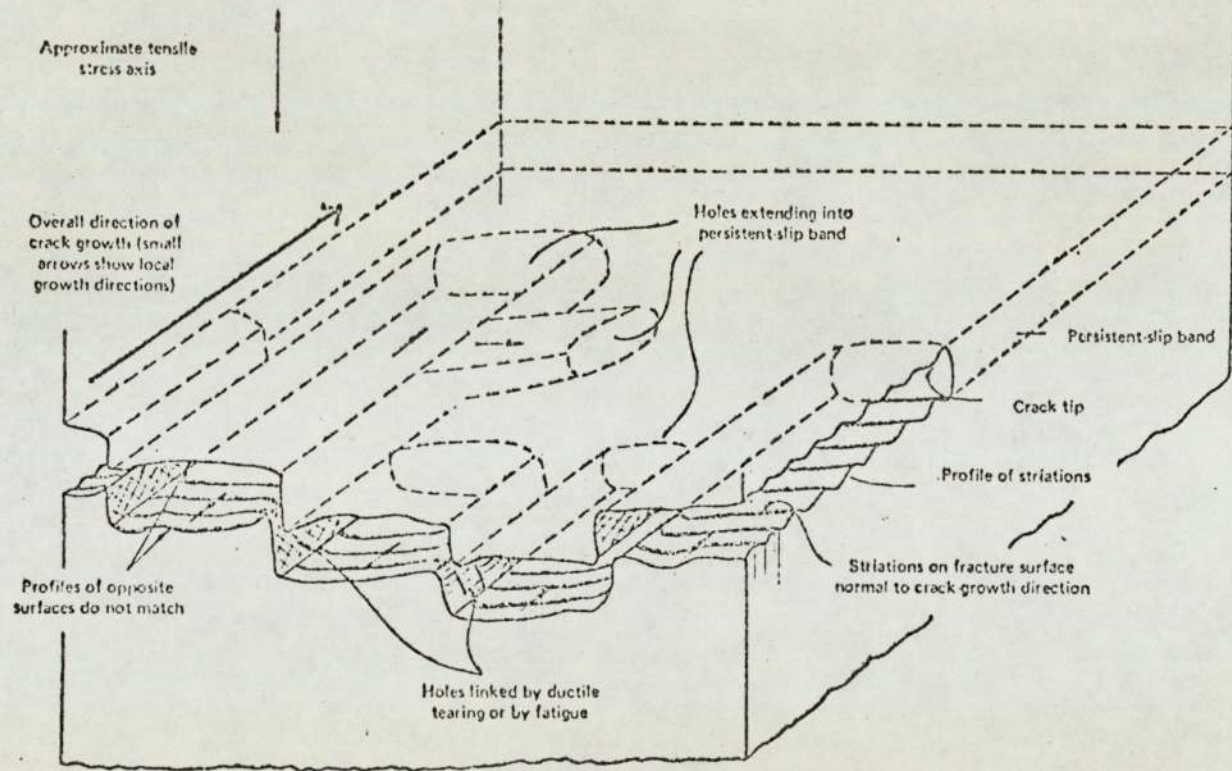


Fig.22. Schematic diagram of stage II crack-tip region.
 (After Ref:76)

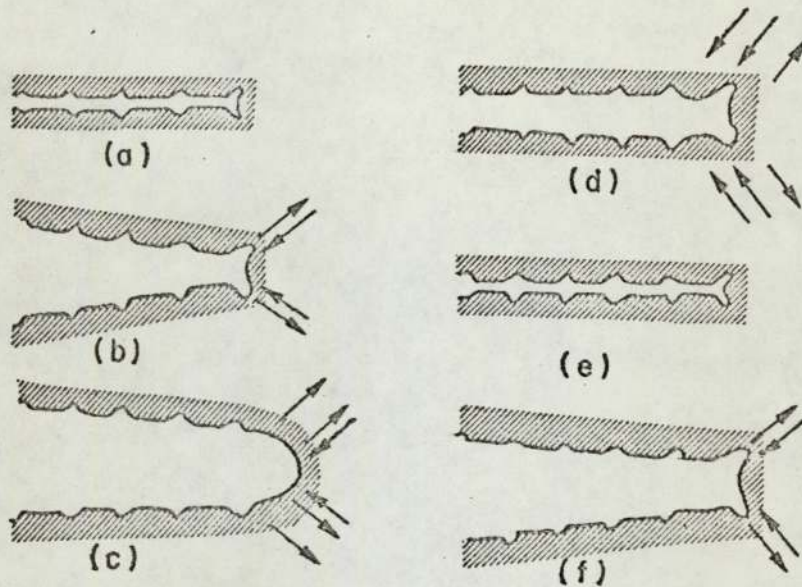


FIG. 23. The plastic blunting process of fatigue crack propagation in the stage II mode: (a) zero load, (b) small tensile load, (c) maximum tensile load, (d) small compressive load, (e) maximum compressive load, and (f) small tensile load. The double arrowheads in (c) and (d) signify the greater width of slip bands at the crack in these stages of the process. The stress axis is vertical. (After Ref:88)

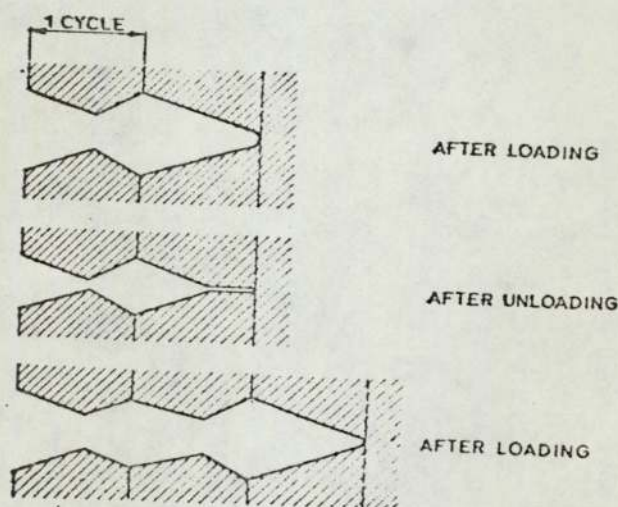


FIG. 24. Crack tip sharpening during unloading. (After Schijve (100))

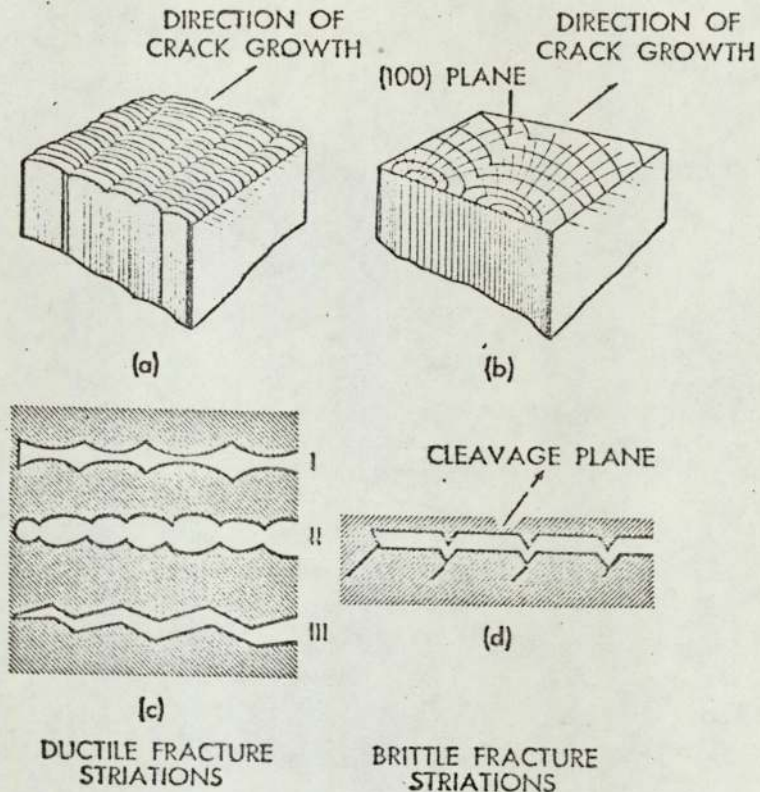
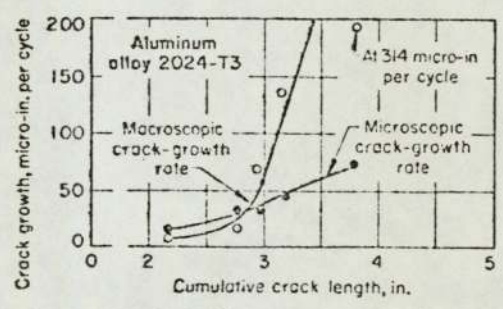


FIG. 25. Different Types of Ductile and Brittle Fatigue Striations; (a) and (b) Are Taken from Forsyth (85)

(After Beachem and Pelloux (102))



Data were obtained on specimens of aluminum alloy 2024-T3, 0.050 in. thick, fatigue tested at a frequency of 1000 cycles per minute. Microscopic rate was determined by striation spacing. Macroscopic rate was estimated from observed crack growth in successive groups of stress pulses.

Fig.26. Relation between microscopic and macroscopic crack-growth rates and cumulative crack length in fatigue fracture

(After Ref:107)

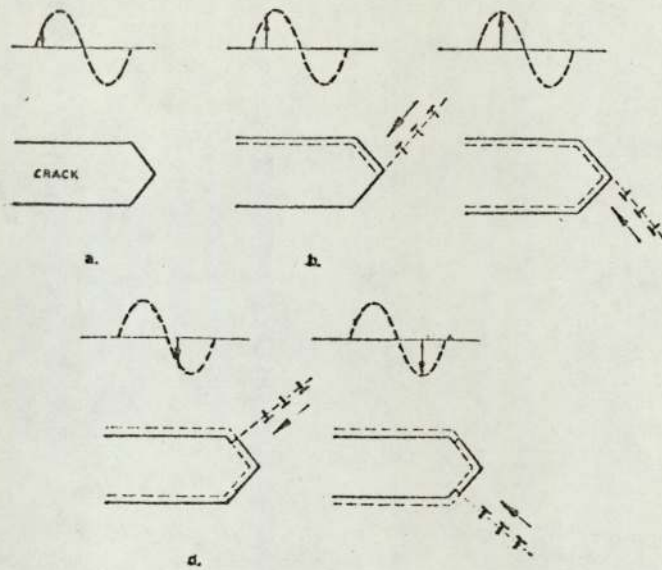


FIG. 27. Crack extension in one load cycle by dislocation movements on two different sets of crystallographic planes (After Ref:109)

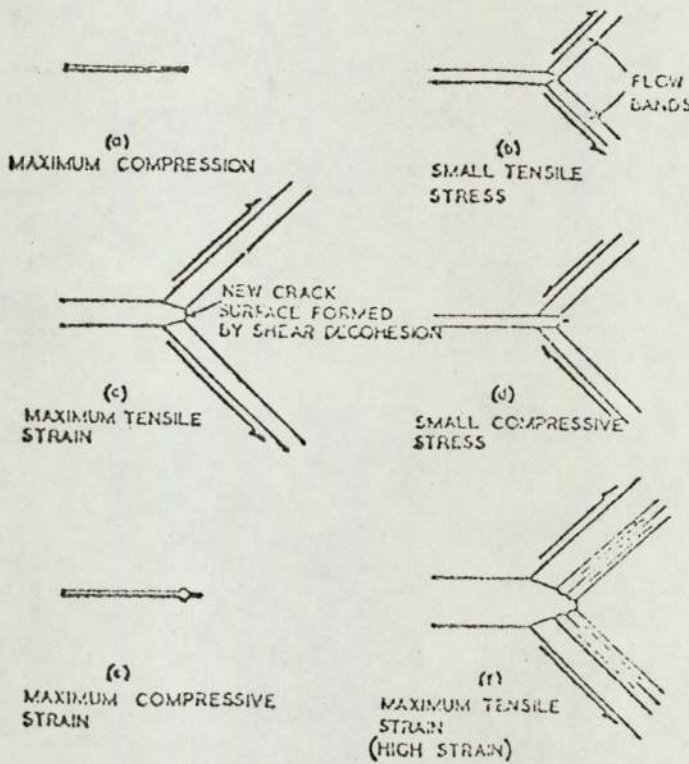


Fig. 28. Shear decohesion mechanism for Stage II crack growth. (After Ref:112)

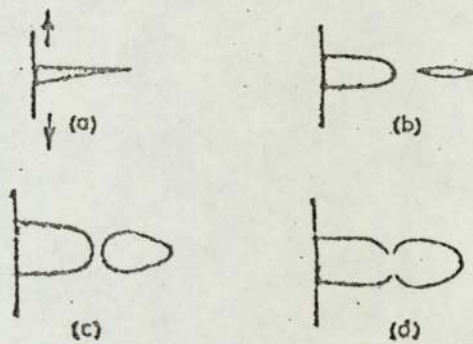


Fig. 29. Fatigue crack growth during one cycle of stress : (a) end of compressive half cycle, which may have cracked inclusions ahead of crack tip; (b) tensile half cycle blunts crack tip and produces void ahead of crack in region of triaxial tension; (c) thinning of unfractured bridge under biaxial tension; (d) final separation of bridge by thinning.

(After Ref: 116)

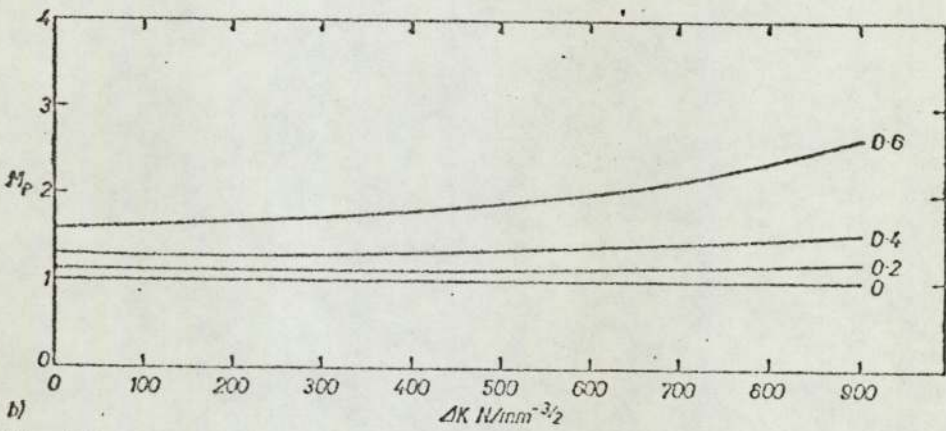
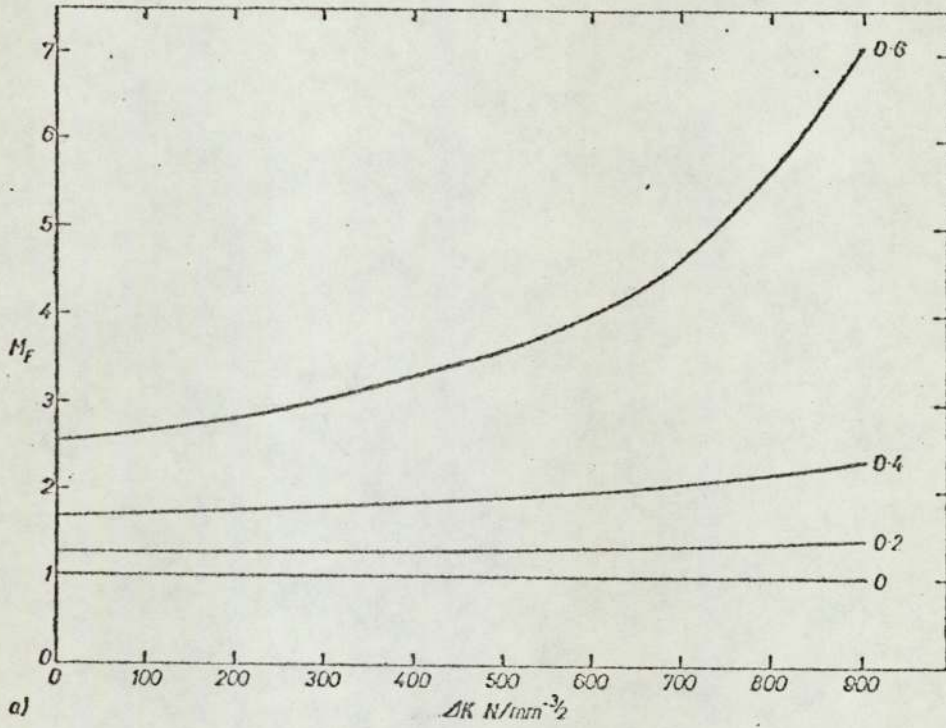


Fig. 30. Comparison of variation in crack propagation magnification factors proposed by (a) Forman [31] and (b) Pearson [14] with ΔK , for a high toughness value ($K_{Ic} = 3000 \text{ N mm}^{-3/2}$).

(After Maddox (146))

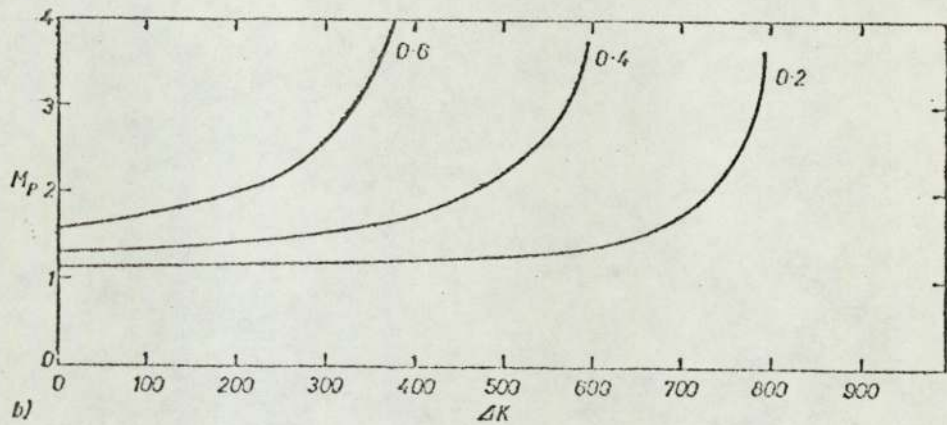
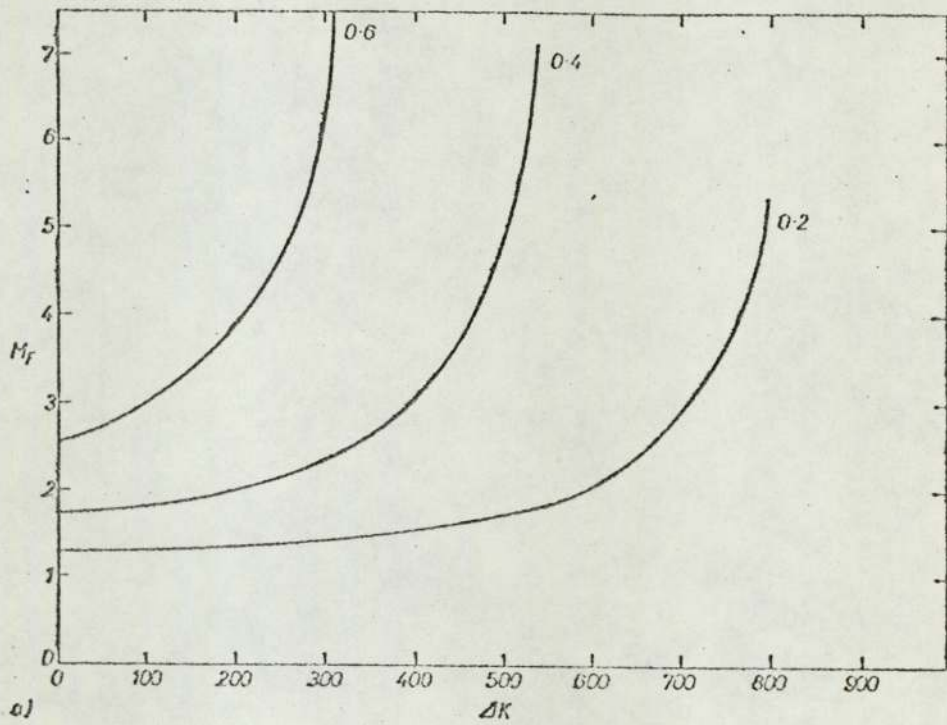
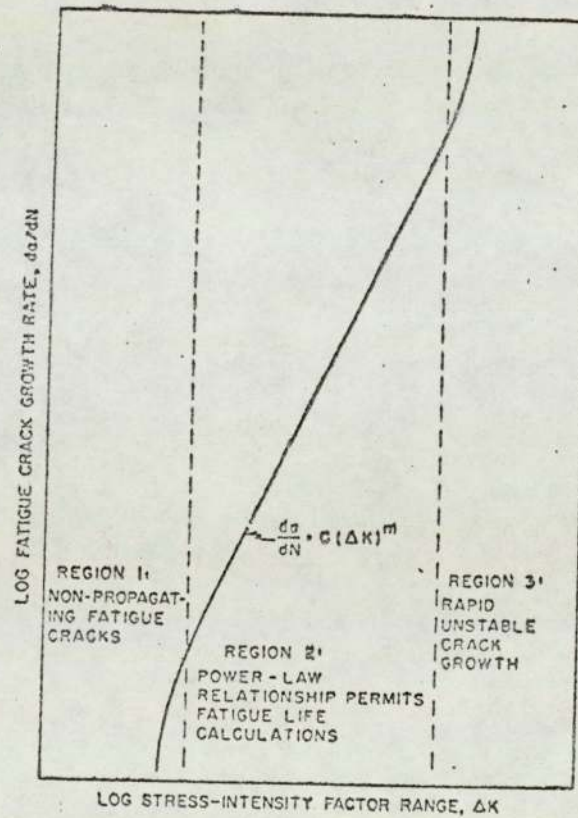


Fig 31 Comparison of variation in crack propagation magnification factors proposed by (a) Forman [31] and (b) Pearson [14] with ΔK , for a low toughness value ($K_{Ic} = 1000 \text{ N mm}^{-3/2}$).

(After Ref:146)

Fig. 32. Schematic illustration of the typical sigmoidal crack-growth-rate curve for structural alloys as plotted on logarithmic coordinates
 (After Crooker (154))



8. EXPERIMENTAL DETAILS

8.1 OBJECTIVES WITH AN OUTLINE OF EXPERIMENTAL WORK

It has been stated in the introduction of the review that there is a general lack of data on the fracture toughness and fatigue properties of sintered components, which are, by definition and nature, heterogeneous. So an attempt has been made to extract some data to evaluate their fracture toughness, fatigue crack initiation and propagation characteristics by applying the concepts developed for homogeneous continuum material models.

The experimental work had been designed primarily to study the influence of sintered densities, % dilution, etc. on toughness and fatigue resistance using the concept of Linear Elastic Fracture Mechanics (L.E.F.M.). In this way, the major factors affecting the growth of cracks or defects in sintered materials could be quantitatively described so as to provide meaningful engineering design data. In conjunction with this work, investigations had also been directed towards the understanding of some of the mechanisms involved in fatigue and fatigue crack extension.

In order to simplify the experimental observations, and the interpretation of the data, rectangular cross-sectional specimens with single edge notches (S.E.N) had been used.

8.2 POWDER MATERIALS

The basic maraging steel material, in the as-received condition, was in the form of pre-alloyed atomised powder, -60 mesh size, supplied in two grades W127 and W119, the main difference being in the Ti content.

The other material, Ancoloy SA (Höganäs) was also in the form of pre-alloyed powder made from sponge iron to which the finely divided alloying elements had been diffusion bonded.

The maraging steel powder, grade W127 (high Ti), had been diluted with iron powder of grade ASC.100.29 (Höganäs) which is extremely pure with very high compressibility. The chemical compositions of (a) maraging steel powder of grade W127 (high Ti), (i) in the as-received condition, (ii) after compaction, sintering and final heat treatment, and (iii) after 25% and 50% dilution with pure iron powder are given below. Also given below are the compositions of (b) low Ti maraging steel powder, grade W119 and of (c) Ancology SA.

(a) Powder Grade Code W127Compositions (Wt %)

In as-received condition	After compaction and sintering	After dilution* with iron Powder (I.P.)	
		with 25% I.P.	with 50% I.P.
C - 0.010	0.02	0.015	0.01
Ni - 18.30	17.30	12.975	8.65
Co - 8.00	8.17	6.1275	4.085
Mo - 5.50	6.14	4.605	3.07
Ti - 0.99	1.20	0.90	0.60
Al - 0.008	0.18	0.135	0.09
S - 0.017	0.018	0.0135	0.009
Zr - 0.015	-	-	-
B - 0.002	0.001	-	-
Ca - 0.020	-	-	-
Si - 0.070	0.11	0.0825	0.055
P - 0.015	0.018	0.0135	0.009
Cr - 0.10	0.08	0.06	0.04
Mn - 0.05	0.03	0.0225	0.015
H ₂ loss (1150°C) 0.02			
Fe - Balance	Balance	Balance	Balance

* Estimated composition, after dilution, compaction, sintering and heat-treatment.

(b) Powder Grade Code W119 -- In as-received condition only.

(Low Ti Grade)

C - 0.02

Ni - 17.60

Co - 8.90

Mo - 4.60

Ti - 0.01

S - 0.018

Si - 0.010

P - 0.014

(c) Ancoloy SA

In as-received condition (i)	After compacting and sintering (ii)	After (ii) + quenching and Tempering
Cu - 1.50	1.42	1.43
Ni - 1.75	1.64	1.66
Mo - 0.50	0.55	0.56
C - 0.01	0.65	0.79
SiO ₂ - 0.16	0.20	0.20
H ₂ -loss - 0.10	-	-
Fe - Balance	Balance	Balance

8.3 SPECIMEN PREPARATION - COMPACTION, CALIBRATION

As recommended by the supplier, Högans of Sweden, 0.60% graphite + 0.65% Zn Stearate had been added to ANCOLOY SA powder, which was then mixed in a rotary drum for 25 minutes. Two lots of the admixed powder had been compacted using a specially designed die-system, Fig.33, to pressures ranging from 398 to 598 MN/m² to achieve green densities of 6.7 and 7.0 Mg/m³.

A fixed amount of maraging steel powder, grade W127, had been compacted at pressures P_1 , P_2 and P_3 (let us call this M_1). Then two lots of maraging steel powder, grade W127 had been mixed with 25% and 50% Högans iron powder (grade ASC.100.29) in a rotary drum for 25 minutes. We call these M_2 and M_3 respectively. The same amount, as in M_1 , of diluted maraging steel powder was then compacted using the same set of pressures P_1 , P_2 and P_3 to yield densities, d_4 , d_5 , d_6 and d_7 , d_8 and d_9 for M_2 and M_3 respectively, where $(d_1, d_4, d_7) < (d_2, d_5, d_8) < (d_3, d_6, d_9)$, Fig. 34.

Then corresponding to the three fixed green density levels of P_1 , P_2 , and P_3 , compaction pressures P_1, P_2, P_3 were read out for each of the materials compacted, namely M_1 (maraging steel powder compacts only), M_2 (M.S.P. + 25% iron powder compacts) and M_3 (M.S.P. + 50% iron powder compacts). This method yielded more or less the same green densities when compacted at the pre-selected or calibrated pressures, e.g. :-

<u>Green Densities</u>	<u>Compaction Pressures</u>	<u>Compacted Materials</u>
$P_1 (5.8 \text{ Mg/m}^3)$	P_1	M_3
	P_2	M_2
	P_3	M_1
$P_2 (6.1 \text{ Mg/m}^3)$	P_4	M_3
	P_5	M_2
	P_6	M_1
	P_7	M_3
$P_3 (6.4 \text{ Mg/m}^3)$	P_8	M_2
	P_9	M_1

or re-written as following, yields :

<u>Compacted Materials</u>	<u>Green Densities</u>	<u>Compacted Pressures</u>
M_1	P_1	P_3
	P_2	P_6
	P_3	P_9
M_2	P_1	P_2
	P_2	P_5
	P_3	P_8
	P_1	P_1
M_3	P_2	P_4
	P_3	P_7

8.4 TEST SPECIMENS

These were of the single-edge-notched (S.E.N.) type for use in three point bending and machined and notched to the average dimensions, Fig. 35, after treatments as detailed in section 8.5.

The maraging steel powder compacts (with Ti \sim 1.0%) and diluted ones had been designed to the following matrix :

M_{11}	M_{12}	M_{13}
M_{21}	M_{22}	M_{23}
M_{31}	M_{32}	M_{33}

where M_1 = maraging steel powder compacts (Ti \sim 1.0%)

M_2 = M_1 + 25% pure iron powder compacts,

M_3 = M_1 + 50% pure iron powder compacts,

and where, second subscripts refer to the three levels of sintered (and final) densities. The specimens in M_{13} , M_{23} , M_{33} and M_{32} of the matrix had $\frac{\text{notch depth}}{\text{width}}$ i.e. $(\frac{a}{W})$ ratio = 0.1, and those in the rest of the matrix and specimens with low Ti had $a/W = 0.3$, with the nominal range of notch root radii from 0.127 to 0.762 mm. Ancoloy SA compacts, sintered, and sintered-quenched-tempered ones were made in two levels of densities with $\frac{a}{W} = 0.3$, and notch root radii of 0.127 mm. Fracture toughness tests had been made on all types of compacts, and also crack initiation and propagation studies had been carried out on all types of compacts, except on those made from Ancoloy SA compacts.

8.5 TREATMENT OF SPECIMENS

The green maraging steel compact specimens had been sintered at 1300°C for 3 hours in a vacuum furnace and cooled in the same furnace. The specimens were then annealed at 815°C for an hour per 25.4 mm. (1.0 inch) of thickness, in 90/10 N_2/H_2 atmosphere, followed by cooling at one end of the annealing furnace using the same atmosphere. After annealing, the specimens were machined to a tolerance of ± 0.025 mm (± 0.001 inch) on the major dimensions and notched to

dimensions, as shown in Fig. 35. The specimens were finally aged at 485°C for 3 hours in 90/10 N₂/H₂ atmosphere.

The green Ancoloy SA (ASA for short) compacts were sintered at 1120°C for an hour using the mixed gas of 90/10 N₂/H₂ as the furnace atmosphere, and cooled at one end of the furnace with the same atmosphere. The specimens, after sintering, were machined and notched, Fig. 35, and then austenitized at 850°C for 30 minutes, quenched in oil, and finally tempered at 175°C for an hour in air. The compact specimens needed surface grinding to the extent of about 0.025 mm. to remove fine surface scales.

8.6 PLANE STRAIN FRACTURE TOUGHNESS TESTING

Single-edge-notch (S.E.N.) bend specimens loaded in 3-point bending were used for determination of fracture toughness. Tests were done on a 50KN-capacity Instron machine operating at a constant rate of 0.02 cm/min. (cross-head speed). Method of mounting clip-in displacement gauge is shown in Fig. 36. Four 350 ohm strain gauges were connected in a Wheatstone Bridge balanced circuit and excited by a C₅₂ transducer amplifier unit.

The amplified response from the clip gauge together with the load signal from the Instron load cell, was fed into a Bryan's X - Y plotter. Location of the clip gauge across the notch was by means of attachable knife edges positioned accurately with the help of a spacer blade.

Bend specimens were tested on an adjustable bend jig. Overall span to specimen width ratio of 4:1 was used, as recommended by B.I.S.R.A. (155).

To produce a suitable starting crack for a toughness test, each specimen notch had to be extended by fatiguing. Fatigue pre-cracking was done on an Amsler Vibrophore fatigue machine using a 2 ton dynamometer, Fig. 37. The final length of the fatigue crack had been generally maintained between the a/w ratios of 0.45 and 0.55, as recommended by B.S.I.⁽¹⁵⁶⁾. The figure of $0.0005E$ suggested by B.I.S.R.A.⁽¹⁵⁷⁾ as an estimate of the fatigue crack propagation stress intensity range was not found satisfactory for the sintered specimens and it was necessary to exceed this value⁽¹⁵⁸⁾.

Fatigue pre-cracking was followed with the help of a low power binocular microscope, and the final 1.25 mm. (0.050 in.) of crack growth was estimated from graduations made at an interval of 0.50 mm. (0.020 in.) on the surface of the specimens. The last 1.25 mm. of crack extension was always made to take place over at least 50,000 cycles, according to the A.S.T.M. recommended practice⁽⁶⁵⁾.

A load/opening displacement record was obtained from each test from the Bryan's X - Y plotter attached to the Instron machine. The critical load was determined from the load/displacement record using the 5% offset procedure, recommended by B.S.I.⁽¹⁵⁶⁾, Fig. 38. All tests were carried out at least in duplicate, and whenever possible, in triplicate.

8.7 CALCULATION OF KQ

The provisional value of K_{IC} , i.e. KQ, was calculated from PQ, Fig. 38, using the following relationship⁽¹⁵⁶⁾ :

$$\begin{aligned}
 KQ = \frac{3PQ \cdot L}{BW^{3/2}} & \left[1.93 \left(\frac{a}{W} \right)^{1/2} - 3.07 \left(\frac{a}{W} \right)^{3/2} \right. \\
 & + 14.53 \left(\frac{a}{W} \right)^{5/2} - 25.11 \left(\frac{a}{W} \right)^{7/2} \\
 & \left. + 25.80 \left(\frac{a}{W} \right)^{9/2} \right] \dots\dots\dots (35A)
 \end{aligned}$$

(where $L = 2W = \frac{S}{2}$)

which can be written as

$$KQ = \frac{Y \cdot PQ}{BW^{3/2}} \dots\dots\dots (35B)$$

where

- P is the load
- B is the specimen thickness
- W is the specimen width
- a is the crack length
- S is the span between supports

and where the values of Y for specific values of $\frac{a}{W}$ are given in tables for different types of specimen and loading conditions.

8.8 CRACK GROWTH MEASUREMENT

Apart from direct observation of the specimen surface, various other means of monitoring the initiation, growth and instability of cracks, have been developed and these are summarized in Table II^(159,160).

TABLE II
CRACK GROWTH MEASUREMENT TECHNIQUES

<u>METHOD</u>	<u>USAGE</u>	<u>ADVANTAGES</u>	<u>DISADVANTAGES</u>
Microscopy techniques	Sheet and plate test-pieces. Photography sometimes used	Cheap. Easy installation.	Difficulty of crack tip location without stroboscopic light. Only surface measurements possible during test. Difficult to automate.
Mechanical methods	Rotating bend test pieces. Sheet, plate, and others depending on displacement gauge used	Use of compliance change which can be measured externally away from specimen.	Restricted to tests where compliance calibration (relationship between specimen stiffness and crack length) is known.
Acoustic methods	Applicable to most types of test-piece	Very small probe required, can be mounted easily; useful in low- and high-temperature tests.	Errors due to back-ground noise and calibration is difficult
Electrical techniques	Continuity gauges usually used on sheet and plate samples, could be used for surface measurements on other test-pieces	Electrical signal gives easy automation.	Difficulty of connecting wire and foil gauges. Gauges must break when crack passes. Only surface measurement.

Eddy currents	Used on surface crack monitoring of sheet test-pieces; others should be possible.	Easily adapted to automatic process. Small probe which is not in contact with test-piece.	Not yet used on thicker samples, may only be useful for surface measurement. Expensive.
Electrical resistance or potential measurement	Used on sheet and plate test-pieces	Easily adapted to automatic process. Only four leads attached to specimen, therefore ideally suited for high- or low-temperature tests	Problems of insulating the test-piece. Initial calibration problem thought to be overcome.
Ultrasonics	Ideally suited to compact fracture toughness test-pieces.	Easily adapted to automatic process. Internal measurement of crack front.	Expensive compared to other techniques. Measurement restricted to thicker type test-pieces.

In fatigue testing, it is required to measure the length of the crack with respect to the number of cycles so that data could be analysed by Fracture Mechanics, and the selection of any of the techniques mentioned must take account of its accuracy, speed of operation, reproducibility, cost, probability of automation, ease of application, whether continuous and flexible enough to apply to most standard test geometries and environments including tests at low ($\sim -100^{\circ}\text{C}$) and high ($\sim 500^{\circ}\text{C}$) temperatures. Since the electrical potential method seemed to satisfy all the requirements desired, it was adopted as the crack monitoring device used in this investigation.

Though first used by Barnett and Troiano⁽¹⁶¹⁾ in 1957 in fracture research studies, the electrical potential drop (p.d.) technique had been reported in detail in 1966 by Gilbey and Pearson⁽¹⁶²⁾.

The basis of the p.d. method is that in a current carrying body, there will be a disturbance in the potential field about any discontinuity in that body. For the purpose of monitoring crack growth, the method thus entails passing a stabilized current through a cracked test-piece under load, and measuring the electrical potential difference across the crack. As this crack extends, the uncracked cross-sectional area of the test-piece decreases, its electrical resistance increases, and the potential difference between two points on either side of the crack rises. By monitoring this potential increase (V_a) and comparing it with that across a unit length measured elsewhere on the uncracked test-piece (V_o), preferably in a region which is not affected by crack growth, the crack length (a) may be deduced from graphs relating V_a/V_oW to a/W , where W is the width of the specimen. A set of typical graphs of V_a/V_oW versus a/W is shown in Fig. 39 with the location of potential lead in the specimen, Fig.39A.

The sensitivity of the p.d. technique can be changed by different mode and amount of current application, the positioning of potential measuring points and their distance of separation. The sensitivity also depends on the instruments used to measure the potentials which are usually of micro-volt range. Possible sources of inaccuracy in the data resulting from using the p.d. technique can be stated as :

- a) Instability of constant current power supply.
- b) Error from thermo-electric E.M.F.s. generated due to dissimilar metals being connected between potential leads and the specimen.
- c) Temperature variation in the specimen or in the testing environment.

- d) Inefficient insulation of specimen and earthing.
- e) Drift of amplifying system.

By passing a current of 15 amps through the specimen, the sensitivity of monitoring crack advance by the p.d. technique was of the order of 0.005 W, i.e. about 0.12 mm., which compared favourably with Ritchie's⁽¹⁶⁴⁾ and Pisárski's⁽¹¹⁴⁾ figures. In the present investigation, a highly stabilized Farnell constant power source of maximum 50 amps. capacity was used. A current of 15 amps. was passed to the specimen through cleaned and polished copper strips screwed at the ends of the specimens, thus minimising or eliminating errors due to instability of the p.d. measurements. The potential leads used were nichrome wires ('Brightray C'), 0.193 mm. in diameter spot welded to the specimen. The potential drop was measured by a Rikadenki D.C. micro-voltmeter which gave a 100 μ V full-scale deflection. As the potential drop exceeded 100 μ V with the growth of the crack, a back-off voltage, supplied from a potentiometer, was used to maintain the full-scale deflections. A schematic diagram of the potential drop method is shown in Fig. 40. The output from the voltmeter was recorded on a Kent Chart Recorder in order to obtain a permanent record of the voltage reading. From the knowledge of the cycling frequency of the fatigue test, the time axis was converted to the number of cycles elapsed.

8.9 POTENTIAL DROP CALIBRATION

The current leads were connected to the specimen via copper strips screwed to the ends of the specimen to reduce contact resistance. The p.d., V_a , was measured across the notch by using nichrome wire leads spot welded at $x = 0$ (i.e. crack length = 0) for maximum sensitivity,

and at $y = 0.05W$ on either side of the notch centre-line. The uncracked potential gradient V_0 was measured on the specimen surface using a lead spacing of about 5 mm, Fig. 39A; the reading obtained of V_0 was then multiplied by a factor to get V_0W , so that the final lead spacing was equivalent to unit length of specimen width, W . This yielded greater accuracy in V_0W , instead of measuring V_0 simply across specimen width W .

Electrical insulations of the specimen and screening of leads from the specimen to the D.C. microvoltmeter were found necessary to prevent the pick-up of extraneous electrical signals. The specimen was insulated from the three contact loading areas by using paxolin sheet.

Constant current was passed through the specimen for about 2 hours before any readings were taken. Before settling down to a constant value, the p.d. across the notch dropped by about 20 to 40 $\mu V.$, and once stabilised the monitored voltage remained stable within $\pm 0.25 \mu V.$ Variation in laboratory temperature or closeness to electric lamp was found to affect the voltage reading. So utmost care was taken to minimise errors from these sources.

The fatigue crack was allowed to grow after the initiation event; however, the growth (for two different sets of specimens, one set with notch depth = $0.3W$ and the other with notch depth = $0.1W$) was stopped at an interval of about 200 $\mu V.$ potential drop (V_a) reading; the specimens were then broken open by partially sawing through from the side opposite to the notch and fracturing the remaining ligament at liquid N_2 temperature, Fig. 41. The crack length on the fatigue zone was optically measured at several points (15 to 20) and the average length was taken, corresponding to the particular potential drop reading. The values of a/W corresponding to different values of $\frac{V_a}{V_0W}$

were then plotted, Fig. 42. Standard 1900 Fortran language (application programme UA01) was used to fit 5th. order polynomials through the plotted points. The values of a/W corresponding to $\frac{V_a}{V_{0W}}$ were then tabulated at intervals of 0.001, for notch depths of $0.3W$ and $0.1W$, and for locations of potential leads as indicated in Fig. 39A. The equations of the calibrated curve at $x = 0$, $y = \pm 0.05W$ is described by the following polynomial :

$$a/W = C_0 + C_1 X^1 + C_2 X^2 + C_3 X^3 + C_4 X^4 + C_5 X^5$$

where $X = V_a/V_{0W}$

and (for notch depth = $0.3W$) (for notch depth = $0.1W$)

$$C_0 = -0.37923$$

$$C_0 = -0.038728$$

$$C_1 = 1.08720$$

$$C_1 = 0.39111$$

$$C_2 = 0.18724$$

$$C_2 = 0.58961$$

$$C_3 = -0.86128$$

$$C_3 = -0.84611$$

$$C_4 = 0.51272$$

$$C_4 = 0.44153$$

$$C_5 = -0.097861$$

$$C_5 = -0.083686$$

In Fig. 42 is also shown the theoretical calibration curve derived by Gilbey and Pearson⁽¹⁶²⁾ using the electrical potential method, for comparison. From this figure, it could be seen that calibration through separate notch lengths produce a distinctly separate curve from that for a crack only. For a particular notch depth, the fatigue crack, once initiated, extends from the notch and approaches the crack only curve and finally merges with Gilbey and Pearson's theoretical curve for the same positioning of potential leads in the specimen. The reduction in initial slope of the curves (a) and (b), Fig. 42, also means that the potential drop method is less sensitive in measuring short growth of a crack from a notch than for measuring the subsequent increase in length of a crack alone.

Gilbey and Pearson⁽¹⁶²⁾ have found the results obtained with p.d. technique in very good agreement with optical measurements of the crack on the specimens surface and were within the accuracy of the optical method, which was taken as 0.13 mm. ($\sim 0.005''$).

The essential difference between visual method and potential drop technique is that the former gives only the surface crack length, whereas the latter measures the average crack length of a bowed crack front, bowing being more pronounced at short crack lengths. Taking into account this aspect of crack front bowing makes the potential drop technique more reliable; it is also capable of detecting the crack initiation event long before the crack is visible on the surface.

8.10 METHOD OF CRACK GROWTH RATE CALCULATION

The fatigue growth rate had been calculated by using the method of finite differences. This involved using the ratio of finite differences in crack lengths to the number of cycles, i.e.

$$\frac{da}{dN} = \frac{a_{n+1} - a_n}{N_{n+1} - N_n} \quad \text{at } a = (a_{n+1} + a_n) / 2 \dots\dots\dots(36)$$

For an acceptable low level of scatter in the crack growth rate, the intervals between the crack length measurements, i.e. $(a_{n+1} - a_n)$ were taken to be sufficiently large, i.e. about 0.5 mm. The raw data from the fatigue tests were processed using a simple computer programme so that the input of potential drop, number of cycles, load amplitude, specimen dimensions etc., resulted in the output of crack growth rate, and ΔK , the stress intensity factor range. No plastic zone correction was made.

Other method of measuring crack growth rate involves differentiating 'a Vs N' curve (i.e. crack length Vs. number of cycles) or

graphically drawing tangents to the curve at various points. This method tends to be laborious and can be inaccurate at low and high crack growth rates. Difficulties in fitting polynomials to the $a - N$ data have also been reported by Davies and Feddersen⁽¹⁶⁵⁾.

8.11 FATIGUE CRACK INITIATION

Crack initiation studies were carried out on maraging and diluted maraging steel powder-compact specimens having notch root radii of 0.127 mm. and 0.762 mm., and having three different density levels. The notch root radii were measured individually; they were viewed at X100 magnification on the screen of a Vicker's projection microscope. The magnified radii of the image was then measured by a specially prepared transparent sheet bearing concentric semicircles with radii ranging from 5 to 80 mm. in 5 mm. increments. In view of the fact that the notch roots tended not to be of constant radius around their circumference, the smallest radius in each case was located and measured; this method was repeated for the other side of the notch. The accuracy of machining notch root radii was found to be within ± 0.02 mm. (~ 0.001 ").

The initiation load (for 3-point loading in compression) was calculated using the following equation,

$$\frac{\sigma_y}{Kt^G} = \sigma_{\text{gross}} = \frac{M \cdot y}{I} \text{ i.e. } \frac{6P}{BW} \dots\dots\dots(37)$$

whence $P_{\text{max.}} = \frac{\sigma_y}{Kt^G} \cdot \frac{BW}{6} \dots\dots\dots(38)$

where Kt^G = gross stress concentration factor calculated using a computer programme on the basis of Neuber's equations (127, Appendix-I)

$$= Kt_{\text{nett}} \cdot \left(\frac{W}{w}\right)^2 ,$$

and $M = \frac{PL}{2}$

$$y = \frac{W}{2}$$

$$L = 2W$$

$$I = \frac{BW^3}{12}$$

$$P = P_{\text{max}} = \Delta P \quad (\text{when } P_{\text{min.}} = 0)$$

B = thickness of specimen

W = width of specimen

w = nett width of specimen.

Knowing σ_y , the yield strength of the materials, Kt^G , B and W, $P_{\text{max.}}$ or ΔP , the load amplitude, was calculated. For each set of specimens, there were two different types of notch root radii, 0.127 and 0.762 mm.; for each type of root radius, the initiation tests were carried out on specimens $\ll 3$ in number, using varying load amplitudes, based, of course, on the calculated one. The overall stress range used for the initiation tests was from 43.4 MN/m² to 237.6 MN/m² and tests were done on an Amsler Vibrophore fatigue testing machine using a fixed frequency of 130 to 140 hz depending on the nature of the materials.

The point of initiation was detected by using the electrical potential drop technique. The actual point of initiation was taken to be the number of cycles at which the initial potential drop across the notch had first shown a definite increase on the chart recorder.

8.12 CONSTANT LOAD FATIGUE TESTS

In order to generate a wide range of ΔK values over the range of crack lengths for which compliance function was available, a suitable load range was selected for both low and high ΔK values. After initiation of the fatigue crack from the notch at relatively high load as indicated in section 7.11, the test load was applied. The constant amplitude test load for low and high ΔK values ranged from (1.4 ± 1.2) to (2.2 ± 2.0) KN for the sintered specimens of density level 1, from (1.5 ± 1.3) to (2.6 ± 2.4) KN for density level 2, and from (1.8 ± 1.6) to (3.0 ± 2.8) KN for density level 3 at a stress ratio of $R \sim 0.07$. The constant load amplitude for test at the higher stress ratio of $R = 0.3$ was 5.6 KN i.e. (5.2 ± 2.8) KN. The crack growth measurement was started at about $0.35 W$ (for specimens with notch depth = $0.3 W$) and $0.15 W$ (for specimens with notch depth = $0.1 W$) using the potential drop equipment. With Amsler Vibrophore fatigue testing machine, it was found that the constant load amplitude could be maintained to a maximum crack length of about $0.65 W$.

8.13 MECHANICAL TESTING

Tensile tests were carried out on No. 12 Hounsfield test pieces machined from the fractured half of toughness testing specimens. A Hounsfield tensometer fitted with a 2-ton beam and split collets was used for this purpose. Meaningful results for % reduction in area and elongations were not expected from these small tensile specimens. For accuracy and consistency, all the tests were duplicated and in some cases, triplicated. Hardness measurements were made on samples representative of each series. To avoid unreliable results due to porosity, Brinell hardness tester was used with a 10 mm. ball indenter and a load of 1000 Kgf. Each result quoted is the mean of 10 hardness readings.

8.14 PHYSICAL EXAMINATIONS

8.14.1 METALLOGRAPHIC SPECIMENS

The metallographic specimens were impregnated with a combination of araldite/hardener (10:1) under low vacuum, left overnight for curing or setting, and normal metallographic techniques used in hot mounting and polishing. Impregnation with araldite/hardener mixture helped in preventing fine debris being lodged inside the pores on the polished specimen surface. 2% Nital was used for etching incoloy S.A. compact specimens, and a special reagent, 3 HCl 3 picral in alcohol, was used for etching maraging and diluted maraging steel compact specimens. Ordinary Vickers projection microscope had been used for obtaining photographs of the microstructures, and in some special cases, Reichert projection microscope had been used.

8.14.2 SCANNING ELECTRON MICROFRACTOGRAPHY

Fractographic survey on fractured surfaces was made on a Cambridge Scanning Electron Microscope (S.E.M.). The S.E.M. technique can be used for direct viewing of the fractured surface. In this, a finely focussed beam of electrons is made to scan the specimen surface and causes emission of secondary and back scattered electrons which are picked up by a detector. This signal is amplified and displayed on a cathode-ray tube as an image of the specimen surface. Contrast in the image is dependent on the nature and topography of the surface.

For use in S.E.M., the specimens were prepared by cutting to a depth of 3.5 mm. (about 1/8") parallel to the fractured face, and mounting on a special flat stud for insertion into the specimen chamber.

8.14.3 ELECTRON MICROPROBE ANALYSIS AND ELECTRON MICROSCOPY

A Cambridge Microscan 5 X-ray Microanalyser was used to identify the discrete phases present in the sintered compact materials, and to get an idea of the extent of diffusion into the matrix. With this equipment, quantitative analysis of small volumes ($\sim 1.0 \mu^3$) can be obtained by comparison of the x-ray intensity of a given element in the sample with that of a pure standard.

A Transmission Electron Microscope, made in Japan (JEOL 100 B) was also used to study the fractured surface. The surface was dipped in acetone, then covered with Bex-film (cellulose tri-acetate) which was stripped dry carefully; carbon was evaporated on the replica followed by shadowing with gold-palladium.

Extraction replicas, first introduced by Fisher⁽¹⁶⁶⁾ had proved particularly useful for inclusion identification and for studying their size distributions, morphology, and structure. For obtaining a reasonable extraction replica, it was necessary to etch or electropolish away the matrix in order to free the inclusions with a solution of (90/10) acetic acid glacial/Perchloric acid.

After evaporating carbon, the extraction carbon replica was then released from specimen by etching with a solution a 10% HCl/methanol.

The main drawback with the extraction replica technique is that extraction may modify the particles. In case of coherent or semi-coherent precipitates, coherency is lost by extraction. Moreover, extraction replicas tend to give an exaggerated idea of the volume fraction of particles in a sample, but it may give some idea of their location, for example, at grain boundaries.

8.14.4. QUANTITATIVE IMAGE ANALYSIS

To study the influence of distribution and number of pores on the mechanical properties of the sintered materials, the quantitative image analysing system, Quantimet 720 was used. Samples parallel with the plane of fracture were taken from the fractured half of the toughness specimens. After normal grinding and diamond polishing they were etched with 5% Nital to remove materials that might have flowed plastically into the pores during grinding. To remove all traces of etching and to represent a true section through the specimens, they were then repolished.

To obtain the area fraction value, which is the same as volume fraction, the actual area occupied by the pores and inclusions in 250 fields of view were measured and the result was a simple percentage of the area of pores and inclusions over the area examined in 250 fields which is 2.87 sq. mm. in fields of 0.0115 sq. mm. The optical magnification used was 315X, which on projection through the QTM 720 became finally 1300X.

9. RESULTS

9.1 MECHANICAL PROPERTIES, Etc.

Investigations of the mechanical properties, crack initiation and propagation characteristics had been carried out in the sintered maraging and diluted maraging steel powder compacts, but only the mechanical properties had been studied in Ancoloy SA compacts in the sintered, and sintered-quenched-tempered conditions.

The test results of the various mechanical properties, etc. studied are given in Table III. Fracture Toughness Validity test results are shown in Table IV.

The effect of % porosity on yield stress (σ_{ys}) and fracture toughness (K_{IC}) is shown in Fig. 43. It is very clear from this figure that the porosity content has a significant effect on yield stress and fracture toughness. Reduction in porosity below ~13% causes a marked rise in yield stress, while increase in porosity above ~13% causes a drop in yield stress, though the rise or drop in yield stress values in the case of material M_3 (maraging steel compacts diluted with 50% iron powder) is somewhat sluggish. There is, however, a significant rise in fracture toughness with reduction in % porosity. In the case of material M_3 , the gain in fracture toughness with the loss of porosity is remarkable.

In Fig. 44 has been shown the relationship between the fracture toughness (K_{IC}) and yield stress (σ_{ys}) for the three types of sintered steels investigated. In the case of material M_1 (maraging steel compacts) though the toughness increases with yield stress, there is a tendency for drop in the toughness values at higher yield stress, while with the material M_3 , the sharp increase in toughness values yields only a small increase in yield stress. The material

M_2 (M_1 diluted with 25% iron powder), however, shows a remarkable balance between increase in toughness and yield stress values.

Fig. 45 shows the elastic modulus (E_N) as a function of % porosity. The elastic modulus has been calculated by using the McAdam's⁽⁴⁶⁾ equation given by

$$E_N = 29 (1 - \epsilon)^{3.4} \times 10^6 \text{ psi.}$$

where E_N = elastic modulus of sintered steel, and

ϵ = fractional porosity.

9.2 PORE DISTRIBUTION

Table V shows the number and sizes of pores obtained by using the QTM 720 technique. The size distribution recorded was obtained by feature analysis, where the area of each 'pore' was considered individually and the number falling into each size category was recorded. The area parameter for each phase was chosen since the voids were of irregular shapes of random orientation, and particle diameter would not have given as true a measure of size distribution.

An attempt had been made to measure the inclusion content of the specimens, but it failed due to the fact that the inclusions were predominantly fine oxides and had a similar reflectivity to the 'pores'. Consequently separate detection 'thresholds' for pores and inclusions could not be operated, and therefore, only one result was recorded combining the voids and inclusions, and termed as 'pores'.

Treating the inclusions as pores should not be too inaccurate⁽¹⁶⁷⁾ since the particle/matrix interfacial strength is not particularly high. Moreover, it simplifies the analysis.

In Fig. 46 is shown the distribution of 'pores' in some of the sintered materials investigated. Predominantly large number of

'pores' are in the size range of $3 - 8 \mu\text{m}^2$. The nearest approximation would be to consider that the majority of inclusions are in this size range, and that the majority of voids are in the size range of $100 - 200 \mu\text{m}^2$. The existence of the wide range of size and shape of voids is also supported by the use of the Scanning Electron Microscope.

9.3 INITIATION RESULTS

In Table VI is shown all the relevant data relating to initiation studies for sintered and heat treated M_1 , M_2 , M_3 and LTM compacts. In Fig. 47 is plotted $Kt \cdot \Delta S$ (where Kt is the Neuber elastic stress concentration factor for the particular notch and ΔS is the range of nominal stress from zero to S_{max}), against N_i (number of cycles for initiation) for the notch root radii of specimens M_1 , M_2 , M_3 at three density levels, also of specimens LTM. The same N_i has been plotted against $\Delta K/\rho^{\frac{1}{2}}$ as shown in Fig. 48. The initiation behaviour of the two plots follows the same pattern. The 'banding' effect of notch root radii on initiation behaviour stands out markedly clear. This effect persists even if all the initiation results are plotted together, as shown in Fig. 49 for N_i Vs. $\Delta K/\rho^{\frac{1}{2}}$. However, when the same N_i is plotted against ΔK , Fig. 50, as shown separately for compacts at different density levels, the banding effect of notch root radii gives way to broader scatter band. The banding effect practically vanishes if a plot of N_i Vs. ΔK is made of all the initiation results, Fig. 51.

Judging from the slopes of the plots in Figs. 47 and 48, higher the density, higher were the number of cycles for initiation for compacts M_1 , M_2 and M_3 ; but for the same lower density d_1 , M_2

compacts needed higher number of cycles for initiation than M_3 compacts, only reason for which might lie in the distribution, size and shape of the pores in the vicinity of the notch tip in these low density compacts.

9.4 CRACK GROWTH RESULTS

Constant load amplitude tests at constant mean load (load profile in Fig. 52) were carried out at a stress ratio R of (a) ~ 0.07 for compacts M_{11} , M_{12} , M_{13} , M_{21} , M_{22} , M_{23} , M_{31} , M_{32} , M_{33} , L.T.M., and (b) 0.3 for compacts M_{13} , M_{23} and M_{33} . Crack propagation rates obtained by the method of finite differences have been plotted as a function of stress intensity ranges ΔK , Fig. 53 (a - k).

For growth rates at $R \sim 0.07$, there is the characteristic change in slope from stage 1 to stage 2 in the growth curve. The transition occurs at $\Delta K = 9 - 11 \text{ MN/m}^{3/2}$ for $R \sim 0.07$. Growth rate curves for $R = 0.3$ also show a transition at a slight higher value of $\Delta K \approx 12 \text{ MN/m}^{3/2}$. That is, at very low values of stress intensity factor and crack growth rate, a threshold for crack growth is approached for the types of sintered materials tested. The linear relationship obtained between $\log \Delta K$ and $\log \frac{da}{dN}$ in stage 2 is as predicted by equation (27). The stage 3 is not clearly defined since the increase in gradient of the curve occurs at very high crack growths which are difficult to measure.

It can be seen from table VII that the values of crack growth exponent m varies from 2.26 to 3.39 for compacts of M_1 series, from 2.87 to 4.38, for M_2 series and from 4.29 to 4.50 for compacts of M_3 series. The corresponding values of the pre-exponent C varies from 4.59 to 10^{-2} to 91.83×10^{-2} , from 0.63×10^{-2} to 7.55×10^{-2} and from 0.12×10^{-3} to 9.7×10^{-3} , when the growth rate is in nm/cycle,

and stress intensity in $\text{MN}/\text{m}^{3/2}$. For compacts of L.T.M. series, the values of m obtained is 5.17 and of C is 0.27×10^{-3} .

TABLE VII
THE VALUES OF m and C

MATERIALS CODE	DENSITY LEVELS					
	1		2		3	
	m	$C \times 10^{-2}$	m	$C \times 10^{-2}$	m	$C \times 10^{-2}$
M_1	2.26	24.77	2.81	91.83	3.39	4.59
M_2	2.87	1.62	3.59	7.55	4.38	0.63
M_3	4.50	0.97	4.29	0.47	4.50	0.012
LTM	m			$C \times 10^{-3}$		
	5.17			0.27		

The crack growth rate curves for M_{12} and M_{21} compact materials, when the stress ratio R is ~ 0.07 , are identical and nearly fall on the same scatter band, Fig. 54, the growth rate being 1.7 to 2.0 times faster than for M_{11} compact material, Fig. 53a over the range of ΔK considered (10 to $35 \text{ MN}/\text{m}^{3/2}$). Similar pattern has been noted for M_{13} and M_{22} materials, Fig. 55, the growth rate being 2.8 to 3.0 times faster than for M_{11} materials; the same thing also goes for M_{23} , M_{31} , M_{32} and M_{33} compact materials, Fig. 56, where the growth rates are about 6.7 to 7.0 times faster than for M_{11} material. For L.T.M.

material, the growth rate, Fig. 53j, has been found to be about 10.7 times faster than for M_{11} material.

At higher stress ratio ($R = 0.3$) the growth rate curves for M_{13} , M_{23} and M_{33} materials are also identical and nearly fall on the same scatter band, the rate being 2.2 to 2.5 times faster than for M_{13} and 6.0 to 6.2 times faster than for M_{11} compacts tested at the stress ratio of $R \sim 0.07$.

The above observations show that the crack growth curves for M_1 , M_2 and M_3 materials fall on four distinctly separate scatter bands, when the stress ratio R is ~ 0.07 . At the higher stress ratio of $R = 0.3$ and only at the highest density of compacts tested, another separate scatter band for crack growth data has been found. The same goes for the L.T.M. materials tested at $R \sim 0.07$, for which also a distinctly separate scatter band has been obtained. Though the values of m obtained are roughly indicative of this trend, it is the combination of the values of m and of the pre-exponent C that determines the rates of crack growth in each of these materials.

9.5 METALLOGRAPHIC OBSERVATIONS

An examination of the etched specimen of M_1 series in the sintered and fully heat-treated condition showed that the microstructure was essentially martensitic and massive in nature, Fig. 59, with pores more or less rounded in higher density compacts. Specimens of M_2 , M_3 and LTM series showed the martensitic structures with fair amount of ferrite, Fig. 60, 61. Pores of different geometry were visible in the specimens, their shape and size depending on the density of the compacts. Higher the density, finer and more rounded the pores. In the sintered condition, the structure for M_1 series of compacts was austenitic with well-defined grains and pores, Fig. 62.

Microstructures of Ancoloy SA compacts showed ferrite and lamellar pearlite in the sintered condition, Fig. 63, and tempered martensite (troostite) in the quenched and tempered condition, Fig. 64 with random distribution of pores of different geometry, depending, as before, on the density of the compacts.

Scanning Electron Microscope-image of the deeply etched microstructures showed clearly the random orientations of the martensitic plates in the M_1 series of compacts, Fig. 65. Some of the particles revealed by longer etching with the special reagent of 3 HCl 3 Picral in alcohol had been analysed to be some intermetallic compound of Ti, possibly Ti (C,N), Fig. 66.

The distribution of the elements in the maraging (M_1 series) and diluted maraging (M_2 and M_3 series) compacts was investigated by the electron probe microanalyser. It was found that the elements were finely well-distributed except for Ti, Mo and Co, Fig. 67, which showed some segregation.

Though mostly in clusters, two distinctly different types of inclusions had been observed in the unetched metallographic sections of M_1 , M_2 and M_3 series of compacts under unfiltered illumination in the light microscope, Fig. 68, 69, 70.

- (a) Angular inclusions, usually square or hexagonal. These appeared light pink or orange.
- (b) Elongated inclusions, appearing grey with a slight mauve or violet tinge.

Electron microprobe analysis showed that type (a) inclusions contained Ti and sometimes some Zr in the centre. Type (b) inclusions contained Ti, S and some Zr. It might be that the angular pink-orange inclusions were carbonitrides, in agreement with the description of

Ti (C,N) in the literature (168). Zirconium present in the centre of Ti (C,N) might be in the form of Zirconia or Zirconium Carbonitride. It is possible that, by analogy with Titanium Oxide (168), the Zirconium Oxide is read, while Zirconium Carbonitride is of the same colour as Titanium Carbonitride. Accurate analysis of the inclusions was not possible in the Electron Microprobe Analyser, since the inclusions were smaller compared to the cross-section of the electron beam resulting in the interference signals from the matrix around the inclusions. The qualitative results obtained with the Microprobe Analyser were confirmed by using a 'KEVEX' Energy Dispersive X-ray Analyser attached to the Stereoscan Electron Microscope.

The crack path was closely studied and found to be mainly influenced by the alignment, distribution, and shape and size of the pores ahead of the crack tip. The presence of numerous inclusions, mainly intermetallic compounds of Ti, on the path of the cracks also influenced the rate and direction of crack growth. The crack paths were not straight as shown in Fig. 71, 72 in the unetched condition. In all the powdered compact specimens, the effects of the distribution and alignment of pores (D.A.P.) on the crack path was so predominant that the favourable orientation effect of grain-boundary with respect to the direction of crack growth was difficult to assess. Also, the D.A.P. effects were clearly reflected in crack-forking, Fig. 73, - branching, Fig. 74, - arching, Fig. 75, island and pseudo-island formation, as shown in Fig. 76, 77. The extent of the D.A.P. effect could be gauged by observation of the crack tip, Fig. 78, where the crack tip seemed to lose its identity in the clusters of pores.

The formation of island, and branch cracks was the most general features of the powder compacts, due mostly to the D.A.P. effect.

These branch cracks were mainly inter-granular. The main branch of the crack seemed to be influenced by the presence of pores and inclusions in its path, whereas the branch cracks seemed to have been influenced by the presence of the pores, Fig. 79, 80. The extent of crack branching was such that it frequently caused the formation of islands in the crack path, Fig. 81.

9.6 FRACTOGRAPHIC OBSERVATIONS

The fractured surfaces of the compact specimens were closely investigated by the Steroscan Electron Microscope. The porous materials all had, more or less, a similar fracture surface with extensive plastic deformation and dimples, and some tendency to grain-boundary separation. The micromechanism of fracture was the coalescence of the microvoids in which case the internal linking drew out the walls of the pre-existing voids until the linkage occurred. The micromechanism was of the ductile dimple type in every case, Fig. 82, and the presence of pores evidently decreased the tendency to brittle cleavage fracture.

There was found no significant difference between fatigue and fast fracture surfaces as is normally found in non-compact materials. Also, no striations were observed on the fracture surfaces; there was no definite trend of a particular type of cracking associated with a particular stress intensity level.

Round particles found in the fracture surfaces were original powder-particles and least amenable to sinter-bonding, Fig. 83. The inclusions and the second-phase particles seemed to play a prominent role in the fracture process. In Fig. 84, the matrix did not adhere to the cubic Ti (C,N) inclusion which allowed the voids to open early

in the fracture process leading to tensile dimple rupture. Dimples shown in Fig. 82 were composed of more than two different sizes. The larger dimples probably formed at the Ti(C,N) particles. All of the dimples were probably caused by particles of some sort. Ti (C,N) particle shown in Fig. 85 triggering the formation of voids might have split before the void opened.

Some larger pores, Fig. 86, opened up during the fracture process by intergranular cracking, besides containing some remnants of Ti (C,N) particles being fusion-bonded to the internal pore surfaces, bore evidence of thermal etching undergone due to sintering at high temperature for a long time. Decohesion of inclusions from the matrix was also observed. Fig. 87 shows an iron-rich particle decohesed from the matrix during the fatigue crack propagation. Fracture surfaces also revealed some deep branch cracks running along the grain-boundaries, Fig. 88.

Transmission Electron Microscopy was also used in the study of the fracture surfaces. Thermal etching effects, left on the internal pore surfaces due to high temperature sintering had been revealed by Transmission Electron Microfractography. These fine markings should not be confused with striation markings which give an indication of micro crack growth rates. In Fig. 89 is shown a combination of big and small dimples and thermal etchings.

Using the Extraction Replica Technique and the Transmission Electron Microscopy, the precipitates extracted from the fractured specimens and shown in Fig. 90 were identified to be $\text{Ni}_3(\text{Al,Ti})$ and $\eta\text{-Al}_2\text{O}_3$. Other precipitates were much smaller and could not be analysed due to their size being smaller than the cross-section of the electron-beam.

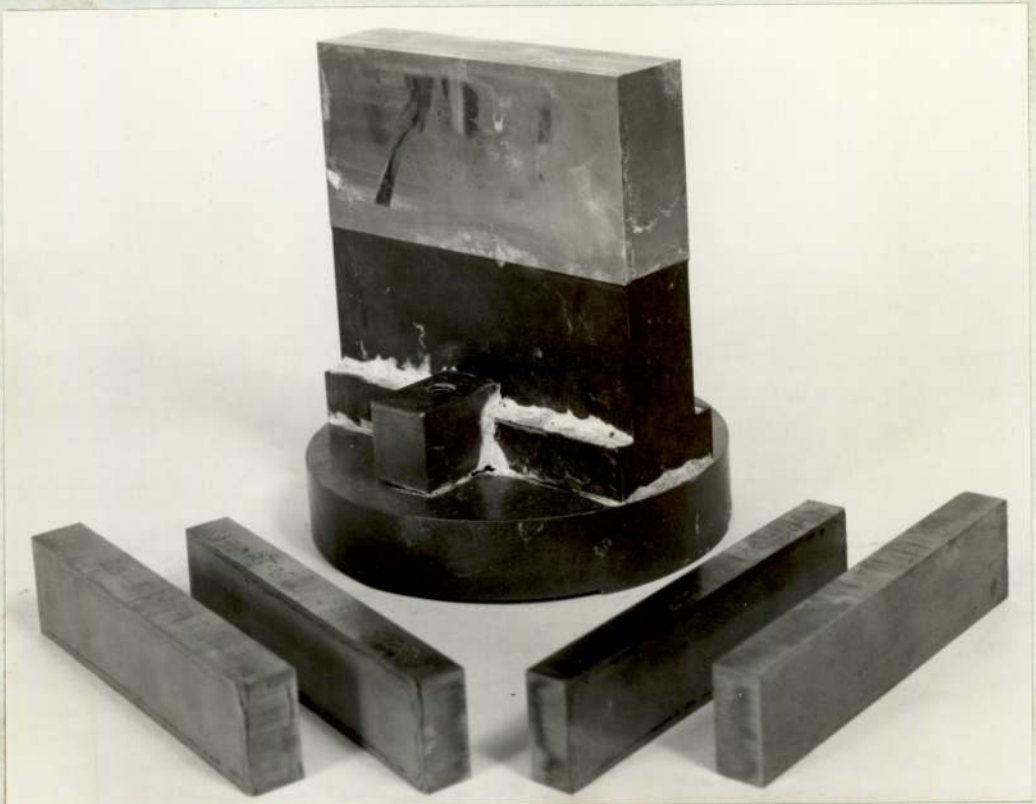
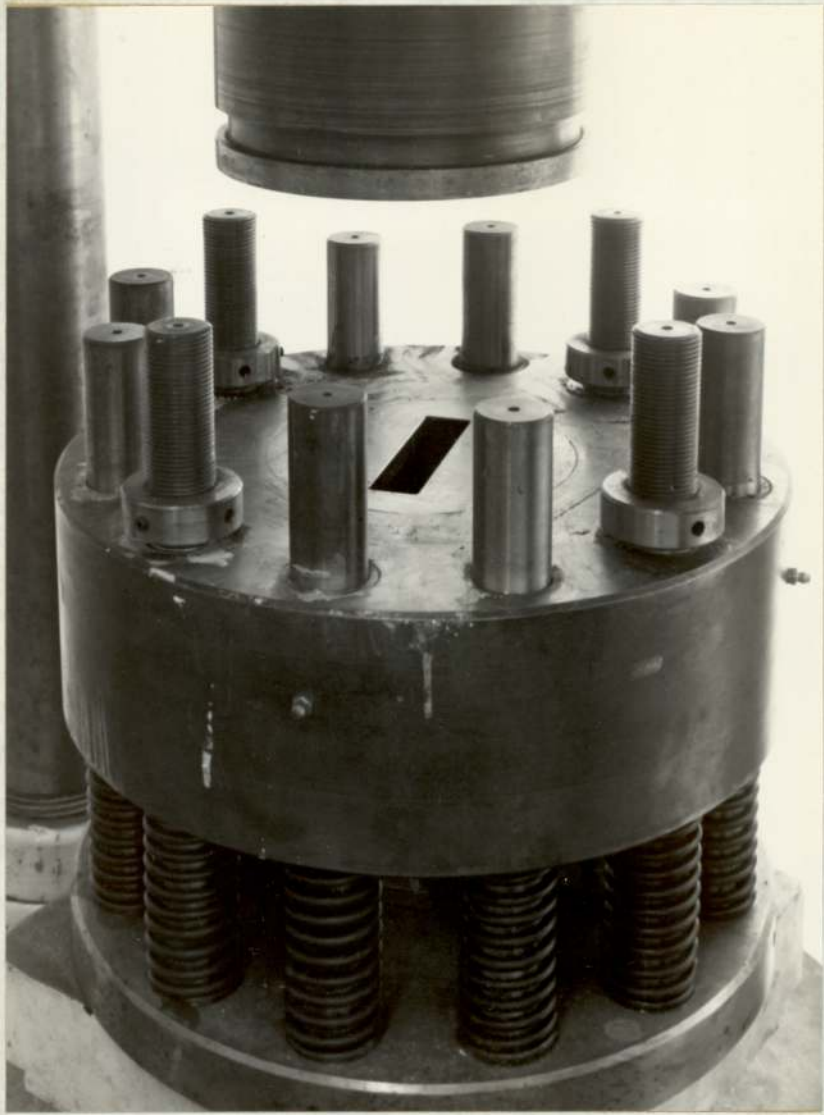


Fig.33. The Die-System and the Compacted Specimens.

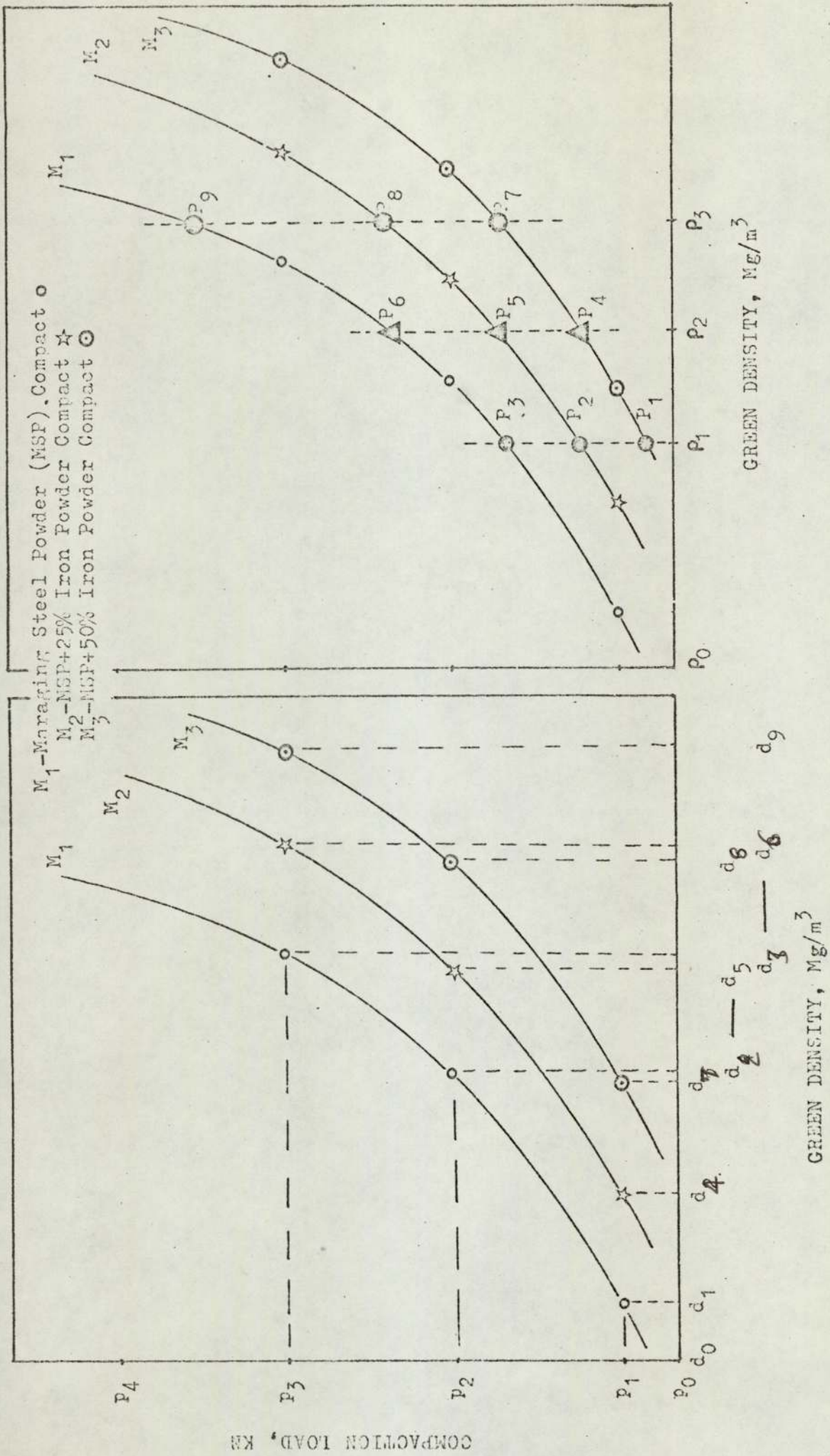


Fig. 34. Schematic representation for obtaining Calibration Curves of Compaction Load Vs Green Density.

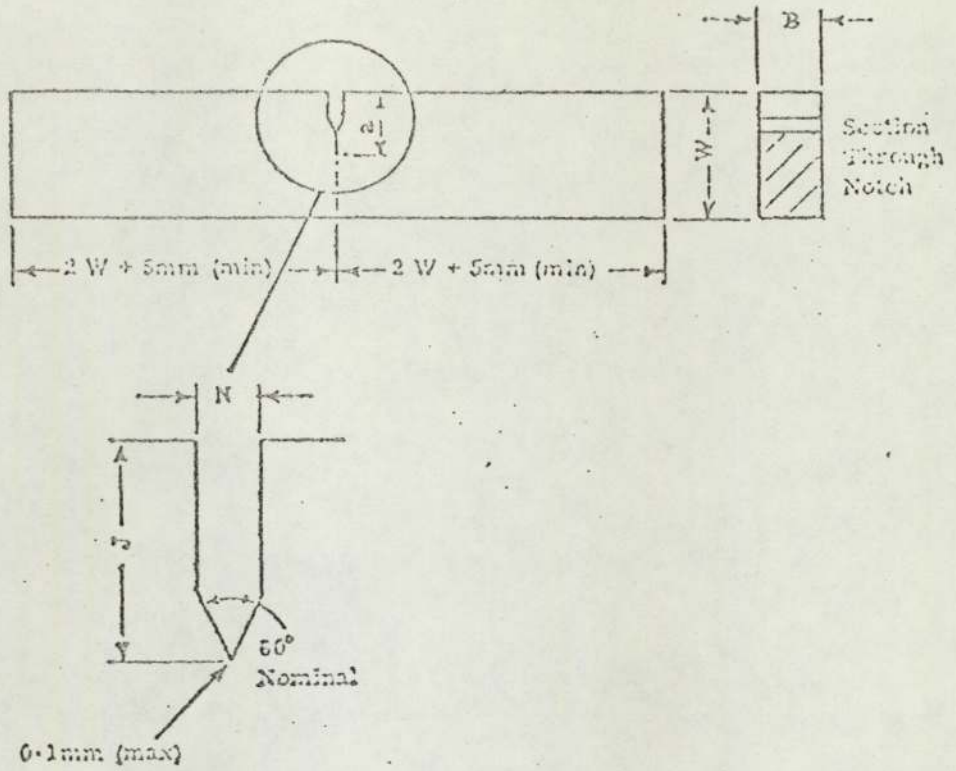


Fig.35. Dimensions of Single-Edge-Notch Bend Test-Piece.

MATERIAL A: Maraging and Diluted Maraging Steel Powder Compact, Sintered and Heat-Treated.

W	B	J	N	NOTCH ROOT RADIUS	NOMINAL ANGLE	TOTAL LENGTH
23.50 & 22.50	11.75 & 11.25	7.05 & 2.25	1.5	0.127, 0.762	60°	110

MATERIAL B: ANCOLOY SA Powder Compact, Sintered and Heat-Treated.

W	B	J	N	NOTCH ROOT RADIUS	NOMINAL ANGLE	TOTAL LENGTH
25.00	12.50	7.50	1.5	0.127, 0.254 0.508, 0.762	60°	110

Dimensions are in mm.

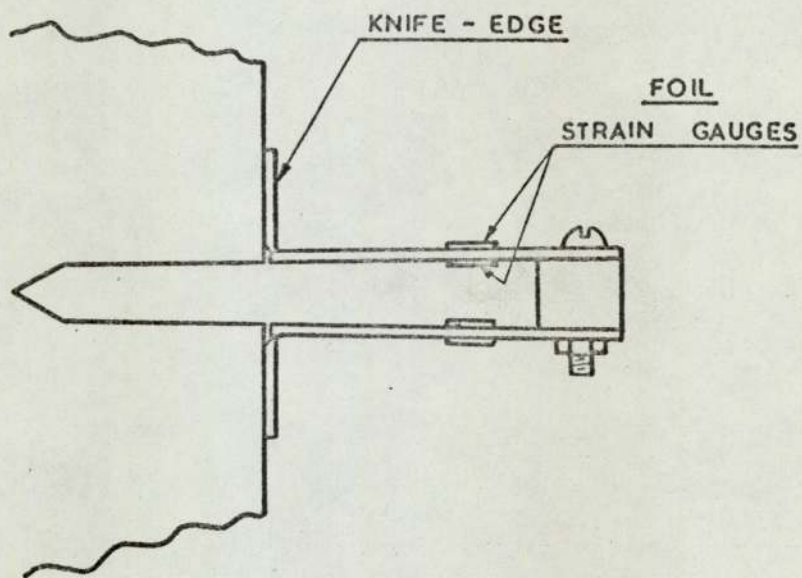


Fig.36. Clip-in Displacement Gauge and Method of Mounting.

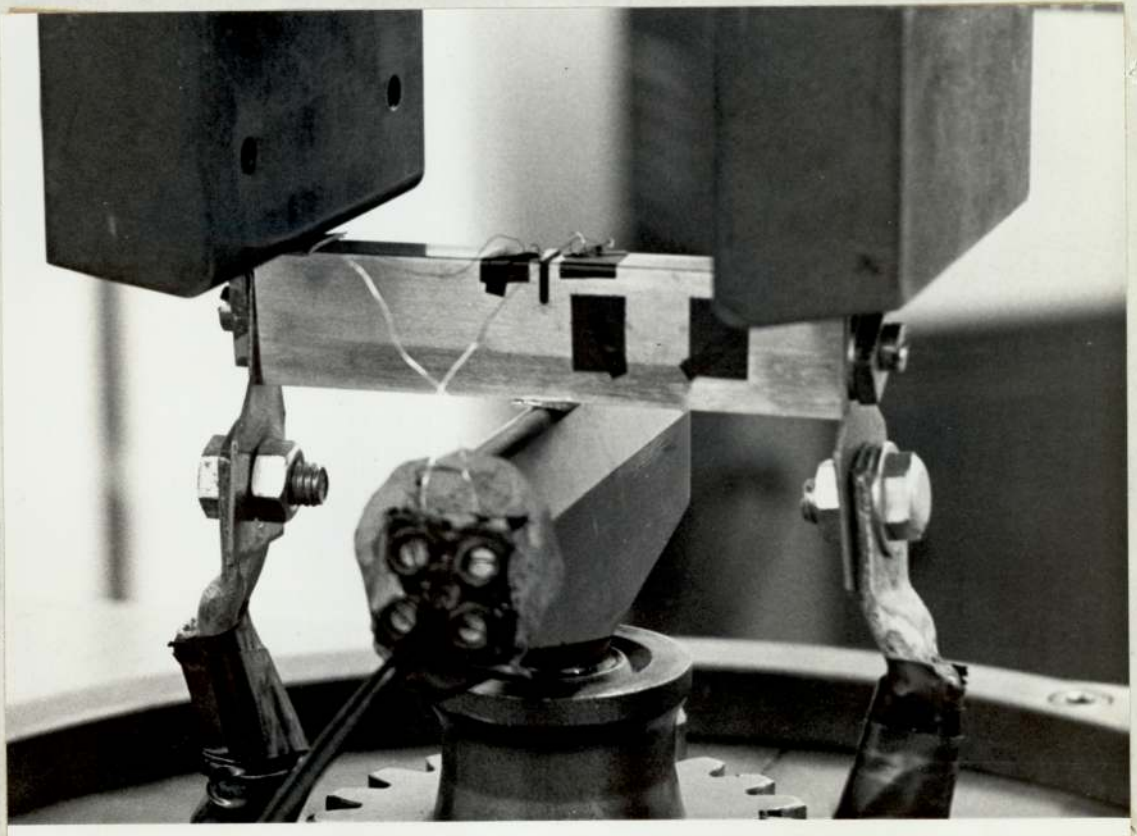


Fig.37. Amsler Vibrophore Fatigue Testing Machine and Potential Drop Unit with the Close-up of Specimen Connections.

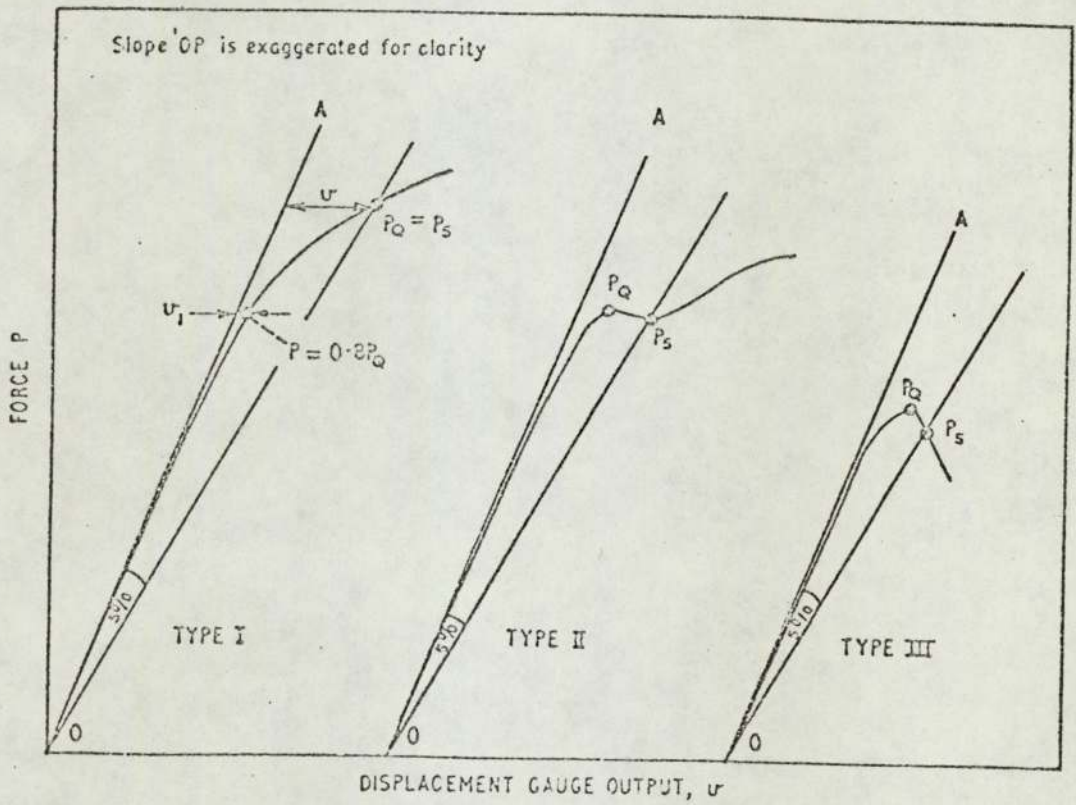


Fig. 38. Principal types of force/displacement records showing quantities involved in analysis (After B.S.I. (156)).

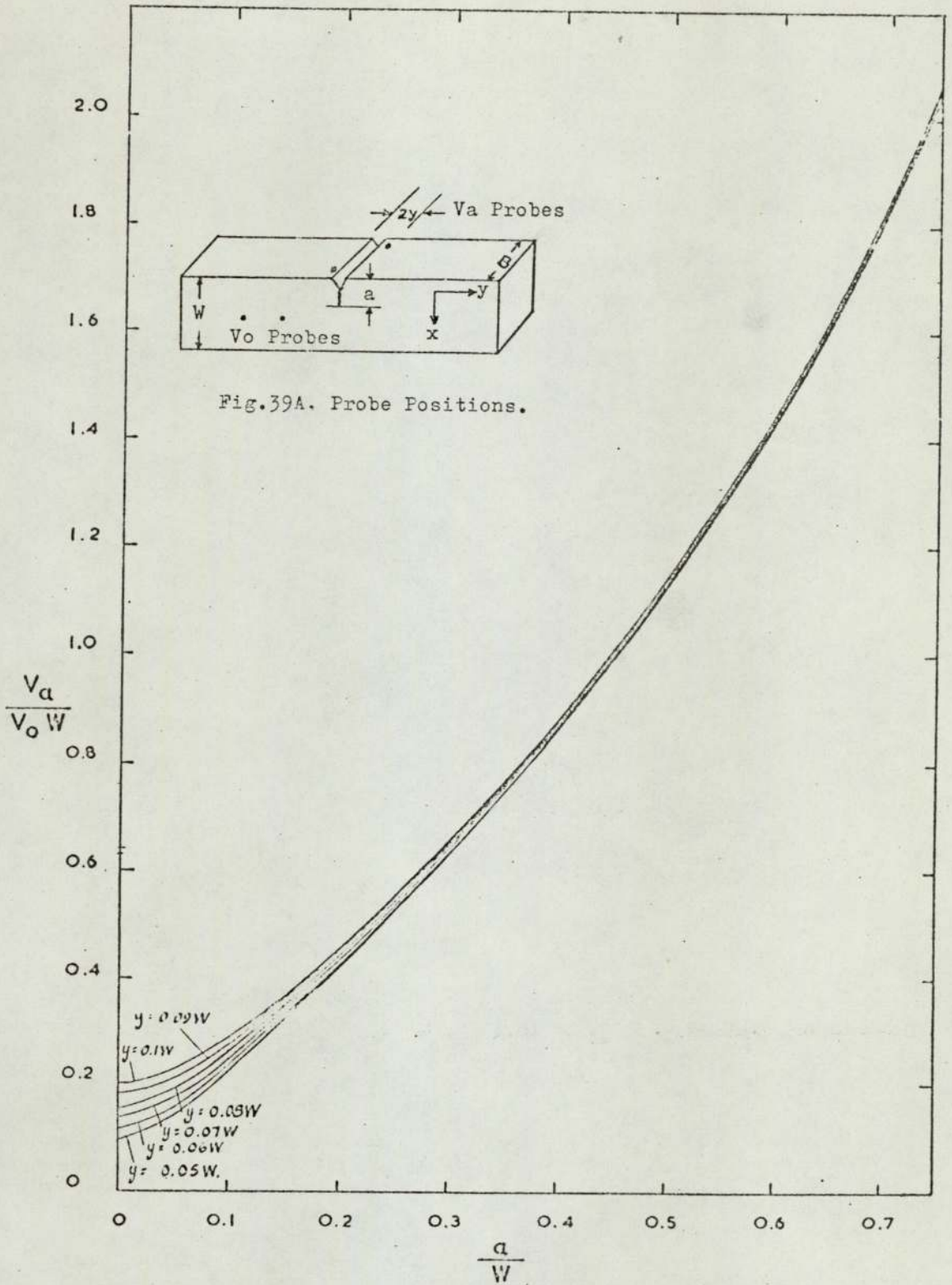


Fig. 39. GRAPH OF $\frac{V_a}{V_o W}$ VERSUS $\frac{a}{W}$ FOR POTENTIAL MEASURING POINTS AT $x = 0$, $y = \pm$ VALUES SHOWN.

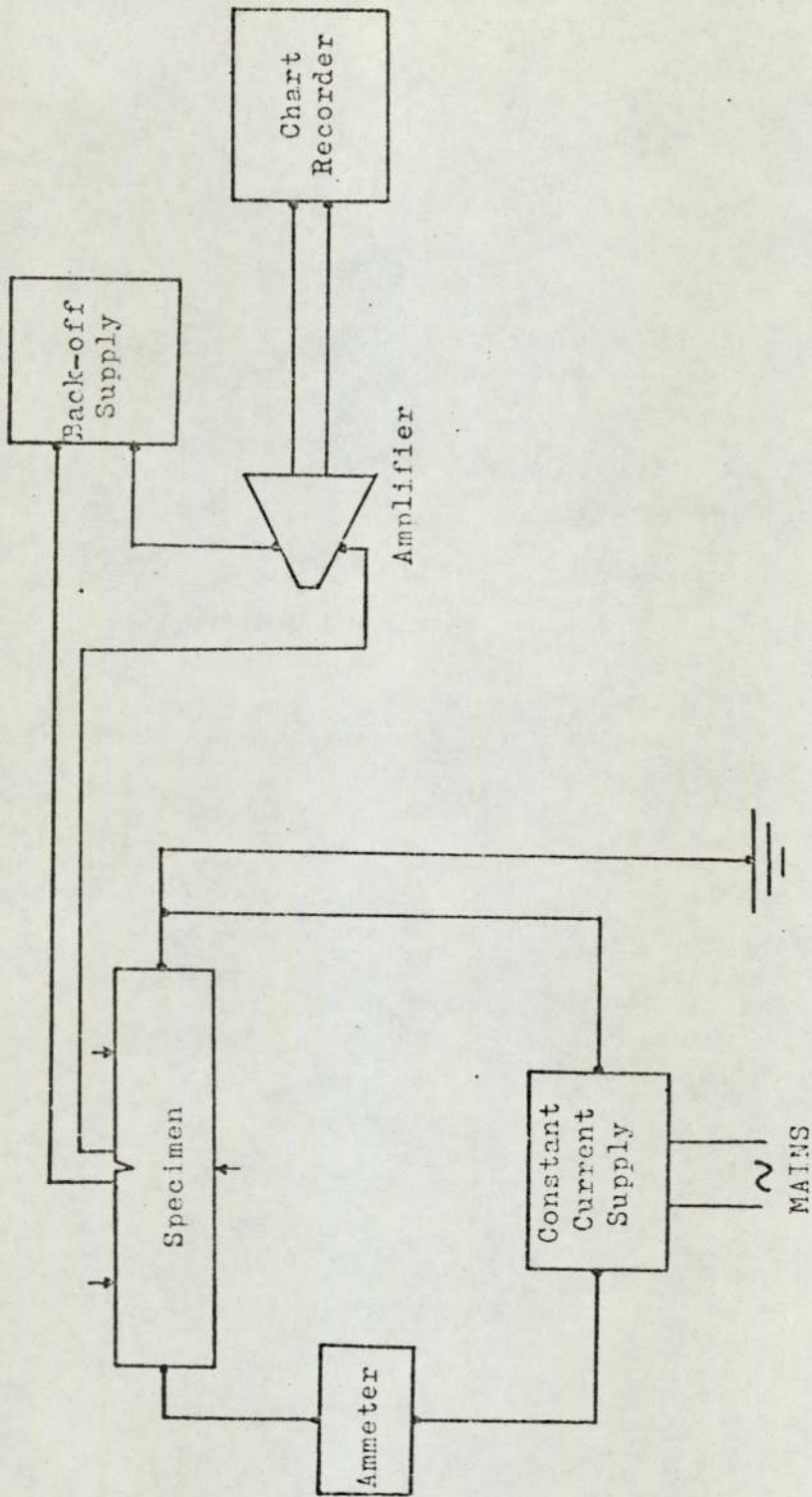


Fig.40. A Schematic Diagram of the Potential Drop Circuit.

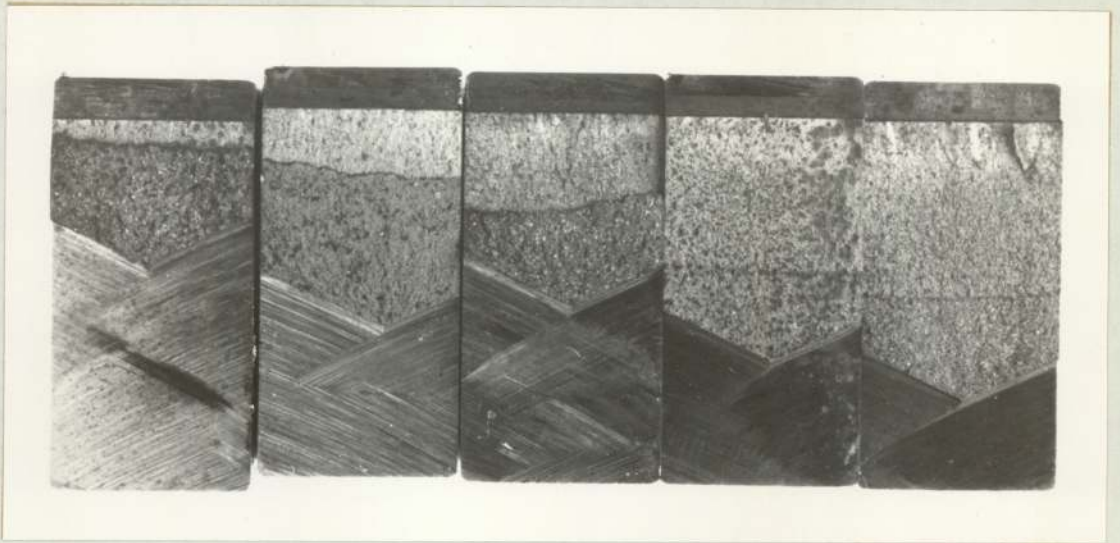


Fig.41. Examples of the Fractured Halves of Sintered Specimens for deriving the Calibration Curves of V_a/V_{oW} Vs. a/W .

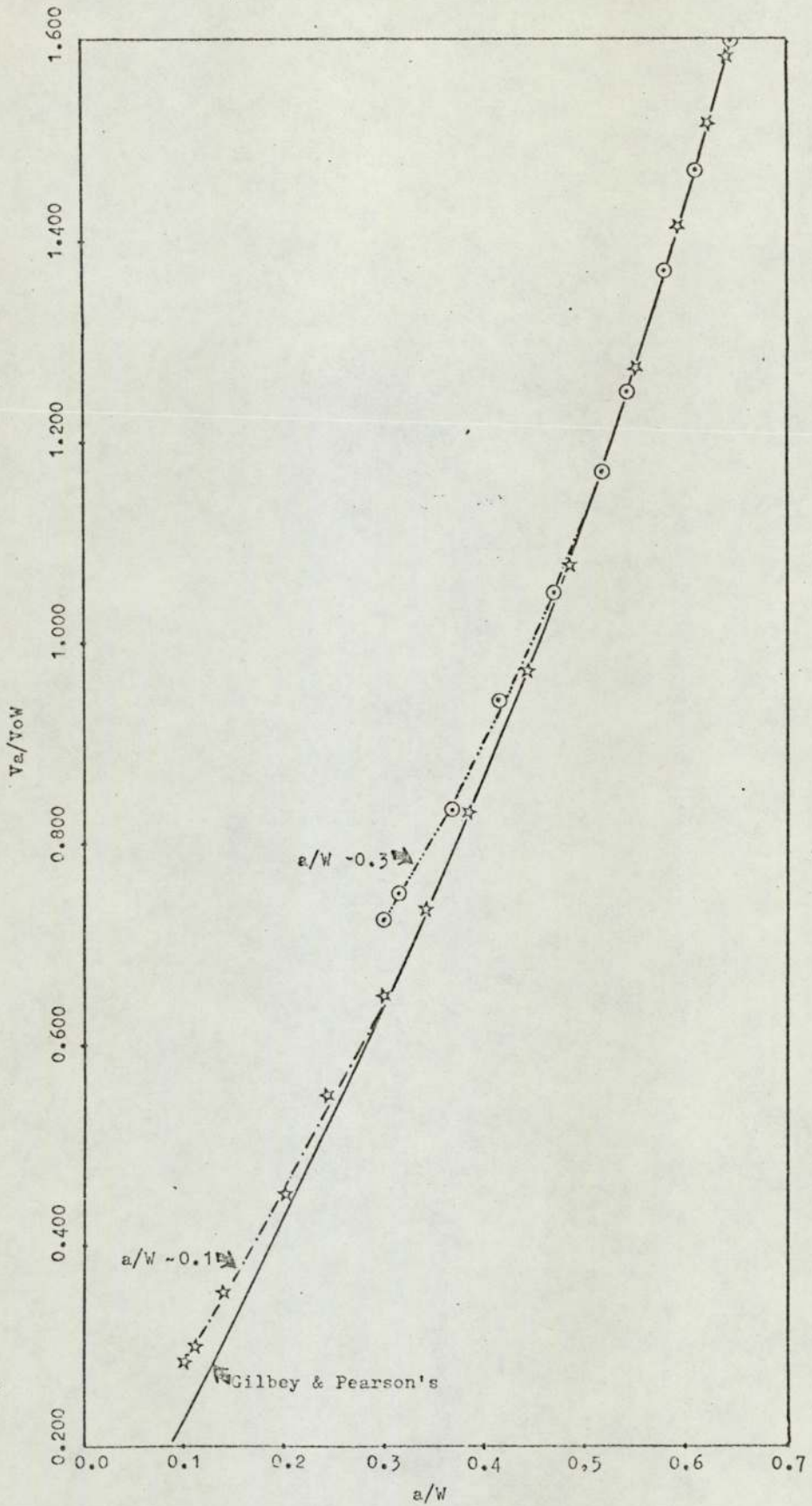


Fig.42. Potential Drop Calibration Curves for compact specimens with different a/W ratios.

TABLE III

ROOM TEMPERATURE MECHANICAL PROPERTIES

DENSITY LEVELS	1	2	3
Final Density, Mg/m ³ (After sintering and Heat-Treatment)	6.9	7.1	7.3

MATERIALS CODE M₁ (Maraging Steel Powder Compacts with high T_i)

K _{IC} , MN/m ^{3/2}	26.2	29.6	34.1
U.T.S. (Y.S), MN/m ²	842	899	1134
% E	2.5	2.5	2.5
% R.A	<0.5	<0.5	<0.5
Hardness, B.H.N.	250	292	368
Porosity, %	16.3	13.7	11.4
Elastic Modulus (E _N), GN/m ²	109	121	132

MATERIALS CODE M₂ (M₁ + 25% Iron Powder Compacts)

K _{IC} , MN/m ^{3/2}	27.5	30.4	34.7
U.T.S. (Y.S), MN/m ²	642	770	966
% E	3.5	2	2.5
% R.A	<0.5	<0.5	1.0
Hardness, B.H.N	188	205	270
Porosity %	16.1	12.9	9.8
Elastic Modulus (E _N), GN/m ²	110	125	141

MATERIALS CODE M₃ (M₁ + 50% Iron Powder Compacts)

K_{IC} , MN/m ^{3/2}	29.1	32.0	35.8
U.T.S. MN/m ²	521	562	639
Y.S. (* 0.2 % P.S.), MN/m ²	521	531*	601*
% E	3.0	3.0	5.0
% R.A	0.5	0.5	1.0
Hardness, B.H.N	120	145	173
Porosity, %	15.7	11.2	8.9
Elastic Modulus (E_N), GN/m ²	112	133	146

MATERIALS CODE LEM (Maraging steel Powder Compacts with Low Ti)

Final Density, Mg/m ³	6.6
K_{IC} , MN/m ^{3/2}	22.9
U.T.S. (I.S), MN/m ²	612
% E	1.5
% R.A	<0.5
Hardness, B.H.N	190
Porosity, %	18.9
Elastic Modulus (E_N), GN/m ²	98

ANCOLOY SA COMPACTS

DENSITY LEVELS	1	2
Final Density, Mg/m ³	6.7	6.9
Porosity, %	15.5	12.2
Elastic Modulus (E_N), GN/m ²	113	128

TABLE III - Cont'd.

MATERIALS CODE ASA-S (Ancoloy SA Powder Compacts, Sintered)

K_{IC} , MN/m ^{3/2}	24.9	28.5
U.T.S. (Y.S), MN/m ²	427	471
% E	2.5	3.0
% R.A.	<0.5	<0.5
Hardness, B.H.N.	149	179

MATERIALS CODE ASA-SQT (Ancoloy SA Powder Compacts, Sintered, Quenched and Tempered)

K_{IC} , MN/m ^{3/2}	25.8	29.6
U.T.S. (Y.S), MN/m ²	658	733
% E	1.5	1.5
% R.A.	<0.5	<0.5
Hardness, B.H.N.	327	372

TABLE IV

FRACTURE TOUGHNESS

VALIDITY TEST DATA

MATERIALS CODE	KQ MN/m ^{3/2}	$\sigma_{y.s.}$ MN/m ²	$2.5 \left(\frac{KQ}{\sigma_{ys}} \right)^2$ mm.	Thickness B, mm.
M ₁₁	26.2	842	2.42	11.75
M ₁₂	29.6	899	2.71	11.75
M ₁₃	34.1	1134	2.26	11.25
M ₂₁	27.5	642	4.62	11.75
M ₂₂	30.4	770	3.90	11.75
M ₂₃	34.7	966	3.22	11.25
M ₃₁	29.1	521	7.78	11.75
M ₃₂	32.0	531	9.06	11.75
M ₃₃	35.8	601	8.88	11.25
LTM	22.9	612	3.50	11.75
ASA-S (1)	24.9	427	8.52	12.50
ASA-S (2)	28.5	471	9.18	12.50
ASA-SQT (1)	25.8	658	3.83	12.50
ASA-SQT (2)	29.6	733	4.07	12.50

TABLE V

QTM720 IMAGE ANALYSIS OF THE NUMBER AND SIZES OF 'PORES'

MATERIALS CODE	VOL. FRACTION OF 'PORES' (%)	NUMBER OF 'PORES' WITH AREAS IN SIZES SHOWN IN pp*							
		<20	(20 -100)	(100-200)	(200-500)	(500-1000)	1000-5000	5000-10,000	<10,000
M ₁₁	16.3	13011	8191	965	1215	841	1320	332	147
M ₁₂	13.7	17682	12324	1338	1263	943	1485	263	66
M ₁₃	11.4	20632	15020	1375	1543	1095	1432	127	40
M ₂₁	16.1	15206	9460	1423	1434	935	1515	288	151
M ₂₂	12.9	19445	13594	1783	1654	845	1268	222	79
M ₂₃	9.8	18083	11805	2070	1836	100	1243	109	20
M ₃₁	15.7	12070	6399	1586	1498	884	1232	294	177
M ₃₂	11.2	13405	7353	1647	1630	1048	1385	220	122
M ₃₃	8.9	14400	8434	1900	1837	915	1163	124	25
ASA-S ₁	15.5	12707	6596	1769	1970	951	1138	193	90
ASA-S ₂	12.2	13167	6983	2048	1846	946	1134	133	76

* lpp = 1 picture point on the QTM screen = 0.227 μm diameter, \therefore lpp² = 0.0515 μm^2 .

TABLE VI

INITIATION RESULTS

MATERIALS CODE	P_{min} .	ΔP KN	ΔS MN/m ²	ΔK MN/m ^{3/2}	$Kt, \Delta S$	$\Delta K / \rho^{\frac{1}{2}}$	Ni x 10 ³ Cycles
M ₁₁	0.127	2.4	52.4	8.1	436.0	718.8	42
		3.2	69.4	10.6	576.9	958.4	90
		5.8	125.9	19.6	1046.6	1739.3	3
		5.4	117.2	18.2	974.5	1615.1	6
		2.2	48.0	7.4	399.1	656.7	170
	0.762	5.4	118.0	18.2	435.9	659.4	2
		2.8	60.9	9.4	225.2	340.6	21
		2.6	56.5	8.8	209.2	318.8	130
		4.0	86.9	13.5	321.6	489.1	4
	M ₁₂	0.127	3.8	82.4	12.8	685.2	1135.9
2.2			47.8	7.4	397.5	656.7	98
3.0			65.1	10.1	541.2	896.3	12
3.4			74.0	11.5	615.1	1020.5	10
2.6			55.5	8.8	469.5	780.9	48
0.762		5.8	126.8	19.6	469.0	710.1	5
		3.4	73.9	11.5	273.7	416.7	91
		3.0	65.4	10.1	242.1	365.9	240
		6.0	130.3	20.2	482.1	731.9	2
M ₁₃		0.127	8.8	210.1	17.6	1521.3	1561.8
	5.2		123.6	10.4	895.2	922.9	29
	8.6		205.5	17.2	1493.5	1526.3	4
	4.8		114.2	9.6	827.1	851.9	55

TABLE VI (Cont'd.)

MATERIALS CODE	$P_{lim.}$	ΔP KN	ΔS MN/m ²	ΔK MN/m ^{3/2}	Kt. ΔS	$\Delta K/\rho^{1/2}$	Ni x 10 ³ cycles
M ₂₁	0.762	9.0	214.6	18.0	1559.5	1597.3	3
		5.0	118.8	10.0	860.0	887.4	47
		4.4	104.7	8.8	758.3	780.9	130
		9.6	229.4	19.2	784.9	695.7	23
		8.4	200.8	16.8	686.1	608.7	12
		10.0	237.6	20.0	812.9	724.6	3
		9.2	218.8	18.4	748.5	666.7	9
		9.0	195.7	18.0	724.2	652.2	5
		8.0	174.2	16.0	644.6	579.7	20
	6.0	130.3	12.0	482.0	434.8	129	
	0.127	2.8	60.7	9.4	504.9	834.1	127
		3.0	65.2	10.1	542.2	896.3	28
		3.2	69.4	10.8	577.0	958.4	148
		3.6	78.4	12.1	651.7	1073.7	3
		0.762	5.8	126.0	19.6	466.6	710.1
5.2	113.0		17.5	418.5	634.1	27	
3.8	82.4		12.8	305.1	463.8	68	
4.0	86.8		13.5	321.7	489.1	180	
M ₂₂	0.127	4.4	95.3	14.8	792.1	1313.3	4
		3.0	65.0	10.1	540.2	896.3	57
		4.8	104.2	16.2	865.8	1437.6	2
		4.0	87.0	13.5	723.2	1198.0	18

TABLE VI (Cont'd)

MATERIALS CODE	$P_{min.}$	ΔP KN	ΔS MN/m ²	ΔK MN/m ^{3/2}	Kt. ΔS	$\Delta K/\rho^{\frac{1}{2}}$	Ni x 10 ³ cycles
M ₂₃	0.762	5.6	121.6	18.9	450.5	684.8	4
		3.8	82.5	12.8	305.7	463.8	27
		5.6	121.6	18.9	449.8	684.8	5
		5.4	117.3	18.2	434.3	659.4	20
		3.6	78.2	12.1	289.7	438.4	98
	0.127	5.2	123.6	10.4	895.0	922.9	66
		5.6	133.3	11.2	968.8	993.9	56
		4.4	104.8	8.8	761.9	780.9	484
		6.0	143.0	12.0	1043.2	1064.9	9
		6.2	147.6	12.4	1073.0	1100.4	5
	0.762	8.6	205.4	17.2	702.7	623.2	9
		8.8	209.3	17.6	716.0	637.7	16
		9.6	228.5	19.2	781.8	695.7	7
		7.8	185.3	15.6	633.8	555.2	91
		8.4	200.4	16.8	685.7	608.7	19
M ₃₁	0.127	3.4	73.8	11.5	613.3	1020.5	13
		3.8	82.5	12.8	685.5	1135.9	4
		2.4	52.2	8.1	433.6	718.8	350
		4.4	95.5	14.8	794.0	1313.3	2
	0.762	3.2	69.5	10.8	257.3	391.3	92
		5.8	125.7	19.6	465.4	710.1	2
		3.0	65.1	10.1	241.2	365.9	310

TABLE VI (Cont'd)

MATERIALS CODE	$P_{mm.}$	ΔP KN	ΔS MN/m ²	ΔK MN/m ^{3/2}	$Kt \Delta S$	$\Delta K / \rho^{\frac{1}{2}}$	Ni x 10 ³ cycles
M ₃₂	0.127	5.6	121.6	18.9	450.3	684.8	6
		3.4	80.8	6.8	584.7	603.4	381
		3.8	90.2	7.6	653.1	674.4	37
		3.6	85.6	7.2	624.5	638.9	188
	0.762	5.6	133.1	11.2	967.1	993.9	3
		6.4	151.7	12.8	519.0	463.8	16
		6.0	142.2	12.0	486.4	434.8	118
		8.0	189.7	16.0	649.1	579.7	2
		6.8	161.4	13.6	552.1	492.8	37
		8.0	189.7	16.0	649.1	579.7	2
M ₃₃	0.127	5.8	137.7	11.6	1000.6	1029.4	17
		4.8	114.4	9.6	828.0	851.9	100
		5.6	132.9	11.2	965.6	993.9	55
		5.0	119.0	10.0	868.6	887.4	68
		6.4	152.2	12.8	1106.0	1135.9	4
	0.762	8.0	190.8	16.0	652.6	579.7	26
		8.8	209.7	17.6	717.3	637.7	3
		9.2	218.9	18.4	748.7	666.7	6
		8.4	200.6	16.8	686.2	603.7	18
		7.2	171.3	14.4	585.9	521.7	150

TABLE VI (Cont'd)

MATERIALS CODE	$P_{min.}$	ΔP KN	ΔS MN/ m ²	ΔK MN/m ^{3/2}	Kt. ΔS	$\Delta K/P^{1/2}$	Ni x 10 ³ cycles	
LTM (low Ti sintered Maraging compact)	0.127	5.4	117.5	18.2	976.4	1615.1	1	
		4.4	95.3	14.8	792.3	1313.3	2	
		2.4	52.0	8.1	432.2	718.8	10	
		2.0	43.4	6.7	360.9	594.6	58	
		2.2	47.8	7.4	397.5	656.7	30	
	0.762	6.0	129.9	20.2	481.0	731.9	2	
		3.2	69.4	10.8	257.0	391.3	12	
		2.6	56.4	8.8	208.7	318.8	45	
		2.4	52.2	8.1	193.0	293.5	91	
		4.8	104.1	16.2	385.4	587.0	4	
	Notch depth for M ₁₁ , M ₁₂ , M ₂₁ , M ₂₂ , M ₃₁ , M ₃₂ , and LTM Compacts ~ 0.3 W; Notch depth for M ₁₃ , M ₂₃ and M ₃₃ Compacts ~ 0.1W.							

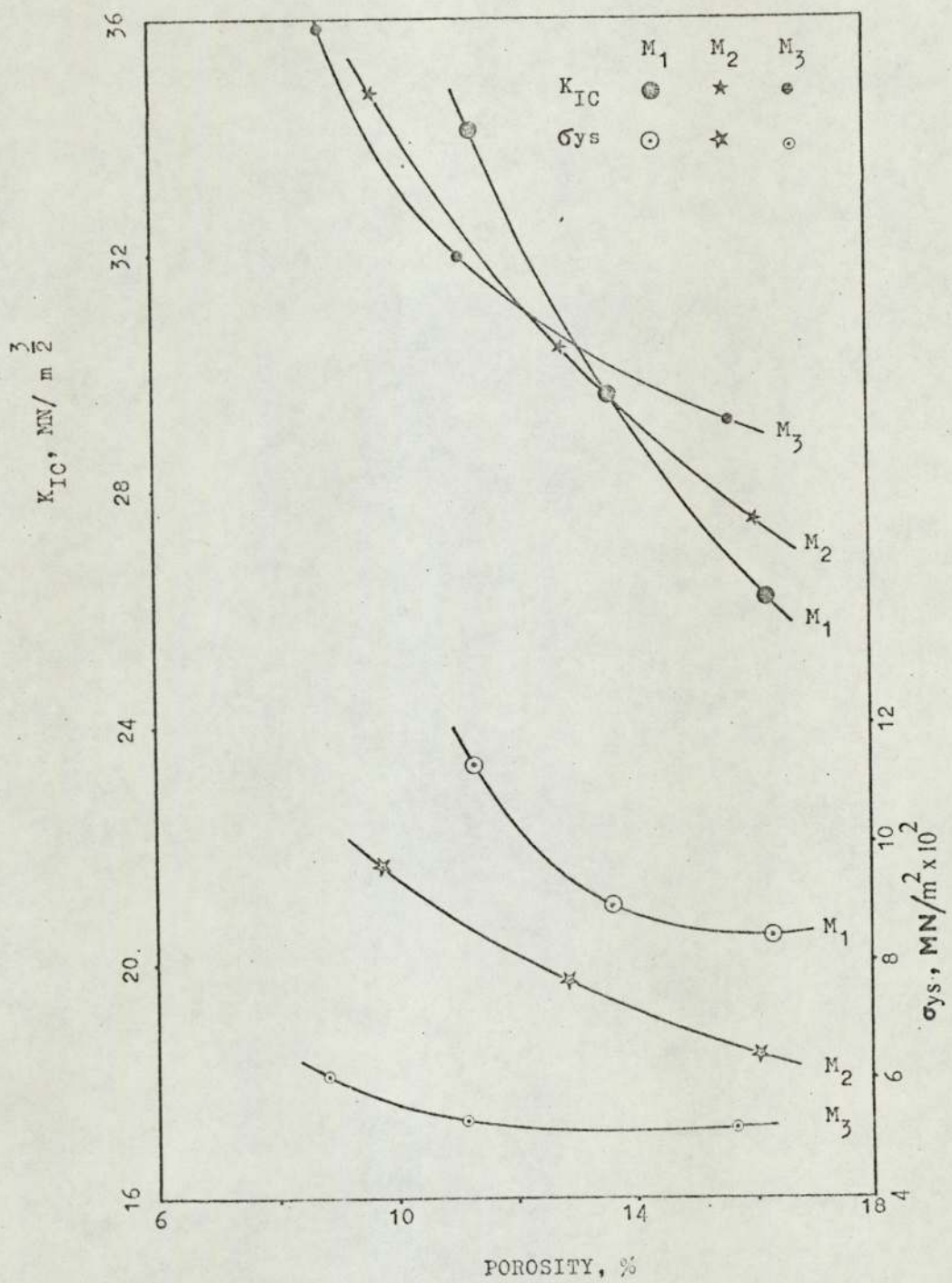


Fig.43. Fracture Toughness, K_{IC} and Yield Stress, σ_{ys} as a function of %Porosity.

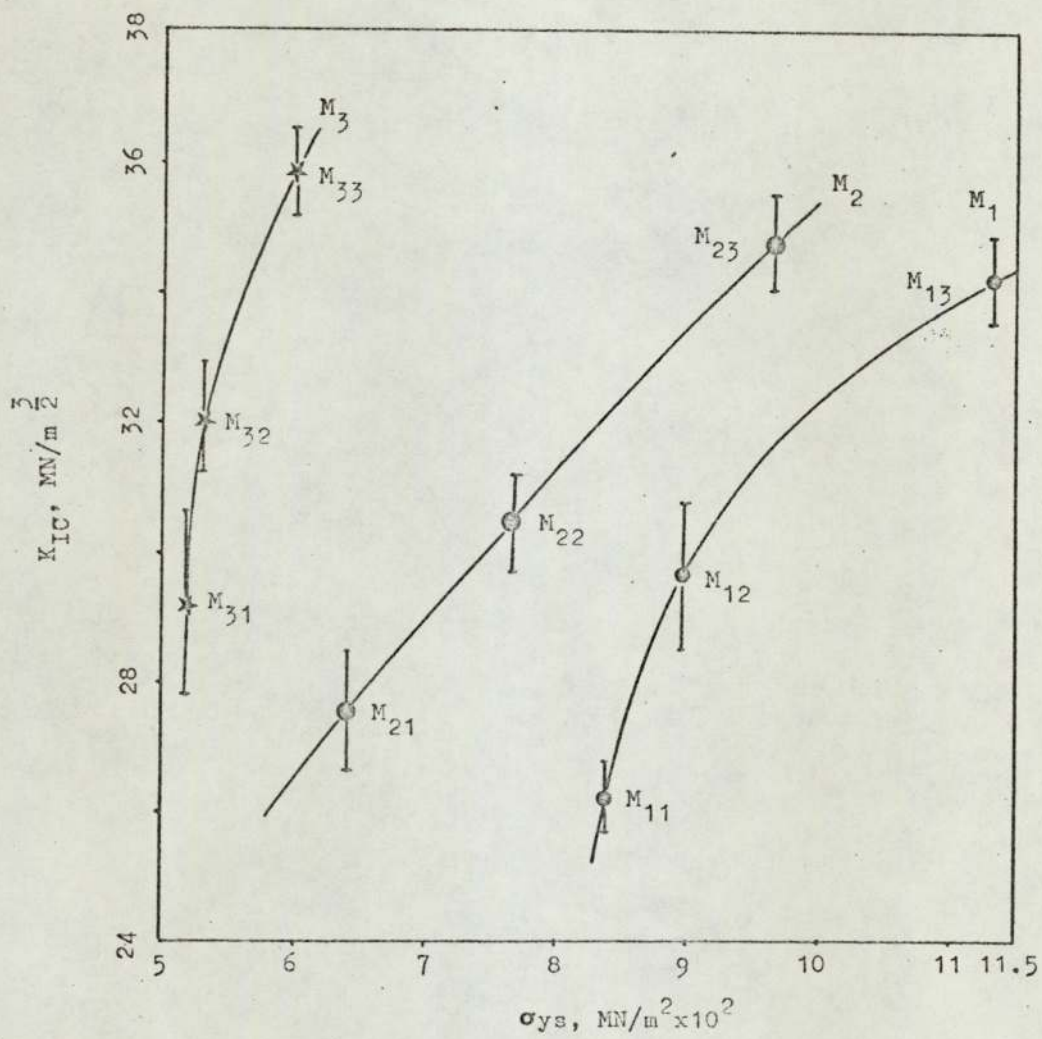


Fig.44. Fracture Toughness as a function of yield stress for the three types of sintered steels investigated.

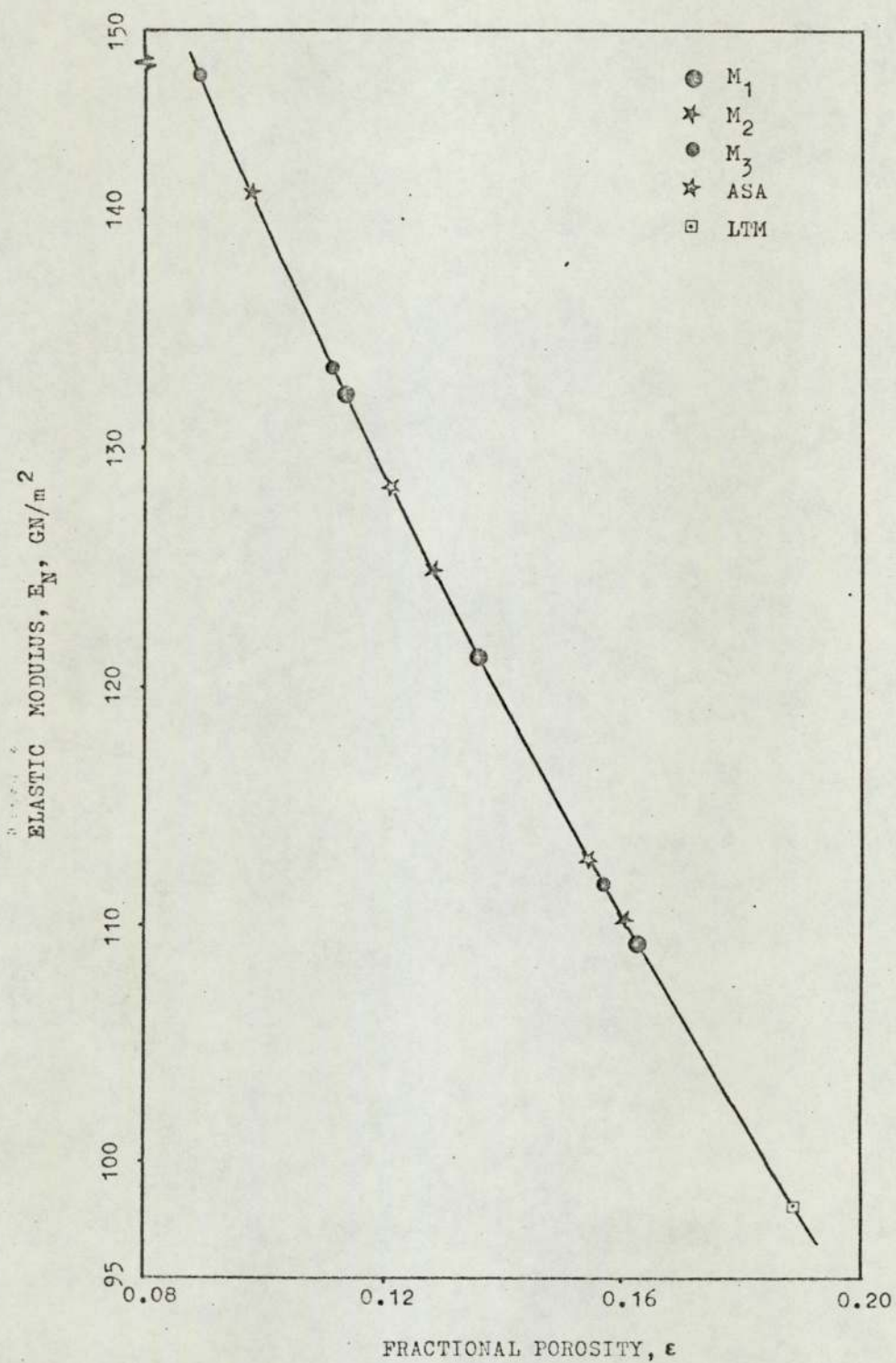


Fig.45. Elastic Modulus, E_N vs. % Porosity for all the materials tested.

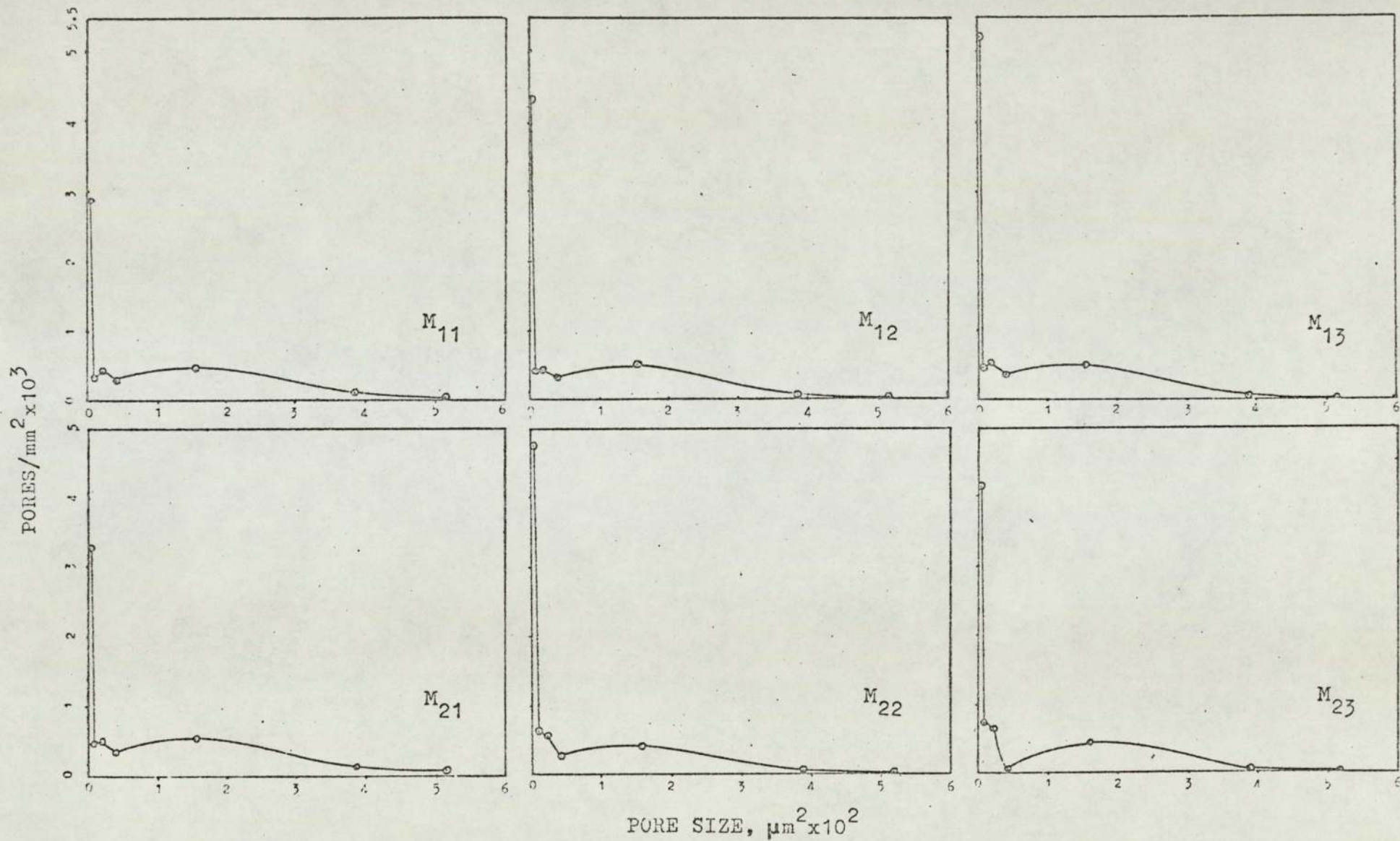


Fig.46. Pore distribution of different sintered steels investigated.

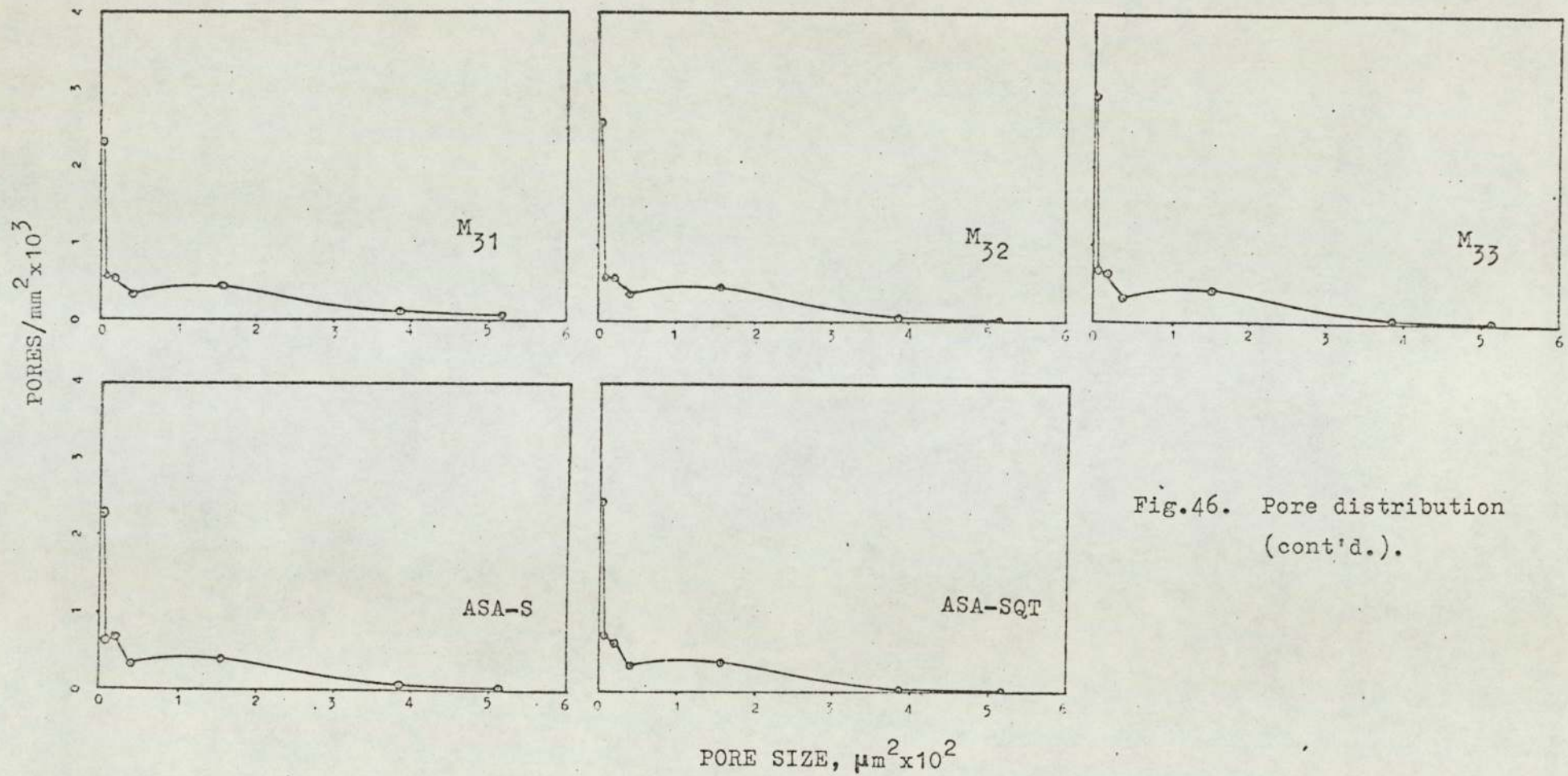


Fig.46. Pore distribution
(cont'd.).

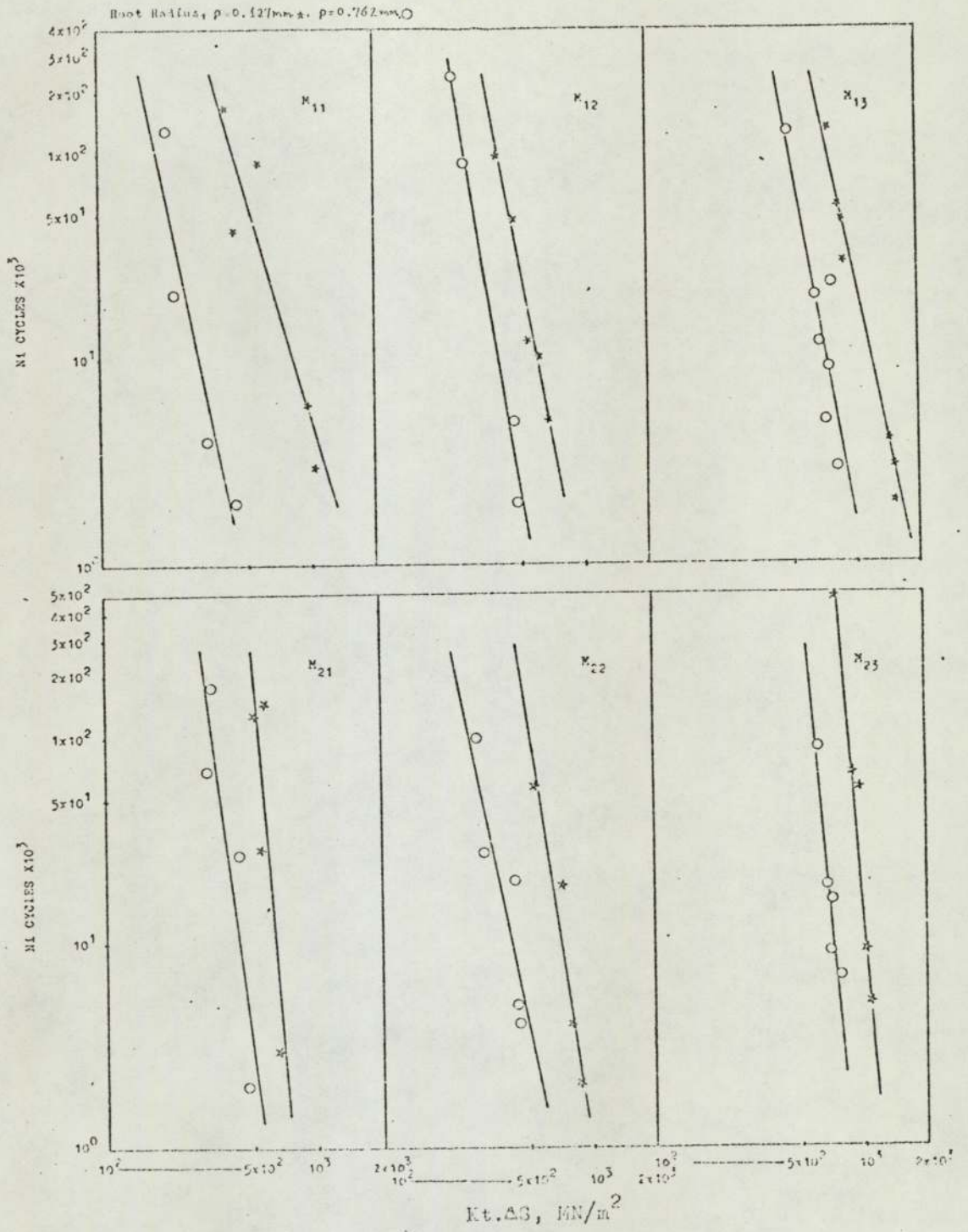


Fig.47. Plot of N_i , no. of cycles for initiation, Vs $K_t.SG$.

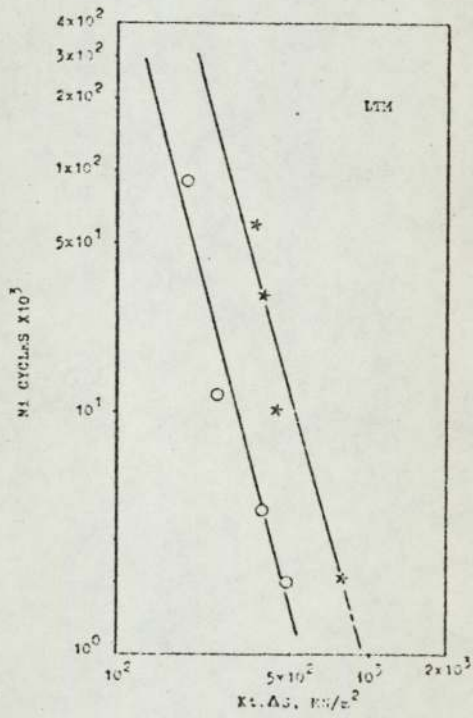
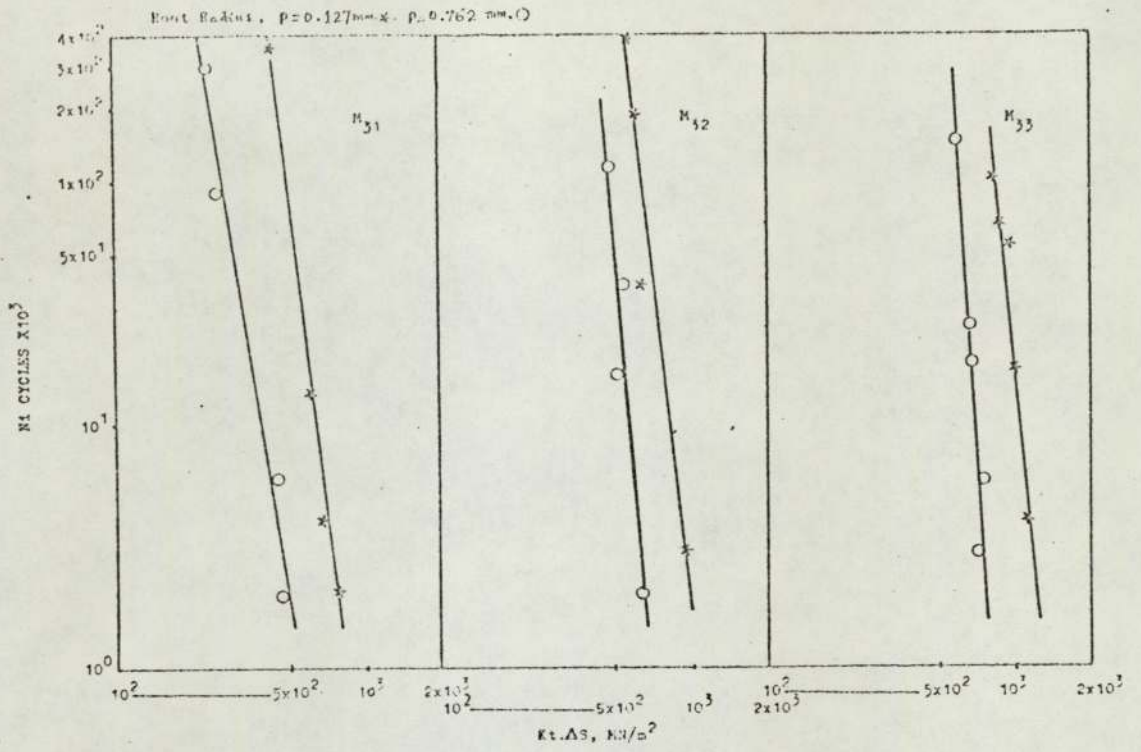


Fig.47. Plot of N_i Vs $Kt.AS$
(cont'd.).

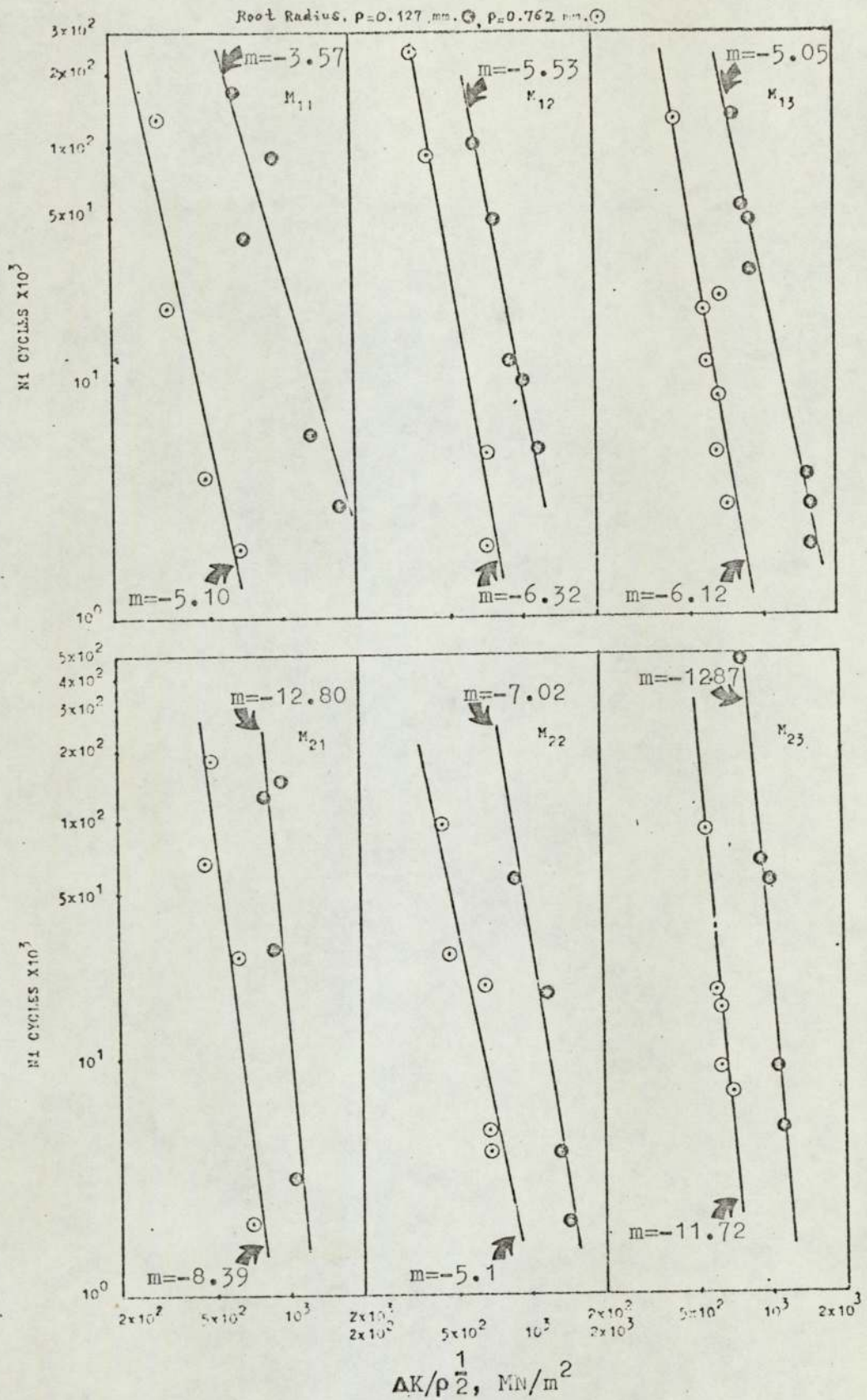


Fig.48. Plot of N_i , no. of cycles for initiation, Vs $\Delta K/\rho^{1/2}$.

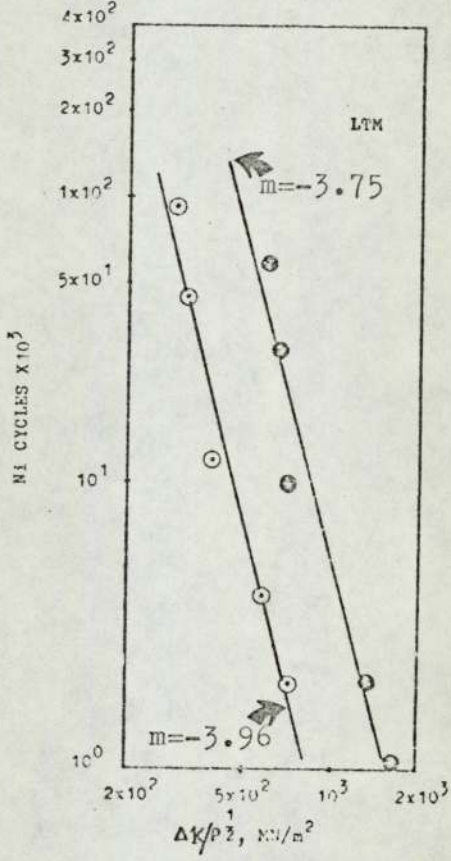
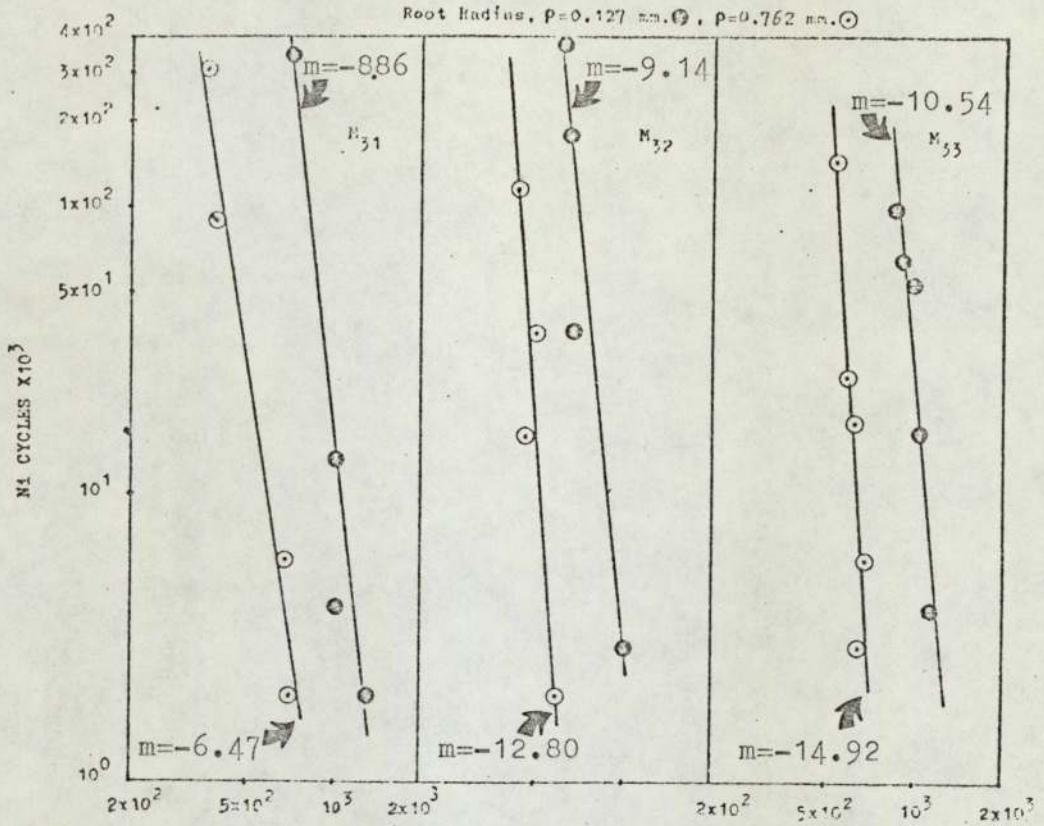


Fig. 48. Plot of N_i Vs $\Delta K / \rho^{1/2}$
(cont'd.).

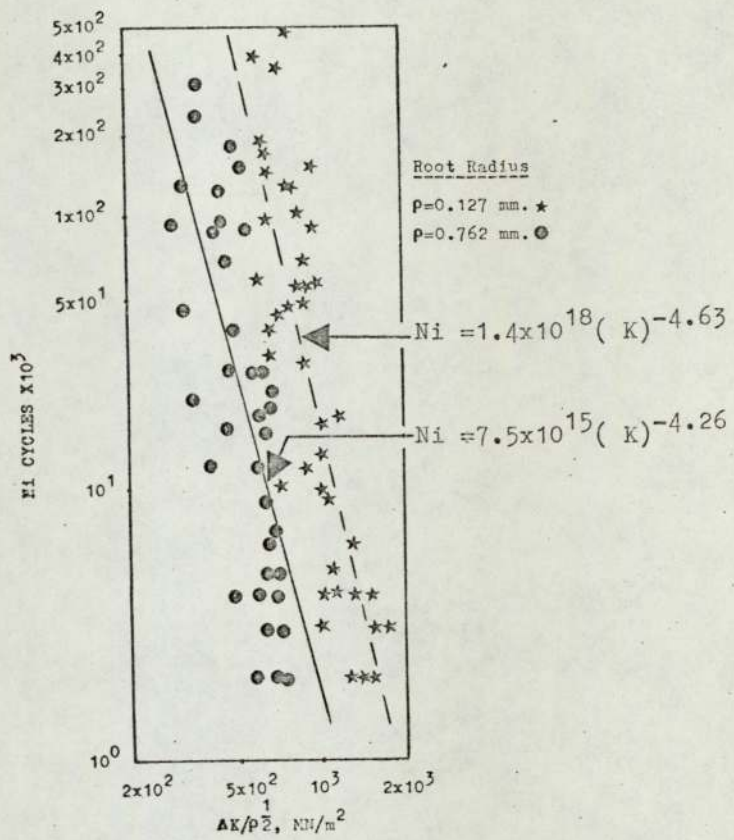


Fig.49. Initiation data for all the materials tested.

Root Radius, $\rho = 0.127$ mm. \circ . $\rho = 0.762$ mm. \odot

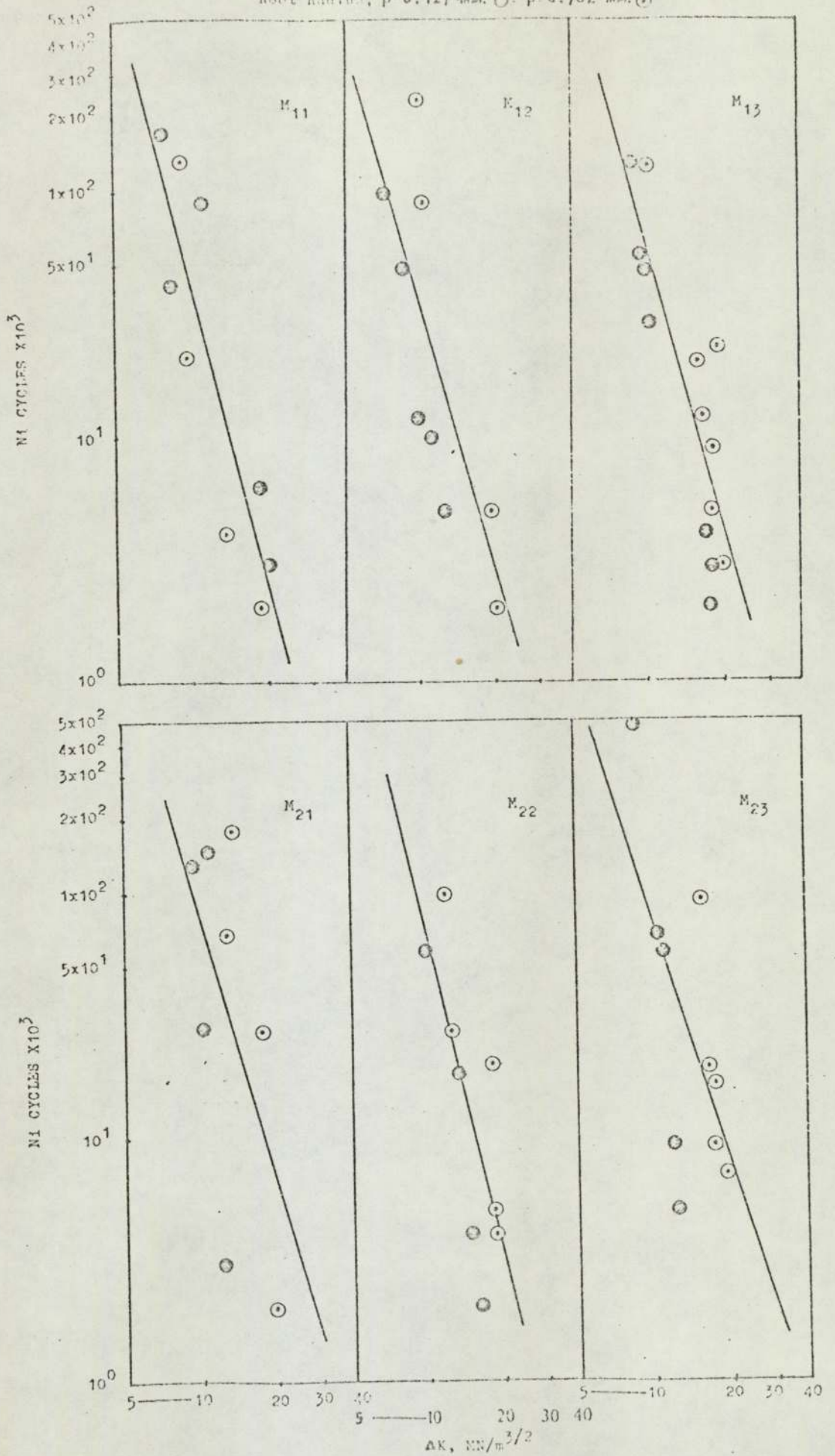


FIG. 50. Plot of N₁ Vs ΔK.

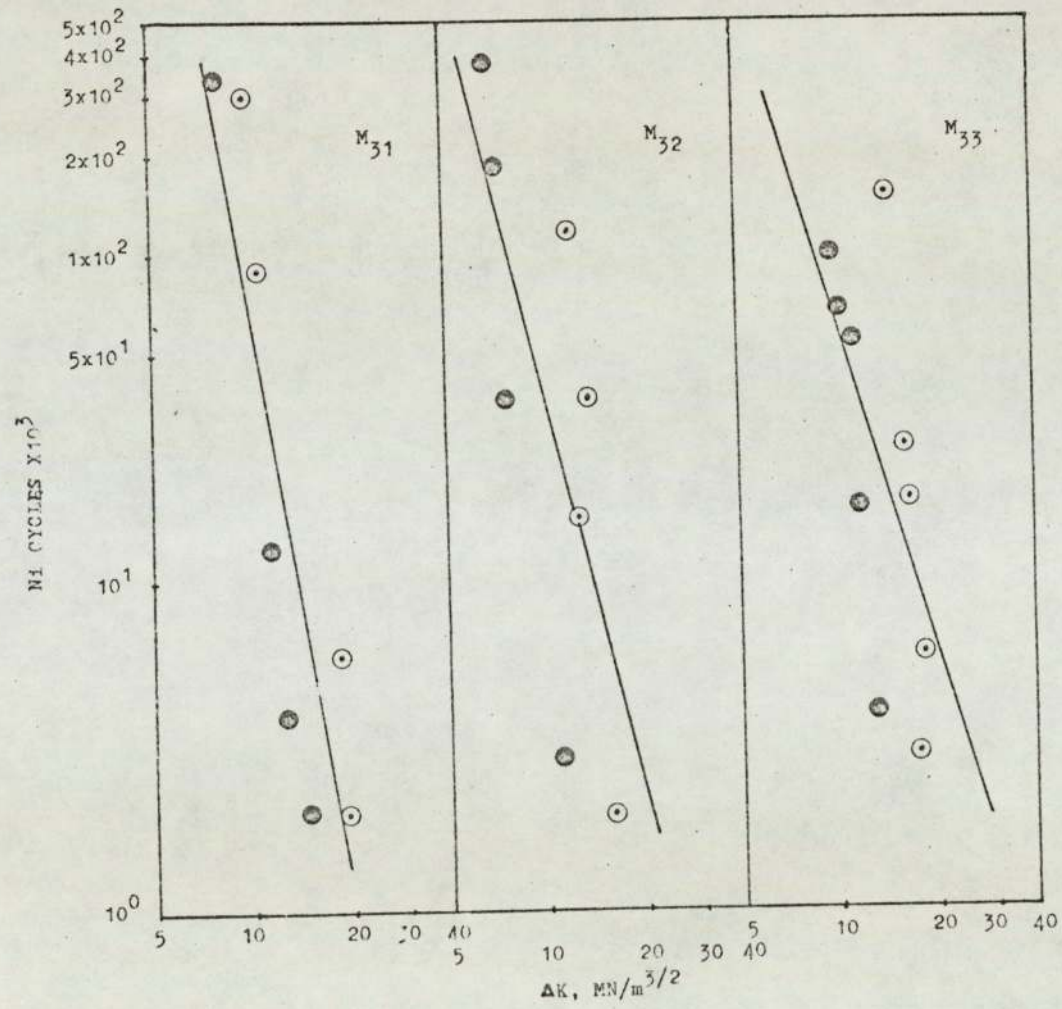


Fig. 50. Plot of N1 Vs ΔK (cont'd).

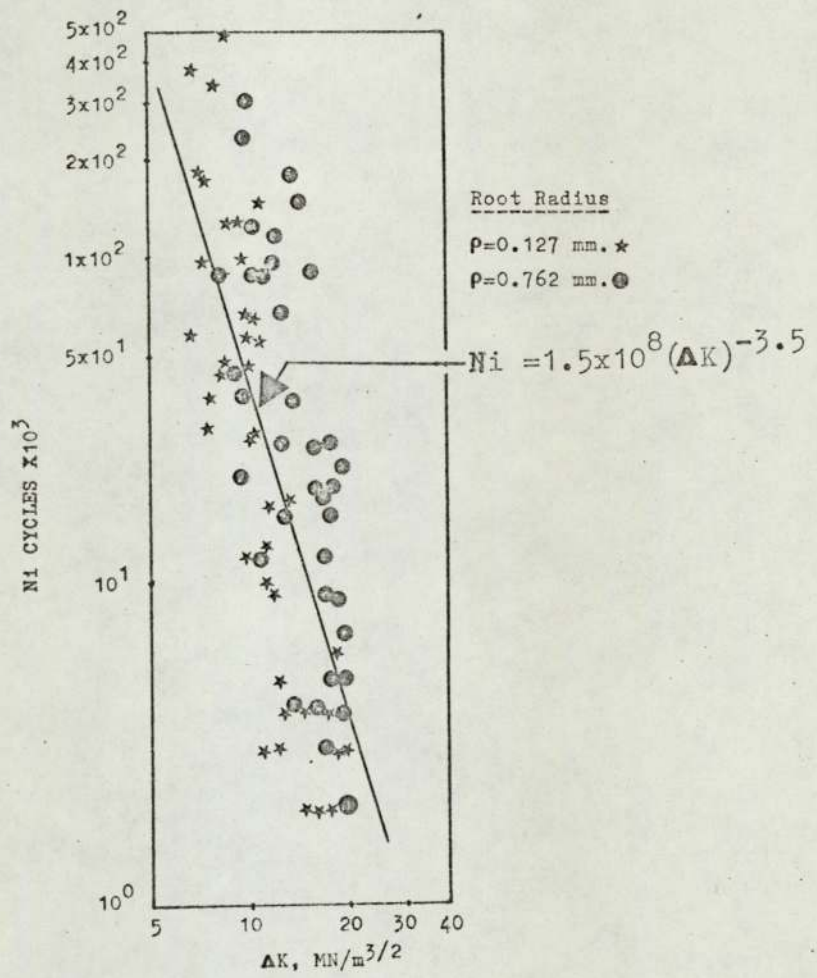


Fig. 51. Correlation of Ni Vs ΔK .

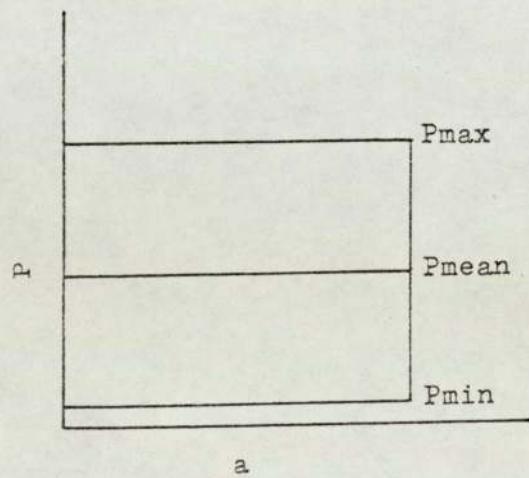


Fig.52. (Constant) Load Profile.

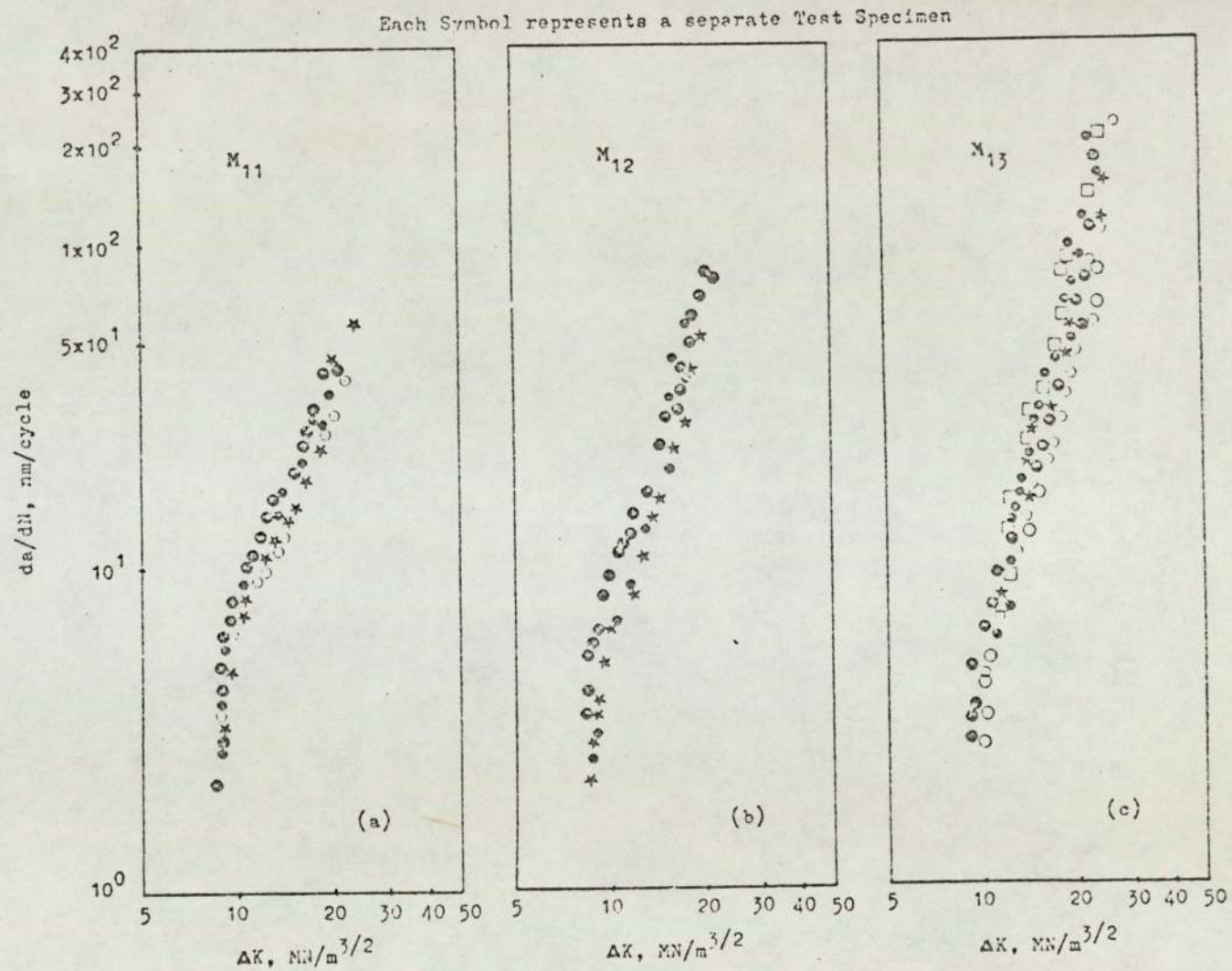


Fig.53. Crack Growth results for the different compact materials investigated, $R=0.07$.

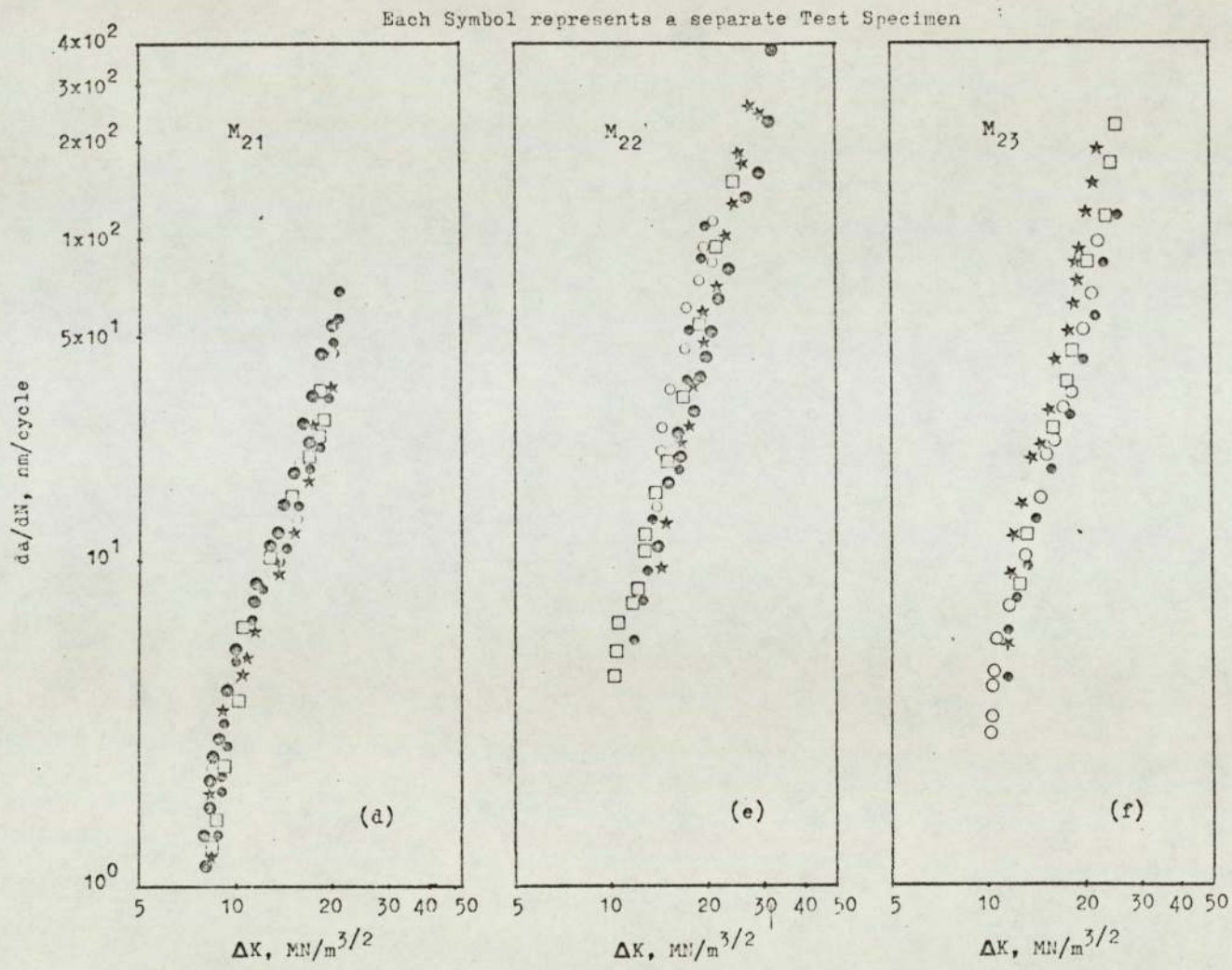


Fig.53. Crack Growth results (Cont'd).

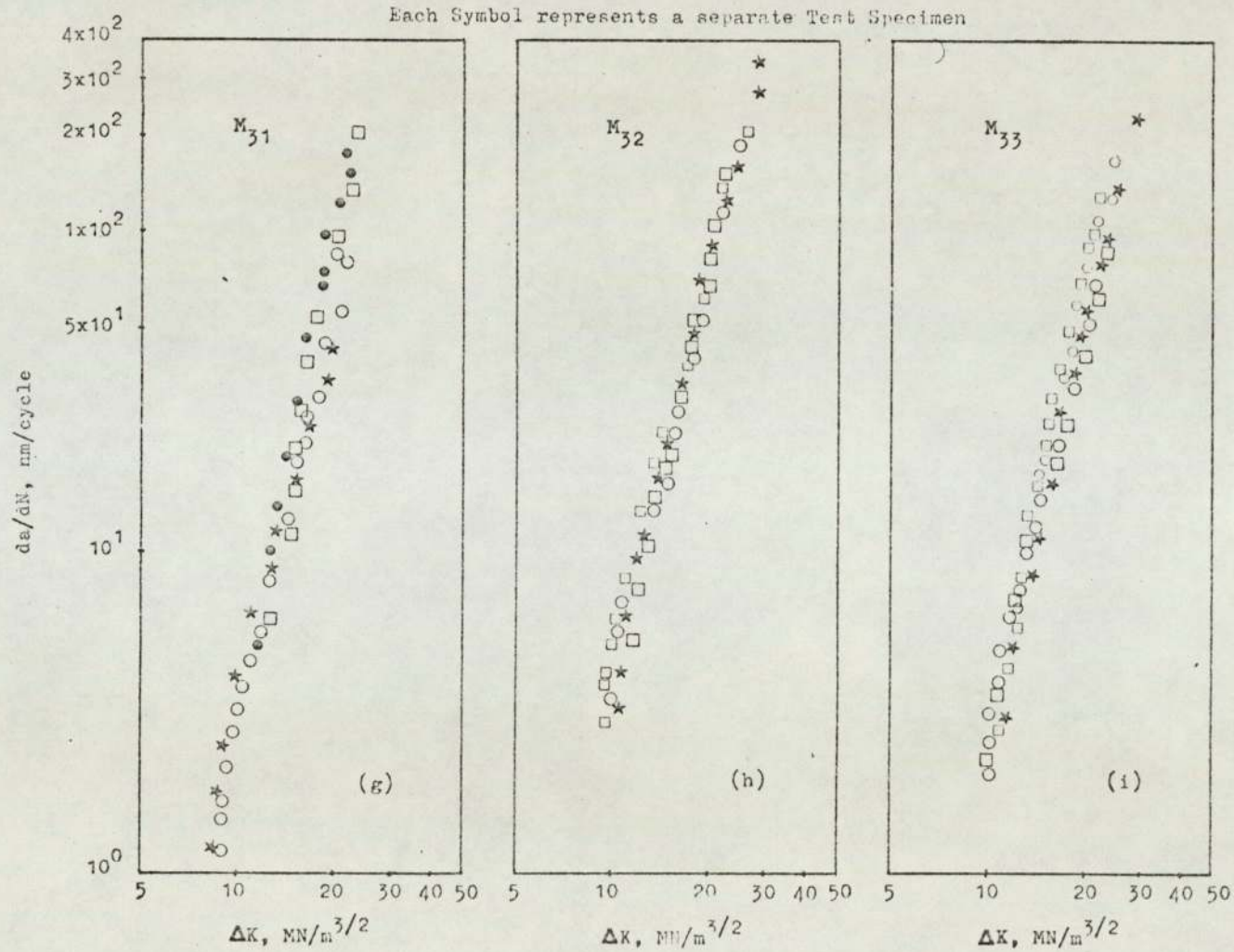


Fig.53. Crack Growth results
(Cont'd).

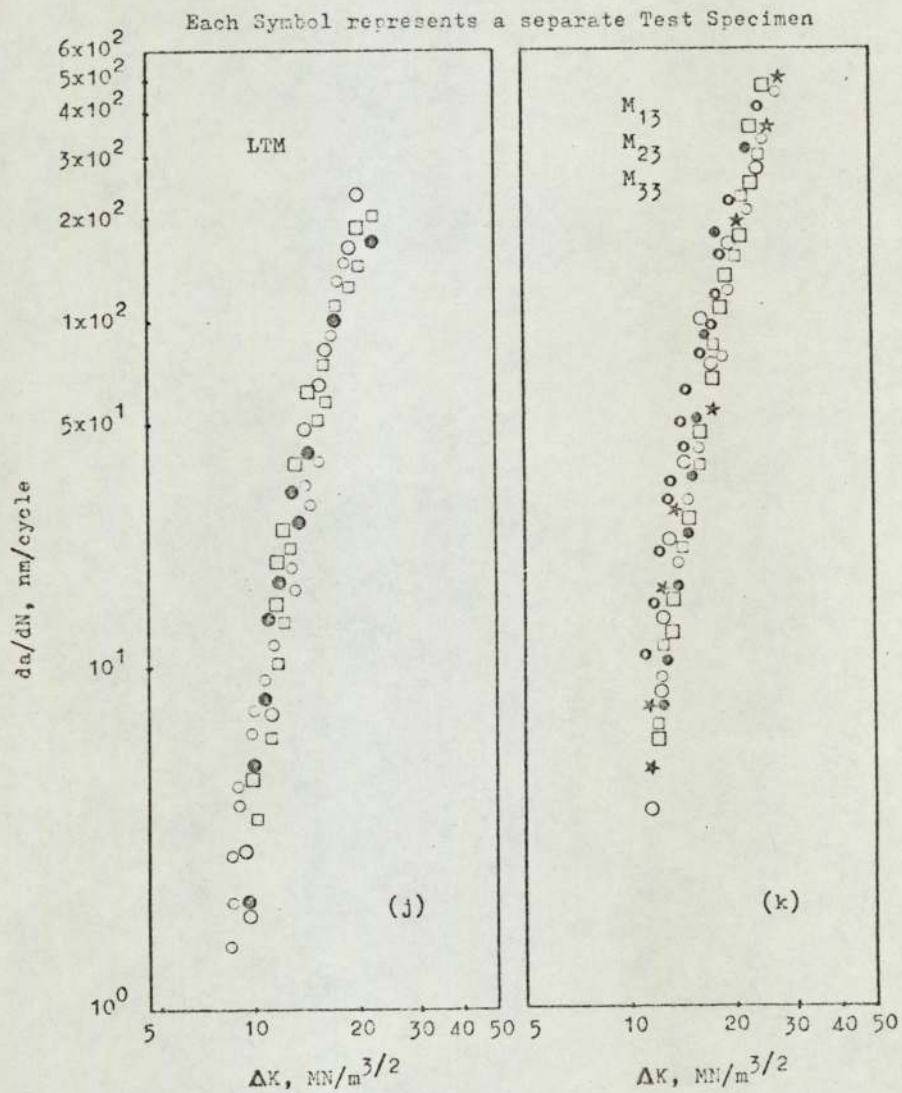


Fig. 53. Crack Growth Results for (j) LTM Compacts, at $R=0.07$, and for (k) M_{13} , M_{23} , M_{33} Compacts at $R=0.3$.

Each Symbol represents a separate Test Specimen

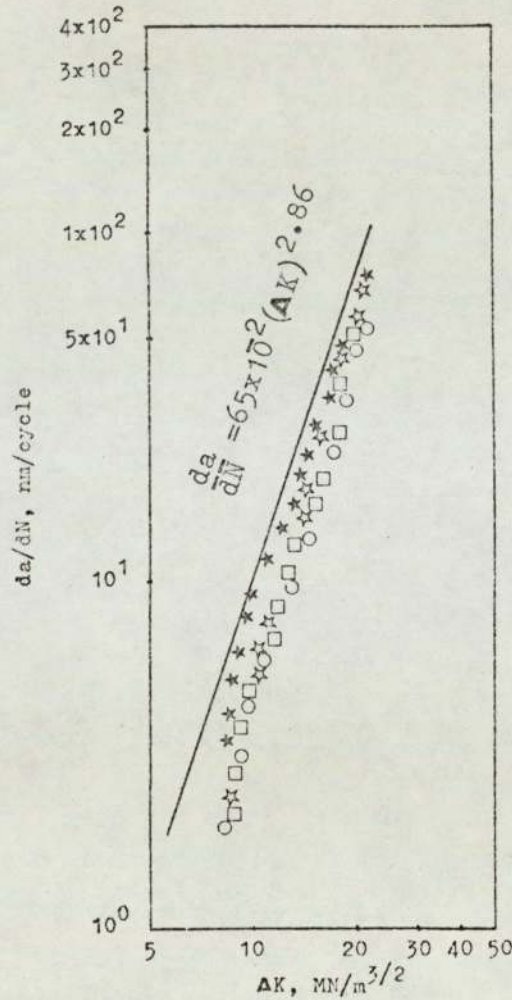


Fig.54. Crack Growth results for M_{12} and M_{21} Compacts at $R \sim 0.07$ shown to be falling on the same scatter band.

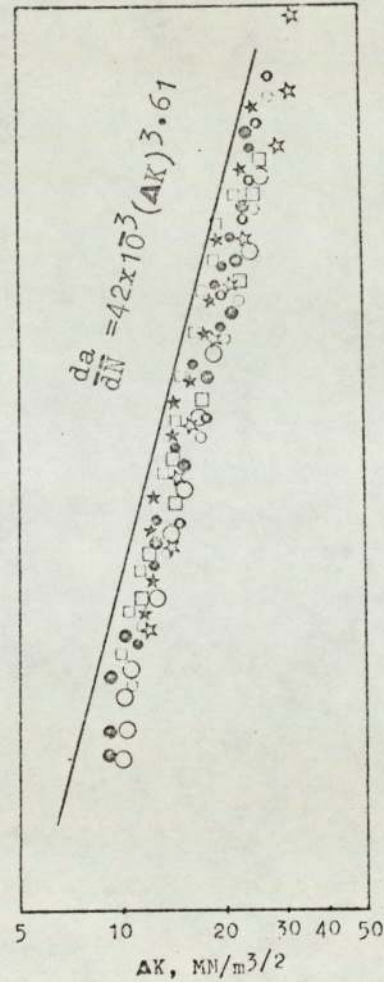


Fig.55. As in Fig.54 for M_{13} and M_{22} Compacts.

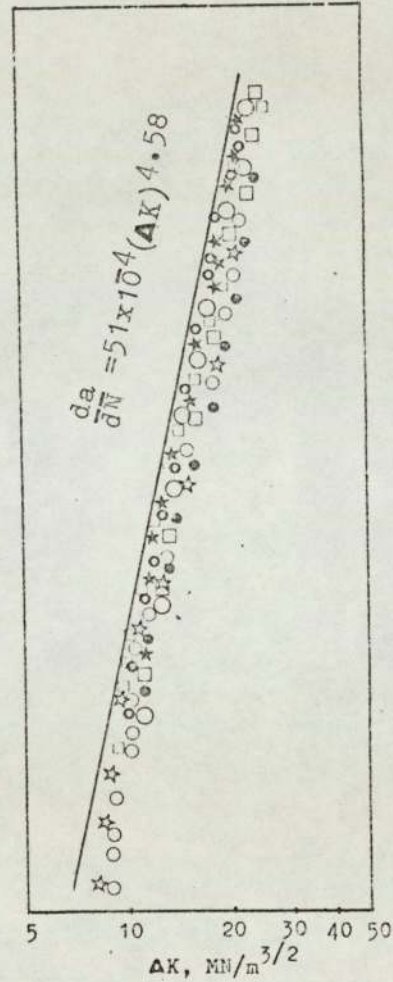


Fig.56. As in Fig.54 for M_{23} , M_{31} , M_{32} and M_{33} Compacts.

Particle Size (P.S.) of Maraging Steel
Pre-alloyed Powders $\sim 250\mu$.



→ 1/25 P.S. ←

Fig.57. A cluster of Maraging Steel
Powder Particles.



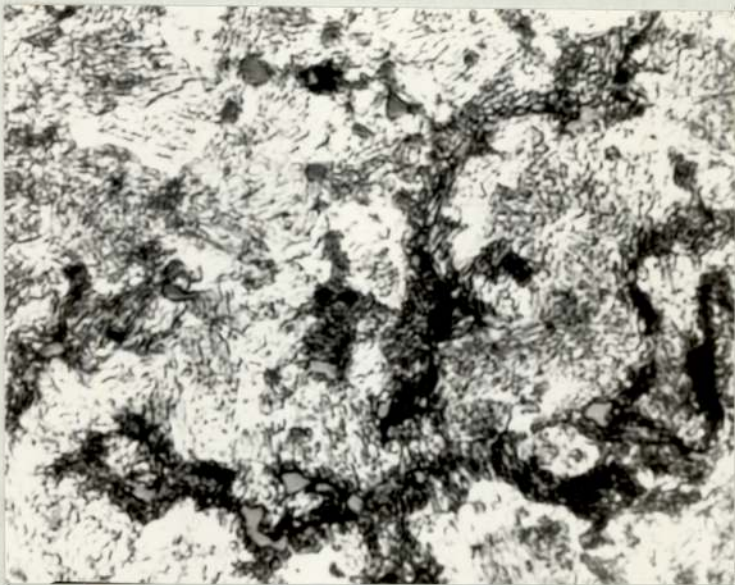
→ 1/5 P.S. ←

Fig.58. Green Maraging Steel Powder
Compact.



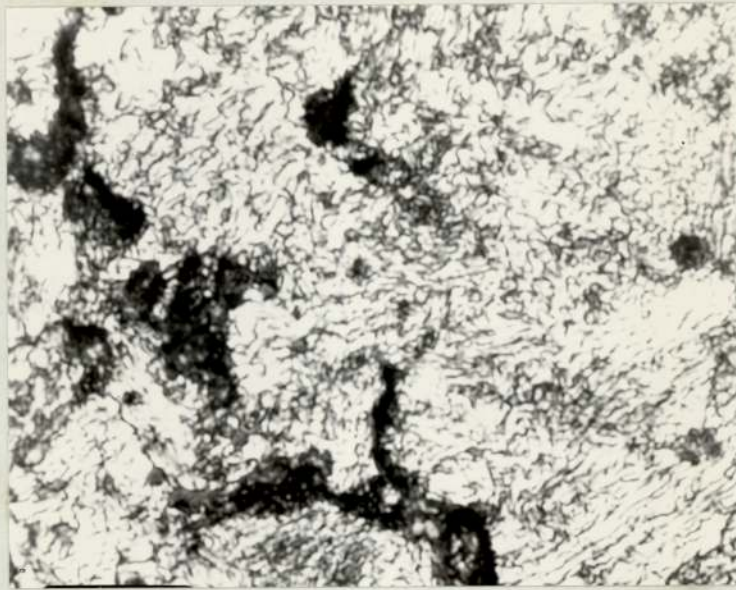
← 1/10 P.S. →

Fig.59. Typical Microstructure of M₁ series of Maraging Steel (M.S.) Compact. Sintered and Heat-Treated (S.H.T.)



← 1/10 P.S. →

Fig.60. Microstructure of M₂ Series of Diluted M.S. Compact. S.H.T.



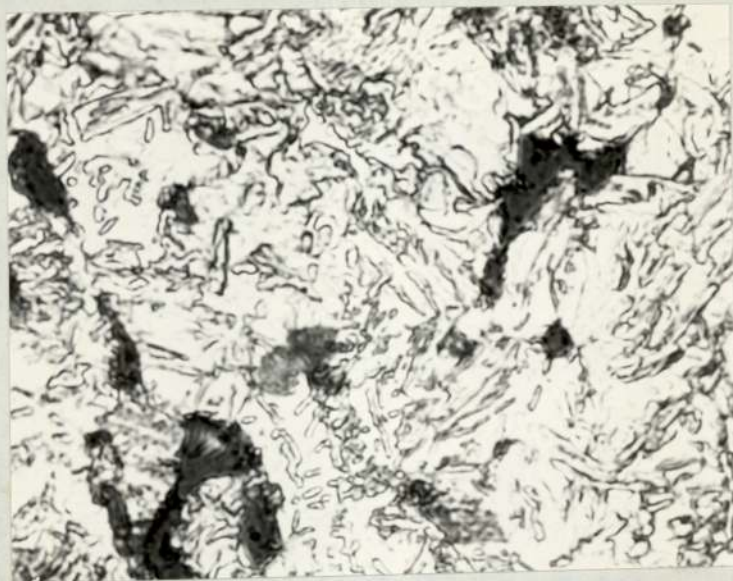
←1/10 P.S.→

Fig.61. Typical Microstructure of M_2 Series of Diluted M.S. Compact. S.³H. T.



←1/10 P.S.→

Fig.62. Microstructure of M_1 Series of M.S. Compact. Sintered only.



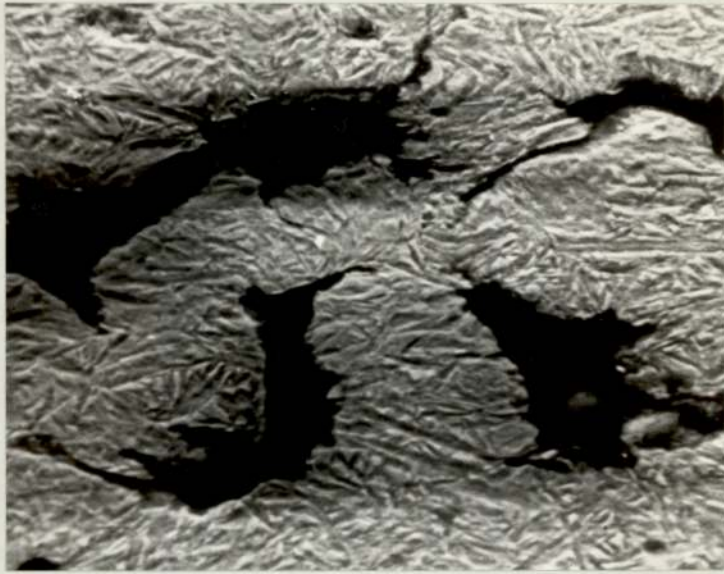
←1/10 P.S.→

Fig.63. Typical Microstructure of Ancoloy SA Compact. Sintered.



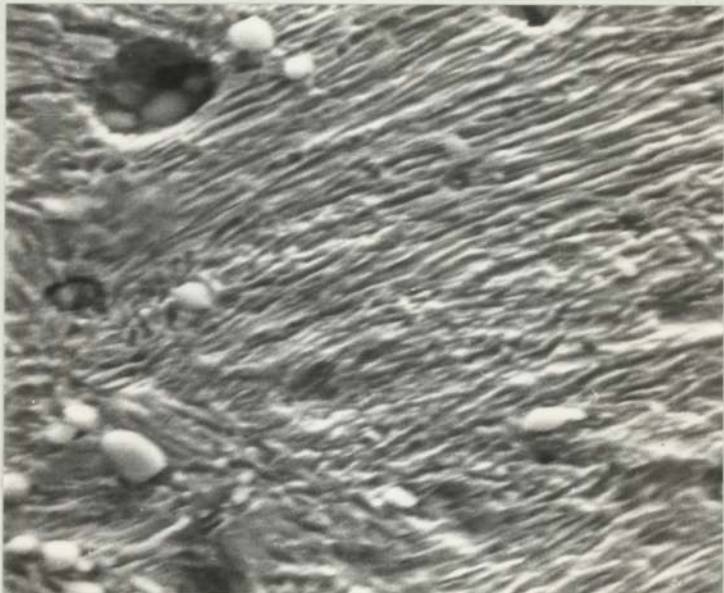
←1/10 P.S.→

Fig.64. Microstructure of Ancoloy SA Compact. Sintered, Quenched and Tempered.



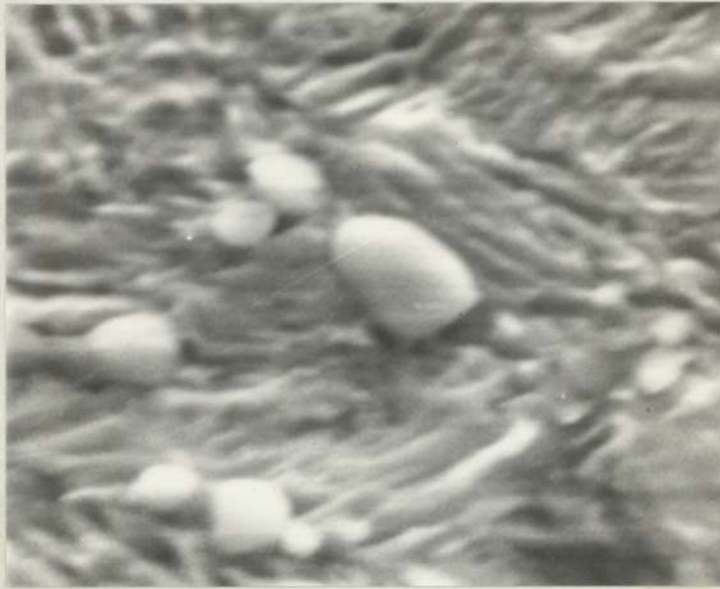
←1/25 P.S.→

Fig.65. S.E.M.-Image of Typical Microstructure of M_1 Series of M.S. Compact. S.H.T.



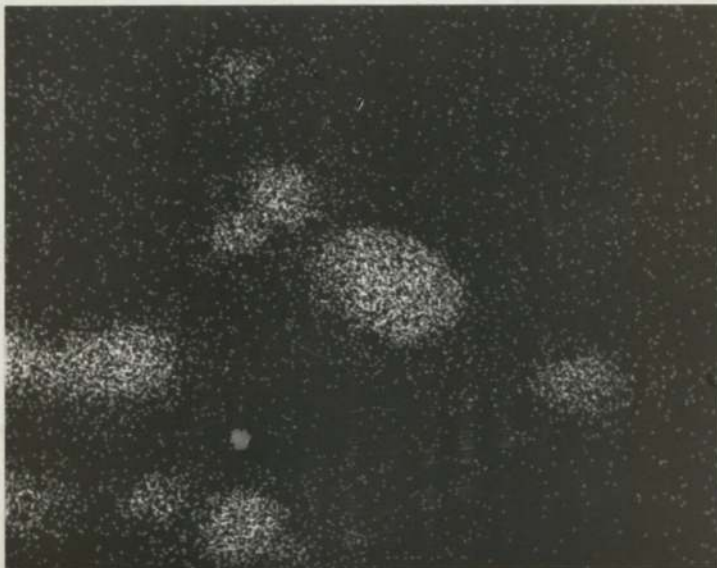
←1/25 P.S.→

Fig.66(a). S.E.M.-Image of Microstructure of M_1 Series of M.S. Compacts. S.H.T.



←1/50 P.S.→

Fig.66 (b). Same as in Fig.66(a) at High Magnification.



←1/50 P.S.→

Fig.66 (c). Ti X-Ray Image of Area in Fig.66(b).

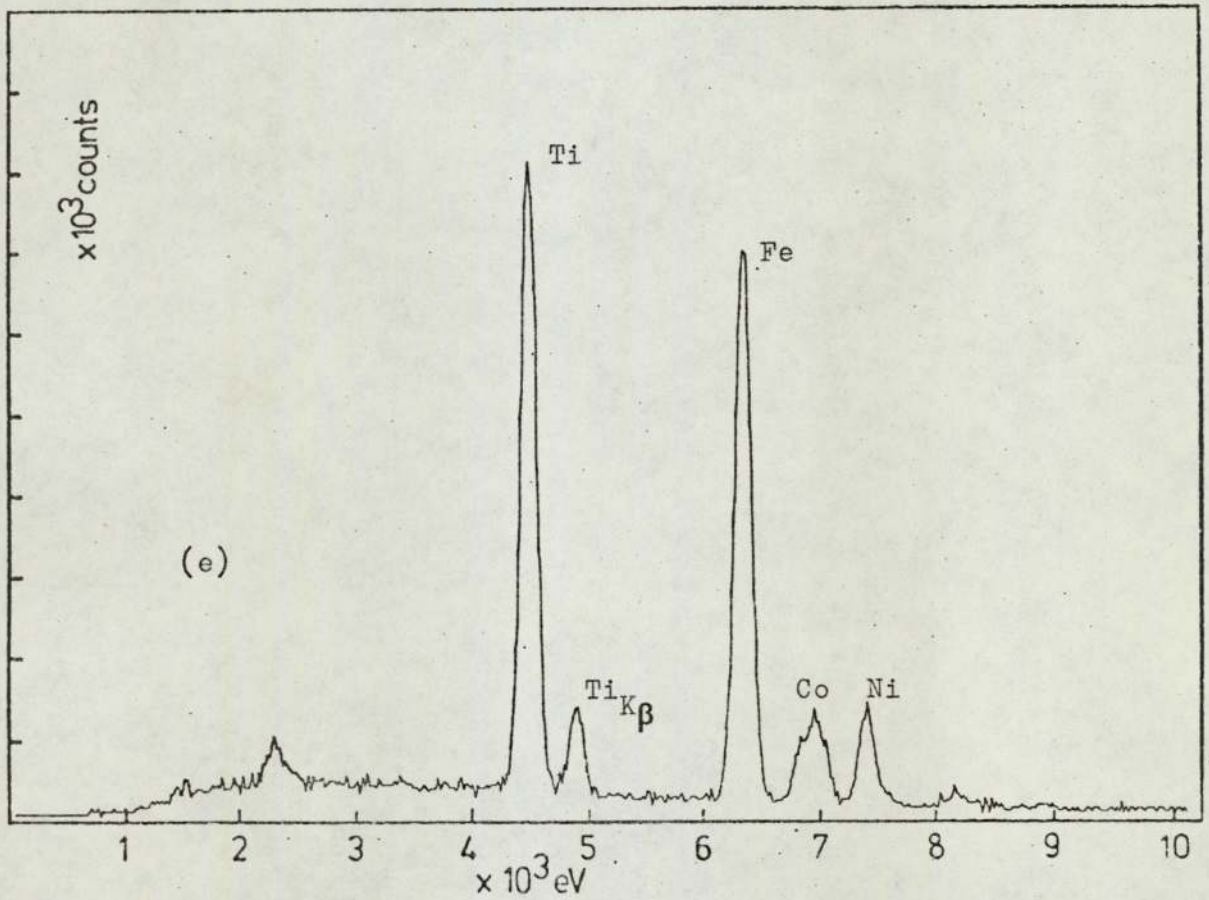
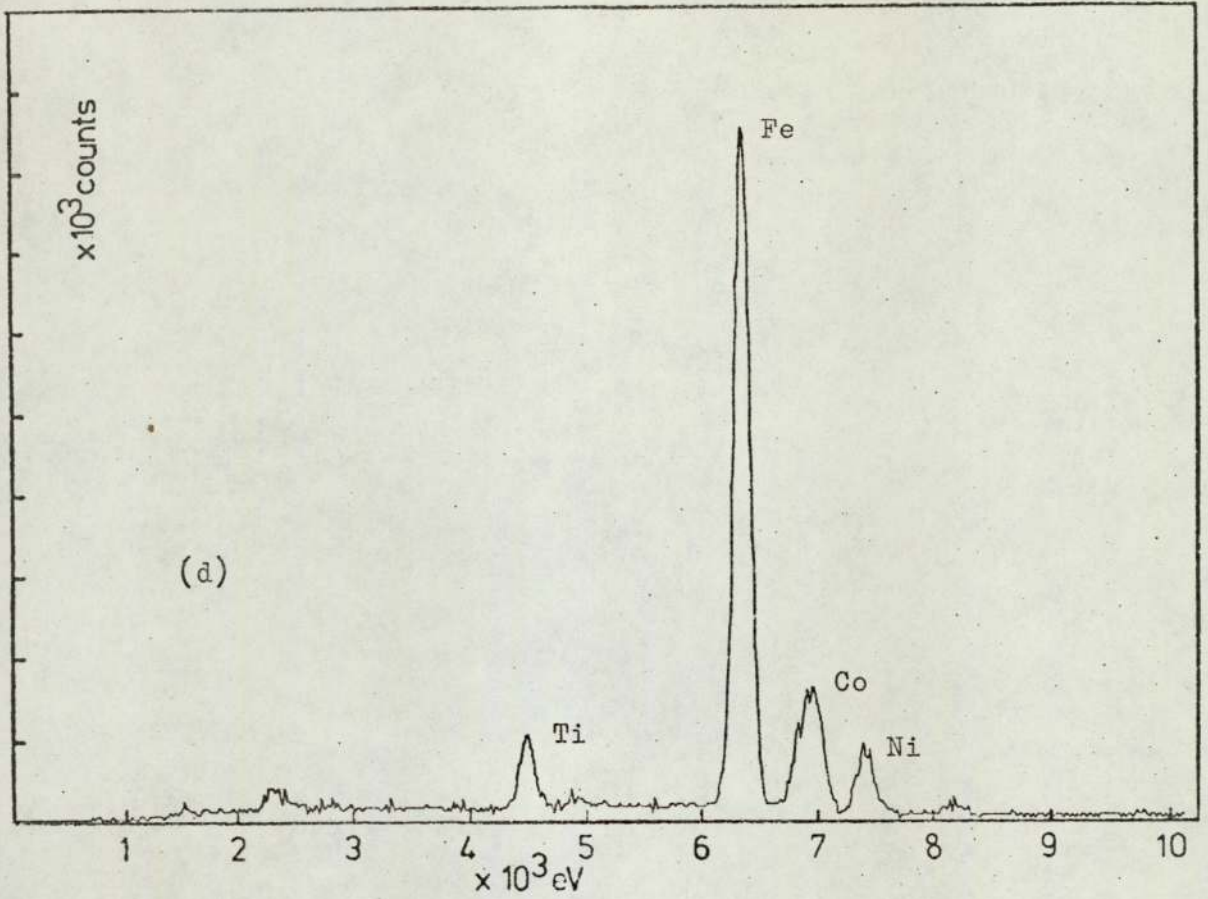
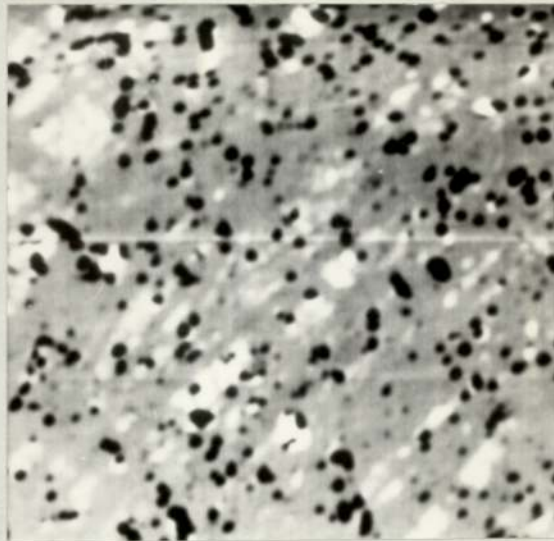


Fig.66(d). Area Analysis of Elements in the Matrix of Fig.66(b).
 (e). Spot Analysis of Elements in a Particle of Fig.66(b).



→1/20 P.S.←

Fig.67(a). Electron-Image (Reversed) and Line of Trace of a Selected Area of Matrix of M_1 Series of M.S. Compact.

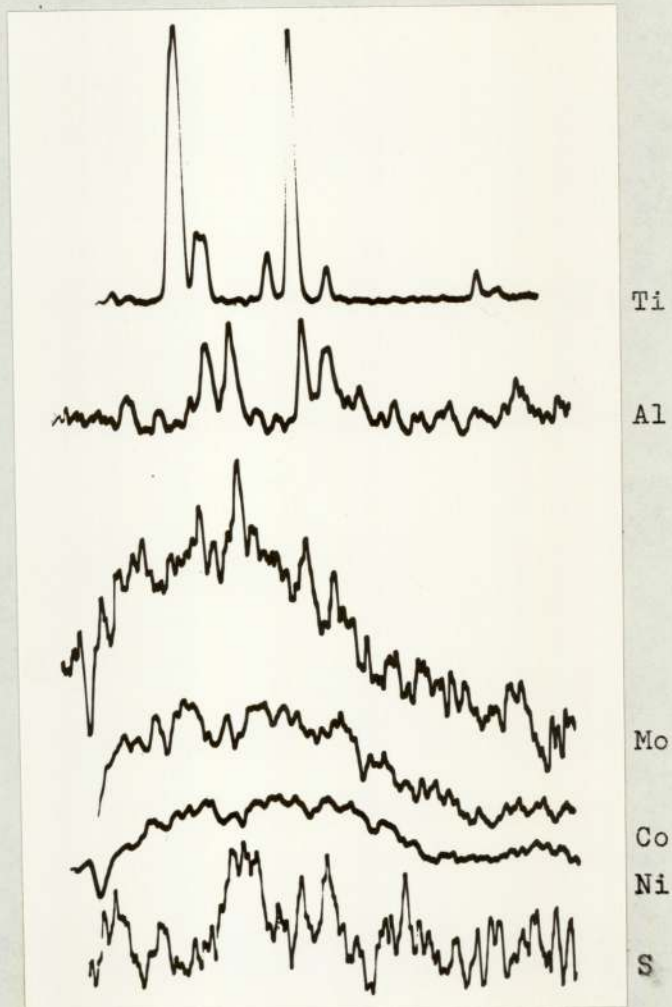


Fig.67(b). Typical Distribution Pattern of Elements along the Line of Trace of Fig.67(a).



|←1/10 P.S.→|

Fig.68. Typical Distribution Pattern of Inclusions
in M_1 Series of M.S. Compacts. Unetched.



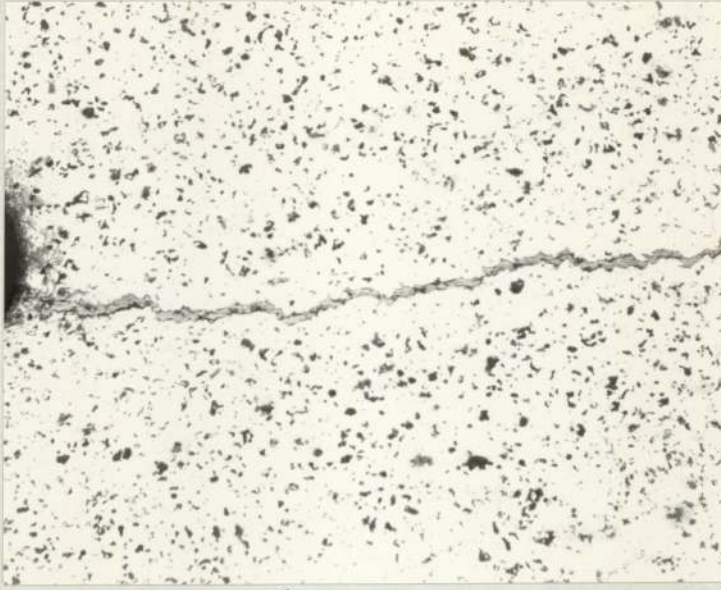
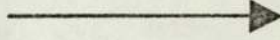
|←1/10 P.S.→|

Fig.69. Typical Distribution Pattern of Inclusions
in M_2 Series of Diluted M.S. Compacts.
Unetched.



←1/10 P.S.→

Fig.70. Typical Distribution Pattern of Inclusions
in M_3 Series of Diluted M.S. Compacts.
Unetched.



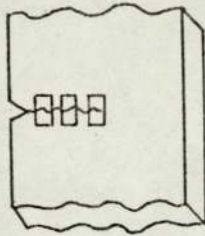
←2×P.S.→

Fig.71. Uneven Crack-Path in the Unetched Condition.

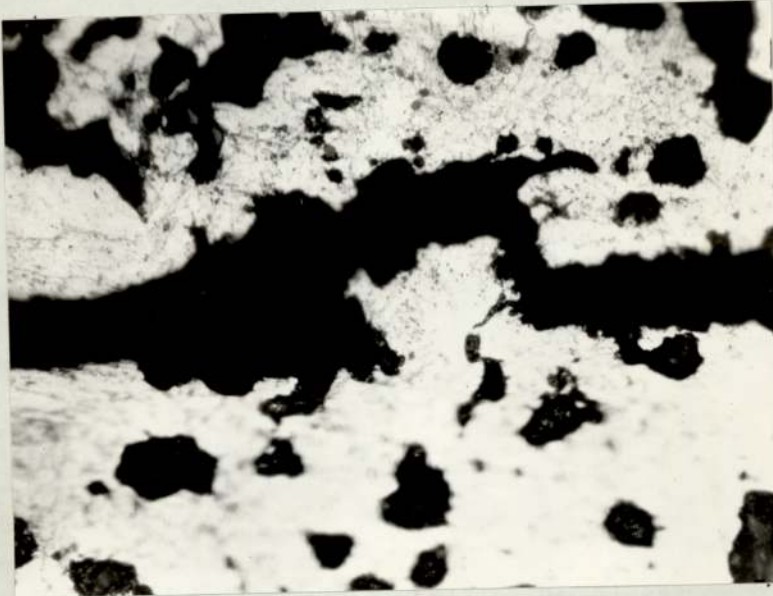
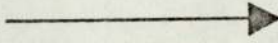


←2×P.S.→

Fig.72. Island Formation along the Crack-Path. Unetched.



Locations of the Distinctive Features of,
and along, Crack-Path.



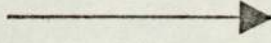
|←1/10 P.S.→|

Fig.73. Crack-Forking and Arching.



|←1/10 P.S.→|

Fig.74. Crack-Branching.



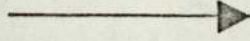
←1/10 P.S.→

Fig.75. Crack-Arching.



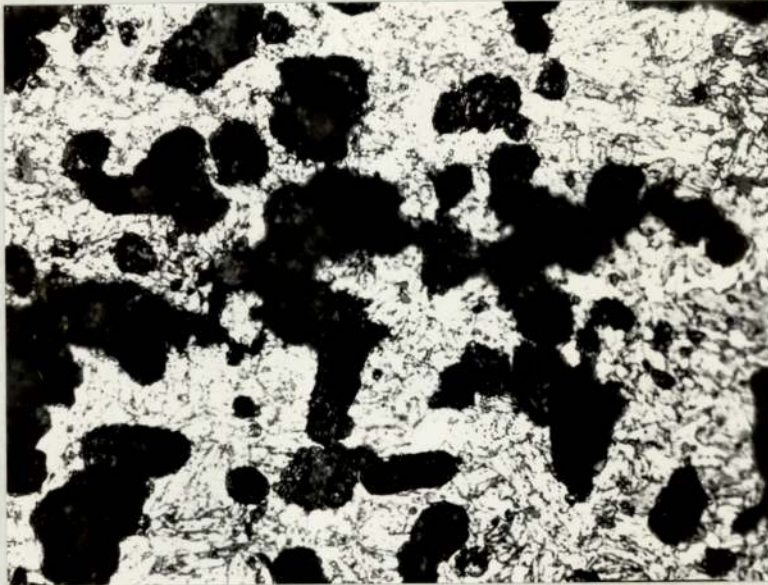
←1/10 P.S.→

Fig.76. Island Formation.



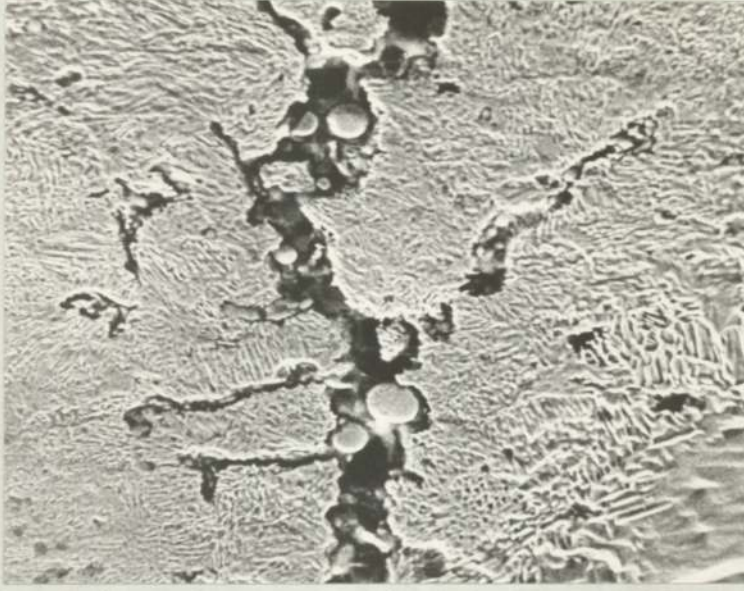
←1/10 P.S.→

Fig.77. Pseudo-Island Formation.



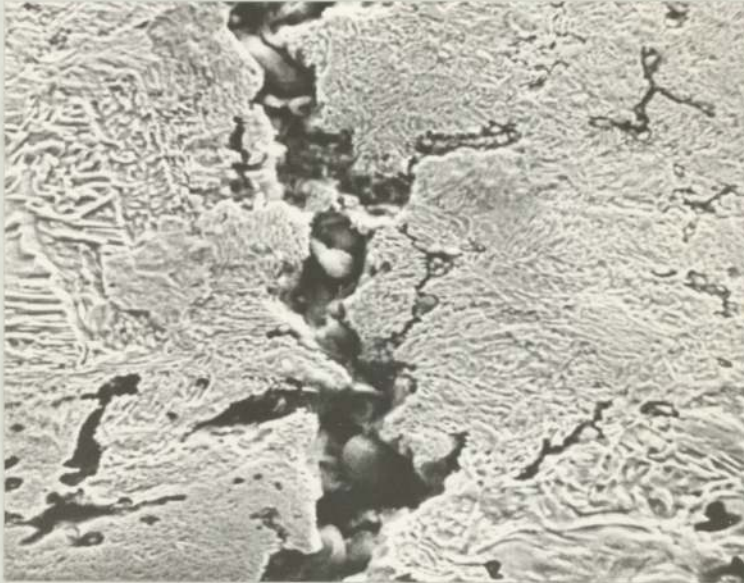
←1/10 P.S.→

Fig.78. Crack-Tip Lost in Clusters of Pores.



← 1/5 P.S. →

Fig.79. S.E.M.-Image of Crack-Path Showing Effect of Pores and Inclusions in Crack Extension.



← 1/5 P.S. →

Fig.80. S.E.M.-Image of Crack Damage.





←1/10 P.S.→

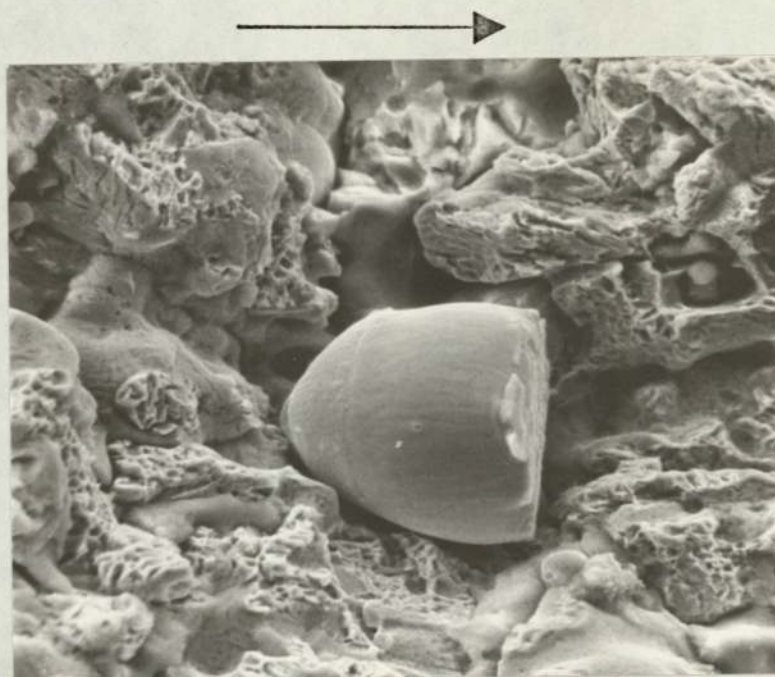
Fig.81. S.E.M.-Image of Island Formation.



←1/20 P.S.→

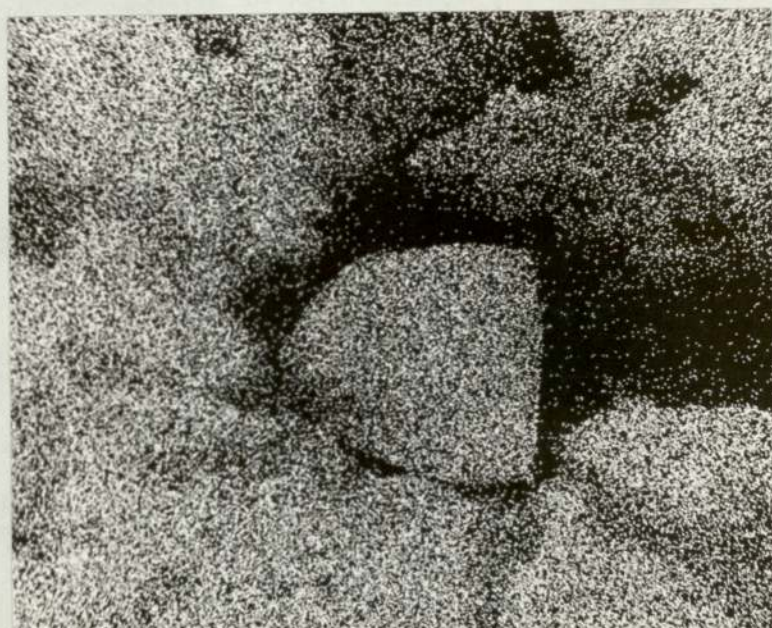
Fig.82. S.E.M.-View of Fracture Surface Showing Tensile Dimples of Various Sizes.





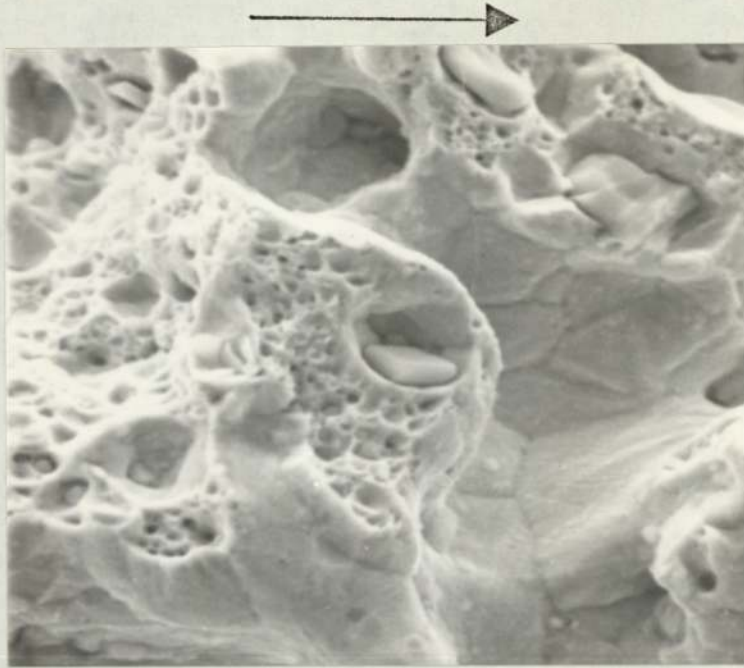
←1/10 P.S.→

Fig.83(a). Round Particle in the Fatigue Surface Showing Least Tendency to Sinter-Bonding.



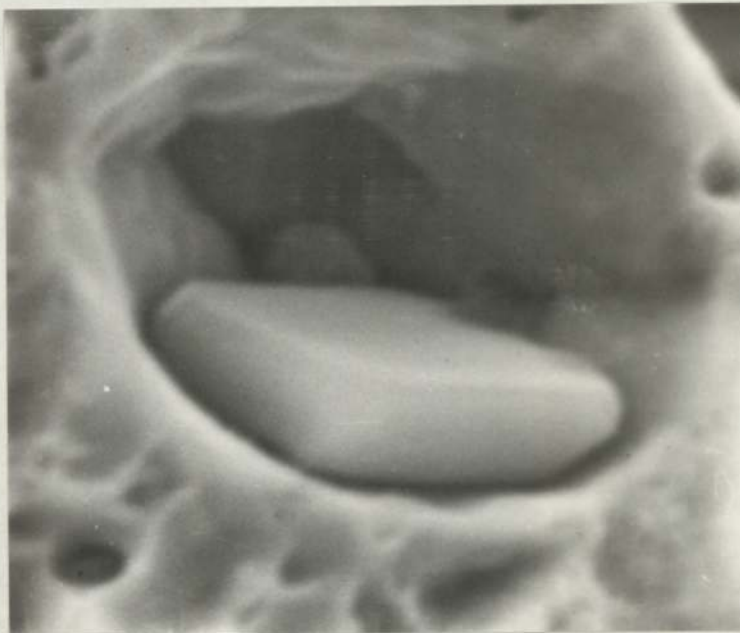
←1/10 P.S.→

Fig.83(b). Fe X-Ray Image of the Particle in Fig.83(a).



←1/25 P.S.→

Fig.84(a). S.E.M.-View of Fast Fracture Surface with Well-Defined Grain Boundaries imprinted in the Internal Surface of the Pores.



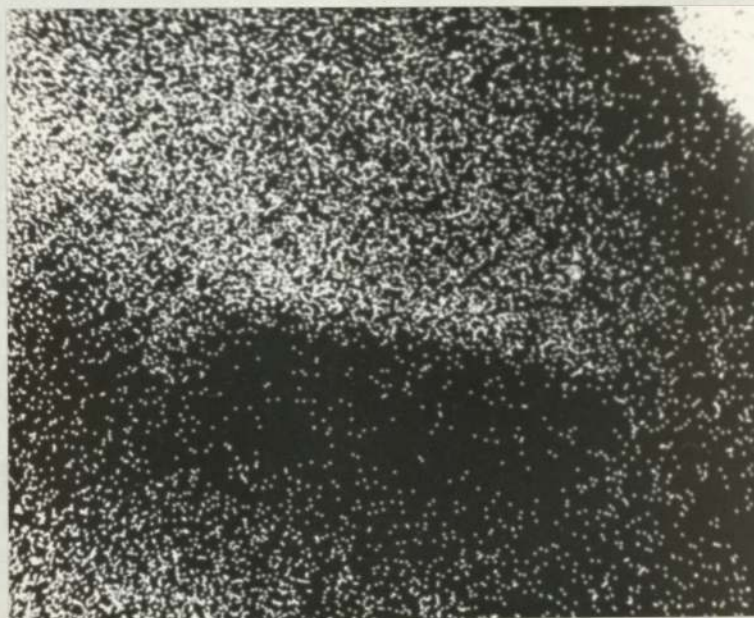
←1/100 P.S.→

Fig.84(b). Cubic Ti (C,N) Particle Shown in Fig.84(a) at High Magnification.



←1/100 P.S.→

Fig.84(c). Ti X-Ray Image of the Enlarged Particle shown in Fig.84(b).



←1/100 P.S.→

Fig.84(d). Fe X-Ray Image of the same Particle.



←1/100 P.S.→

Fig.85(a). Split Ti(C,N) Particle in the Fracture Surface.

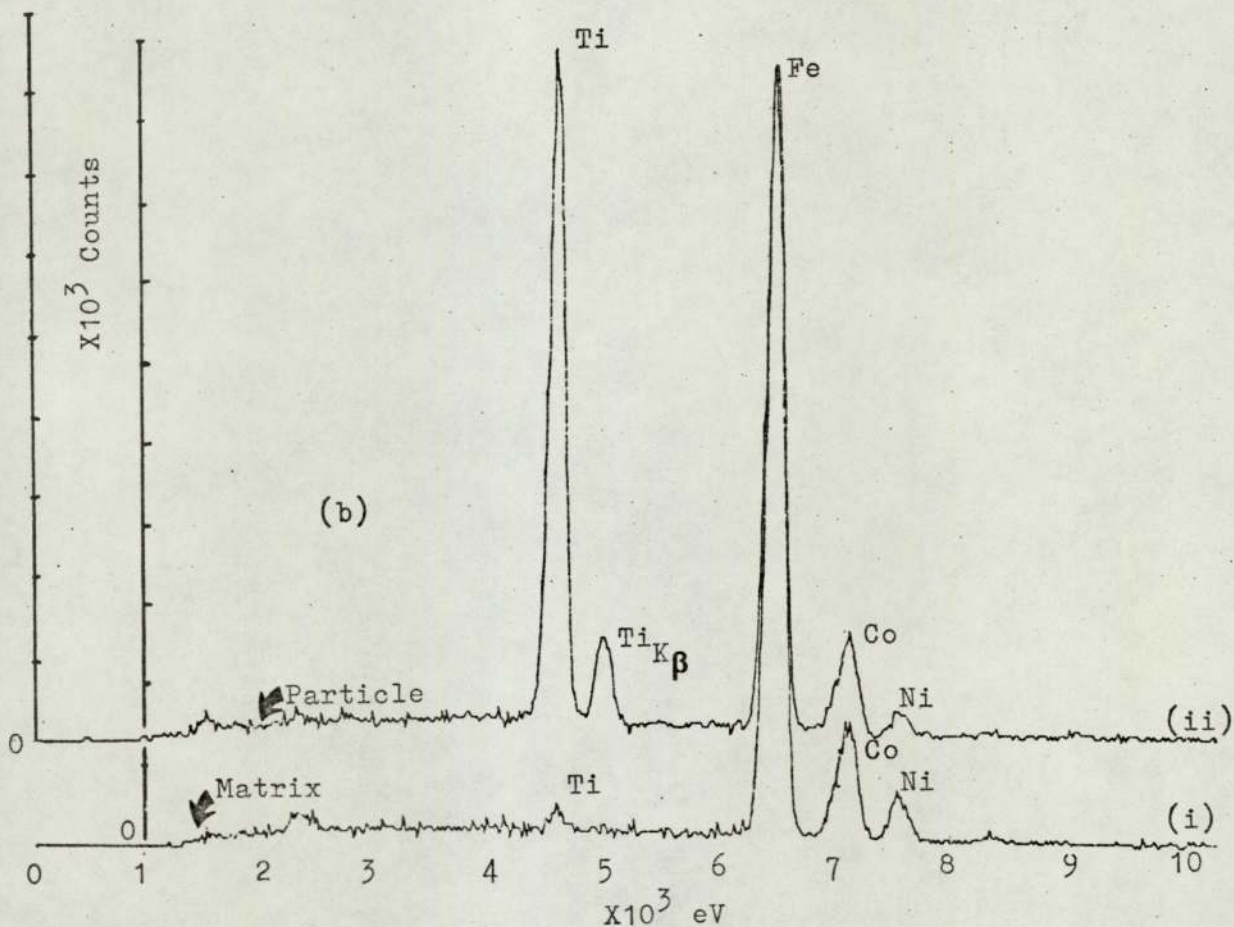


Fig.85(b). (i) Area Analysis of Elements in the Matrix of Fig.85(a).
(ii) Spot Analysis of Elements in the Split Particle of Fig.85(a).

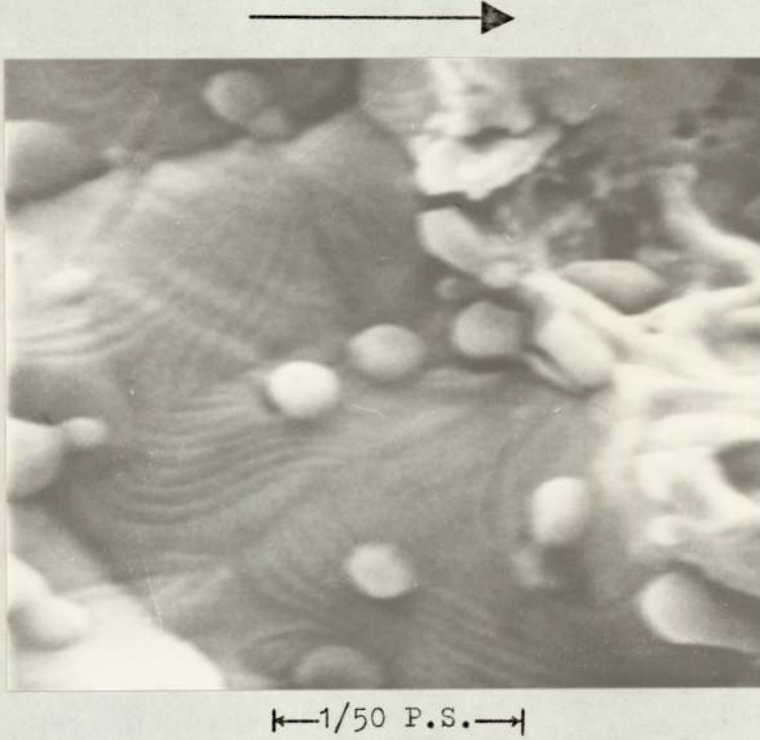


Fig.86. Ti (C,N) Particle Fusion-Bonded to the Internal Pore Surfaces with Signs of Thermal Etchings.

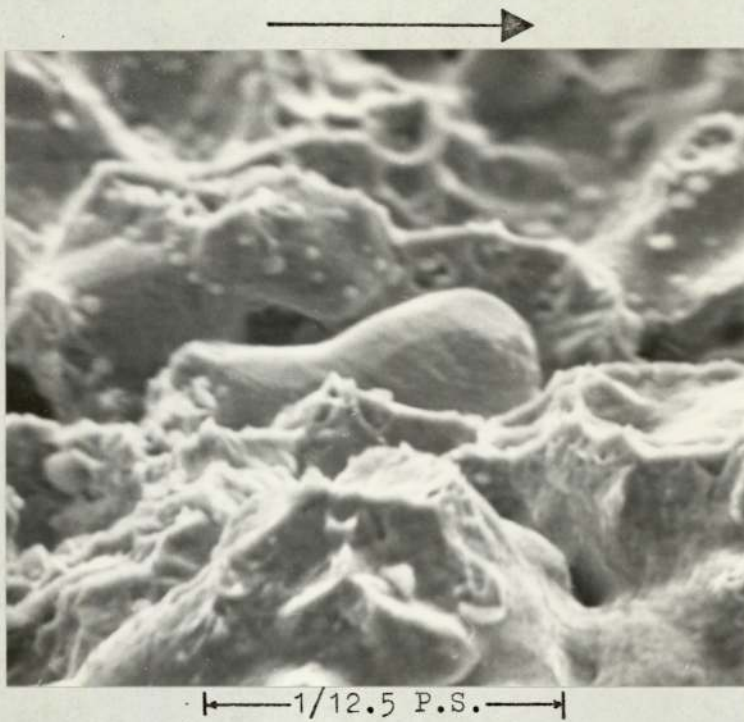


Fig.87(a). Decohesion of an Iron-Rich Particle.

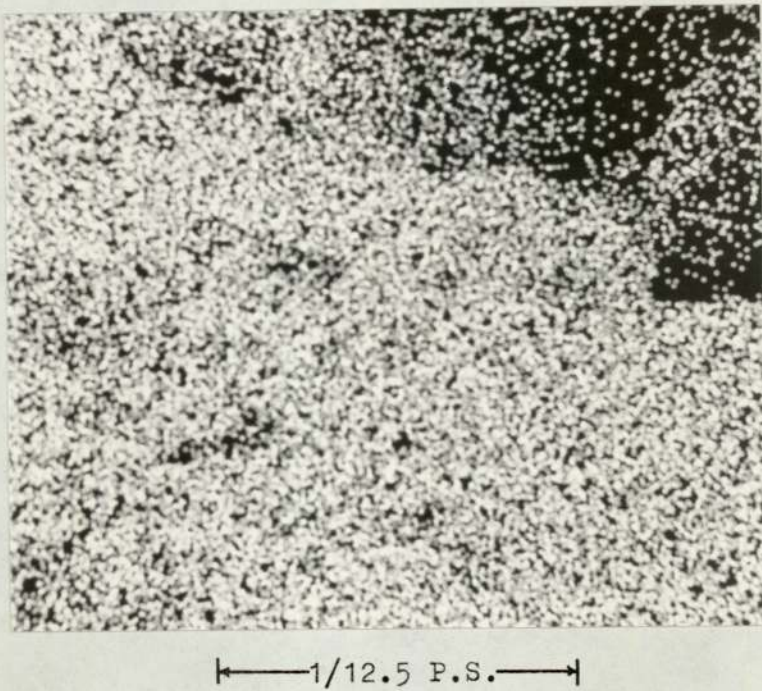
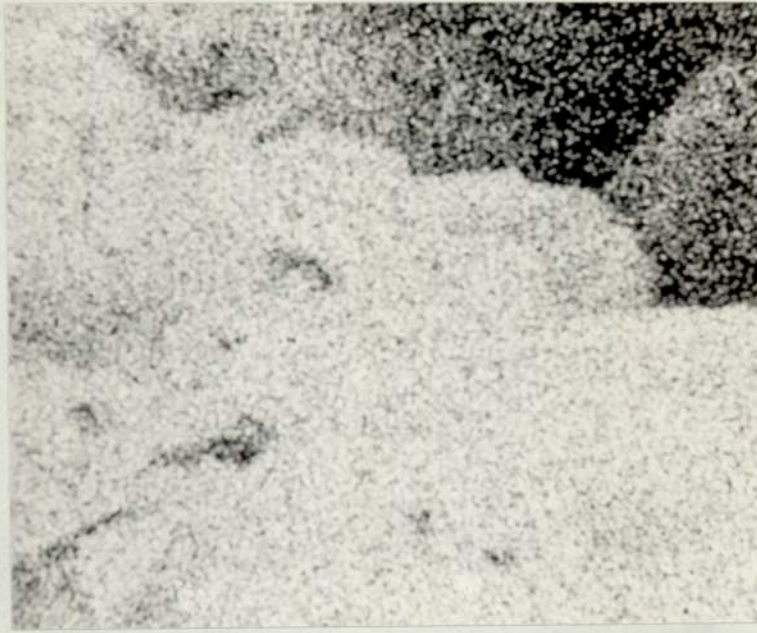
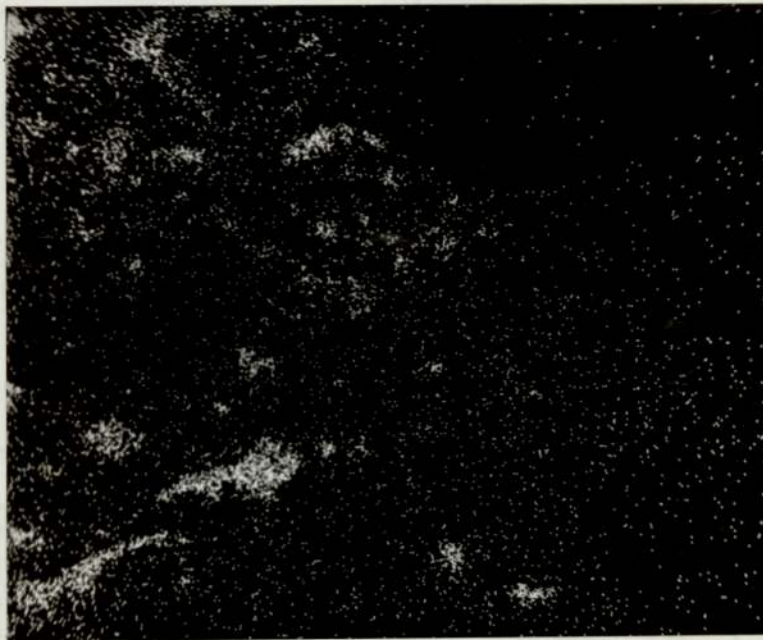


Fig.87(b). Co X-Ray Image of Fig.87(a).



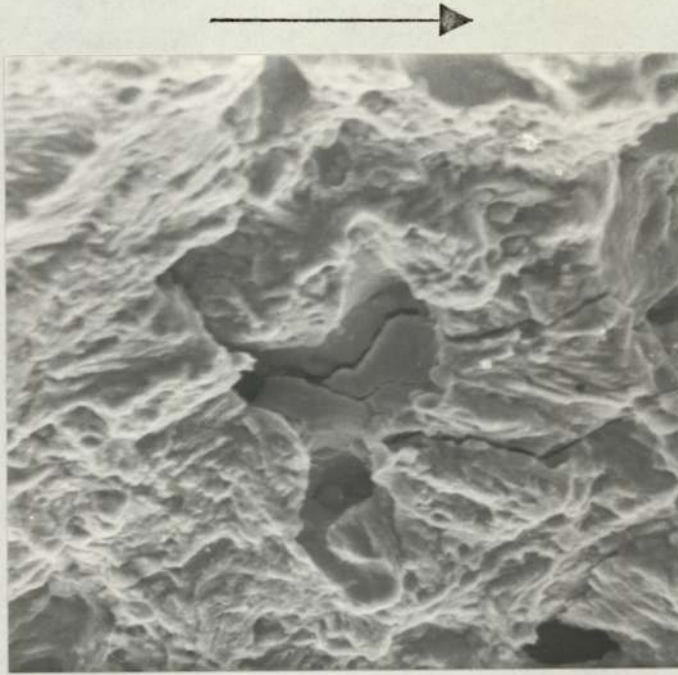
←1/12.5 P.S.→

Fig.87(c). Fe X-Ray Image of Fig.87(a).



←1/12.5 P.S.→

Fig.87(d). Ti X-Ray Image of Fig.87(a).



←1/20 P.S.→

Fig.88. Deep Intergranular Branch Cracks.



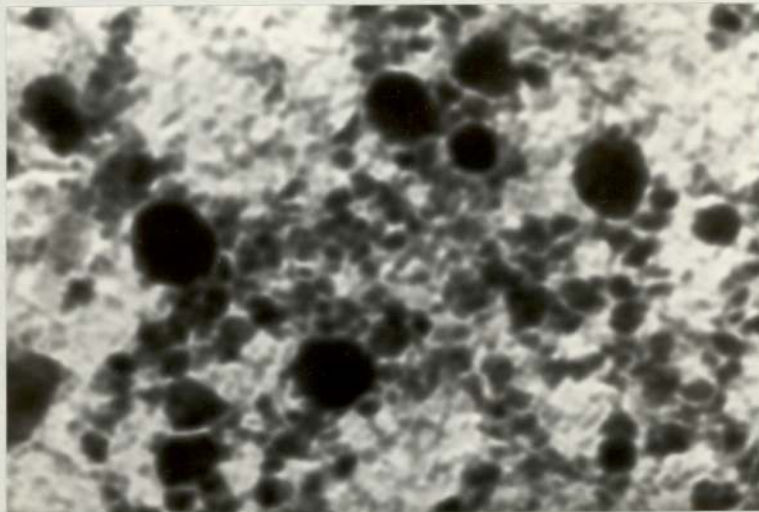
←1/100 P.S.→

Fig.89. T.E.M.-View of Different Types of Dimples and Thermal Etchings.



1/500 P.S.

Fig.90. Extraction Replica Micrographs of
(a) $\text{Ni}_3(\text{Al},\text{Ti})$ Precipitates and



1/1000 P.S.

Fig.90. (b) $\eta\text{-Al}_2\text{O}_3$ Precipitates.

10. DISCUSSION

From an inspection of the sintered density data on maraging and diluted maraging steel compacts, Table III, it has been found that the original "Green Density Vs. Compaction Pressure" matrix, which was designed and found satisfactory with minimum of experimental error, has shifted to the left, as shown below, in stages ('target' green densities and corresponding sintered densities obtained in each level are also shown):

		<u>Green Density Levels</u>				
		<u>1</u>	<u>2</u>	<u>3</u>		
(a)	M_1	d_1 (5.8)	d_2 (6.1)	d_3 (6.4)	}	
	M_2	d_1 (5.8)	d_2 (6.1)	d_3 (6.4)		ORIGINAL MATRIX
	M_3	d_1 (5.8)	d_2 (6.1)	d_3 (6.4)		

		<u>Sintered Density Levels</u>		
		<u>1</u>	<u>2</u>	<u>3</u>
(b)	M_1	d_1 (M_1) (6.9)	d_2 (M_1) (7.1)	d_3 (M_1) (7.3)
	M_2	d_1 (M_2) (6.7)	d_2 (M_2) (6.9)	d_3 (M_2) (7.1)
	M_3	d_1 (M_3) (6.5)	d_2 (M_3) (6.7)	d_3 (M_3) (6.9)

where, due to shift in sintered density,

$$d_1 (M_1) = d_2 (M_2) = d_3 (M_3) \text{ and}$$

$$d_2 (M_1) = d_3 (M_2), \text{ as shown}$$

Written in proper order, the new sintered density levels can be arranged as:

New Sintered Density Levels

			<u>1</u>	<u>2</u>	<u>3</u>
M_1			$d_1(M_1)$ (6.9)	$d_2(M_1)$ (7.1)	$d_3(M_1)$ (7.3)
M_2	$d_1(M_2)$		$d_2(M_2)$ (6.9)	$d_3(M_2)$ (7.1)	(-)
M_3	$d_1(M_3)$		$d_3(M_3)$ (6.9)	(-)	(-)
	(Left Hand Side)			(Right Hand Side)	

creating voids (-) or imbalances in the matrix.

To maintain proper balance and symmetry in the matrix, specimens with sintered density shown on the left hand side of the matrix have been discarded, while sets of new specimens have been compacted following extrapolation of calibration curves to complete the right hand side of the matrix.

The shift in the sintered density seems to arise from the particular sintering behaviour of maraging steel powder when combined or diluted with iron powder in different proportions. The variation of density, as indicated in the green and sintered density matrix shows that for the same green density level 1 (green density 5.8 Mg/m^3) compacts in the M_{11} group have the highest gain in sintered density, the lowest gain being shown by compacts in the M_{31} group. The same trend is shown by compacts at progressively higher green density levels (6.1 and 6.4 Mg/m^3). This gain in density has been manifest in the contracted specimens after sintering. Maraging steel powder, when mixed in definite proportion with pure iron powder, results in compacts less dense than compacts made of maraging steel powder after sintering.

Since no dilution had been carried out with iron powder in case of Ancoloy SA (ASA in short) compacts, there was no disproportionate shift in sintered density. The sintered density obtained in these compacts was lower than the initial green density and this was due to carbon-loss during sintering.

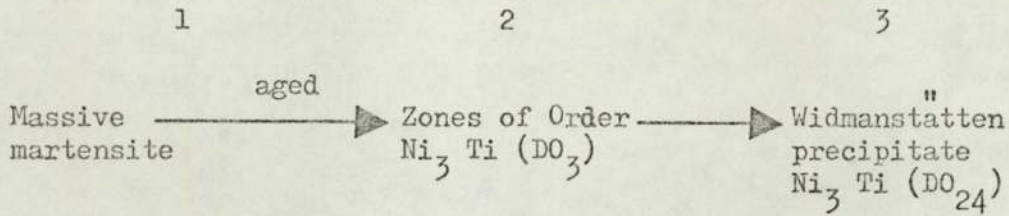
10.1 IMPORTANCE OF TITANIUM IN MARAGING STEELS.

The influence of titanium on the properties of the sintered maraging steel compacts can be best understood by considering its importance in the wrought maraging steel, as detailed in section 3.5.2. The higher strengths in the 18% Ni maraging steels are achieved mainly by increasing the titanium content and its importance can be realised from the fact that, in wrought form, for each 0.1% Ti, the yield strength is increased by 68.9 MN/m^2 (10 Ksi). The NTS/TS ratio decreases in air melts containing more than 0.4% Ti, Fig. 5. This drop-off is very sharp for maraging at 485°C (905°F), dropping to a NTS/TS ratio of 1 at 0.6 to 0.7% Ti. A Ti content of 0.7% was found to be the upper limit by Decker et al.⁽¹⁰⁾ Banerjee and Hauser⁽²⁰⁾, quoted an upper limit of Ti ~1.1% in 18% Ni-Fe base material without adverse effects on mechanical properties; in fact, it was shown to develop a Hardness of about 43 Rc, Fig. 91. The figure also shows the effect of low Ti or lack of it (as in LTM group of compacts in the present work) on 18% Ni-Fe base. Low Ti has also adverse effect on the NTS/TS ratio, as shown in Fig. 5.

The particular mechanism, which operates contributing to hardening, depends upon the nature, size and density of the precipitate distribution. Much work has been done towards identifying the composition and structure of these precipitates, but the results to analyse the precipitate phases are by no means in agreement. A general trend, however, suggests that Mo precipitates out as Ni_3Mo under normal ageing conditions. This is a metastable phase, being replaced, on overaging, by Fe_2Mo or a sigma phase. Ti generally appears to form Ni_3Ti , but this is generally difficult to identify in the presence of Ni_3Mo , and so a complex $\text{Ni}_3(\text{Mo}, \text{Ti})$ may actually exist^(27,34). Other

elements are normally found to be present in these precipitates, but Co is the exception, appearing to remain entirely in solution. In the present study, the only precipitates that could be analysed were extracted from the fractured surfaces, and analysed as $Ni_3(Al,Ti)$ and $\eta-Al_2O_3$; other precipitates were too small to be analysed by electron diffraction.

The hardening effect of titanium is due to the fact that its addition to 18% Ni maraging steels results in the formation, in the overaged condition, of a lath-like Widmanstätten precipitate formed with its long axis parallel to the $\langle 111 \rangle$ direction of the matrix, and having the composition and structure of Ni_3Ti . However, in the condition of maximum hardness, although a Widmanstätten precipitate is present in thin foils as observed by Miller and Mitchell⁽³¹⁾ and can be associated with streaking of the thin-foil diffraction patterns, a fine spheroidal precipitate is also present in an amount much too plentiful to result from the viewing of the Laths end-on. Miller and Mitchell⁽³¹⁾ found faint spots in the $\{100\}$ matrix reflection position, but these cannot result from either streaking caused by the precipitate, or double diffraction, but are an indication of ordering. It seems probable that ordering may occur as a pre-precipitation reaction, involving the spheroidal zones. This ordering could possibly be based on the $NiTi, B_2$ structure, or more likely on a metastable Ni_3Ti, DO_3 structure. Co, which also forms ordered b.c.c. compounds with Fe, could possibly stabilize formation of these ordered zones at peak hardness even though, in the final equilibrium precipitate, Co is not present in detectable amounts. Thus the hardening mechanism of Ti may be suggested as:



where peak hardness occurs between 2 and 3.

Though it is important to have the right percentage of titanium content in the 18% Ni sintered maraging steel to develop and realise the potential mechanical properties, difficulties have been encountered in the production of the pre-alloyed maraging steel powder with the specified titanium content, due mainly to the tendency of titanium to oxidise, segregate, and separate out only to combine with dross and film which may be developing in the melt. It is, therefore, essential to have an inert atmosphere melting plant to avoid loss of titanium.

10.2 CRACK INITIATION RESULTS

Taylor⁽¹⁶⁹⁾ and Parkin⁽²⁷⁾ dealing with initiation studies on maraging steel, found that the initiation characteristics depend on the condition of the material. For the maraging steel, Taylor and Parkin found that the initiation life is better in the solution treated, machined and aged condition than in the fully heat treated and machined condition. In the former, the ageing temperature is too low for recrystallisation, but there will be a tendency for residual stresses, which are compressive, to be relieved and the surface will be oxidised if the treatment is carried out in air. Moreover, there will be an additional major change, which is the precipitation of the hardening phase on dislocations. Since the surface of the notch contains a high dislocation density, as a result of the machining operation, this structure will be effectively locked in by the precipitation, forming a strong surface layer. This argument is supported by the higher hardness value in the vicinity of notch surface than the bulk material. Taylor⁽¹⁶⁹⁾ and Parkin⁽²⁷⁾ could find no hardness increase on the surfaces of specimens machined after ageing. This means that the strengthening effects of precipitation more than balances the weakening effects of oxidation and stress relieving.

The significance of the above observations lies in the fact that the sintered specimens used in the present study were sintered, solution treated, machined/notched and aged. Whatever the beneficial effect of this sequence of operations in the initiation, there was found no significant hardness increase in the vicinity of the notch tip in these specimens aged after machining and notching operations. Since no other heat treatment sequence was followed for these compact specimens, the change in initiation behaviour encountered in the

material of such compact nature, may arise from some combination of the following factors:

- (a) the specimens being compacted to different density levels and
- (b) made to different compositions by dilution with pure iron powder in certain proportions
- (c) the particular distribution and alignment of pores at the notch tip, and
- (d) the presence of residual compressive stresses, however slight, after the low temperature ageing operation.

Early attempts to study the material behaviour in fatigue crack initiation used a stress concentration factor approach which yielded design information expressed as a relationship between N_i , the number of cycles to initiation of a fatigue crack from a notch, and $K_T \cdot \Delta S$, where K_T is the Neuber elastic stress concentration factor for the particular notch, and ΔS is the range of nominal stress from zero to S max.

Following the examples of Weertman⁽¹⁴⁸⁾, Bilby and Heald⁽¹⁷⁰⁾, Jack and Price⁽¹²³⁾, a stress intensity approach has been used in the present study to provide a general description of crack initiation and propagation in the notched specimens. Weertman⁽¹⁴⁸⁾, Bilby and Heald⁽¹⁷⁰⁾ used a model of plastic relaxation at the crack tip to develop an expression relating N_i , the number of cycles to initiate a crack to the stress intensity factor range ΔK in the form

$$N_i = \frac{2 Y G}{\pi a \sigma^2} (\approx \Delta K^2) \dots \dots \dots (39)$$

where $Y = \Phi_c \cdot \sigma_y$ is a measure of the plastic work done per unit area of fracture Φ_c is the critical value of the cumulative displacement at which the crack initiation is considered to occur,

and G is the shear modulus. It was assumed here that, when the sum of the plastic displacements at the crack tip exceeded the critical value Φ_C , the crack would extend.

Though this approach provides no significant improvement to the design criteria, it leads to an unified approach in crack initiation and propagation in the notched specimens and enables comparisons with other workers.

The initiation results plotted as N_i Vs. $K_{T\sqrt{AS}}$ for the compact specimens, Fig. 47, show a distinct banding effect in the two levels of notch root radii tested. This effect exists even if plotted as N_i against $\Delta K/\rho^{1/2}$, Fig. 48, where ΔK is the range of stress intensity factor which would exist if the notch were a sharp crack of the same depth as the notch, ρ being the measured root radius for the notch. Jack and Price⁽¹²³⁾ used mild steel specimens, which were annealed after notching, and obtained good correlation of N_i with the parameter $\Delta K/\rho^{1/2}$, without much scatter or any banding effect. The initiation data, on the other hand, replotted as N_i Vs ΔK with a lower powdered exponent of root radius, Fig. 92 shows that the banding effect is markedly reduced, though some scatter still persists in the plot. A possible explanation could be found in the existence of residual stresses and/or work-hardening in the notch due to machining.

According to Neuber⁽¹¹⁸⁾, K_T has a roughly $\frac{1}{\rho^{1/2}}$ dependency (Appendix I), and taking into account of the fact that residual compressive stress, even after low temperature ageing operation, is an additional source of stress superimposed on the existing stress concentration, the real relationship between N_i and $\Delta K/\rho^n$ tends to become empirical in order to compensate for the variation in stresses needed to initiate cracks from blunt and sharp notches. The plot in Fig. 92 is based purely on empirical analysis of the data where a lower power of ρ ($n = 0.3$) in the relationship

$$N_i = B \left(\frac{\Delta K}{\rho^n} \right)^q \dots\dots\dots (40)$$

has been employed, whereby the banding effect has been markedly minimised. Pearson⁽¹²⁵⁾ also found distinct banding effect when his initiation results were plotted according to notch root radius. He used notched aluminium alloy specimens without heat-treatment subsequent to notching, and so these specimens contained any residual stresses and/or work-hardening.

The initiation data as plotted in terms of N_i Vs. ΔK , Fig.51, also show reduced banding effect, though with some scatter, which should not be considered unusual for materials of such sintered nature. In this plot, it has been found that $N_i \propto (\Delta K)^{-n}$, where $n \approx 3.5$, similar to Jack and Price's⁽¹²³⁾ plot, where n was found to be 4.

From the Fig. 51, it is also clear that the blunter notches have better initiation life than sharper notches. From an inspection of the initiation plots in Fig. 48, it is found that the higher density and higher % dilution with iron powder generally result in superior initiation life. In other words, the lower density compacts are notch-sensitive, and need lower number of cycles for initiation from notches.

Jack and Price⁽¹²³⁾ observed that, below a certain critical root radius, initiation was independent of root radius, this critical value being independent of the stress and notch depth. Jack⁽¹²⁶⁾ examined Weibull's⁽⁷⁷⁾ work on aluminium alloys and found that the results were consistent with the existence of a critical root radius. A similar conclusion can be drawn from the work of Wilkins and Smith⁽¹⁷¹⁾ on an Al-Mg alloy. This means that a critical root radius may exist for all alloys, and in the present case, if it exists at all, it must be less than 0.127 mm. Pearson⁽¹²⁵⁾ also, more or less came to the same conclusion.

Since the detection of a fatigue crack is the sole criteria of crack initiation, some crack growth must occur in order to be sure that the initiation has taken place. So, in general,

$$N_{\text{measured}} = N_{\text{true}} + N_{\text{Propagation}}$$

In order to make the stresses equal at the tips of two notches of unequal root radius, a higher nominal stress must be applied to the specimen with the blunter notch. Now, since the notch stresses are made equal, the N_{true} values will be equal (ignoring the size effect). Once cracks have nucleated at the notch tips, then to a first approximation, the nuclei and notch can be considered a single crack. Since the specimen with the blunter notch has a higher applied stress, the crack in that specimen will grow to the defined initiation length faster.

Attempts have been made by some researchers to explain banding encountered in initiation data by considering certain initiation criteria as the number of cycles for a crack to attain a 'length' of, say, 0.127 mm. Taylor⁽¹⁶⁹⁾ used Jack and Price's⁽¹²³⁾ parameter of $\Delta K/\rho^{\frac{1}{2}}$ and a crack length of 0.125 mm. as the criteria for initiation in the fully heat treated and machined maraging steel specimens. He observed evidence of banding and a broader scatter band than for his original data, without any 'length' criteria for initiation. He repeated the process for machined titanium alloy specimens, but failed to get any evidence of banding, when compared to his original data for the material without any 'length' criteria for initiation. Gowda et al.⁽¹²²⁾ also found that mild steel and Al alloy 7075-T6 are insensitive to the definition of N_i . So it is safe to suggest that sensitivity to the definition of N_i depends on the alloy being tested. Since no investigation was carried out into this aspect using the

present material, the explanation for banding still needs further exploration.

The banding effect as shown by the compact materials, when the initiation data is plotted as Ni against $K_{T} \cdot \Delta S$ or $\Delta K / \rho^{1/2}$, might be characteristic of these materials due to their inherent inhomogeneity. Although the attempts to plot the initiation data and unify the results within a single scatter band by such parameter as $\Delta K / \rho^{0.3}$ or simply ΔK against Ni might conceal this characteristic, it helps providing an adequate method for engineering design. In other words, the initiation data as presented in Fig. 51, 92 fulfills the requirements for safe design criteria for the compact materials tested. This information enables one to draw a conservative line below which initiation would not occur, and then scale down from this line by applying a safety factor on the allowable stresses.

For specimens containing sharp notches in plane strain, Jack's⁽¹²⁶⁾ relationship between Ni and the range of stress intensity factor was of the type $Ni \propto (\Delta K)^{-4}$, whereas, for the sintered specimens, a relationship of the type $Ni \propto (\Delta K)^{-3.5}$ has been observed. Weertman⁽¹⁴⁸⁾ and Bilby and Heald⁽¹⁷⁰⁾ predicted a relationship of the type $Ni \propto (\Delta K)^{-2}$ as shown in equation (39).

A possible reason for the discrepancy is due to the fact that the theoretical results are dependent on the assumed material behaviour built into the mathematical models. Bilby and Heald⁽¹⁷⁰⁾ obtained their expression for ϕ_c , the critical crack tip displacement at which the initiation is considered to occur, by linear summation of the displacements resulting from each cycle, and these displacements are assumed to be confined to a single slip plane in this model. In practice, it is likely that deformation occurs randomly on several slip planes. Others are statistical models^(172, 173) in which the

accumulation of fatigue damage is proportional to the square of the plastic strain to obtain theoretical justification for the Manson-Coffin relationship. There is also some experimental evidence from results on austenitic steel in high strain fatigue⁽¹⁷⁴⁾ which can be used to show that N_i is inversely proportional to the square of the plastic strain range for plastic strains of less than 1%. If it is assumed that the critical displacement Φ_c in the Bilby and Heald's⁽¹⁷⁰⁾ analysis is obtained by summation of the squares of the individual displacements i.e. a random rather than a linear summation, their expression becomes

$$N_i \propto (\Delta K)^{-4}$$

which agrees with the results for sharp notches in some materials⁽¹²³⁾. Although Bilby and Heald's analysis⁽¹⁷⁰⁾ applied strictly to sharp cracks, Smith⁽¹⁷⁵⁾ has shown that this treatment should be applicable to notches. Smith's analysis predicts that the displacement at the notch tip is reduced by a factor of about 2 as the root radius increases from 0 to 0.250 mm. for a 2.5 mm. deep notch. The present results show that experimentally there is no effect of root radius in this range. Similar behaviour has been observed in brittle fracture where it has been found⁽¹⁷⁶⁾ that there is a critical notch root radius below which further sharpening does not reduce the fracture toughness. This effect is generally ascribed to the fact that a particular mechanism requires a minimum volume or critical element over which to operate.

The dependence of N_i on a particular inverse power of ΔK or on the effective range of stress intensity factor in the form of $\Delta K/\rho^{\frac{1}{2}}$ or $\Delta K/\rho^{0.3}$ can be understood by studying the actual material behaviour in terms of the appropriate microstructural processes. In the sintered steels studied, the measured notch root

radius ρ may not be effectively the machined notch root radius, since the effective root radius of the notch may have been affected by the presence of the pores at the base of the notch, also plastic blunting may disturb the actual radius and may have a bigger effect at high ΔK values. So it may be argued that the effective range of stress intensity factor $\Delta K/\rho^{\frac{1}{2}}$ or $\Delta K/\rho^{0.3}$ does not adequately represent the real ΔK . In fact, there are calculations⁽¹⁷⁰⁾ which incorporates correction factors taking care of the presence of the blunt notch of root radius ρ . The effective stress intensity factor (K_{eff}) for a blunt notch is related to that for a sharp crack or notch by

$$K_{\text{eff}} = K \left(\frac{\rho_0}{\rho_e} \right)^{\frac{1}{2}} \dots\dots\dots (41)$$

where ρ_0 is the critical value of ρ

ρ_e is the effective root radius

$$\rho_e = \rho \quad \text{when} \quad \rho \geq \rho_0$$

$$\rho_e = \rho_0 \quad \text{when} \quad \rho \leq \rho_0$$

i.e. no correction would seem necessary once ρ is less than ρ_0 , the limiting sharpness for the material. Experiment by Jack⁽¹²⁶⁾ indicates a dependence of N_i on ΔK^{-4} when $\rho < \rho_0$. Eventually as the fatigue crack grows and reaches beyond the range of the radius ρ , no correction would seem necessary.

As mentioned earlier, Jack and Price⁽¹²³⁾ found a critical root radius of 0.25 mm (0.010") below which N_i was not reduced. A similar feature was also mentioned by Cottrell⁽¹⁷⁶⁾ who showed that notches of less than a critical radius must blunt to that critical radius prior to crack propagation in fast fracture and so did not reduce fracture toughness. Jack⁽¹²⁶⁾ justified his finding of the existence of such a critical root radius by demonstrating that the distance, r_0 , ahead of his notches at which the stress was equal to

that for a sharp crack was equal to one quarter of the root radius. Thus, for a 0.250 mm. (0.010") notch, this distance was of the order of the grain size of the material used by Jack, which may be described as a critical element or a minimum volume of material over which the prevailing mechanism can operate. Ahead of blunter notches, the stress at the tip of this critical element is less than at the same distance ahead of a sharp crack, and so N_i will be increased. Jack⁽¹²⁶⁾ based his argument on an approximate expression developed by Weiss and Yukawa⁽⁶⁰⁾ for the longitudinal stress distribution at a distance r ahead of the notch of root radius ρ ; in its simplified form, the expression can be written as:

$$\sigma_1 = \sigma \left[2 \left(\frac{a}{\rho} \right)^{\frac{1}{2}} + 1 \right] + \left[\frac{\rho}{\rho + 4r} \right]^{\frac{1}{2}} \dots \dots \dots (42)$$

where σ_1 is the longitudinal stress,

Weiss and Yukawa's approximation, in conjunction with the critical element size can be used to develop the modified stress intensity factor which describes crack initiation from a blunt notch.

when $a \gg \rho \gg r$,

$$\sigma_1 = 2 \sigma \left(\frac{a}{\rho} \right)^{\frac{1}{2}} \dots \dots \dots (43)$$

Hence the ratio of stresses σ_a / σ_b arising from the notches of root radii ρ_a , ρ_b is given by

$$\frac{\sigma_a}{\sigma_b} = \left(\frac{\rho_b}{\rho_a} \right)^{\frac{1}{2}} \dots \dots \dots (44)$$

At the end of the critical element, the stress for a notch of root radius ρ is given by the stress intensity factor, and it follows that, for notches of larger root radii

$$\sigma = \frac{K}{(2\pi r)^{\frac{1}{2}}} \left(\frac{\rho_0}{\rho} \right)^{\frac{1}{2}} \dots \dots \dots (45)$$

It must be assumed that the stress intensity factor controls displacements at the end of the critical element, and that N_i is controlled by these displacements rather than those at the notch root. On this basis, a more appropriate treatment would be to consider these displacements using the plastic relaxation model.

10.3. CRACK GROWTH RATE

The room temperature fatigue crack growth rate properties have been presented in Fig. 53 through Fig. 56 in terms of the stress intensity factor range (ΔK) Vs. crack growth rate (da/dN).

An inspection of the effect of stress ratio on fatigue threshold shows that the high load ratio (i.e. $R = 0.3$) used in the test, yields a threshold $\Delta K_{th} \sim 12 \text{ MN/m}^{3/2}$, while the lowest load ratio (i.e. $R \sim 0.07$) appears to indicate a ΔK_{th} value somewhere between 8 and 11 $\text{MN/m}^{3/2}$. This influence of stress ratio on fatigue threshold is not consistent with the findings reported by Bucci et al. (177), for ASTM A517 Grade F(T-1) steel, by Paris (178) for several high strength steels, and by Schmidt (179) for a Ti - 6Al - 4V alloy. They found that, higher the stress ratio, lower the threshold ΔK_{th} value.

Above the ΔK_{th} threshold value, an increase in stress ratio is accompanied by an increase in growth rate for equivalent ΔK . This trend is similar to that reported by other workers for many different alloys (178, 144).

The nearly linear relationship in stage 2 between $\log (da/dN)$ and $\log \Delta K$ shown in Figs. 53 through 56 is typical of the most fatigue crack growth rate data. Since this linear relationship exists, the crack growth rate data has been expressed in terms of the generalised fatigue crack growth rate law developed by Paris (66):

$$\frac{da}{dN} = C (\Delta K)^m$$

where da/dN is the rate of crack growth, C is an intercept constant determined from the $\log (da/dN)$ Vs. $\log \Delta K$ plot, m is the slope of the log - log plot and ΔK is the stress intensity factor range. As the

upper scatter band data represent a conservative estimate of the materials crack growth rate properties, the generalised crack growth rate expression describing this line is normally reported as the materials crack growth rate properties.

As reported earlier, in section 9.4, the growth rate for M_{12} and M_{21} compacts has been found to be 1.7 to 2.0 times faster than for M_{11} compacts at $R \sim 0.07$, over the range of ΔK considered (10 to 35 MN/m^{3/2}); for M_{13} and M_{22} compacts, the rate is 2.8 to 3.0 times faster than for M_{11} compacts, and for M_{23} , M_{31} , M_{32} , M_{33} compacts, the rate is 6.7 to 7.0 times faster than for M_{11} material. The rate for LTM compacts has been found to be 10.7 times faster than for M_{11} compacts. At higher stress ratio, $R = 0.3$, the growth rate for M_{13} , M_{23} and M_{33} has been found to be 6.0 to 6.2 times faster than for M_{11} compacts tested at $R \sim 0.07$.

In general terms, the above findings show that at lower stress ratio, $R \sim 0.07$, the growth rate curves for M_1 , M_2 and M_3 compacts fall on four distinctly separate scatter bands; also separate scatter bands have been obtained for LTM compacts at $R \sim 0.07$, and for M_{13} , M_{23} and M_{33} compacts at $R = 0.3$.

Fig. 93 summarises the fatigue crack growth data represented by the upper scatter bands for the compact materials. The slope (m) in all the crack growth expressions in Fig. 93 (a) is within the range 2.25-4.58, and 4.4 to 5.13 for the remaining two crack growth expressions as shown in Fig. 93 (b). The upper scatter band for M_{13} has been added in Fig. 93(b) for comparison. It is evident from Fig. 93(a) that the crack growth rate expression for the $M_{23}/M_{31}/M_{32}/M_{33}$ groups of compacts is the least conservative and will yield the greatest rate of crack growth. Therefore, the growth rate expression

$$\frac{da}{dN} = 5.1 \times 10^{-3} (\Delta K)^{4.58} \dots\dots\dots(46)$$

should be employed when making fatigue life predictions or calculating initial allowable flaw sizes applicable to M_1 , M_2 and M_3 groups maraging and diluted maraging steel compacts subjected to room temperature air environment. The Fig. 93(a) also shows that the crack growth rate expression for M_{11} compacts yields the slowest rate of crack growth. Therefore, from the point of view of fatigue crack growth rate, M_{11} compacts are significantly superior to other compacts in M_1 , M_2 and M_3 groups when tested at the low stress ratio.

Fig. 93(b) shows the influence of stress ratio on crack growth rate. Here the increased stress ratio R is accompanied by an increase in crack growth rate for the range of ΔK and growth rate considered. The crack growth rate for M_{13} , M_{23} and M_{33} compacts at $R = 0.3$ is 2.2 to 2.5 times faster than for M_{13} compacts tested at $R \sim 0.07$, and about 6.0 to 6.2 times faster than for M_{11} compacts tested at $R \sim 0.07$, as shown in Fig. 93 (b). This figure also shows that the growth rate is slower in the lower density M_1 compacts than in the higher density M_1 compacts, but in case of LTM compacts tested at a lower density (6.6 Mg/m^3) than the lowest of the M_1 compacts (6.9 Mg/m^3), the growth rate is remarkably high; in fact, it is higher than $M_{13}/M_{23}/M_{33}$ compacts (density 7.3 Mg/m^3) tested at $R = 0.3$. This means that there is perhaps a critical density or critical porosity content in the compact materials that governs the crack growth rate.

From a study of the room temperature properties of maraging M_1 and LTM compacts, Table III, it seems that the critical porosity content lies somewhere between 16.3 and 18%, when the crack growth rate trend is reversed, that is, the growth rate is increased with

increased porosity. In case of M_2 compacts, which is basically maraging compacts diluted with 25% pure iron powder, the resulting microstructure, with lesser amount of martensites and correspondingly higher amount of ferrite, is jointly responsible along with the porosity content for generally faster growth rate. The growth rate is still faster in M_{31} , M_{32} and M_{33} compacts ($M_1 + 50\%$ iron powder, density levels 1, 2, 3), where the effect of microstructure with still higher amount of ferrite and lesser amount of martensites, is most likely the predominant feature, the role of porosity seems marginal or not significant enough. That is, on the softer microstructural side of the microstructure - porosity relationship that an explanation is to be found for the higher crack growth rate in the M_3 compacts.

Evaluation of the results on the basis of fatigue crack growth rate behaviour associated with the scatter of results, Fig. 53a, 54, 55, seemingly indicate, as also stated earlier, that the compacts in M_1 group with the lowest density exhibit somewhat superior growth rate properties than the compacts with highest density. A speculative explanation for this behaviour may be that the presence of bigger and irregular shaped porosities in the M_{11} compacts results in delayed crack growth, and, consequently, decreased growth rates. Similar behaviour has also been reported in structural steels with discontinuities⁽¹⁷⁷⁾, due to weld defects. It appears that when the main fatigue crack front encounters 'defects' of the appropriate size, type and orientation, "blunting" of the crack tip occurs and growth stops until enough cycles have elapsed to sharpen the crack tip. Unfortunately, the effect of defects or discontinuities on fatigue crack growth is not repeatably uniform. Depending on the size, shape and orientation of discontinuities present, they can also significantly increase the rate of crack growth. For this reason, one generally

encounters comparatively large amounts of scatter in the crack growth rate data obtained from compact materials containing porosities or discontinuities.

In the case of the compacts in M_3 group, where the matrix is sufficiently soft due to the presence of large amount of ferrite, the crack blunting effect due to porosities is not operative, being largely superceded by the presence of the softer ferrite. The higher crack growth rate in this group can be explained mainly due to the presence of this softer constituents. The scatter band for the growth rate for compacts in the M_3 group can effectively accommodate any small differences in the growth rates due to the small differences in the sintered densities in this group. On the other hand, the M_2 group of compacts still retain an effect of porosities in spite of the presence of lesser amount of ferrite than in M_3 group of compacts. This effect is shown by the different growth rates obtained in this group due to the different porosity levels.

For M_1 group of compacts with a martensitic matrix, it is the orientation, concentration and shape of 'voids' which seems to control the rate of crack growth. Slower growth rate at lower densities has been explained by the 'blunting' effect of the crack tip, due to the presence of bigger and irregular shaped 'voids' along the crack path. At higher densities, one would expect the presence of smaller and rounder voids with lesser surface area in the compacted mass. Of course, it would not also be difficult for one to expect, at higher densities, a significant amount of these 'voids' to be severely compressed or 'squashed' with sharp corners and favourably oriented along the crack path. It could be that the compaction pressure, and sintering time and temperature, though high, were not sufficient enough to close or absorb these 'voids' into the matrix, or even

render the corners sufficiently harmless by making them somewhat blunter by the sintering mechanism.

It is the presence of these type of voids in adequate numbers, and favourably oriented along the crack path, which may have contributed to the lower fatigue resistance in this group of compacts at higher densities. This also seems to be the speculative explanation for the faster growth rate with increasing density, for the M_2 group of compacts.

At the present state of the art, sufficient information regarding the influence of defect characterisation on fatigue crack growth is not available to permit further generalisations.

The slopes of the crack growth rate curves for M_{11} , M_{12}/M_{21} , Table VII, are in good agreement with the work of Miller⁽¹³⁹⁾ who found a slope of 2.88 for a '200' grade maraging steel and 2.53 for a '250' grade maraging steel. Van Swam et al.⁽¹⁷⁾ found a slope of 2.0 for a '300' grade maraging steel, all tested in air. The slopes of the growth rate curves for M_{13}/M_{22} etc. are higher, and so, from the point of view of crack growth rate, the compacts in M_{11} and M_{12}/M_{21} groups stand a good chance of competing with the above grade of normal maraging steels.

10.4 Fractographic and other observations.

In non-sintered materials, specially in maraging steels, the fracture generally show striated surfaces characteristic of micro-crack growth rate, and fairly indicative of macroscopic crack growth rate. In none of the fracture surfaces of the compact materials was seen any striation markings even at high magnification. Some marking, which was seen, was the characteristic thermal etching effects due to the high temperature sintering.

The particular shape and size of pores* including 'inclusions', and their general distribution, and orientation are the determining factor in the crack growth rate for M_1 group for maraging steel compacts. In the case of the compacts in the M_3 group, it is the softer microstructural features that govern the macroscopic crack growth rate. In between the two extremes lies the compacts of the M_2 group, where it is the balance between the porosity and microstructure that governs the crack growth rate.

The fracture surfaces for the sintered specimens are microscopically entirely flat, without any sheer lips. These surfaces show the characteristic ductile dimple type of failure and the presence of dimples indicates that the fracture process is basically the necking down between the crack tip and the adjacent voids. At the tip of a crack in a fully dense material, the plane strain condition promotes

* Throughout the discussion, the term 'pore' has been used to combine the sense of 'voids and inclusions', as detailed in section 9.2. Treating the inclusions as part of the 'pores' should not be too inaccurate, as the particle/matrix interfacial strength is not particularly high.

fairly high normal stresses (all three >0) and the normal/shear stress ratio is high. Such a stress situation can affect cleavage fracture before plastic deformation (associated with high shear stresses) can cause a ductile failure. However, when appreciable porosity is present, the shear/normal stress ratio is increased because of relaxation of strict plane strain conditions (approaches plane stress) on a micro scale. This allows the attainment locally of the critical shear stress for plastic deformation before cleavage and a ductile dimple failure results. With increasing porosity, the tensile strength at a micro level and hence the fracture toughness are reduced (decreasing cross-section of micro-tensile specimens). Poor toughness can also result from inclusions and second-phase particles which initiate large fracture dimples or from a fine dispersion of very small particles which initiate many small fracture dimples. It may be that the volume of the material deformed, that is, the depth of the pores and dimples in addition to their size, determines the toughness of the compact materials. If this is true, a study of the fracture surface in three dimensions would be required to obtain a correlation between the volume of metal deformed and the toughness.

In the range of sintered materials tested, the toughness increases with decreasing porosity content and is clearly dominated by the resulting yield strength. In fact, toughness increases with increase in yield strength as shown in Fig. 44, in the range of sintered density considered. The yield stress is, of course, controlled by the strength of the necks of metal around the voids which result in less than the theoretical density. Basically, the fracture process involves drawing out the neck between the crack tip and the adjacent voids on a micro scale, and this process determines the fracture energy consumption and therefore, the fracture toughness.

Basic trend of the increase in toughness with the increased yield stress is illustrated in Fig. 94, which also contains results from previous work of the author and other workers, on sintered materials. This relationship between toughness and yield strength is the opposite of that which normally arises in, say, high-strength steels, aluminium or titanium alloys.

The increase in toughness with yield strength is an interesting feature of the behaviour of sintered steels, since it suggests the possibility that high strength, highly alloyed, sintered steels could match the high-strength wrought steels, titanium and aluminium alloys, as illustrated in Fig. 95. Toughness data comparing these materials have been abstracted from Pellini's work⁽¹⁸⁰⁾ and the high toughness figures correspond to the energies absorbed in a drop-weight test⁽¹⁸¹⁾, whereas the lower toughness figures are K_{IC} values. The sintered materials examined in the present study compare well with the high-strength aluminium and titanium alloys, but an extrapolation of the toughness/yield stress trend would carry them into competition with high-strength wrought steels. There is no doubt that this possibility will tempt other investigators to venture into this meaningful field.

An attempt was made to pin down the 'effective' notch root radius (P_e), above which the apparent values of fracture toughness show a noticeable increase. With this value of P_e was compared the minimum root radius of pores (P_{min}) measured in the sintered and heat treated maraging, diluted maraging steel and Ancoloy SA (ASA) compacts, after light etching. Also, the relationships of crack opening displacement ($\frac{\delta_c}{2}$) with P_e and P_{min} were looked into, in the above

sintered materials, and the possibility of improving toughness by manipulating P_{\min} of pores was explored (Details are set out in Appendix - II).

From the results given in Appendix - II, it has been found that

$$P_{\min} < \frac{\delta_c}{2} \ll P_e.$$

In fact, the minimum root radius of the pores have been found to be extremely small compared to the 'effective' notch root radius (P_e) of specimens, above which the K apparent values tend to go up with root radius ρ . This means that some of the defects or pores in the compact materials are isolated, but with very sharp root radius. They are like any other defects in non-compact materials, and do not become operative in toughness testing situations unless they are favourably oriented. This finding is preliminary at this stage and needs further exploration.

11.

CONCLUSIONS

A distinct banding effect, possibly characteristic of the sintered materials tested had been observed when the initiation data were plotted as Ni against $K_{T0} \Delta S$ or $\Delta K / \rho^{\frac{1}{2}}$ for the two levels of notch root radii of 0.127 and 0.762 mm.

Banding effect was markedly reduced when the initiated data was replotted as Ni against ΔK or an empirical parameter $\Delta K / \rho^{0.3}$.

No critical notch root radius was found below which initiation was independent of root radius.

There was perhaps a critical density or critical porosity level in the sintered materials, below which crack growth rate increased with increased porosity content; above the critical level, decreased fatigue resistance arose from increased sintered density.

Comparatively higher crack growth rate in M_3 group of sintered compacts was due to the presence of soft ferrite in the matrix, which largely superceded the crack blunting effect due to porosities.

The micromechanism of fracture was of ductile dimple type in every case.

No striation markings were observed on fracture surfaces; instead, some characteristic lines found on the internal pore surfaces exposed after fracture were due to thermal etching effects.

Increase in toughness with increased yield stress seemed to be the basic trend in the sintered materials tested so far. This was because the fracture was effected by plastic instability on a micro-level.

12. RECOMMENDATIONS FOR FUTURE WORK

The present work opens up wider areas for further investigation. Some of these potential areas are outlined below:

It would be useful to test sintered specimens which have been machined and notched after full heat-treatment in order to isolate the effect of residual stresses or work hardening on crack initiation.

A 'Length' criterion for crack initiation may be used in future work to see whether sintered materials are sensitive to the definition of Ni and banding.

The concept of critical density or critical porosity level in sintered materials and the absence of striation markings on their fracture surfaces need further exploration.

Besides higher sintered density, infiltration, pore sealing or other approaches appear to be attractive for further improvement of fracture toughness.

Effect of root radius of pores on crack initiation and propagation characteristics and on toughness need careful exploration.

Fracture Mechanics approach, as applied in the present study, may be attempted for the assessment of thermal fatigue characteristics and corrosion damage in the sintered materials.

13.

ACKNOWLEDGEMENTS

It is my pleasure to thank Prof. J.T. Barnby for his valuable guidance and encouragement throughout this Project. The author also wishes to thank Prof. W.O. Alexander for the provision of necessary facilities in the Department which made this Research possible.

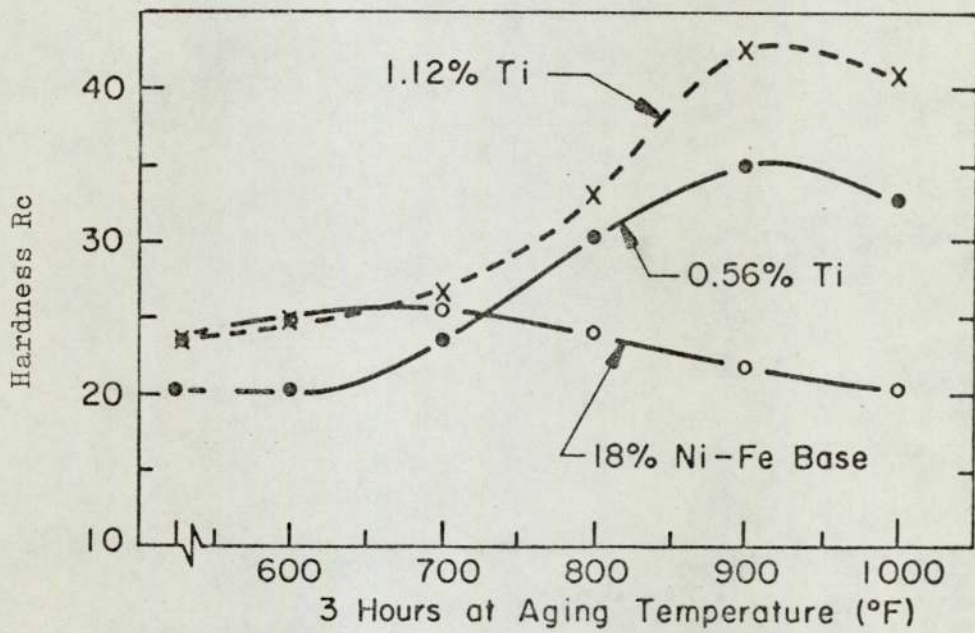


Fig.91. Variation in Hardness of 18 % Ni-Fe Base Alloy with Titanium Content, plotted as a Function of Ageing Temperature.

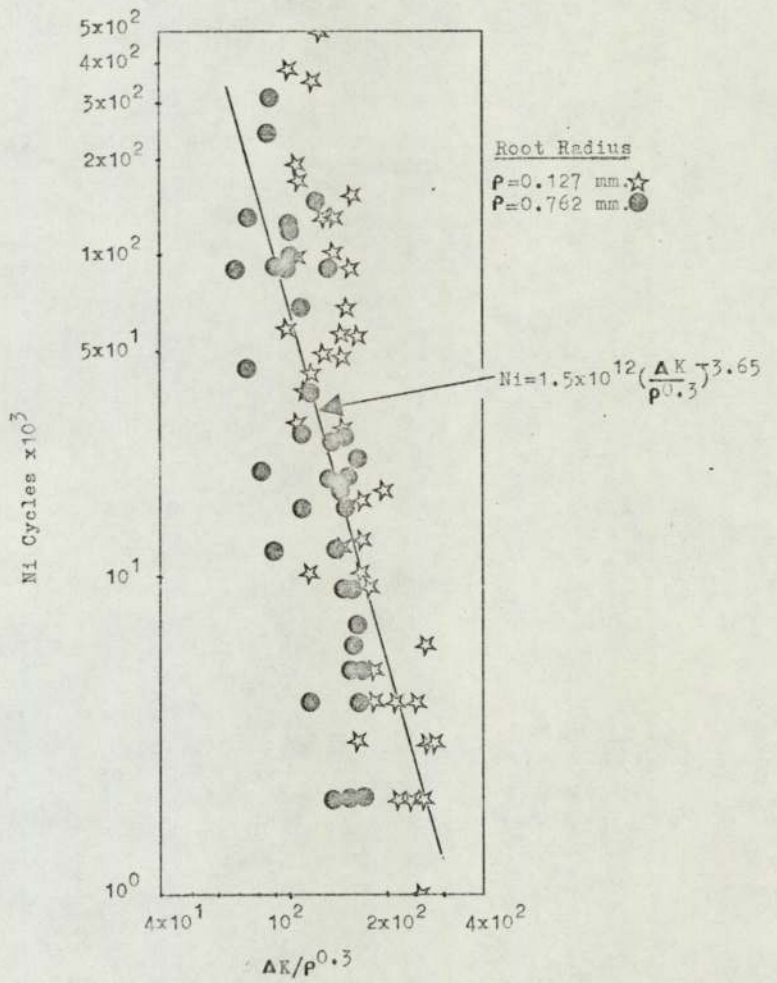


Fig.92. Effect of factors ΔK and ρ combined in a form derived by Regression Analysis on the no. of cycles to crack initiation, N_i .

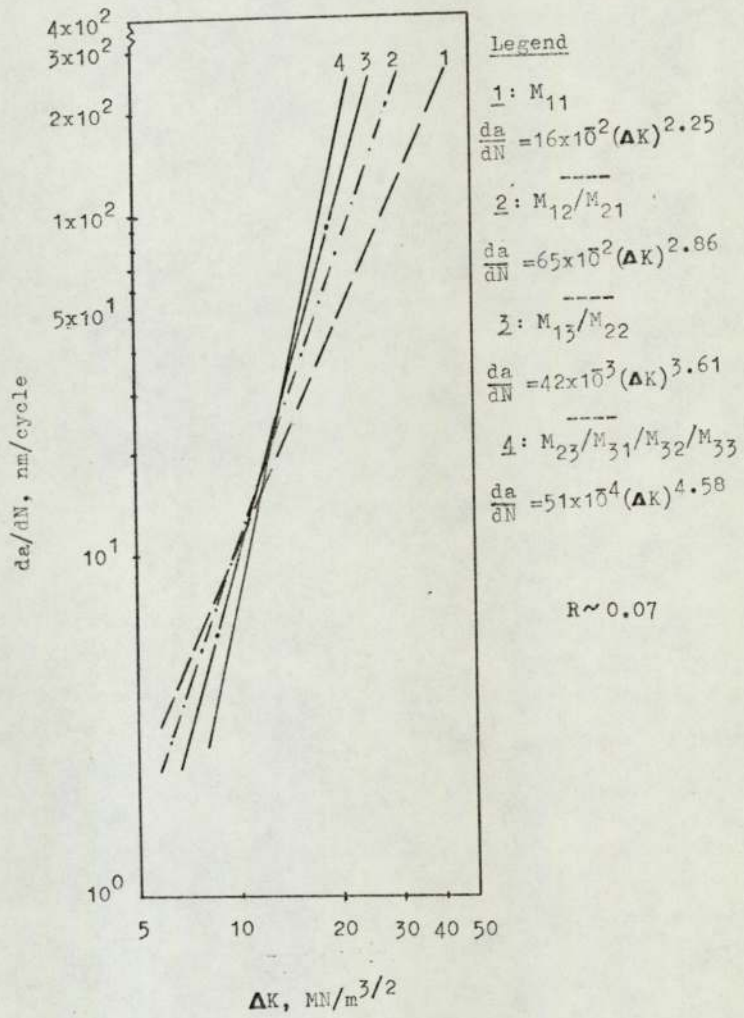


Fig.93(a). Summary of the Fatigue Crack Growth Rate Data generated for the Sintered Materials tested in this work.

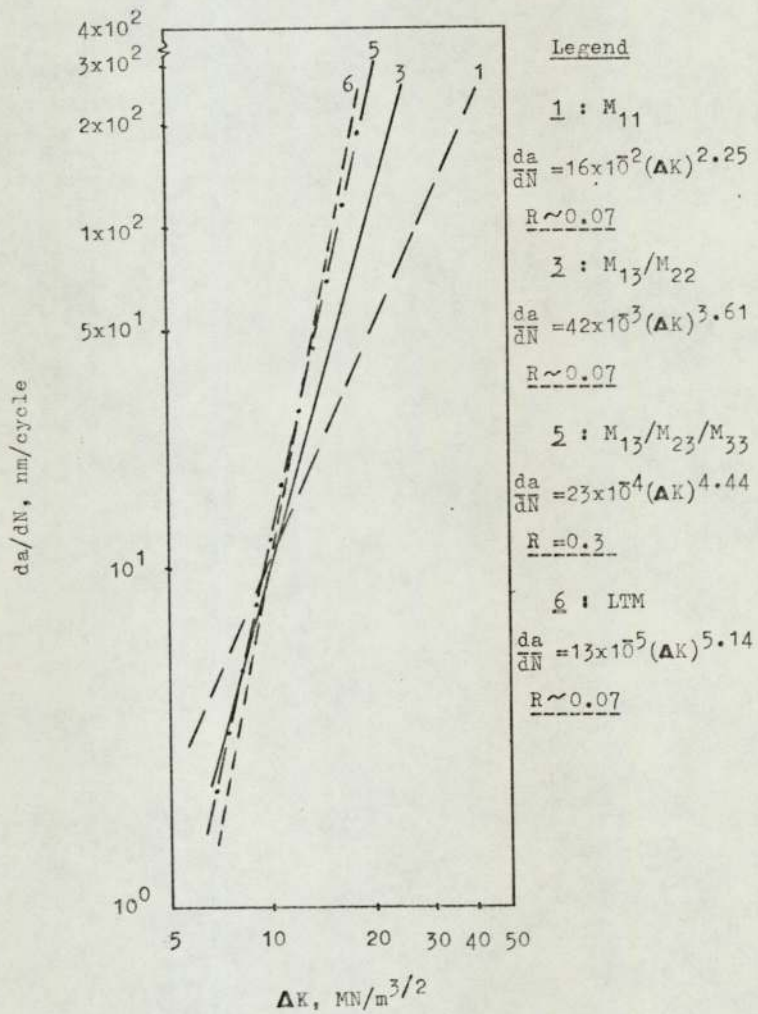


Fig.93(b). Summary of the Fatigue Crack Growth Rate Data (Cont'd.).

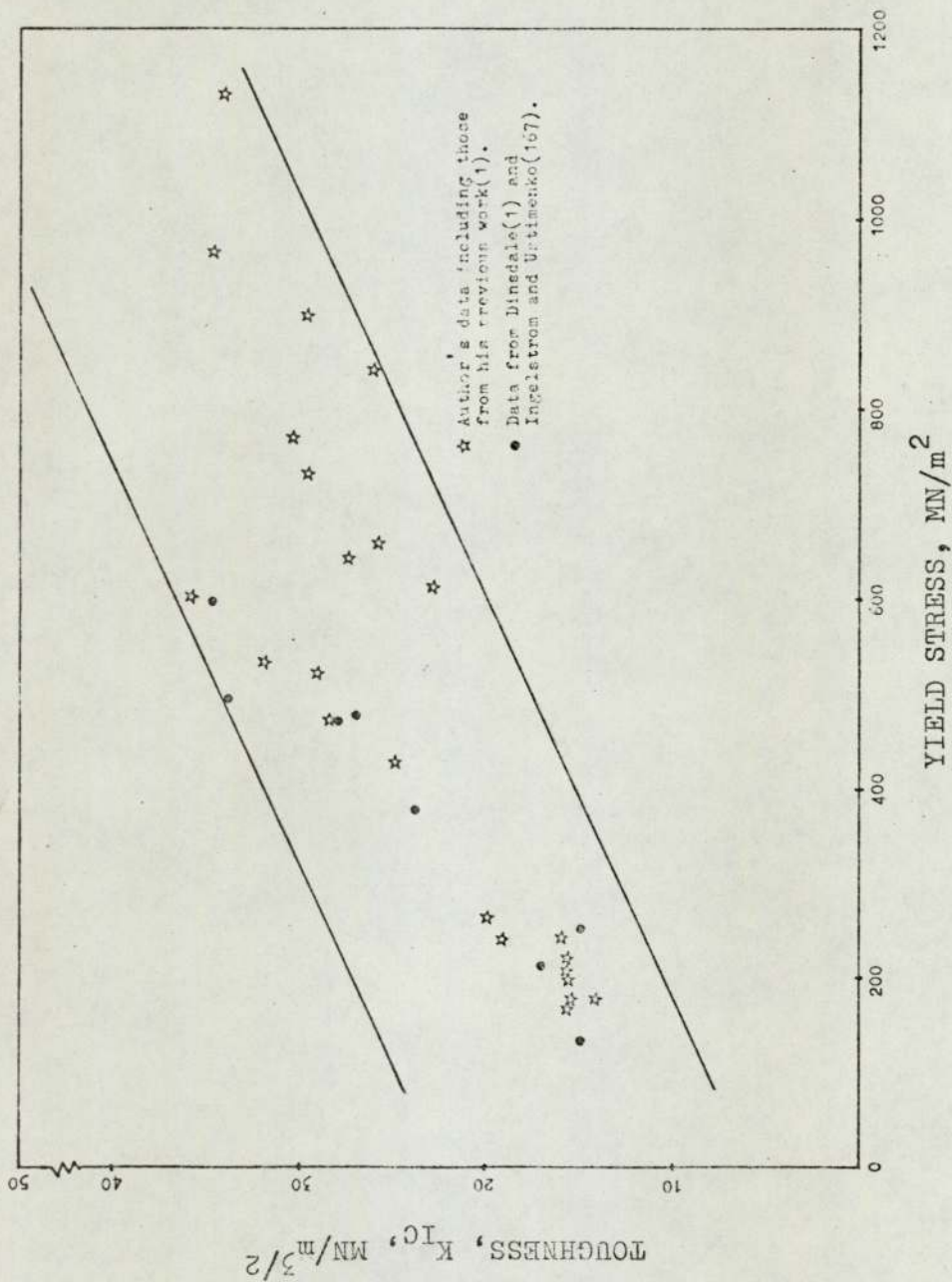


Fig.94. Variation in Toughness with Yield Stress for all the Sintered Materials tested in this work. Also included are data from others as shown.

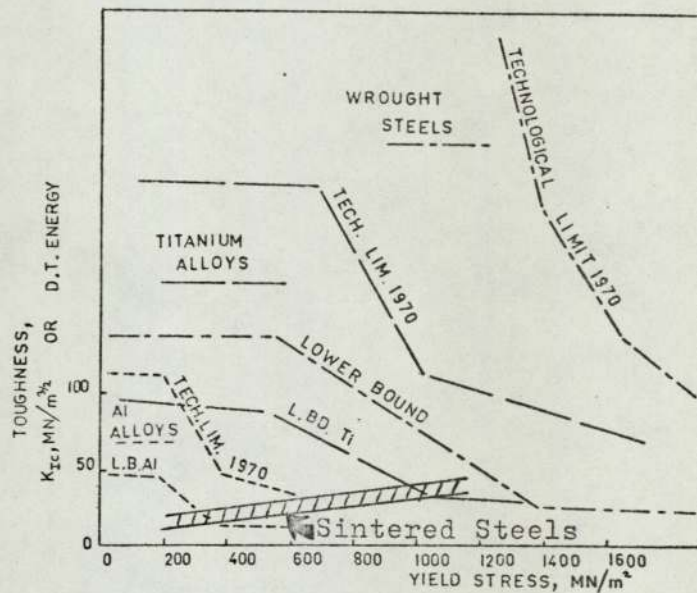


Fig. 95. Toughness/yield-stress relationships for wrought steels, titanium alloys, and aluminium alloys, compared with data on the sintered materials tested in this work.

1. Barnby, J.T., Powder Metallurgy, 16 (31),
Ghosh, D.C. and 1973, p.55.
Dinsdale, K.
2. Haynes, R. Powder Metallurgy, 13 (26),
1970, p.465.
3. Talmage, R. Mod. Dev. in P.M., 3, p.227
Plenum Press, 1966.
4. U. S. Patent No. 2, 769, 709.
5. Floreen, S. and A.S.M. Trans. Qrt. 57 (3),
Speich, G.R. 1964, p.714.
6. Spitzig, W.A., Engg. Fract. Mech. 1, 1968,
Talda, P.M. and p.155.
Wei, R.P.
7. Spitzig, W.A. and Engg. Fract. Mech., 1, 1970,
Wei, R.A. p.719.
8. Coleman, M.C. and Metal Tech., Jan. 1974,
Jordan, M.F. p.24.
9. Yoder, G.R. Met. Trans. 3, 1972, p.1851.
10. Decker, R.F., Trans. of A.S.M., 55, 1962,
Eash, J.T. and p.58.
Goldman, D.A.
11. Yates, D.H., and Metal Progress, 82 (Sept.),
Hamakar, J. 1962, p.97.
12. Floreen, S. and A.S.M. Qrt. Trans., 55 (3),
Decker, R.F. 1962 (March), p.518.
- 12A. Snape, E. and Powder Metallurgy, 15 (30),
Veltry, F. 1972, p.332.

13. Fisher, J.J. Int. J. of Powder Met., 2 (4),
1966, p.37.
14. Pampillo, C.A. and Met. Trans., 3, 1972 p.2895.
Paxton, H.W.
15. Tuffnell, G.W. and A.S.M. Trans. Qrt., 61
Cairns, R.L. 1968, p.798.
16. Floreen, S. Met. Rev. no. 126 (13),
1968, p.115.
17. Van Swam, L.F., et al. Met. Trans., 6 (1),
1975 (January), p.45.
18. Pellisier, G.E. Weld Imperfections, p.427.
19. Decker, R.F., J. of Metals, 19, 1967, p.60.
Novak, C.J. and
Landig, T.W.
20. Banerjee, B.R. and Tech. Report, Wright Patterson
Hauser, J.J. AFB, Ohio, AFML-TR-66-166, March, 1966.
21. Decker, R.F., et al. A.S.M. Trans., 55, 1962, p.58.
22. Owen, E.A. and J.I.S.I., 163, 1949, p.132
Liu, Y.H.
23. Jones, W. and J.I.S.I. 163, 1949, p.121
Pumphrey, W.
24. Kaufman, L. and Trans., A.I.M.E., 206,
Cohen, M. 1956, 1393.
25. Owen, W.S., High Strength Materials, 1965,
Wilson, E.A. p.167 (John Wiley, New York &
and Bell, T. London)
26. Patterson, R.L. and A.M., 14, 1966, p.347.
Wayman, C.M.

27. Parkin, J.R. M.Sc. Project, 1973, University of
Aston in Birmingham (U.O.A.B.)
28. Yeo, R.G.B. Trans. A.I.M.E., 227, 1963,
p.884.
29. Weltzin, R.D. and Met. Eng. Qrtly., 14,
Berger, C.M. May, 1974, p.62.
30. Peters, D.T. and Trans. A.I.M.E., 236, 1966,
Cupp, C.R. p.1420.
31. Miller, G.P. and J.I.S.I., 203, 1965, p.899.
Mitchell, W.I.
32. Perkass, M.D. Met. Sci. and Heat Treatment,
7-8, 1970, p.558.
33. Baker, A.J. and Trans. Qrt. A.S.M., 57, 1964,
Swann, P.R. p.1008.
34. Reisdorf, B.G. and Wright Patterson AFB, Ohio,
Baker, A.J. Tech. Report (AFML-TR-64-390), 1965.
35. Detert, K. Trans. Quart. A.S.M., 59, 1966,
p.262.
36. Detert, K. Arch. Eisenhüttenwesen, 37, 1966,
p.579.
37. Banerjee, B.R., et al. Tech. Report on The Fourth Maraging
Steel Project Review, A.F.M.L.-TDR.64.
- 37A. " " Hogan, A.B. Iron Powder Information, P.M. 70-1.
38. " Thummler, F. and Met. Rev. No. 115, 1967,
" Thomma, W. p.69.
39. Lenel, F.V., Mod. Dev. in Powder Met., 4,
Ansell, G.S. and 1971, p.199.
Morris, R.C.

40. Rhines, F.N. and Dehoff, R.T. Mod. Dev. in Powder Met., 4, 1971, p.173.
41. Sauerwald, F. Z. Physikal. Chem., 209, 1958, p.206.
42. Herring, C. Nabarro, F.R.N. J. Appl. Physics, 21, 1950, p.301. Report of Conf. on 'Strength of Solids', 1948, p.75.
43. Kuczynski, G.C. Trans. A.I.M.M.E., 185, 1949, p.169.
44. Jones, W.D. Fundamental Pr. of Powder Met., Arnold (London), 1960, p.386.
45. Kingery, W.D. J. Appl. Physics, 30, 1959, p.301.
46. Mc Adam, G.D. J.I.S.I. 168, 1951 1951 (August), p.346.
47. Rolfe, S.T. Int. Met. Rev. No. 186, 19, Sept. 1974, p.183.
48. Griffith, A.A. Phil. Trans. Ry. Soc. (London), Series A, (1920), 221, p.163.
49. Irwin, G.R. J. Appl. Mechanics, 24, 1957, p.361.
50. Orowan, E. Welding Res. Supplement, 20, 1955, p.157.
51. Inglis, C.E. Trans. Inst. Nav. Architects, 60, 1913, p.219.
52. Brown, W.F. and Srawley, J.E. A.S.T.M. - S.T.P. 410, 1966, p.9.
53. Walker, E.F. and May, M.J. B.I.S.R.A. Open Report No. MG/E/307/67.
54. Irwin, G.R. and Kies, J.A. Welding Journal, 33, 1954, p.193.

55. Sullivan, A.M. Mat. Res. and Std., 4, 1964,
p.20.
56. Johnson, H.H. and Engg. Fract. Mech. 1,
Paris, P.C. 1968, p.3.
57. Paris, P.C. and A.S.T.M. - S.T.P. 381,
Sih, G.C. 1965, p.30.
58. Barnby, J.T. N.D.T. Dec. 1971, p.387.
59. Pook, L.P. N.E.L. Report No. 465, 1970, p.1.
60. Weiss, V. and A.S.T.M. - S.T.P. 381, 1965,
Yukawa, S. p.6.
61. Barnby, J.T. Welding and Metal Fab.,
Feb. 1969, p.72.
62. Hahn, G.T. and Acta Met., 13, 1965,
Rosenfield, A.R. p.293.
63. Pook, L.P. N.E.L. Report No. 465, 1970, p.4.
64. Srawley J.E. and A.S.T.M. - S.T.P. 381, 1965,
Brown, W.F. p.133.
65. Brown, W.F. and A.S.T.M. - S.T.P. 410, 1966.
Srawley, J.E.
66. Paris, P.C. Proc. of 10th. Sagamore Army Conf.,
1964, Syracuse Univ. Press, p.107.
67. Rice, J.R. A.S.T.M., STP. 415, 1967, p.247.
68. Dobson, M.O. 'Fract. Fract. Mech. for Struct.
Steel', Chapman & Hall, London, 1969, Bl.
69. Walton, D. and Int. Met. Rev. No. 163, p.100
Ellison, E.G.

70. Forsyth, P.J.E. Proc. Crack Prop. Symp. 1961,
Cranfield, p.76.
71. Ewing, Sir J.A. and Phil. Trans., A. 200,
Humfrey, J.W.C. 1903, p.241.
72. Forsyth, P.J.E. Int. Conf. on the Fatigue of Metals,
London. Inst. Mech. Engrs.
73. Allery, M.B.P. and Engg. Fract. Mech., 4, 1972,
Birkbeck, G. p.325.
74. Thompson, N., Phil. Mag. 1, 1956, p.113.
Wadsworth, N.J.
and Louat, N.
75. Kennedy, A.J. Processes of Creep and Fatigue in Metals,
Oliver and Boyd, London, 1962.
76. Lynch, S.P. Met. Sc., 2 (9), Sept. 1975, p.401.
77. Weibull, W. Proc. of Crack Prop. Symp.,
Sweden, 1961, p.271.
78. Hoepfner, D.W. A.S.T.M. S.T.P.-415, 1967, p.486.
79. GrossKreutz, J.G. Physica Status Solidi (b), 47,
1971, p.359.
80. Plumbridge, W.J. Met. Rev. 14, 1969, p.119.
and Ryder, D.A.
81. Forsyth, P.J.E. "Physical Basis of Metal Fatigue",
1969, Blackie (London).
82. Lynch, S.P. A.R.L. Met. Report No. 94, 1974.
83. Cottrell, A.H. 'Mech. Properties of Matter',
p.373, 1964, John Wiley & Sons
(New York).

84. Lynch, S.P. and 'Aluminium', 49 (11), 1973,
Ryder, D.A. p.748.
85. Forsyth, P.J.E. Acta Met., 11, 1963, p.703.
86. Stubbington, C.A. ibid., 12, p.931.
87. Lynch, S.P. Met. Sc. J. 7, 1973, p.93.
88. Laird, C. A.S.T.M. S.T.P. 415, 1967, p.131
89. McEvily, A.J. and Acta Met., 11, 1963, p.725.
Boettner, R.C.
90. Zappfe, C.A. and Trans. A.S.M., 41, 1949, p.396.
Worden, C.D.
91. Crussard, C. Proc. of Int. Conf. on Fatigue of
Metals, p.784, Inst. of Mech. Eng.,
London, 1956.
92. Ryder, D.A. R.A.E. Tech. Note (Met. 288), 1958.
93. Forsyth, P.J.E. and Aircraft Engg., 32, 1960, p.96.
Ryder, D.A.
94. Plumbridge, W.J. and Met. Rev. No. 136, 2, 1968, p.119.
Ryder, D.A.
95. Richards, C.E. Acta Met., 19, 1971, p.583.
96. Lindley, T.C. and I.S.I. Report 145, 1971, p.119
Richards, C.E.
97. Jacoby, G. N.A.T.O. - A.G.A.R.D. Report (541),
1966.
98. Metals Handbook 2, 1974, p.69 (A.S.M.)
99. Zaman, K. Ph.D. Thesis, 1973, U.O.A.B.
100. Schijve, J. A.S.T.M. S.T.P. 415, 1967, p.533

101. Forsyth, P.J.E.,
Stubbington, C.A.
and Clark, D. J. Inst. of Metals, 90, 1961-62,
p.238.
102. Beachem, C.D. and
Pelloux, R.M.N. A.S.T.M. - S.T.P. 381,
1965, p.210.
103. Forsyth, P.J.E. R.A.E., Tech. Note (Met. 257) 1957.
104. Laird, C. and
Smith, G.C. Phil. Mag. 7, 1962, p.847.
105. Forsyth, P.J.E. and
Sampson, E.G.E. R.A.E. Tech. Report (65 158),
1965.
106. Whiteson, B.V., et al. A.S.T.M., S.T.P. 436, 1968,
p.151.
107. Metals Handbook 9, 1974, p.86, (A.S.M.)
108. Laird, C. and
Kaplan, H. Trans. of Met. Soc. of A.I.M.E.
T.M.S.A.A., 239, 1967, p.1017.
109. Schijve, J. A.S.T.M., S.T.P. 415, 1967, p.415.
110. Broek, D. Int. Met. Rev. No. 185, 19,
Sept. 1974, p.135.
111. Pelloux, R.M.N. Engg. Fract. Mech., 1, 1970, p.697.
112. Tomkins, B. Phil. Mag. 18, 1968, p.1041.
113. Pelloux, R.M.N. Trans. A.S.M., 57 (5), 1964, p.11
114. Pisarsky, H. Ph.D. Thesis, 1974, U.O.A.B.
115. GrossKreutz, J.C.
and Shaw, G. 'Fracture', 1969, p.620.
Chapman & Hall, London
116. Forsyth, P.J.E. and
Ryder, D.A. Metallurgia, 63, 1961, p.117.

117. EL-Soudani, S.M. and Pelloux, R.M.N. Met. Trans., 4, 1973, p.519.
118. Neuber, H. J. of App. Mech., Dec. 1961, p.554.
119. Wetzel, R.M. J. of Materials, 3 (3), Sept. 1968, p.646.
120. Topper, T.H., Wetzel, R.M. and Morrow Jo Dean. J. of Materials, 4, 1969, p.200.
121. Morrow, J., Wetzel, R.M. and Topper, T.H. A.S.T.M., S.T.P. 462, 1970, p.74.
122. Gowda, C.V.B., Topper, T.H. and Leiss, B.N. Proc. Int. Conf. on Mech. Behaviour of Materials, Kyoto, Japan, Vol. II, 1971, p.187.
123. Jack, A.R. and Price, A.T. Int. J. of Fract. Mech., 6, 1970, p.401.
124. Bilby, B.A., Cottrell, A.H. and Swinden, K.H. Proc. Roy. Soc. A 272, 1963, p.304.
125. Pearson, S. R.A.E. Tech. Report No. 71109, May, 1971.
126. Jack, A.R. Ph.D. Thesis, 1971, U.O.A.B.
127. Dinsdale, K. Private communication. 1973, U.O.A.B.
128. Forman, R.G. Engg. Fract. Mech., 4, 1972, p.333.
129. Creager, M. and Paris, P.C. Int. J. of Fract. Mech. 3, 1967, p.247.
130. Manson, S.S. Exp. Mech., 1965, p.193.

131. Barnby, J.T.,
Dinsdale, K. and
Holder, R. Conf. on Fract. Mech. Camb. Un.,
Paper No. 26, 1974.
132. Head, A.K. Phil. Mag. 44, 1953, p.925.
133. Frost, N.E. and
Dugdale, D.S. J. of Mech. and Physics of Solids,
6, (2), 1958, p.92.
134. Liu, H.W. Trans. A. Soc. of Mech. Engg., 85,
Series D. 1963, p.116.
135. Frost, N.E. J. of Mech. Eng. Soc., 1(2),
Sept. 1959, p.151.
136. Tomkins, B. and
Biggs, W.D. J. of Mat. Sc., 4, (6), 1969.
137. Tomkins, B. Phil. Mag. 18 (155), Nov. 1968.
138. Paris, and
Erdogan, Trans. of A.S.M.E., Series D,
1963, p.528.
139. Miller, G.A. Trans. A.S.M.E., 61, 1968, p.442.
140. Clark, W.G. Metal Progress, 79, 1970, p.81.
141. Forman, R.G.,
Kearney, V.E. and
Engle, R.M. J. of Basic Engg. A.S.M.E. Trans.
89, 1967, p.459.
142. Broek, D. and
Schijve, J. N.L.R. - TR M2111, Jan. 1963.
143. Illg, W. and
McEvily, A.J. NASA TN D - 52, Oct. 1959.
144. Crooker, T.W. and
Lange, E.A. NRL Report No. 6805,
Nov. 1968.
145. Pearson, S. R.A.E. Tech. Report 68297,
Dec. 1968.

146. Maddox, S.J. Int. J. of Fracture, 11 (3), June, 1975, p.389.
147. Heald, P.T.,
Lindley T.C. and
Richards, C.E. Mat. Sc. Engg., 10, 1972, p.235.
148. Weertman, J. Int. J. of Fract. Mech. 2, 1966,
p.460.
149. Roberts, R. and
Erdogan, F. Trans. A.S.M.E., Series D,
89, 1967, p.885.
150. Klensil, M. and
Lucas, P. Engg. Fract. Mech., 4,
1972, p.77.
151. Cooke, R.J. and
Beevers, C.J. Int. Report, B'ham University,
1973.
152. Donahue, R.J.,
et al. Int. J. of Fract. Mech. 8 (2),
1972, p.209.
153. Richards, C.E. and
Lindley, T.C. Engg. Fract. Mech., 4 (4), 1972,
p.951.
154. Crooker, T.W. N.R.L. Report 7347, p.8.
155. Walker, E.F. and
May, M.J. B.I.S.R.A. Open Report
No. MG/E/307/67
D.D.3. 1971.
156. B.S.I. Draft
D.D.3. 1971.
157. B.I.S.R.A. Report Proposed Spec. for Fract. Toughness
of High Strength Materials, Report,
MG/EB/312/67.
158. Pook, L.P. N.E.L. Report No. 449,
April 1970, p.1.
159. Nicholson, C.E. BISRA Report MG/EF/202/69, 1969.

160. Frost, N.E.,
Marsh, K.J.
and Pook, L.P. Metal Fatigue, Clarendon Press,
1974.
161. Barnett, W.J. and
Troiano, A.R. J. of Metals, 9, 1957, p.486.
162. Gilbey, D.M. and
Pearson, S. R.A.E. Tech. Report No. 66402,
1966.
163. Jack, A.R. and
Yeldham, D.E. C.E.G.B. Report, SSD/MID/R/215/70,
1970.
164. Ritchie, R.O. Camb. Un. Report, Jan. 1972.
165. Davies, K.B. and
Fedderson, C.E. Int. J. of Fracture, 9, 1973,
p.116.
166. Fisher, R.M. J. Appl. Phys., 24, 1953, p.113.
167. Ingelstrom, N. and
Ustimenko, V. Powder Met., 18, (36)
1975, p.303.
168. Allmand, T.R. BISRA report on "Microscopic identification
of inclusions in Steel", 1962.
169. Taylor, E. External Report, University of Aston
in Birmingham, Sept. 1973.
170. Bilby, B.A. and
Heald, P.T. Proc. Roy. Soc., A.305,
1968, p.429.
171. Wilkins, M.A. and
Smith, G.C. Met. Sc. J., 5, 1971,
p.139.
172. May, A.N. Nature, 188, 1960,
p.573.
173. Gittus, J.H. Nature 202,
1964, p.788.

174. Dawson, R.A.T.,
Elder, W.J.,
Hill, G.J. and
Price, A.T. Int. Conf. 1967, Metals and
Metallurgy Trust Monograph and
Report No. 325, 239.
175. Smith, E. Proc. Roy. Soc. A 299, 1967,
p.455.
176. Cottrell, A.H. Proc. Roy. Soc. A.285,
1965, p.10.
177. Bucci, R.J., Clark, W.G. ASTM - STP 513,
and Paris, P.C. 1971, p.177.
178. Paris, P.C. M.T.S. Closed Loop Magazine,
2 (5), 1970.
179. Schmidt, R.A. M.S. Thesis, Lehigh University
U.S.A., 1970.
180. Pellini, W.S. Nat. Res. Lab. Report 7406,
1972.
181. "Conducting Drop-Weight Tear Testing to Determine Nil
Ductility Transition Temperature of Ferrite Steels",
ASTM Stand. E208-69.
182. Heckel, R.W.,
Lanam, R.D. and
Tanzilli, R.A. Perspectives in Powder Metallurgy,
5, p.139, Plenum Press, New York,
London, 1970.

15. Appendix I.

According to Neuber⁽¹¹⁸⁾, the equation for the maximum stress or the stress concentration factor at the base of a notch is written as:

$$\sigma_{\max} = \frac{p \times 2 (a/\rho + 1) (a/\rho)^{\frac{1}{2}}}{(a/\rho + 1) \arctan (a/\rho)^{\frac{1}{2}} + (a/\rho)^{\frac{1}{2}}},$$

for tension case

and

$$\sigma_{\max} = \frac{p \times 4 (a/\rho) (a/\rho)^{\frac{1}{2}}}{3 [(a/\rho)^{\frac{1}{2}} + (a/\rho - 1) \text{Arctan} (a/\rho)^{\frac{1}{2}}]}$$

for bending case

whence,

$$\frac{\sigma_{\max}}{p} = \alpha_1,$$

for tension case

$$\frac{\sigma_{\max}}{p} = \alpha_2,$$

for bending case

where $p = \sigma_{\text{nom.}}$

The equation for $K_{T \text{ NET}}$, according to Neuber, can be written as:

$$K_{T \text{ NET}} = \frac{1 + (K_S - 1) (K_D - 1)}{[(K_S - 1)^2 + (K_D - 1)^2]^{\frac{1}{2}}}$$

and

$$K_{T \text{ GROSS}} = K_{T \text{ NET}} \times \frac{w^2}{(w-t)^2}$$

where

$$K_D = \frac{2(a/\rho + 1) - \alpha_1 (a/\rho + 1)^{\frac{1}{2}}}{(4(a/\rho + 1)/\alpha_2) - 3 \alpha_1}$$

and

$$K_S = 1 + 2(t/\rho)^{\frac{1}{2}}$$

where K_D is defined as the stress concentration factor for the deep notch (where the depth of notch is not too small compared to the width of the specimens) and K_S is the stress concentration factor for a shallow notch (where the depth of notch is very small compared to

the width of the specimens), and where

t = depth of notch

p = notch root radius

W = width of specimen

a = (width - depth of the notch)

16. APPENDIX II

Relationships between P_e , P_{min} and $\frac{\delta_c}{2}$.

An attempt was made to pin down the 'effective' notch root radius (P_e), above which the apparent values of fracture toughness show a noticeable increase. With this value of P_e was compared the minimum root radius of pores (P_{min}) measured in the sintered and heat-treated maraging, diluted maraging steel and ancoloy SA (ASA) compacts, after light etching. An attempt was also made to find out the relationships of crack opening displacement ($\frac{\delta_c}{2}$) with P_e and P_{min} in the above compact materials, and to explore the possibility of improving toughness by manipulating P_{min} of pores.

Four sets of specimens (2 in each set) of sintered and heat-treated maraging (M_{12}), diluted maraging (M_{21}), and ASA compacts in 2 levels of densities, were each machined/notched to a depth of $0.45W$ with root radii of 0.127, 0.254, 0.508 and 0.762 mm. as shown in the Table AI (appendix). One set of 2 specimens of the above mentioned compact materials, in both levels of densities, were initially machine-notched to a depth of $0.3W$, with root radius of 0.127 mm. and fatigue-cracked to a depth of $\sim 0.45W$. This helped to produce infinitely small root radius ($\rightarrow 0$) at the crack tip. Results of apparent fracture toughness are also given in Table AI.

TABLE AI

Apparent Fracture Toughness corresponding to different
Notch Root Radii.

Materials Code	Notch Depth W=23.50 mm.	Notch Root Radius, mm.	Apparent Fracture Toughness K.App., MN/m ^{3/2}		
			Density levels	1	2
				6.9, Mg/m ³	7.1, Mg/m ³
M ₁₂	0.45W	0.127		31.39	30.50
				29.61	
		0.254		31.25	32.70
				34.15	
	0.508		38.41	36.68	
			34.95		
	0.762		43.55	41.76	
			39.97		
	0.3W ↓ (0.45W)	0.127 ↓ (0.0)		30.10	29.60*
M ₂₁	0.45W	0.127	31.42	28.97	
			26.52		
		0.254	29.86	30.20	
			30.54		
	0.508	33.67	33.72		
		33.77			
	0.762	38.49	39.45		
		40.41			
	0.3W ↓ (0.45W)	0.127 ↓ (0.0)	28.12	27.53*	
			26.94		

* Valid K_{IC} Values

TABLE AI (CONT'D)

Apparent Fracture Toughness corresponding to different Notch Root Radii.

Materials Code	Notch Depth W = 250 mm.	Notch Root Radius, mm.	Apparent Fracture Toughness			
			K app., MN/m ^{3/2}			
			Density levels	1	2	
				6.7, Mg/m ³	6.9, Mg/m ³	
ASA-S (Ancoloy SA, sintered)	0.45W	0.127	25.69	26.11 (av.)	31.15	31.44
			26.54		31.73	
		0.254	28.39	28.15	31.79	32.16
			27.91		32.53	
	0.508	29.86	30.01	35.95	35.77	
		30.16		35.59		
	0.762	32.89	32.71	37.14	37.11	
		32.54		37.09		
0.3W ↓ (0.45W)	0.127 ↓ (0.0)	24.73	24.92	27.92	28.54	
		25.11		29.16		
ASA-SQT (Ancoloy SA, sintered, quenched and tempered)	0.45W	0.127	27.73	27.03	32.51	31.72
			26.34		30.93	
		0.259	32.43	31.94	33.35	34.50
			31.46		35.65	
	0.508	35.84	36.03	41.31	39.70	
		36.23		38.09		
	0.762	38.47	37.89	32.08	43.43	
		37.32		44.79		
0.3W ↓ (0.45W)	0.127 ↓ (0.0)	25.63	25.77	28.20	29.61	
		25.92		31.02		

* Valid K_{IC} Values

From the graphs of K-apparent Vs Notch Root Radius, Fig. 1A, & 2A, it is difficult to pin down the Effective Notch Root Radius of Specimens, P_e (at which K-apparent values tend to go up gradually with Root Radius P); however, it seems that it lies somewhere at Notch Root Radius ~ 0.0635 mm. for M_{12} & M_{21} compacts, and ~ 0.03175 mm. for Ancoloy SA compacts. In Table-A II is given the relationships between $\frac{\delta_c}{2}$ & P_e , obtained by using the formula,

$$G_c = \frac{\pi}{4} \cdot \sigma_{ys} \cdot \delta_c, \text{ for Plane stress}$$

$$= \frac{\pi}{2} \cdot \sigma_{ys} \cdot \delta_c, \text{ for Plane strain.}$$

also, $G_c = \frac{K_c^2 (1 - \nu^2)}{E}$, for Plane strain

TABLE-A II

Materials Code	P_e (Effective ρ) (μ)	$P_{min.}$ (from Root Radius of pores) ($\times 10^3 \mu$)	G_c ($\frac{KN}{m}$)	$\frac{\delta_c}{2}$ (μ)
M_{12}	63.5	48.1	6.59	2.3
M_{21}	63.5	100.0	6.26	3.1
M_{12}	63.5	64.5	6.59	2.3
ASA-S(1)	31.75	86.2	4.99	3.7
ASA-SQT(2)	31.75	76.9	6.23	2.7
ASA-S (2)	31.75	121.4	5.78	3.9

In all cases, $P_{min.} < \frac{\delta_c}{2} \ll P_e$.

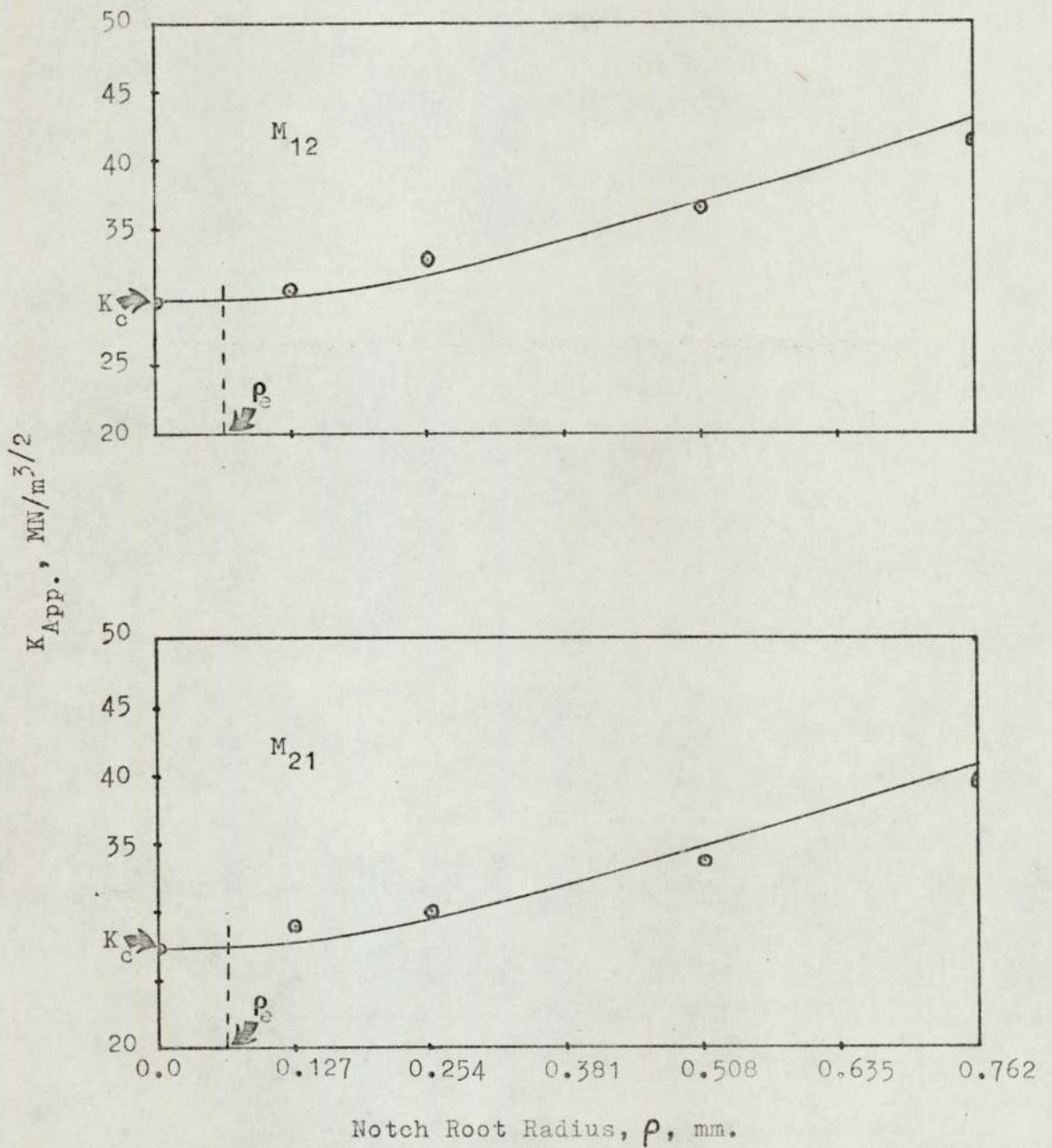


Fig.1A. Variation of Apparent Fracture Toughness with Notch Root Radii.

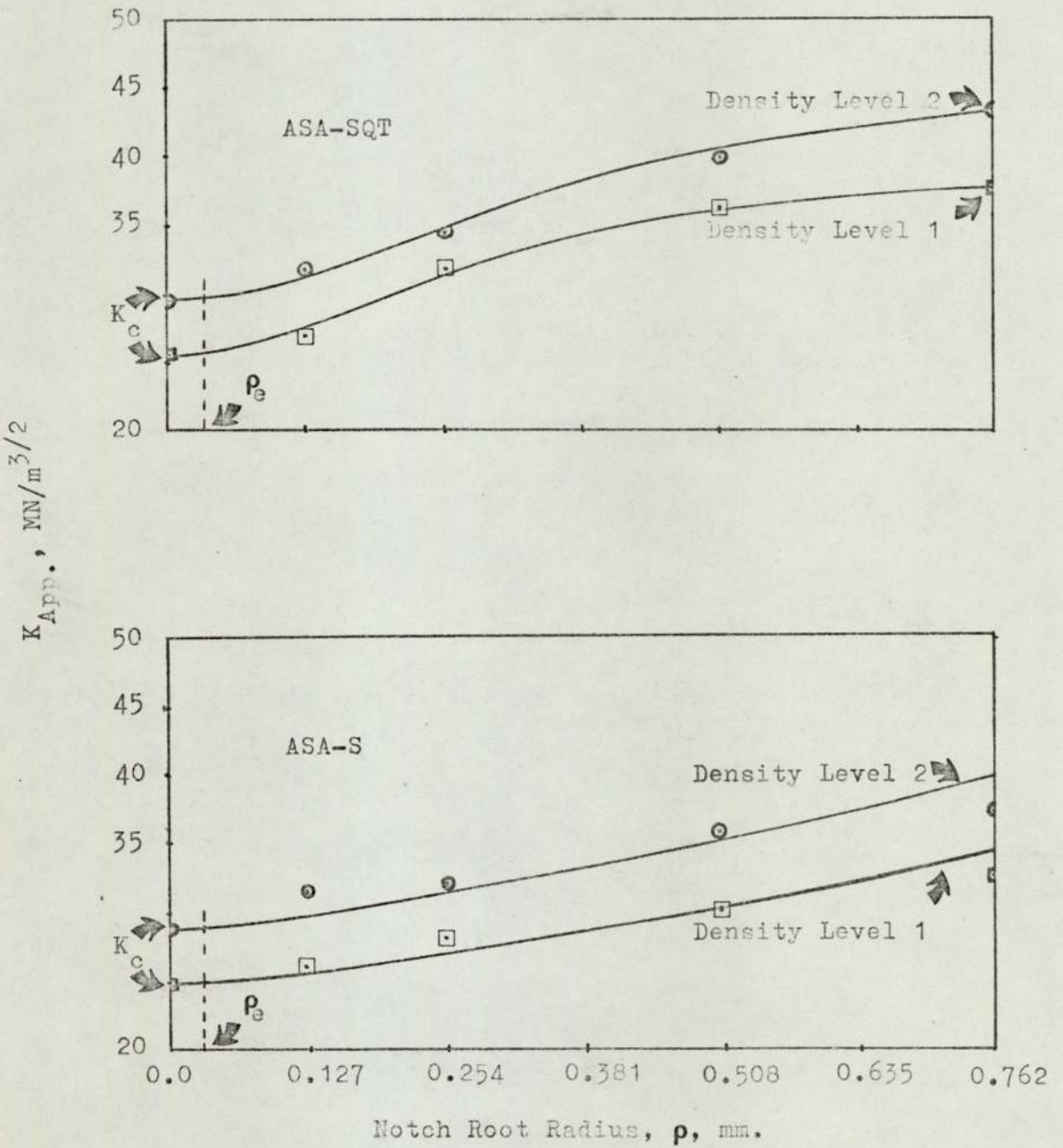
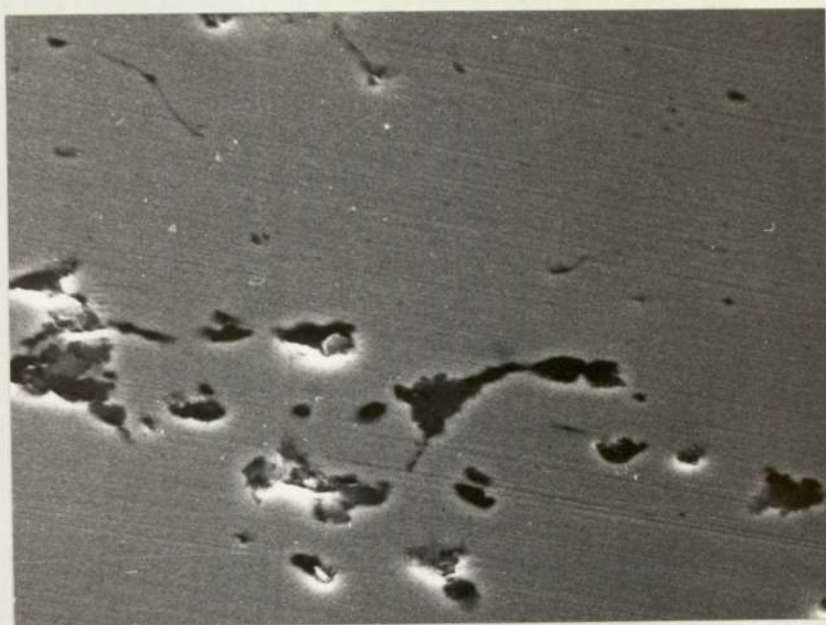


Fig.2A. Variation of Apparent Fracture Toughness with Notch Root Radii.

EXAMPLES OF PORES WITH VERY SHARP ROOT RADII IN
THE SINTERED MATERIALS TESTED.



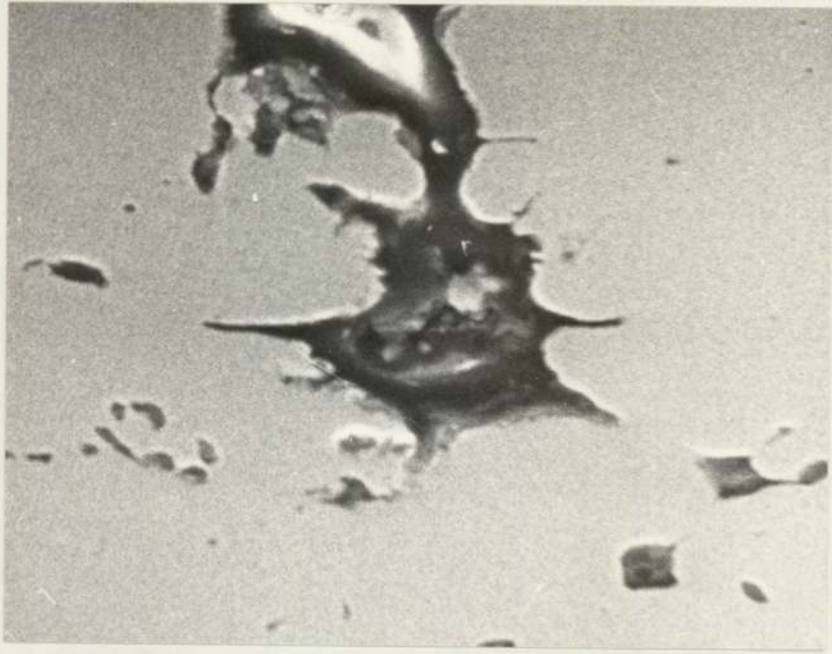
←1/50 P.S.→

Fig.1A1. M_{12} Sintered Compacts.
 $R_{min.} = 48.1 \times 10^3 \mu.$



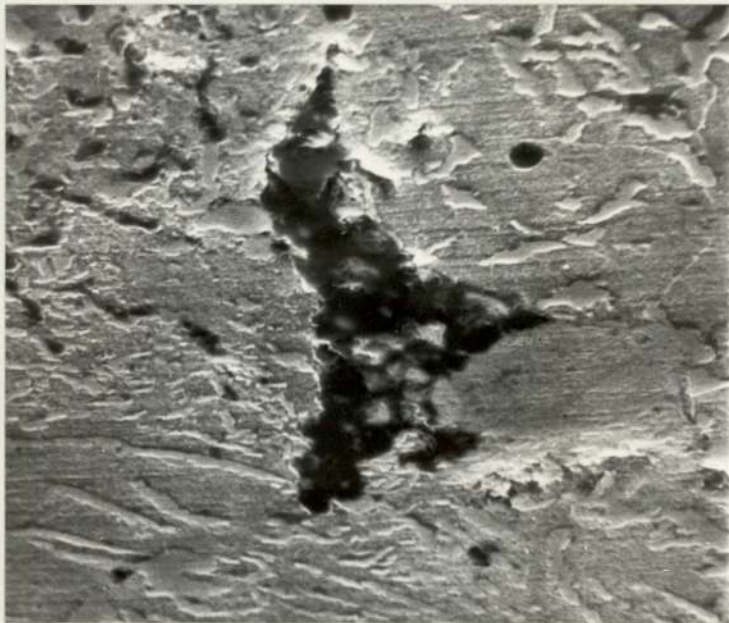
←1/10 P.S.→

Fig.1A2. M_{21} Sintered Compacts.
 $R_{min.} = 100 \times 10^3 \mu.$



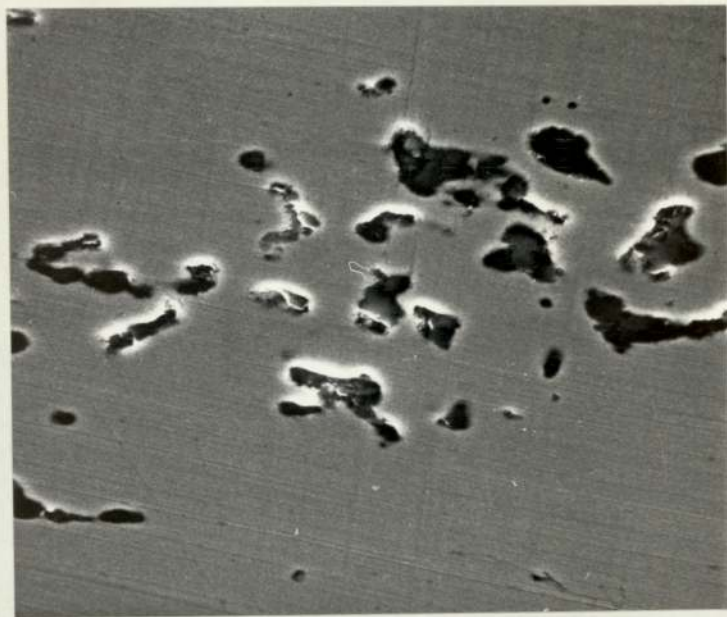
←1/10 P.S. →

Fig.1A3. M_{12} Sintered Compacts.
 $P_{\min.} = 64.5 \times 10^3 \mu.$



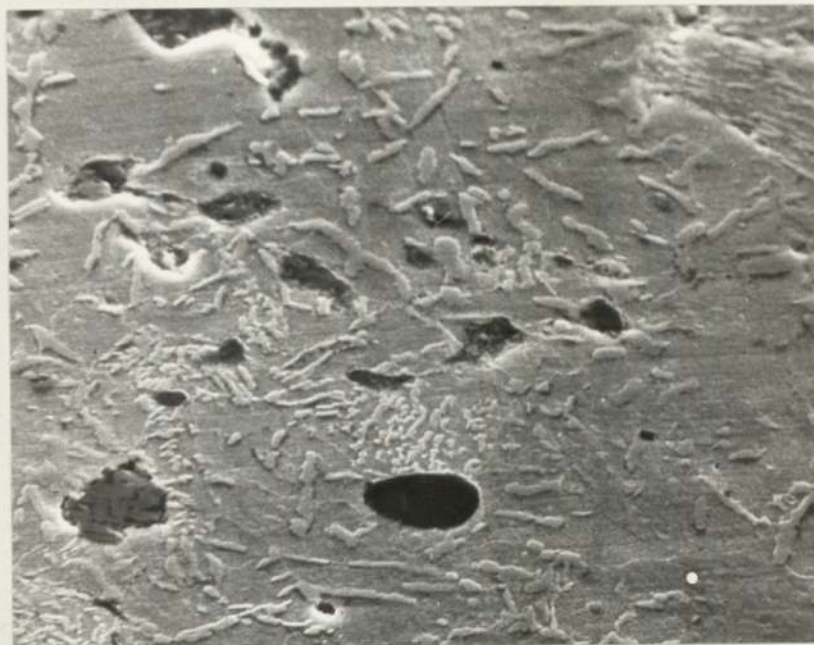
←1/50 P.S. →

Fig.2A1. ASA-S(1) Sintered Compacts.
 $P_{\min.} = 86.2 \times 10^3 \mu.$



←1/20 P.S.→

Fig.2A2. ASA-SQT(2) Sintered Compacts.
 $P_{\min.} = 76.9 \times 10^3 \mu.$



←1/50 P.S.→

Fig.2A3. ASA-S(2) Sintered Compacts.
 $P_{\min.} = 121.4 \times 10^3 \mu.$

FRACTURE TOUGHNESS
AND
FATIGUE RESISTANCE
OF A
RANGE OF SINTERED STEELS

BY
DULAL CHANDRA GHOSH
B.TECH.(HONS.), M.Sc.

A THESIS SUBMITTED TO THE
UNIVERSITY OF ASTON IN BIRMINGHAM
FOR THE DEGREE OF
DOCTOR OF PHILOSOPHY.

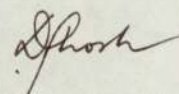
DECEMBER, 1976

SYNOPSIS

A range of notched, sintered maraging and diluted maraging steel compacts have been fatigue tested in three point bending with two levels of notch root radii. The number of cycles to produce a detectable fatigue crack correlated well with an empirical parameter of the form $(\Delta K / \rho^{0.3})$, thereby minimising the banding effect, possibly characteristic in these sintered steels. Decreased fatigue resistance have been observed with increased sintered density above a critical porosity level. Comparatively higher crack growth rate have been found in the highly diluted maraging steel compacts due to the presence of soft ferrite in the matrix, which largely superceded the crack blunting effect due to porosities. The micromechanism of fracture was of ductile dimple type in every case.

In the sintered materials tested so far, including some sintered specimens of the Ancoloy SA (Hoganas) variety, the increase in toughness value with the increased yield stress seemed to be the basic trend - a trend which would carry them into competition with the high-strength wrought steels.

I certify that to the best of my knowledge, no part of the work described in this thesis was done in collaboration unless specifically mentioned, and that the work has not been submitted for any other award.



D.C. Ghosh,
Dec., 1976.

CONTENTS

SYNOPSIS	I
1. INTRODUCTION	1
2. LITERATURE REVIEWS	6
3. LITERATURE REVIEW PART I (a) - MARAGING STEELS	6
3.1. Introduction	6
3.2. Some Basic Characteristics	6
3.3. Main Types of Maraging Steels	8
3.4. Heat Treatment and Properties	9
3.5. The Structure of Maraging Steels	10
3.5.1. The Matrix	10
3.5.2. Effects of Alloying Elements	11
3.5.3. Physical Metallurgy and Hardening	15
Mechanisms of Maraging Steels	
4. LITERATURE REVIEW PART I(b)	19
4.1. Ancoloy SA.	19
5. LITERATURE REVIEW PART II - GENERAL PRINCIPLES OF SINTERING	20
5.1. Introduction	20
5.2. Sintering Mechanism	21
5.3. The Stages of Sintering	22
5.4. Possible Mechanisms of Material Transport	23
5.5. Sintering of Multicomponent Systems	25
5.6. Liquid Phase Sintering	26
5.7. The Homogenisation Behaviour of Maraging Steel Powder and Iron Powder Mixes	28
6. LITERATURE REVIEW PART III	31

6.1.	Relation Between Young's Modulus and Porosity	31
7.	LITERATURE REVIEW PART IV - THE MECHANICS OF FRACTURE	32
7.1.	Introduction to Fracture Mechanics	32
7.2.	Criteria for Fracture	34
7.3.	The Effect of Yielding	38
7.4.	Micromechanisms of Initiation and Growth of Fatigue Cracks	41
7.4.1.	Introduction	41
7.4.2.	Mechanism of Crack Initiation	41
7.4.3.	Accepted Model of Mechanism for Initiation	42
7.4.4.	Mechanisms of Fatigue Crack Growth	43
7.5.	Fatigue Crack Initiation	49
7.5.1.	Introduction	49
7.5.2.	Review of Criteria for Correlating Fatigue Crack Initiation Data in Notched Specimens	50
7.5.2.1.	Stress-Strain Concentration Approach	50
7.5.2.2.	Fracture Mechanics Approach	52
7.6.	Fatigue Crack Propagation Laws	54
7.6.1.	Introduction	54
7.6.2.	Crack Propagation Laws	55
8.	EXPERIMENTAL DETAILS	62
8.1.	Objectives with An Outline of Experimental Work	62
8.2.	Powder Materials	62
8.3.	Specimen Preparation - Compaction, Calibration	66
8.4.	Test Specimens	67
8.5.	Treatment of Specimens	68
8.6.	Plane Strain Fracture Toughness Testing	69

8.7.	Calculation of KQ	71
8.8.	Crack Growth Measurement	71
8.9.	Potential Drop Calibration	75
8.10.	Method of Crack Growth Rate Calculation	78
8.11.	Fatigue Crack Initiation	79
8.12.	Constant Load Fatigue Tests	81
8.13.	Mechanical Testing	81
8.14.	Physical Examinations	82
8.14.1.	Metallographic Specimens	82
8.14.2.	Scanning Electron Microfractography	82
8.14.3.	Electron Microprobe Analysis and Electron Microscopy	83
8.14.4.	Quantitative Image Analysis	84
9.	RESULTS	85
9.1.	Mechanical Properties etc	85
9.2.	Pore Distribution	86
9.3.	Initiation Results	87
9.4.	Crack Growth Results	88
9.5.	Metallographic Observations	90
9.6.	Fractographic Observations	93
10.	DISCUSSIONS	95
10.1.	Importance of Titanium in Maraging Steels	97
10.2.	Crack Initiation Results	100
10.3.	Crack Growth Rate	110
10.4.	Fractographic and other observations	116
11.	CONCLUSIONS	120
12.	RECOMMENDATIONS FOR FUTURE WORK	121
13.	ACKNOWLEDGEMENTS	122
14.	BIBLIOGRAPHY	123

15. APPENDIX I

136

16. APPENDIX II

138

1. INTRODUCTION

The most common cause of failure in modern machineries and components is due to fatigue, and disasters have been reported to result from a failure to anticipate its occurrence. A component whose service conditions are known, may be designed to have either a finite or an infinite fatigue life, depending on the economics of operating high strength-to-weight structures or using too great a mass of material at a low level of stress. A number of contemporary structures require, however, the utmost in materials utilisation, in terms of stiffness-to-weight or strength-to-weight ratios, and these requirements have led to several imaginative innovations in materials engineering. One of these innovations has been the development of composite materials, such as the diffusion-hardened metals and pre-alloyed sintered compacts, which are introducing or about to introduce new and interesting combinations of mechanical properties.

In another direction, the techniques of fracture safe design has evolved around the discipline of Linear Elastic Fracture Mechanics (L.E.F.M). This approach introduced the concept that the relevant property of a material is the force required to extend a crack through a structural member, and this crack extension force parameter can be used to rank materials in some order of fracture resistance.

Linear Fracture design approaches a structural problem in a pragmatic fashion, attempting to answer the following questions: For a given design stress, what is the largest crack which can be tolerated without failure (or vice-versa)? The fantasies of perfect materials and infallible fabrication are swept away, and the designer considers, instead, the resolving power of the best inspection he is willing to provide for a particular application, and this is true for statically loaded as well as cyclically loaded structures.

There is a profusion of data on fatigue behaviour of homogeneous continuum metals and alloys, and these data are more or less readily amenable to be processed and analysed by applying the concept of L.E.F.M. However, despite the rapidly increasing application of sintered metal parts over the past thirty-five years, little attention has been paid to their toughness and fatigue behaviour. Sintered materials are, by definition and nature, heterogeneous materials. So, a persistent question is concerned with the applicability of the concepts and results developed for homogeneous material models to heterogeneous materials. A partial answer to this question has been provided by previous experience of the present author et al.,⁽¹⁾ with Fe - C, Fe - Cu and Fe - C - Cu compacts. One should also bear in mind that the early use and much recent use of sintered parts has been in situations in which the parts have been subjected to little or no mechanical stress. However, during the past several years sintered alloys have been developed which are now chosen for applications involving stressing. In fact, sintered components are giving satisfactory service under conditions of repeated stressing as bearings, synchroniser hubs and baulk rings in motor-car gear boxes, connecting rods, gears in hydraulic pumps, valve rocker brackets in internal combustion engines, sliding clutches in bicycle three-speed hub gears, sewing machine components⁽²⁾, etc.

The distinguishing feature of the majority of sintered materials is their porosity, and it is this that exercises the primary influence on fatigue. Some engineers believe that the inherent porosity of sintered materials produces a multitude of stress raisers, but according to Talmage⁽³⁾, this is probably influential only at very high stress level, providing the pores are small. Such small porosity is relatively easy to produce in a 90% - dense sintered part, and its uniformity

and consistency can be very high in comparison to castings, forgings, and even wrought metal. In practice, castings have always been plagued with surface and sub-surface porosity due to gas effects, and erratic molten metal-flow. Forgings and wrought metals have inclusions, and porosity which often appear at the surface and can be concentrated in some areas to make the condition worse. Forgings also have oxides in the surface caused by the hammering of oxidised billets.

In fatigue, it is recognised that one of the most influential factors is the quality of the surface finish. Sintered steel is excellent in this regard. The ease with which a very high quality of finish can be produced is well-known, particularly with parts that are as dense as 90%. This ability, it is believed, can produce a better fatigue-life picture than that now found in production of parts made of conventional material.

If a higher order of fatigue strength is desired, there is available a rather simple and comparatively inexpensive patented method of improving it considerably⁽³⁾. This involves the shot peening of a porous sintered surface to close the pores and then re-sintering to bond the closure surface⁽⁴⁾. This has proved very successful in the production of some sintered parts, e.g. roller chain bushings used in cars.

Another factor that is important in this comparison with conventional materials, is the fact that a normal sintered-metal part has none of the disparities found in castings due to liquid-metal flow or differences in rates of freezing. Also, it has the same properties in the transverse as in the longitudinal direction. This is a major strength reducer in forgings where the transverse properties can be 50% lower. Moreover, mass production of simple sintered components to close tolerances at competitive cost is already a reality in automotive industry.

Maraging steels made a commanding appearance in the metallurgical scene in the early sixties as one of those super-alloys, with the interesting combination of high strength and toughness values^(2,5,10-16). In subsequent years, an abundance of data have been extracted on their crack propagation characteristics and fracture toughness, weldability etc.,^(6-9, 17, 18), and as a consequence, these steels have already found applications in aircraft landing gears, aircraft arrester hooks, space vehicle cases, gimbal bearings, hydrofoil struts, torque transmission shafts, bolts, dies for cold forging, extrusion press rams, etc.⁽¹⁹⁾. However, as stated before, there is a general lack of data on fatigue behaviour of sintered materials, and sintered maraging steels are no exception.

In the present study, the fracture toughness and fatigue behaviour of a representative maraging steel produced from pre-alloyed powders, have been investigated. Properties of sintered maraging steel compacts made from elemental powders have been found by Snape and Veltry^(12A) to be inferior to those made from pre-alloyed powders. Based on the experiences of Fischer⁽¹³⁾ and Yates and Hamaker⁽¹¹⁾, a composition of 0.03 C max, 17.50 to 18.50 Ni, 7 to 8 Co, 4.5 to 5.5 Mo, 0.4 to 0.6 Ti, 0.01 P max, 0.10 Si max, 0.1 Mn max, 0.01 S max, 0.10 Al, 0.01 Zr and 0.003 B had been selected and subsequently diluted with 25% and 50% iron powder, grade ASC.100.29 ("Hoganas"), to yield two more varieties of sintered powder compacts. Besides these, another variety of powder compact made from pre-alloyed powders with the patent name of Ancoloy SA ("Hoganas") and containing 1.50 Cu, 0.50 Mo, 1.75 Ni, 0.01 C, 0.16 SiO₂, 95.98 Fe, had been tested after sintering and heat treatment. A low titanium variety of maraging steel compacts had also been tested for toughness, crack initiation and propagation studies.

The present investigation is primarily aimed at assessing toughness, crack initiation and propagation characteristics of the range of sintered materials mentioned earlier, using the concept of Fracture Mechanics.

Often engineers and designers are reluctant to use sintered materials despite their advantages in certain situations. Therefore it seems highly desirable that their attention should be drawn to the potential of sintered materials and that data about their properties and behaviour, including fatigue, should be available to them. Only when they become aware of the potential will sintered materials be exploited most effectively and be presented as viable materials to compete with high strength steels and other materials.

2. LITERATURE REVIEWS

In order to limit this review to sensible proportions, only the literature directly relevant to the present study has been included, and only interesting aspects on some related topics has been touched upon.

3. LITERATURE REVIEW PART I (a) - MARAGING STEEL

3.1. Introduction

Because of the high strength and toughness combinations achievable in the maraging steels by age - hardening of their iron-nickel martensitic microstructures, these materials have come under intensive study in recent years, specially by aerospace designers and missile system engineers ⁽²⁰⁾. This is particularly true of the important iron-based 18% Ni, Co and Mo alloys, additionally hardened with Ti and Al. But, in spite of the rapidly increasing volume of data on these alloys, there is still no satisfactory understanding of the basic physical metallurgy of these complex precipitation - hardened martensitic alloys. Indeed the basic hardening mechanisms involved are still open to much question. For example, though synergistic effects of Co-Mo interactions have been suggested by Decker et al. ⁽²¹⁾, no clearly defined mechanism for this has yet been demonstrated ⁽²⁰⁾.

3.2 Some basic characteristics

Several basic characteristics of maraging steels are directly related to the characteristics of the iron-rich end of the iron-nickel phase diagram. Actually two diagrams must be considered. The first

is the equilibrium diagram, Fig. 1, as given by Owen and Liu⁽²²⁾. The essential point to be noted is that at lower temperatures, the equilibrium phases for alloys containing 3-30% Ni are ferrite and austenite.

The austenite-martensite transformation characteristics in iron-nickel alloy have been studied by several investigators^(23,24) and are shown in the metastable equilibrium diagram of Jones and Pumphrey⁽²³⁾, Fig. 2. In practice, if an alloy containing, say, 18% Ni is cooled, from the austenite field, the austenite will not decompose into the equilibrium austenite and ferrite compositions, even if held for very long times in the two-phase region. Instead, with further cooling, the austenite transforms to martensite that has a b.c.c. crystal structure.

If the martensite is reheated, one of two things may happen. If the alloy is brought to a temperature below the A_s temperature (i.e. the start of the $\alpha \rightarrow \gamma$ transformation shown in Fig.2), the martensite will decompose into the equilibrium austenite and ferrite compositions i.e. the martensite reverts to the equilibrium structures given by Fig. 1. The rate of this reversion reaction depends upon the temperature, and fortunately for maraging steels, the rate at temperatures of the order of 485°C (900°F) is slow enough for considerable precipitation hardening to be achieved before the reversion reaction predominates.

If, on the other hand, the alloy is heated above the A_s temperature the martensite transforms by a shear reaction back to an austenite of the same composition. Fig. 2 indicates only that alloys containing up to 33% Ni transform martensitically.

The martensites at 18% Ni and above, form by diffusionless shear as in conventional steels, but the nature of transformation and

product contrast sharply with that of conventional carbon steels in that:

(a) Section-size effects are small due to an insensitivity of the martensite reaction to cooling rate and the lack of higher temperature-diffusion controlled austenite decomposition to carbide phases. Thus rapid quenching is not required and hardenability is no problem.

(b) The transformation can proceed both athermally and isothermally.

(c) The martensite structure exhibits no tetragonality; but rather, is body-centred cubic.

(d) Tempering does not occur upon reheating of the martensite. As in (c) and (d) above, this is due to absence of carbon. Finally, the hysteresis of the transformation seen in Fig. 2 allows considerable reheating of the martensite for ageing (in the presence of alloying additions) before reversion to austenite occurs. This step is designated as maraging⁽¹⁰⁾.

It is desired to further strengthen this iron-nickel martensite to a level of engineering interest, but with a minimum loss of toughness. In the 18% Ni maraging steel selected, the hardening is achieved mainly by Co, Mo and Ti.

3.3 Main types of maraging steels

Three main types of maraging steel currently exist and are specified by their nickel contents. These are the 20% and 25% Ni maraging steels, which still persist despite their inherently complicated treatments, and the 18% Ni variety. The 18% Ni maraging steel is the most popular and is subdivided according to the attainable yield strengths which vary due to slight differences in composition

and treatment. The three common grades are designated as 18 Ni (200) (250) and (300), the figures in brackets referring to the yield strengths in Ksi. A very comprehensive review of all these steels along with their physical and mechanical properties is given by Decker et al ⁽¹⁰⁾. The essential difference between the 18% Ni grades and the higher nickel types is the absence of Co and Mo in the latter and consequently these attain strengths only equivalent to those of the 18% Ni (250) grade. Detailed discussion of higher %Ni types of maraging steel is beyond the scope of this review.

3.4 Heat Treatment and Properties

Basically maraging steels require a solution treatment which serves to dissolve the precipitate phase elements into the matrix and to render the matrix martensitic on cooling. This is the most suitable conditions for working operations as it is relatively soft and ductile. To harden the steel, the precipitates must be formed by an ageing treatment i.e. by holding at an elevated temperature which is sufficient to accelerate the precipitation process without causing any reversion of the martensite back to austenite.

The standard heat treatment of the 18% Ni maraging steel is annealing for an hour per inch of thickness at 815°C (1500°F), followed by air cooling to room temperature, and then ageing at 485°C (905°F) for 3 hours. Higher annealing temperatures produce coarse grain sizes which reduce strength and ductility. That the choice of annealing temperature can markedly affect the final properties of the steel ⁽¹²⁾ is illustrated in Fig. 3, which clearly shows the optimum annealing temperature to be 815°C. Based on this figure, an ageing temperature of 485°C. (905°F). has been selected not entirely for optimum properties, but to approach such properties in a reasonable ageing time.

It is also interesting to observe from the figure that the hardness rises rapidly e.g. from 400 to 450 D.P.N. within the first ten minutes of ageing at 485°C. Softening at this ageing temperature does not occur until over 200 hours. The softening has been shown to be due mainly to reversion to austenite rather than over ageing of this precipitate. Increasing the ageing temperature causes the peak hardness to occur at shorter times.

Ageing between 470°C (880°F) and 500°C (930°F) results in yield strengths of 1929 MN/m² (280 Ksi) to 1964 MN/m² (285 Ksi) and tensile strengths of 1998 MN/m² (290 Ksi) to 2033 MN/m² (295 Ksi) combined with 12% elongation and 55% reduction in area. For such strength levels, this ductility is very high, Fig. 4.

The M_s and M_f temperatures for the 18% Ni maraging steel are 160°C and 100°C respectively so that on air cooling to room temperature, the structure is fully martensitic. However, raising the percentage of Nickel lowers the M_s and causes austenite to be retained at room temperature. Ni lowers M_s by 40°C for every additional 1%.

3.5 The Structure of Maraging Steels

3.5.1. The Matrix

The matrix of maraging steel is ductile B.C.C. martensite formed by a diffusionless shear reaction. The phase diagram shows that the equilibrium phase of these iron-nickel alloys is either alpha or alpha + gamma. In practice, slow cooling results in the formation of martensites in all but those alloys containing less than 10% Ni which can form alpha and those alloys containing more than 33% which remain austenitic. The type of martensites formed in the 10-25% Ni alloys is termed "massive"⁽¹⁶⁾. The composition limits are not exact

and vary not only with cooling rate, but also the annealing temperature and interstitial content ⁽²⁵⁾. There is evidence that after ageing, a massive martensitic matrix gives better toughness than a twinned martensite encountered in maraging steels containing more than 25% Ni. The structure of massive martensites consists of a series of elongated laths or platelets with wavy interfaces and containing a high density of dislocations. According to Patterson and Wayman ⁽²⁶⁾, the dislocations in structures of this kind tend to lie in $[111]$ directions. The platelets lie in parallel groups separated from neighbouring groups by low angle boundaries. Typically, three such groups may lie within the boundary of an old austenite grain which will itself be a high angle boundary. The masses are made up of parallel shear plates and individual shear plates are not resolvable by etching. The martensite plate orientation relationships follow the Kurdjumov-Sachs rule i.e.

$$\begin{aligned} (111)_\gamma &\parallel (011)_\alpha \\ [\bar{1}\bar{1}0]_\gamma &\parallel [\bar{1}\bar{1}1]_\alpha \end{aligned}$$

It can be seen that the coincidence of the slip planes and direction of the parent and product lattices allows simple slip to form one from the other without any twinning, somewhat similar to the reaction which occur in very low carbon steels ⁽²⁷⁾.

3.5.2. Effects of Alloying Elements

Many different substitutional alloying elements can produce age-hardening in Fe-Ni martensites. The degree of hardening, however, may vary appreciably with changes in the Ni content or with variations in the ageing kinetics or the reversion reaction. In addition, there can be rather strong interactions between particular combinations of elements, such as that between Co and Mo. Qualitatively, though one

can classify the alloying additions roughly as follows: elements that produce "strong" age hardening (Ti); "moderate" hardeners (Al, Mo, Mn, Si); and "weak" hardeners (Co, Zr).

The higher strengths in the 18% Ni maraging steels are achieved mainly by increasing the Ti content. For each 0.1% Ti, the yield strength is increased by 68.9 MN/m^2 (10 Ksi). The NTS/TS ratio decreases in air melts containing more than 0.4% Ti. This drop-off is very sharp for maraging at 485°C (905°F) dropping to a NTS/TS ratio of 1 at 0.6 to 0.7% Ti. A Ti content of 0.7% was found to be the upper limit by Decker et al ⁽¹⁰⁾, to preserve the excellent air melting characteristics of these alloys, Fig. 5. Above this level, dross and films develop.

Ti also causes segregation and the fact that Ti lowers the M_s temp. by 40°C per 1% addition means that excessive amounts of Ti may result in bands of retained austenite ⁽²⁸⁾. Ti also neutralises residual carbon and nitrogen by removing them from solution in the martensite.

Mo is a less powerful hardener, increasing strength by only 14 MN/m^2 ($\sim 2\text{Ksi}$) for 0.1% addition. Mo (up to 5.4%) in Fe-Ni alloys had been claimed to increase toughness by preventing segregation or precipitation at the grain boundaries thereby lowering the propensity to failure through grain boundary cracking ⁽⁵⁾. However, Banerjee and Hauser ⁽²⁰⁾ dispute this claim. They did find grain boundary precipitation in Mo containing Fe-Ni alloys. In previous studies by Floreen and Speich ⁽⁵⁾, these precipitates might have been missed because of etching specificity. Banerjee and Hauser, in their turn, however, could not put forward any alternative explanation for the toughening by Mo.

Perhaps the most interesting strengthening effect in maraging steels is that due to the combination of Co and Mo. Decker et al. ⁽¹⁰⁾ found that the hardening when these two elements were present together was much greater than the sum of the strength increments produced when they were added individually. Although this effect was not observed by Banerjee and Hauser ⁽²⁰⁾, the data of at least three other investigators ^(5, 29, 30) show this general trend.

As pointed out before, moderate age-hardening results from Mo additions. In fig.6 are shown the effects of Mo and Mo+7% Co on maraged hardness. A strong additional effect from the presence of Co can be seen. Fig.7 reveals the synergistic effect (defined as 'the co-operative action of discrete agencies such that the total effect is greater than the sum of the two effects taken independently' ⁽²⁰⁾) of Co with Mo on maraging steel between 427°C (800°F) and 485°C (905°F). Maraged hardness increased linearly as the product, Co times Mo, increased between the limits of 1.7 Co., 1.8 Mo to 7 Co, 5.4 Mo. It is possible by increasing this product to obtain alloys that show only a change from Rockwell C-25, in the absence of both Co and Mo, to Rockwell C-30 in the annealed martensitic condition, but then exhibit very strong maraging to give hardness above Rockwell C-50.

With this balance of strong maraging effect and weak solid solution hardening, a tough martensite matrix is maintained even with high strength. This appears to be the key to the remarkable toughness of the Ni-Co-Mo steels.

In the Mo-containing alloys, the strength increases by 517 MN/m² (75 Ksi) by the Co addition, though Co itself supplies only a relatively small, roughly additive strengthening contribution. The addition of Co results in a finer dispersion of precipitates in the Mo-bearing Fe-Ni alloys; since Co has not been found by Floreen ⁽¹⁶⁾

to be present to any extent in the Mo precipitates, he considered that Co might have lowered the solubility of Mo in the matrix and this increased the amount of Mo precipitate. Miller and Mitchell⁽³¹⁾ also came to this conclusion. It is considered that a Mo-based precipitate is nucleated on dislocations within the martensite plates and that this precipitate will be most affected by Co addition. Co may also lower the solubility of Mo in the matrix so that an improved distribution of the precipitate and an increased volume fraction of the precipitate could be formed for a given Mo content. Strengthening due to Co addition increases in a continuous fashion and it is thought that hardening at the 18% Ni-8% Co level may be due to a low degree of long-range ordering, Co is also considered to lower the resistance of the matrix to the passage of dislocations and to lower the interaction energy between dislocations and interstitial atoms⁽³²⁾. According to Banerjee and Hauser⁽²⁰⁾, the matrix strengthening by Co addition is due to lowering of stacking fault energy (SFE) of the matrix. The lowered SFE discourages cross slip and retards cell growth. Thus, the average dislocation density is increased, which provides more numerous nucleation sites for precipitation. The resulting increased barrier to dislocation movement causes the observed increased hardness.

In the 18% Ni maraging steels, Mn and Si should be kept below 0.1% and C should be 0.03% (maximum), otherwise ductility and notched tensile strength will be markedly reduced.

As only a small amount of Mn is available for sulphide formation, a maximum S content of 0.01% is specified. P content should also be kept below 0.01%.

Because of the need for low Si and Mn contents to ensure adequate deoxidation and desulphurisation, Al and Ca are added. B and Zr additions are used to suppress harmful grain boundary precipitation, thereby improving toughness and stress corrosion⁽³²⁾.

3.5.3. Physical Metallurgy and Hardening Mechanisms of Maraging Steel

The primary attribute of maraging steels is their excellent combination of strength and toughness. This seems to be especially true of the 18% Ni grades, which in general have a toughness superior to that of the other grades at higher strength levels.

In the case of strengthening mechanisms, the yield strengths of unaged maraging steels are typically $\sim 700 \text{ MN/m}^2$. After maraging, the increase in yield strengths of the various 18% Ni steels range from 700 MN/m^2 to 1400 MN/m^2 . The precipitation strengthening of this magnitude can be accounted for quite reasonably by an Orwan relationship, e.g.

$$\sigma = \sigma_0 + \frac{\alpha G b}{\lambda} \quad \dots (1)$$

where σ is the total strength, σ_0 the matrix strength, α is a constant, G the shear modulus, b the Burgers vector, and λ the interparticle spacing. After maraging, the values of λ are of the order of 300-500 angstroms, and the corresponding strength increments are ~ 700 - 1400 MN/m^2 . Thus an Orwan-type hardening involving dislocation motion between the precipitate particles can account for the strengths observed (33,34).

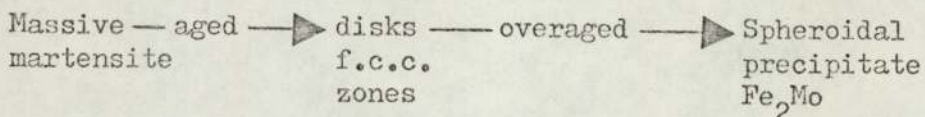
On the other hand, Detert^(35, 36) has suggested that hardening could be controlled by the stress necessary to shear through the precipitate particles. Reisdorf and Baker⁽³⁴⁾ have observed however, that the structure of the 18% Ni (250) steel showed tangles of dislocation around the precipitate particles, and also instances of dislocations bowing between the particles.

The reasons for the superior toughness of the 18% Ni maraging steels are not clear. It has often been noted that the elimination of C and other deleterious impurities should be beneficial. Also the relatively uniform precipitate distribution achieved by age-hardening in a massive martensite matrix would be helpful.

The particular mechanism, which operates contributing to hardening, depends upon the nature, size and density of the precipitate distribution. Much work has been done towards identifying the composition and structure of these precipitates. Floreen ⁽¹⁶⁾ has reviewed the results of 22 efforts to analyse the precipitate phases which are by no means in agreement. A general trend, however, suggests that Mo precipitates out as Ni_3Mo under normal ageing conditions. This is a metastable phase, being replaced, on overageing, by Fe_2Mo or a sigma phase. Ti generally appears to form Ni_3Ti but this is generally difficult to identify in the presence of Ni_3Mo , and so a complex $Ni_3(Mo,Ti)$ may actually exist ⁽²⁷⁾. Other elements are found to be present in these precipitates but Co is the exception, appearing to remain entirely in solution. Most workers ^(5,16,20,34,37) consider Mo to be the primary hardening element and Ti as the secondary hardener.

Much of the controversy arises out of the need to overage precipitates in order to extract them for analysis and the existence of Fe_2Mo and austenite in the matrix are undoubtedly due to this. Miller and Mitchell ⁽³¹⁾ quote Fe_2Mo in preference to Ni_3Mo as the primary hardening precipitate. They consider that in maraging steels, in the overaged condition, the Fe_2Mo precipitate is spheroidal, but in the fully aged condition, the precipitate is disk shaped, having a f.c.c. structure. This suggests that the hardening mechanism of

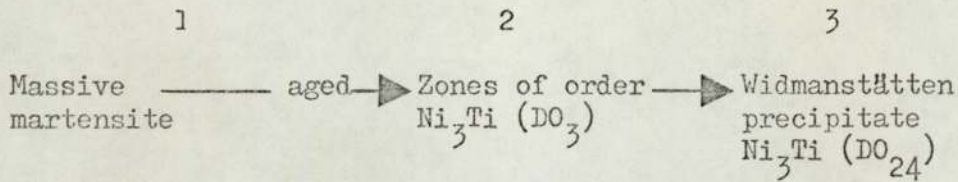
Mo may be summarised as:



By this mechanism, there is a gradual increase in the packing density of the atoms and by examination of interplanar spacing, it may be assumed that the {110} ferrite planes are parallel to the {100} planes of the f.c.c. zones which, in turn, are parallel to the {112} Fe₂Mo planes. Floreen⁽¹⁶⁾ describes Ni₃Mo as H.C.P. structured and rod or ribbon shaped which forms coherently and whose growth is limited in that form by increased coherency stresses and these may lead to the nucleation of the equilibrium precipitate.

The addition of Ti to 18% Ni maraging steels results in the formation, in the overaged condition, of a lath-like Widmanstätten precipitate formed with its long axis parallel to the <111> direction of the matrix, and having the composition and structure of Ni₃Ti. However, in the condition of maximum hardness, although a Widmanstätten precipitate is present in thin foils as observed by Miller and Mitchell⁽³¹⁾ and can be associated with streaking of the thin foil diffraction patterns, a fine spheroidal precipitate is also present in an amount much too plentiful to result from the viewing of laths end-on. Miller and Mitchell⁽³¹⁾ found faint spots in the {100} matrix reflection positions, but these cannot result from either streaking caused by the precipitate, or double diffraction, but are an indication of ordering. It seems probable that ordering may occur as a pre-precipitation reaction, involving the spheroidal zones. This ordering could possibly be based on the NiTi, B₂ structure or more likely on a metastable Ni₃Ti, DO₃, structure. Co, which also forms ordered b.c.c. compounds with Fe, could possibly stabilize formation of these ordered zones at peak hardness even though, in the final equilibrium precipitate,

Co is not present in detectable amounts. Thus the hardening mechanism of Ti may be suggested as:



where peak hardness occurs between 2 and 3.

Although ordering by Co addition would be a convenient explanation, and strength has been found to increase with Co content without its presence in the precipitate form, and even without Mo present in the alloy, the ordering theory has not been widely accepted and no evidence has been put forward to support it (16), because in the ordered Fe-Ni-Co alloys, it is difficult to obtain direct structural evidence by X-Ray or electron diffraction techniques. Miller and Mitchell (31) suggest that the peak hardness due to the Co-Mo interaction would be reached slightly later than that due to the Ti precipitate.

The ultra high strength with good ductility, which characterizes the 18%Ni maraging steel is probably due to the combination of the ferrite/austenite transformation with the conventional precipitation hardening mechanisms. Thus, a larger quantity of precipitate can be dissolved in the austenite at a fairly low solution temperature, a grain-refining process occurring at the same time as the solution of the precipitate and the massive martensite transformation which occurs during cooling results in a matrix with a high dislocation density ideal for precipitation hardening.

4. LITERATURE REVIEW PART I (b)4.1 Ancoloy SA

Ancoloy SA^(37A) is an iron powder containing Cu, Ni and Mo. Mixed with graphite, it is especially intended for parts to be heat treated. After hardening and tempering, a high ultimate tensile strength in combination with a certain ductility is achieved. The alloying elements facilitate the hardening, and very consistent hardness without any soft spots is achieved.

Ancoloy SA is manufactured from sponge iron and the individual particles, therefore, have a spongy irregular shape contributing to a high green strength of the compacted component. The individual particles mainly consist of unaffected pure iron (ferrite) to which the finely divided alloying elements are diffusion bonded. Therefore, Ancoloy SA has a very high compressibility. The risk of segregation of the alloying elements in the mixture is eliminated. As the alloying elements are added in a very finely divided form, they diffuse rapidly into the iron particles during sintering. Thus, the additions are well utilized. The addition of Cu and Ni are so balanced that a very small dimensional change takes place during sintering and heat treatment. The Mo added raises the hardenability considerably, and consequently, the material becomes less sensitive to minor changes of hardening variables. All three of the alloying additives have less affinity to oxygen than iron. Therefore, when sintering ancloy S.A. the same atmosphere can be used as for the sintering of normal iron powder with low H₂-loss. If close tolerances with regard to the amount of combined carbon in the sintered part are desired, the carbon potential of the sintering atmosphere has to be thoroughly controlled or closed sintering boxes should be used.

5. LITERATURE REVIEW PART II - GENERAL PRINCIPLES OF SINTERING

5.1 Introduction

The term "sintering" is commonly used to refer to the annealing treatment by which powders are consolidated into coherent and/or dense polycrystalline aggregates. The technological importance of this process hardly needs emphasizing. It is one of the most important and versatile methods of integration of materials in metallurgy and ceramics. Fast development of the art of powder technology in modern times necessitated better scientific understanding of the processes involved in sintering, the central problem of powder technology.

To be generally valid, however, a definition of sintering must satisfy the following essential factors:

- (a) A liquid phase is present only to the extent that it leaves a solid skeleton behind.
- (b) A decrease in free enthalpy of the system, which represents the driving force of the sintering process, results from:
 - (i) Diminution in the specific surface area due to initiation and/or growth of contacts (necks).
 - (ii) Decrease in pore volume and/or the surface area of the pores.
 - (iii) Elimination of non-equilibrium states in the lattice.
 - (iv) Important properties approximate to those of the compact, porosity free material.

On these bases, Thummler and Thomma⁽³⁸⁾ have proposed the following definitions:

'By sintering is understood the heat treatment of a system of individual particles or of a porous body, with or without the

application of external pressure, in which some or all of the properties of the system are changed with the reduction of the free enthalpy in the direction of the porosity-free system. In this connection, at least enough solid phases remain to ensure shape stability.'

It is clear that sintering of powders involves two broad phenomena: (a) adhesion or welding of surfaces together and (b) change in shape of the particles to permit more and more of adhesion. Without (a) there is no sintering at all, and without (b), there cannot be any densification.

5.2 Sintering Mechanism

It is not possible to deal with all the aspects of this complex field in this survey, so only the main factors of influence will be considered.

The tendency of a system to assume its state of lowest free energy is the driving force for sintering. At high temperature, the powder compact approximates to the stable state, with the co-operation of all the transport mechanisms concerned. The excess free energy exists in the compact in the form of surface energy of all interfaces, including grain boundaries, and as excess lattice energy in the form of vacancies, dislocations and internal stresses.

The surface energy remains more or less constant during compaction, as it is an intrinsic property of the powder. What is dependent upon the compacting operation to a greater extent, however, is the lattice, or internal energy factor, and the number of metal-to-metal contacts. The former increases due to the formation of dislocation vacancies, and internal stresses, and the latter increases with compacting pressure. The high free energy level of the compact

leads to the sintering reactions which occur at high temperatures.

5.3. The stages of Sintering

There are three distinct interconnected stages of sintering:

(a) The early stage of neck growth. In this stage, neck growth proceeds according to an exponential time law, and the powder particles remain as individual, since it is still not possible for strong grain growth to take place beyond the original particle. The tensile stresses resulting from surface tension maintain the grain boundaries between two adjacent particles in the plane of contact. However, the occasional formation of new grains is possible. The midpoints of the particles approach only slightly corresponding to a small contraction, but a marked decrease in surface activity takes place.

(b) The stage of densification and grain growth. When the x/a ratio, Fig. 8, exceeds a certain value after intensified neck growth, the separate particles begin to lose their identity. Most of the shrinkage takes place at this stage, where a coherent network of pores is formed, and grain growth continues. This is somewhat overlapping start of third stage sintering. As channels are lost, the geometric form of the pore network becomes simplified (40). Instead of a complete network, the disconnected parts degenerate into trees, with systems of branches that connect to nothing else. The tips of the branches may be absorbed into the parent limb, or they may be cut off to become isolated pores, Fig. 9.

(c) The final stage with closed pore spaces. At this stage, the "genus" or connectivity of the pore network becomes zero, with very small tendency to densify further. This is because the isolated pore shapes tend to become spheroidised. The third stage

is finally characterized by a reduction in the number of these isolated spheroidised pores.

5.4 Possible Mechanisms of Material Transport

Table 1 enumerates all the conceivable mechanisms of material transport that can occur in sintering processes⁽³⁸⁾.

TABLE 1

Possible elementary processes (transport mechanisms) during sintering

A Without material transport	Adhesion	
B With material transport (Movement of atoms over increased distances)	Surface diffusion Lattice diffusion via vacancies Lattice diffusion via interstitials Grain boundary diffusion Vaporisation and re-condensation	Movements of individual lattice structural components
C With material transport (movement of atoms over very small distances)	Plastic flow Grain-boundary Slip	Movements of lattice regions
	Recovery or recrystallisation	

Although adhesion occurs in every type of particle contact, it is not likely to constitute the dominating mechanism except in impact sintering.⁽⁴¹⁾

The transport mechanisms listed in Table IB might be supplemented by viscous flow associated with self diffusion co-efficients. This is the same as 'diffusion creep' according to the Nabarro-Herring mechanism⁽⁴²⁾, where an 'oriented' diffusion is activated by external stresses.

It is extremely probable that surface diffusion occurs in all sintering processes. The rounding off of the internal and external surfaces and pores is produced by surface diffusion which requires the least activation energy of all types of diffusion.

Lattice diffusion by a vacancy mechanism is the most important. Vacancy gradients exist between the undistorted lattice and both curved surfaces and pore edges, between surfaces having different curvatures and between the distorted and undistorted lattice. Vacancy sources can be small pores or concave surfaces, while vacancy sinks can be larger pores, convex surfaces, and grain boundaries. This process can lead to densification.

Interstitial diffusion has not been studied in much detail. In cases where it might have a strong influence, for example, on neck growth, phase separation must always occur.

Vaporisation and recondensation have been observed to be the predominant mechanism in some cases, mainly in metallic oxides where the vapour pressure is high. Flow processes are no longer thought to be of major importance, but have enabled the mechanisms of hot pressing to be understood.

The relative importance of the above mechanisms depend solely upon the system concerned. Kuczynski⁽⁴³⁾ has carried out an

experimental approach to the determination of these mechanisms by using wire-wire and wire-bar models. Herring⁽⁴²⁾ formulated his 'scaling laws' from these model data and suggested experiments in which a group of particles of the same material with different radii a_1 and a_2 with $a_1 = \lambda a_2$ are sintered until their necks bear the relationship $x_1 = \lambda x_2$ Fig. 8. The times required to reach this neck radius relationship would be t_1 and t_2 with $t_1 = H t_2$, where H is Herring's Scaling factor. The relationships between H and λ would then determine the mechanism, with $H = \lambda^3$ for volume diffusion, $H = \lambda^4$ for surface diffusion etc.⁽³⁹⁾ The time law of neck growth can thus give an indication of the predominant sintering mechanism⁽⁴⁴⁾.

5.5. Sintering of multicomponent systems

In the case of mutual solubility of the systems, it is necessary to differentiate between:

- (a) Sintering homogeneous solid solutions (with a concentration gradient)
- (b) Sintering with simultaneous homogenisation
- (c) Sintering with the decomposition of solid solutions

"
Thummler studied the systems Fe-Sn, Fe-Mo, Fe-Ni and Cu-Sn with up to ~ 2 at.% of the second metal in homogeneous solid solution. He found the sintering behaviour to be closely related to the physical, and thermodynamic properties of the solid solutions. Strong promoting or inhibiting effects can be observed due to the different partial diffusion co-efficients of the constituents. New vacancies are continually formed and if they coagulate to form new pores, they have an inhibiting action, by producing the Kirkendall effect (preferential penetration of one phase into the other). The formation of a new phase (reaction sintering) is associated with expansion

phenomena in many cases. The result of the different atom mobilities is that a large amount of diffusion porosity is formed and along with the inherent brittleness of many phases, this can lead to premature failure of some compacts.

5.6. Liquid Phase Sintering

This field occupies a special position attributable to the different mechanisms such as:

- (a) The ease of diffusion in melts
- (b) The possibilities of re-ordering of the phase remaining solid in the melt, and
- (c) Rapid dissolution and re-precipitation

These play a major part in solid/liquid systems compared to the predominance of diffusion in the solid state.

Based on phenomenological observations, Kingery⁽⁴⁵⁾ considered three distinguishable stages:

1. Rearrangement of the particles of the residual solid phase by viscous flow in the liquid phase. In this case, wetting of the solid by the liquid is the important factor, not solubility.
2. Dissolution and re-precipitation. At least limited solubility is necessary and densification is slower because transport is dependent upon solution and diffusion in the melt. Small grains with strongly convex curvatures disappear while larger ones assume a more regular shape. The driving force is the enhanced chemical potential in the contact zones due to higher compressive stresses. This leads to dissolution in these regions and precipitation in regions of lower stress. In case of complete wetting (angle of contact = 0°), the grains remain separated by films of liquid.
3. Coalescence. In the case of incomplete wetting

(angle of contact $<90^\circ$), the solid grains are partly in contact without the interposition of the melt, and processes such as those formed with solid phase sintering can occur, and become rate-determining.

A non-wetting liquid phase (contact Angle $>90^\circ$) is ineffective or inhibiting and usually exudes partially from the sintered compact in the form of droplets.

In the case of Fe-Cu, the liquid metal dissolves into the iron matrix giving a growth component in addition to shrinkage upon sintering. This enables closer tolerances to be achieved, and so is of some technological advantage.

5.7 THE HOMOGENISATION BEHAVIOUR OF MARAGING STEEL POWDER AND IRON POWDER MIXES.

The homogenisation behaviour of maraging steel and pure iron powder mixes can be understood by considering the geometry of the compacted mass, which may be idealised to spherical particles of the minor constituent (i.e. 25% pure iron powder in case of M_2 series) embedded in a continuous matrix of the major constituent (i.e. maraging steel powder in the rest of M_2 series). This situation is shown in Fig. 9A. The idealised geometry can be referred to as the concentric-sphere model wherein each minor constituent particle has associated with a shell of matrix. (182)

The homogenisation behaviour of powder compacts that approximate the idealised, concentric-sphere geometry may be compared to the behaviour of ordinary diffusion couples. The principal differences between the concentric sphere model and diffusion couples are the diffusion geometry (spherical Vs. planar) and the fact that diffusion distances in couples are usually small compared to the size of the couples, whereas, in the concentric-sphere model, the diffusion is to be considered over the entire sphere-shell composite. The similarities between the concentric-sphere model and diffusion couples include:

- (a) the general form of the concentration-distance profiles,
- (b) the applicability of Fick's laws of diffusion,
- (c) the development of Kirkendall effect
- (d) the validity of the approximation that equilibrium compositions are present at interfaces between phases in the multi-phase system.

To delve deeper into these aspects of homogenisation is beyond the scope of the present work. Only those points of some

significance and applicable to the present work will be dwelt ^{with} here.

The progress of homogenisation in the idealised, concentric-sphere model, and concentration-distance profiles for the microstructures can be shown schematically in Fig. 9B . The shaded areas represent the areas of inter-diffusion.

From this, it appears that, for M_2 groups of compacts, Fig. 9B (a,b) after sintering and heat-treatment, ferritic areas are embedded in a martensitic matrix, with interparticle and intraparticle porosities randomly distributed throughout the compacted mass, and equilibrium compositions being present at interfaces between the phases in the martensite-ferrite system. The pockets of ferritic zones might act as buffer between the surrounding martensites, and thus reduce volume contraction, as experienced by the maraging steel compacts of M_1 group, while sintering.

For M_3 group of compacts which consist of a compacted mass of maraging steel Powder diluted with 50% pure iron powder, the idealised geometry can be referred to as a concentric-sphere model wherein each constituent particle (iron particle or pre-alloyed maraging steel particle) has associated with it a shell of the matrix, which is more or less equally dominated by either of the constituent particles. Fig. 9B(c,d) . The shaded areas, as usual represent the areas of inter-diffusion. In this group of compacts, the continuity of martensites is broken, after sintering and heat-treatment by the presence of an equal amount of ferrite, more or less evenly distributed throughout the compacted mass.

The variations that may exist between the idealised, concentric-sphere model and actual powder compacts are primarily geometric. The interparticle porosity, non-uniform distribution of particles, particle size distributions of the minor constituent, and

non-spherical minor constituent shape can cause variations in homogenisation behaviour from that predicted from the idealised model. In addition to these geometry effects, interparticle and intraparticle porosity can give rise to enhanced mass transport through the compact. These effects would, therefore, result in variations between homogenisation behaviour predicted by volume interdiffusion models and experimentally-determined behaviour.

Since the variation of concentration with distance is the principal structural feature to be studied in homogenisation, microprobe scans across the microstructure provide a direct measurement of the degree of heterogeneity. In Fig. 67 is shown a typical distribution of the elements in the sintered compacts studied. As stated in section 9.5, the distribution of Ti, Co and Mo is not uniform, and the abrupt fluctuations in the distribution curve for Ti, Al, are due to the presence of some complex titanium or aluminium precipitates.

The structure of sintered materials is inhomogeneous, at least over short distances, as a result of irregularities in the particle stacking, etc, and over greater distances in compacted structures. If a sample containing several hundred particles is analysed, small scale inhomogeneities are averaged out. Any long range variation in the topological properties can, in principle, be detected by analysing samples at various locations in the sinter body, but it is a time consuming undertaking which has not been attempted for the present work.

6. LITERATURE REVIEW PART III6.1. Relation between Young's Modulus and Porosity

The elastic modulus E_N of sintered steels and iron-based alloys is influenced mainly by the void content in the material and is relatively insensitive to changes in composition. The elasticity ratio E_N/E has been related to the porosity (ϵ) by McAdam⁽⁴⁶⁾ by the expression:

$$E_N = E(1 - \epsilon)^{3/4} \times 10^6 \text{ psi.} \quad (2)$$

where E_N = elastic modulus of sintered steels and iron-base alloys
 E = elastic modulus of steel
 ϵ = fractional porosity.

This limits the elasticity of these alloys to a range $0-29 \times 10^6$ psi. corresponding to porosities of 100% and 0 respectively.

The plot of E_N Vs. fractional porosity for a series of porous iron-base compacts is shown in Fig. 10. The elasticity of all porous compacts is lowered by increasing the porosity. The decrease is progressively more rapid for products with more than 20% void and is independent of the dimensions of the particles.

7. LITERATURE REVIEW PART IV — THE MECHANICS OF FRACTURE7.1. Introduction to Fracture Mechanics

An overwhelming amount of research on brittle fracture in engineering structures has shown that numerous factors (e.g. service, temperature, material toughness, design, residual stresses, fatigue, etc.) can contribute to brittle fracture. However, the recent development of Linear Elastic Fracture Mechanics (L.E.F.M.) has shown that three primary factors control the susceptibility of a structure to brittle fracture. These are:

(1) Material Toughness (K_{Ic} , K_{IC}),

Material toughness can be defined as the resistance to crack propagation in the presence of a notch and can be described in terms of the static critical stress-intensity factor under conditions of plane stress or plane strain. In addition to metallurgical factors such as composition and heat-treatment, the notch toughness of a structure also depends on the application temperature, loading rate, and constraint (state-of-stress) ahead of the notch.

(2) Flaw Size (a).

Brittle fractures initiate from flaws or discontinuities of various kinds. These discontinuities can vary from extremely small cracks to much larger weld or fatigue cracks. Complex structures are not fabricated without discontinuities (porosity, lack of fusion, mis-match, etc), although good fabrications practice and inspections can minimize the original size and number of flaws. Even though only 'small' flaws may be present initially, static loading can cause them to enlarge, possibly to a critical size.

(3) Stress Level (σ)

Tensile stresses (nominal, residual or both) are necessary for brittle fracture to occur. The stresses in many complex structures are difficult to analyse because of the complexity of possible dynamic loading, and because of the stress concentrations present throughout a structure that increase the local stress levels, as well as the residual stresses.

All three of these basic factors are inter-related in brittle fractures in structures. All other factors such as temperature, loading rate, residual stresses, etc., merely affect the above three primary factors.

Engineers have known these facts for many years and have reduced the susceptibility of structures to brittle fractures by applying these concepts qualitatively, and in recent years, the engineers are endeavouring to specify design guidelines to evaluate the relative performance and economic trade-offs between design, fabrication and materials in quantitative manner.

The fundamental principle of Fracture Mechanics is that the stress field ahead of a sharp crack can be characterized in terms of a single parameter K , the stress intensity factor, having units of $\text{MN/m}^{3/2}$ ($\text{Ksi } \sqrt{\text{in.}}$). This single parameter, K , is related to both the stress level (σ) and flaw size (a). When the particular combination of σ and a (represented by K) reaches a critical value of K , called K_c , unstable crack growth occurs.

By knowing the critical value of K_I at failure (K_c, K_{IC}) for a given structure of a particular thickness and at a specific temperature and loading rate, the designer can determine flaw sizes that can be tolerated in structural members for a given design stress level. Conversely, he can determine the design stress level that can be

safely used for a flaw size that may be present in a structure.

This general relationship between material toughness (K_c), nominal stress (σ) and flaw size (a) is shown schematically in Fig.11. If a particular combination of stress and flaw size in a structure (K_I) reaches the K_c value, fracture can occur. Thus, there are many combinations of stress and flaw size (e.g. σ_f and a_f) that may cause fracture in a structure having a particular value of K_c at a particular service temperature, loading rate and plate thickness. Conversely, there are many combinations of stress and flaw size (e.g. σ_o and a_o) that will not cause failure of a particular structure i.e. below the K_c line.

The preceding L.E.F.M. analysis pertains to conditions at fracture. For most structural members, the tolerable flaw sizes are much larger than any initial undetected flaws. However, for structures subjected to fatigue loading, these initial cracks can grow throughout the life of the structure. L.E.F.M. provides a means to analyse the subcritical crack growth behaviour of structures under fatigue loading using the same conditions as at fracture. L.E.F.M. philosophy assumes the existence of small flaw or flaws of certain geometry in structures after fabrication and that this flaw can either cause brittle fracture or grow by fatigue to the critical size. To ensure that the structure does not fail by fracture, the calculated critical crack size, a_{cr} , at design load, must be sufficiently large, and the number of cycles of loading required to grow a small crack to a critical crack must be greater than the design life of the structure⁽⁴⁷⁾.

7.2 Criteria for Fracture

The first notable contribution to fracture was due to Griffith⁽⁴⁸⁾, who proposed an energy criterion for the extension of

such a crack. This involved a balance between the elastic strain energy released and the surface energy created due to an incremental increase in its length. Thus at equilibrium, the stress was given by

$$\sigma_f = \left(\frac{2EY}{\pi a} \right)^{\frac{1}{2}} \dots\dots\dots (2A)$$

where a = half crack length
 E = Young's modulus and
 Y = Surface energy

The Griffiths equation is valid only for a completely brittle solid; for metals where crack extension is accompanied by plastic flow, the increase in surface energy considered in Griffith's equation is several orders of magnitude less than the energy expended in plastic deformation. So, Griffith's criterion was subsequently modified by Irwin⁽⁴⁹⁾ and Orowan⁽⁵⁰⁾ to account for the predominantly plastic work that is involved in most metal fractures under normal conditions, and energy of plastic deformations or crack extension force G replaced the surface energy, as the controlling factor in brittle fracture. Thus the applied stress required to propagate an elliptical crack of length 2a within a large plate under conditions of plane stress is given by

$$\sigma_f = \left(\frac{G_c E}{\pi a} \right)^{\frac{1}{2}} \dots\dots\dots (3)$$

where E is the Young's modulus and G_c represents the total work consumed in producing unit area of new crack surface and known as 'critical strain-energy release rate', the suffix c denoting its value at instability. Further rationalisation of this criteria by Irwin⁽⁴⁹⁾ realised the parameter K_c, defined as the 'critical stress intensification factor' or the 'Fracture toughness parameter' and is regarded as a basic material property and the basis of Fracture Mechanics concept, and which enables direct comparison between materials.

In contrast to Inglis⁽⁵¹⁾ work, where he considered the stress concentration at a crack tip, Irwin considers the stress distribution at the close vicinity of the tip and thus plasticity effects can be appreciated. For conditions of plane stress, K_c and G_c are related by:

$$K_c = (G_c E)^{\frac{1}{2}} \dots\dots\dots (4)$$

and for plane strain

$$K_c = \left[\frac{G_c E}{1-\nu^2} \right]^{\frac{1}{2}} \dots\dots\dots (5)$$

where ν is the Poisson's ratio.

From equations (3) and (4), it is evident that

$$K_c \propto \sigma_f (a)^{\frac{1}{2}},$$

which satisfies Griffith's analysis and is normally used in the form

$$K_c = Y \cdot \sigma_f (a)^{\frac{1}{2}} \dots\dots\dots (6)$$

where Y is called the compliance function and depends on crack length and specimen or component geometry and has been evaluated for many situations using boundary collocation techniques^(52,53) and experimental compliance calibration^(54,55). Through the use of this geometrical factor, the data generated from the laboratory tests can be used in real situations.

Subsequent to the development for monotonic loading, L.E.F.M. found its application to fatigue as well. Substituting the σ term in the equation (6) by $\Delta\sigma$, σ_{\min} , σ_{\max} and σ_{mean} , the corresponding stress intensity terms can be obtained. In fact, many research workers⁽⁵⁶⁾ have related fatigue crack growth rates in a variety of materials to stress intensity factors by means of simple equations. The L.E.F.M. approach is now widely used to evaluate the resistance of materials to fatigue crack propagation.

Three basic modes of crack surface displacement⁽⁵⁷⁾ have been isolated, shown in Fig. 12. These are:

(I) The tensile opening mode. The crack surfaces move directly apart; analogous to an edge dislocation.

(II) The edge sliding mode. The crack surfaces move normal to the crack front and remain in the crack plane, also analogous to an edge dislocation.

(III) The shear mode. The crack surfaces move parallel to the crack front and remain in the crack plane; analogous to a screw dislocation⁽⁵⁹⁾.

K_I denotes the stress intensification level for the tensile opening mode, and at the level of instability becomes K_{IC} . Irwin's analysis of the stress field at the tip of a crack for mode I crack surface displacement in a homogeneous elastic solid can be specified by Westergaard's⁽⁶⁰⁾ stress field equation for cracks:

$$\begin{aligned}\sigma_x &= \frac{K_I}{\sqrt{2\pi r}} \cos \frac{\theta}{2} \left(1 - \sin \frac{\theta}{2} \sin \frac{3\theta}{2}\right) \\ \sigma_y &= \frac{K_I}{\sqrt{2\pi r}} \cos \frac{\theta}{2} \left(1 + \sin \frac{\theta}{2} \sin \frac{3\theta}{2}\right) \\ \tau_{xy} &= \frac{K_I}{\sqrt{2\pi r}} \cos \frac{\theta}{2} \sin \frac{\theta}{2} \cos \frac{3\theta}{2}\end{aligned} \quad (7)$$

$$\sigma_z = \nu (\sigma_x + \sigma_y) \quad (\text{Plane Strain})$$

$$\tau_{xz} = \tau_{yz} = 0, \quad \sigma_z = 0 \quad (\text{Generalised Plane Stress})$$

$$u = \frac{K_I}{G} \left(\frac{r}{2\pi}\right)^{\frac{1}{2}} \cos \frac{\theta}{2} \left(1 - 2\nu + \sin^2 \frac{\theta}{2}\right)$$

$$v = \frac{K_I}{G} \left(\frac{r}{2\pi}\right)^{\frac{1}{2}} \sin \frac{\theta}{2} \left(2 - 2\nu - \cos^2 \frac{\theta}{2}\right)$$

$$w = 0$$

where (r, θ) denotes the polar co-ordinates of a point in the stress field taking the crack tip as origin; u, v, w are displacements in the x, y, z directions; G is the shear modulus, ν is the Poisson's ratio, and which indicate that identical stress fields are obtained for identical K_I values. The co-ordinate system is shown in fig. 13. Elastic stresses are inversely proportional to the square root of the distance from the crack tip, and become infinite at the crack tip.

7.3 The Effect of Yielding

An uncracked metal plate loaded in uniaxial tension is in a state of plane stress. The insertion of a crack does not affect the plate remote from the crack tip, which remains in plane stress, but the highly stressed material near the crack tip is prevented from contracting in the thickness direction by the material further away from the crack, and is, therefore, in a state of plane strain. In the interior of the plate, there is a transverse stress⁽⁶¹⁾ of the form.

$$\sigma_z = \nu (\sigma_x + \sigma_y) \quad \dots \quad (8)$$

where ν is the Poisson's ratio, Fig. 14. All the plate surfaces, however, will still be in a state of plane stress.

In a metal, the yield stress is exceeded near the crack tip and a plastic zone develops; the approximate extent of this plastic zone can be estimated by substituting a yield criterion into the stress field equation. If the plastic zone is small compared with the plate thickness, transverse yielding is restricted and conditions near the crack tip approximate to plane strain through most of the plate thickness. In Fracture Mechanics, this localized plane strain situation is called plane strain, Fig. 15 and 16, and exists in most metals, provided the thickness is at least

$$2.5 \left(\frac{K_{IC}}{\sigma_y} \right)^2$$

where σ_y is the yield stress (usually taken as the 0.2% proof stress). A large plastic zone means that σ_z is not fully developed through the specimen thickness; when the plastic zone size becomes comparable with the thickness, yielding can take place on 45° planes, Fig. 17, and the stress state near the crack tip changes to plane stress. This happens when the thickness $\ll 2.5 \left(\frac{K_{IC}}{\sigma_y} \right)^2$ and in Fracture Mechanics is referred to as plane stress.

The actual size and shape of plastic zone, Fig. 18, depends on the plastic flow properties of the material, but it is proportional to $(K_{IC}/\sigma_y)^2$. The relaxation of stress, caused by yielding inside the plastic zone means that to maintain equilibrium, the stresses outside the plastic zone must increase slightly. The plastic zone, thus, increases the effective length of the crack. This effective increase, called r_y (a symbol for nominal plastic zone radius) is given approximately by Irwin⁽⁴⁹⁾ as

$$r_y = \frac{1}{2\pi} \left(\frac{K_{IC}}{\sigma_y} \right)^2, \text{ for plane stress } \dots\dots (9)$$

$$r_y = \frac{1}{6\pi} \left(\frac{K_{IC}}{\sigma_y} \right)^2, \text{ for plane strain } \dots\dots (10)$$

These corrections are only applicable when the plastic zone is small compared with specimen dimensions in the plane of the plate, and are, therefore, within the region where the stresses are reasonably accurately described by the stress intensity factor⁽⁶³⁾. If the plastic zone becomes too large, which happens when the net section stress exceeds about $0.8 \sigma_y$ ⁽⁶⁴⁾, the L.E.F.M. is no longer applicable. It is not always possible to define the net section stress unambiguously and other criteria may be adopted⁽⁶⁵⁾, for example, the crack length is at least $2.5 \left(\frac{K_{IC}}{\sigma_y} \right)^2$.

It is interesting to note that Paris⁽⁶⁶⁾ and Rice⁽⁶⁷⁾ independently stated that the equations (9) and (10) do not apply to fatigue situations. Due to extreme stress concentration at the crack tip, plasticity is always present in the material. When the load is reversed as in the case of fatigue, plasticity occurs at the crack tip in the reversed sense. The new plastic zone starts to form within the old plastic zone from the maximum load.

Since to cause plasticity in the reversed direction, the yield stress should be doubled, the new fatigue plastic zone size is approximated by

$$r_y = \frac{\Delta K^2}{2\pi(2\sigma_{ys})^2} = \frac{1}{8\pi} \left(\frac{\Delta K}{\sigma_{ys}} \right)^2 \quad \text{for Plane stress}$$

$$\text{and } r_y = \frac{\Delta K^2}{2\pi(\sqrt{3}2\sigma_{ys})^2} = \frac{1}{24\pi} \left(\frac{\Delta K}{\sigma_{ys}} \right)^2 \quad \text{for Plane strain} \quad (11)$$

For fatigue cycling with a stress amplitude of ΔP , the cyclic plastic zone depends on ΔP only and is independent of the maximum stress provided that no crack closure occurs during compressive part of the load cycle. The formation of the cyclic plastic zone within the maximum plastic zone is shown schematically in Fig. 19.

The value of K_c is normally a minimum under plane strain conditions as shown in Fig. 16; it becomes a material property denoted as K_{IC} , in the same sense as the 0.2% proof stress. The existence of K_{IC} as a material property is the main justification for the application of Linear Elastic Fracture Mechanics to brittle fracture problems.

When a specimen containing a crack is loaded, the crack tip opens without extension of the crack. This movement is called the crack opening displacement (COD) and is associated with the development of plastic zone. Its critical value δ_c , when the crack starts

to grow, is roughly constant⁽⁶⁸⁾, and approximately equals G_c / σ_y ; δ_c is used as a measure of toughness for low strength steels and has the advantage that it still has meaning at, and beyond general yield.

7.4 Micromechanisms of Initiation and Growth of Fatigue Cracks

7.4.1. Introduction

The early work of relating initiation sites and topography of fracture surfaces to their causes and basic mechanisms was severely restricted by the inherent limitations of optical microscopy. The recent application of electron microscopy with its far larger depth of field and higher resolving power has, to a great extent, overcome the limitations imposed by optical microscopy in the study of fracture surfaces. With the help of this technique, usually referred to as electron micro-fractography (using scanning and transmission electron microscopes), at high magnification, more details are visible, and need to be categorized and described if the fractographs are to be related to the micromechanisms of crack initiation and propagation.

Fatigue is a complex phenomenon, involving microscopic flow processes and macroscopic crack extension, to final fracture. Forsyth⁽⁷⁰⁾ divided fatigue cracking into three stages - initiation, Stage I or slip band growth (crystallographic) and Stage II growth on planes normal to the maximum tensile stress (non-crystallographic).

7.4.2. Mechanism of Crack Initiation

It was first noted by Ewing and Humphrey⁽⁷¹⁾ that the process of crack initiation in un-notched specimens takes place at slip bands. During further investigation of these slip bands in fatigued specimens, Forsyth⁽⁷²⁾ observed that metal was extruded

from the slip bands ('extrusions'), and at the same time, fine crevices, generally termed 'intrusions' were formed within the bands. These intrusions developed into cracks and crack initiation was loosely defined as the formation of a 'viable' crack from a slip band intrusion. While little attention has been paid to the number of cycles taken to initiate cracks in un-notched specimens, it has been shown that crack initiation occupies the majority of the life in high cycle fatigue^{(73), (74)}.

It is well established that surface conditions greatly influence the fatigue life, rough surfaces giving shorter lives than smooth surfaces and this is attributed to the presence of favourable sites for the early formation of slip bands at stress concentrations such as surface scratches. Several mechanisms for the formation of extrusions and intrusions have been proposed, and have been summarized by Kennedy⁽⁷⁵⁾ and Lynch⁽⁷⁶⁾, Fig. 20. These mechanisms, although differing in details, postulate reversed slip mechanisms on planes of maximum resolved shear stress. While there have been many investigations concerned with the effect of notches on fatigue life, crack initiations in notched or pre-cracked specimens has been almost entirely neglected, it being generally assumed that crack initiation takes place immediately at sharp cracks, and after a small proportion of the fatigue life from blunt notches. Exceptions to this are the investigations of Weibull⁽⁷⁷⁾ and Hoepfner⁽⁷⁸⁾ who showed that crack initiation could occupy a significant proportion of the fatigue life of notched specimens.

7.4.3. Accepted Model of Mechanism for Initiation

While specific dislocation mechanisms have been proposed to account for extrusion and intrusion during fatigue^(79, 80, 81, 82),

Cottrell⁽⁸³⁾ proposed that extrusions would result when soft material in slip bands was squeezed out plastically during the compressive phase of the fatigue cycle and not sucked back during the tensile phase, Fig. 20. In many materials, cyclic stressing may locally remove strengthening components⁽⁷⁶⁾ within persistent-slip bands (PSB's), where extrusion/intrusion commonly occurs, and PSB's should then be softer than their surrounding matrix. In age-hardened Al alloys, PSB's are thin layers of material, usually $\sim 0.1 \mu\text{m}$ thick, in which re-resolution or overaging of precipitates has occurred^(84, 85, 86). In these alloys, fatigue initially produces narrow discrete bands of high dislocation density; these bands form along "quench bands", which usually contain only a slightly lower than normal density of precipitates and are already present before fatigue⁽⁸⁷⁾. Re-resolution of precipitates within these bands of high dislocation density, probably involving dislocation enhanced diffusion, enables the dislocations within the bands to re-arrange into a fine sub-grain structure. In cold-worked Al, fatigue can induce localised recrystallisation along slip bands⁽⁷⁰⁾. In other alloy systems, the same mechanisms of crack initiation may be seen to operate.

7.4.4. Mechanisms of Fatigue Crack Growth

Stage I fatigue crack growth, Fig. 21, is characterized by propagation of the crack on a plane oriented at approximately 45° to the stress axis and by crystallographic fracture facets changing direction slightly⁽⁸⁹⁾ with orientation at grain boundaries, and it is considered by Forsyth⁽⁷⁰⁾ to be an extension of the reversed slip process responsible for crack initiation. According to the model of mechanisms of crack initiation⁽⁷⁶⁾, Stage I cracks initiating from intrusions, propagate along PSB's (and grain boundaries) and

their crack-tip regions often consist of series of holes (tunnels), extending to different depths into PSB's which subsequently link up, Fig 20. This mode of growth can continue for an appreciable proportion of the life in un-notched specimens, particularly under torsional loading, but persists only through a few grains in notched specimens after which Stage II takes over.

In Stage II, plane of crack propagation is at 90° to the stress axis and it is generally characterized by certain microscopic features, known as fatigue striations on the fracture surface. These fatigue striations first wrongly observed by Zappfe and Worden⁽⁹⁰⁾ as some micro-cellular structure in metals, are characteristic to fatigue crack growth only, running more or less parallel to the crack front, Fig. 22. Crussard⁽⁹¹⁾ suggested that each striation represented the crack growth by ten load cycles. Tests employing single programme loading, however, showed that each striation was produced by a single cycle^(92, 93), an observation confirmed by many workers and providing the basis for subsequent quantitative work. The converse of this statement i.e. 'that every load cycle produces one striation' is not necessarily valid, since the crack-tip stress resulting from some cycles may be too small to produce an increment of crack length, especially in programme or block loading⁽⁹⁴⁾. In many alloys, for example, aluminium alloys and 3% silicon iron⁽⁹⁵⁾ striations are well defined, but they are less clearly visible in ferritic and bainitic structures and their presence in tempered martensitic structures has not been conclusively demonstrated. The regularity of striations is also distorted by the presence of large volume fractions of second phase particles as in spheroidised 1% carbon steel⁽⁹⁶⁾.

The presence of numerous well-defined striations on a fracture surface unambiguously defines that failure was by fatigue. Their absence does not preclude the possibility of fatigue fracture. Invisibility of striations on a fracture produced by cyclic load may arise from:

(a) Their spacing being too small to be resolved by the observational technique used. The smallest inter-striation spacing reported is a $\sim 200 \text{ \AA}$ (97).

(b) Insufficient ductility at the crack tip to produce a ripple by plastic deformation large enough to be subsequently observed.

(c) The operation of a fatigue fracture mode that does not produce striations.

(d) Their obliteration by damage subsequent to fracture (97).

The striations that are formed at very low crack growth rates ($< 5 \times 10^{-6}$ in./cycle or 127 nm/c) are difficult to resolve and often cannot be distinguished from the network of slip lines and slip-bands associated with plastic deformation at, and near the fracture surface. Under these circumstances, measurement of striation spacing is difficult, if not impossible (98).

The main mechanisms for Stage II crack growth and the striation formation can be listed as:

- (i) Plastic blunting process of crack growth
- (ii) Cyclic slip and movement of dislocations
- (iii) By shear and decohesions.
- (iv) Microvoid coalescence and growth.

All the models relate to damage by cycling at the vicinity of the crack tip, differing only in the way in which the damage occurs.

In his plastic blunting process, Laird⁽⁸⁸⁾ assumes that a small double notch exists at the crack tip from prior damage. As a tensile load is applied, the double notch at the crack tip serves to concentrate slip band along planes at 45° to the plane of the crack and to maintain a square geometry of the tip. When the specimen is deformed to the maximum tensile strain, the stress concentration effect of the crack is lessened, and the crack tip blunts to a semi-circular shape due to the broadening of the slip bands at the tip. Upon application of compressive load, reversed slip occurs, and the new crack surface created in tension is forced into the plane of the crack and partly folded by buckling of the very front of the crack tip into another notch. The process then repeats and crack growth occurs, Fig. 23. Depending on the inclusions, grain boundaries etc., slip zones may not remain symmetric. Moreover, variation of the position of slip planes with respect to the stress axis for different orientation of the cycles at the crack tip may cause asymmetry of the notch tip⁽⁹⁹⁾. Subsequent loading may induce plastic blunting in the most advanced part of the crack. Thus, in effect, crack growth occurs, according to Laird⁽⁸⁸⁾, during the increasing part of the load cycle only, but Schijve⁽¹⁰⁰⁾ believes that crack tip sharpening occurs during unloading, as depicted in Fig. 24.

Basically alternate blunting and re-sharpening of the crack tip give rise to striation formations, Fig. 23,24. Forsyth et al⁽¹⁰¹⁾ have distinguished between two types of fatigue fracture striation: Type A or 'ductile' striations, each consisting of a light and dark band, lying on irregular non-crystallographic plateau, e.g. Al-Zn-Mg alloy. Type B or 'brittle' striation lying on fan-shaped crystallographic facets, as on $\{100\}$ facets in corrosion-fatigue tested Al-Zn-Mg alloy and hydrogen-charged iron⁽⁹⁴⁾ Fig. 25. These facets often

exhibit 'river markings' and the striations show limited ductility. The spacing of both types of striation increases with the stress at the crack tip; their curvature is away from the origin of failure and large local variations in spacing and orientation have been observed in immediately adjacent areas of fractures in specimens cycled at constant load; the plateaux or facets on which striations lie are usually at different levels joined by regions of ductile tearing^(97,103,104). Both types of striation have been reported on grain boundaries⁽¹⁰⁵⁾. The spacing of fatigue striations does not correlate well with macroscopic crack growth rates⁽¹⁰⁶⁾, especially at higher crack growth rate, Fig. 26. The macroscopic crack growth rate is the sum of the normal fatigue process causing striations and the dimple fracture component caused by tensile tearing.

According to Laird⁽¹⁰⁸⁾ and Schijve⁽¹⁰⁹⁾, the Stage II crack propagation is an extension of Stage I crack propagation. On cycling, dislocation movement occurs on one or two sets of crystallographic planes at 45° to the crack plane, Fig. 27. Depending on the stress condition, crack tip may act as source or sink. Thus the crack extension occurs in each cycle as a consequence of a 'sliding off' mechanism⁽⁹⁹⁾. According to Broek⁽¹¹⁰⁾, striation depth could be larger on one fracture surface than on its mating part, depending on the orientation of the slip planes.

According to Pelloux⁽¹¹¹⁾, deformation at the crack tip may be caused either by alternate shears or simultaneous shear on two shear bands. If shear starts on one plane and strain hardening occurs, it could be easier to shear on the other plane, and this process may alternate.

If the material is non-hardening, or the hardening is saturated, crack blunting will take place by simultaneous shear. Due to high strain at the crack tip, void nucleation and growth may occur by further blunting and re-sharpening of the crack tip. On the other hand, Tomkins⁽¹¹²⁾ considers that the shear decohesion along the inner edges of both the flaw bands occurs during the tensile part of the fatigue cycle. During compression, the reversed slip occurs, and the crack closes without significant re-cohesion of the newly cracked surface. Due to this process, Fig. 28, according to Tomkins, the familiar ripple patterns on the fatigue fracture surface can form and this mechanism is also active in Stage I crack growth, but only on one plane.

Second phase particles can nucleate voids and cracks can extend by growth and coalescence of these voids. Pelloux⁽¹¹³⁾ proposed that the effects of second phase particles on crack growth rate depends on the ratio of fatigue plastic zone size, r_p , to the interparticle spacing S . He suggested that when

(a) $r_p < 10S$, crack growth rate depends on the matrix properties;

(b) $r_p \approx S$, crack growth is a result of propagation through the matrix and second phase particles;

(c) $10 r_p \geq S$, crack growth is mainly a result of crack extension through and around second phase particles⁽¹¹⁴⁾. Broek⁽¹¹⁰⁾ shows

that at low ΔK , fracture occurs around second phase particles, but at high ΔK , voids form due to loss of coherency of the second phase particles with the matrix. However, Grosskreutz and Shaw⁽¹¹⁵⁾ have

shown that at low values of ΔK , second phase particles effectively hold up propagation and act as crack arresters, which is the opposite of the relationship proposed by Pelloux⁽¹¹³⁾. A mechanism of void formation and coalescence by second phase particles has been proposed

by Forsyth and Ryder⁽¹¹⁶⁾. In this mechanism, the high hydrostatic stresses ahead of the crack tip cause voids to form probably at some discontinuity in the matrix. e.g. a brittle particle. These voids eventually link up by thinning of the unfractured bridges under biaxial stresses, resulting in crack extension, Fig. 29. Therefore, it can be expected that plane stress situations would be more favourable to void coalescence than plane strain condition, although void coalescence has been observed to occur under plane strain conditions. El Soudani and Pelloux⁽¹¹⁷⁾ noted that the extent of void coalescence could be reduced by decreasing the volume fraction of inclusions in the matrix.

7.5. FATIGUE CRACK INITIATION

7.5.1. Introduction

Much of the data relating to the resistance of materials to fatigue failure has been obtained using smooth specimens. The data thus generated are of limited use, because engineering components almost invariably contain stress concentrators due either to design, in the form of section changes, notches, keyways etc., or to fabrication difficulties in the form of defects such as laps, microporosity etc. In these circumstances, the choice of a safe design criterion depends on the working conditions of each individual component. If the stresses are low, then the defects may be assumed to be sharp cracks, and from a knowledge of the fatigue crack propagation rate, the time taken for the crack to reach a critical size, and hence the safe working life of the component, may be calculated. In these cases the application of fracture mechanics concepts has been found very successful. However, if the stresses are high, fatigue crack

propagation rate is rapid, and it becomes necessary to design against the initiation of cracking at the stress concentrators.

7.5.2. Review of Criteria for Correlating Fatigue Crack initiation data in notched specimens.

7.5.2.1. Stress-Strain Concentration Approach

The theoretical stress concentration factor, K_t applies only when the material at the notch root remains elastic. Neuber⁽¹¹⁸⁾ analysed a specific notch geometry and loading and derived a rule which applies when the material at the notch root deforms non-linearly. Recent work has shown that this rule adequately describes the more general case of plastic action in notched axial specimen^(119, 120). According to Neuber, the theoretical stress concentration factor K_t is equal to the geometric mean of the actual stress and strain concentration factors i.e.

$$K_t = (K_\sigma \cdot K_\epsilon)^{\frac{1}{2}}, \text{ Neuber's Rule } \dots\dots\dots (12)$$

Topper et al.⁽¹²⁰⁾ used the Neuber's rule to take into account plastic deformation at the notch root. This rule was derived for shear strained prismatical bodies containing deep longitudinal notches.

In applying Neuber's Rule to the notched fatigue problem, K_t is replaced by K_f , 'fatigue concentration factor', and K_σ , K_ϵ are written in terms of the nominal stress and strain ranges ΔS and Δe i.e.

$$K_f = \left(\frac{\Delta \sigma}{\Delta S} \cdot \frac{\Delta \epsilon}{\Delta e} \right)^{\frac{1}{2}} \dots\dots\dots (13)$$

where $\Delta \sigma$ and $\Delta \epsilon$ are local stress and strain ranges at the notch root.

Rearranging and multiplying both sides by Young's modulus, E , we can write:

$$K_f (\Delta S \Delta \epsilon E)^{\frac{1}{2}} = (\Delta \sigma \Delta \epsilon E)^{\frac{1}{2}} \dots \dots \dots (14)$$

and if the nominal stress and strain are limited to the elastic region,

$$K_f \Delta S = (\Delta \sigma \Delta \epsilon E)^{\frac{1}{2}} \dots \dots \dots (15)$$

The expression (14) is useful and important because it shows that a function of nominal stress and strain $(\Delta S \Delta \epsilon E)^{\frac{1}{2}}$ need only be multiplied by an experimentally determined constant concentration factor to obtain the value of $(\Delta \sigma \Delta \epsilon E)^{\frac{1}{2}}$ at the notch root (120).

The special case where ΔS is elastic but $\Delta \sigma$ and $\Delta \epsilon$ are inelastic, is important, because it covers most problems of engineering interest. At even longer lives, and lower values of ΔS , the notch root remains essentially elastic and equation (14) reduces to the familiar form

$$K_f \Delta S = \Delta \sigma \dots \dots \dots (16)$$

This equation is frequently used at shorter lives when the material near the notch behaves inelastically.

The relationship in equation (14) can be interpreted as furnishing indexes of equal fatigue damage in notched and unnotched specimens, or in other words, a notched specimen and a smooth specimen will form detectable cracks after the same number of cycles, provided $K_f (\Delta S \Delta \epsilon E)^{\frac{1}{2}}$ for the notched specimen is equal to $(\Delta \sigma \Delta \epsilon E)^{\frac{1}{2}}$ for the smooth specimen. Thus, if a master curve of $(\Delta \sigma \Delta \epsilon E)^{\frac{1}{2}}$ versus crack initiation (or life, as an approximation, provided the specimens are small) is obtained for smooth specimens, the life of a notched specimen can be obtained from the value of $K_f \Delta S$ on the $(\Delta \sigma \Delta \epsilon E)^{\frac{1}{2}}$ axis. This correlation has been checked experimentally and reasonable agreement has been found between the predicted and observed notch behaviour (121, 122).

A limitation of this method is that it only applies to constant amplitude, completely reversed (i.e. the stress ratio, $R = \frac{\sigma_{\max}}{\sigma_{\min}} = -1$) strain controlled loading. However, while direct correlation between smooth and notched specimens is only possible for $R = -1$, examination of equation (15) indicates that for other R values crack initiation data for different notches can be correlated using the parameter $K_f \Delta S$.

7.5.2.2. Fracture Mechanics approach

Several workers^(123, 124) have related the number of cycles, N_i , to initiate growth of a crack to the stress intensity range, ΔK , by an equation of the form

$$N_i = A (\Delta K)^{-n} \dots \dots \dots (17)$$

where A and n are constants for a given material in a given condition. Since fracture mechanics analysis applies strictly to sharp cracks, then, for defects with blunt tips some sort of adjustment to ΔK is required. Jack and Price⁽¹²³⁾ measured initiation at notches in mild steel and found that for sharp notches of root radius $\rho \leq 0.25$ mm., N_i was independent of root radius, and equation (17) applied.

Above the critical notch root radius, N_i is a function of root radius, written in the form $\Delta K / \rho^{1/2}$. Thus the effective stress intensity factor (K_{eff}) for a blunt notch is related to that for a sharp notch or crack by:

$$K_{eff} = K \left(\frac{\rho_0}{\rho'} \right)^{1/2} \dots \dots \dots (18)$$

where ρ_0 is the critical value of ρ and equal to 0.25mm. for mild steel⁽¹²³⁾,

ρ' is the effective root radius and

$$\rho' = \rho \quad \text{when} \quad \rho \geq \rho_0$$

$$\rho' = \rho_0 \quad \text{when} \quad \rho \leq \rho_0$$

Pearson⁽¹²⁵⁾ was unable to determine whether a critical root radius existed for a high strength aluminium alloy and he suggested that, if it did exist, it must be less than the 0.254 mm obtained by Jack⁽¹²⁶⁾ for mild steels. Pearson also described his initiation results in terms of the parameter $\Delta K/\rho^{1/2}$. Scatter was found to be fairly extreme. This could possibly be attributed to his criteria for initiation, which he defined as the load cycle when a 0.127 mm crack was first observed. Forman's⁽¹²⁸⁾ initiation data plotted in terms of the parameter $\Delta K/\rho^{1/2}$ also resulted in some scatter⁽¹²⁷⁾. Here again, an explanation can be found by properly defining the initiation event.

According to Forman⁽¹²⁸⁾, crack initiation, analogous to crack growth rate, should be a function of the relative stress intensity parameter, $\frac{\Delta K}{K_c}$, where K_c is the fracture toughness. For blunt notches, he replaced K_c by an apparent fracture toughness K_a , which is corrected for the finite root radius. K_a is defined as the product of K_c and the ratio of the size of the plastic zone r at the tip of the blunt notch to the size of the plastic zone w at the tip of the sharp crack; thus

$$K_a = K_c \cdot \frac{r}{w} \dots\dots\dots (19)$$

Values of $\frac{r}{w}$ were calculated using the equation derived by Creager and Paris⁽¹²⁹⁾ for the stresses at the tip of blunt notches.

Various initiation criteria cannot be tested accurately by experiment but crack growth law can be accurately measured by experiment. According to Forman⁽¹²⁸⁾, a satisfactory approach for predicting cycles to initiation of an 'engineering size' crack is to use crack propagation theory in which it is assumed that crack growth begins with the first load cycle. Forman correlated his initiation data extracted from sheet specimens of 7075-T6 aluminium alloy with $\frac{\Delta K}{K_a}$.

For his data, N_i was for the initiation of an average crack length of 0.254 mm. He also showed that data obtained by Manson⁽¹³⁰⁾ for 2014-T6 aluminium alloy could be correlated with $\frac{\Delta K}{K_a}$. For this data, crack initiation was defined as the load cycle when a 0.063 mm. crack was first observed.

It is apparent that several methods have been employed for correlating fatigue crack initiation behaviour at notches. Each method appears to correlate specific sets of data. An explanation lies in the fact that, in order to know that initiation has taken place, some crack growth must occur, since detection of a fatigue crack is the sole criteria of initiation. Thus the experimental value of N_i , is in general,

$$N_i \text{ measured}_{(N_i)} = N_i \text{ true}_{(N_o)} + N \text{ propagation}_{N(a)} \dots\dots\dots (20)$$

The criteria of initiation may be very sensitive and then the $N(a)$ contribution to N_i is small, or vice versa⁽¹³¹⁾.

Both from a fundamental and a design point of view, it is important to know how N_i varies as the initiation criteria is varied from the presence of a large fatigue 'nucleus' to a very small 'nucleus'. This study of the very early stages of propagation is necessary in order to judge how conservative a particular criteria of nucleation is⁽¹³¹⁾.

7.6 Fatigue Crack Propagation Laws

7.6.1. Introduction

In recent years, considerable effort has been focussed on the crack propagation phase of fatigue failures in an attempt to develop useful design rules. Analytical solutions have stemmed from several distinct disciplines of engineering science and to review all

such models, a broad classification of crack propagation laws has been necessary.

The various approaches can be divided into those involving dislocation theories, those based on the mechanics of fracture and dimensional consideration, and those founded on empirical studies of cyclic material behaviour and damage accumulation.

7.6.2. Crack Propagation Laws

The first continuum model for fatigue crack propagation was presented by Head ⁽¹³²⁾ in 1953, in the following form:

$$\frac{da}{dN} = \frac{C \Delta \sigma^3 a^3 / 2}{(\sigma_{ys} - \Delta \sigma) r_y^{\frac{1}{2}}} \dots \dots \dots (21)$$

where C is a material constant

$\Delta \sigma$ is the stress range

σ_{ys} is the yield strength

a is the crack length and

r_y is the plastic zone size at the crack tip,

and is assumed to be constant.

Frost and Dugdale ⁽¹³³⁾ showed on the basis of experimental results that plastic zone size is proportional to crack length.

Further they concluded that the crack propagation rate is linearly dependent on the crack length which in turn is proportional to $\Delta \sigma^3$.

Thus they proposed the following model.

$$\frac{da}{dN} = A \Delta \sigma^3 a \dots \dots \dots (22)$$

where A is a constant.

Liu ⁽¹³⁴⁾ modified the above equation, in subsequent work, to

$$\frac{da}{dN} = A \Delta \sigma^2 a \dots \dots \dots (23)$$

Frost and Dugdale⁽¹³³⁾, and later, Frost⁽¹³⁵⁾, examined the effect of mean stress on the rate of crack propagations in several materials, including an annealed mild steel, cold rolled mild steel and 18/8 austenitic steel, and a crack growth relationship of the form:

$$\frac{da}{dN} = (P + Q \sigma_m) \Delta\sigma^3 a \dots\dots\dots (24)$$

was proposed, where P, Q are constants and σ_m is the mean stress.

Tomkins and Biggs⁽¹³⁶⁾ deduced a mechanism of fracture in terms of plastic deformation at the crack tip and this formed the basis of Tomkin's theory⁽¹³⁷⁾. Essentially, he calculated the crack tip decohesion which would occur as a result of the plastic strain at the crack tip and equated this to da/dN . The result was a relationship similar to that obtained experimentally by Frost⁽¹³⁵⁾, equation 24. It was

$$\frac{da}{dN} = A \Delta\sigma^3 \sigma_m a \dots\dots\dots (25)$$

Equation (24) would be the same as equation (25) if $P = 0$ as was found for aluminium alloys.

According to Paris and Erdogan⁽¹³⁸⁾, the laws of Head, equation (21), Frost and Dugdale, equation (22) and Liu equation (23), can all be approximated by the form

$$\frac{da}{dN} = \frac{\Delta\sigma^m a^n}{C} \dots\dots\dots (26)$$

where C is a constant and $n = \frac{m}{2}$

Paris⁽⁶⁶⁾ adopted an energy approach to crack propagation. This was based on the assumption that the rate of change of elastic energy during fracture equals the rate of absorption of energy as plastic deformation. Assuming that all the plastic work is absorbed at the crack tip, the work is proportional to the area of the plastic zone per unit thickness, which in turn, is proportional to K^4 . He

went on to suggest that, in fatigue, the alternating plastic zone⁽⁶⁷⁾, based on ΔK , is relevant, so that the crack propagation relationship is

$$\frac{da}{dN} = C (\Delta K)^m \dots\dots\dots (27)$$

Thus Paris' theory predicts a value of $m = 4$, in equation (27) and no influence of mean stress on fatigue crack propagation.

According to Liu's⁽¹³⁴⁾ analysis, the value of $m = 2$. He argued that this value holds good for results with maximum stress levels. Since the elastic strain energy released is a function of maximum stress, the maximum stress should give reasonable correlation. Liu admitted that the value of m will have to be modified if σ_{max} is not the same.

Although a good fit for a variety of experimental data has been observed with Paris type equation, it has been well established that m can have values ranging from 2 to 6^(139, 140).

Forman et al.⁽¹⁴¹⁾ noted that Paris's equation was not a good fit for higher load ratios and crack growth rates. They attributed this to the onset of fast fracture as K_{max} approached K_c , the fracture toughness of the material. Forman et al.⁽¹⁴¹⁾ suggested that the approach to K_c could be incorporated in the crack propagation relationship by adopting the criterion

$$\lim_{K_{max} \rightarrow K_c} \frac{da}{dN} = \infty$$

Putting $K_{max} = \Delta K / (1-R)$, where R is the stress ratio (K_{min}/K_{max}), this may be expressed as

$$\lim_{\Delta K \rightarrow (1-R) K_c} \frac{da}{dN} = \infty$$

So, the crack propagation relationship suggested to include this condition can be written as:

$$\frac{da}{dN} = \frac{C (\Delta K)^m}{(1-R) K_c - \Delta K} \dots\dots\dots (28)$$

This equation fitted nicely Broek and Schijves⁽¹⁴²⁾ results, and also those obtained by Illg and McEvilly⁽¹⁴³⁾ for $R = -1$. Later Hudson and Scardina⁽¹⁴⁴⁾ also used equation (28) and found that it fitted their data for $R > 0$, those for $R \leq 0$ being fitted by the simpler equation (27), if the compressive part of a cycle was ignored.

Crooker and Lange⁽¹⁴⁴⁾ were less successful in unifying their data for steel when they applied Forman's equation. It should be noted that, since K_c is geometry and environment dependent, it cannot be regarded as a material constant. The value used in equation (28) would be appropriate to the test specimen geometry. This places a serious limitation on the use of the equation in practical situations.

Pearson⁽¹⁴⁵⁾ investigated the effect of mean stress using thick (12.7mm) bend specimens, in which plane strain conditions are maintained until failure. This contrasts with the tests using thin specimens in which the fracture mode would be plane stress when final failure occurred. Hence, using equation (28) with K_c replaced by its plane strain value K_{IC} , and further modifying the equation to bias the effect of stress ratio towards high values of ΔK , Pearson obtained

$$\frac{da}{dN} = \frac{C (\Delta K)^m}{[(1-R) K_{IC} - \Delta K]^{\frac{1}{2}}} \dots\dots\dots (29)$$

to secure better fit with his data.

This equation (29) still complies with the criterion that $\frac{da}{dN} = \infty$ when $K_{max} = K_{IC}$. Pearson's equation was also successful in correlating Broek and Schijves data⁽¹⁴²⁾, as well as Maddox's⁽¹⁴⁶⁾ data at $R = 0$ and $+0.5$.

An indication of how the two equations (28 and 29 predict the influence of mean stress over a range of ΔK values, for high and low toughness materials, may be provided graphically as follows.

First, the predicted magnifications (M) in $\frac{da}{dN}$ for given values of R , K_{IC} and ΔK , have been redefined relative to the values for $R = 0$, and are given by

$$M_F = \frac{1}{(1-R)K_{IC} - \Delta K} \div \frac{1}{K_{IC} - \Delta K} = \frac{K_{IC} - \Delta K}{(1-R)K_{IC} - \Delta K} \dots\dots\dots (30A)$$

$$M_P = \frac{1}{[(1-R)K_{IC} - \Delta K]^{\frac{1}{2}}} \div \frac{1}{(K_{IC} - \Delta K)^{\frac{1}{2}}} = \left[\frac{K_{IC} - \Delta K}{(1-R)K_{IC} - \Delta K} \right]^{\frac{1}{2}} \quad (30B)$$

where suffix F refers to Forman's and suffix P refers to Pearson's equation (146). Secondly, the magnification factors have been plotted against ΔK for various stress ratios and two arbitrary K_{IC} values in Figs. 30 and 31. It will be seen from Fig. 30 (high toughness) that Forman's equation predicts the greatest influence of stress ratio, although the two factors do not differ widely for low values of R and ΔK . Thus, the effect of R on plots of $\log (da/dN)$ vs. $\log \Delta K$ would be to shift the curves along the $\log (da/dN)$ axis to give approximately parallel curves, as found in the results obtained by Broek and Schijve (142). Clearly, either expression would be suitable for correlating such data over a wide range of R and ΔK values. In contrast, the factors for a low toughness material, Fig. 31, differ widely over the whole range of ΔK and R values, especially at high values, Forman's equation giving the highest values. The data obtained by Pearson for low toughness materials were consistent with his equation, while Forman's equation (28) was not suitable.

A fuller attempt to take account of the material properties, has been made by Heald et al.⁽¹⁴⁷⁾. Basing their equation on one given by Weertman⁽¹⁴⁸⁾, they proposed the following modified equation

$$\frac{da}{dN} = A \left[\frac{\Delta K^4}{\sigma_c^2 (K_c^2 - K_{max}^2)} \right]^n \dots\dots\dots (31)$$

where A is a constant, n lies between 0.5 to 1 and Kc is the fracture toughness of the component. Besides predicting an effect of Kmax, where K max approaches Kc, this expression describes an effect of microstructure, principally through the parameter Kc. Heald et al.⁽¹⁴⁷⁾ showed that the fatigue crack growth results obtained from heat-treating a 1.0 percent carbon steel to different micro-structures were in good agreement with the equation (31).

Roberts and Erdogan⁽¹⁴⁹⁾ analysed the results of Broek and Schijve⁽¹⁴²⁾ on 2024-T6 aluminium sheet specimens in tension and some of their own results on 2024-T₃ in bending and showed that the dependency of crack growth rate on mean stress and ΔK can be satisfactorily represented by an equation of the form

$$\frac{da}{dN} = B (K_{max})^m (\Delta K)^n \dots\dots\dots (32)$$

where B is constant. The values of m and n were both found to be 2.

Klensil and Lukas⁽¹⁵⁰⁾ reviewed evidence suggesting the existence of a threshold value of ΔK below which cracks will not propagate, and modified the Paris's equation to take ΔK_{th} into account i.e.

$$\frac{da}{dN} = C (\Delta K_a^n - \Delta K_{th}^n) \dots\dots\dots (33)$$

where ΔK_{th} is related to ΔK_a by the equation

$$\Delta K_{th} = \Delta K_{thb}^{1-\alpha} \cdot \Delta K_a^\alpha \dots\dots\dots (34)$$

where ΔK_{th} = threshold stress intensity following the stress intensity of ΔK_a

ΔK_{thb} = basic threshold value of stress intensity factor

independent of the strength of the material.

α = material constant dependent on strength

Cooke and Beavers⁽¹⁵¹⁾ have also found evidence of threshold stress intensities in five medium carbon steels and concluded that ΔK_{th} depends on load ratio R . Prior loading could also be responsible for the existence of threshold ΔK values as found by Donahue et al⁽¹⁵²⁾ and Klensil and Lukas⁽¹⁵⁰⁾.

Finally, to provide an equation which predicts fatigue crack propagation from very small values of ΔK to impending unstable failure, a combination of equations (31 and 33) have been suggested by Richards and Lindley⁽¹⁵³⁾ in the form

$$\frac{da}{dN} = A' \left[\frac{(\Delta K - \Delta K_0)^4}{\sigma_c^2 (K_c^2 - K_{max}^2)} \right]^n \dots \dots \dots (35)$$

where ΔK_0 is the threshold stress intensity value and A' is a constant. The equation (35) represents an attempt to extend the prediction of fatigue crack propagation rates to extreme cyclic stress intensity regimes.

The complete relationship between fatigue crack growth rate and stress intensity factor, schematically plotted on logarithmic co-ordinates has been shown to be sigmoidal, consisting of three regions, Fig. 32. While most of the crack propagation laws is applicable to the linear middle portion of the sigmoidal curve, the rest of the curve is sensibly covered by incorporating the threshold stress intensity factor (ΔK_{th}) at very low values of ΔK and K_c term for very high values of ΔK close to catastrophic failure.

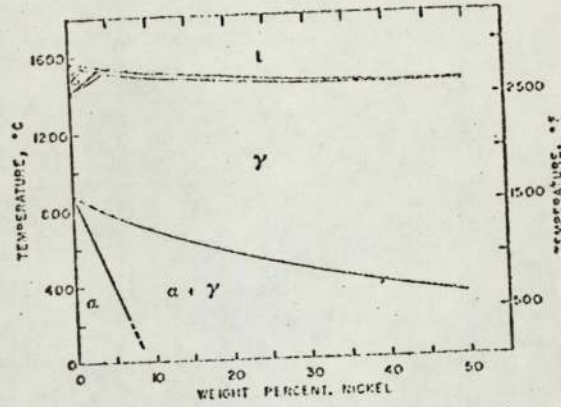


Fig.1. Iron-rich portion of the iron-nickel equilibrium diagram.
 (After Ref:22) [Courtesy Iron Steel Inst.]

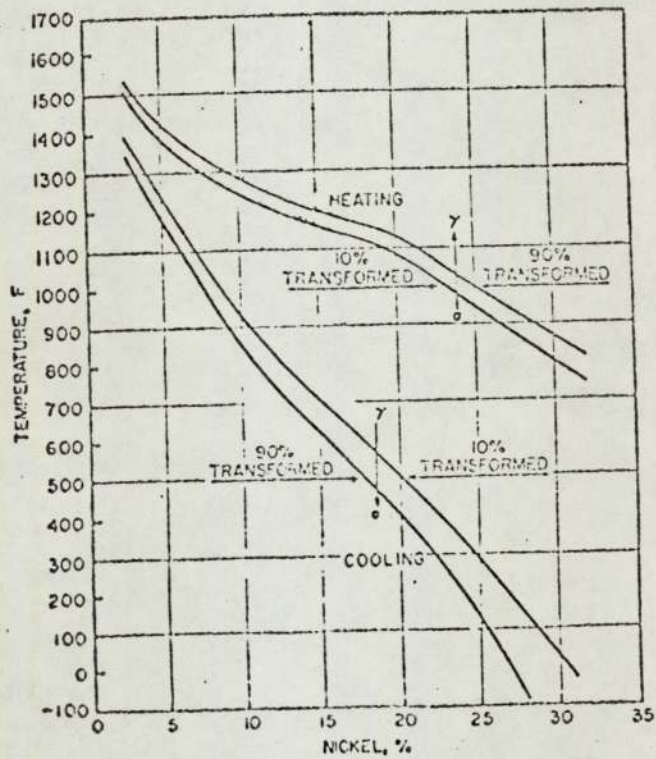


Fig.2. The Fe-Ni transformation diagram
 (After Ref:10)

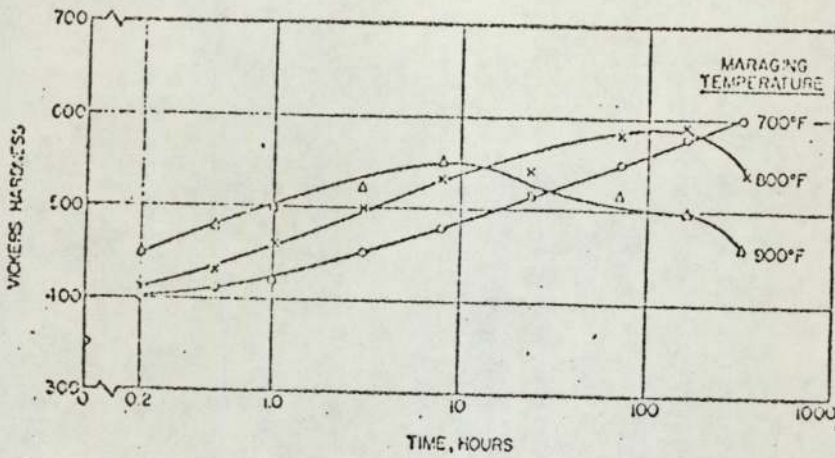


Fig. 3. Effect of maraging on hardness of 18% Ni steel. Initially annealed at 1500°F.
(After Ref: 12)

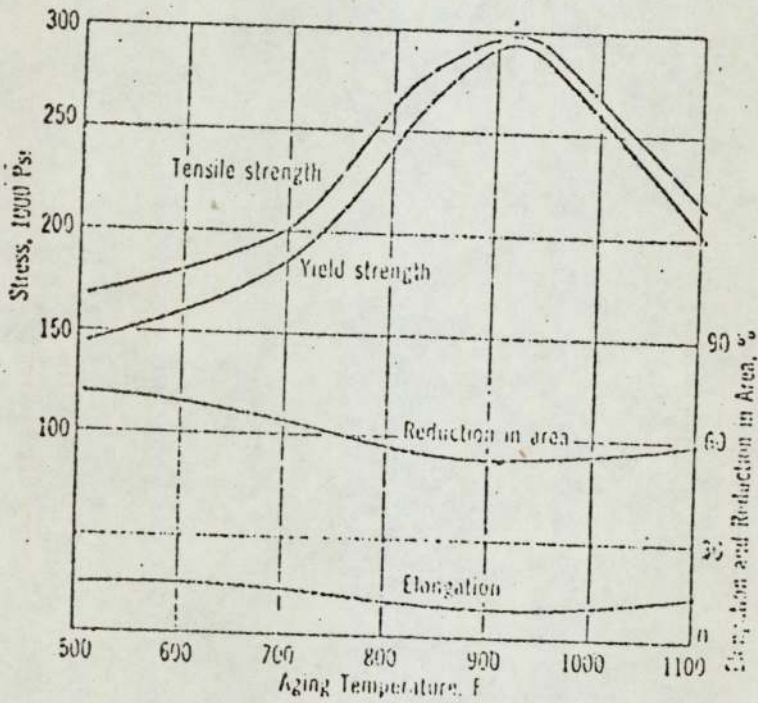


Fig. 4. Effect of Ageing Temp. on mechanical properties of a 18% Ni Maraging steel
(After Ref: 11)

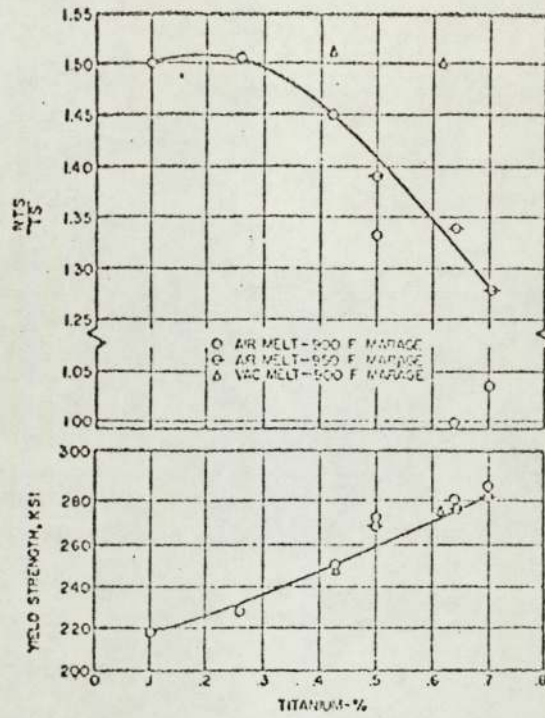


Fig. 5. Effect of titanium on yield strength and NTS/TS of 18.5 Ni, 7 to 7.5 Co, 6 Mo-Fe alloys 30 lb melts. Annealed 1 hr at 1500 F, maraged.

(After Ref: 10)

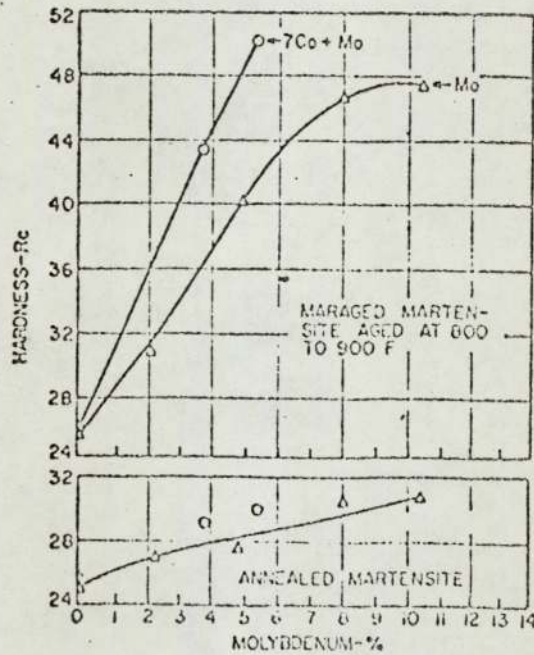


Fig. 6. Effect of molybdenum and molybdenum + 7% Co on maximum hardness of 18.5 to 20.1 Ni-Fe alloys. Solution annealed 1 hr at 1600 F, air cooled; maraged

(After Ref: 10)

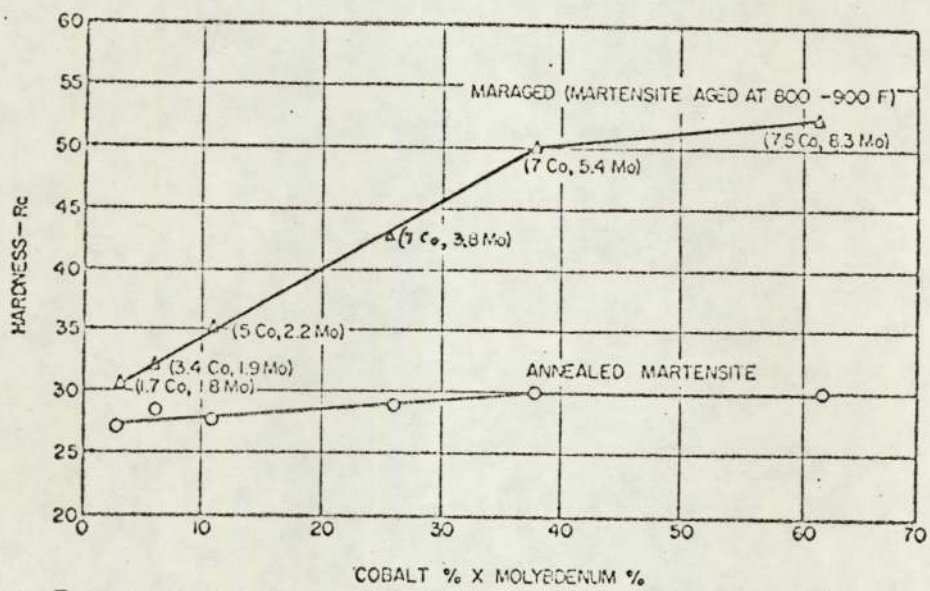


Fig. 7. Effect of product of cobalt X molybdenum on maximum hardness of 18.5 to 20.1 Ni-Fe alloys. Solution annealed 1 hr at 1600 F, air cooled; maraged 3 to 10 hr at 800 to 900 F.
(After Ref:10)

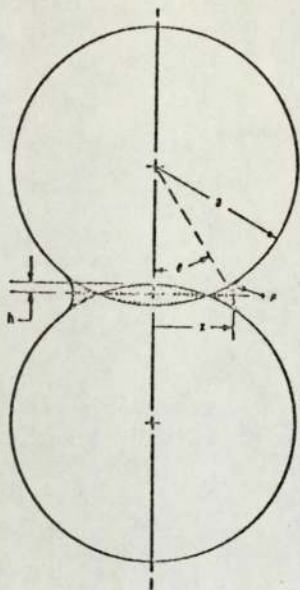


Fig.8. Two Sphere Model with interpenetration.
(After Ref:39)

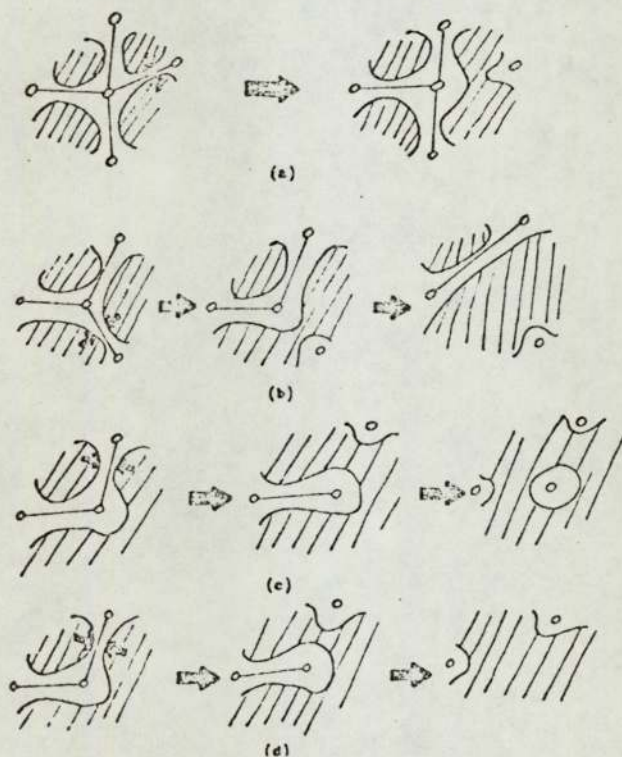


Fig.9. Whether a given pore is isolated (c) or adsorbed (d) into the main network depends upon the competition between shrinkage and surface rounding mechanisms, as well as upon the shape of the last connecting channel.
(After Rhines and DeHoff (40))

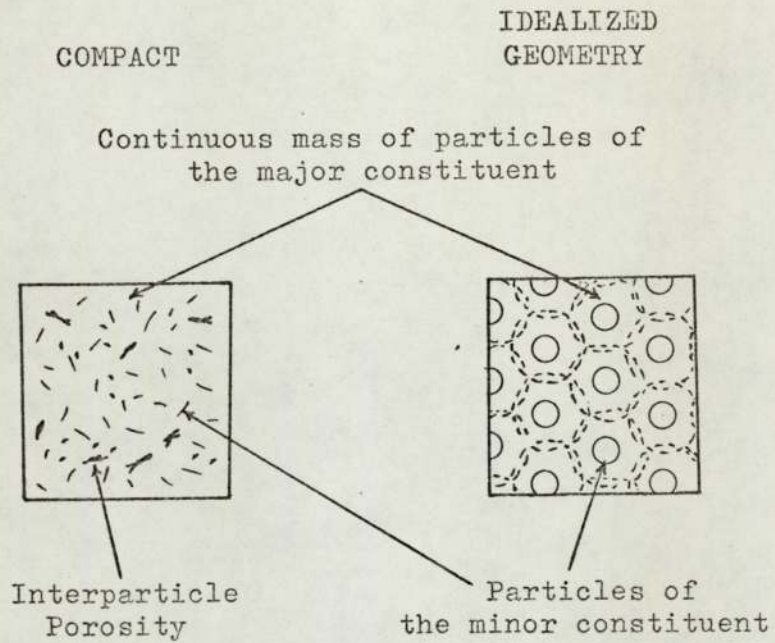


Fig.9A. Schematic representation of a Sintered Compact along with the Idealized Geometry of the Concentric-Sphere Model.

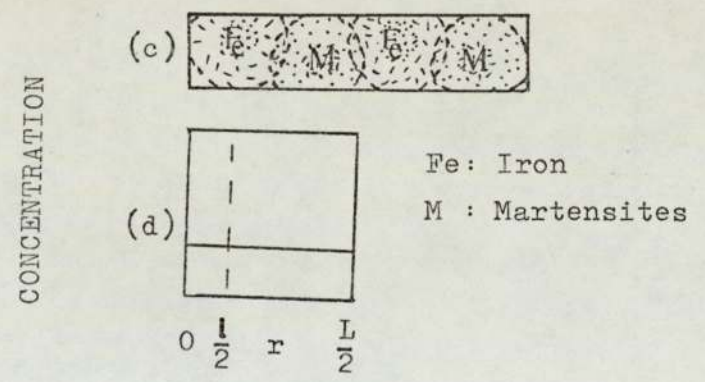
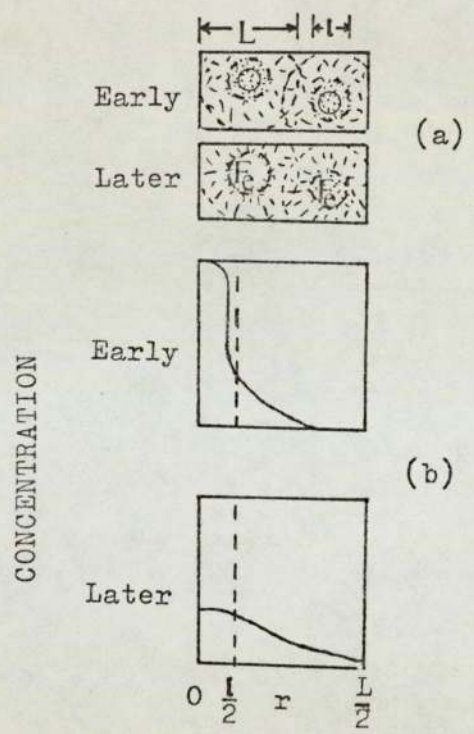


Fig.9B. Schematic representation of the Homogenisation Process for Martensite-Iron System in terms of the Microstructural Changes and Composition-Distance Profile.

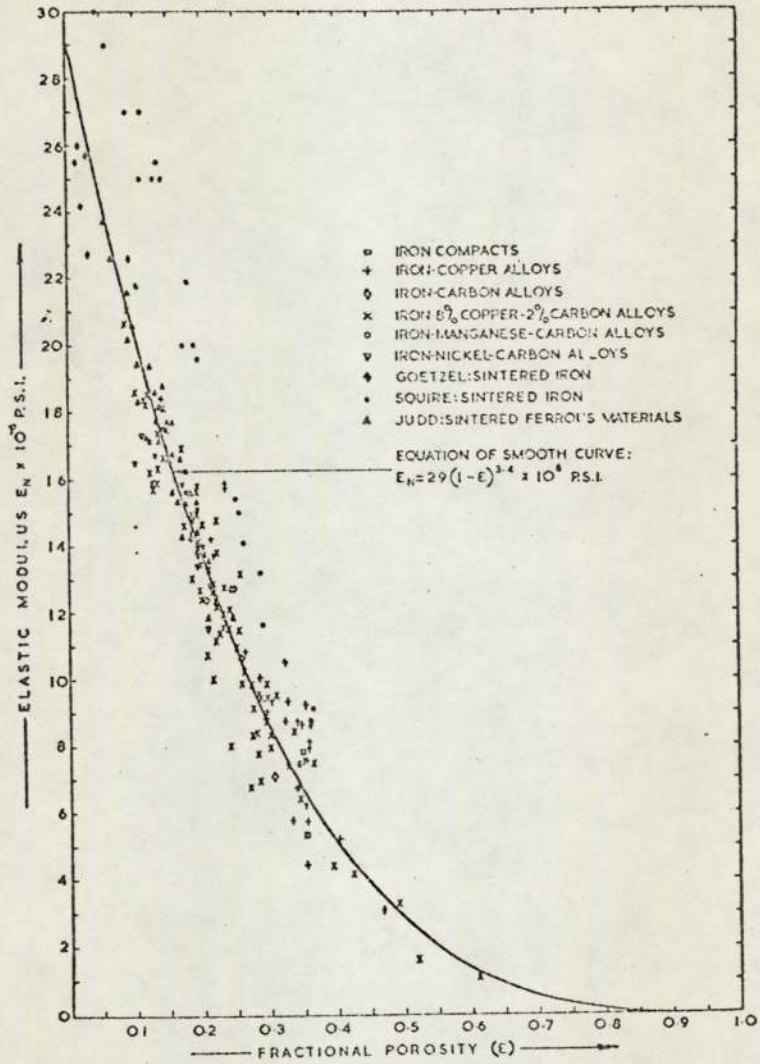


Fig. 10. Relation between elastic modulus and fractional porosity of iron-base alloy compacts.

(After McAdam (46))

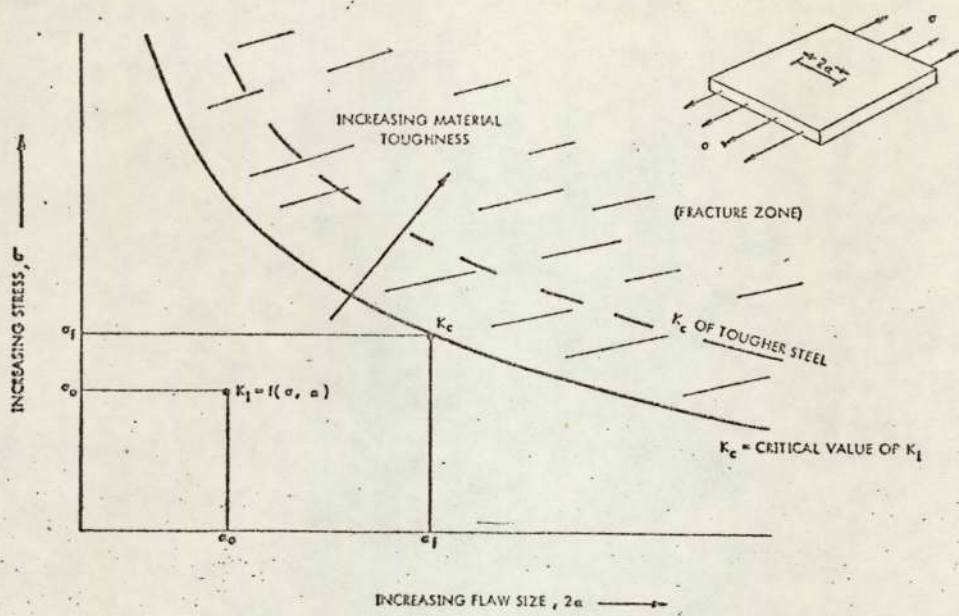


Fig.11. Schematic relation between stress, flaw size, and material toughness. (After Rolfe (47))

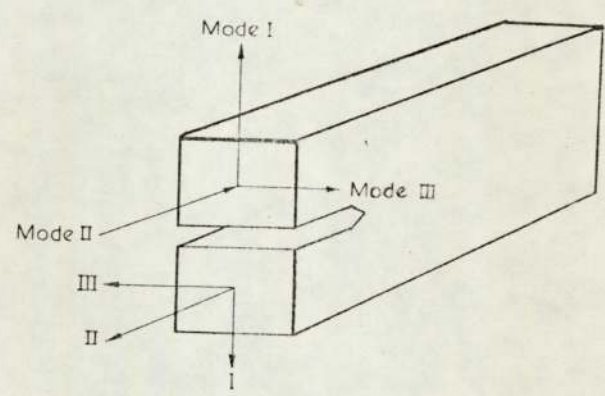


Fig.12. Diagram showing directions of Mode I, II and III cracking. It is possible to crack a body with shear loadings in Modes II or III. (After Ref:58)

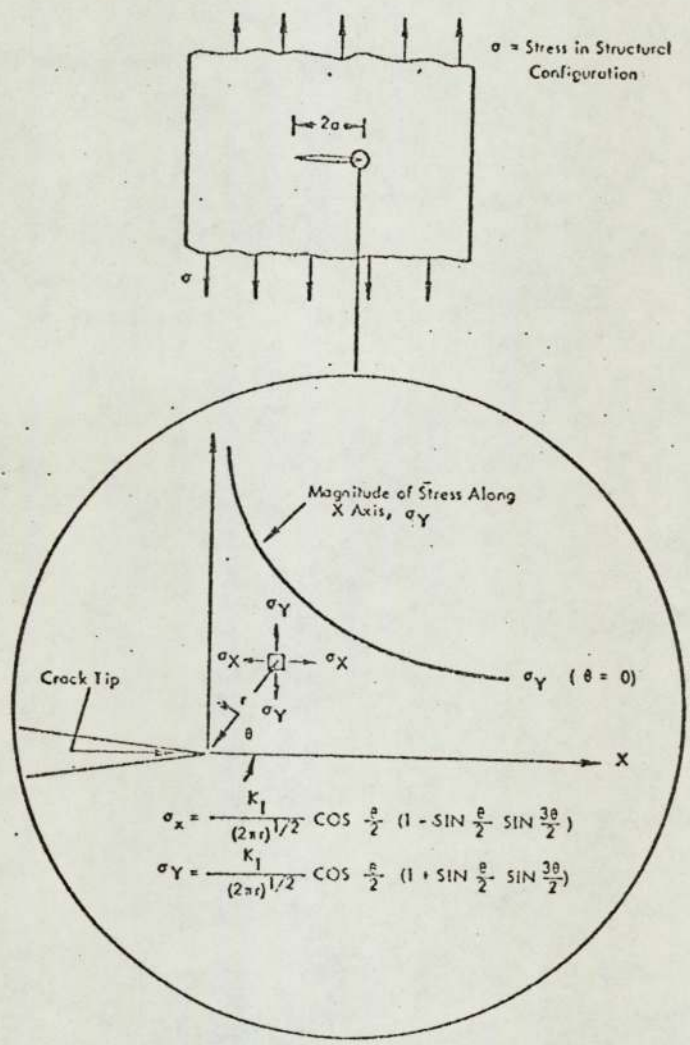


Fig.13. Elastic-stress-field distribution ahead of a crack.
(After Ref:47)

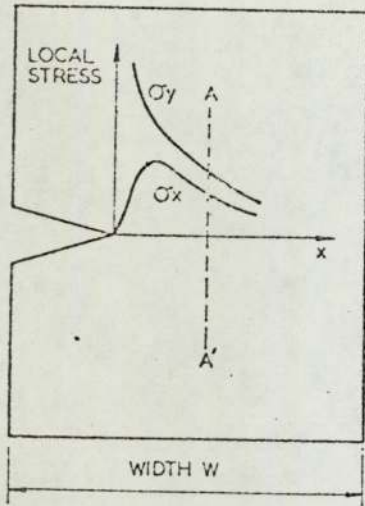


Fig.(a). Variation of σ_y and σ_x across width. Elastic condition.

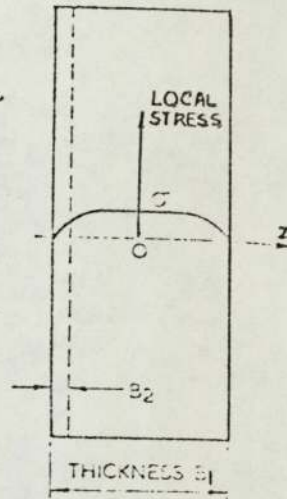


Fig.(b) Section at AA', $\sigma_z = \nu(\sigma_y + \sigma_x)$. Variation of σ_z through the thickness at section AA'. Elastic condition.

Fig. 14. Development of Constraint Stresses through width and thickness of a notched plate. (After Ref:61)

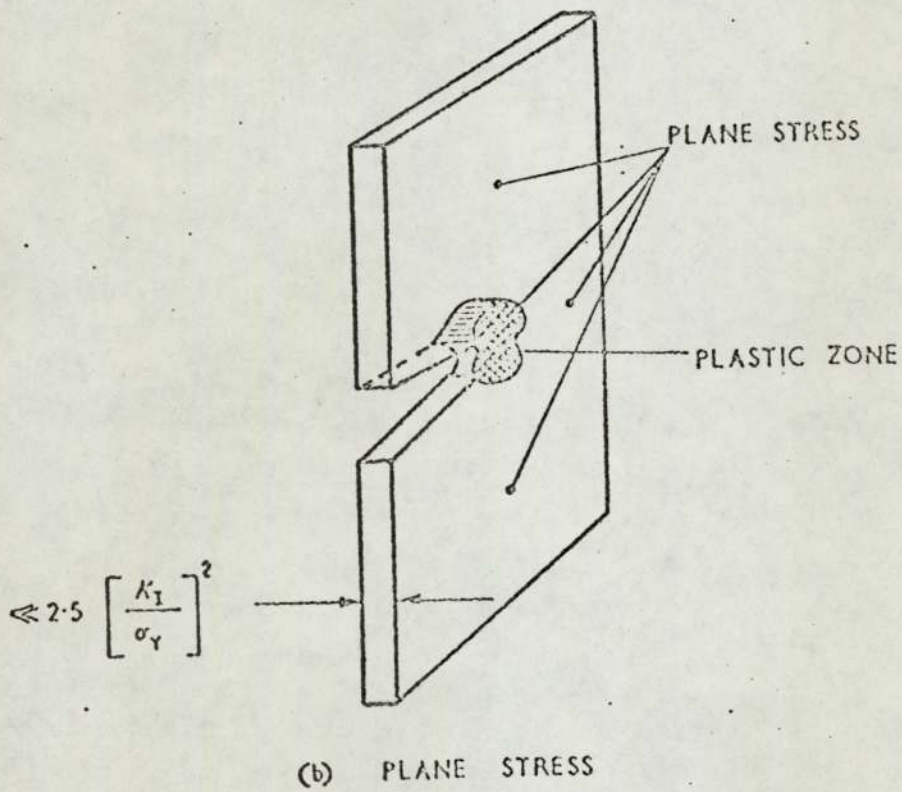
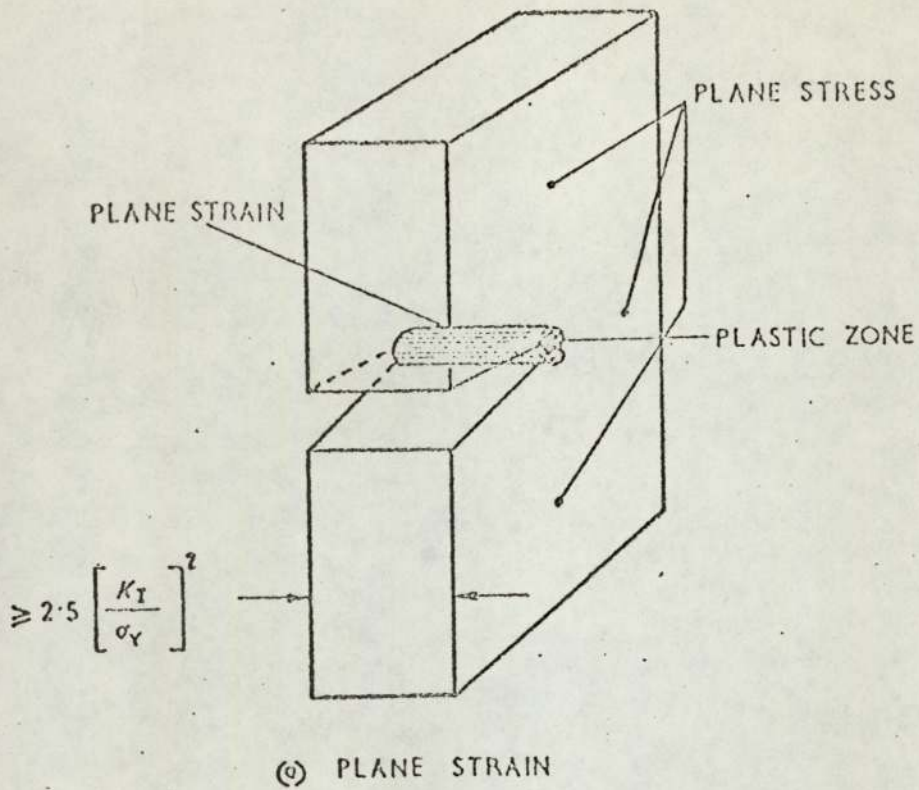


FIG. 15. NOMENCLATURE FOR THE STATE OF STRESS IN A CRACKED PLATE
(After Ref:59)

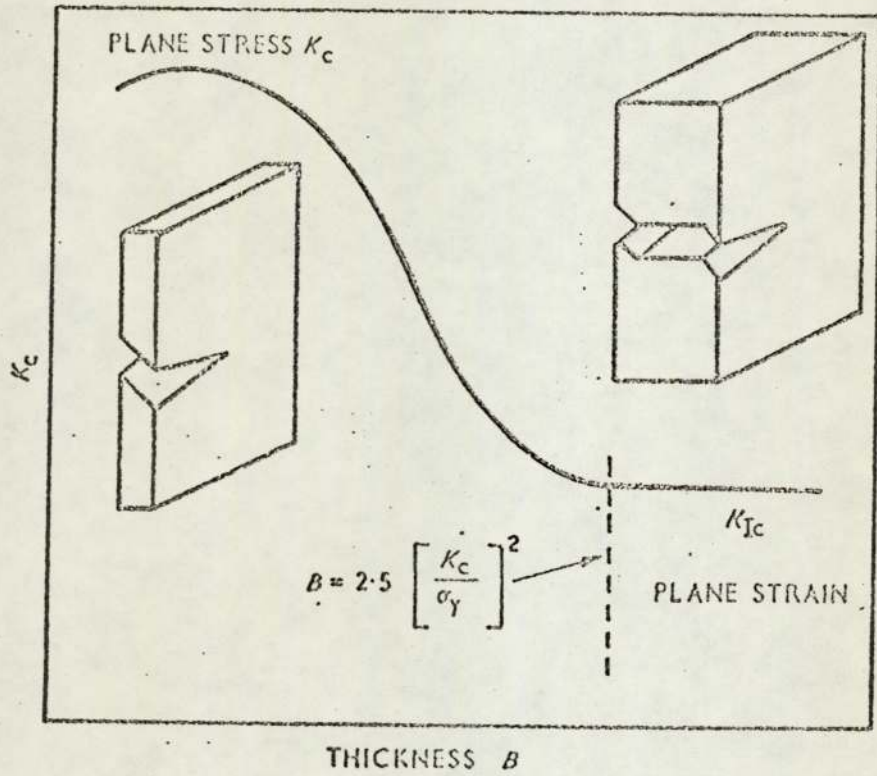
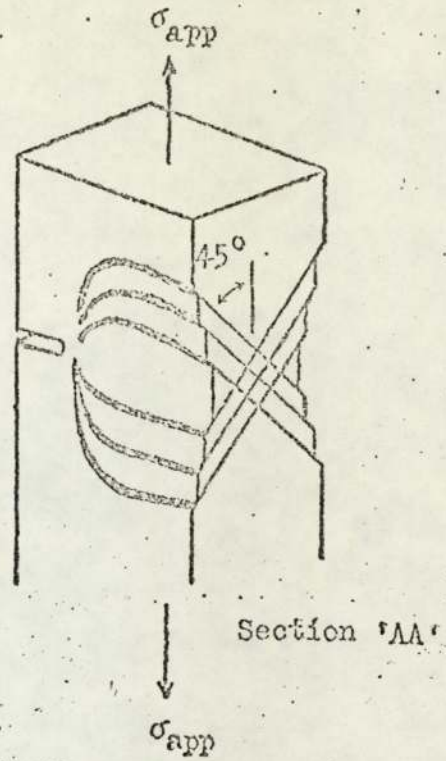
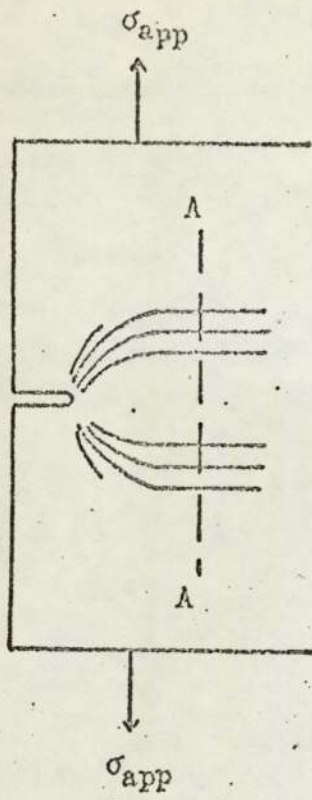
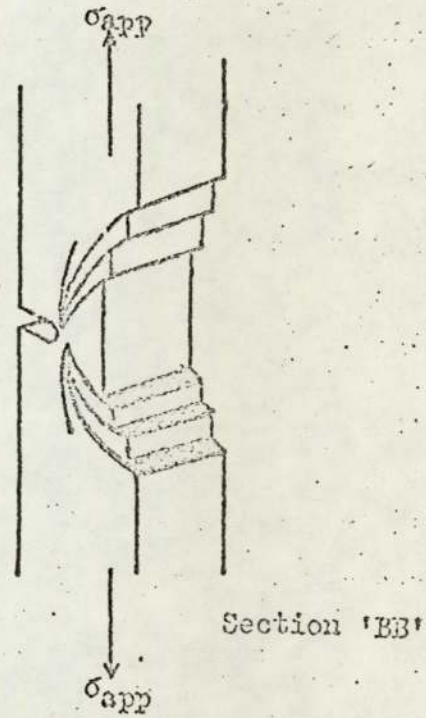
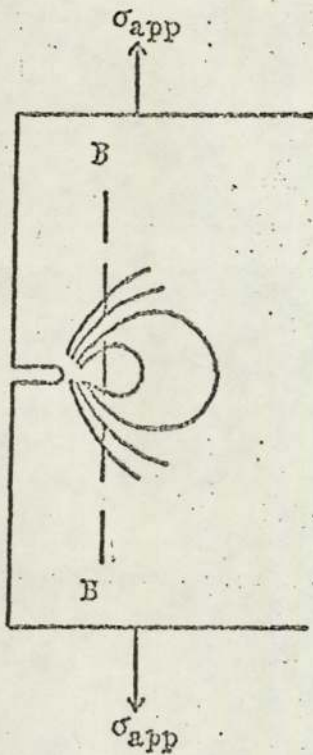


FIG.16. RELATIONSHIP BETWEEN THICKNESS AND K_c
 (After Pook (59))



(a) Plane Stress.



(b) Plane Strain.

Fig.17. Yield Zones through the Cross Section of a Cracked Plate in Plane Stress and Plane Strain. (After Ref:62)

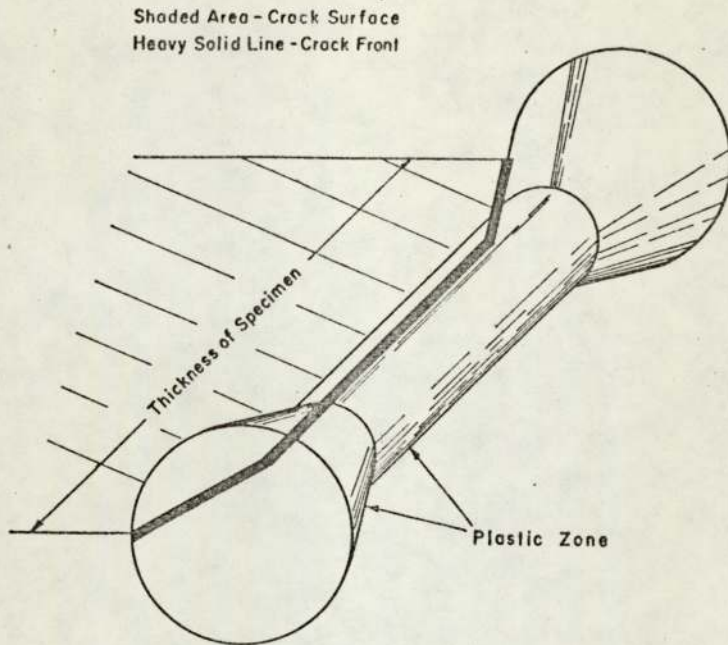


FIG. 18. Three-Dimensional Schematic Diagram of the Crack Surface, the Crack Front and the Plastic Zone.
(After Ref:60)

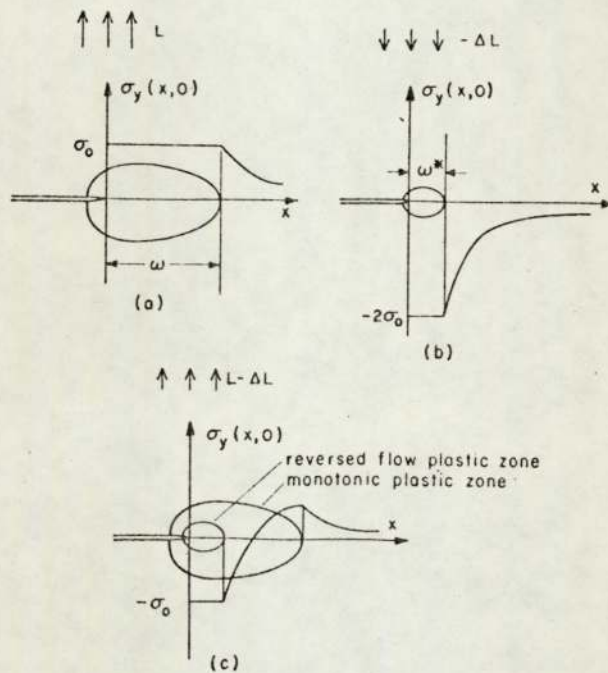


FIG. 19. Plastic superposition for unloading. Adding (b) for load $-\Delta L$ with a doubled yield stress to (a) gives the solution (c) resulting after unloading from L to $L-\Delta L$. Reloading, $L-\Delta L$ to L , restores (a).

(After Rice (67))

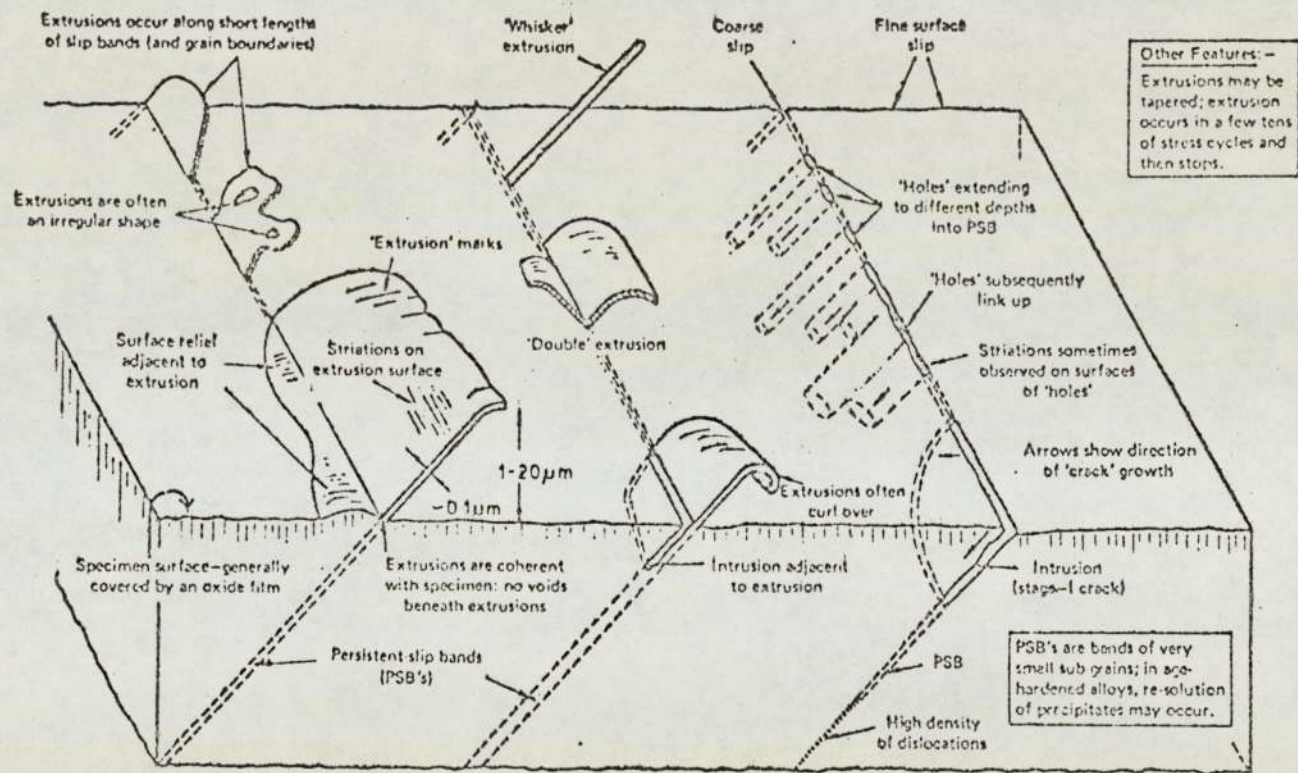


Fig. 20. Diagrammatic summary of important features of slip-band extrusion and intrusion. Specific details depend on material, stress, environment, etc.

(After Lynch (76))

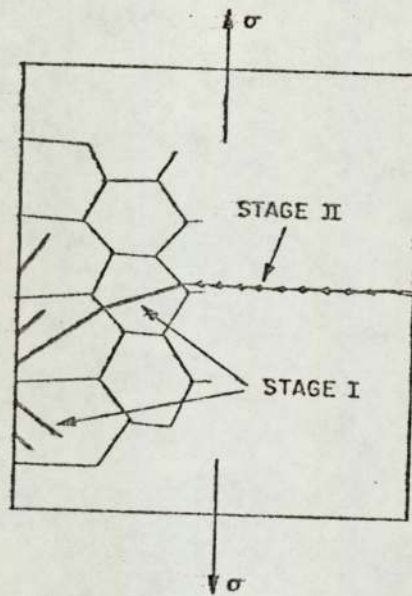


FIG. 21 Schematic representation of the two stages of crack propagation.
(After Ref:88)

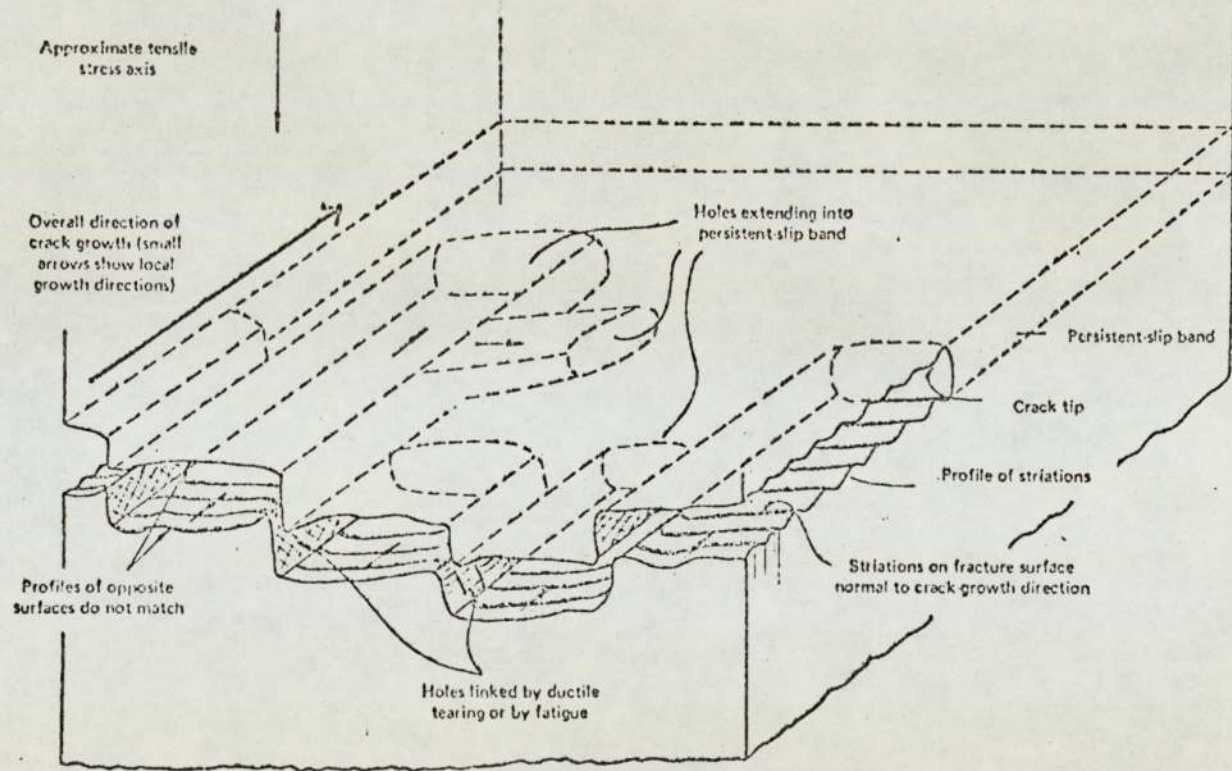


Fig.22. Schematic diagram of stage II crack-tip region.
 (After Ref:76)

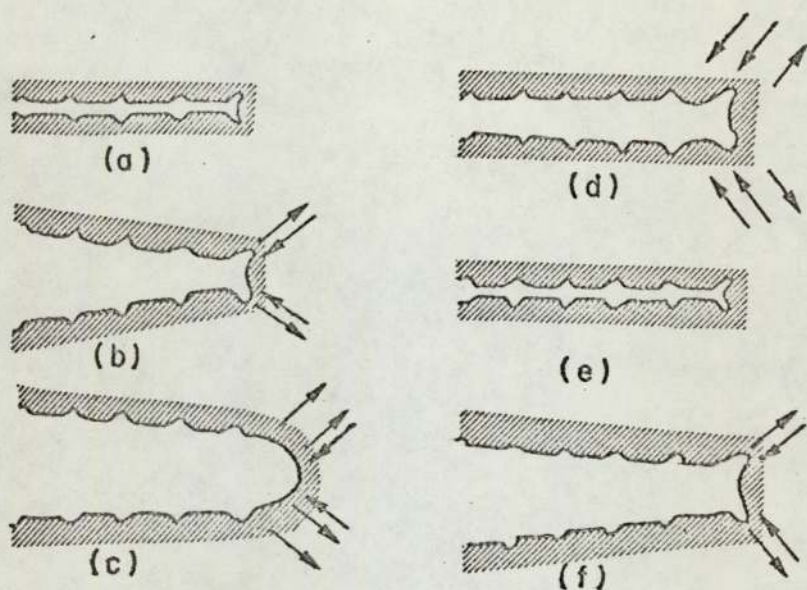


FIG. 23. The plastic blunting process of fatigue crack propagation in the stage II mode: (a) zero load, (b) small tensile load, (c) maximum tensile load, (d) small compressive load, (e) maximum compressive load, and (f) small tensile load. The double arrowheads in (c) and (d) signify the greater width of slip bands at the crack in these stages of the process. The stress axis is vertical. (After Ref:88)

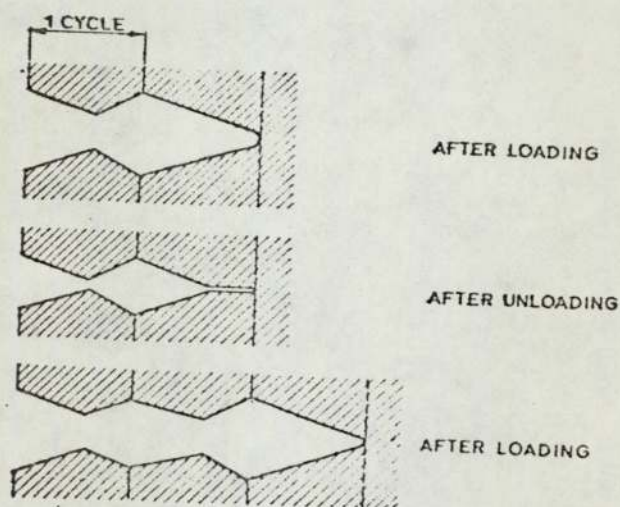


FIG. 24. Crack tip sharpening during unloading. (After Schijve (100))

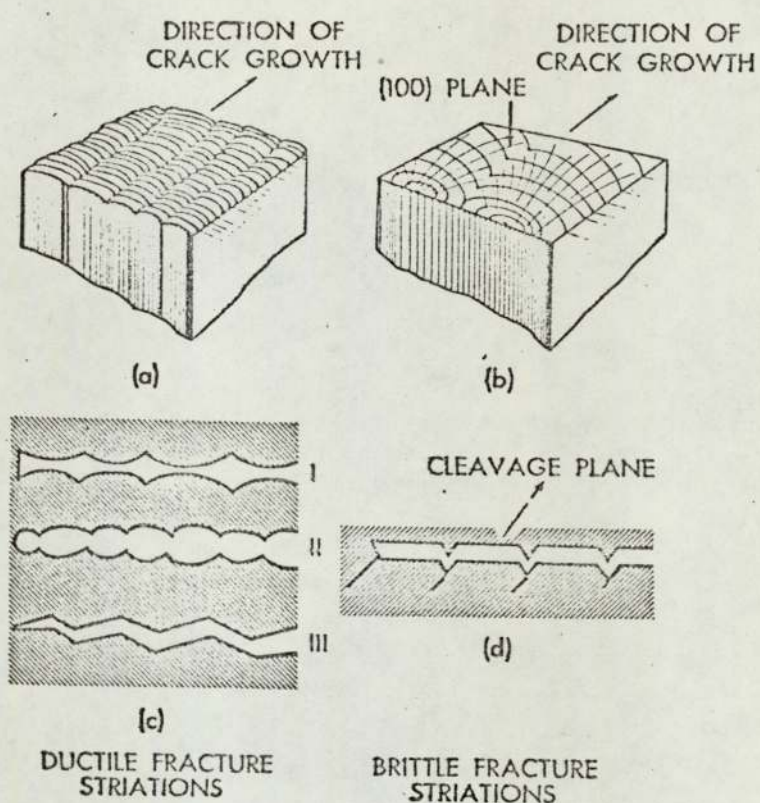
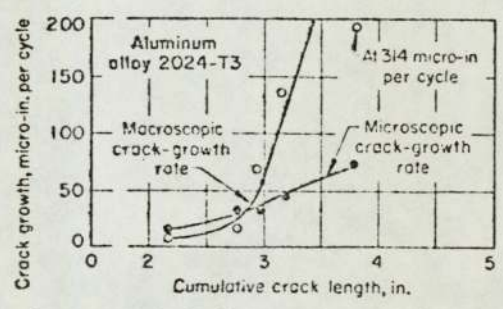


FIG. 25. Different Types of Ductile and Brittle Fatigue Striations; (a) and (b) Are Taken from Forsyth (85)

(After Beachem and Pelloux (102))



Data were obtained on specimens of aluminum alloy 2024-T3, 0.050 in. thick, fatigue tested at a frequency of 1000 cycles per minute. Microscopic rate was determined by striation spacing. Macroscopic rate was estimated from observed crack growth in successive groups of stress pulses.

Fig.26. Relation between microscopic and macroscopic crack-growth rates and cumulative crack length in fatigue fracture

(After Ref:107)

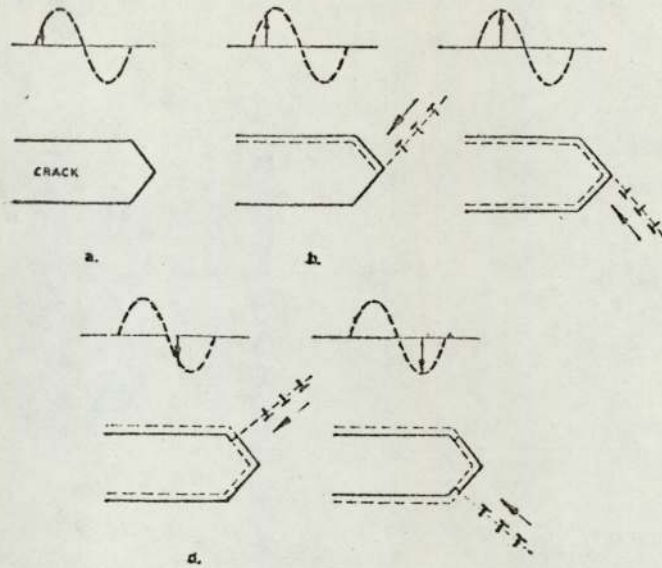


FIG. 27. Crack extension in one load cycle by dislocation movements on two different sets of crystallographic planes (After Ref:109)

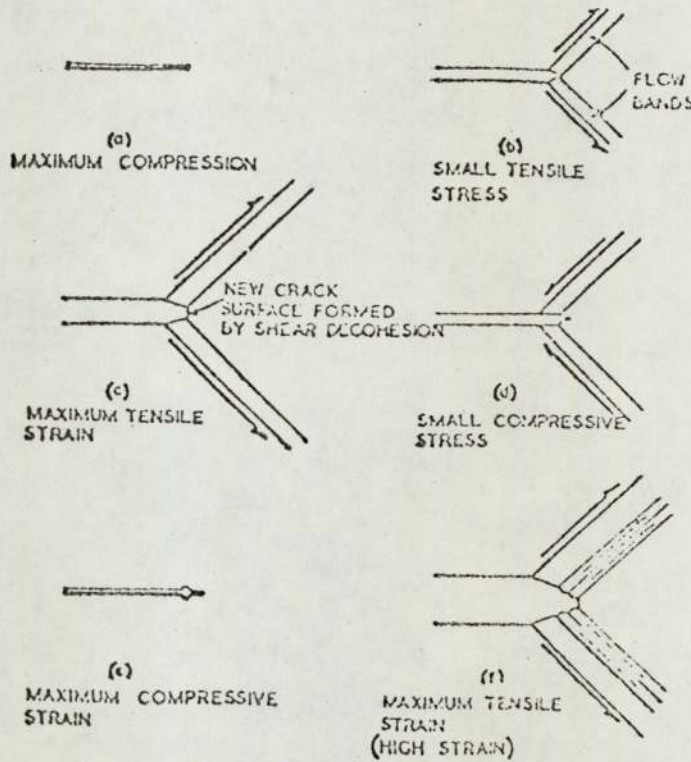


Fig. 28. Shear decohesion mechanism for Stage II crack growth. (After Ref:112)

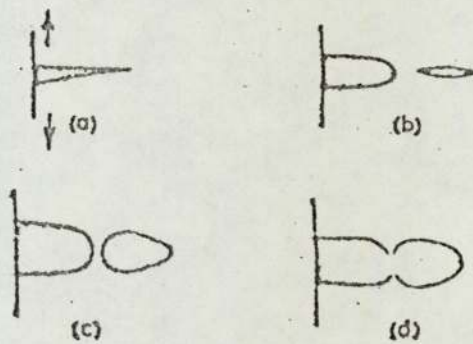


Fig. 29. Fatigue crack growth during one cycle of stress : (a) end of compressive half cycle, which may have cracked inclusions ahead of crack tip; (b) tensile half cycle blunts crack tip and produces void ahead of crack in region of triaxial tension; (c) thinning of unfractured bridge under biaxial tension; (d) final separation of bridge by thinning.

(After Ref: 116)

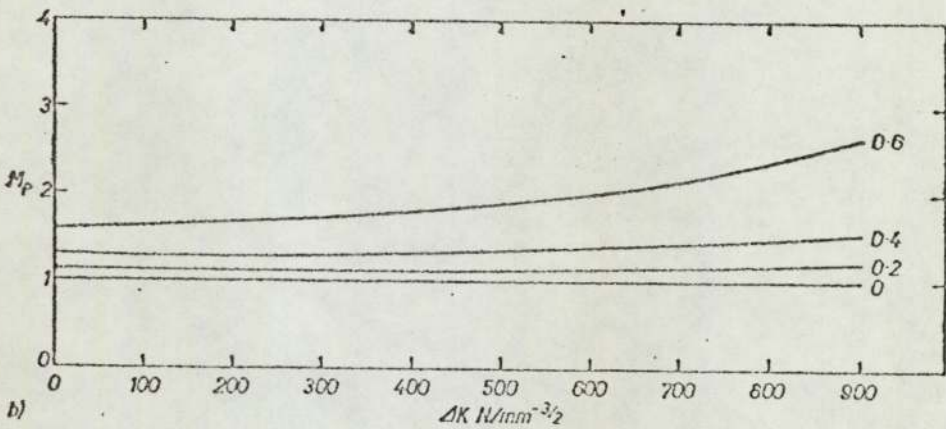
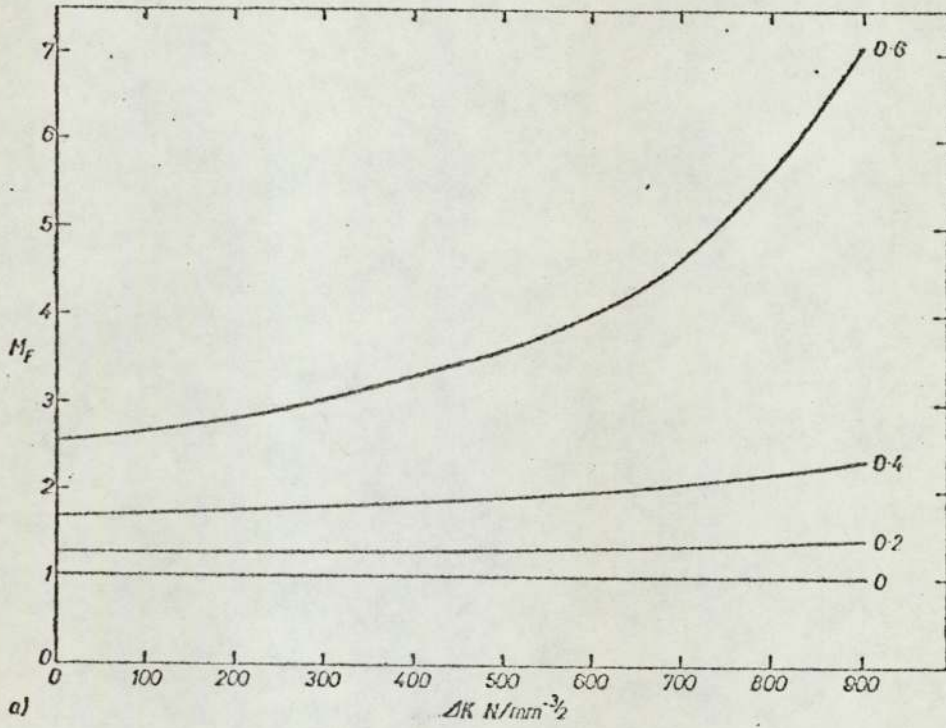


Fig. 30. Comparison of variation in crack propagation magnification factors proposed by (a) Forman [31] and (b) Pearson [14] with ΔK , for a high toughness value ($K_{Ic} = 3000 \text{ N mm}^{-3/2}$).

(After Maddox (146))

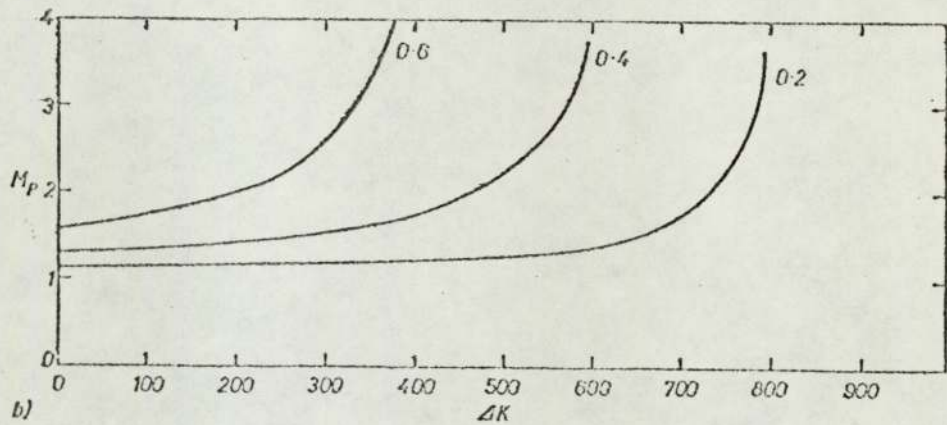
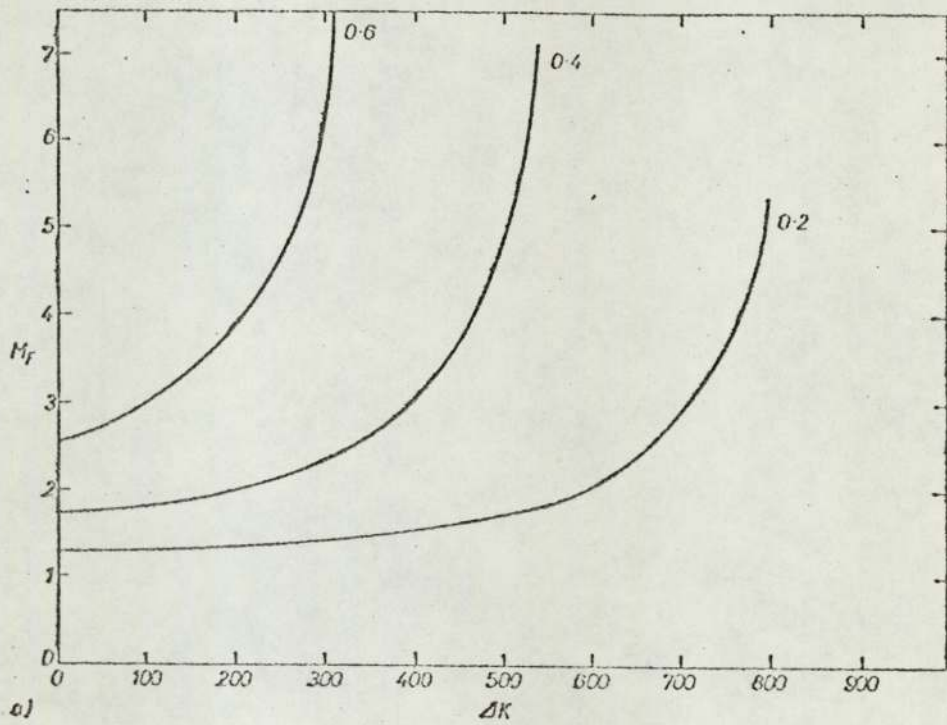
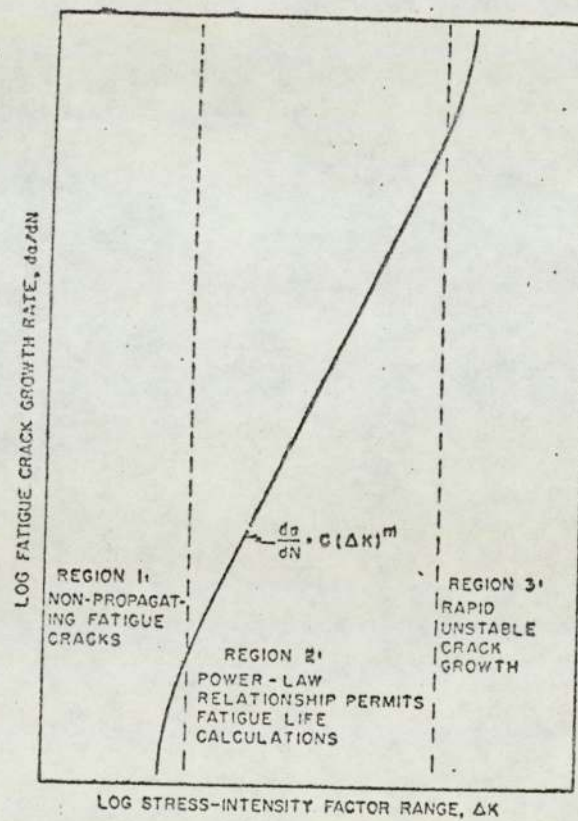


Fig 31 Comparison of variation in crack propagation magnification factors proposed by (a) Forman [31] and (b) Pearson [14] with ΔK , for a low toughness value ($K_{Ic} = 1000 \text{ N mm}^{-3/2}$).

(After Ref: 146)

Fig. 32. Schematic illustration of the typical sigmoidal crack-growth-rate curve for structural alloys as plotted on logarithmic coordinates
 (After Crooker (154))



8. EXPERIMENTAL DETAILS

8.1 OBJECTIVES WITH AN OUTLINE OF EXPERIMENTAL WORK

It has been stated in the introduction of the review that there is a general lack of data on the fracture toughness and fatigue properties of sintered components, which are, by definition and nature, heterogeneous. So an attempt has been made to extract some data to evaluate their fracture toughness, fatigue crack initiation and propagation characteristics by applying the concepts developed for homogeneous continuum material models.

The experimental work had been designed primarily to study the influence of sintered densities, % dilution, etc. on toughness and fatigue resistance using the concept of Linear Elastic Fracture Mechanics (L.E.F.M.). In this way, the major factors affecting the growth of cracks or defects in sintered materials could be quantitatively described so as to provide meaningful engineering design data. In conjunction with this work, investigations had also been directed towards the understanding of some of the mechanisms involved in fatigue and fatigue crack extension.

In order to simplify the experimental observations, and the interpretation of the data, rectangular cross-sectional specimens with single edge notches (S.E.N) had been used.

8.2 POWDER MATERIALS

The basic maraging steel material, in the as-received condition, was in the form of pre-alloyed atomised powder, -60 mesh size, supplied in two grades W127 and W119, the main difference being in the Ti content.

The other material, Ancoloy SA (Höganäs) was also in the form of pre-alloyed powder made from sponge iron to which the finely divided alloying elements had been diffusion bonded.

The maraging steel powder, grade W127 (high Ti), had been diluted with iron powder of grade ASC.100.29 (Höganäs) which is extremely pure with very high compressibility. The chemical compositions of (a) maraging steel powder of grade W127 (high Ti), (i) in the as-received condition, (ii) after compaction, sintering and final heat treatment, and (iii) after 25% and 50% dilution with pure iron powder are given below. Also given below are the compositions of (b) low Ti maraging steel powder, grade W119 and of (c) Ancology SA.

(a) Powder Grade Code W127Compositions (Wt %)

In as-received condition	After compaction and sintering	After dilution* with iron Powder (I.P.)	
		with 25% I.P.	with 50% I.P.
C - 0.010	0.02	0.015	0.01
Ni - 18.30	17.30	12.975	8.65
Co - 8.00	8.17	6.1275	4.085
Mo - 5.50	6.14	4.605	3.07
Ti - 0.99	1.20	0.90	0.60
Al - 0.008	0.18	0.135	0.09
S - 0.017	0.018	0.0135	0.009
Zr - 0.015	-	-	-
B - 0.002	0.001	-	-
Ca - 0.020	-	-	-
Si - 0.070	0.11	0.0825	0.055
P - 0.015	0.018	0.0135	0.009
Cr - 0.10	0.08	0.06	0.04
Mn - 0.05	0.03	0.0225	0.015
H ₂ loss (1150°C) 0.02			
Fe - Balance	Balance	Balance	Balance

* Estimated composition, after dilution, compaction, sintering and heat-treatment.

(b) Powder Grade Code W119 -- In as-received condition only.

(Low Ti Grade)

C - 0.02

Ni - 17.60

Co - 8.90

Mo - 4.60

Ti - 0.01

S - 0.018

Si - 0.010

P - 0.014

(c) Ancoloy SA

In as-received condition (i)	After compacting and sintering (ii)	After (ii) + quenching and Tempering
Cu - 1.50	1.42	1.43
Ni - 1.75	1.64	1.66
Mo - 0.50	0.55	0.56
C - 0.01	0.65	0.79
SiO ₂ - 0.16	0.20	0.20
H ₂ -loss - 0.10	-	-
Fe - Balance	Balance	Balance

8.3 SPECIMEN PREPARATION - COMPACTION, CALIBRATION

As recommended by the supplier, Högans of Sweden, 0.60% graphite + 0.65% Zn Stearate had been added to ANCOLOY SA powder, which was then mixed in a rotary drum for 25 minutes. Two lots of the admixed powder had been compacted using a specially designed die-system, Fig.33, to pressures ranging from 398 to 598 MN/m² to achieve green densities of 6.7 and 7.0 Mg/m³.

A fixed amount of maraging steel powder, grade W127, had been compacted at pressures P_1 , P_2 and P_3 (let us call this M_1). Then two lots of maraging steel powder, grade W127 had been mixed with 25% and 50% Högans iron powder (grade ASC.100.29) in a rotary drum for 25 minutes. We call these M_2 and M_3 respectively. The same amount, as in M_1 , of diluted maraging steel powder was then compacted using the same set of pressures P_1 , P_2 and P_3 to yield densities, d_4 , d_5 , d_6 and d_7 , d_8 and d_9 for M_2 and M_3 respectively, where $(d_1, d_4, d_7) < (d_2, d_5, d_8) < (d_3, d_6, d_9)$, Fig. 34.

Then corresponding to the three fixed green density levels of P_1, P_2, P_3 , compaction pressures were read out for each of the materials compacted, namely M_1 (maraging steel powder compacts only), M_2 (M.S.P. + 25% iron powder compacts) and M_3 (M.S.P. + 50% iron powder compacts). This method yielded more or less the same green densities when compacted at the pre-selected or calibrated pressures, e.g. :-

<u>Green Densities</u>	<u>Compaction Pressures</u>	<u>Compacted Materials</u>
$P_1 (5.8 \text{ Mg/m}^3)$	P_1	M_3
	P_2	M_2
	P_3	M_1
$P_2 (6.1 \text{ Mg/m}^3)$	P_4	M_3
	P_5	M_2
	P_6	M_1
	P_7	M_3
$P_3 (6.4 \text{ Mg/m}^3)$	P_8	M_2
	P_9	M_1

or re-written as following, yields :

<u>Compacted Materials</u>	<u>Green Densities</u>	<u>Compacted Pressures</u>
M_1	P_1	P_3
	P_2	P_6
	P_3	P_9
M_2	P_1	P_2
	P_2	P_5
	P_3	P_8
M_3	P_1	P_1
	P_2	P_4
	P_3	P_7

8.4 TEST SPECIMENS

These were of the single-edge-notched (S.E.N.) type for use in three point bending and machined and notched to the average dimensions, Fig. 35, after treatments as detailed in section 8.5.

The maraging steel powder compacts (with Ti \sim 1.0%) and diluted ones had been designed to the following matrix :

M_{11}	M_{12}	M_{13}
M_{21}	M_{22}	M_{23}
M_{31}	M_{32}	M_{33}

where M_1 = maraging steel powder compacts (Ti \sim 1.0%)

M_2 = M_1 + 25% pure iron powder compacts,

M_3 = M_1 + 50% pure iron powder compacts,

and where, second subscripts refer to the three levels of sintered (and final) densities. The specimens in M_{13} , M_{23} , M_{33} and M_{32} of the matrix had $\frac{\text{notch depth}}{\text{width}}$ i.e. ($\frac{a}{W}$) ratio = 0.1, and those in the rest of the matrix and specimens with low Ti had $a/W = 0.3$, with the nominal range of notch root radii from 0.127 to 0.762 mm. Ancoloy SA compacts, sintered, and sintered-quenched-tempered ones were made in two levels of densities with $\frac{a}{W} = 0.3$, and notch root radii of 0.127 mm. Fracture toughness tests had been made on all types of compacts, and also crack initiation and propagation studies had been carried out on all types of compacts, except on those made from Ancoloy SA compacts.

8.5 TREATMENT OF SPECIMENS

The green maraging steel compact specimens had been sintered at 1300°C for 3 hours in a vacuum furnace and cooled in the same furnace. The specimens were then annealed at 815°C for an hour per 25.4 mm. (1.0 inch) of thickness, in 90/10 N_2/H_2 atmosphere, followed by cooling at one end of the annealing furnace using the same atmosphere. After annealing, the specimens were machined to a tolerance of ± 0.025 mm (± 0.001 inch) on the major dimensions and notched to

dimensions, as shown in Fig. 35. The specimens were finally aged at 485°C for 3 hours in 90/10 N₂/H₂ atmosphere.

The green Ancoloy SA (ASA for short) compacts were sintered at 1120°C for an hour using the mixed gas of 90/10 N₂/H₂ as the furnace atmosphere, and cooled at one end of the furnace with the same atmosphere. The specimens, after sintering, were machined and notched, Fig. 35, and then austenitized at 850°C for 30 minutes, quenched in oil, and finally tempered at 175°C for an hour in air. The compact specimens needed surface grinding to the extent of about 0.025 mm. to remove fine surface scales.

8.6 PLANE STRAIN FRACTURE TOUGHNESS TESTING

Single-edge-notch (S.E.N.) bend specimens loaded in 3-point bending were used for determination of fracture toughness. Tests were done on a 50KN-capacity Instron machine operating at a constant rate of 0.02 cm/min. (cross-head speed). Method of mounting clip-in displacement gauge is shown in Fig. 36. Four 350 ohm strain gauges were connected in a Wheatstone Bridge balanced circuit and excited by a C₅₂ transducer amplifier unit.

The amplified response from the clip gauge together with the load signal from the Instron load cell, was fed into a Bryan's X - Y plotter. Location of the clip gauge across the notch was by means of attachable knife edges positioned accurately with the help of a spacer blade.

Bend specimens were tested on an adjustable bend jig. Overall span to specimen width ratio of 4:1 was used, as recommended by B.I.S.R.A. (155).

To produce a suitable starting crack for a toughness test, each specimen notch had to be extended by fatiguing. Fatigue pre-cracking was done on an Amsler Vibrophore fatigue machine using a 2 ton dynamometer, Fig. 37. The final length of the fatigue crack had been generally maintained between the a/w ratios of 0.45 and 0.55, as recommended by B.S.I.⁽¹⁵⁶⁾. The figure of $0.0005E$ suggested by B.I.S.R.A.⁽¹⁵⁷⁾ as an estimate of the fatigue crack propagation stress intensity range was not found satisfactory for the sintered specimens and it was necessary to exceed this value⁽¹⁵⁸⁾.

Fatigue pre-cracking was followed with the help of a low power binocular microscope, and the final 1.25 mm. (0.050 in.) of crack growth was estimated from graduations made at an interval of 0.50 mm. (0.020 in.) on the surface of the specimens. The last 1.25 mm. of crack extension was always made to take place over at least 50,000 cycles, according to the A.S.T.M. recommended practice⁽⁶⁵⁾.

A load/opening displacement record was obtained from each test from the Bryan's X - Y plotter attached to the Instron machine. The critical load was determined from the load/displacement record using the 5% offset procedure, recommended by B.S.I.⁽¹⁵⁶⁾, Fig. 38. All tests were carried out at least in duplicate, and whenever possible, in triplicate.

8.7 CALCULATION OF KQ

The provisional value of K_{IC} , i.e. KQ, was calculated from PQ, Fig. 38, using the following relationship⁽¹⁵⁶⁾ :

$$\begin{aligned}
 KQ = \frac{3PQ \cdot L}{BW^{3/2}} & \left[1.93 \left(\frac{a}{W} \right)^{1/2} - 3.07 \left(\frac{a}{W} \right)^{3/2} \right. \\
 & + 14.53 \left(\frac{a}{W} \right)^{5/2} - 25.11 \left(\frac{a}{W} \right)^{7/2} \\
 & \left. + 25.80 \left(\frac{a}{W} \right)^{9/2} \right] \dots\dots\dots (35A)
 \end{aligned}$$

(where $L = 2W = \frac{S}{2}$)

which can be written as

$$KQ = \frac{Y \cdot PQ}{BW^{3/2}} \dots\dots\dots (35B)$$

where

- P is the load
- B is the specimen thickness
- W is the specimen width
- a is the crack length
- S is the span between supports

and where the values of Y for specific values of $\frac{a}{W}$ are given in tables for different types of specimen and loading conditions.

8.8 CRACK GROWTH MEASUREMENT

Apart from direct observation of the specimen surface, various other means of monitoring the initiation, growth and instability of cracks, have been developed and these are summarized in Table II^(159,160).

TABLE II
CRACK GROWTH MEASUREMENT TECHNIQUES

<u>METHOD</u>	<u>USAGE</u>	<u>ADVANTAGES</u>	<u>DISADVANTAGES</u>
Microscopy techniques	Sheet and plate test-pieces. Photography sometimes used	Cheap. Easy installation.	Difficulty of crack tip location without stroboscopic light. Only surface measurements possible during test. Difficult to automate.
Mechanical methods	Rotating bend test pieces. Sheet, plate, and others depending on displacement gauge used	Use of compliance change which can be measured externally away from specimen.	Restricted to tests where compliance calibration (relationship between specimen stiffness and crack length) is known.
Acoustic methods	Applicable to most types of test-piece	Very small probe required, can be mounted easily; useful in low- and high-temperature tests.	Errors due to back-ground noise and calibration is difficult
Electrical techniques	Continuity gauges usually used on sheet and plate samples, could be used for surface measurements on other test-pieces	Electrical signal gives easy automation.	Difficulty of connecting wire and foil gauges. Gauges must break when crack passes. Only surface measurement.

Eddy currents	Used on surface crack monitoring of sheet test-pieces; others should be possible.	Easily adapted to automatic process. Small probe which is not in contact with test-piece.	Not yet used on thicker samples, may only be useful for surface measurement. Expensive.
Electrical resistance or potential measurement	Used on sheet and plate test-pieces	Easily adapted to automatic process. Only four leads attached to specimen, therefore ideally suited for high- or low-temperature tests	Problems of insulating the test-piece. Initial calibration problem thought to be overcome.
Ultrasonics	Ideally suited to compact fracture toughness test-pieces.	Easily adapted to automatic process. Internal measurement of crack front.	Expensive compared to other techniques. Measurement restricted to thicker type test-pieces.

In fatigue testing, it is required to measure the length of the crack with respect to the number of cycles so that data could be analysed by Fracture Mechanics, and the selection of any of the techniques mentioned must take account of its accuracy, speed of operation, reproducibility, cost, probability of automation, ease of application, whether continuous and flexible enough to apply to most standard test geometries and environments including tests at low ($\sim -100^{\circ}\text{C}$) and high ($\sim 500^{\circ}\text{C}$) temperatures. Since the electrical potential method seemed to satisfy all the requirements desired, it was adopted as the crack monitoring device used in this investigation.

Though first used by Barnett and Troiano⁽¹⁶¹⁾ in 1957 in fracture research studies, the electrical potential drop (p.d.) technique had been reported in detail in 1966 by Gilbey and Pearson⁽¹⁶²⁾.

The basis of the p.d. method is that in a current carrying body, there will be a disturbance in the potential field about any discontinuity in that body. For the purpose of monitoring crack growth, the method thus entails passing a stabilized current through a cracked test-piece under load, and measuring the electrical potential difference across the crack. As this crack extends, the uncracked cross-sectional area of the test-piece decreases, its electrical resistance increases, and the potential difference between two points on either side of the crack rises. By monitoring this potential increase (V_a) and comparing it with that across a unit length measured elsewhere on the uncracked test-piece (V_o), preferably in a region which is not affected by crack growth, the crack length (a) may be deduced from graphs relating V_a/V_oW to a/W , where W is the width of the specimen. A set of typical graphs of V_a/V_oW versus a/W is shown in Fig. 39 with the location of potential lead in the specimen, Fig.39A.

The sensitivity of the p.d. technique can be changed by different mode and amount of current application, the positioning of potential measuring points and their distance of separation. The sensitivity also depends on the instruments used to measure the potentials which are usually of micro-volt range. Possible sources of inaccuracy in the data resulting from using the p.d. technique can be stated as :

- a) Instability of constant current power supply.
- b) Error from thermo-electric E.M.F.s. generated due to dissimilar metals being connected between potential leads and the specimen.
- c) Temperature variation in the specimen or in the testing environment.

- d) Inefficient insulation of specimen and earthing.
- e) Drift of amplifying system.

By passing a current of 15 amps through the specimen, the sensitivity of monitoring crack advance by the p.d. technique was of the order of 0.005 W, i.e. about 0.12 mm., which compared favourably with Ritchie's⁽¹⁶⁴⁾ and Pisárski's⁽¹¹⁴⁾ figures. In the present investigation, a highly stabilized Farnell constant power source of maximum 50 amps. capacity was used. A current of 15 amps. was passed to the specimen through cleaned and polished copper strips screwed at the ends of the specimens, thus minimising or eliminating errors due to instability of the p.d. measurements. The potential leads used were nichrome wires ('Brightray C'), 0.193 mm. in diameter spot welded to the specimen. The potential drop was measured by a Rikadenki D.C. micro-voltmeter which gave a 100 μ V full-scale deflection. As the potential drop exceeded 100 μ V with the growth of the crack, a back-off voltage, supplied from a potentiometer, was used to maintain the full-scale deflections. A schematic diagram of the potential drop method is shown in Fig. 40. The output from the voltmeter was recorded on a Kent Chart Recorder in order to obtain a permanent record of the voltage reading. From the knowledge of the cycling frequency of the fatigue test, the time axis was converted to the number of cycles elapsed.

8.9 POTENTIAL DROP CALIBRATION

The current leads were connected to the specimen via copper strips screwed to the ends of the specimen to reduce contact resistance. The p.d., V_a , was measured across the notch by using nichrome wire leads spot welded at $x = 0$ (i.e. crack length = 0) for maximum sensitivity,

and at $y = 0.05W$ on either side of the notch centre-line. The uncracked potential gradient V_0 was measured on the specimen surface using a lead spacing of about 5 mm, Fig. 39A; the reading obtained of V_0 was then multiplied by a factor to get V_0W , so that the final lead spacing was equivalent to unit length of specimen width, W . This yielded greater accuracy in V_0W , instead of measuring V_0 simply across specimen width W .

Electrical insulations of the specimen and screening of leads from the specimen to the D.C. microvoltmeter were found necessary to prevent the pick-up of extraneous electrical signals. The specimen was insulated from the three contact loading areas by using paxolin sheet.

Constant current was passed through the specimen for about 2 hours before any readings were taken. Before settling down to a constant value, the p.d. across the notch dropped by about 20 to 40 $\mu V.$, and once stabilised the monitored voltage remained stable within $\pm 0.25 \mu V.$ Variation in laboratory temperature or closeness to electric lamp was found to affect the voltage reading. So utmost care was taken to minimise errors from these sources.

The fatigue crack was allowed to grow after the initiation event; however, the growth (for two different sets of specimens, one set with notch depth = $0.3W$ and the other with notch depth = $0.1W$) was stopped at an interval of about 200 $\mu V.$ potential drop (V_a) reading; the specimens were then broken open by partially sawing through from the side opposite to the notch and fracturing the remaining ligament at liquid N_2 temperature, Fig. 41. The crack length on the fatigue zone was optically measured at several points (15 to 20) and the average length was taken, corresponding to the particular potential drop reading. The values of a/W corresponding to different values of $\frac{V_a}{V_0W}$

were then plotted, Fig. 42. Standard 1900 Fortran language (application programme UA01) was used to fit 5th. order polynomials through the plotted points. The values of a/W corresponding to $\frac{V_a}{V_{0W}}$ were then tabulated at intervals of 0.001, for notch depths of $0.3W$ and $0.1W$, and for locations of potential leads as indicated in Fig. 39A. The equations of the calibrated curve at $x = 0$, $y = \pm 0.05W$ is described by the following polynomial :

$$a/W = C_0 + C_1 X^1 + C_2 X^2 + C_3 X^3 + C_4 X^4 + C_5 X^5$$

where $X = V_a/V_{0W}$

and (for notch depth = $0.3W$) (for notch depth = $0.1W$)

$$C_0 = -0.37923$$

$$C_0 = -0.038728$$

$$C_1 = 1.08720$$

$$C_1 = 0.39111$$

$$C_2 = 0.18724$$

$$C_2 = 0.58961$$

$$C_3 = -0.86128$$

$$C_3 = -0.84611$$

$$C_4 = 0.51272$$

$$C_4 = 0.44153$$

$$C_5 = -0.097861$$

$$C_5 = -0.083686$$

In Fig. 42 is also shown the theoretical calibration curve derived by Gilbey and Pearson⁽¹⁶²⁾ using the electrical potential method, for comparison. From this figure, it could be seen that calibration through separate notch lengths produce a distinctly separate curve from that for a crack only. For a particular notch depth, the fatigue crack, once initiated, extends from the notch and approaches the crack only curve and finally merges with Gilbey and Pearson's theoretical curve for the same positioning of potential leads in the specimen. The reduction in initial slope of the curves (a) and (b), Fig. 42, also means that the potential drop method is less sensitive in measuring short growth of a crack from a notch than for measuring the subsequent increase in length of a crack alone.

Gilbey and Pearson⁽¹⁶²⁾ have found the results obtained with p.d. technique in very good agreement with optical measurements of the crack on the specimens surface and were within the accuracy of the optical method, which was taken as 0.13 mm. ($\sim 0.005''$).

The essential difference between visual method and potential drop technique is that the former gives only the surface crack length, whereas the latter measures the average crack length of a bowed crack front, bowing being more pronounced at short crack lengths. Taking into account this aspect of crack front bowing makes the potential drop technique more reliable; it is also capable of detecting the crack initiation event long before the crack is visible on the surface.

8.10 METHOD OF CRACK GROWTH RATE CALCULATION

The fatigue growth rate had been calculated by using the method of finite differences. This involved using the ratio of finite differences in crack lengths to the number of cycles, i.e.

$$\frac{da}{dN} = \frac{a_{n+1} - a_n}{N_{n+1} - N_n} \quad \text{at } a = (a_{n+1} + a_n) / 2 \dots\dots\dots(36)$$

For an acceptable low level of scatter in the crack growth rate, the intervals between the crack length measurements, i.e. $(a_{n+1} - a_n)$ were taken to be sufficiently large, i.e. about 0.5 mm. The raw data from the fatigue tests were processed using a simple computer programme so that the input of potential drop, number of cycles, load amplitude, specimen dimensions etc., resulted in the output of crack growth rate, and ΔK , the stress intensity factor range. No plastic zone correction was made.

Other method of measuring crack growth rate involves differentiating 'a Vs N' curve (i.e. crack length Vs. number of cycles) or

graphically drawing tangents to the curve at various points. This method tends to be laborious and can be inaccurate at low and high crack growth rates. Difficulties in fitting polynomials to the $a - N$ data have also been reported by Davies and Feddersen⁽¹⁶⁵⁾.

8.11 FATIGUE CRACK INITIATION

Crack initiation studies were carried out on maraging and diluted maraging steel powder-compact specimens having notch root radii of 0.127 mm. and 0.762 mm., and having three different density levels. The notch root radii were measured individually; they were viewed at X100 magnification on the screen of a Vicker's projection microscope. The magnified radii of the image was then measured by a specially prepared transparent sheet bearing concentric semicircles with radii ranging from 5 to 80 mm. in 5 mm. increments. In view of the fact that the notch roots tended not to be of constant radius around their circumference, the smallest radius in each case was located and measured; this method was repeated for the other side of the notch. The accuracy of machining notch root radii was found to be within ± 0.02 mm. (~ 0.001 ").

The initiation load (for 3-point loading in compression) was calculated using the following equation,

$$\frac{\sigma_y}{Kt^G} = \sigma_{\text{gross}} = \frac{M \cdot y}{I} \text{ i.e. } \frac{6P}{BW} \dots\dots\dots(37)$$

whence $P_{\text{max.}} = \frac{\sigma_y}{Kt^G} \cdot \frac{BW}{6} \dots\dots\dots(38)$

where Kt^G = gross stress concentration factor calculated using a computer programme on the basis of Neuber's equations (127, Appendix-I)

$$= Kt_{\text{nett}} \cdot \left(\frac{W}{w}\right)^2 ,$$

and $M = \frac{PL}{2}$

$$y = \frac{W}{2}$$

$$L = 2W$$

$$I = \frac{BW^3}{12}$$

$$P = P_{\text{max}} = \Delta P \quad (\text{when } P_{\text{min.}} = 0)$$

B = thickness of specimen

W = width of specimen

w = nett width of specimen.

Knowing σ_y , the yield strength of the materials, Kt^G , B and W, $P_{\text{max.}}$ or ΔP , the load amplitude, was calculated. For each set of specimens, there were two different types of notch root radii, 0.127 and 0.762 mm.; for each type of root radius, the initiation tests were carried out on specimens $\llcorner 3$ in number, using varying load amplitudes, based, of course, on the calculated one. The overall stress range used for the initiation tests was from 43.4 MN/m² to 237.6 MN/m² and tests were done on an Amsler Vibrophore fatigue testing machine using a fixed frequency of 130 to 140 hz depending on the nature of the materials.

The point of initiation was detected by using the electrical potential drop technique. The actual point of initiation was taken to be the number of cycles at which the initial potential drop across the notch had first shown a definite increase on the chart recorder.

8.12 CONSTANT LOAD FATIGUE TESTS

In order to generate a wide range of ΔK values over the range of crack lengths for which compliance function was available, a suitable load range was selected for both low and high ΔK values. After initiation of the fatigue crack from the notch at relatively high load as indicated in section 7.11, the test load was applied. The constant amplitude test load for low and high ΔK values ranged from (1.4 ± 1.2) to (2.2 ± 2.0) KN for the sintered specimens of density level 1, from (1.5 ± 1.3) to (2.6 ± 2.4) KN for density level 2, and from (1.8 ± 1.6) to (3.0 ± 2.8) KN for density level 3 at a stress ratio of $R \sim 0.07$. The constant load amplitude for test at the higher stress ratio of $R = 0.3$ was 5.6 KN i.e. (5.2 ± 2.8) KN. The crack growth measurement was started at about $0.35 W$ (for specimens with notch depth = $0.3 W$) and $0.15 W$ (for specimens with notch depth = $0.1 W$) using the potential drop equipment. With Amsler Vibrophore fatigue testing machine, it was found that the constant load amplitude could be maintained to a maximum crack length of about $0.65 W$.

8.13 MECHANICAL TESTING

Tensile tests were carried out on No. 12 Hounsfield test pieces machined from the fractured half of toughness testing specimens. A Hounsfield tensometer fitted with a 2-ton beam and split collets was used for this purpose. Meaningful results for % reduction in area and elongations were not expected from these small tensile specimens. For accuracy and consistency, all the tests were duplicated and in some cases, triplicated. Hardness measurements were made on samples representative of each series. To avoid unreliable results due to porosity, Brinell hardness tester was used with a 10 mm. ball indenter and a load of 1000 Kgf. Each result quoted is the mean of 10 hardness readings.

8.14 PHYSICAL EXAMINATIONS

8.14.1 METALLOGRAPHIC SPECIMENS

The metallographic specimens were impregnated with a combination of araldite/hardener (10:1) under low vacuum, left overnight for curing or setting, and normal metallographic techniques used in hot mounting and polishing. Impregnation with araldite/hardener mixture helped in preventing fine debris being lodged inside the pores on the polished specimen surface. 2% Nital was used for etching incoloy S.A. compact specimens, and a special reagent, 3 HCl 3 picral in alcohol, was used for etching maraging and diluted maraging steel compact specimens. Ordinary Vickers projection microscope had been used for obtaining photographs of the microstructures, and in some special cases, Reichert projection microscope had been used.

8.14.2 SCANNING ELECTRON MICROFRACTOGRAPHY

Fractographic survey on fractured surfaces was made on a Cambridge Scanning Electron Microscope (S.E.M.). The S.E.M. technique can be used for direct viewing of the fractured surface. In this, a finely focussed beam of electrons is made to scan the specimen surface and causes emission of secondary and back scattered electrons which are picked up by a detector. This signal is amplified and displayed on a cathode-ray tube as an image of the specimen surface. Contrast in the image is dependent on the nature and topography of the surface.

For use in S.E.M., the specimens were prepared by cutting to a depth of 3.5 mm. (about 1/8") parallel to the fractured face, and mounting on a special flat stud for insertion into the specimen chamber.

8.14.3 ELECTRON MICROPROBE ANALYSIS AND ELECTRON MICROSCOPY

A Cambridge Microscan 5 X-ray Microanalyser was used to identify the discrete phases present in the sintered compact materials, and to get an idea of the extent of diffusion into the matrix. With this equipment, quantitative analysis of small volumes ($\sim 1.0 \mu^3$) can be obtained by comparison of the x-ray intensity of a given element in the sample with that of a pure standard.

A Transmission Electron Microscope, made in Japan (JEOL 100 B) was also used to study the fractured surface. The surface was dipped in acetone, then covered with Bex-film (cellulose tri-acetate) which was stripped dry carefully; carbon was evaporated on the replica followed by shadowing with gold-palladium.

Extraction replicas, first introduced by Fisher⁽¹⁶⁶⁾ had proved particularly useful for inclusion identification and for studying their size distributions, morphology, and structure. For obtaining a reasonable extraction replica, it was necessary to etch or electropolish away the matrix in order to free the inclusions with a solution of (90/10) acetic acid glacial/Perchloric acid.

After evaporating carbon, the extraction carbon replica was then released from specimen by etching with a solution a 10% HCl/methanol.

The main drawback with the extraction replica technique is that extraction may modify the particles. In case of coherent or semi-coherent precipitates, coherency is lost by extraction. Moreover, extraction replicas tend to give an exaggerated idea of the volume fraction of particles in a sample, but it may give some idea of their location, for example, at grain boundaries.

8.14.4. QUANTITATIVE IMAGE ANALYSIS

To study the influence of distribution and number of pores on the mechanical properties of the sintered materials, the quantitative image analysing system, Quantimet 720 was used. Samples parallel with the plane of fracture were taken from the fractured half of the toughness specimens. After normal grinding and diamond polishing they were etched with 5% Nital to remove materials that might have flowed plastically into the pores during grinding. To remove all traces of etching and to represent a true section through the specimens, they were then repolished.

To obtain the area fraction value, which is the same as volume fraction, the actual area occupied by the pores and inclusions in 250 fields of view were measured and the result was a simple percentage of the area of pores and inclusions over the area examined in 250 fields which is 2.87 sq. mm. in fields of 0.0115 sq. mm. The optical magnification used was 315X, which on projection through the QTM 720 became finally 1300X.

9. RESULTS

9.1 MECHANICAL PROPERTIES, Etc.

Investigations of the mechanical properties, crack initiation and propagation characteristics had been carried out in the sintered maraging and diluted maraging steel powder compacts, but only the mechanical properties had been studied in Ancoloy SA compacts in the sintered, and sintered-quenched-tempered conditions.

The test results of the various mechanical properties, etc. studied are given in Table III. Fracture Toughness Validity test results are shown in Table IV.

The effect of % porosity on yield stress (σ_{ys}) and fracture toughness (K_{IC}) is shown in Fig. 43. It is very clear from this figure that the porosity content has a significant effect on yield stress and fracture toughness. Reduction in porosity below ~13% causes a marked rise in yield stress, while increase in porosity above ~13% causes a drop in yield stress, though the rise or drop in yield stress values in the case of material M_3 (maraging steel compacts diluted with 50% iron powder) is somewhat sluggish. There is, however, a significant rise in fracture toughness with reduction in % porosity. In the case of material M_3 , the gain in fracture toughness with the loss of porosity is remarkable.

In Fig. 44 has been shown the relationship between the fracture toughness (K_{IC}) and yield stress (σ_{ys}) for the three types of sintered steels investigated. In the case of material M_1 (maraging steel compacts) though the toughness increases with yield stress, there is a tendency for drop in the toughness values at higher yield stress, while with the material M_3 , the sharp increase in toughness values yields only a small increase in yield stress. The material

M_2 (M_1 diluted with 25% iron powder), however, shows a remarkable balance between increase in toughness and yield stress values.

Fig. 45 shows the elastic modulus (E_N) as a function of % porosity. The elastic modulus has been calculated by using the McAdam's⁽⁴⁶⁾ equation given by

$$E_N = 29 (1 - \epsilon)^{3.4} \times 10^6 \text{ psi.}$$

where E_N = elastic modulus of sintered steel, and

ϵ = fractional porosity.

9.2 PORE DISTRIBUTION

Table V shows the number and sizes of pores obtained by using the QTM 720 technique. The size distribution recorded was obtained by feature analysis, where the area of each 'pore' was considered individually and the number falling into each size category was recorded. The area parameter for each phase was chosen since the voids were of irregular shapes of random orientation, and particle diameter would not have given as true a measure of size distribution.

An attempt had been made to measure the inclusion content of the specimens, but it failed due to the fact that the inclusions were predominantly fine oxides and had a similar reflectivity to the 'pores'. Consequently separate detection 'thresholds' for pores and inclusions could not be operated, and therefore, only one result was recorded combining the voids and inclusions, and termed as 'pores'.

Treating the inclusions as pores should not be too inaccurate⁽¹⁶⁷⁾ since the particle/matrix interfacial strength is not particularly high. Moreover, it simplifies the analysis.

In Fig. 46 is shown the distribution of 'pores' in some of the sintered materials investigated. Predominantly large number of

'pores' are in the size range of $3 - 8 \mu\text{m}^2$. The nearest approximation would be to consider that the majority of inclusions are in this size range, and that the majority of voids are in the size range of $100 - 200 \mu\text{m}^2$. The existence of the wide range of size and shape of voids is also supported by the use of the Scanning Electron Microscope.

9.3 INITIATION RESULTS

In Table VI is shown all the relevant data relating to initiation studies for sintered and heat treated M_1 , M_2 , M_3 and LTM compacts. In Fig. 47 is plotted $Kt \cdot \Delta S$ (where Kt is the Neuber elastic stress concentration factor for the particular notch and ΔS is the range of nominal stress from zero to S_{max}), against N_i (number of cycles for initiation) for the notch root radii of specimens M_1 , M_2 , M_3 at three density levels, also of specimens LTM. The same N_i has been plotted against $\Delta K/\rho^{\frac{1}{2}}$ as shown in Fig. 48. The initiation behaviour of the two plots follows the same pattern. The 'banding' effect of notch root radii on initiation behaviour stands out markedly clear. This effect persists even if all the initiation results are plotted together, as shown in Fig. 49 for N_i Vs. $\Delta K/\rho^{\frac{1}{2}}$. However, when the same N_i is plotted against ΔK , Fig. 50, as shown separately for compacts at different density levels, the banding effect of notch root radii gives way to broader scatter band. The banding effect practically vanishes if a plot of N_i Vs. ΔK is made of all the initiation results, Fig. 51.

Judging from the slopes of the plots in Figs. 47 and 48, higher the density, higher were the number of cycles for initiation for compacts M_1 , M_2 and M_3 ; but for the same lower density d_1 , M_2

compacts needed higher number of cycles for initiation than M_3 compacts, only reason for which might lie in the distribution, size and shape of the pores in the vicinity of the notch tip in these low density compacts.

9.4 CRACK GROWTH RESULTS

Constant load amplitude tests at constant mean load (load profile in Fig. 52) were carried out at a stress ratio R of (a) ~ 0.07 for compacts M_{11} , M_{12} , M_{13} , M_{21} , M_{22} , M_{23} , M_{31} , M_{32} , M_{33} , L.T.M., and (b) 0.3 for compacts M_{13} , M_{23} and M_{33} . Crack propagation rates obtained by the method of finite differences have been plotted as a function of stress intensity ranges ΔK , Fig. 53 (a - k).

For growth rates at $R \sim 0.07$, there is the characteristic change in slope from stage 1 to stage 2 in the growth curve. The transition occurs at $\Delta K = 9 - 11 \text{ MN/m}^{3/2}$ for $R \sim 0.07$. Growth rate curves for $R = 0.3$ also show a transition at a slight higher value of $\Delta K \approx 12 \text{ MN/m}^{3/2}$. That is, at very low values of stress intensity factor and crack growth rate, a threshold for crack growth is approached for the types of sintered materials tested. The linear relationship obtained between $\log \Delta K$ and $\log \frac{da}{dN}$ in stage 2 is as predicted by equation (27). The stage 3 is not clearly defined since the increase in gradient of the curve occurs at very high crack growths which are difficult to measure.

It can be seen from table VII that the values of crack growth exponent m varies from 2.26 to 3.39 for compacts of M_1 series, from 2.87 to 4.38, for M_2 series and from 4.29 to 4.50 for compacts of M_3 series. The corresponding values of the pre-exponent C varies from 4.59 to 10^{-2} to 91.83×10^{-2} , from 0.63×10^{-2} to 7.55×10^{-2} and from 0.12×10^{-3} to 9.7×10^{-3} , when the growth rate is in nm/cycle,

and stress intensity in $\text{MN}/\text{m}^{3/2}$. For compacts of L.T.M. series, the values of m obtained is 5.17 and of C is 0.27×10^{-3} .

TABLE VII
THE VALUES OF m and C

MATERIALS CODE	DENSITY LEVELS					
	1		2		3	
	m	$C \times 10^{-2}$	m	$C \times 10^{-2}$	m	$C \times 10^{-2}$
M_1	2.26	24.77	2.81	91.83	3.39	4.59
M_2	2.87	1.62	3.59	7.55	4.38	0.63
M_3	4.50	0.97	4.29	0.47	4.50	0.012
LTM	m			$C \times 10^{-3}$		
	5.17			0.27		

The crack growth rate curves for M_{12} and M_{21} compact materials, when the stress ratio R is ~ 0.07 , are identical and nearly fall on the same scatter band, Fig. 54, the growth rate being 1.7 to 2.0 times faster than for M_{11} compact material, Fig. 53a over the range of ΔK considered (10 to $35 \text{ MN}/\text{m}^{3/2}$). Similar pattern has been noted for M_{13} and M_{22} materials, Fig. 55, the growth rate being 2.8 to 3.0 times faster than for M_{11} materials; the same thing also goes for M_{23} , M_{31} , M_{32} and M_{33} compact materials, Fig. 56, where the growth rates are about 6.7 to 7.0 times faster than for M_{11} material. For L.T.M.

material, the growth rate, Fig. 53j, has been found to be about 10.7 times faster than for M_{11} material.

At higher stress ratio ($R = 0.3$) the growth rate curves for M_{13} , M_{23} and M_{33} materials are also identical and nearly fall on the same scatter band, the rate being 2.2 to 2.5 times faster than for M_{13} and 6.0 to 6.2 times faster than for M_{11} compacts tested at the stress ratio of $R \sim 0.07$.

The above observations show that the crack growth curves for M_1 , M_2 and M_3 materials fall on four distinctly separate scatter bands, when the stress ratio R is ~ 0.07 . At the higher stress ratio of $R = 0.3$ and only at the highest density of compacts tested, another separate scatter band for crack growth data has been found. The same goes for the L.T.M. materials tested at $R \sim 0.07$, for which also a distinctly separate scatter band has been obtained. Though the values of m obtained are roughly indicative of this trend, it is the combination of the values of m and of the pre-exponent C that determines the rates of crack growth in each of these materials.

9.5 METALLOGRAPHIC OBSERVATIONS

An examination of the etched specimen of M_1 series in the sintered and fully heat-treated condition showed that the microstructure was essentially martensitic and massive in nature, Fig. 59, with pores more or less rounded in higher density compacts. Specimens of M_2 , M_3 and LTM series showed the martensitic structures with fair amount of ferrite, Fig. 60, 61. Pores of different geometry were visible in the specimens, their shape and size depending on the density of the compacts. Higher the density, finer and more rounded the pores. In the sintered condition, the structure for M_1 series of compacts was austenitic with well-defined grains and pores, Fig. 62.

Microstructures of Ancoloy SA compacts showed ferrite and lamellar pearlite in the sintered condition, Fig. 63, and tempered martensite (troostite) in the quenched and tempered condition, Fig. 64 with random distribution of pores of different geometry, depending, as before, on the density of the compacts.

Scanning Electron Microscope-image of the deeply etched microstructures showed clearly the random orientations of the martensitic plates in the M_1 series of compacts, Fig. 65. Some of the particles revealed by longer etching with the special reagent of 3 HCl 3 Picral in alcohol had been analysed to be some intermetallic compound of Ti, possibly Ti (C,N), Fig. 66.

The distribution of the elements in the maraging (M_1 series) and diluted maraging (M_2 and M_3 series) compacts was investigated by the electron probe microanalyser. It was found that the elements were finely well-distributed except for Ti, Mo and Co, Fig. 67, which showed some segregation.

Though mostly in clusters, two distinctly different types of inclusions had been observed in the unetched metallographic sections of M_1 , M_2 and M_3 series of compacts under unfiltered illumination in the light microscope, Fig. 68, 69, 70.

- (a) Angular inclusions, usually square or hexagonal. These appeared light pink or orange.
- (b) Elongated inclusions, appearing grey with a slight mauve or violet tinge.

Electron microprobe analysis showed that type (a) inclusions contained Ti and sometimes some Zr in the centre. Type (b) inclusions contained Ti, S and some Zr. It might be that the angular pink-orange inclusions were carbonitrides, in agreement with the description of

Ti (C,N) in the literature (168). Zirconium present in the centre of Ti (C,N) might be in the form of Zirconia or Zirconium Carbonitride. It is possible that, by analogy with Titanium Oxide (168), the Zirconium Oxide is read, while Zirconium Carbonitride is of the same colour as Titanium Carbonitride. Accurate analysis of the inclusions was not possible in the Electron Microprobe Analyser, since the inclusions were smaller compared to the cross-section of the electron beam resulting in the interference signals from the matrix around the inclusions. The qualitative results obtained with the Microprobe Analyser were confirmed by using a 'KEVEX' Energy Dispersive X-ray Analyser attached to the Stereoscan Electron Microscope.

The crack path was closely studied and found to be mainly influenced by the alignment, distribution, and shape and size of the pores ahead of the crack tip. The presence of numerous inclusions, mainly intermetallic compounds of Ti, on the path of the cracks also influenced the rate and direction of crack growth. The crack paths were not straight as shown in Fig. 71, 72 in the unetched condition. In all the powdered compact specimens, the effects of the distribution and alignment of pores (D.A.P.) on the crack path was so predominant that the favourable orientation effect of grain-boundary with respect to the direction of crack growth was difficult to assess. Also, the D.A.P. effects were clearly reflected in crack-forking, Fig. 73, - branching, Fig. 74, - arching, Fig. 75, island and pseudo-island formation, as shown in Fig. 76, 77. The extent of the D.A.P. effect could be gauged by observation of the crack tip, Fig. 78, where the crack tip seemed to lose its identity in the clusters of pores.

The formation of island, and branch cracks was the most general features of the powder compacts, due mostly to the D.A.P. effect.

These branch cracks were mainly inter-granular. The main branch of the crack seemed to be influenced by the presence of pores and inclusions in its path, whereas the branch cracks seemed to have been influenced by the presence of the pores, Fig. 79, 80. The extent of crack branching was such that it frequently caused the formation of islands in the crack path, Fig. 81.

9.6 FRACTOGRAPHIC OBSERVATIONS

The fractured surfaces of the compact specimens were closely investigated by the Steroscan Electron Microscope. The porous materials all had, more or less, a similar fracture surface with extensive plastic deformation and dimples, and some tendency to grain-boundary separation. The micromechanism of fracture was the coalescence of the microvoids in which case the internal linking drew out the walls of the pre-existing voids until the linkage occurred. The micromechanism was of the ductile dimple type in every case, Fig. 82, and the presence of pores evidently decreased the tendency to brittle cleavage fracture.

There was found no significant difference between fatigue and fast fracture surfaces as is normally found in non-compact materials. Also, no striations were observed on the fracture surfaces; there was no definite trend of a particular type of cracking associated with a particular stress intensity level.

Round particles found in the fracture surfaces were original powder-particles and least amenable to sinter-bonding, Fig. 83. The inclusions and the second-phase particles seemed to play a prominent role in the fracture process. In Fig. 84, the matrix did not adhere to the cubic Ti (C,N) inclusion which allowed the voids to open early

in the fracture process leading to tensile dimple rupture. Dimples shown in Fig. 82 were composed of more than two different sizes. The larger dimples probably formed at the Ti(C,N) particles. All of the dimples were probably caused by particles of some sort. Ti (C,N) particle shown in Fig. 85 triggering the formation of voids might have split before the void opened.

Some larger pores, Fig. 86, opened up during the fracture process by intergranular cracking, besides containing some remnants of Ti (C,N) particles being fusion-bonded to the internal pore surfaces, bore evidence of thermal etching undergone due to sintering at high temperature for a long time. Decohesion of inclusions from the matrix was also observed. Fig. 87 shows an iron-rich particle decohesed from the matrix during the fatigue crack propagation. Fracture surfaces also revealed some deep branch cracks running along the grain-boundaries, Fig. 88.

Transmission Electron Microscopy was also used in the study of the fracture surfaces. Thermal etching effects, left on the internal pore surfaces due to high temperature sintering had been revealed by Transmission Electron Microfractography. These fine markings should not be confused with striation markings which give an indication of micro crack growth rates. In Fig. 89 is shown a combination of big and small dimples and thermal etchings.

Using the Extraction Replica Technique and the Transmission Electron Microscopy, the precipitates extracted from the fractured specimens and shown in Fig. 90 were identified to be $\text{Ni}_3(\text{Al},\text{Ti})$ and $\eta\text{-Al}_2\text{O}_3$. Other precipitates were much smaller and could not be analysed due to their size being smaller than the cross-section of the electron-beam.

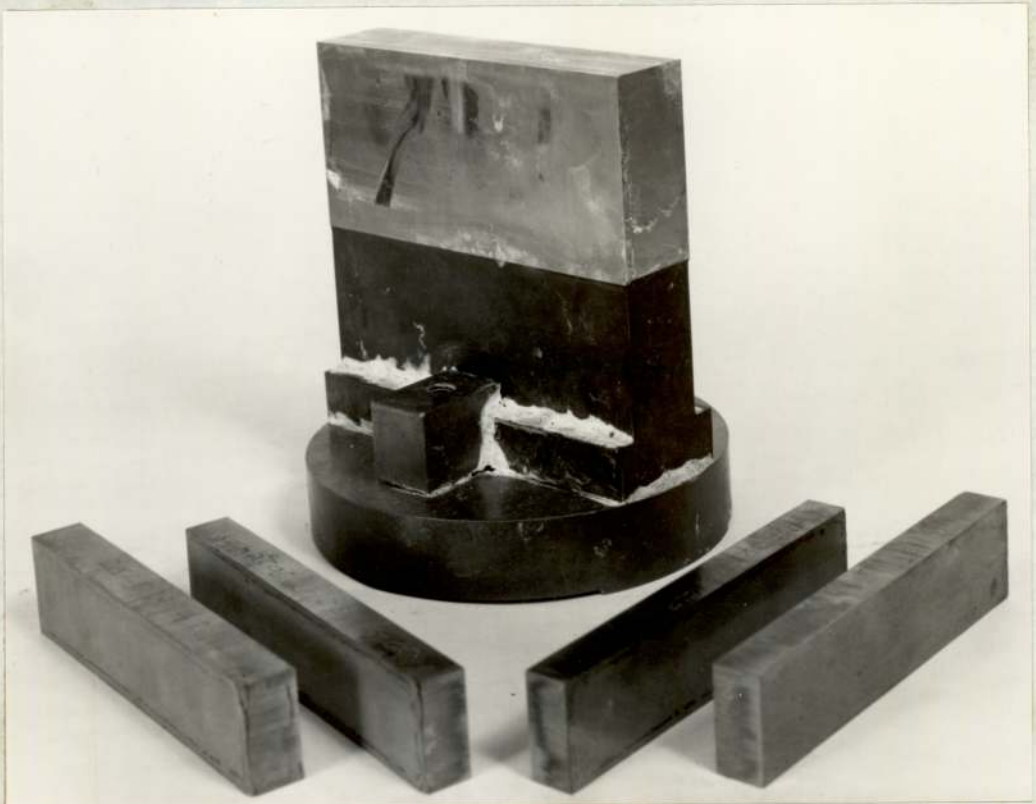
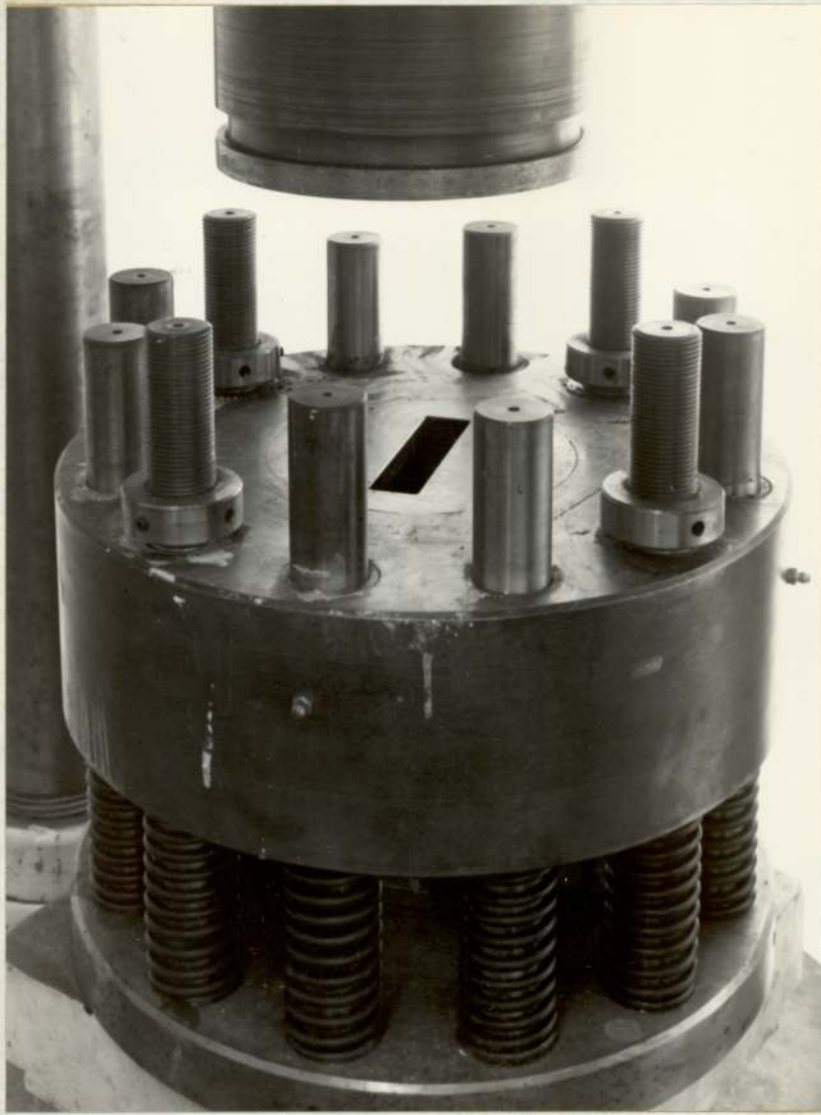


Fig.33. The Die-System and the Compacted Specimens.

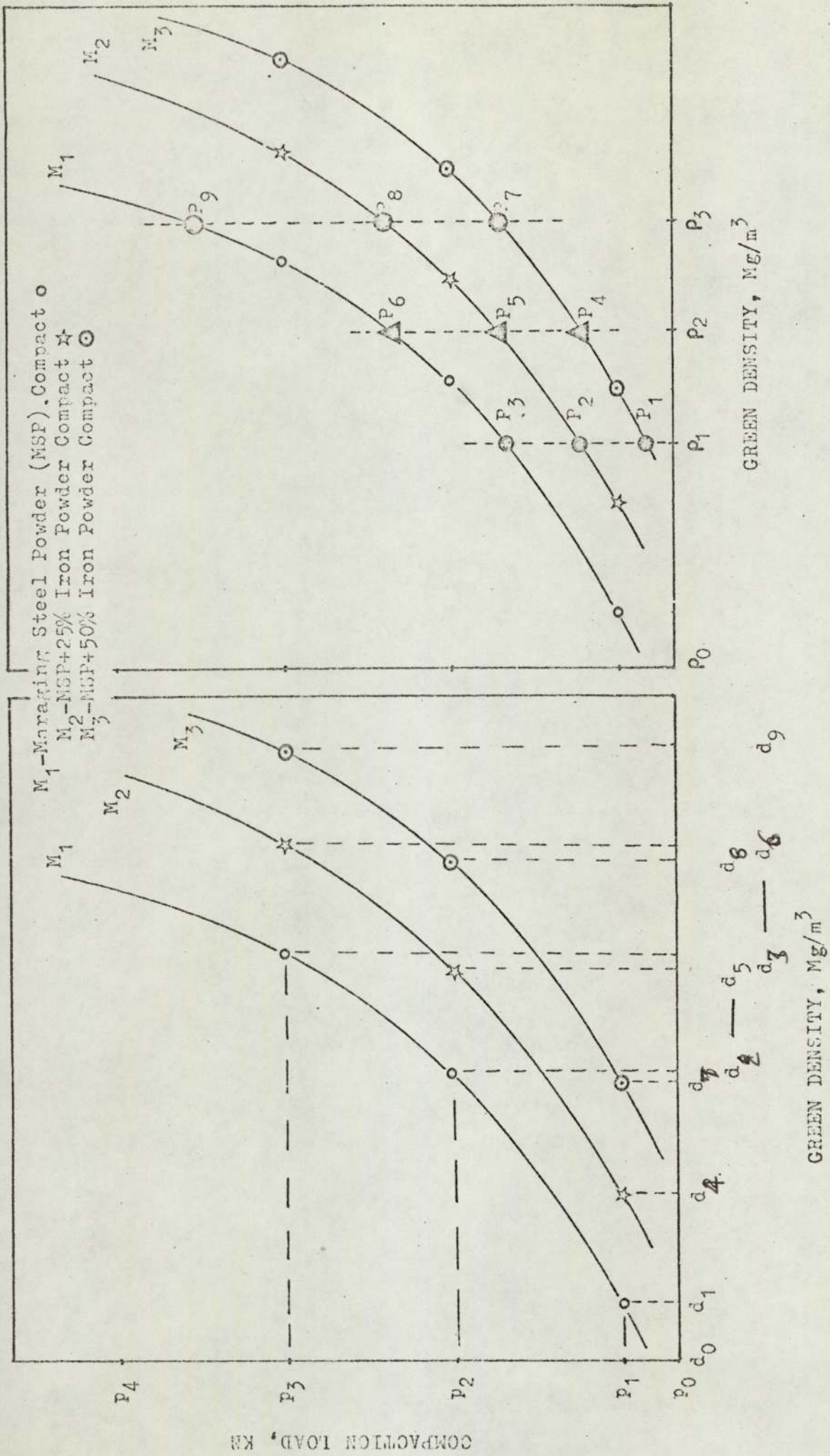


Fig. 34. Schematic representation for obtaining Calibration Curves of Compaction Load Vs Green Density.

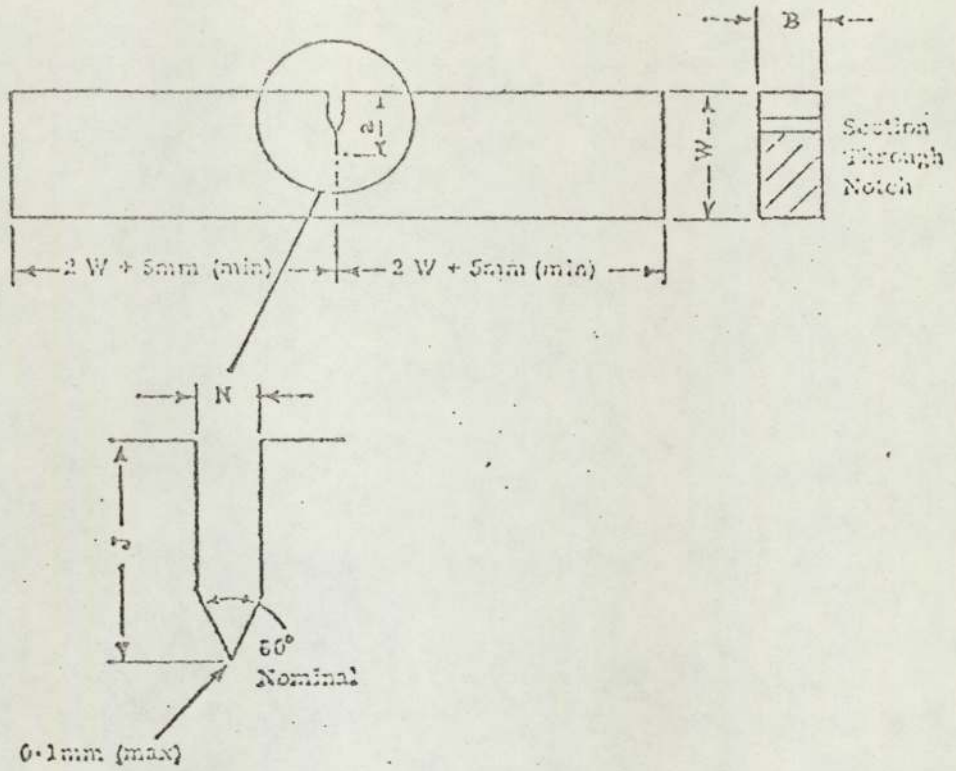


Fig.35. Dimensions of Single-Edge-Notch Bend Test-Piece.

MATERIAL A: Maraging and Diluted Maraging Steel Powder Compact, Sintered and Heat-Treated.

W	B	J	N	NOTCH ROOT RADIUS	NOMINAL ANGLE	TOTAL LENGTH
23.50 & 22.50	11.75 & 11.25	7.05 & 2.25	1.5	0.127, 0.762	60°	110

MATERIAL B: ANCOLOY SA Powder Compact, Sintered and Heat-Treated.

W	B	J	N	NOTCH ROOT RADIUS	NOMINAL ANGLE	TOTAL LENGTH
25.00	12.50	7.50	1.5	0.127, 0.254 0.508, 0.762	60°	110

Dimensions are in mm.

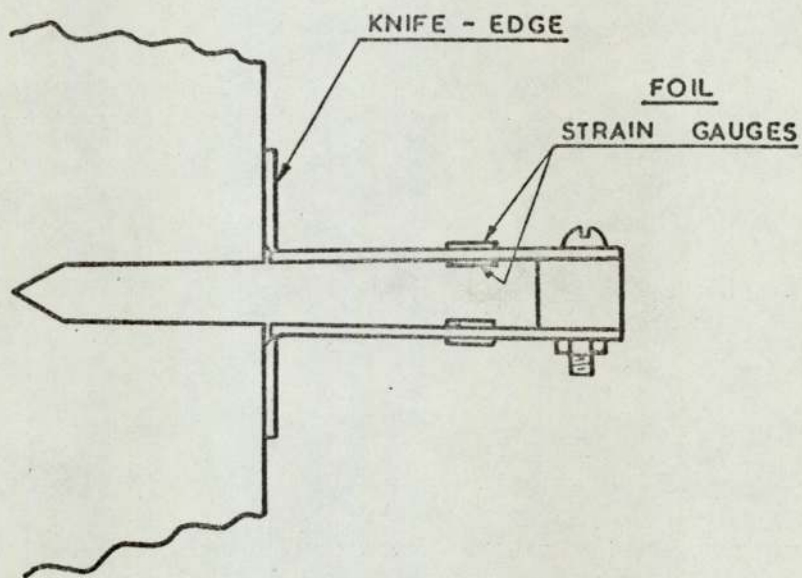


Fig.36. Clip-in Displacement Gauge and Method of Mounting.

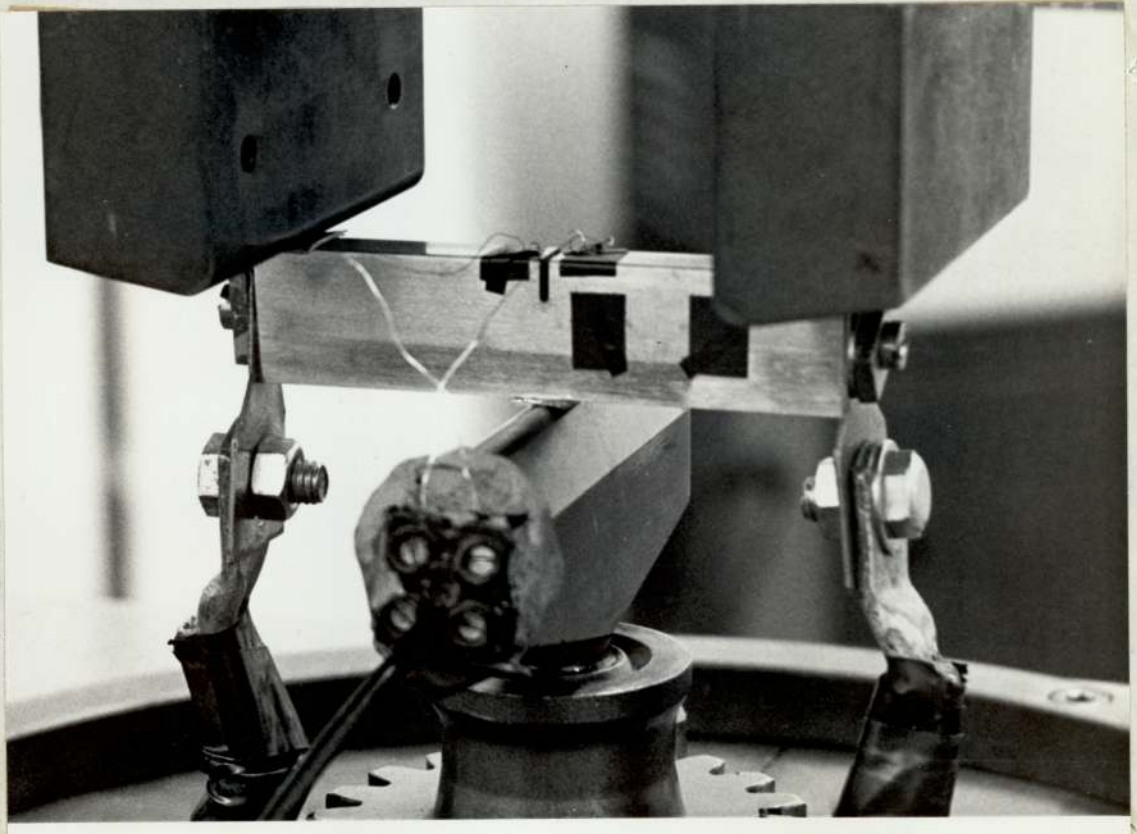


Fig.37. Amsler Vibrophore Fatigue Testing Machine and Potential Drop Unit with the Close-up of Specimen Connections.

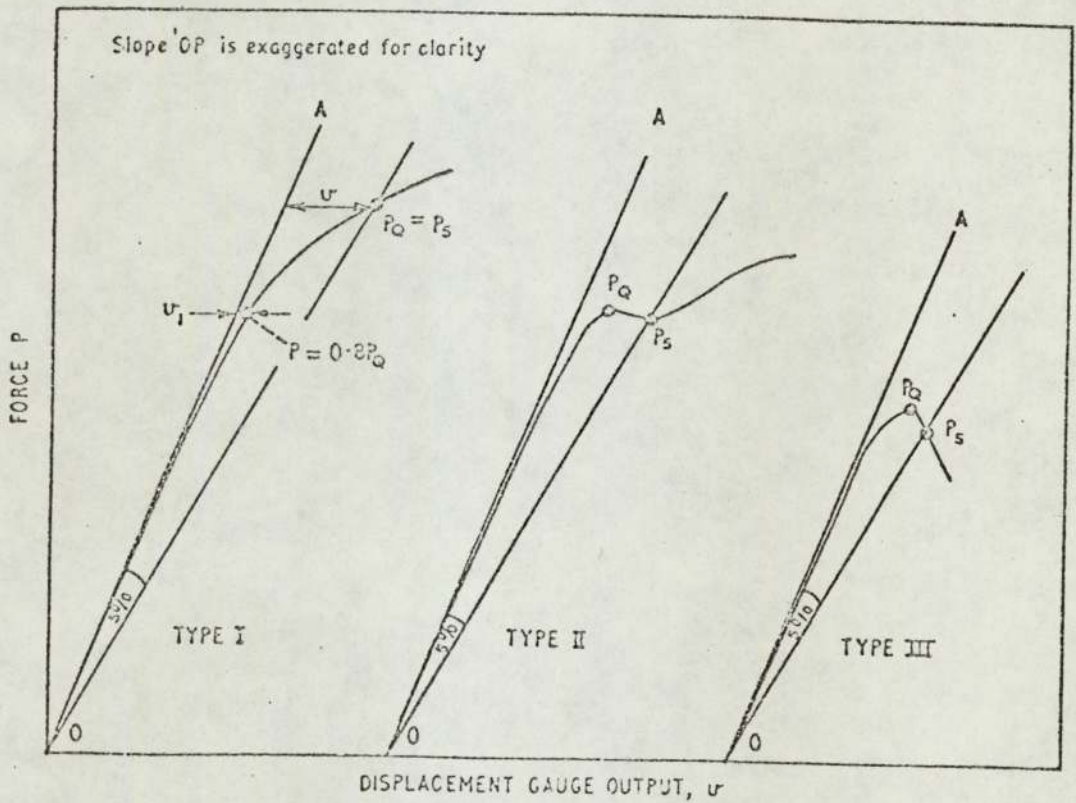


Fig. 38. Principal types of force/displacement records showing quantities involved in analysis (After B.S.I. (156)).

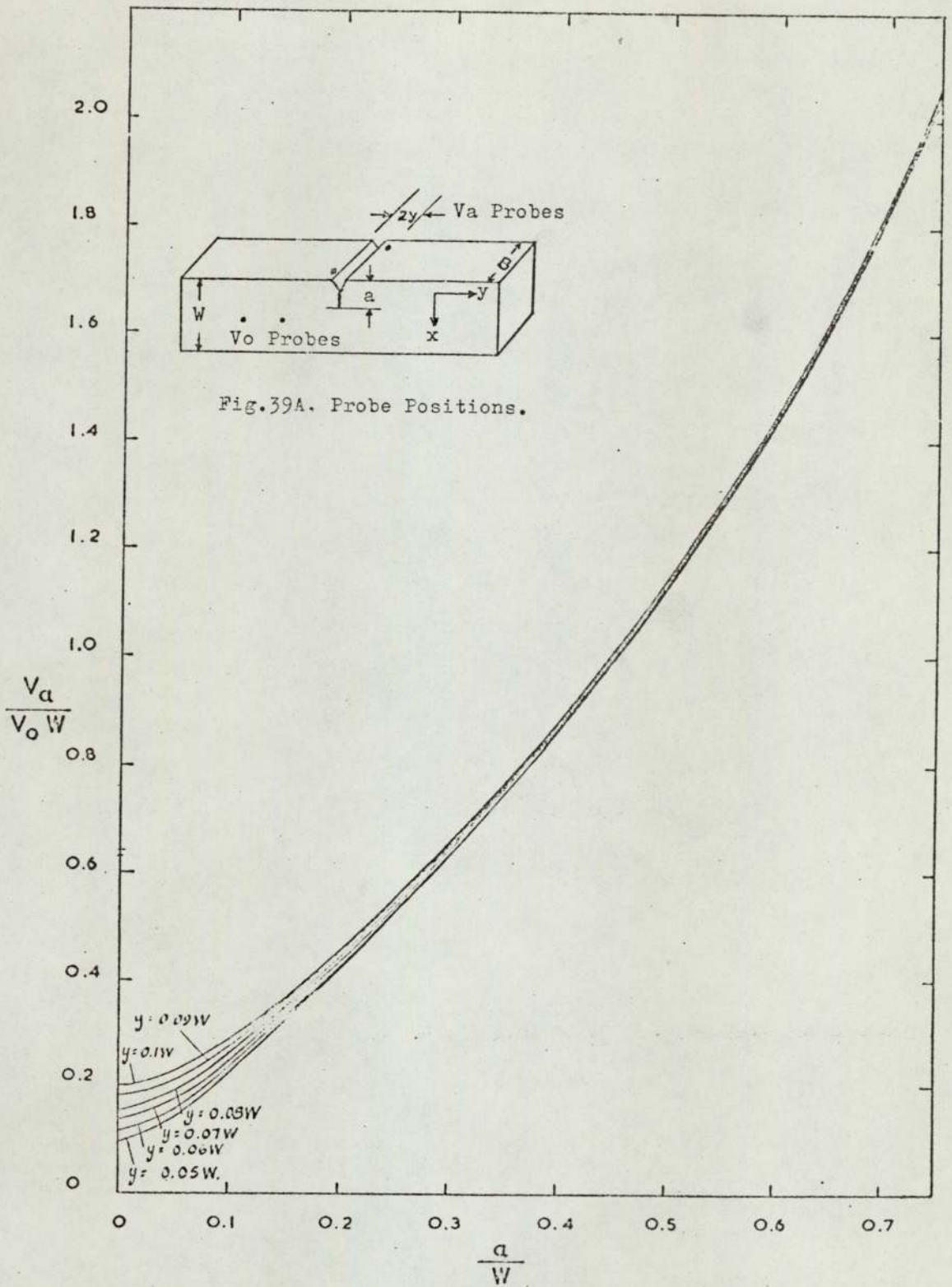


Fig.39A. Probe Positions.

Fig.39. GRAPH OF $\frac{V_a}{V_o W}$ VERSUS $\frac{a}{W}$ FOR POTENTIAL MEASURING POINTS AT $x = 0$, $y = \pm$ VALUES SHOWN.

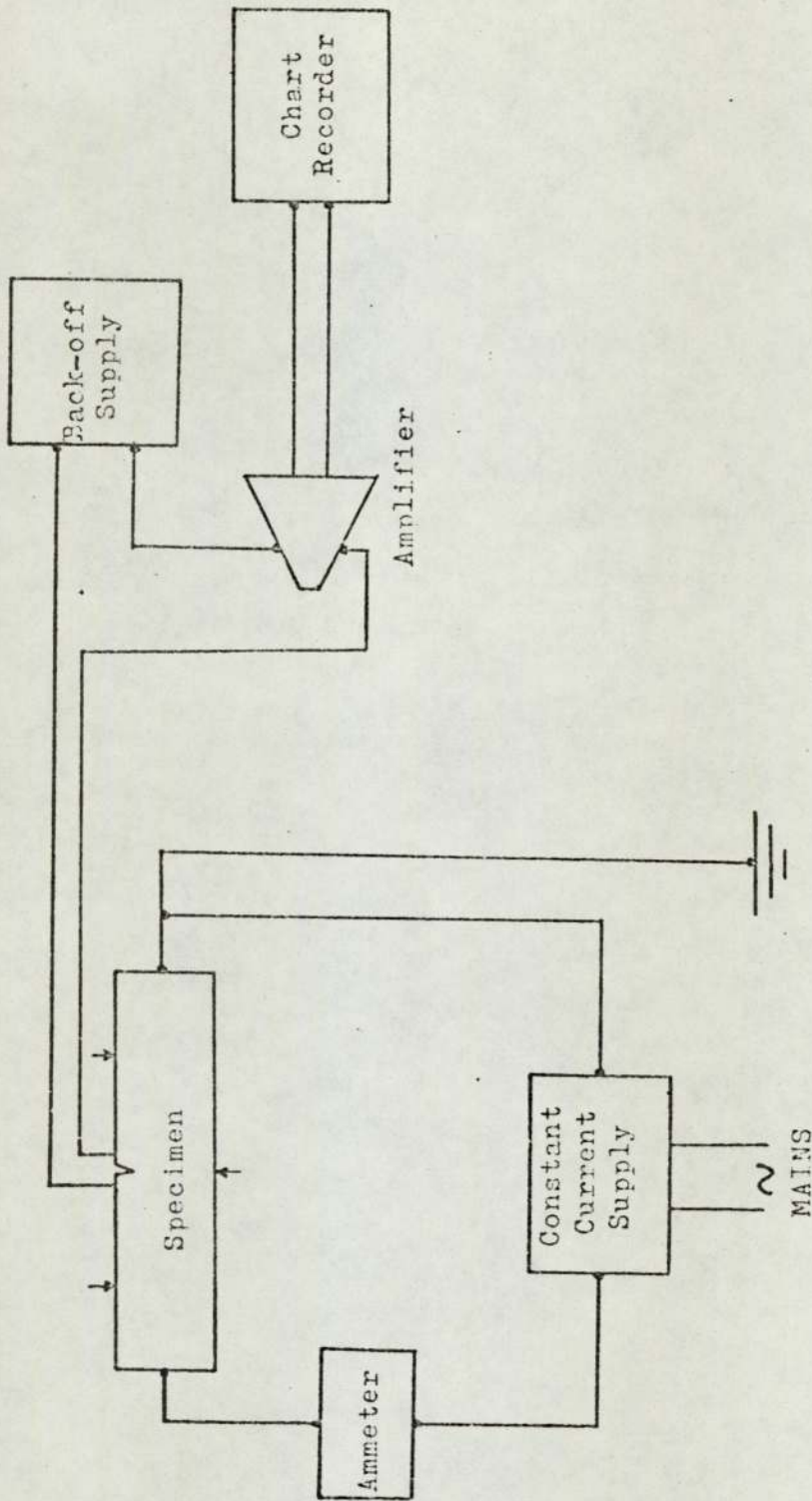


Fig.40. A Schematic Diagram of the Potential Drop Circuit.

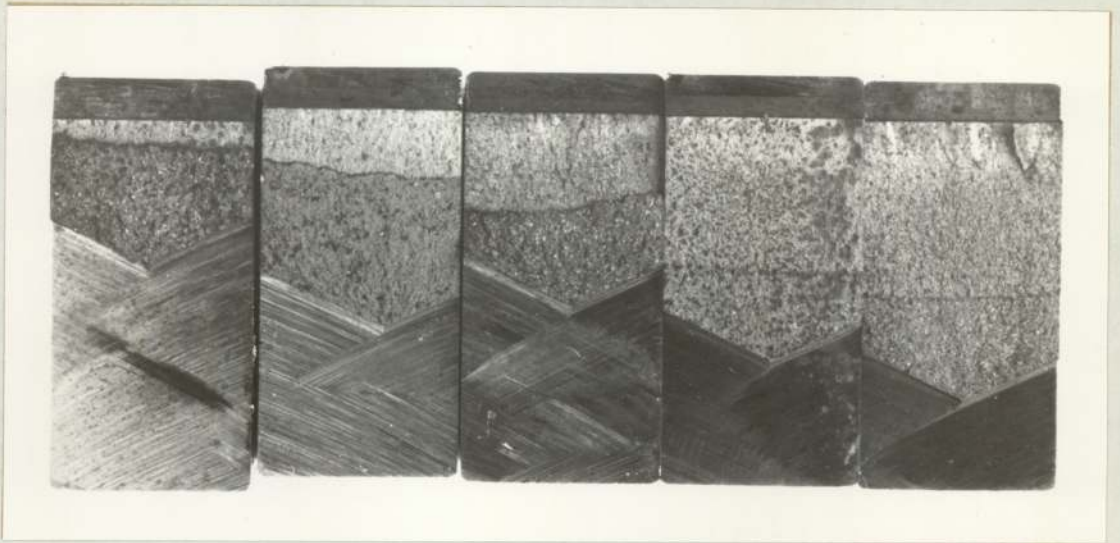


Fig.41. Examples of the Fractured Halves of Sintered Specimens for deriving the Calibration Curves of V_a/V_{oW} Vs. a/W .

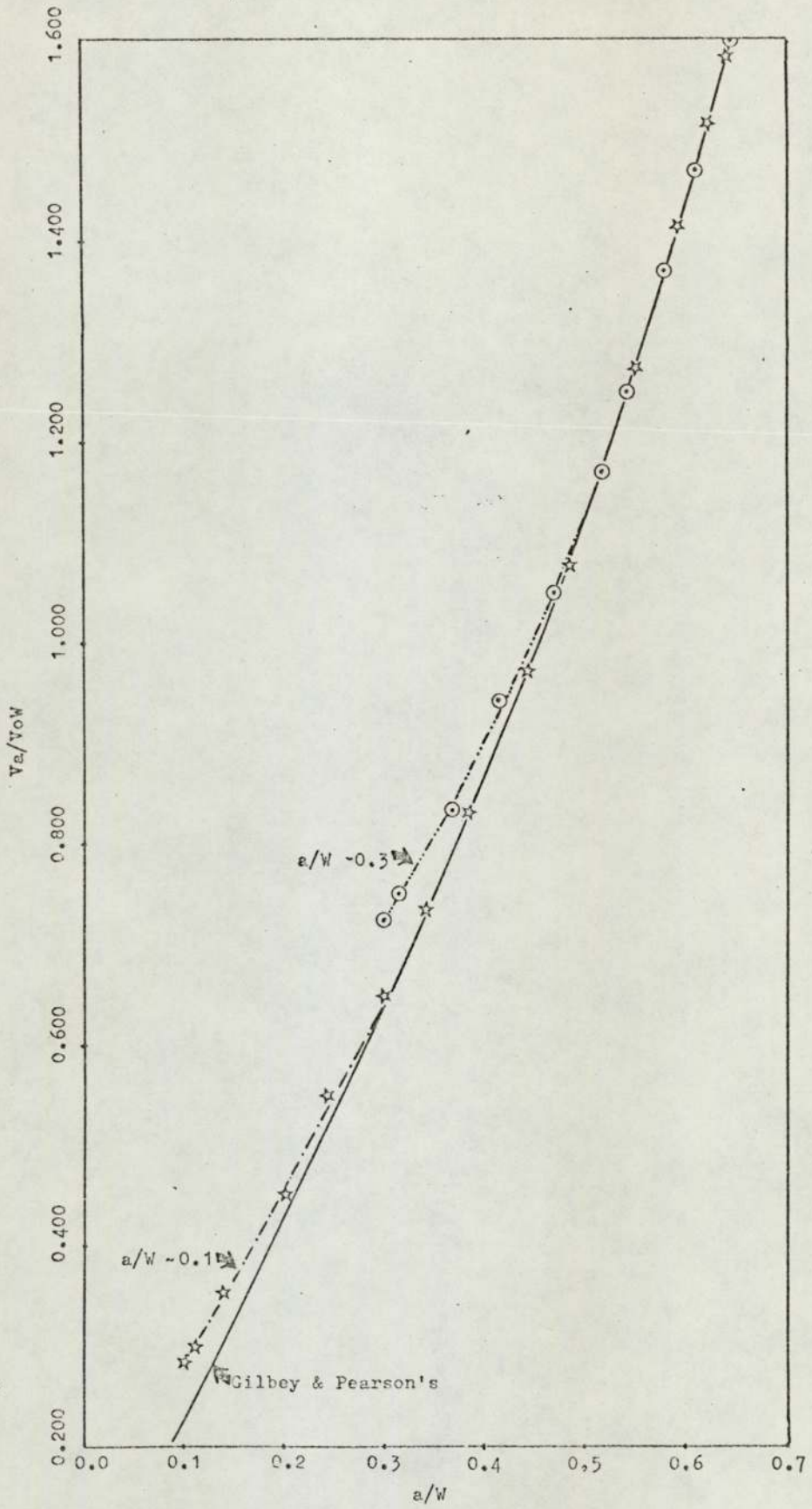


Fig.42. Potential Drop Calibration Curves for compact specimens with different a/W ratios.

TABLE III

ROOM TEMPERATURE MECHANICAL PROPERTIES

DENSITY LEVELS	1	2	3
Final Density, Mg/m ³ (After sintering and Heat-Treatment)	6.9	7.1	7.3

MATERIALS CODE M₁ (Maraging Steel Powder Compacts with high T_i)

K _{IC} , MN/m ^{3/2}	26.2	29.6	34.1
U.T.S. (Y.S), MN/m ²	842	899	1134
% E	2.5	2.5	2.5
% R.A	<0.5	<0.5	<0.5
Hardness, B.H.N.	250	292	368
Porosity, %	16.3	13.7	11.4
Elastic Modulus (E _N), GN/m ²	109	121	132

MATERIALS CODE M₂ (M₁ + 25% Iron Powder Compacts)

K _{IC} , MN/m ^{3/2}	27.5	30.4	34.7
U.T.S. (Y.S), MN/m ²	642	770	966
% E	3.5	2	2.5
% R.A	<0.5	<0.5	1.0
Hardness, B.H.N	188	205	270
Porosity %	16.1	12.9	9.8
Elastic Modulus (E _N), GN/m ²	110	125	141

MATERIALS CODE M₃ (M₁ + 50% Iron Powder Compacts)

K_{IC} , MN/m ^{3/2}	29.1	32.0	35.8
U.T.S. MN/m ²	521	562	639
Y.S. (* 0.2 % P.S.), MN/m ²	521	531*	601*
% E	3.0	3.0	5.0
% R.A	0.5	0.5	1.0
Hardness, B.H.N	120	145	173
Porosity, %	15.7	11.2	8.9
Elastic Modulus (E_N), GN/m ²	112	133	146

MATERIALS CODE LEM (Maraging steel Powder Compacts with Low Ti)

Final Density, Mg/m ³	6.6
K_{IC} , MN/m ^{3/2}	22.9
U.T.S. (I.S), MN/m ²	612
% E	1.5
% R.A	<0.5
Hardness, B.H.N	190
Porosity, %	18.9
Elastic Modulus (E_N), GN/m ²	98

ANCOLOY SA COMPACTS

DENSITY LEVELS	1	2
Final Density, Mg/m ³	6.7	6.9
Porosity, %	15.5	12.2
Elastic Modulus (E_N), GN/m ²	113	128

TABLE III - Cont'd.

MATERIALS CODE ASA-S (Acoloy SA Powder Compacts, Sintered)

K_{IC} , MN/m ^{3/2}	24.9	28.5
U.T.S. (Y.S), MN/m ²	427	471
% E	2.5	3.0
% R.A.	<0.5	<0.5
Hardness, B.H.N.	149	179

MATERIALS CODE ASA-SQT (Acoloy SA Powder Compacts, Sintered, Quenched and Tempered)

K_{IC} , MN/m ^{3/2}	25.8	29.6
U.T.S. (Y.S), MN/m ²	658	733
% E	1.5	1.5
% R.A.	<0.5	<0.5
Hardness, B.H.N.	327	372

TABLE IV

FRACTURE TOUGHNESS

VALIDITY TEST DATA

MATERIALS CODE	KQ MN/m ^{3/2}	$\sigma_{y.s.}$ MN/m ²	$2.5 \left(\frac{KQ}{\sigma_{ys}} \right)^2$ mm.	Thickness B, mm.
M ₁₁	26.2	842	2.42	11.75
M ₁₂	29.6	899	2.71	11.75
M ₁₃	34.1	1134	2.26	11.25
M ₂₁	27.5	642	4.62	11.75
M ₂₂	30.4	770	3.90	11.75
M ₂₃	34.7	966	3.22	11.25
M ₃₁	29.1	521	7.78	11.75
M ₃₂	32.0	531	9.06	11.75
M ₃₃	35.8	601	8.88	11.25
LTM	22.9	612	3.50	11.75
ASA-S (1)	24.9	427	8.52	12.50
ASA-S (2)	28.5	471	9.18	12.50
ASA-SQT (1)	25.8	658	3.83	12.50
ASA-SQT (2)	29.6	733	4.07	12.50

TABLE V

QTM720 IMAGE ANALYSIS OF THE NUMBER AND SIZES OF 'PORES'

MATERIALS CODE	VOL. FRACTION OF 'PORES' (%)	NUMBER OF 'PORES' WITH AREAS IN SIZES SHOWN IN pp*							
		<20	(20 -100)	(100-200)	(200-500)	(500-1000)	1000-5000	5000-10,000	<10,000
M ₁₁	16.3	13011	8191	965	1215	841	1320	332	147
M ₁₂	13.7	17682	12324	1338	1263	943	1485	263	66
M ₁₃	11.4	20632	15020	1375	1543	1095	1432	127	40
M ₂₁	16.1	15206	9460	1423	1434	935	1515	288	151
M ₂₂	12.9	19445	13594	1783	1654	845	1268	222	79
M ₂₃	9.8	18083	11805	2070	1836	100	1243	109	20
M ₃₁	15.7	12070	6399	1586	1498	884	1232	294	177
M ₃₂	11.2	13405	7353	1647	1630	1048	1385	220	122
M ₃₃	8.9	14400	8434	1900	1837	915	1163	124	25
ASA-S ₁	15.5	12707	6596	1769	1970	951	1138	193	90
ASA-S ₂	12.2	13167	6983	2048	1846	946	1134	133	76

* lpp = 1 picture point on the QTM screen = 0.227 μm diameter, \therefore lpp² = 0.0515 μm^2 .

TABLE VI

INITIATION RESULTS

MATERIALS CODE	P_{nm}	ΔP KN	ΔS MN/m ²	ΔK MN/m ^{3/2}	$Kt, \Delta S$	$\Delta K / P^{\frac{1}{2}}$	Ni x 10 ³ Cycles
M ₁₁	0.127	2.4	52.4	8.1	436.0	718.8	42
		3.2	69.4	10.6	576.9	958.4	90
		5.8	125.9	19.6	1046.6	1739.3	3
		5.4	117.2	18.2	974.5	1615.1	6
		2.2	48.0	7.4	399.1	656.7	170
	0.762	5.4	118.0	18.2	435.9	659.4	2
		2.8	60.9	9.4	225.2	340.6	21
		2.6	56.5	8.8	209.2	318.8	130
		4.0	86.9	13.5	321.6	489.1	4
	M ₁₂	0.127	3.8	82.4	12.8	685.2	1135.9
2.2			47.8	7.4	397.5	656.7	98
3.0			65.1	10.1	541.2	896.3	12
3.4			74.0	11.5	615.1	1020.5	10
2.6			55.5	8.8	469.5	780.9	48
0.762		5.8	126.8	19.6	469.0	710.1	5
		3.4	73.9	11.5	273.7	416.7	91
		3.0	65.4	10.1	242.1	365.9	240
		6.0	130.3	20.2	482.1	731.9	2
M ₁₃		0.127	8.8	210.1	17.6	1521.3	1561.8
	5.2		123.6	10.4	895.2	922.9	29
	8.6		205.5	17.2	1495.5	1526.3	4
	4.8		114.2	9.6	827.1	851.9	55

TABLE VI (Cont'd.)

MATERIALS CODE	$P_{lim.}$	ΔP KN	ΔS MN/m ²	ΔK MN/m ^{3/2}	Kt. ΔS	$\Delta K/\rho^{1/2}$	Ni x 10 ³ cycles
M ₂₁	0.762	9.0	214.6	18.0	1559.5	1597.3	3
		5.0	118.8	10.0	860.0	887.4	47
		4.4	104.7	8.8	758.3	780.9	130
		9.6	229.4	19.2	784.9	695.7	23
		8.4	200.8	16.8	686.1	608.7	12
		10.0	237.6	20.0	812.9	724.6	3
		9.2	218.8	18.4	748.5	666.7	9
		9.0	195.7	18.0	724.2	652.2	5
		8.0	174.2	16.0	644.6	579.7	20
	6.0	130.3	12.0	482.0	434.8	129	
	0.127	2.8	60.7	9.4	504.9	834.1	127
		3.0	65.2	10.1	542.2	896.3	28
		3.2	69.4	10.8	577.0	958.4	148
		3.6	78.4	12.1	651.7	1073.7	3
		0.762	5.8	126.0	19.6	466.6	710.1
5.2	113.0		17.5	418.5	634.1	27	
3.8	82.4		12.8	305.1	463.8	68	
4.0	86.8		13.5	321.7	489.1	180	
M ₂₂	0.127	4.4	95.3	14.8	792.1	1313.3	4
		3.0	65.0	10.1	540.2	896.3	57
		4.8	104.2	16.2	865.8	1437.6	2
		4.0	87.0	13.5	723.2	1198.0	18

TABLE VI (Cont'd)

MATERIALS CODE	$P_{min.}$	ΔP KN	ΔS MN/m ²	ΔK MN/m ^{3/2}	Kt. ΔS	$\Delta K/\rho^{1/2}$	Ni x 10 ³ cycles
M ₂₃	0.762	5.6	121.6	18.9	450.5	684.8	4
		3.8	82.5	12.8	305.7	463.8	27
		5.6	121.6	18.9	449.8	684.8	5
		5.4	117.3	18.2	434.3	659.4	20
		3.6	78.2	12.1	289.7	438.4	98
	0.127	5.2	123.6	10.4	895.0	922.9	66
		5.6	133.3	11.2	968.8	993.9	56
		4.4	104.8	8.8	761.9	780.9	484
		6.0	143.0	12.0	1043.2	1064.9	9
		6.2	147.6	12.4	1073.0	1100.4	5
	0.762	8.6	205.4	17.2	702.7	623.2	9
		8.8	209.3	17.6	716.0	637.7	16
		9.6	228.5	19.2	781.8	695.7	7
		7.8	185.3	15.6	633.8	555.2	91
		8.4	200.4	16.8	685.7	608.7	19
M ₃₁	0.127	3.4	73.8	11.5	613.3	1020.5	13
		3.8	82.5	12.8	685.5	1135.9	4
		2.4	52.2	8.1	433.6	718.8	350
		4.4	95.5	14.8	794.0	1313.3	2
	0.762	3.2	69.5	10.8	257.3	391.3	92
		5.8	125.7	19.6	465.4	710.1	2
		3.0	65.1	10.1	241.2	365.9	310

TABLE VI (Cont'd)

MATERIALS CODE	$P_{mm.}$	ΔP KN	ΔS MN/ m ²	ΔK MN/m ^{3/2}	$Kt \Delta S$	$\Delta K / \rho^{\frac{1}{2}}$	Ni x 10 ³ cycles
M ₃₂	0.127	5.6	121.6	18.9	450.3	684.8	6
		3.4	80.8	6.8	584.7	603.4	381
		3.8	90.2	7.6	653.1	674.4	37
		3.6	85.6	7.2	624.5	638.9	188
	0.762	5.6	133.1	11.2	967.1	993.9	3
		6.4	151.7	12.8	519.0	463.8	16
		6.0	142.2	12.0	486.4	434.8	118
		8.0	189.7	16.0	649.1	579.7	2
		6.8	161.4	13.6	552.1	492.8	37
		8.0	189.7	16.0	649.1	579.7	2
M ₃₃	0.127	5.8	137.7	11.6	1000.6	1029.4	17
		4.8	114.4	9.6	828.0	851.9	100
		5.6	132.9	11.2	965.6	993.9	55
		5.0	119.0	10.0	868.6	887.4	68
		6.4	152.2	12.8	1106.0	1135.9	4
	0.762	8.0	190.8	16.0	652.6	579.7	26
		8.8	209.7	17.6	717.3	637.7	3
		9.2	218.9	18.4	748.7	666.7	6
		8.4	200.6	16.8	686.2	603.7	18
		7.2	171.3	14.4	585.9	521.7	150

TABLE VI (Cont'd)

MATERIALS CODE	$P_{min.}$	ΔP KN	ΔS MN/ m ²	ΔK MN/m ^{3/2}	Kt. ΔS	$\Delta K/P^{1/2}$	Ni x 10 ³ cycles	
LTM (low Ti sintered Maraging compact)	0.127	5.4	117.5	18.2	976.4	1615.1	1	
		4.4	95.3	14.8	792.3	1313.3	2	
		2.4	52.0	8.1	432.2	718.8	10	
		2.0	43.4	6.7	360.9	594.6	58	
		2.2	47.8	7.4	397.5	656.7	30	
	0.762	6.0	129.9	20.2	481.0	731.9	2	
		3.2	69.4	10.8	257.0	391.3	12	
		2.6	56.4	8.8	208.7	318.8	45	
		2.4	52.2	8.1	193.0	293.5	91	
		4.8	104.1	16.2	385.4	587.0	4	
	Notch depth for M ₁₁ , M ₁₂ , M ₂₁ , M ₂₂ , M ₃₁ , M ₃₂ , and LTM Compacts ~ 0.3 W; Notch depth for M ₁₃ , M ₂₃ and M ₃₃ Compacts ~ 0.1W.							

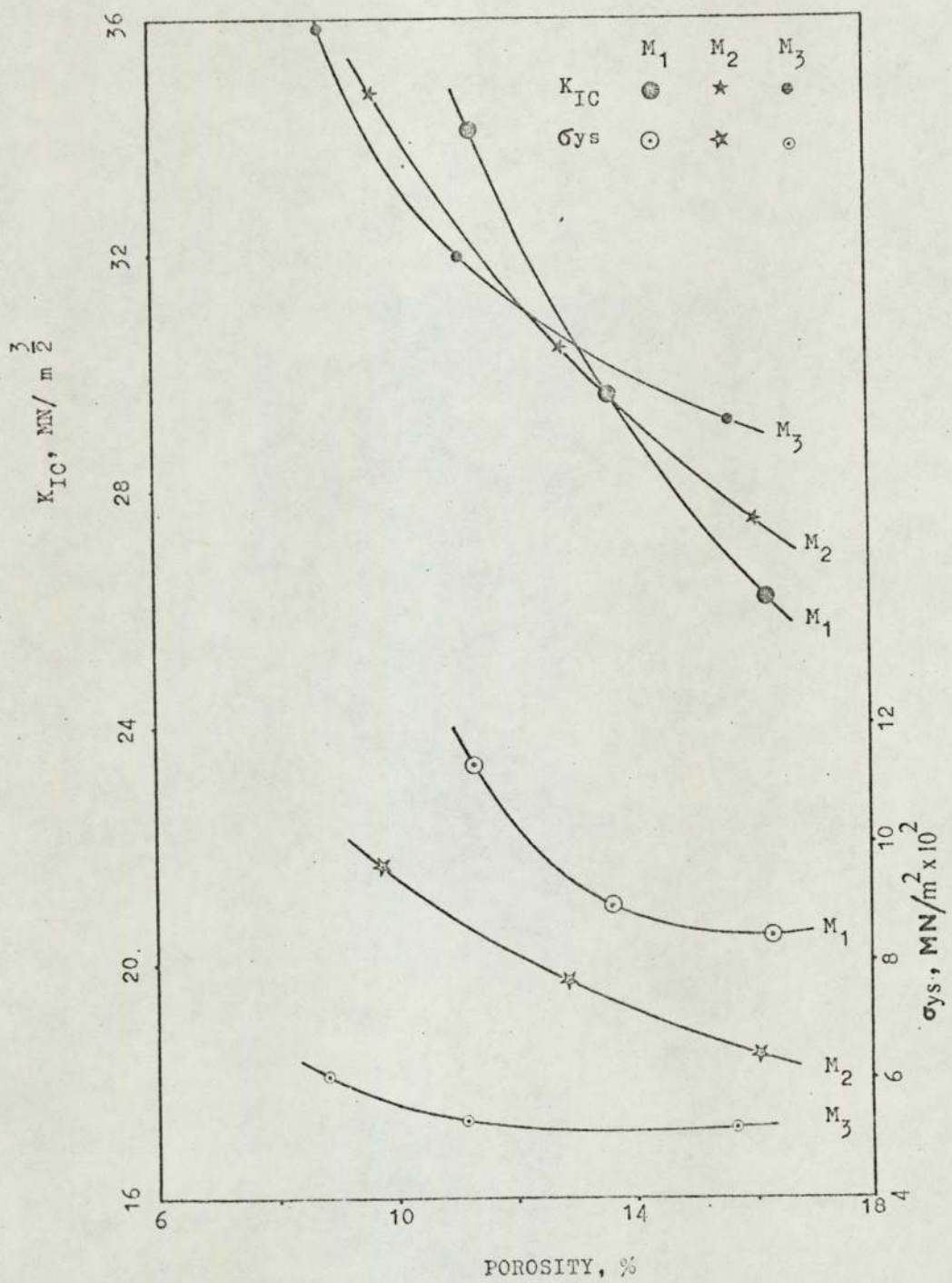


Fig.43. Fracture Toughness, K_{IC} and Yield Stress, σ_{ys} as a function of %Porosity.

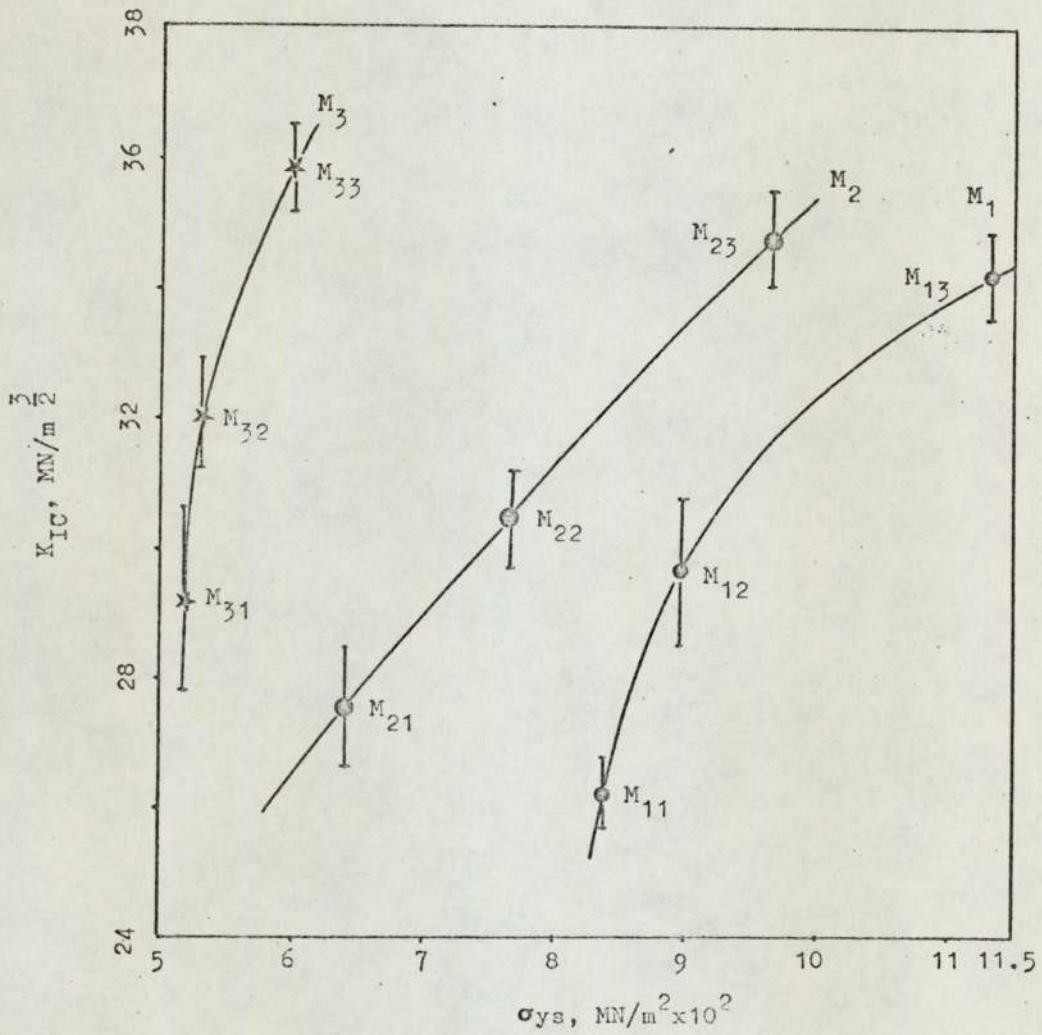


Fig.44. Fracture Toughness as a function of yield stress for the three types of sintered steels investigated.

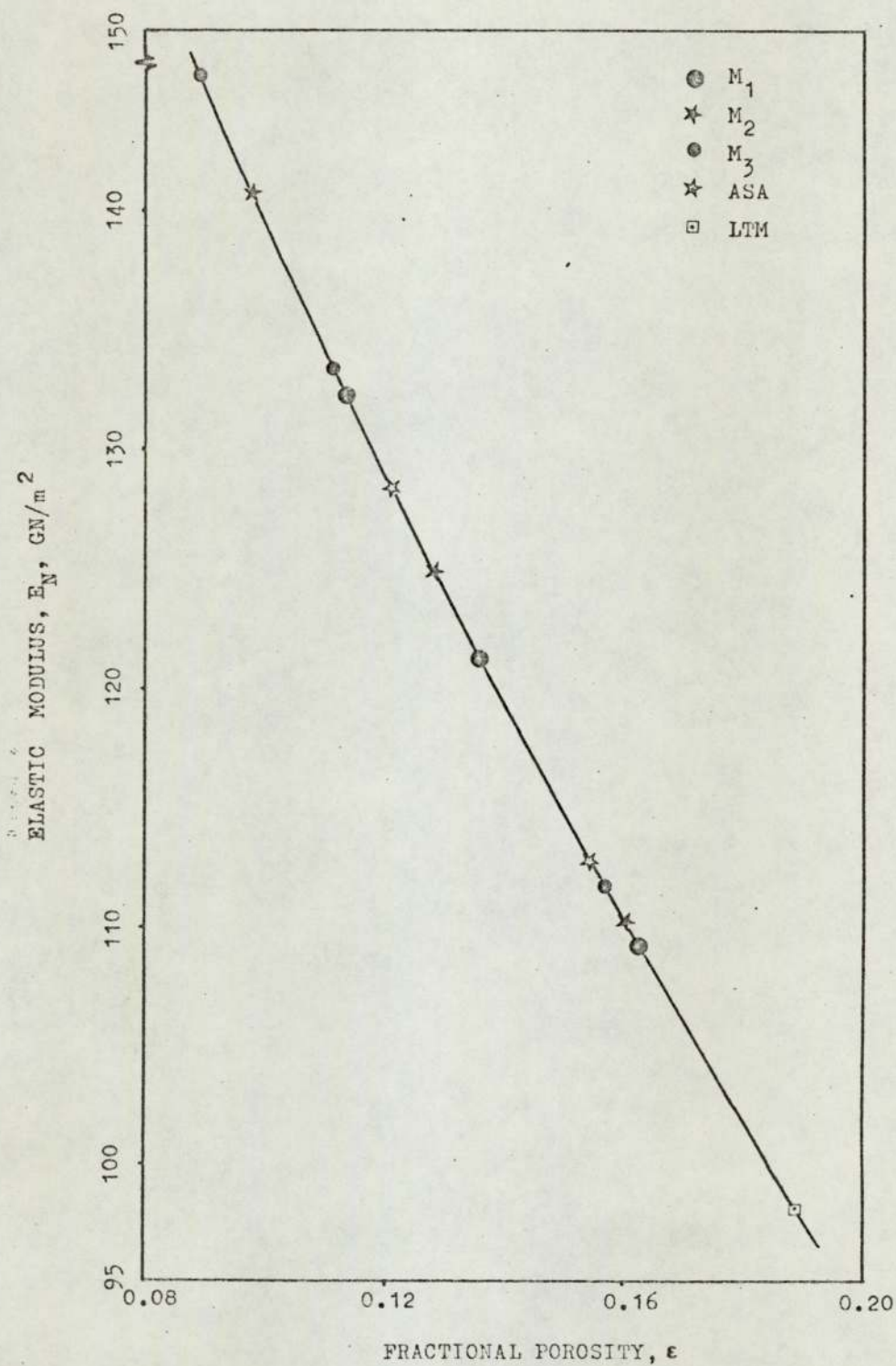


Fig.45. Elastic Modulus, E_N vs. % Porosity for all the materials tested.

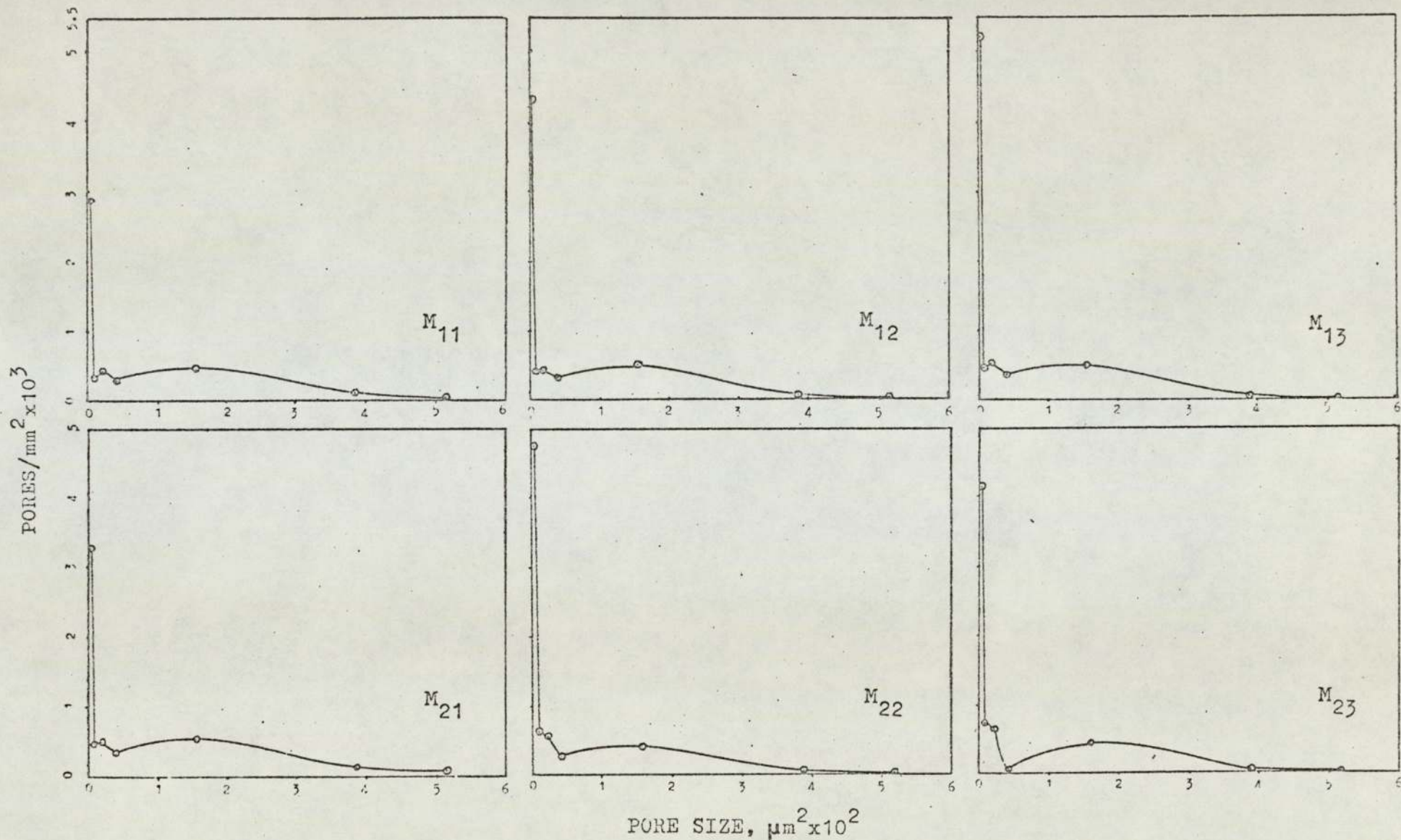


Fig.46. Pore distribution of different sintered steels investigated.

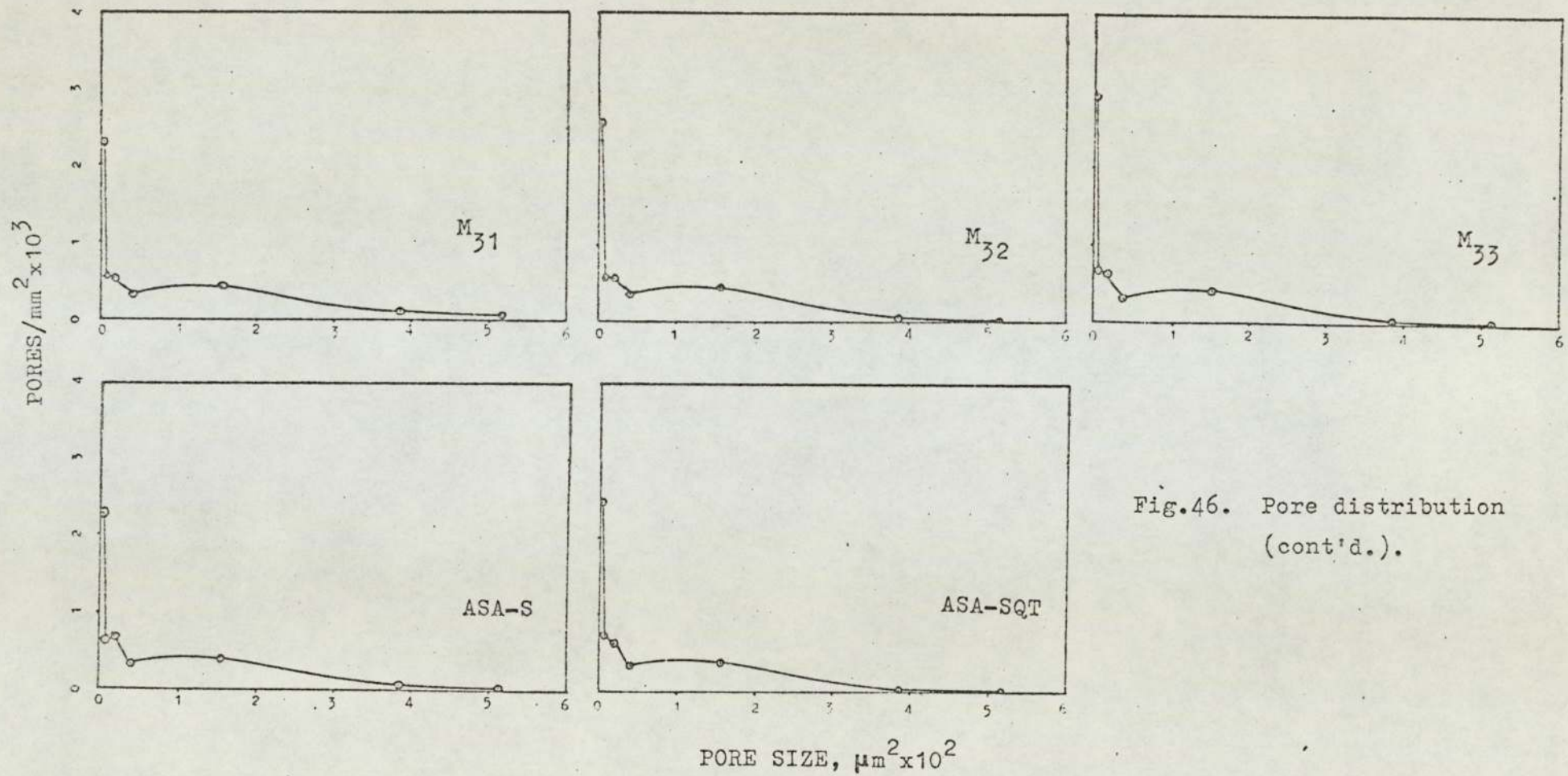


Fig.46. Pore distribution (cont'd.).

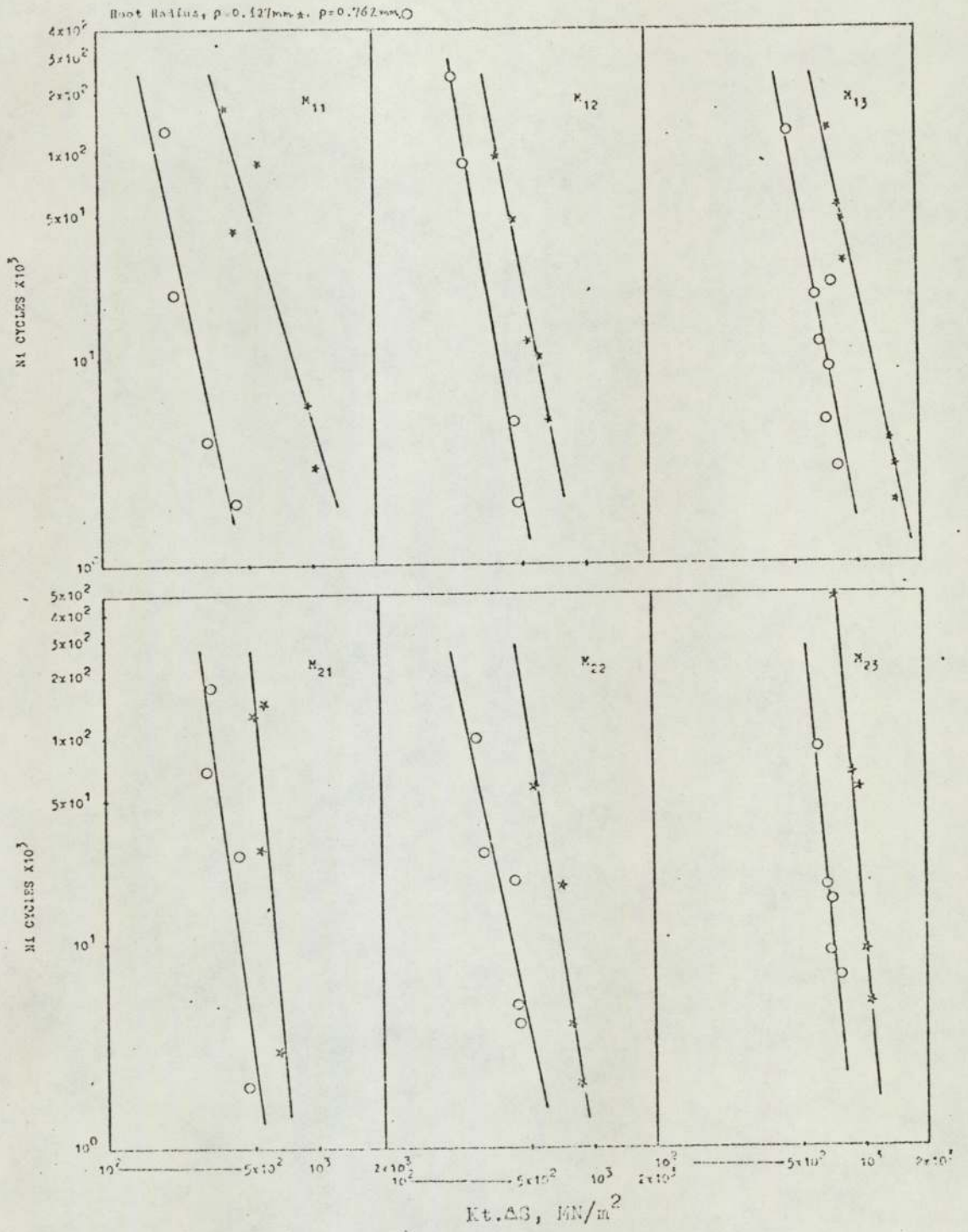


Fig.47. Plot of N_i , no. of cycles for initiation, Vs $Kt.S$.

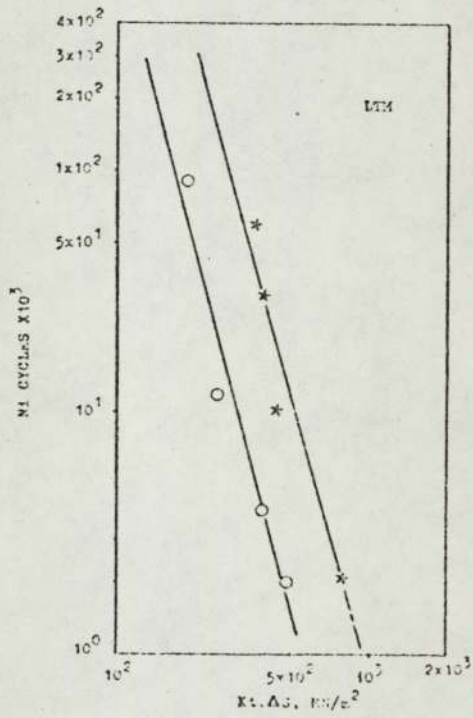
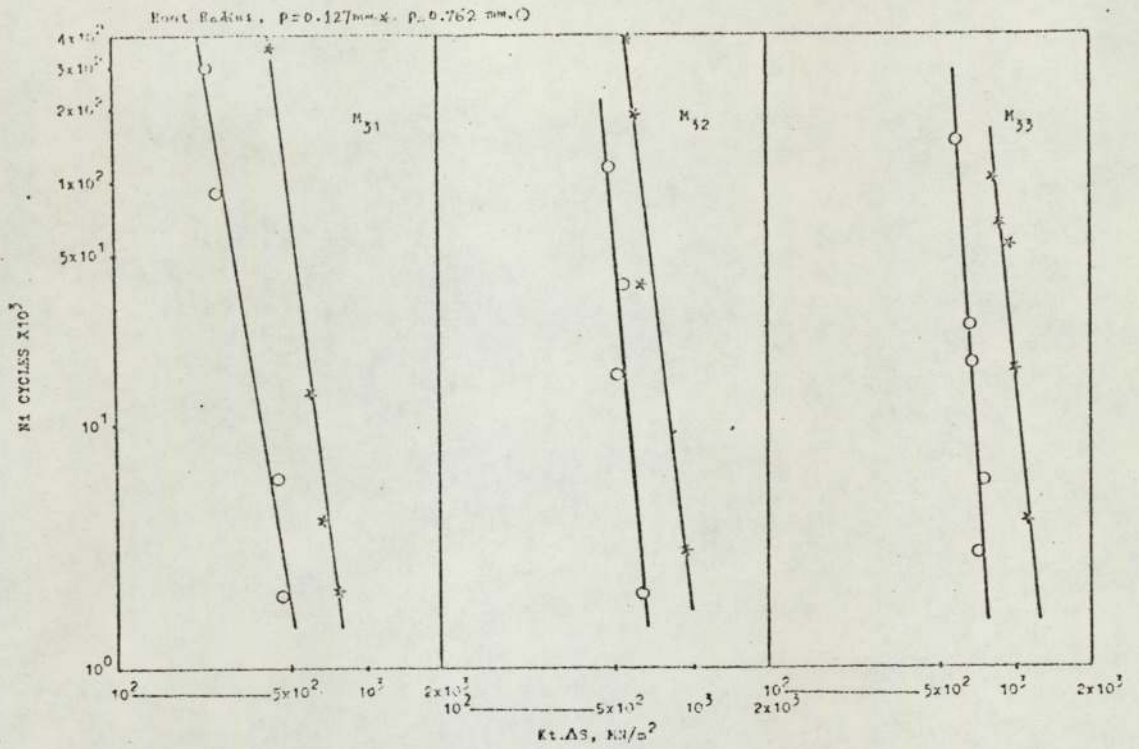


Fig.47. Plot of N_i Vs $Kt.AS$
(cont'd.).

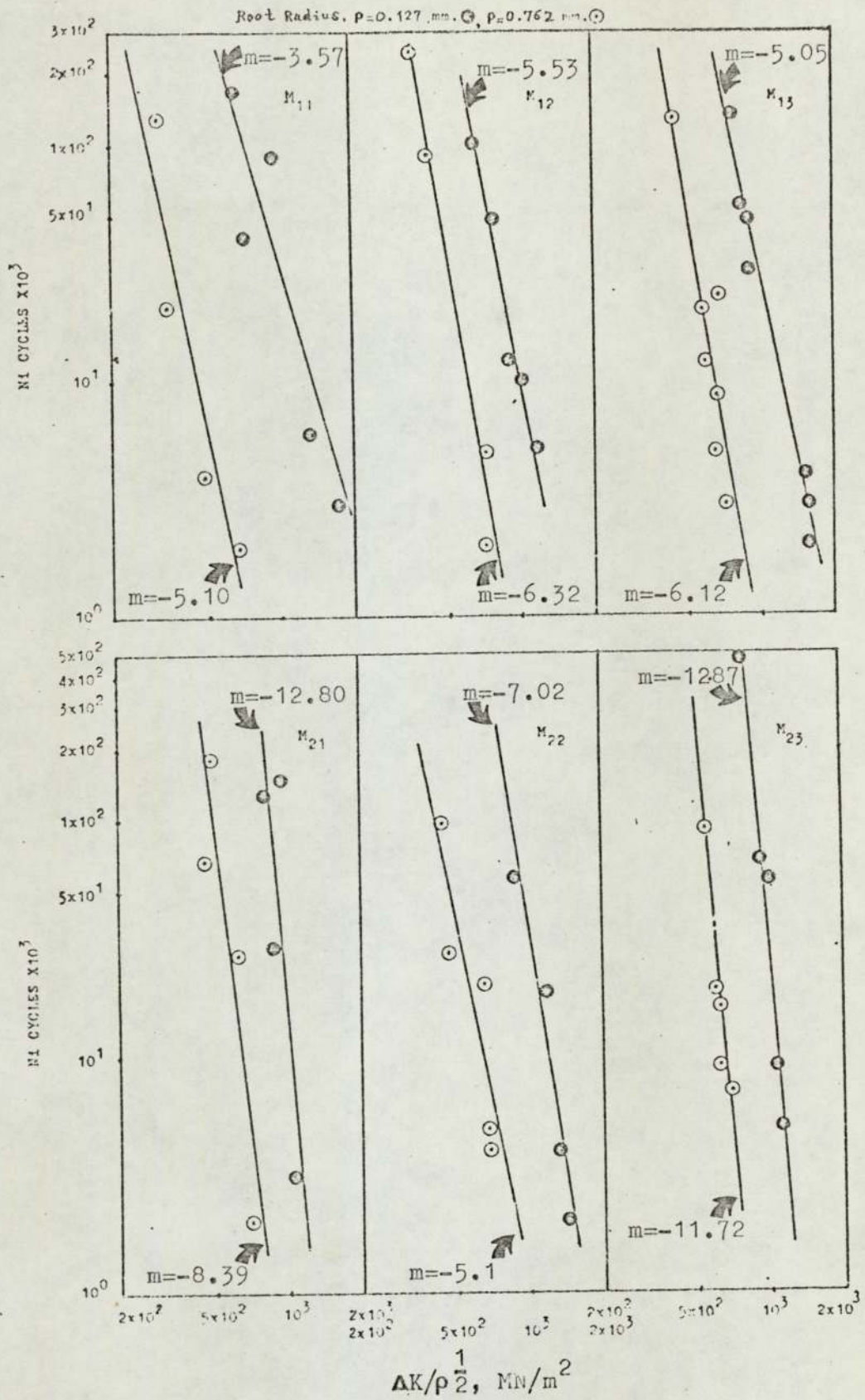


Fig.48. Plot of N_i , no. of cycles for initiation, Vs $\Delta K / \rho^{1/2}$.

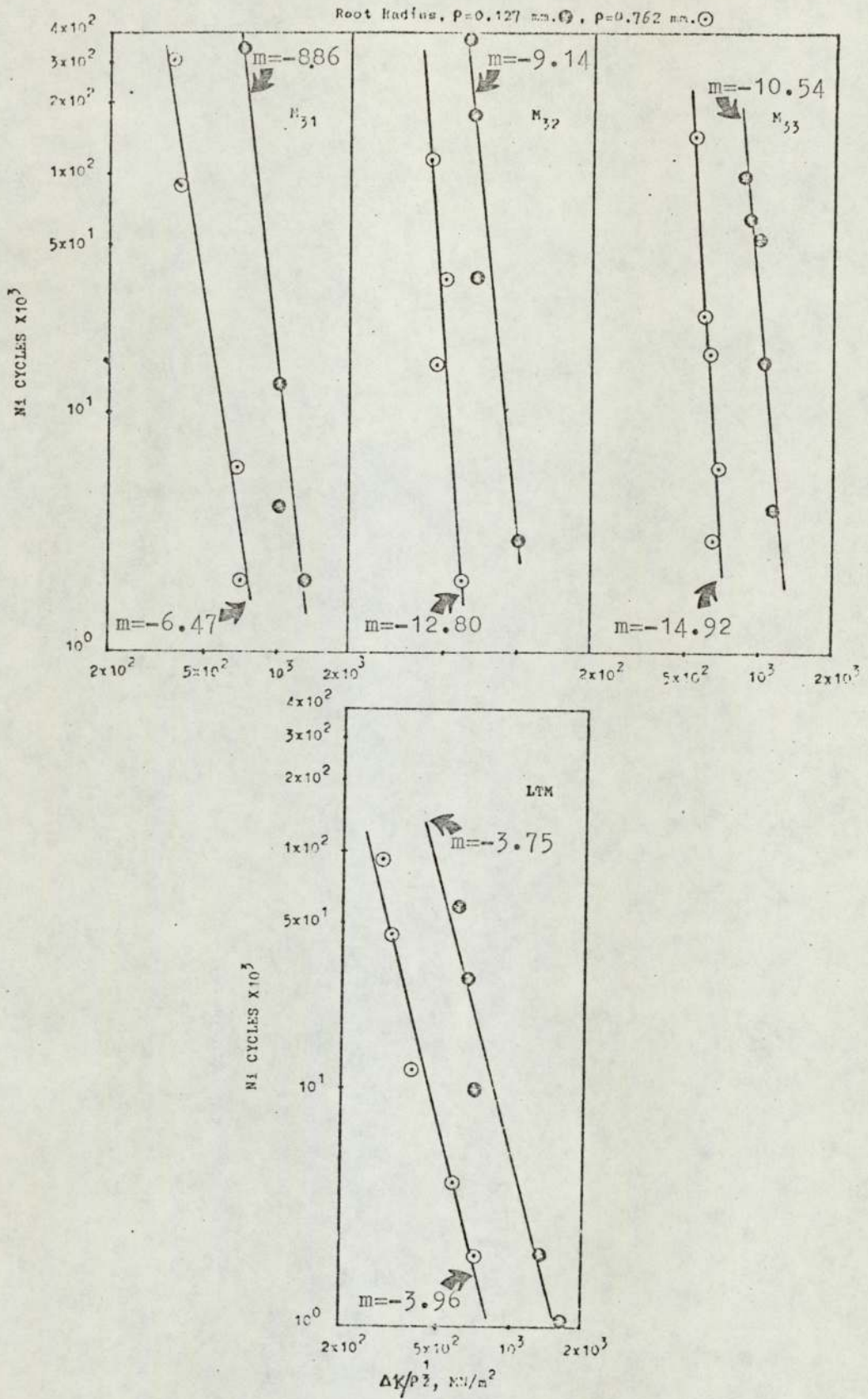


Fig. 48. Plot of N_i Vs $\Delta K / \rho^{1/2}$
(cont'd.).

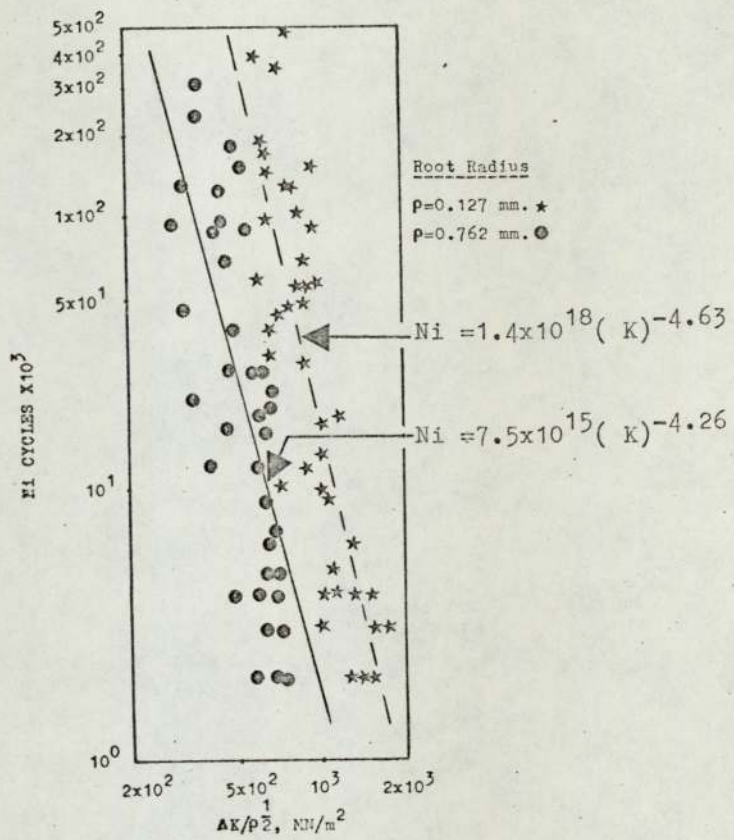


Fig.49. Initiation data for all the materials tested.

Root Radius, $\rho = 0.127$ mm. \odot $\rho = 0.762$ mm. \ominus

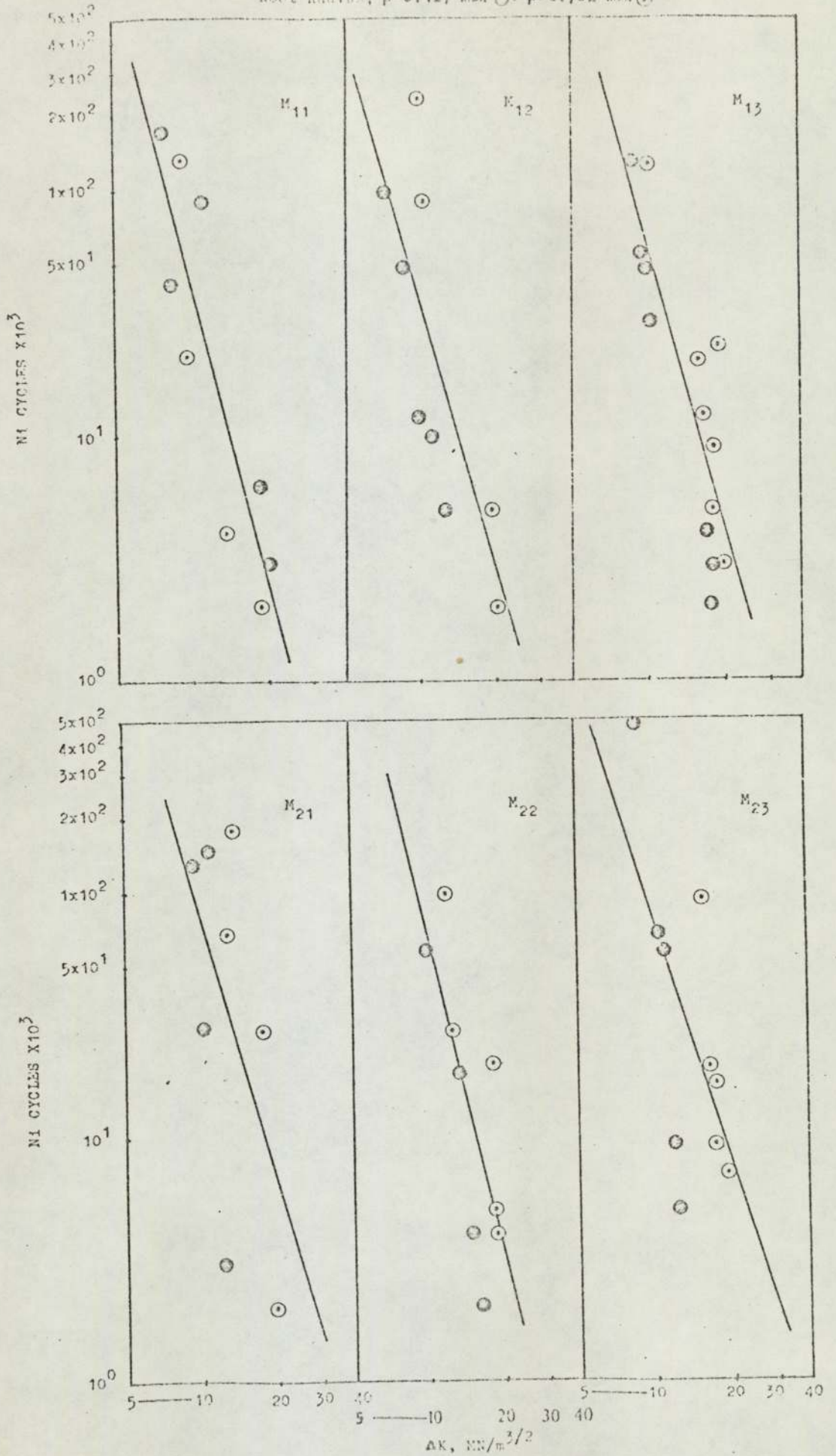


FIG. 50. Plot of N_1 Vs ΔK .

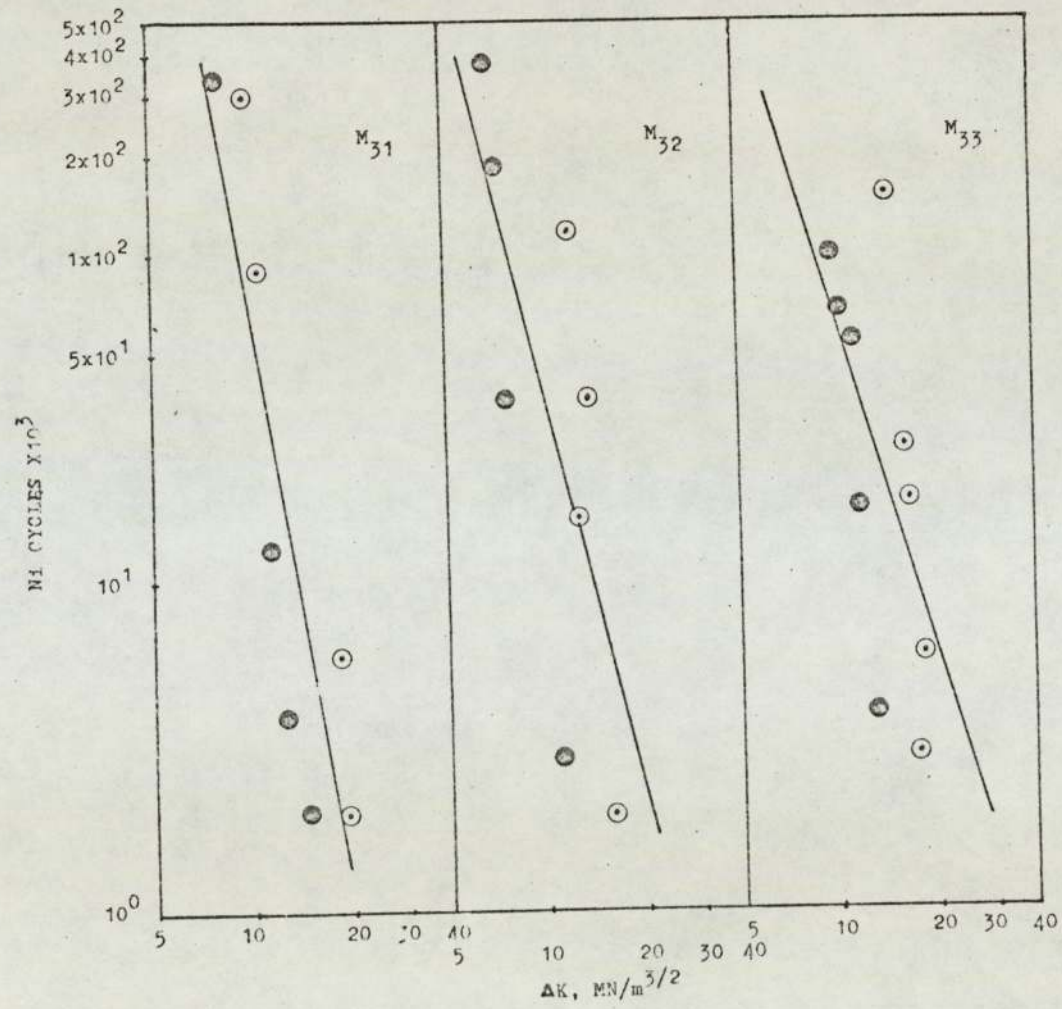


Fig. 50. Plot of N_i Vs ΔK (cont'd).

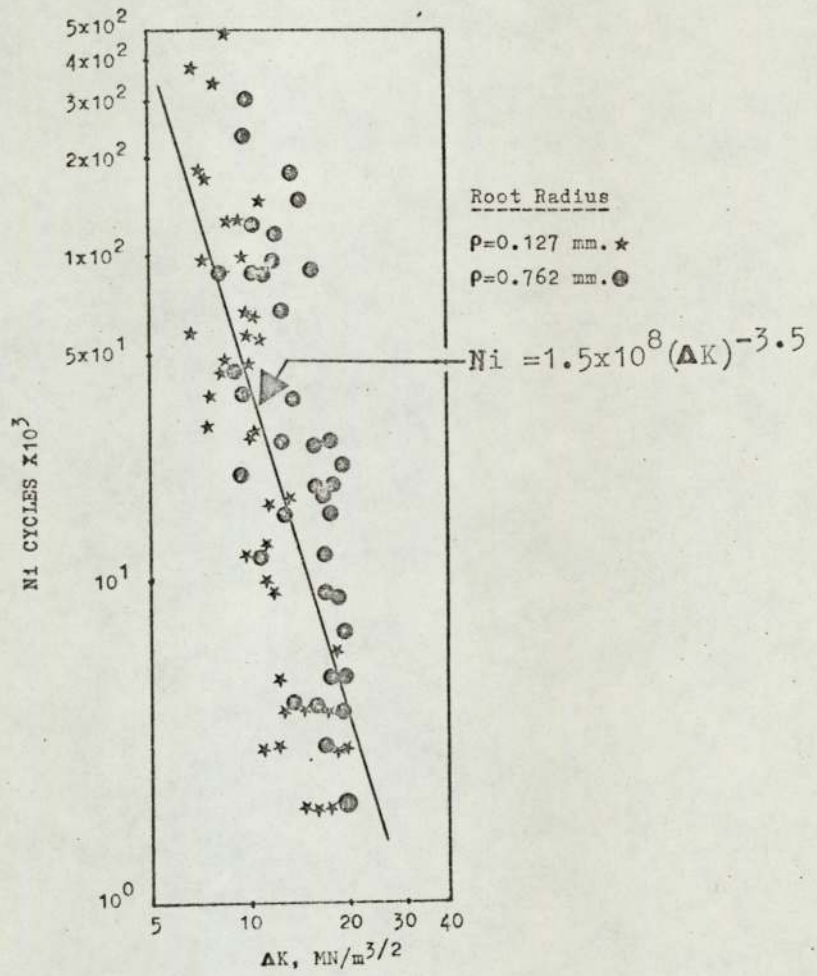


Fig. 51. Correlation of Ni Vs ΔK .

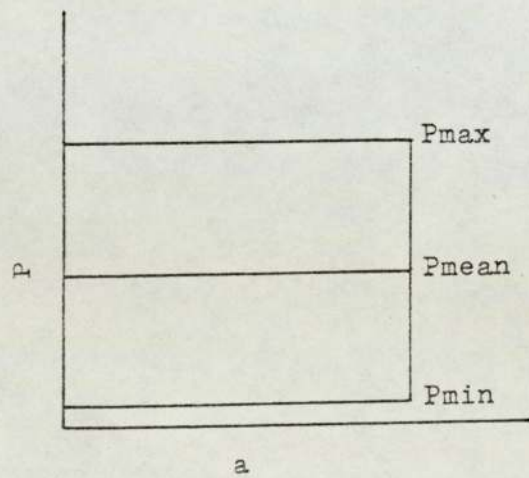


Fig.52. (Constant) Load Profile.

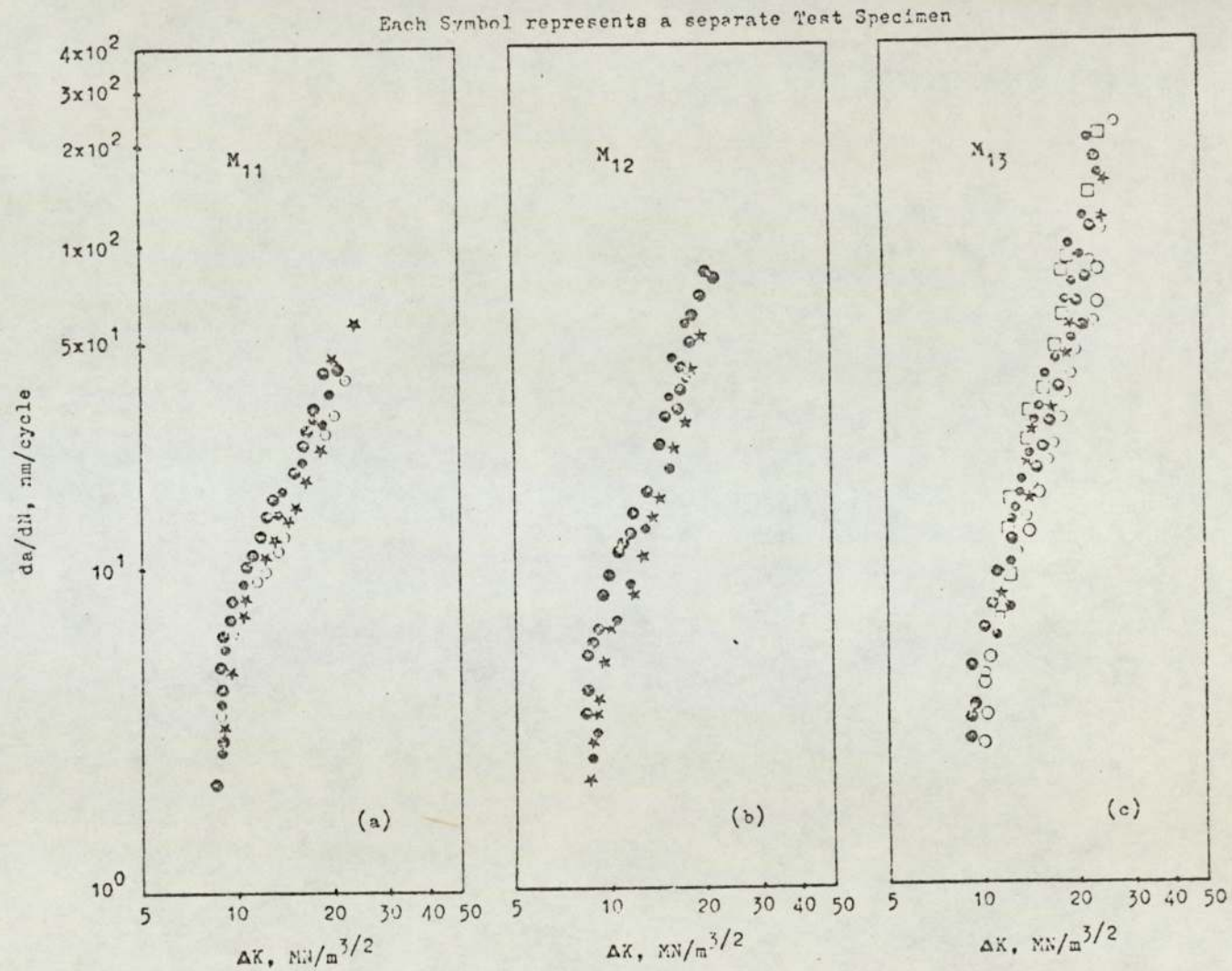


Fig.53. Crack Growth results for the different compact materials investigated, $R=0.07$.

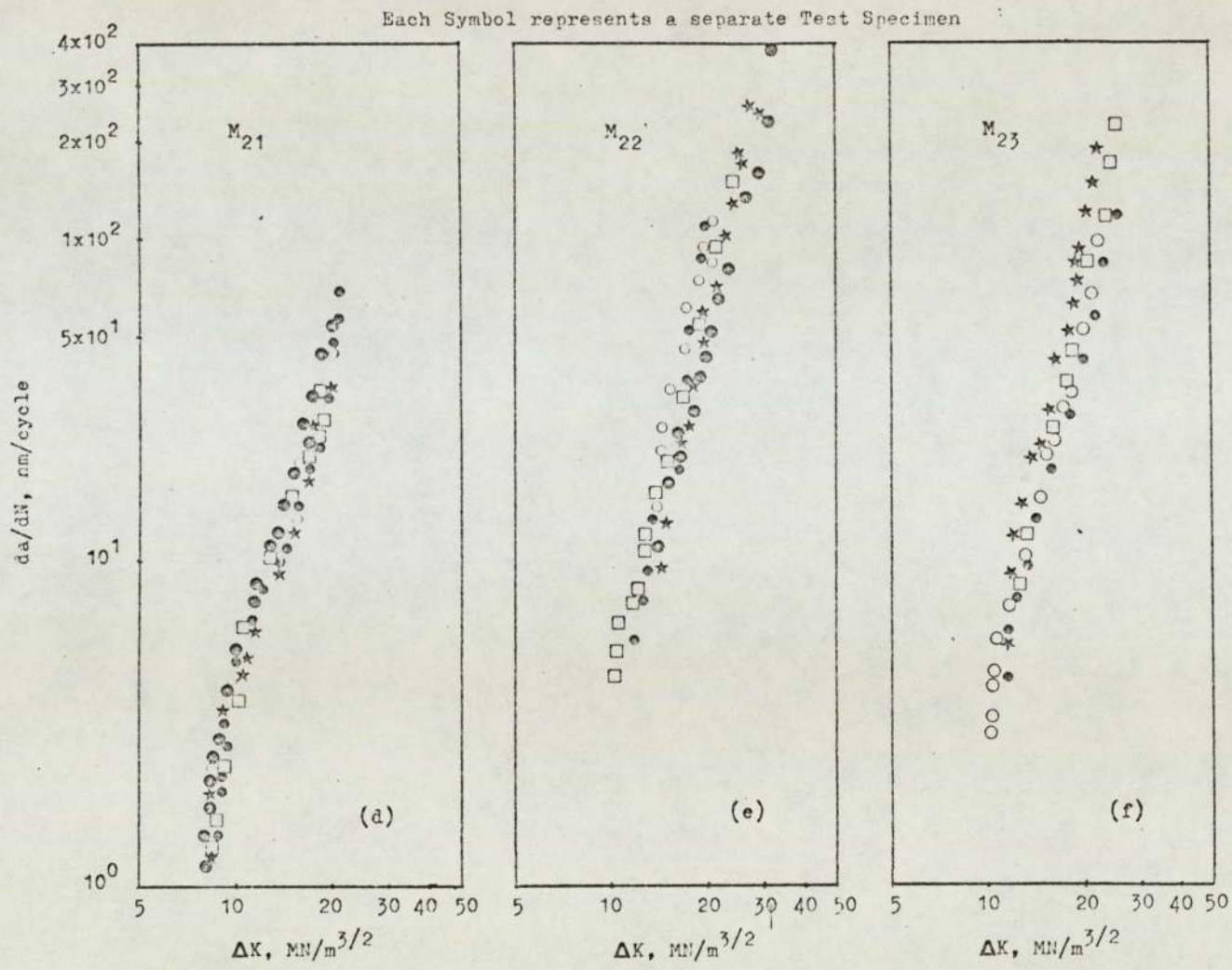


Fig.53. Crack Growth results (Cont'd).

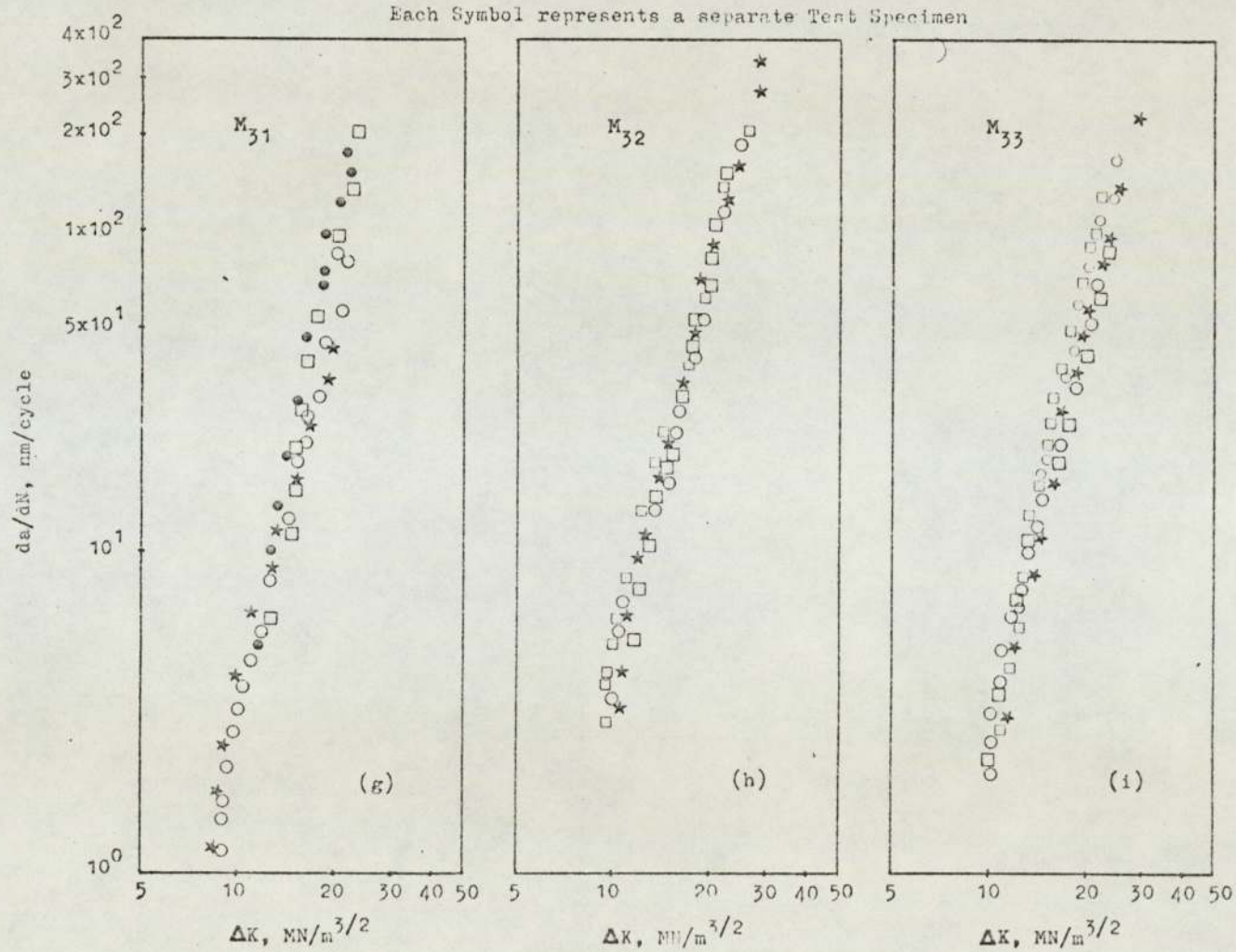


Fig.53. Crack Growth results
(Cont'd).

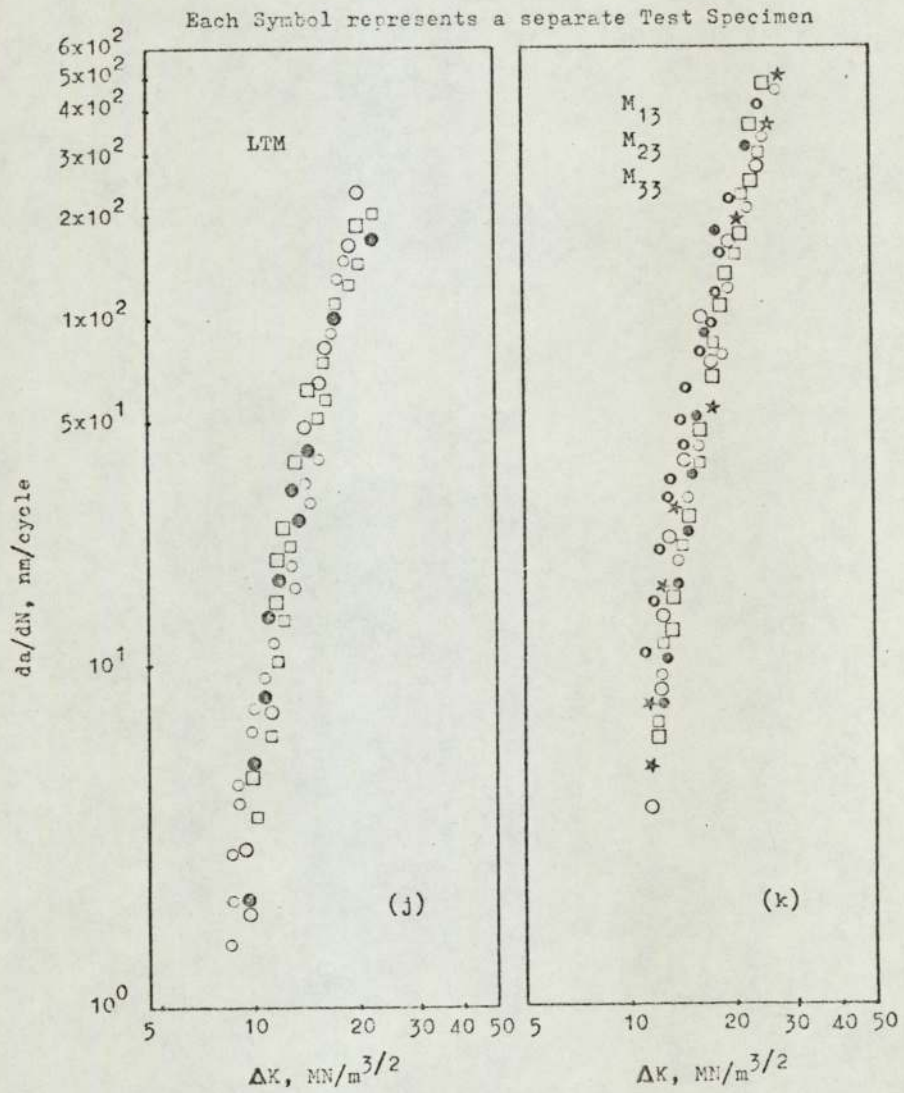


Fig. 53. Crack Growth Results for (j) LTM Compacts, at $R \sim 0.07$, and for (k) M_{13} , M_{23} , M_{33} Compacts at $R \sim 0.3$.

Each Symbol represents a separate Test Specimen

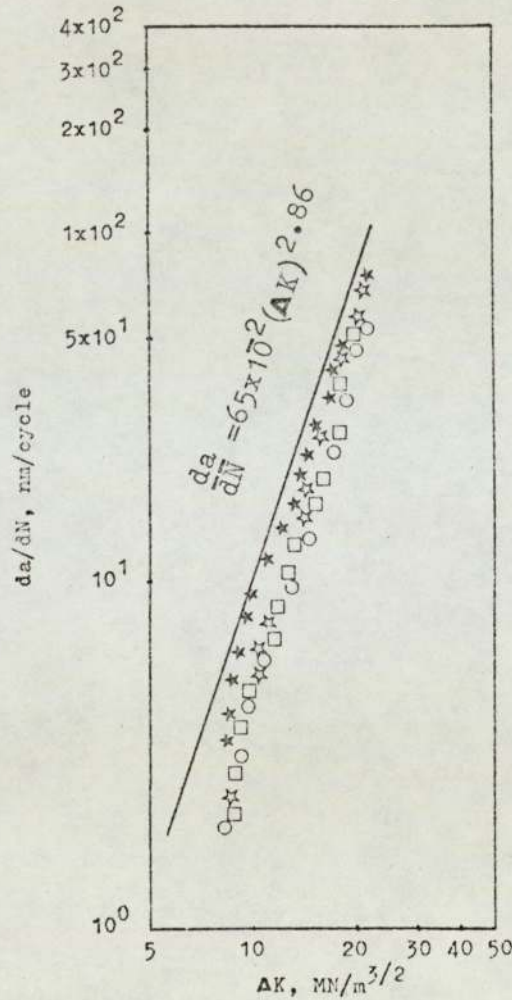


Fig.54. Crack Growth results for M_{12} and M_{21} Compacts at $R \sim 0.07$ shown to be falling on the same scatter band.

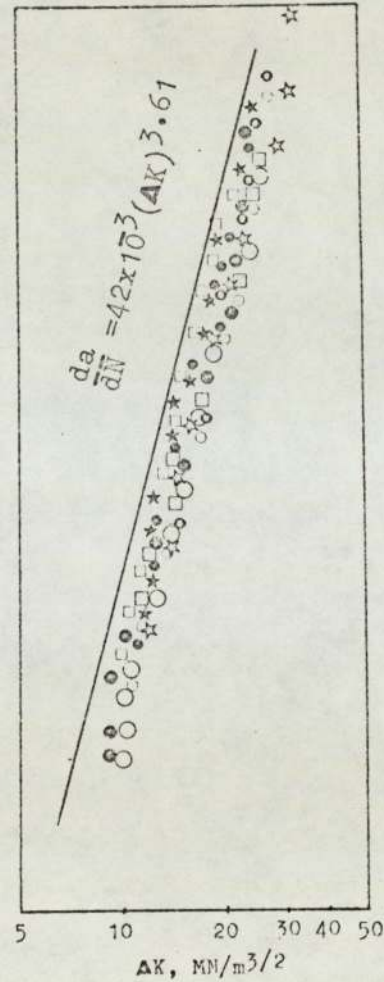


Fig.55. As in Fig.54 for M_{13} and M_{22} Compacts.

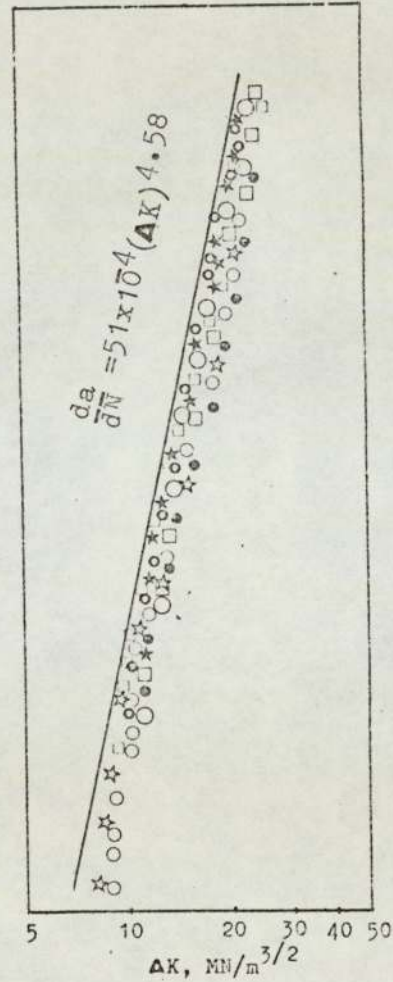
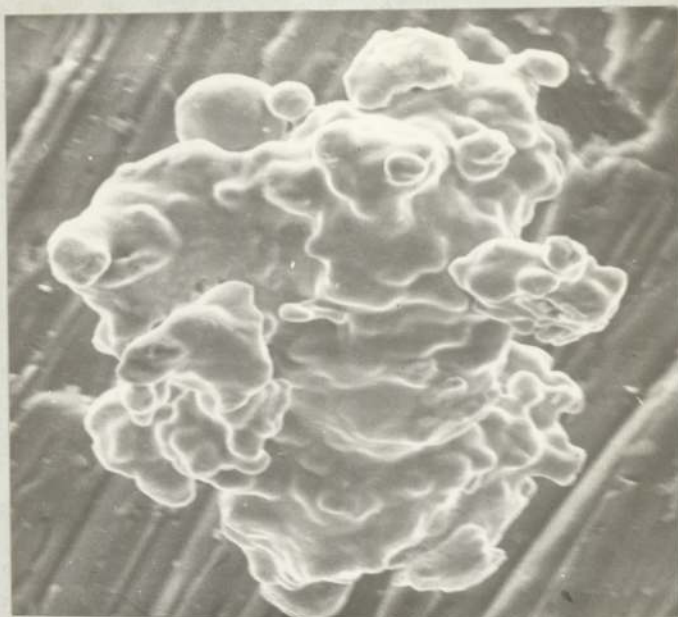


Fig.56. As in Fig.54 for M_{23} , M_{31} , M_{32} and M_{33} Compacts.

Particle Size (P.S.) of Maraging Steel
Pre-alloyed Powders $\sim 250\mu$.



→ 1/25 P.S. ←

Fig.57. A cluster of Maraging Steel
Powder Particles.



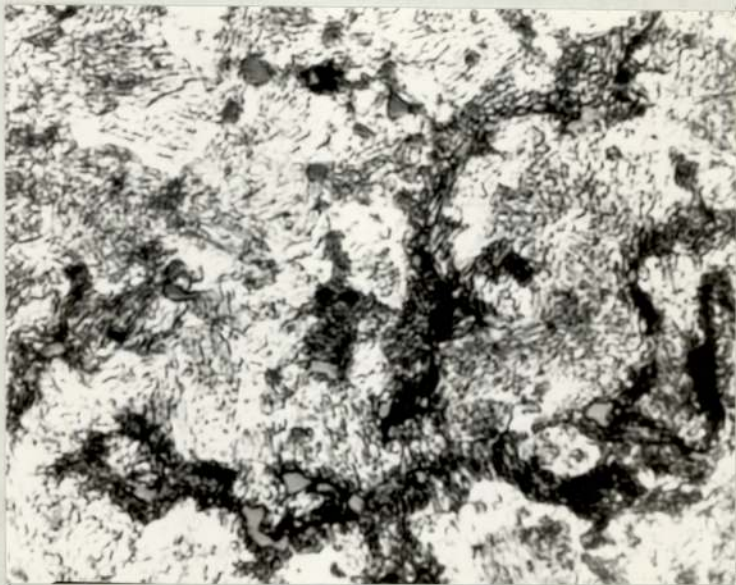
→ 1/5 P.S. ←

Fig.58. Green Maraging Steel Powder
Compact.



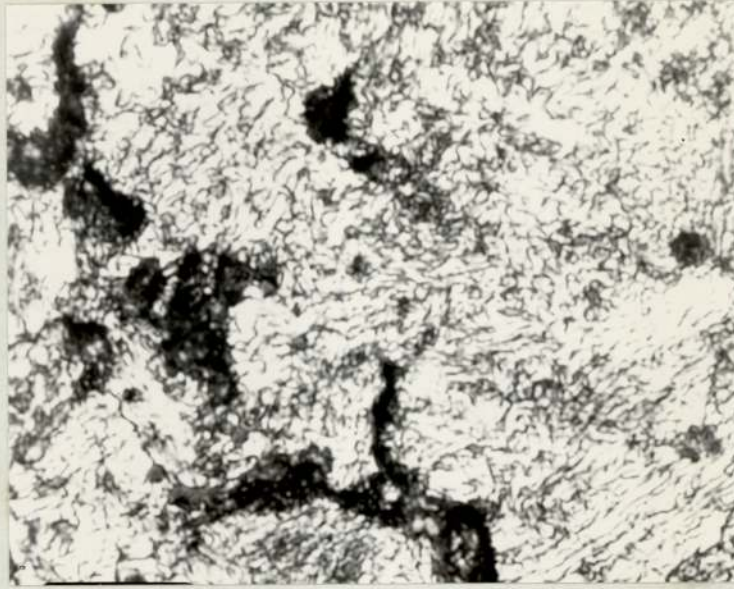
← 1/10 P.S. →

Fig.59. Typical Microstructure of M₁ series of Maraging Steel (M.S.) Compact. Sintered and Heat-Treated (S.H.T.)



← 1/10 P.S. →

Fig.60. Microstructure of M₂ Series of Diluted M.S. Compact. S.H.T.



|←1/10 P.S.→|

Fig.61. Typical Microstructure of M_2 Series of Diluted M.S. Compact. S.³H. T.



|←1/10 P.S.→|

Fig.62. Microstructure of M_1 Series of M.S. Compact. Sintered only.



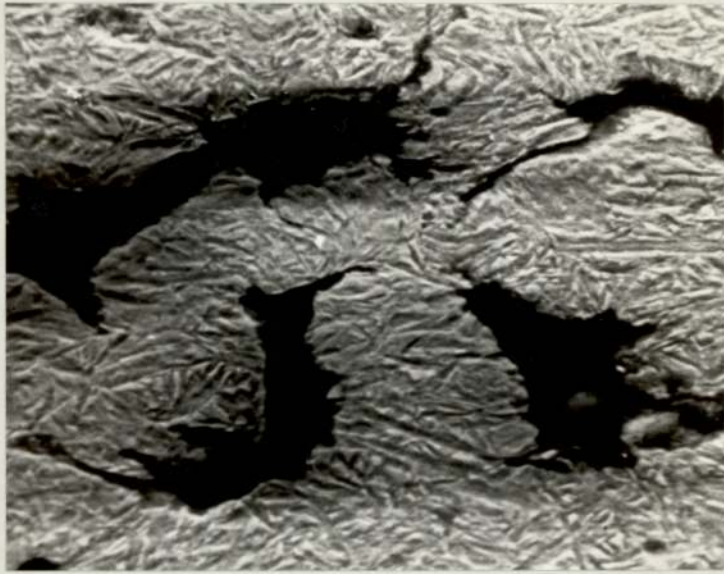
←1/10 P.S.→

Fig.63. Typical Microstructure of Ancoloy SA Compact. Sintered.



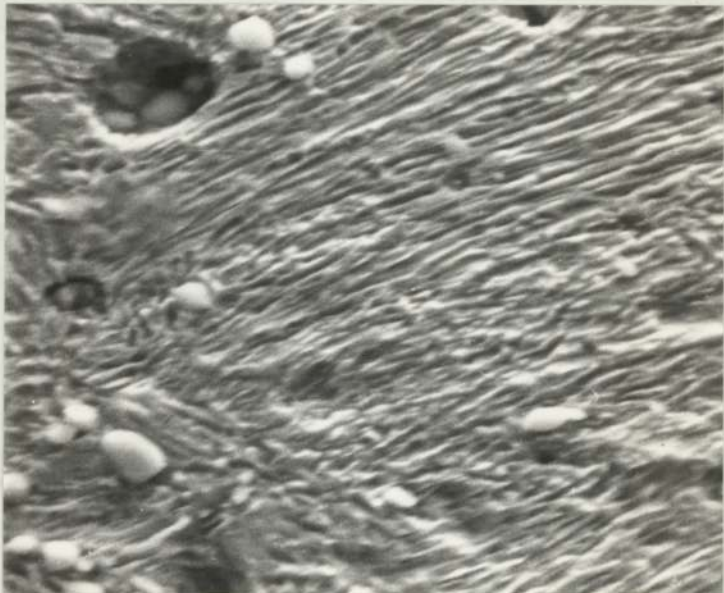
←1/10 P.S.→

Fig.64. Microstructure of Ancoloy SA Compact. Sintered, Quenched and Tempered.



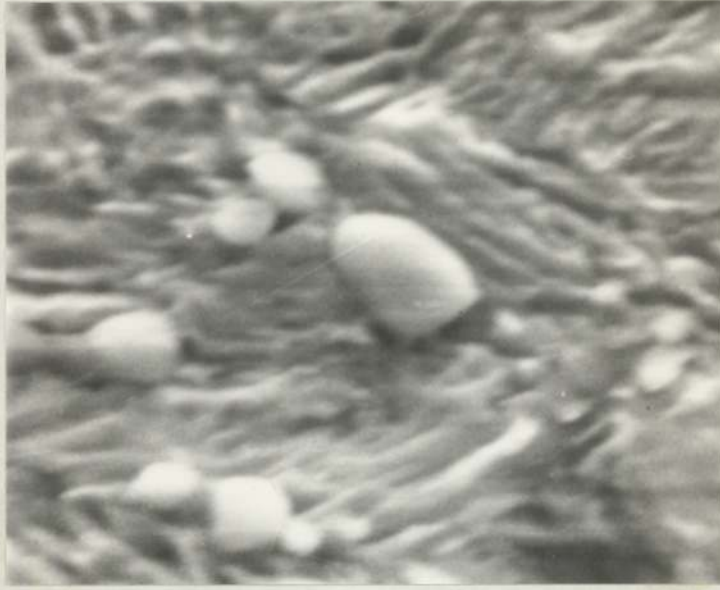
|←1/25 P.S.→|

Fig.65. S.E.M.-Image of Typical Microstructure of M_1 Series of M.S. Compact. S.H.T.



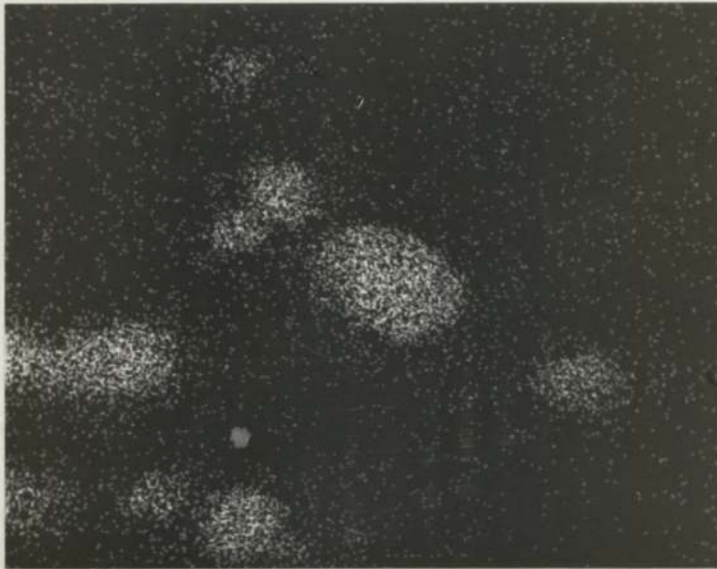
|←1/25 P.S.→|

Fig.66(a). S.E.M.-Image of Microstructure of M_1 Series of M.S. Compacts. S.H.T.



←1/50 P.S.→

Fig.66 (b). Same as in Fig.66(a) at High Magnification.



←1/50 P.S.→

Fig.66 (c). Ti X-Ray Image of Area in Fig.66(b).

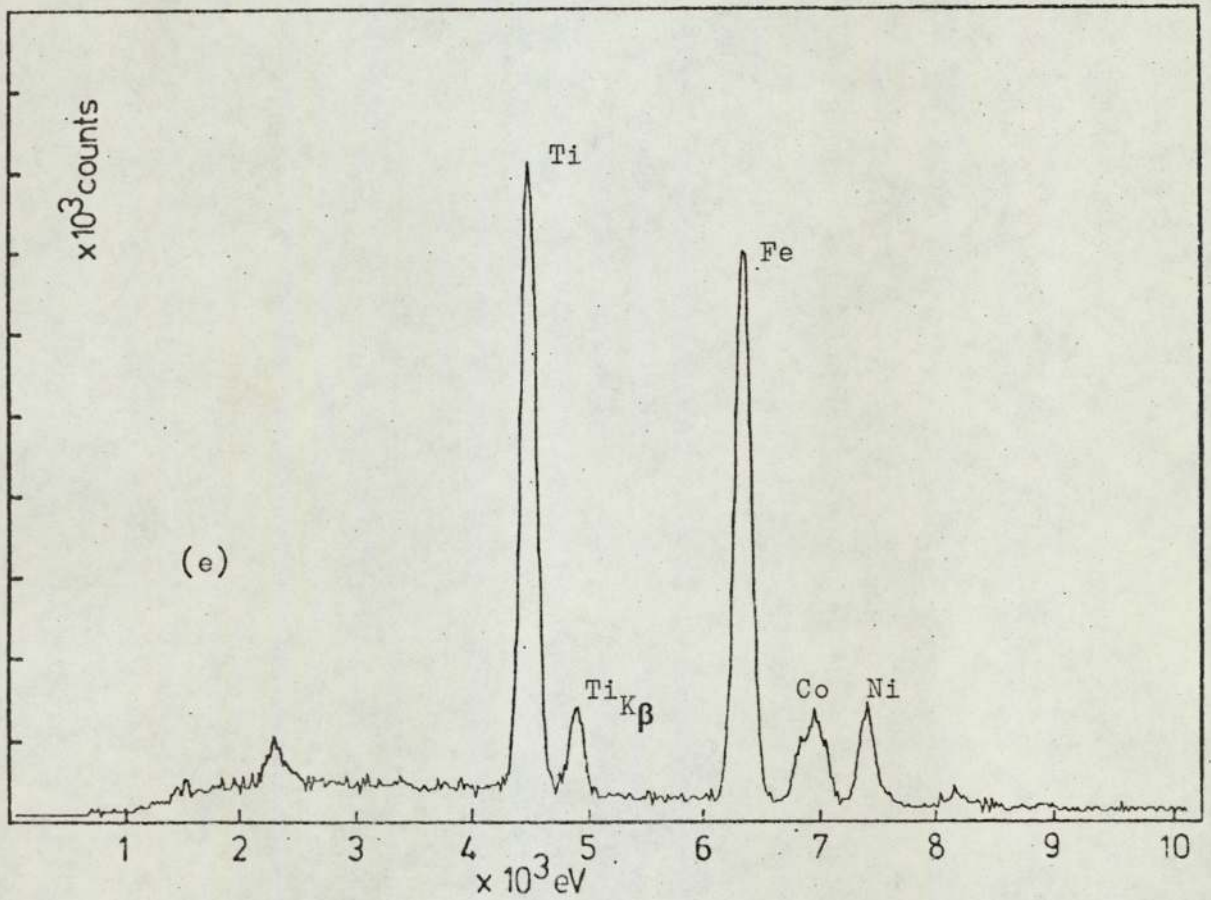
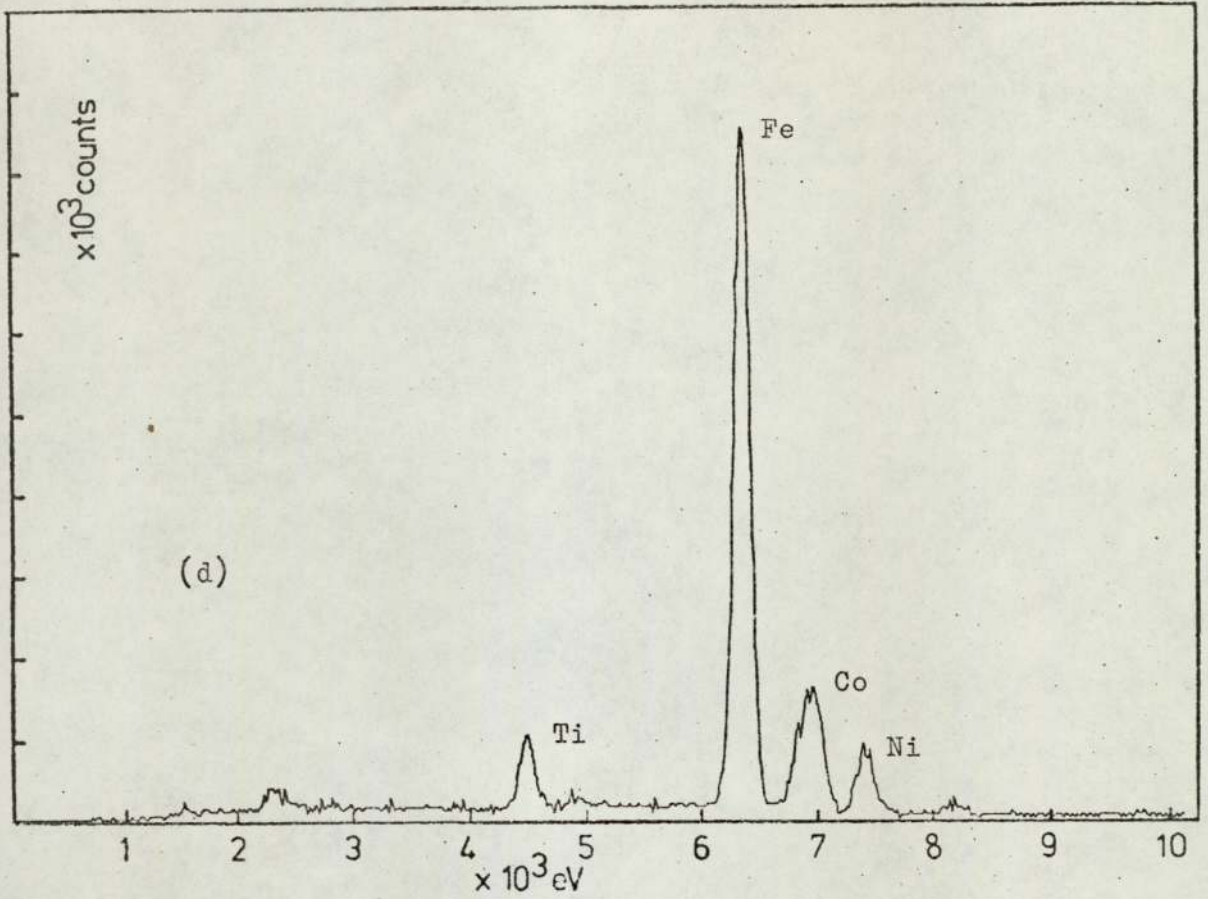
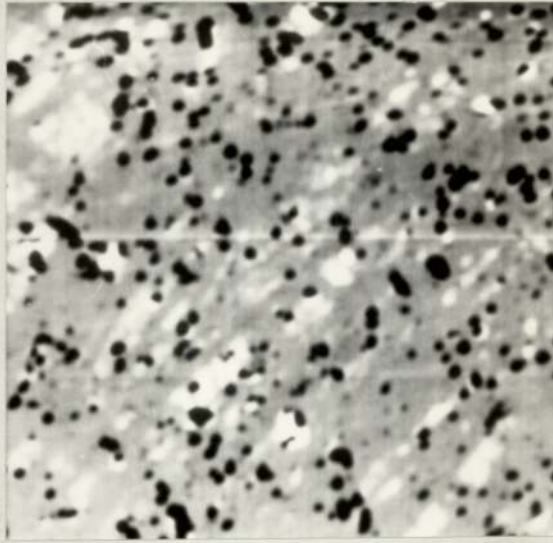


Fig.66(d). Area Analysis of Elements in the Matrix of Fig.66(b).
 (e). Spot Analysis of Elements in a Particle of Fig.66(b).



→1/20 P.S.←

Fig.67(a). Electron-Image (Reversed) and Line of Trace of a Selected Area of Matrix of M_1 Series of M.S. Compact.

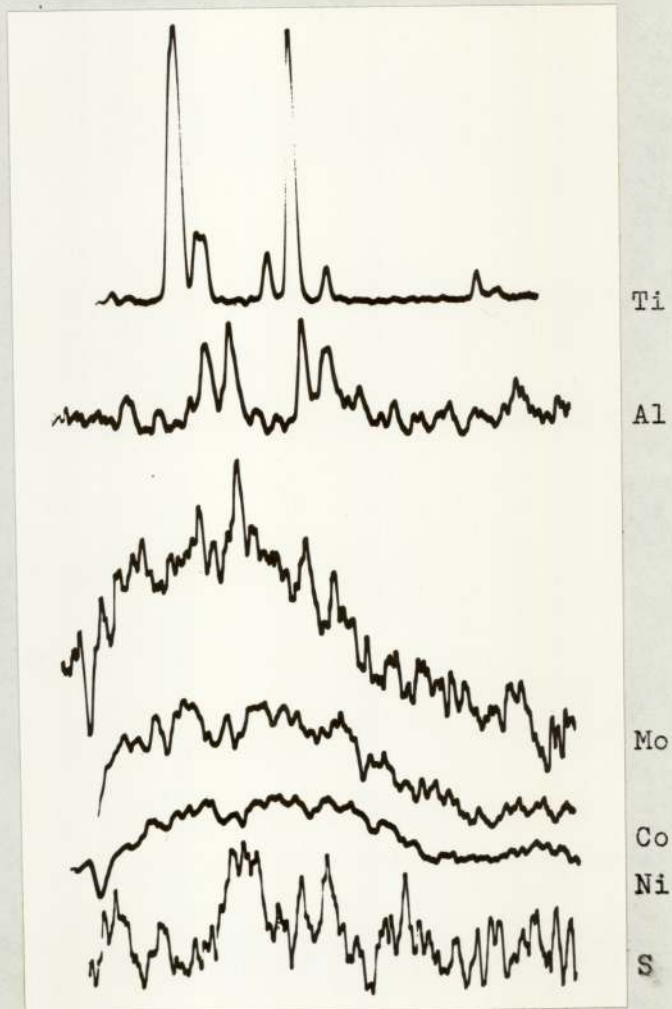


Fig.67(b). Typical Distribution Pattern of Elements along the Line of Trace of Fig.67(a).



|←1/10 P.S.→|

Fig.68. Typical Distribution Pattern of Inclusions
in M_1 Series of M.S. Compacts. Unetched.



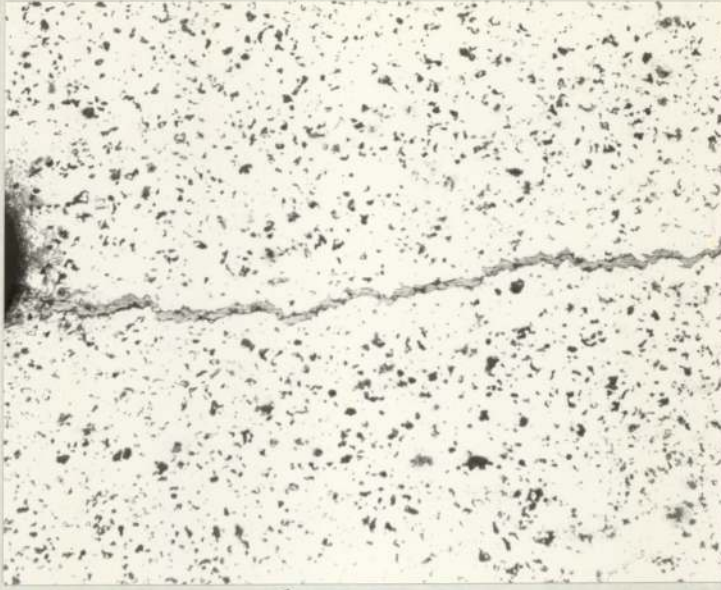
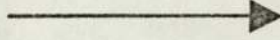
|←1/10 P.S.→|

Fig.69. Typical Distribution Pattern of Inclusions
in M_2 Series of Diluted M.S. Compacts.
Unetched.



←1/10 P.S.→

Fig.70. Typical Distribution Pattern of Inclusions
in M₃ Series of Diluted M.S. Compacts.
Unetched.



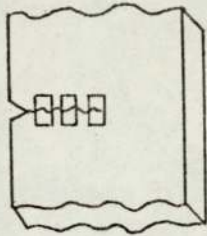
←2×P.S.→

Fig.71. Uneven Crack-Path in the Unetched Condition.

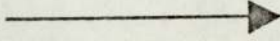


←2×P.S.→

Fig.72. Island Formation along the Crack-Path. Unetched.



Locations of the Distinctive Features of,
and along, Crack-Path.



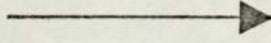
|←1/10 P.S.→|

Fig.73. Crack-Forking and Arching.



|←1/10 P.S.→|

Fig.74. Crack-Branching.



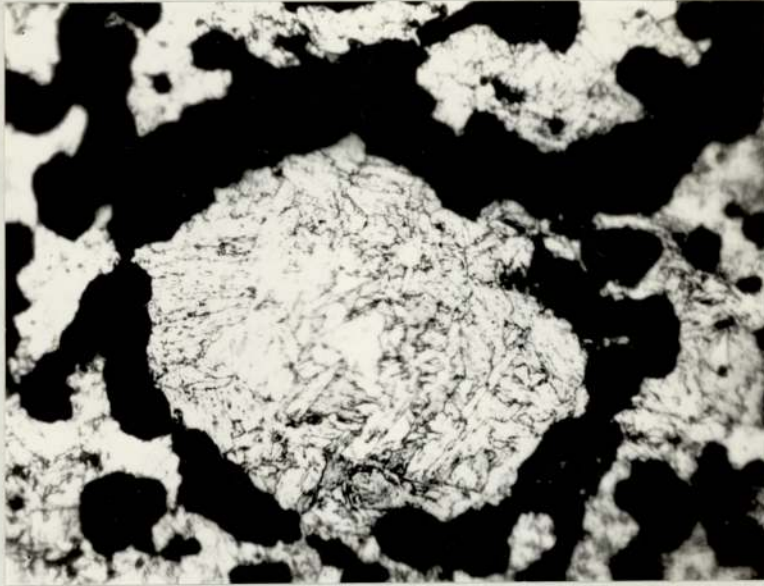
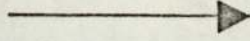
↳1/10 P.S.↳

Fig.75. Crack-Arching.



↳1/10 P.S.↳

Fig.76. Island Formation.



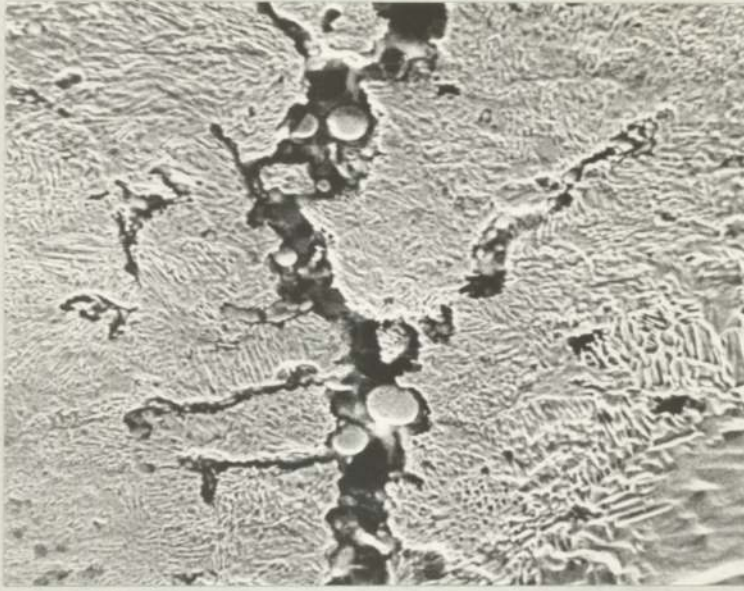
←1/10 P.S.→

Fig.77. Pseudo-Island Formation.



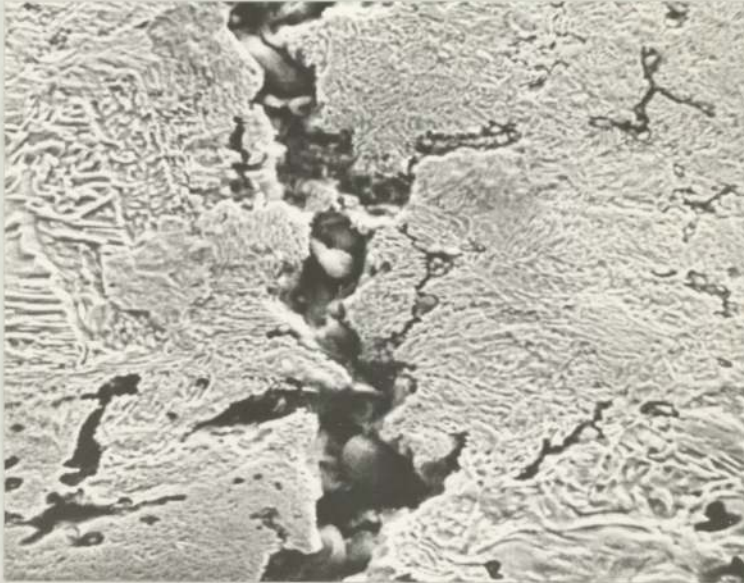
←1/10 P.S.→

Fig.78. Crack-Tip Lost in Clusters of Pores.



← 1/5 P.S. →

Fig.79. S.E.M.-Image of Crack-Path Showing Effect of Pores and Inclusions in Crack Extension.



← 1/5 P.S. →

Fig.80. S.E.M.-Image of Crack Damage.





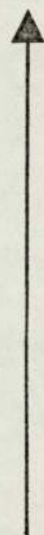
←1/10 P.S.→

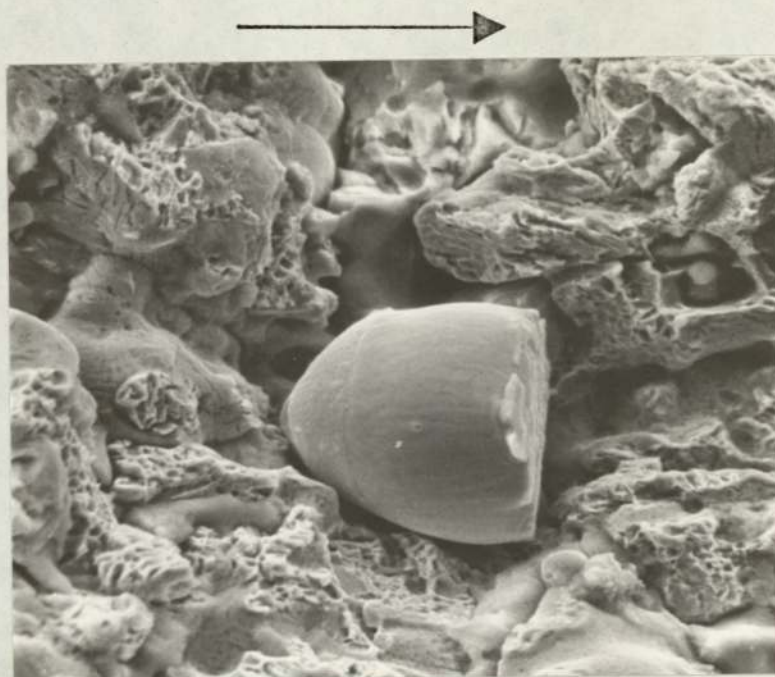
Fig.81. S.E.M.-Image of Island Formation.



←1/20 P.S.→

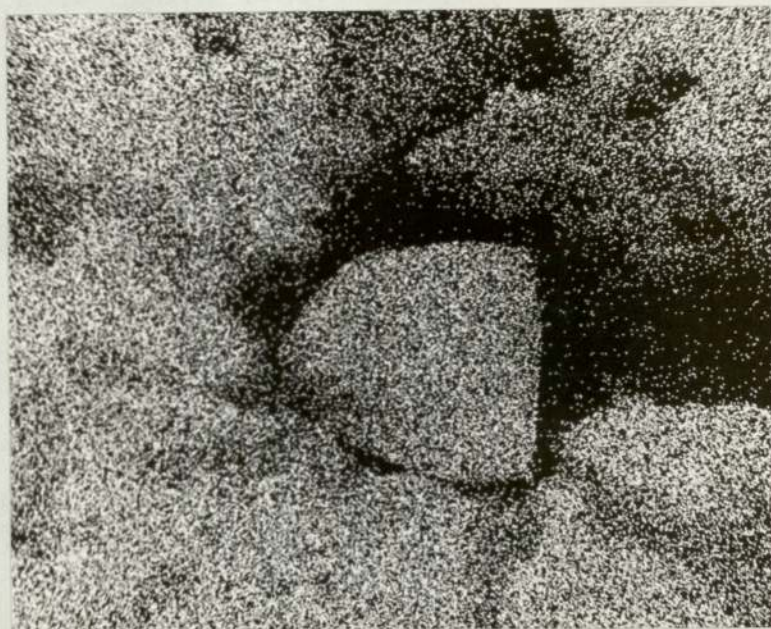
Fig.82. S.E.M.-View of Fracture Surface Showing Tensile Dimples of Various Sizes.





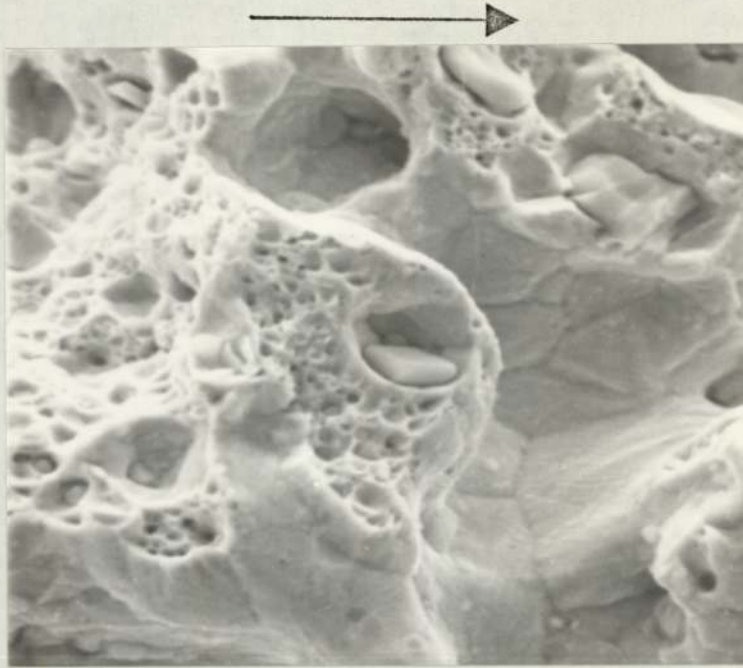
←1/10 P.S.→

Fig.83(a). Round Particle in the Fatigue Surface Showing Least Tendency to Sinter-Bonding.



←1/10 P.S.→

Fig.83(b). Fe X-Ray Image of the Particle in Fig.83(a).



←1/25 P.S.→

Fig.84(a). S.E.M.-View of Fast Fracture Surface with Well-Defined Grain Boundaries imprinted in the Internal Surface of the Pores.



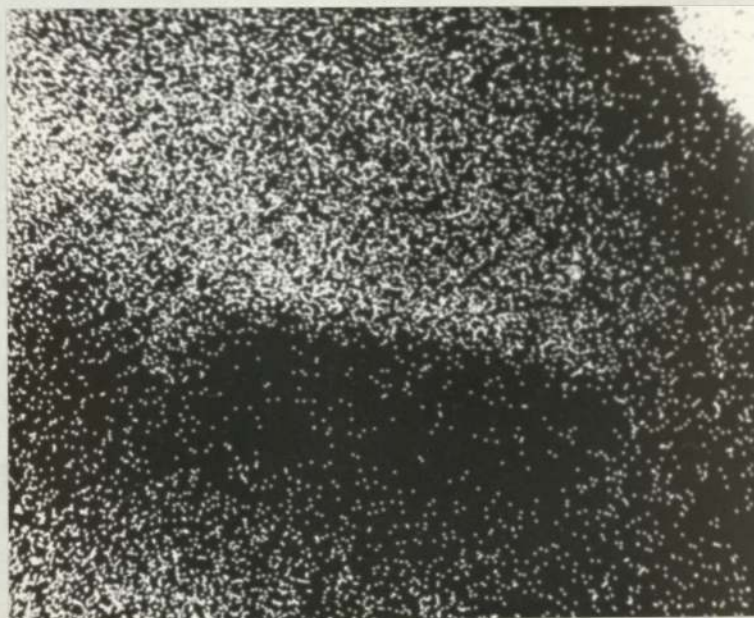
←1/100 P.S.→

Fig.84(b). Cubic Ti (C,N) Particle Shown in Fig.84(a) at High Magnification.



←1/100 P.S.→

Fig.84(c). Ti X-Ray Image of the Enlarged Particle shown in Fig.84(b).



←1/100 P.S.→

Fig.84(d). Fe X-Ray Image of the same Particle.



←1/100 P.S.→

Fig.85(a). Split Ti(C,N) Particle in the Fracture Surface.

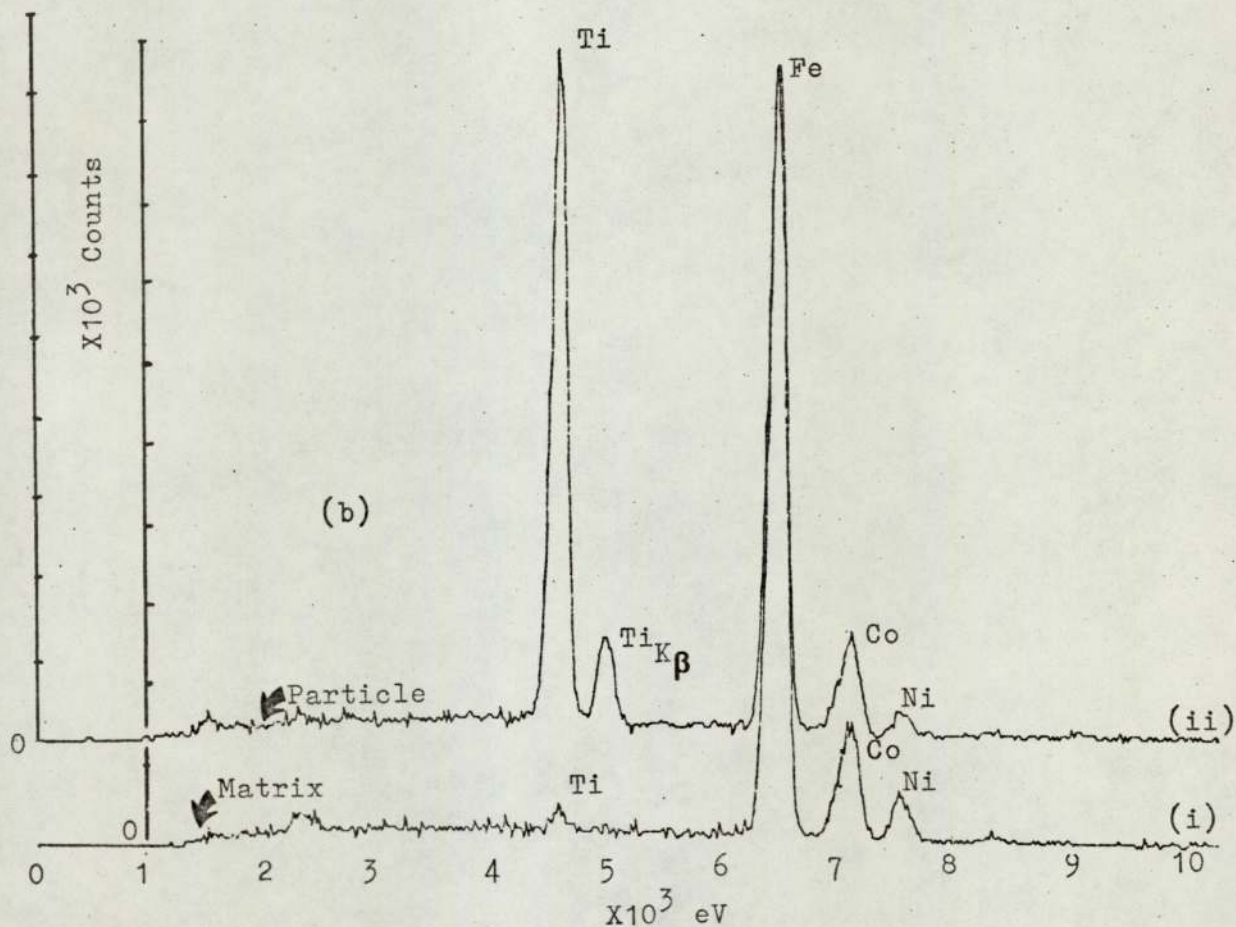


Fig.85(b). (i) Area Analysis of Elements in the Matrix of Fig.85(a).
(ii) Spot Analysis of Elements in the Split Particle of Fig.85(a).

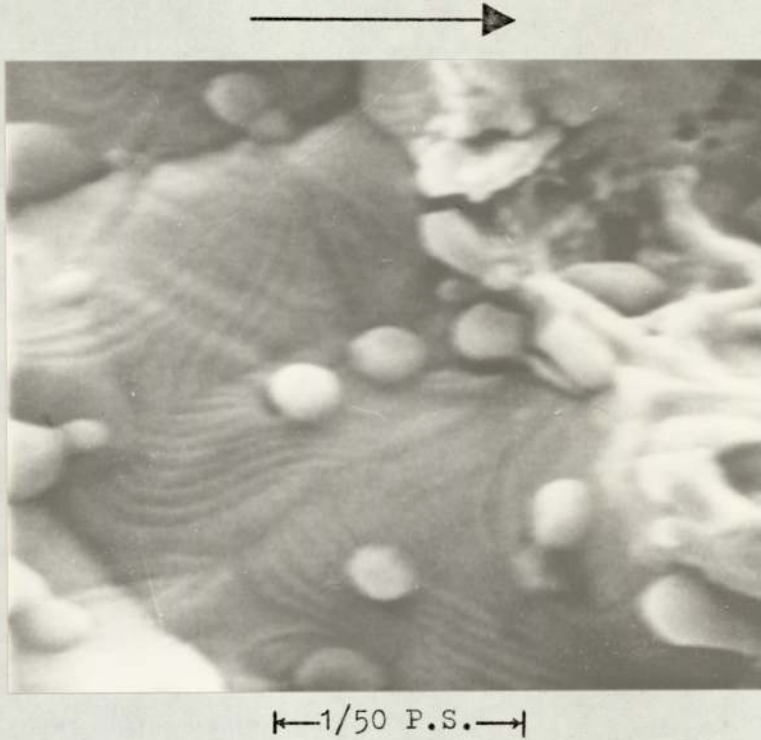


Fig.86. Ti (C,N) Particle Fusion-Bonded to the Internal Pore Surfaces with Signs of Thermal Etchings.

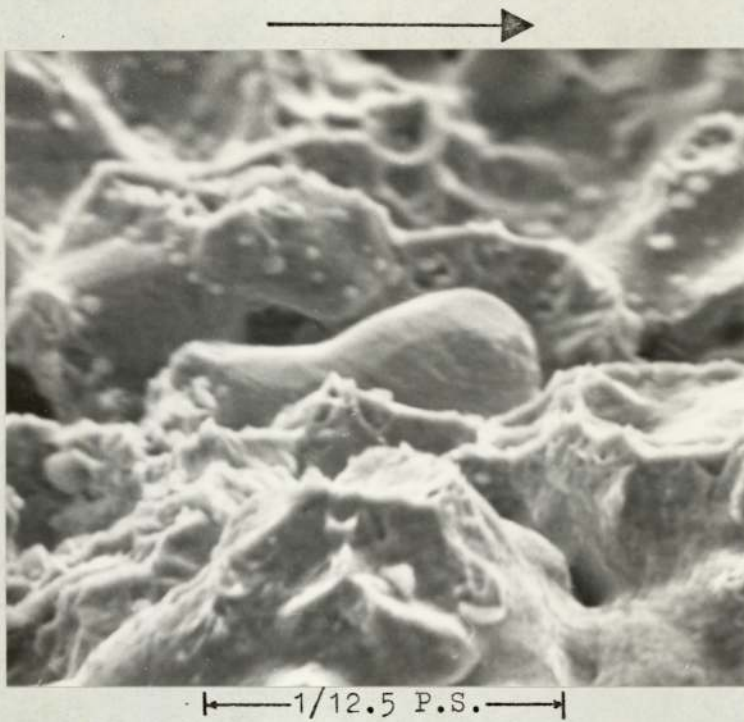


Fig.87(a). Decohesion of an Iron-Rich Particle.

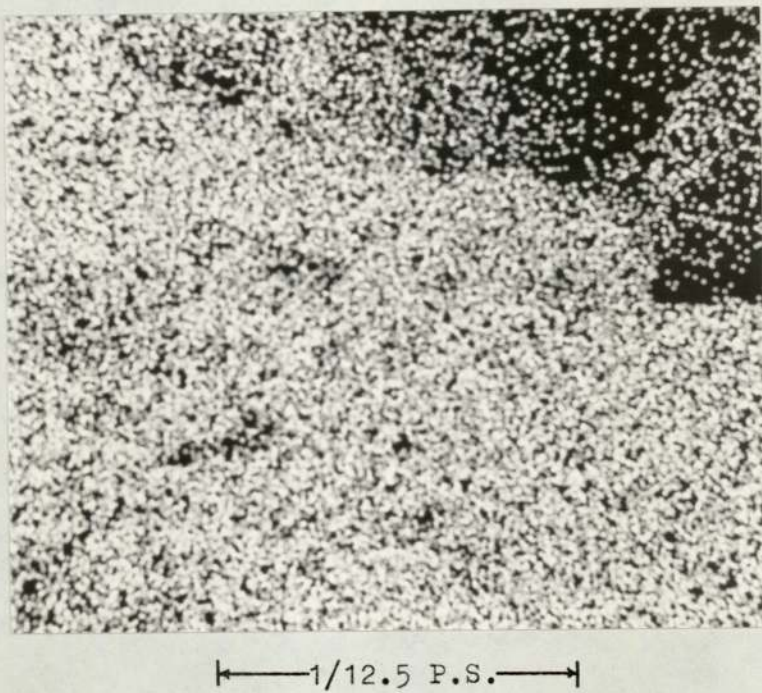
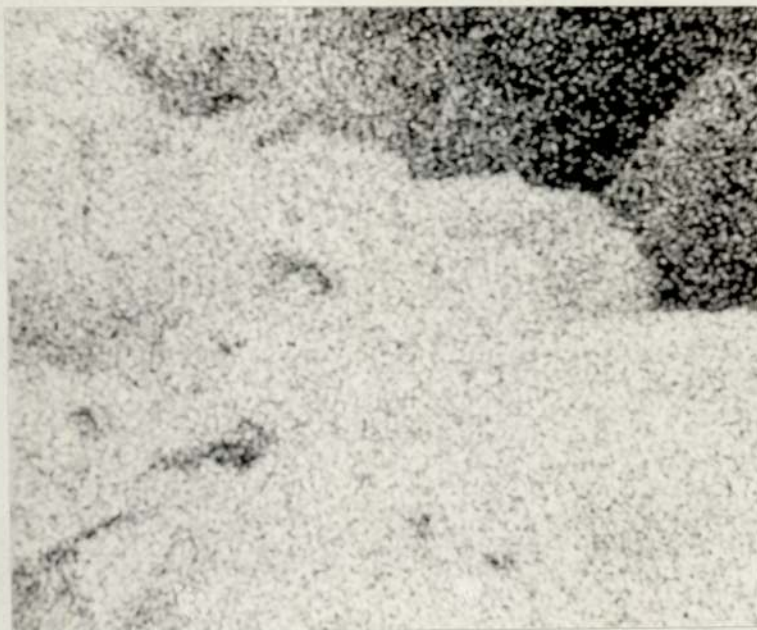
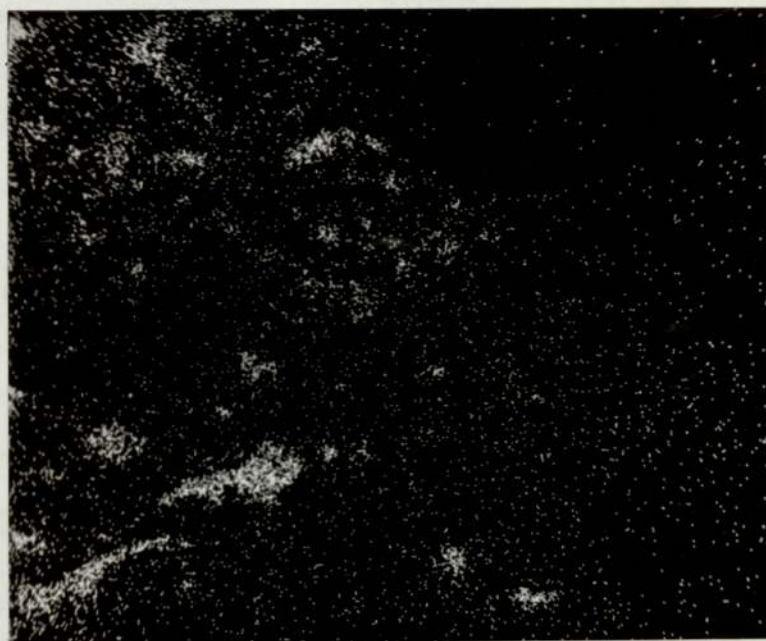


Fig.87(b). Co X-Ray Image of Fig.87(a).



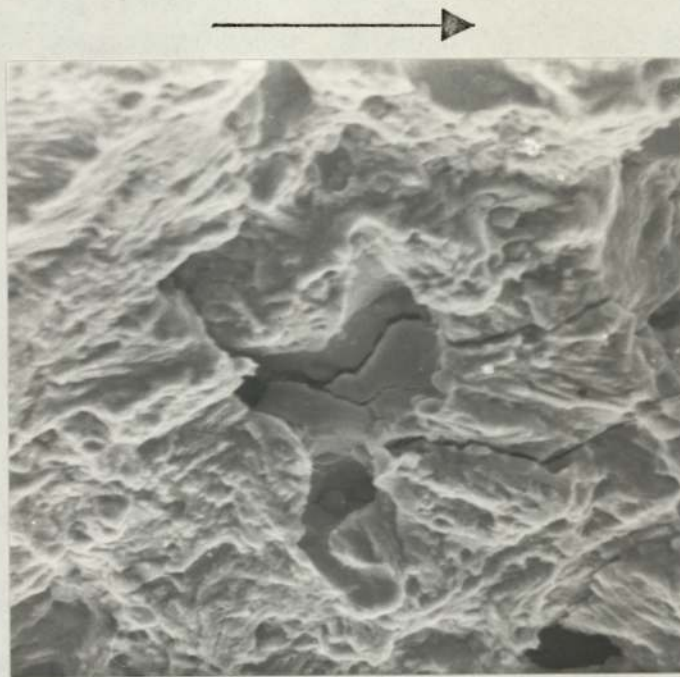
←1/12.5 P.S.→

Fig.87(c). Fe X-Ray Image of Fig.87(a).



←1/12.5 P.S.→

Fig.87(d). Ti X-Ray Image of Fig.87(a).



←1/20 P.S.→

Fig.88. Deep Intergranular Branch Cracks.



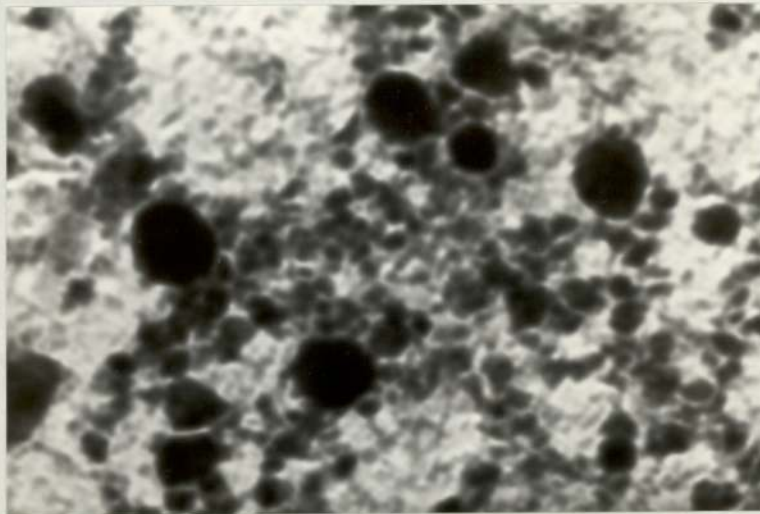
←1/100 P.S.→

Fig.89. T.E.M.-View of Different Types of Dimples and Thermal Etchings.



1/500 P.S.

Fig.90. Extraction Replica Micrographs of
(a) $\text{Ni}_3(\text{Al},\text{Ti})$ Precipitates and



1/1000 P.S.

Fig.90. (b) $\eta\text{-Al}_2\text{O}_3$ Precipitates.

10. DISCUSSION

From an inspection of the sintered density data on maraging and diluted maraging steel compacts, Table III, it has been found that the original "Green Density Vs. Compaction Pressure" matrix, which was designed and found satisfactory with minimum of experimental error, has shifted to the left, as shown below, in stages ('target' green densities and corresponding sintered densities obtained in each level are also shown):

		<u>Green Density Levels</u>			
		<u>1</u>	<u>2</u>	<u>3</u>	
(a)	M_1	d_1 (5.8)	d_2 (6.1)	d_3 (6.4)	} ORIGINAL MATRIX
	M_2	d_1 (5.8)	d_2 (6.1)	d_3 (6.4)	
	M_3	d_1 (5.8)	d_2 (6.1)	d_3 (6.4)	

		<u>Sintered Density Levels</u>		
		<u>1</u>	<u>2</u>	<u>3</u>
(b)	M_1	d_1 (M_1) (6.9)	d_2 (M_1) (7.1)	d_3 (M_1) (7.3)
	M_2	d_1 (M_2) (6.7)	d_2 (M_2) (6.9)	d_3 (M_2) (7.1)
	M_3	d_1 (M_3) (6.5)	d_2 (M_3) (6.7)	d_3 (M_3) (6.9)

where, due to shift in sintered density,

$$d_1 (M_1) = d_2 (M_2) = d_3 (M_3) \text{ and}$$

$$d_2 (M_1) = d_3 (M_2), \text{ as shown}$$

Written in proper order, the new sintered density levels can be arranged as:

New Sintered Density Levels

			<u>1</u>	<u>2</u>	<u>3</u>
M_1			$d_1(M_1)$ (6.9)	$d_2(M_1)$ (7.1)	$d_3(M_1)$ (7.3)
M_2	$d_1(M_2)$		$d_2(M_2)$ (6.9)	$d_3(M_2)$ (7.1)	(-)
M_3	$d_1(M_3)$	$d_2(M_3)$	$d_3(M_3)$ (6.9)	(-)	(-)
(Left Hand Side)			(Right Hand Side)		

creating voids (-) or imbalances in the matrix.

To maintain proper balance and symmetry in the matrix, specimens with sintered density shown on the left hand side of the matrix have been discarded, while sets of new specimens have been compacted following extrapolation of calibration curves to complete the right hand side of the matrix.

The shift in the sintered density seems to arise from the particular sintering behaviour of maraging steel powder when combined or diluted with iron powder in different proportions. The variation of density, as indicated in the green and sintered density matrix shows that for the same green density level 1 (green density 5.8 Mg/m^3) compacts in the M_{11} group have the highest gain in sintered density, the lowest gain being shown by compacts in the M_{31} group. The same trend is shown by compacts at progressively higher green density levels (6.1 and 6.4 Mg/m^3). This gain in density has been manifest in the contracted specimens after sintering. Maraging steel powder, when mixed in definite proportion with pure iron powder, results in compacts less dense than compacts made of maraging steel powder after sintering.

Since no dilution had been carried out with iron powder in case of Ancoloy SA (ASA in short) compacts, there was no disproportionate shift in sintered density. The sintered density obtained in these compacts was lower than the initial green density and this was due to carbon-loss during sintering.

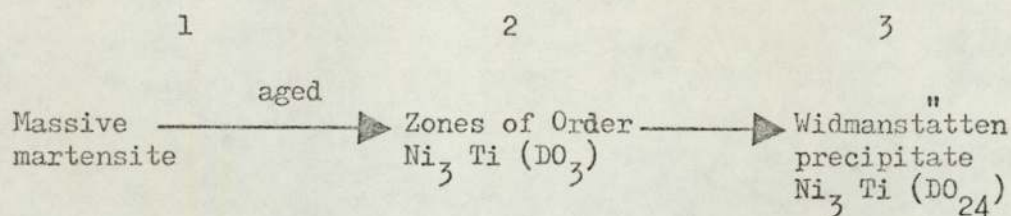
10.1 IMPORTANCE OF TITANIUM IN MARAGING STEELS.

The influence of titanium on the properties of the sintered maraging steel compacts can be best understood by considering its importance in the wrought maraging steel, as detailed in section 3.5.2. The higher strengths in the 18% Ni maraging steels are achieved mainly by increasing the titanium content and its importance can be realised from the fact that, in wrought form, for each 0.1% Ti, the yield strength is increased by 68.9 MN/m^2 (10 Ksi). The NTS/TS ratio decreases in air melts containing more than 0.4% Ti, Fig. 5. This drop-off is very sharp for maraging at 485°C (905°F), dropping to a NTS/TS ratio of 1 at 0.6 to 0.7% Ti. A Ti content of 0.7% was found to be the upper limit by Decker et al.⁽¹⁰⁾ Banerjee and Hauser⁽²⁰⁾, quoted an upper limit of Ti ~1.1% in 18% Ni-Fe base material without adverse effects on mechanical properties; in fact, it was shown to develop a Hardness of about 43 Rc, Fig. 91. The figure also shows the effect of low Ti or lack of it (as in LTM group of compacts in the present work) on 18% Ni-Fe base. Low Ti has also adverse effect on the NTS/TS ratio, as shown in Fig. 5.

The particular mechanism, which operates contributing to hardening, depends upon the nature, size and density of the precipitate distribution. Much work has been done towards identifying the composition and structure of these precipitates, but the results to analyse the precipitate phases are by no means in agreement. A general trend, however, suggests that Mo precipitates out as Ni_3Mo under normal ageing conditions. This is a metastable phase, being replaced, on overaging, by Fe_2Mo or a sigma phase. Ti generally appears to form Ni_3Ti , but this is generally difficult to identify in the presence of Ni_3Mo , and so a complex $\text{Ni}_3(\text{Mo}, \text{Ti})$ may actually exist^(27,34). Other

elements are normally found to be present in these precipitates, but Co is the exception, appearing to remain entirely in solution. In the present study, the only precipitates that could be analysed were extracted from the fractured surfaces, and analysed as $Ni_3(Al,Ti)$ and $\eta-Al_2O_3$; other precipitates were too small to be analysed by electron diffraction.

The hardening effect of titanium is due to the fact that its addition to 18% Ni maraging steels results in the formation, in the overaged condition, of a lath-like Widmanstätten precipitate formed with its long axis parallel to the $\langle 111 \rangle$ direction of the matrix, and having the composition and structure of Ni_3Ti . However, in the condition of maximum hardness, although a Widmanstätten precipitate is present in thin foils as observed by Miller and Mitchell⁽³¹⁾ and can be associated with streaking of the thin-foil diffraction patterns, a fine spheroidal precipitate is also present in an amount much too plentiful to result from the viewing of the Laths end-on. Miller and Mitchell⁽³¹⁾ found faint spots in the $\{100\}$ matrix reflection position, but these cannot result from either streaking caused by the precipitate, or double diffraction, but are an indication of ordering. It seems probable that ordering may occur as a pre-precipitation reaction, involving the spheroidal zones. This ordering could possibly be based on the $NiTi, B_2$ structure, or more likely on a metastable Ni_3Ti, DO_3 structure. Co, which also forms ordered b.c.c. compounds with Fe, could possibly stabilize formation of these ordered zones at peak hardness even though, in the final equilibrium precipitate, Co is not present in detectable amounts. Thus the hardening mechanism of Ti may be suggested as:



where peak hardness occurs between 2 and 3.

Though it is important to have the right percentage of titanium content in the 18% Ni sintered maraging steel to develop and realise the potential mechanical properties, difficulties have been encountered in the production of the pre-alloyed maraging steel powder with the specified titanium content, due mainly to the tendency of titanium to oxidise, segregate, and separate out only to combine with dross and film which may be developing in the melt. It is, therefore, essential to have an inert atmosphere melting plant to avoid loss of titanium.

10.2 CRACK INITIATION RESULTS

Taylor⁽¹⁶⁹⁾ and Parkin⁽²⁷⁾ dealing with initiation studies on maraging steel, found that the initiation characteristics depend on the condition of the material. For the maraging steel, Taylor and Parkin found that the initiation life is better in the solution treated, machined and aged condition than in the fully heat treated and machined condition. In the former, the ageing temperature is too low for recrystallisation, but there will be a tendency for residual stresses, which are compressive, to be relieved and the surface will be oxidised if the treatment is carried out in air. Moreover, there will be an additional major change, which is the precipitation of the hardening phase on dislocations. Since the surface of the notch contains a high dislocation density, as a result of the machining operation, this structure will be effectively locked in by the precipitation, forming a strong surface layer. This argument is supported by the higher hardness value in the vicinity of notch surface than the bulk material. Taylor⁽¹⁶⁹⁾ and Parkin⁽²⁷⁾ could find no hardness increase on the surfaces of specimens machined after ageing. This means that the strengthening effects of precipitation more than balances the weakening effects of oxidation and stress relieving.

The significance of the above observations lies in the fact that the sintered specimens used in the present study were sintered, solution treated, machined/notched and aged. Whatever the beneficial effect of this sequence of operations in the initiation, there was found no significant hardness increase in the vicinity of the notch tip in these specimens aged after machining and notching operations. Since no other heat treatment sequence was followed for these compact specimens, the change in initiation behaviour encountered in the

material of such compact nature, may arise from some combination of the following factors:

- (a) the specimens being compacted to different density levels and
- (b) made to different compositions by dilution with pure iron powder in certain proportions
- (c) the particular distribution and alignment of pores at the notch tip, and
- (d) the presence of residual compressive stresses, however slight, after the low temperature ageing operation.

Early attempts to study the material behaviour in fatigue crack initiation used a stress concentration factor approach which yielded design information expressed as a relationship between N_i , the number of cycles to initiation of a fatigue crack from a notch, and $K_T \cdot \Delta S$, where K_T is the Neuber elastic stress concentration factor for the particular notch, and ΔS is the range of nominal stress from zero to S_{max} .

Following the examples of Weertman⁽¹⁴⁸⁾, Bilby and Heald⁽¹⁷⁰⁾, Jack and Price⁽¹²³⁾, a stress intensity approach has been used in the present study to provide a general description of crack initiation and propagation in the notched specimens. Weertman⁽¹⁴⁸⁾, Bilby and Heald⁽¹⁷⁰⁾ used a model of plastic relaxation at the crack tip to develop an expression relating N_i , the number of cycles to initiate a crack to the stress intensity factor range ΔK in the form

$$N_i = \frac{2 \gamma G}{\pi a \sigma^2} (\approx \Delta K^2) \dots \dots \dots (39)$$

where $\gamma = \Phi_c \cdot \sigma_y$ is a measure of the plastic work done per unit area of fracture Φ_c is the critical value of the cumulative displacement at which the crack initiation is considered to occur,

and G is the shear modulus. It was assumed here that, when the sum of the plastic displacements at the crack tip exceeded the critical value Φ_C , the crack would extend.

Though this approach provides no significant improvement to the design criteria, it leads to an unified approach in crack initiation and propagation in the notched specimens and enables comparisons with other workers.

The initiation results plotted as N_i Vs. $K_T \cdot \Delta S$ for the compact specimens, Fig. 47, show a distinct banding effect in the two levels of notch root radii tested. This effect exists even if plotted as N_i against $\Delta K / \rho^{1/2}$, Fig. 48, where ΔK is the range of stress intensity factor which would exist if the notch were a sharp crack of the same depth as the notch, ρ being the measured root radius for the notch. Jack and Price⁽¹²³⁾ used mild steel specimens, which were annealed after notching, and obtained good correlation of N_i with the parameter $\Delta K / \rho^{1/2}$, without much scatter or any banding effect. The initiation data, on the other hand, replotted as N_i Vs ΔK with a lower powdered exponent of root radius, Fig. 92 shows that the banding effect is markedly reduced, though some scatter still persists in the plot. A possible explanation could be found in the existence of residual stresses and/or work-hardening in the notch due to machining.

According to Neuber⁽¹¹⁸⁾, K_T has a roughly $\frac{1}{\rho^{1/2}}$ dependency (Appendix I), and taking into account of the fact that residual compressive stress, even after low temperature ageing operation, is an additional source of stress superimposed on the existing stress concentration, the real relationship between N_i and $\Delta K / \rho^n$ tends to become empirical in order to compensate for the variation in stresses needed to initiate cracks from blunt and sharp notches. The plot in Fig. 92 is based purely on empirical analysis of the data where a lower power of ρ ($n = 0.3$) in the relationship

$$N_i = B \left(\frac{\Delta K}{\rho^n} \right)^q \dots\dots\dots (40)$$

has been employed, whereby the banding effect has been markedly minimised. Pearson⁽¹²⁵⁾ also found distinct banding effect when his initiation results were plotted according to notch root radius. He used notched aluminium alloy specimens without heat-treatment subsequent to notching, and so these specimens contained any residual stresses and/or work-hardening.

The initiation data as plotted in terms of N_i Vs. ΔK , Fig.51, also show reduced banding effect, though with some scatter, which should not be considered unusual for materials of such sintered nature. In this plot, it has been found that $N_i \propto (\Delta K)^{-n}$, where $n \approx 3.5$, similar to Jack and Price's⁽¹²³⁾ plot, where n was found to be 4.

From the Fig. 51, it is also clear that the blunter notches have better initiation life than sharper notches. From an inspection of the initiation plots in Fig. 48, it is found that the higher density and higher % dilution with iron powder generally result in superior initiation life. In other words, the lower density compacts are notch-sensitive, and need lower number of cycles for initiation from notches.

Jack and Price⁽¹²³⁾ observed that, below a certain critical root radius, initiation was independent of root radius, this critical value being independent of the stress and notch depth. Jack⁽¹²⁶⁾ examined Weibull's⁽⁷⁷⁾ work on aluminium alloys and found that the results were consistent with the existence of a critical root radius. A similar conclusion can be drawn from the work of Wilkins and Smith⁽¹⁷¹⁾ on an Al-Mg alloy. This means that a critical root radius may exist for all alloys, and in the present case, if it exists at all, it must be less than 0.127 mm. Pearson⁽¹²⁵⁾ also, more or less came to the same conclusion.

Since the detection of a fatigue crack is the sole criteria of crack initiation, some crack growth must occur in order to be sure that the initiation has taken place. So, in general,

$$N_{\text{measured}} = N_{\text{true}} + N_{\text{Propagation.}}$$

In order to make the stresses equal at the tips of two notches of unequal root radius, a higher nominal stress must be applied to the specimen with the blunter notch. Now, since the notch stresses are made equal, the N_{true} values will be equal (ignoring the size effect). Once cracks have nucleated at the notch tips, then to a first approximation, the nuclei and notch can be considered a single crack. Since the specimen with the blunter notch has a higher applied stress, the crack in that specimen will grow to the defined initiation length faster.

Attempts have been made by some researchers to explain banding encountered in initiation data by considering certain initiation criteria as the number of cycles for a crack to attain a 'length' of, say, 0.127 mm. Taylor⁽¹⁶⁹⁾ used Jack and Price's⁽¹²³⁾ parameter of $\Delta K/\rho^{\frac{1}{2}}$ and a crack length of 0.125 mm. as the criteria for initiation in the fully heat treated and machined maraging steel specimens. He observed evidence of banding and a broader scatter band than for his original data, without any 'length' criteria for initiation. He repeated the process for machined titanium alloy specimens, but failed to get any evidence of banding, when compared to his original data for the material without any 'length' criteria for initiation. Gowda et al.⁽¹²²⁾ also found that mild steel and Al alloy 7075-T6 are insensitive to the definition of N_i . So it is safe to suggest that sensitivity to the definition of N_i depends on the alloy being tested. Since no investigation was carried out into this aspect using the

present material, the explanation for banding still needs further exploration.

The banding effect as shown by the compact materials, when the initiation data is plotted as Ni against $K_{T} \cdot \Delta S$ or $\Delta K / \rho^{1/2}$, might be characteristic of these materials due to their inherent inhomogeneity. Although the attempts to plot the initiation data and unify the results within a single scatter band by such parameter as $\Delta K / \rho^{0.3}$ or simply ΔK against Ni might conceal this characteristic, it helps providing an adequate method for engineering design. In other words, the initiation data as presented in Fig. 51, 92 fulfills the requirements for safe design criteria for the compact materials tested. This information enables one to draw a conservative line below which initiation would not occur, and then scale down from this line by applying a safety factor on the allowable stresses.

For specimens containing sharp notches in plane strain, Jack's⁽¹²⁶⁾ relationship between Ni and the range of stress intensity factor was of the type $Ni \propto (\Delta K)^{-4}$, whereas, for the sintered specimens, a relationship of the type $Ni \propto (\Delta K)^{-3.5}$ has been observed. Weertman⁽¹⁴⁸⁾ and Bilby and Heald⁽¹⁷⁰⁾ predicted a relationship of the type $Ni \propto (\Delta K)^{-2}$ as shown in equation (39).

A possible reason for the discrepancy is due to the fact that the theoretical results are dependent on the assumed material behaviour built into the mathematical models. Bilby and Heald⁽¹⁷⁰⁾ obtained their expression for ϕ_c , the critical crack tip displacement at which the initiation is considered to occur, by linear summation of the displacements resulting from each cycle, and these displacements are assumed to be confined to a single slip plane in this model. In practice, it is likely that deformation occurs randomly on several slip planes. Others are statistical models^(172, 173) in which the

accumulation of fatigue damage is proportional to the square of the plastic strain to obtain theoretical justification for the Manson-Coffin relationship. There is also some experimental evidence from results on austenitic steel in high strain fatigue⁽¹⁷⁴⁾ which can be used to show that N_i is inversely proportional to the square of the plastic strain range for plastic strains of less than 1%. If it is assumed that the critical displacement Φ_c in the Bilby and Heald's⁽¹⁷⁰⁾ analysis is obtained by summation of the squares of the individual displacements i.e. a random rather than a linear summation, their expression becomes

$$N_i \propto (\Delta K)^{-4}$$

which agrees with the results for sharp notches in some materials⁽¹²³⁾. Although Bilby and Heald's analysis⁽¹⁷⁰⁾ applied strictly to sharp cracks, Smith⁽¹⁷⁵⁾ has shown that this treatment should be applicable to notches. Smith's analysis predicts that the displacement at the notch tip is reduced by a factor of about 2 as the root radius increases from 0 to 0.250 mm. for a 2.5 mm. deep notch. The present results show that experimentally there is no effect of root radius in this range. Similar behaviour has been observed in brittle fracture where it has been found⁽¹⁷⁶⁾ that there is a critical notch root radius below which further sharpening does not reduce the fracture toughness. This effect is generally ascribed to the fact that a particular mechanism requires a minimum volume or critical element over which to operate.

The dependence of N_i on a particular inverse power of ΔK or on the effective range of stress intensity factor in the form of $\Delta K/\rho^{\frac{1}{2}}$ or $\Delta K/\rho^{0.3}$ can be understood by studying the actual material behaviour in terms of the appropriate microstructural processes. In the sintered steels studied, the measured notch root

radius ρ may not be effectively the machined notch root radius, since the effective root radius of the notch may have been affected by the presence of the pores at the base of the notch, also plastic blunting may disturb the actual radius and may have a bigger effect at high ΔK values. So it may be argued that the effective range of stress intensity factor $\Delta K/\rho^{\frac{1}{2}}$ or $\Delta K/\rho^{0.3}$ does not adequately represent the real ΔK . In fact, there are calculations⁽¹⁷⁰⁾ which incorporates correction factors taking care of the presence of the blunt notch of root radius ρ . The effective stress intensity factor (K_{eff}) for a blunt notch is related to that for a sharp crack or notch by

$$K_{\text{eff}} = K \left(\frac{\rho_0}{\rho_e} \right)^{\frac{1}{2}} \dots \dots \dots (41)$$

where ρ_0 is the critical value of ρ

ρ_e is the effective root radius

$$\rho_e = \rho \quad \text{when} \quad \rho \geq \rho_0$$

$$\rho_e = \rho_0 \quad \text{when} \quad \rho \leq \rho_0$$

i.e. no correction would seem necessary once ρ is less than ρ_0 , the limiting sharpness for the material. Experiment by Jack⁽¹²⁶⁾ indicates a dependence of N_i on ΔK^{-4} when $\rho < \rho_0$. Eventually as the fatigue crack grows and reaches beyond the range of the radius ρ , no correction would seem necessary.

As mentioned earlier, Jack and Price⁽¹²³⁾ found a critical root radius of 0.25 mm (0.010") below which N_i was not reduced. A similar feature was also mentioned by Cottrell⁽¹⁷⁶⁾ who showed that notches of less than a critical radius must blunt to that critical radius prior to crack propagation in fast fracture and so did not reduce fracture toughness. Jack⁽¹²⁶⁾ justified his finding of the existence of such a critical root radius by demonstrating that the distance, r_0 , ahead of his notches at which the stress was equal to

that for a sharp crack was equal to one quarter of the root radius. Thus, for a 0.250 mm. (0.010") notch, this distance was of the order of the grain size of the material used by Jack, which may be described as a critical element or a minimum volume of material over which the prevailing mechanism can operate. Ahead of blunter notches, the stress at the tip of this critical element is less than at the same distance ahead of a sharp crack, and so N_i will be increased. Jack⁽¹²⁶⁾ based his argument on an approximate expression developed by Weiss and Yukawa⁽⁶⁰⁾ for the longitudinal stress distribution at a distance r ahead of the notch of root radius ρ ; in its simplified form, the expression can be written as:

$$\sigma_1 = \sigma \left[2 \left(\frac{a}{\rho} \right)^{\frac{1}{2}} + 1 \right] + \left[\frac{\rho}{\rho + 4r} \right]^{\frac{1}{2}} \dots \dots \dots (42)$$

where σ_1 is the longitudinal stress,

Weiss and Yukawa's approximation, in conjunction with the critical element size can be used to develop the modified stress intensity factor which describes crack initiation from a blunt notch.

when $a \gg \rho \gg r$,

$$\sigma_1 = 2 \sigma \left(\frac{a}{\rho} \right)^{\frac{1}{2}} \dots \dots \dots (43)$$

Hence the ratio of stresses σ_a / σ_b arising from the notches of root radii ρ_a , ρ_b is given by

$$\frac{\sigma_a}{\sigma_b} = \left(\frac{\rho_b}{\rho_a} \right)^{\frac{1}{2}} \dots \dots \dots (44)$$

At the end of the critical element, the stress for a notch of root radius ρ is given by the stress intensity factor, and it follows that, for notches of larger root radii

$$\sigma = \frac{K}{(2\pi r)^{\frac{1}{2}}} \left(\frac{\rho_0}{\rho} \right)^{\frac{1}{2}} \dots \dots \dots (45)$$

It must be assumed that the stress intensity factor controls displacements at the end of the critical element, and that N_i is controlled by these displacements rather than those at the notch root. On this basis, a more appropriate treatment would be to consider these displacements using the plastic relaxation model.

10.3. CRACK GROWTH RATE

The room temperature fatigue crack growth rate properties have been presented in Fig. 53 through Fig. 56 in terms of the stress intensity factor range (ΔK) Vs. crack growth rate (da/dN).

An inspection of the effect of stress ratio on fatigue threshold shows that the high load ratio (i.e. $R = 0.3$) used in the test, yields a threshold $\Delta K_{th} \sim 12 \text{ MN/m}^{3/2}$, while the lowest load ratio (i.e. $R \sim 0.07$) appears to indicate a ΔK_{th} value somewhere between 8 and 11 $\text{MN/m}^{3/2}$. This influence of stress ratio on fatigue threshold is not consistent with the findings reported by Bucci et al. (177), for ASTM A517 Grade F(T-1) steel, by Paris (178) for several high strength steels, and by Schmidt (179) for a Ti - 6Al - 4V alloy. They found that, higher the stress ratio, lower the threshold ΔK_{th} value.

Above the ΔK_{th} threshold value, an increase in stress ratio is accompanied by an increase in growth rate for equivalent ΔK . This trend is similar to that reported by other workers for many different alloys (178, 144).

The nearly linear relationship in stage 2 between $\log (da/dN)$ and $\log \Delta K$ shown in Figs. 53 through 56 is typical of the most fatigue crack growth rate data. Since this linear relationship exists, the crack growth rate data has been expressed in terms of the generalised fatigue crack growth rate law developed by Paris (66):

$$\frac{da}{dN} = C (\Delta K)^m$$

where da/dN is the rate of crack growth, C is an intercept constant determined from the $\log (da/dN)$ Vs. $\log \Delta K$ plot, m is the slope of the log - log plot and ΔK is the stress intensity factor range. As the

upper scatter band data represent a conservative estimate of the materials crack growth rate properties, the generalised crack growth rate expression describing this line is normally reported as the materials crack growth rate properties.

As reported earlier, in section 9.4, the growth rate for M_{12} and M_{21} compacts has been found to be 1.7 to 2.0 times faster than for M_{11} compacts at $R \sim 0.07$, over the range of ΔK considered (10 to 35 MN/m^{3/2}); for M_{13} and M_{22} compacts, the rate is 2.8 to 3.0 times faster than for M_{11} compacts, and for M_{23} , M_{31} , M_{32} , M_{33} compacts, the rate is 6.7 to 7.0 times faster than for M_{11} material. The rate for LTM compacts has been found to be 10.7 times faster than for M_{11} compacts. At higher stress ratio, $R = 0.3$, the growth rate for M_{13} , M_{23} and M_{33} has been found to be 6.0 to 6.2 times faster than for M_{11} compacts tested at $R \sim 0.07$.

In general terms, the above findings show that at lower stress ratio, $R \sim 0.07$, the growth rate curves for M_1 , M_2 and M_3 compacts fall on four distinctly separate scatter bands; also separate scatter bands have been obtained for LTM compacts at $R \sim 0.07$, and for M_{13} , M_{23} and M_{33} compacts at $R = 0.3$.

Fig. 93 summarises the fatigue crack growth data represented by the upper scatter bands for the compact materials. The slope (m) in all the crack growth expressions in Fig. 93 (a) is within the range 2.25–4.58, and 4.4 to 5.13 for the remaining two crack growth expressions as shown in Fig. 93 (b). The upper scatter band for M_{13} has been added in Fig. 93(b) for comparison. It is evident from Fig. 93(a) that the crack growth rate expression for the $M_{23}/M_{31}/M_{32}/M_{33}$ groups of compacts is the least conservative and will yield the greatest rate of crack growth. Therefore, the growth rate expression

$$\frac{da}{dN} = 5.1 \times 10^{-3} (\Delta K)^{4.58} \dots\dots\dots(46)$$

should be employed when making fatigue life predictions or calculating initial allowable flaw sizes applicable to M_1 , M_2 and M_3 groups maraging and diluted maraging steel compacts subjected to room temperature air environment. The Fig. 93(a) also shows that the crack growth rate expression for M_{11} compacts yields the slowest rate of crack growth. Therefore, from the point of view of fatigue crack growth rate, M_{11} compacts are significantly superior to other compacts in M_1 , M_2 and M_3 groups when tested at the low stress ratio.

Fig. 93(b) shows the influence of stress ratio on crack growth rate. Here the increased stress ratio R is accompanied by an increase in crack growth rate for the range of ΔK and growth rate considered. The crack growth rate for M_{13} , M_{23} and M_{33} compacts at $R = 0.3$ is 2.2 to 2.5 times faster than for M_{13} compacts tested at $R \sim 0.07$, and about 6.0 to 6.2 times faster than for M_{11} compacts tested at $R \sim 0.07$, as shown in Fig. 93 (b). This figure also shows that the growth rate is slower in the lower density M_1 compacts than in the higher density M_1 compacts, but in case of LTM compacts tested at a lower density (6.6 Mg/m^3) than the lowest of the M_1 compacts (6.9 Mg/m^3), the growth rate is remarkably high; in fact, it is higher than $M_{13}/M_{23}/M_{33}$ compacts (density 7.3 Mg/m^3) tested at $R = 0.3$. This means that there is perhaps a critical density or critical porosity content in the compact materials that governs the crack growth rate.

From a study of the room temperature properties of maraging M_1 and LTM compacts, Table III, it seems that the critical porosity content lies somewhere between 16.3 and 18%, when the crack growth rate trend is reversed, that is, the growth rate is increased with

increased porosity. In case of M_2 compacts, which is basically maraging compacts diluted with 25% pure iron powder, the resulting microstructure, with lesser amount of martensites and correspondingly higher amount of ferrite, is jointly responsible along with the porosity content for generally faster growth rate. The growth rate is still faster in M_{31} , M_{32} and M_{33} compacts ($M_1 + 50\%$ iron powder, density levels 1, 2, 3), where the effect of microstructure with still higher amount of ferrite and lesser amount of martensites, is most likely the predominant feature, the role of porosity seems marginal or not significant enough. That is, on the softer microstructural side of the microstructure - porosity relationship that an explanation is to be found for the higher crack growth rate in the M_3 compacts.

Evaluation of the results on the basis of fatigue crack growth rate behaviour associated with the scatter of results, Fig. 53a, 54, 55, seemingly indicate, as also stated earlier, that the compacts in M_1 group with the lowest density exhibit somewhat superior growth rate properties than the compacts with highest density. A speculative explanation for this behaviour may be that the presence of bigger and irregular shaped porosities in the M_{11} compacts results in delayed crack growth, and, consequently, decreased growth rates. Similar behaviour has also been reported in structural steels with discontinuities⁽¹⁷⁷⁾, due to weld defects. It appears that when the main fatigue crack front encounters 'defects' of the appropriate size, type and orientation, "blunting" of the crack tip occurs and growth stops until enough cycles have elapsed to sharpen the crack tip. Unfortunately, the effect of defects or discontinuities on fatigue crack growth is not repeatably uniform. Depending on the size, shape and orientation of discontinuities present, they can also significantly increase the rate of crack growth. For this reason, one generally

encounters comparatively large amounts of scatter in the crack growth rate data obtained from compact materials containing porosities or discontinuities.

In the case of the compacts in M_3 group, where the matrix is sufficiently soft due to the presence of large amount of ferrite, the crack blunting effect due to porosities is not operative, being largely superceded by the presence of the softer ferrite. The higher crack growth rate in this group can be explained mainly due to the presence of this softer constituents. The scatter band for the growth rate for compacts in the M_3 group can effectively accommodate any small differences in the growth rates due to the small differences in the sintered densities in this group. On the other hand, the M_2 group of compacts still retain an effect of porosities in spite of the presence of lesser amount of ferrite than in M_3 group of compacts. This effect is shown by the different growth rates obtained in this group due to the different porosity levels.

For M_1 group of compacts with a martensitic matrix, it is the orientation, concentration and shape of 'voids' which seems to control the rate of crack growth. Slower growth rate at lower densities has been explained by the 'blunting' effect of the crack tip, due to the presence of bigger and irregular shaped 'voids' along the crack path. At higher densities, one would expect the presence of smaller and rounder voids with lesser surface area in the compacted mass. Of course, it would not also be difficult for one to expect, at higher densities, a significant amount of these 'voids' to be severely compressed or 'squashed' with sharp corners and favourably oriented along the crack path. It could be that the compaction pressure, and sintering time and temperature, though high, were not sufficient enough to close or absorb these 'voids' into the matrix, or even

render the corners sufficiently harmless by making them somewhat blunter by the sintering mechanism.

It is the presence of these type of voids in adequate numbers, and favourably oriented along the crack path, which may have contributed to the lower fatigue resistance in this group of compacts at higher densities. This also seems to be the speculative explanation for the faster growth rate with increasing density, for the M_2 group of compacts.

At the present state of the art, sufficient information regarding the influence of defect characterisation on fatigue crack growth is not available to permit further generalisations.

The slopes of the crack growth rate curves for M_{11} , M_{12}/M_{21} , Table VII, are in good agreement with the work of Miller⁽¹³⁹⁾ who found a slope of 2.88 for a '200' grade maraging steel and 2.53 for a '250' grade maraging steel. Van Swam et al.⁽¹⁷⁾ found a slope of 2.0 for a '300' grade maraging steel, all tested in air. The slopes of the growth rate curves for M_{13}/M_{22} etc. are higher, and so, from the point of view of crack growth rate, the compacts in M_{11} and M_{12}/M_{21} groups stand a good chance of competing with the above grade of normal maraging steels.

10.4 Fractographic and other observations.

In non-sintered materials, specially in maraging steels, the fracture generally show striated surfaces characteristic of micro-crack growth rate, and fairly indicative of macroscopic crack growth rate. In none of the fracture surfaces of the compact materials was seen any striation markings even at high magnification. Some marking, which was seen, was the characteristic thermal etching effects due to the high temperature sintering.

The particular shape and size of pores* including 'inclusions', and their general distribution, and orientation are the determining factor in the crack growth rate for M_1 group for maraging steel compacts. In the case of the compacts in the M_3 group, it is the softer microstructural features that govern the macroscopic crack growth rate. In between the two extremes lies the compacts of the M_2 group, where it is the balance between the porosity and microstructure that governs the crack growth rate.

The fracture surfaces for the sintered specimens are microscopically entirely flat, without any sheer lips. These surfaces show the characteristic ductile dimple type of failure and the presence of dimples indicates that the fracture process is basically the necking down between the crack tip and the adjacent voids. At the tip of a crack in a fully dense material, the plane strain condition promotes

* Throughout the discussion, the term 'pore' has been used to combine the sense of 'voids and inclusions', as detailed in section 9.2. Treating the inclusions as part of the 'pores' should not be too inaccurate, as the particle/matrix interfacial strength is not particularly high.

fairly high normal stresses (all three >0) and the normal/shear stress ratio is high. Such a stress situation can affect cleavage fracture before plastic deformation (associated with high shear stresses) can cause a ductile failure. However, when appreciable porosity is present, the shear/normal stress ratio is increased because of relaxation of strict plane strain conditions (approaches plane stress) on a micro scale. This allows the attainment locally of the critical shear stress for plastic deformation before cleavage and a ductile dimple failure results. With increasing porosity, the tensile strength at a micro level and hence the fracture toughness are reduced (decreasing cross-section of micro-tensile specimens). Poor toughness can also result from inclusions and second-phase particles which initiate large fracture dimples or from a fine dispersion of very small particles which initiate many small fracture dimples. It may be that the volume of the material deformed, that is, the depth of the pores and dimples in addition to their size, determines the toughness of the compact materials. If this is true, a study of the fracture surface in three dimensions would be required to obtain a correlation between the volume of metal deformed and the toughness.

In the range of sintered materials tested, the toughness increases with decreasing porosity content and is clearly dominated by the resulting yield strength. In fact, toughness increases with increase in yield strength as shown in Fig. 44, in the range of sintered density considered. The yield stress is, of course, controlled by the strength of the necks of metal around the voids which result in less than the theoretical density. Basically, the fracture process involves drawing out the neck between the crack tip and the adjacent voids on a micro scale, and this process determines the fracture energy consumption and therefore, the fracture toughness.

Basic trend of the increase in toughness with the increased yield stress is illustrated in Fig. 94, which also contains results from previous work of the author and other workers, on sintered materials. This relationship between toughness and yield strength is the opposite of that which normally arises in, say, high-strength steels, aluminium or titanium alloys.

The increase in toughness with yield strength is an interesting feature of the behaviour of sintered steels, since it suggests the possibility that high strength, highly alloyed, sintered steels could match the high-strength wrought steels, titanium and aluminium alloys, as illustrated in Fig. 95. Toughness data comparing these materials have been abstracted from Pellini's work⁽¹⁸⁰⁾ and the high toughness figures correspond to the energies absorbed in a drop-weight test⁽¹⁸¹⁾, whereas the lower toughness figures are K_{IC} values. The sintered materials examined in the present study compare well with the high-strength aluminium and titanium alloys, but an extrapolation of the toughness/yield stress trend would carry them into competition with high-strength wrought steels. There is no doubt that this possibility will tempt other investigators to venture into this meaningful field.

An attempt was made to pin down the 'effective' notch root radius (P_e), above which the apparent values of fracture toughness show a noticeable increase. With this value of P_e was compared the minimum root radius of pores (P_{min}) measured in the sintered and heat treated maraging, diluted maraging steel and Ancoloy SA (ASA) compacts, after light etching. Also, the relationships of crack opening displacement ($\frac{\delta_c}{2}$) with P_e and P_{min} were looked into, in the above

sintered materials, and the possibility of improving toughness by manipulating P_{\min} of pores was explored (Details are set out in Appendix - II).

From the results given in Appendix - II, it has been found that

$$P_{\min} < \frac{\delta_c}{2} \ll P_e.$$

In fact, the minimum root radius of the pores have been found to be extremely small compared to the 'effective' notch root radius (P_e) of specimens, above which the K apparent values tend to go up with root radius ρ . This means that some of the defects or pores in the compact materials are isolated, but with very sharp root radius. They are like any other defects in non-compact materials, and do not become operative in toughness testing situations unless they are favourably oriented. This finding is preliminary at this stage and needs further exploration.

11.

CONCLUSIONS

A distinct banding effect, possibly characteristic of the sintered materials tested had been observed when the initiation data were plotted as Ni against $K_{T\Delta S}$ or $\Delta K/\rho^{\frac{1}{2}}$ for the two levels of notch root radii of 0.127 and 0.762 mm.

Banding effect was markedly reduced when the initiated data was replotted as Ni against ΔK or an empirical parameter $\Delta K/\rho^{0.3}$.

No critical notch root radius was found below which initiation was independent of root radius.

There was perhaps a critical density or critical porosity level in the sintered materials, below which crack growth rate increased with increased porosity content; above the critical level, decreased fatigue resistance arose from increased sintered density.

Comparatively higher crack growth rate in M_3 group of sintered compacts was due to the presence of soft ferrite in the matrix, which largely superceded the crack blunting effect due to porosities.

The micromechanism of fracture was of ductile dimple type in every case.

No striation markings were observed on fracture surfaces; instead, some characteristic lines found on the internal pore surfaces exposed after fracture were due to thermal etching effects.

Increase in toughness with increased yield stress seemed to be the basic trend in the sintered materials tested so far. This was because the fracture was effected by plastic instability on a micro-level.

12. RECOMMENDATIONS FOR FUTURE WORK

The present work opens up wider areas for further investigation. Some of these potential areas are outlined below:

It would be useful to test sintered specimens which have been machined and notched after full heat-treatment in order to isolate the effect of residual stresses or work hardening on crack initiation.

A 'Length' criterion for crack initiation may be used in future work to see whether sintered materials are sensitive to the definition of Ni and banding.

The concept of critical density or critical porosity level in sintered materials and the absence of striation markings on their fracture surfaces need further exploration.

Besides higher sintered density, infiltration, pore sealing or other approaches appear to be attractive for further improvement of fracture toughness.

Effect of root radius of pores on crack initiation and propagation characteristics and on toughness need careful exploration.

Fracture Mechanics approach, as applied in the present study, may be attempted for the assessment of thermal fatigue characteristics and corrosion damage in the sintered materials.

13.

ACKNOWLEDGEMENTS

It is my pleasure to thank Prof. J.T. Barnby for his valuable guidance and encouragement throughout this Project. The author also wishes to thank Prof. W.O. Alexander for the provision of necessary facilities in the Department which made this Research possible.

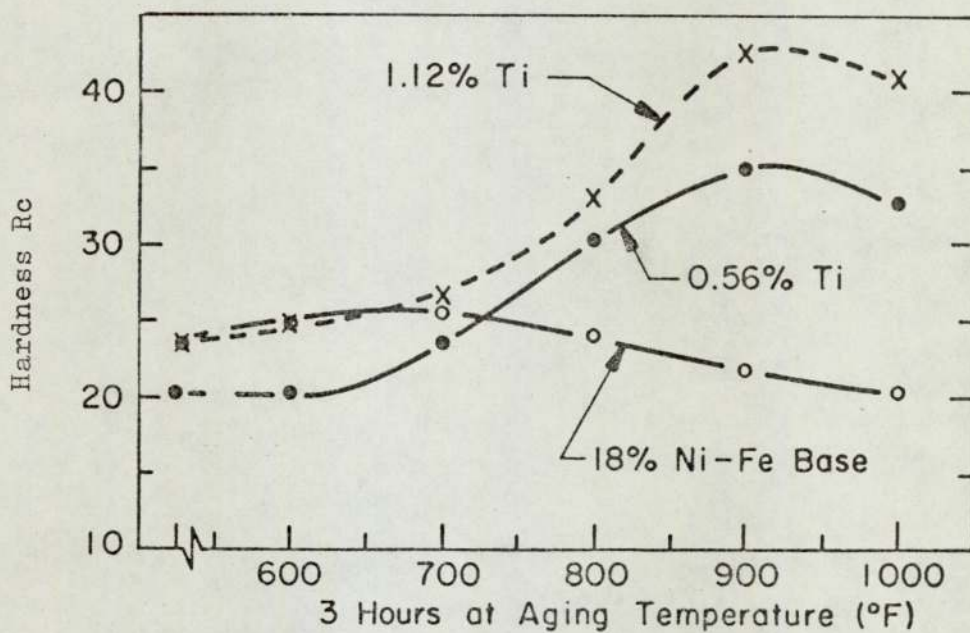


Fig.91. Variation in Hardness of 18 % Ni-Fe Base Alloy with Titanium Content, plotted as a Function of Ageing Temperature.

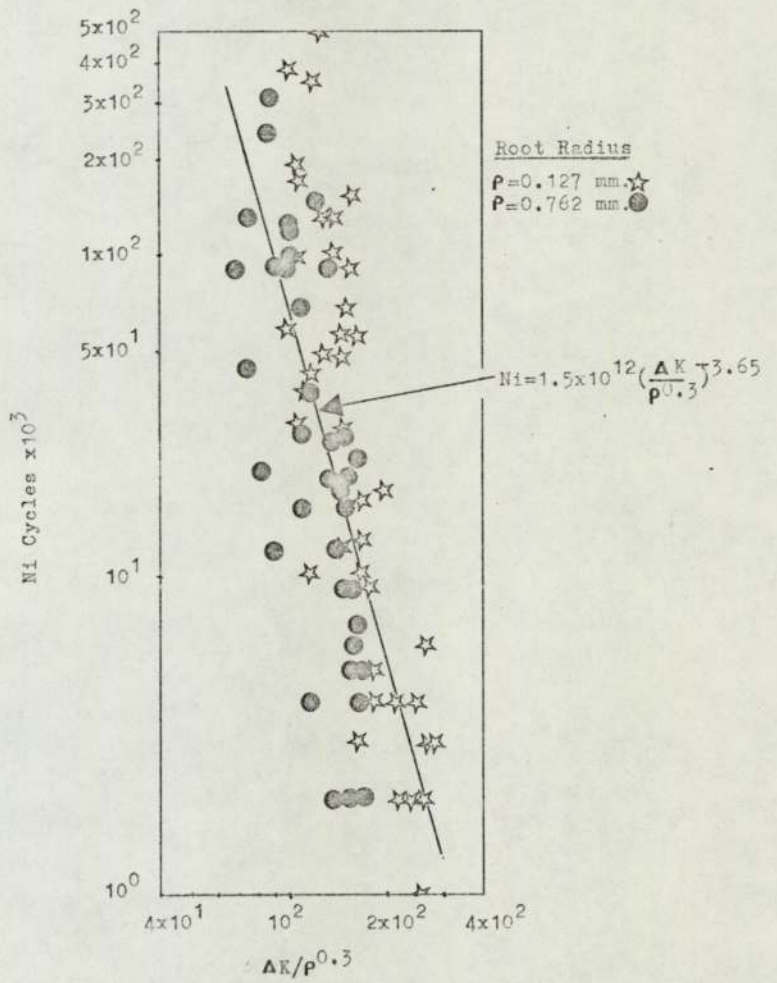


Fig.92. Effect of factors ΔK and ρ combined in a form derived by Regression Analysis on the no. of cycles to crack initiation, N_i .

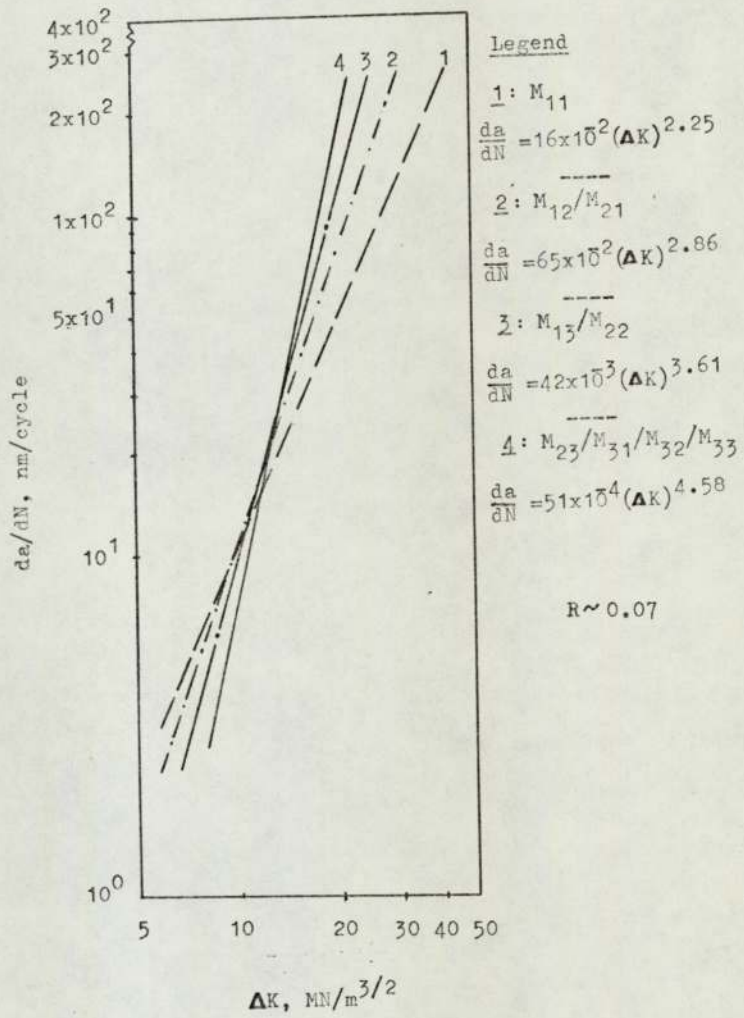


Fig.93(a). Summary of the Fatigue Crack Growth Rate Data generated for the Sintered Materials tested in this work.

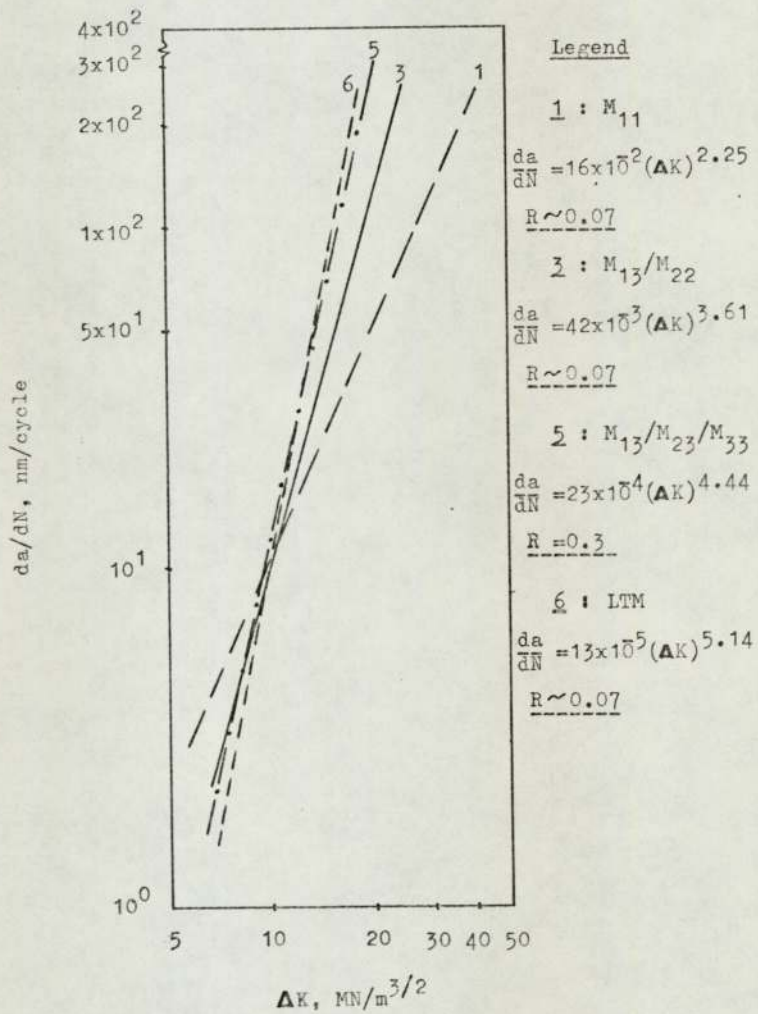


Fig.93(b). Summary of the Fatigue Crack Growth Rate Data (Cont'd.).

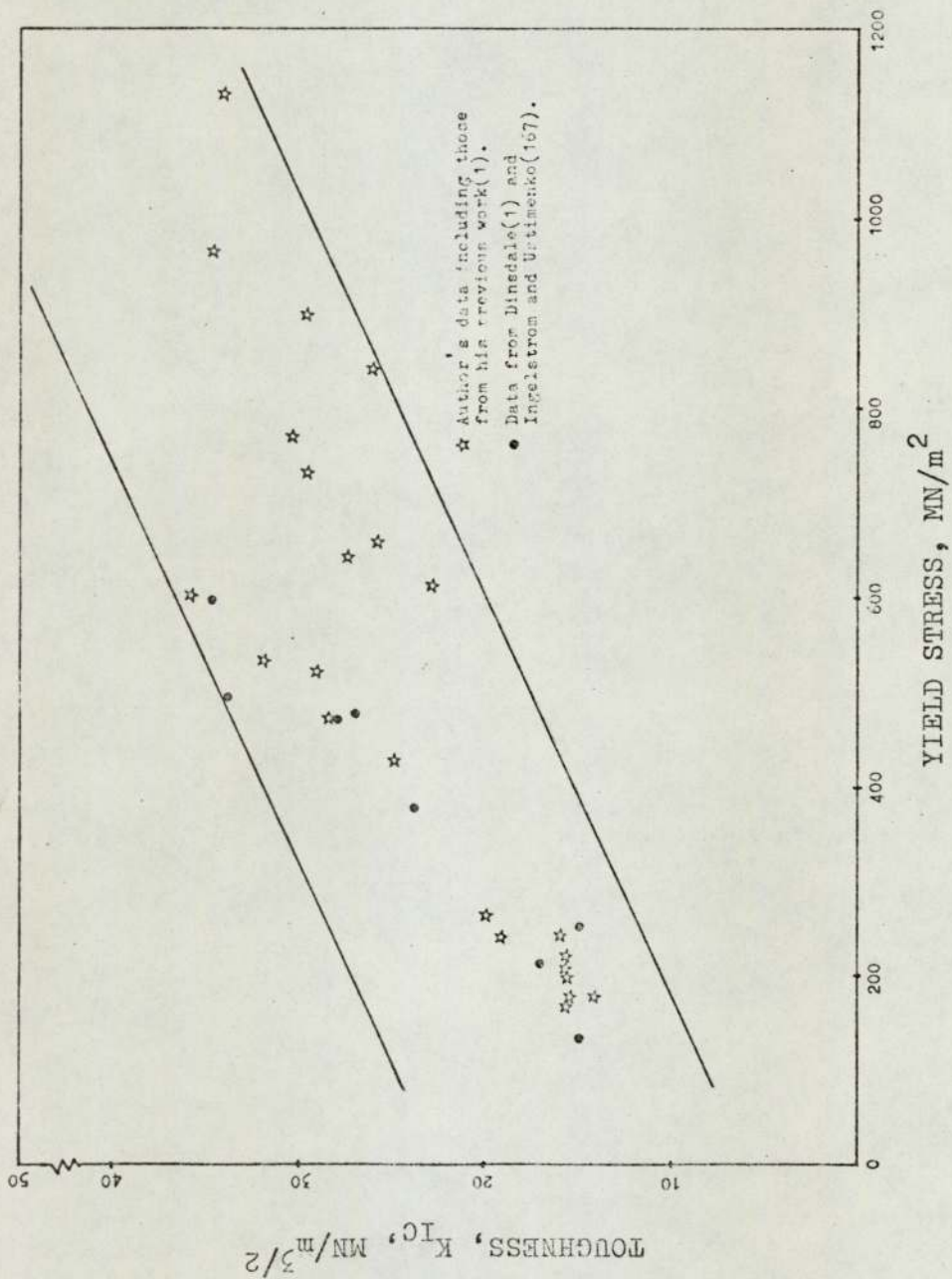


Fig.94. Variation in Toughness with Yield Stress for all the Sintered Materials tested in this work. Also included are data from others as shown.

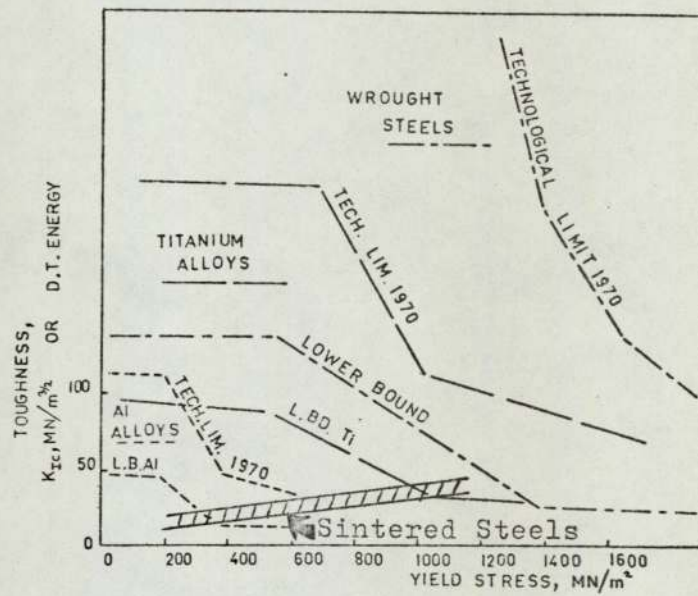


Fig. 95. Toughness/yield-stress relationships for wrought steels, titanium alloys, and aluminium alloys, compared with data on the sintered materials tested in this work.

1. Barnby, J.T., Powder Metallurgy, 16 (31),
Ghosh, D.C. and 1973, p.55.
Dinsdale, K.
2. Haynes, R. Powder Metallurgy, 13 (26),
1970, p.465.
3. Talmage, R. Mod. Dev. in P.M., 3, p.227
Plenum Press, 1966.
4. U. S. Patent No. 2, 769, 709.
5. Floreen, S. and A.S.M. Trans. Qrt. 57 (3),
Speich, G.R. 1964, p.714.
6. Spitzig, W.A., Engg. Fract. Mech. 1, 1968,
Talda, P.M. and p.155.
Wei, R.P.
7. Spitzig, W.A. and Engg. Fract. Mech., 1, 1970,
Wei, R.A. p.719.
8. Coleman, M.C. and Metal Tech., Jan. 1974,
Jordan, M.F. p.24.
9. Yoder, G.R. Met. Trans. 3, 1972, p.1851.
10. Decker, R.F., Trans. of A.S.M., 55, 1962,
Eash, J.T. and p.58.
Goldman, D.A.
11. Yates, D.H., and Metal Progress, 82 (Sept.),
Hamakar, J. 1962, p.97.
12. Floreen, S. and A.S.M. Qrt. Trans., 55 (3),
Decker, R.F. 1962 (March), p.518.
- 12A. Snape, E. and Powder Metallurgy, 15 (30),
Veltry, F. 1972, p.332.

13. Fisher, J.J. Int. J. of Powder Met., 2 (4),
1966, p.37.
14. Pampillo, C.A. and Met. Trans., 3, 1972 p.2895.
Paxton, H.W.
15. Tuffnell, G.W. and A.S.M. Trans. Qrt., 61
Cairns, R.L. 1968, p.798.
16. Floreen, S. Met. Rev. no. 126 (13),
1968, p.115.
17. Van Swam, L.F., et al. Met. Trans., 6 (1),
1975 (January), p.45.
18. Pellisier, G.E. Weld Imperfections, p.427.
19. Decker, R.F., J. of Metals, 19, 1967, p.60.
Novak, C.J. and
Landig, T.W.
20. Banerjee, B.R. and Tech. Report, Wright Patterson
Hauser, J.J. AFB, Ohio, AFML-TR-66-166, March, 1966.
21. Decker, R.F., et al. A.S.M. Trans., 55, 1962, p.58.
22. Owen, E.A. and J.I.S.I., 163, 1949, p.132
Liu, Y.H.
23. Jones, W. and J.I.S.I. 163, 1949, p.121
Pumphrey, W.
24. Kaufman, L. and Trans., A.I.M.E., 206,
Cohen, M. 1956, 1393.
25. Owen, W.S., High Strength Materials, 1965,
Wilson, E.A. p.167 (John Wiley, New York &
and Bell, T. London)
26. Patterson, R.L. and A.M., 14, 1966, p.347.
Wayman, C.M.

27. Parkin, J.R. M.Sc. Project, 1973, University of
Aston in Birmingham (U.O.A.B.)
28. Yeo, R.G.B. Trans. A.I.M.E., 227, 1963,
p.884.
29. Weltzin, R.D. and Met. Eng. Qrtly., 14,
Berger, C.M. May, 1974, p.62.
30. Peters, D.T. and Trans. A.I.M.E., 236, 1966,
Cupp, C.R. p.1420.
31. Miller, G.P. and J.I.S.I., 203, 1965, p.899.
Mitchell, W.I.
32. Perkass, M.D. Met. Sci. and Heat Treatment,
7-8, 1970, p.558.
33. Baker, A.J. and Trans. Qrt. A.S.M., 57, 1964,
Swann, P.R. p.1008.
34. Reisdorf, B.G. and Wright Patterson AFB, Ohio,
Baker, A.J. Tech. Report (AFML-TR-64-390), 1965.
35. Detert, K. Trans. Quart. A.S.M., 59, 1966,
p.262.
36. Detert, K. Arch. Eisenhüttenwesen, 37, 1966,
p.579.
37. Banerjee, B.R., et al. Tech. Report on The Fourth Maraging
Steel Project Review, A.F.M.L.-TDR.64.
- 37A. " " Hogan, A.B. Iron Powder Information, P.M. 70-1.
38. " Thummler, F. and Met. Rev. No. 115, 1967,
" Thomma, W. p.69.
39. Lenel, F.V., Mod. Dev. in Powder Met., 4,
Ansell, G.S. and 1971, p.199.
Morris, R.C.

40. Rhines, F.N. and Dehoff, R.T. Mod. Dev. in Powder Met., 4, 1971, p.173.
41. Sauerwald, F. Z. Physikal. Chem., 209, 1958, p.206.
42. Herring, C. Nabarro, F.R.N. J. Appl. Physics, 21, 1950, p.301. Report of Conf. on 'Strength of Solids', 1948, p.75.
43. Kuczynski, G.C. Trans. A.I.M.M.E., 185, 1949, p.169.
44. Jones, W.D. Fundamental Pr. of Powder Met., Arnold (London), 1960, p.386.
45. Kingery, W.D. J. Appl. Physics, 30, 1959, p.301.
46. Mc Adam, G.D. J.I.S.I. 168, 1951 1951 (August), p.346.
47. Rolfe, S.T. Int. Met. Rev. No. 186, 19, Sept. 1974, p.183.
48. Griffith, A.A. Phil. Trans. Ry. Soc. (London), Series A, (1920), 221, p.163.
49. Irwin, G.R. J. Appl. Mechanics, 24, 1957, p.361.
50. Orowan, E. Welding Res. Supplement, 20, 1955, p.157.
51. Inglis, C.E. Trans. Inst. Nav. Architects, 60, 1913, p.219.
52. Brown, W.F. and Srawley, J.E. A.S.T.M. - S.T.P. 410, 1966, p.9.
53. Walker, E.F. and May, M.J. B.I.S.R.A. Open Report No. MG/E/307/67.
54. Irwin, G.R. and Kies, J.A. Welding Journal, 33, 1954, p.193.

55. Sullivan, A.M. Mat. Res. and Std., 4, 1964,
p.20.
56. Johnson, H.H. and Engg. Fract. Mech. 1,
Paris, P.C. 1968, p.3.
57. Paris, P.C. and A.S.T.M. - S.T.P. 381,
Sih, G.C. 1965, p.30.
58. Barnby, J.T. N.D.T. Dec. 1971, p.387.
59. Pook, L.P. N.E.L. Report No. 465, 1970, p.1.
60. Weiss, V. and A.S.T.M. - S.T.P. 381, 1965,
Yukawa, S. p.6.
61. Barnby, J.T. Welding and Metal Fab.,
Feb. 1969, p.72.
62. Hahn, G.T. and Acta Met., 13, 1965,
Rosenfield, A.R. p.293.
63. Pook, L.P. N.E.L. Report No. 465, 1970, p.4.
64. Srawley J.E. and A.S.T.M. - S.T.P. 381, 1965,
Brown, W.F. p.133.
65. Brown, W.F. and A.S.T.M. - S.T.P. 410, 1966.
Srawley, J.E.
66. Paris, P.C. Proc. of 10th. Sagamore Army Conf.,
1964, Syracuse Univ. Press, p.107.
67. Rice, J.R. A.S.T.M., STP. 415, 1967, p.247.
68. Dobson, M.O. 'Fract. Fract. Mech. for Struct.
Steel', Chapman & Hall, London, 1969, Bl.
69. Walton, D. and Int. Met. Rev. No. 163, p.100
Ellison, E.G.

70. Forsyth, P.J.E. Proc. Crack Prop. Symp. 1961,
Cranfield, p.76.
71. Ewing, Sir J.A. and Phil. Trans., A. 200,
Humfrey, J.W.C. 1903, p.241.
72. Forsyth, P.J.E. Int. Conf. on the Fatigue of Metals,
London. Inst. Mech. Engrs.
73. Allery, M.B.P. and Engg. Fract. Mech., 4, 1972,
Birkbeck, G. p.325.
74. Thompson, N., Phil. Mag. 1, 1956, p.113.
Wadsworth, N.J.
and Louat, N.
75. Kennedy, A.J. Processes of Creep and Fatigue in Metals,
Oliver and Boyd, London, 1962.
76. Lynch, S.P. Met. Sc., 2 (9), Sept. 1975, p.401.
77. Weibull, W. Proc. of Crack Prop. Symp.,
Sweden, 1961, p.271.
78. Hoepfner, D.W. A.S.T.M. S.T.P.-415, 1967, p.486.
79. GrossKreutz, J.G. Physica Status Solidi (b), 47,
1971, p.359.
80. Plumbridge, W.J. Met. Rev. 14, 1969, p.119.
and Ryder, D.A.
81. Forsyth, P.J.E. "Physical Basis of Metal Fatigue",
1969, Blackie (London).
82. Lynch, S.P. A.R.L. Met. Report No. 94, 1974.
83. Cottrell, A.H. 'Mech. Properties of Matter',
p.373, 1964, John Wiley & Sons
(New York).

84. Lynch, S.P. and 'Aluminium', 49 (11), 1973,
Ryder, D.A. p.748.
85. Forsyth, P.J.E. Acta Met., 11, 1963, p.703.
86. Stubbington, C.A. ibid., 12, p.931.
87. Lynch, S.P. Met. Sc. J. 7, 1973, p.93.
88. Laird, C. A.S.T.M. S.T.P. 415, 1967, p.131
89. McEvily, A.J. and Acta Met., 11, 1963, p.725.
Boettner, R.C.
90. Zappfe, C.A. and Trans. A.S.M., 41, 1949, p.396.
Worden, C.D.
91. Crussard, C. Proc. of Int. Conf. on Fatigue of
Metals, p.784, Inst. of Mech. Eng.,
London, 1956.
92. Ryder, D.A. R.A.E. Tech. Note (Met. 288), 1958.
93. Forsyth, P.J.E. and Aircraft Engg., 32, 1960, p.96.
Ryder, D.A.
94. Plumbridge, W.J. and Met. Rev. No. 136, 2, 1968, p.119.
Ryder, D.A.
95. Richards, C.E. Acta Met., 19, 1971, p.583.
96. Lindley, T.C. and I.S.I. Report 145, 1971, p.119
Richards, C.E.
97. Jacoby, G. N.A.T.O. - A.G.A.R.D. Report (541),
1966.
98. Metals Handbook 2, 1974, p.69 (A.S.M.)
99. Zaman, K. Ph.D. Thesis, 1973, U.O.A.B.
100. Schijve, J. A.S.T.M. S.T.P. 415, 1967, p.533

101. Forsyth, P.J.E.,
Stubbington, C.A.
and Clark, D. J. Inst. of Metals, 90, 1961-62,
p.238.
102. Beachem, C.D. and
Pelloux, R.M.N. A.S.T.M. - S.T.P. 381,
1965, p.210.
103. Forsyth, P.J.E. R.A.E., Tech. Note (Met. 257) 1957.
104. Laird, C. and
Smith, G.C. Phil. Mag. 7, 1962, p.847.
105. Forsyth, P.J.E. and
Sampson, E.G.E. R.A.E. Tech. Report (65 158),
1965.
106. Whiteson, B.V., et al. A.S.T.M., S.T.P. 436, 1968,
p.151.
107. Metals Handbook 9, 1974, p.86, (A.S.M.)
108. Laird, C. and
Kaplan, H. Trans. of Met. Soc. of A.I.M.E.
T.M.S.A.A., 239, 1967, p.1017.
109. Schijve, J. A.S.T.M., S.T.P. 415, 1967, p.415.
110. Broek, D. Int. Met. Rev. No. 185, 19,
Sept. 1974, p.135.
111. Pelloux, R.M.N. Engg. Fract. Mech., 1, 1970, p.697.
112. Tomkins, B. Phil. Mag. 18, 1968, p.1041.
113. Pelloux, R.M.N. Trans. A.S.M., 57 (5), 1964, p.11
114. Pisarsky, H. Ph.D. Thesis, 1974, U.O.A.B.
115. GrossKreutz, J.C.
and Shaw, G. 'Fracture', 1969, p.620.
Chapman & Hall, London
116. Forsyth, P.J.E. and
Ryder, D.A. Metallurgia, 63, 1961, p.117.

117. EL-Soudani, S.M. and Pelloux, R.M.N. Met. Trans., 4, 1973, p.519.
118. Neuber, H. J. of App. Mech., Dec. 1961, p.554.
119. Wetzel, R.M. J. of Materials, 3 (3), Sept. 1968, p.646.
120. Topper, T.H., Wetzel, R.M. and Morrow Jo Dean. J. of Materials, 4, 1969, p.200.
121. Morrow, J., Wetzel, R.M. and Topper, T.H. A.S.T.M., S.T.P. 462, 1970, p.74.
122. Gowda, C.V.B., Topper, T.H. and Leiss, B.N. Proc. Int. Conf. on Mech. Behaviour of Materials, Kyoto, Japan, Vol. II, 1971, p.187.
123. Jack, A.R. and Price, A.T. Int. J. of Fract. Mech., 6, 1970, p.401.
124. Bilby, B.A., Cottrell, A.H. and Swinden, K.H. Proc. Roy. Soc. A 272, 1963, p.304.
125. Pearson, S. R.A.E. Tech. Report No. 71109, May, 1971.
126. Jack, A.R. Ph.D. Thesis, 1971, U.O.A.B.
127. Dinsdale, K. Private communication. 1973, U.O.A.B.
128. Forman, R.G. Engg. Fract. Mech., 4, 1972, p.333.
129. Creager, M. and Paris, P.C. Int. J. of Fract. Mech. 3, 1967, p.247.
130. Manson, S.S. Exp. Mech., 1965, p.193.

131. Barnby, J.T.,
Dinsdale, K. and
Holder, R. Conf. on Fract. Mech. Camb. Un.,
Paper No. 26, 1974.
132. Head, A.K. Phil. Mag. 44, 1953, p.925.
133. Frost, N.E. and
Dugdale, D.S. J. of Mech. and Physics of Solids,
6, (2), 1958, p.92.
134. Liu, H.W. Trans. A. Soc. of Mech. Engg., 85,
Series D. 1963, p.116.
135. Frost, N.E. J. of Mech. Eng. Soc., 1(2),
Sept. 1959, p.151.
136. Tomkins, B. and
Biggs, W.D. J. of Mat. Sc., 4, (6), 1969.
137. Tomkins, B. Phil. Mag. 18 (155), Nov. 1968.
138. Paris, and
Erdogan, Trans. of A.S.M.E., Series D,
1963, p.528.
139. Miller, G.A. Trans. A.S.M.E., 61, 1968, p.442.
140. Clark, W.G. Metal Progress, 79, 1970, p.81.
141. Forman, R.G.,
Kearney, V.E. and
Engle, R.M. J. of Basic Engg. A.S.M.E. Trans.
89, 1967, p.459.
142. Broek, D. and
Schijve, J. N.L.R. - TR M2111, Jan. 1963.
143. Illg, W. and
McEvily, A.J. NASA TN D - 52, Oct. 1959.
144. Crooker, T.W. and
Lange, E.A. NRL Report No. 6805,
Nov. 1968.
145. Pearson, S. R.A.E. Tech. Report 68297,
Dec. 1968.

146. Maddox, S.J. Int. J. of Fracture, 11 (3), June, 1975, p.389.
147. Heald, P.T.,
Lindley T.C. and
Richards, C.E. Mat. Sc. Engg., 10, 1972, p.235.
148. Weertman, J. Int. J. of Fract. Mech. 2, 1966,
p.460.
149. Roberts, R. and
Erdogan, F. Trans. A.S.M.E., Series D,
89, 1967, p.885.
150. Klensil, M. and
Lucas, P. Engg. Fract. Mech., 4,
1972, p.77.
151. Cooke, R.J. and
Beevers, C.J. Int. Report, B'ham University,
1973.
152. Donahue, R.J.,
et al. Int. J. of Fract. Mech. 8 (2),
1972, p.209.
153. Richards, C.E. and
Lindley, T.C. Engg. Fract. Mech., 4 (4), 1972,
p.951.
154. Crooker, T.W. N.R.L. Report 7347, p.8.
155. Walker, E.F. and
May, M.J. B.I.S.R.A. Open Report
No. MG/E/307/67
156. B.S.I. Draft D.D.3. 1971.
157. B.I.S.R.A. Report Proposed Spec. for Fract. Toughness
of High Strength Materials, Report,
MG/EB/312/67.
158. Pook, L.P. N.E.L. Report No. 449,
April 1970, p.1.
159. Nicholson, C.E. BISRA Report MG/EF/202/69, 1969.

160. Frost, N.E.,
Marsh, K.J.
and Pook, L.P. Metal Fatigue, Clarendon Press,
1974.
161. Barnett, W.J. and
Troiano, A.R. J. of Metals, 9, 1957, p.486.
162. Gilbey, D.M. and
Pearson, S. R.A.E. Tech. Report No. 66402,
1966.
163. Jack, A.R. and
Yeldham, D.E. C.E.G.B. Report, SSD/MID/R/215/70,
1970.
164. Ritchie, R.O. Camb. Un. Report, Jan. 1972.
165. Davies, K.B. and
Fedderson, C.E. Int. J. of Fracture, 9, 1973,
p.116.
166. Fisher, R.M. J. Appl. Phys., 24, 1953, p.113.
167. Ingelstrom, N. and
Ustimenko, V. Powder Met., 18, (36)
1975, p.303.
168. Allmand, T.R. BISRA report on "Microscopic identification
of inclusions in Steel", 1962.
169. Taylor, E. External Report, University of Aston
in Birmingham, Sept. 1973.
170. Bilby, B.A. and
Heald, P.T. Proc. Roy. Soc., A.305,
1968, p.429.
171. Wilkins, M.A. and
Smith, G.C. Met. Sc. J., 5, 1971,
p.139.
172. May, A.N. Nature, 188, 1960,
p.573.
173. Gittus, J.H. Nature 202,
1964, p.788.

174. Dawson, R.A.T.,
Elder, W.J.,
Hill, G.J. and
Price, A.T. Int. Conf. 1967, Metals and
Metallurgy Trust Monograph and
Report No. 325, 239.
175. Smith, E. Proc. Roy. Soc. A 299, 1967,
p.455.
176. Cottrell, A.H. Proc. Roy. Soc. A.285,
1965, p.10.
177. Bucci, R.J., Clark, W.G. ASTM - STP 513,
and Paris, P.C. 1971, p.177.
178. Paris, P.C. M.T.S. Closed Loop Magazine,
2 (5), 1970.
179. Schmidt, R.A. M.S. Thesis, Lehigh University
U.S.A., 1970.
180. Pellini, W.S. Nat. Res. Lab. Report 7406,
1972.
181. "Conducting Drop-Weight Tear Testing to Determine Nil
Ductility Transition Temperature of Ferrite Steels",
ASTM Stand. E208-69.
182. Heckel, R.W.,
Lanam, R.D. and
Tanzilli, R.A. Perspectives in Powder Metallurgy,
5, p.139, Plenum Press, New York,
London, 1970.

15. Appendix I.

According to Neuber⁽¹¹⁸⁾, the equation for the maximum stress or the stress concentration factor at the base of a notch is written as:

$$\sigma_{\max} = \frac{p \times 2 (a/\rho + 1) (a/\rho)^{\frac{1}{2}}}{(a/\rho + 1) \arctan (a/\rho)^{\frac{1}{2}} + (a/\rho)^{\frac{1}{2}}},$$

for tension case

and

$$\sigma_{\max} = \frac{p \times 4 (a/\rho) (a/\rho)^{\frac{1}{2}}}{3 [(a/\rho)^{\frac{1}{2}} + (a/\rho - 1) \text{Arctan} (a/\rho)^{\frac{1}{2}}]}$$

for bending case

whence,

$$\frac{\sigma_{\max}}{p} = \alpha_1,$$

for tension case

$$\frac{\sigma_{\max}}{p} = \alpha_2,$$

for bending case

where $p = \sigma_{\text{nom.}}$

The equation for $K_{T \text{ NET}}$, according to Neuber, can be written as:

$$K_{T \text{ NET}} = \frac{1 + (K_S - 1) (K_D - 1)}{[(K_S - 1)^2 + (K_D - 1)^2]^{\frac{1}{2}}}$$

and

$$K_{T \text{ GROSS}} = K_{T \text{ NET}} \times \frac{w^2}{(w-t)^2}$$

where

$$K_D = \frac{2(a/\rho + 1) - \alpha_1 (a/\rho + 1)^{\frac{1}{2}}}{(4(a/\rho + 1)/\alpha_2) - 3 \alpha_1}$$

and

$$K_S = 1 + 2(t/\rho)^{\frac{1}{2}}$$

where K_D is defined as the stress concentration factor for the deep notch (where the depth of notch is not too small compared to the width of the specimens) and K_S is the stress concentration factor for a shallow notch (where the depth of notch is very small compared to

the width of the specimens), and where

t = depth of notch

p = notch root radius

W = width of specimen

a = (width - depth of the notch)

16. APPENDIX II

Relationships between P_e , P_{min} and $\frac{\delta_c}{2}$.

An attempt was made to pin down the 'effective' notch root radius (P_e), above which the apparent values of fracture toughness show a noticeable increase. With this value of P_e was compared the minimum root radius of pores (P_{min}) measured in the sintered and heat-treated maraging, diluted maraging steel and ancoloy SA (ASA) compacts, after light etching. An attempt was also made to find out the relationships of crack opening displacement ($\frac{\delta_c}{2}$) with P_e and P_{min} in the above compact materials, and to explore the possibility of improving toughness by manipulating P_{min} of pores.

Four sets of specimens (2 in each set) of sintered and heat-treated maraging (M_{12}), diluted maraging (M_{21}), and ASA compacts in 2 levels of densities, were each machined/notched to a depth of $0.45W$ with root radii of 0.127, 0.254, 0.508 and 0.762 mm. as shown in the Table AI (appendix). One set of 2 specimens of the above mentioned compact materials, in both levels of densities, were initially machine-notched to a depth of $0.3W$, with root radius of 0.127 mm. and fatigue-cracked to a depth of $\sim 0.45W$. This helped to produce infinitely small root radius ($\rightarrow 0$) at the crack tip. Results of apparent fracture toughness are also given in Table AI.

TABLE AI

Apparent Fracture Toughness corresponding to different
Notch Root Radii.

Materials Code	Notch Depth W=23.50 mm.	Notch Root Radius, mm.	Apparent Fracture Toughness K.App., MN/m ^{3/2}		
			Density levels	1	2
				6.9, Mg/m ³	7.1, Mg/m ³
M ₁₂	0.45W	0.127		31.39	30.50
				29.61	
		0.254		31.25	32.70
				34.15	
	0.508		38.41	36.68	
			34.95		
	0.762		43.55	41.76	
			39.97		
	0.3W ↓ (0.45W)	0.127 ↓ (0.0)		30.10	29.60*
M ₂₁	0.45W	0.127	31.42	28.97	
			26.52		
		0.254	29.86	30.20	
			30.54		
	0.508	33.67	33.72		
		33.77			
	0.762	38.49	39.45		
		40.41			
	0.3W ↓ (0.45W)	0.127 ↓ (0.0)	28.12	27.53*	
			26.94		

* Valid K_{IC} Values

TABLE AI (CONT'D)

Apparent Fracture Toughness corresponding to different Notch Root Radii.

Materials Code	Notch Depth W = 250 mm.	Notch Root Radius, mm.	Apparent Fracture Toughness			
			K app., MN/m ^{3/2}			
			Density levels	1	2	
				6.7, Mg/m ³	6.9, Mg/m ³	
ASA-S (Ancoloy SA, sintered)	0.45W	0.127	25.69	26.11 (av.)	31.15	31.44
			26.54		31.73	
		0.254	28.39	28.15	31.79	32.16
			27.91		32.53	
	0.508	29.86	30.01	35.95	35.77	
		30.16		35.59		
	0.762	32.89	32.71	37.14	37.11	
		32.54		37.09		
	0.3W ↓ (0.45W)	0.127 ↓ (0.0)	24.73	24.92	27.92	28.54
			25.11		29.16	
ASA-SQT (Ancoloy SA, sintered, quenched and tempered)	0.45W	0.127	27.73	27.03	32.51	31.72
			26.34		30.93	
		0.259	32.43	31.94	33.35	34.50
			31.46		35.65	
	0.508	35.84	36.03	41.31	39.70	
		36.23		38.09		
	0.762	38.47	37.89	32.08	43.43	
		37.32		44.79		
	0.3W ↓ (0.45W)	0.127 ↓ (0.0)	25.63	25.77	28.20	29.61
			25.92		31.02	

* Valid K_{IC} Values

From the graphs of K-apparent Vs Notch Root Radius, Fig. 1A, & 2A, it is difficult to pin down the Effective Notch Root Radius of Specimens, P_e (at which K-apparent values tend to go up gradually with Root Radius P); however, it seems that it lies somewhere at Notch Root Radius ~ 0.0635 mm. for M_{12} & M_{21} compacts, and ~ 0.03175 mm. for Ancoloy SA compacts. In Table-A II is given the relationships between $\frac{\delta_c}{2}$ & P_e , obtained by using the formula,

$$G_c = \frac{\pi}{4} \cdot \sigma_{ys} \cdot \delta_c, \text{ for Plane stress}$$

$$= \frac{\pi}{2} \cdot \sigma_{ys} \cdot \delta_c, \text{ for Plane strain.}$$

also, $G_c = \frac{Kc^2 (1 - \nu^2)}{E}$, for Plane strain

TABLE-A II

Materials Code	P_e (Effective ρ) (μ)	$P_{min.}$ (from Root Radius of pores) ($\times 10^3 \mu$)	G_c ($\frac{KN}{m}$)	$\frac{\delta_c}{2}$ (μ)
M_{12}	63.5	48.1	6.59	2.3
M_{21}	63.5	100.0	6.26	3.1
M_{12}	63.5	64.5	6.59	2.3
ASA-S(1)	31.75	86.2	4.99	3.7
ASA-SQT(2)	31.75	76.9	6.23	2.7
ASA-S (2)	31.75	121.4	5.78	3.9

In all cases, $P_{min.} < \frac{\delta_c}{2} \ll P_e$.

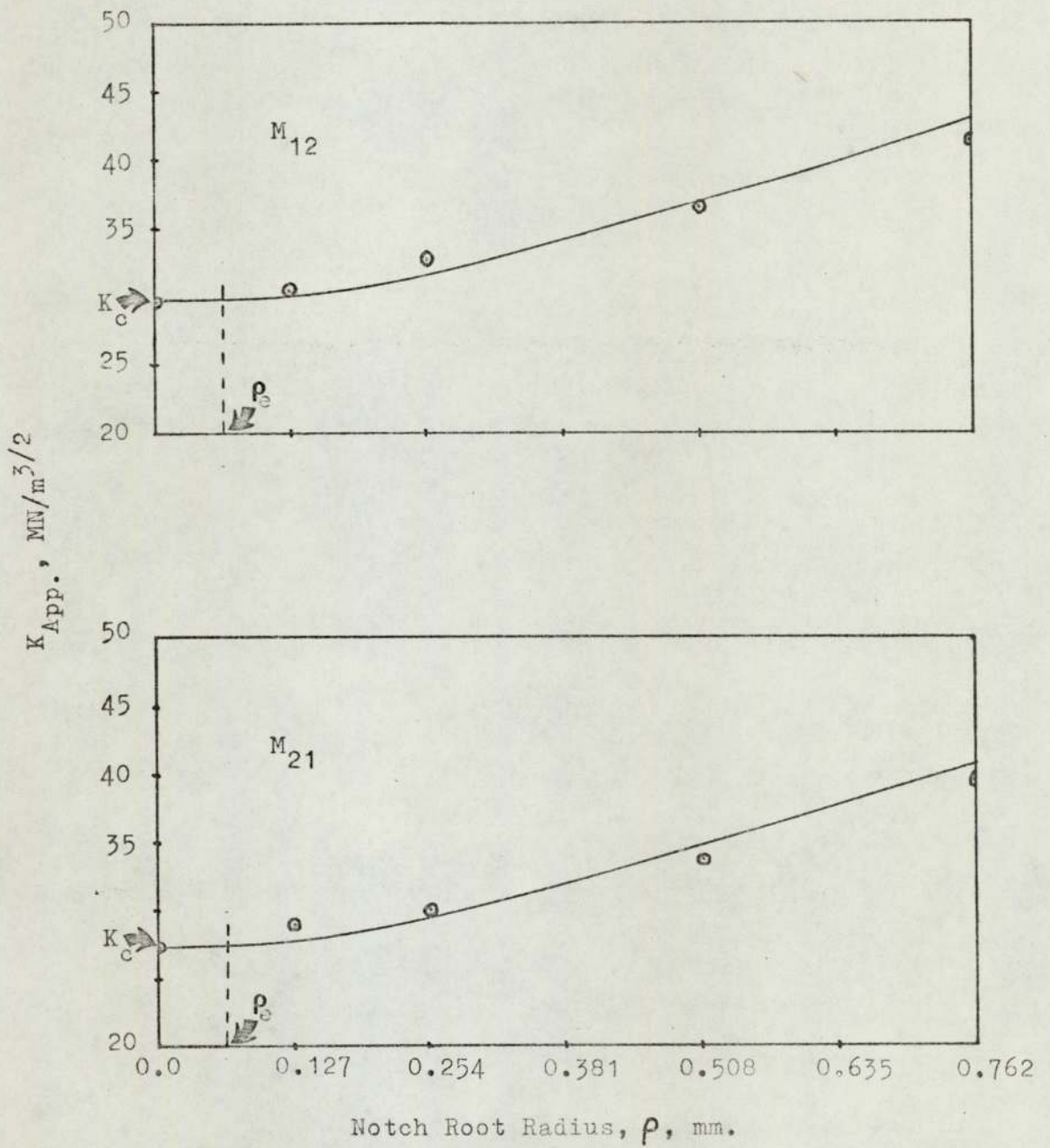


Fig.1A. Variation of Apparent Fracture Toughness with Notch Root Radii.

$K_{App.}, MN/m^{3/2}$

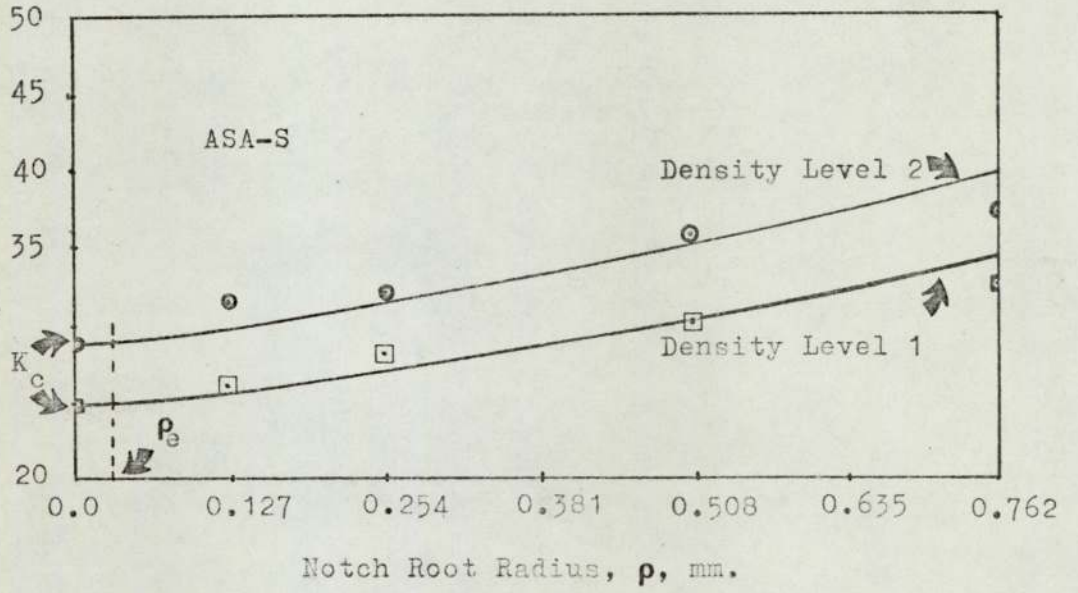
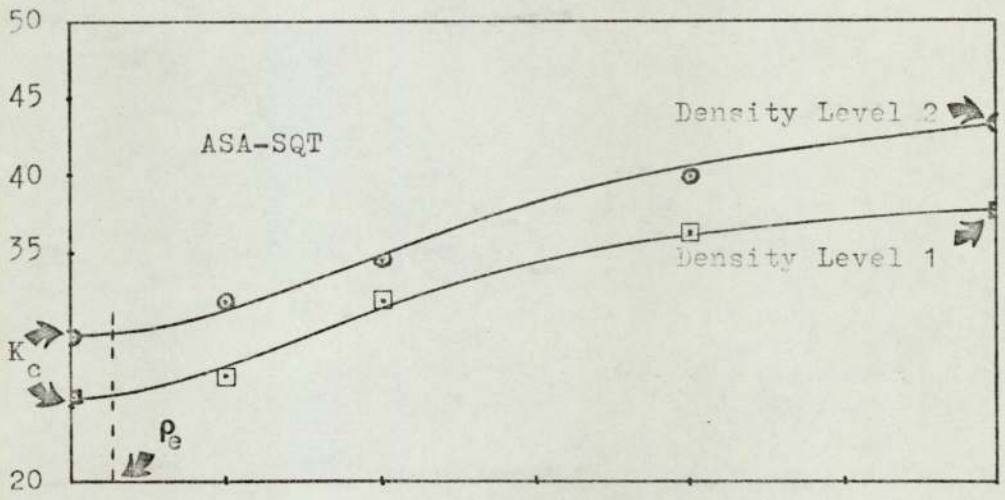
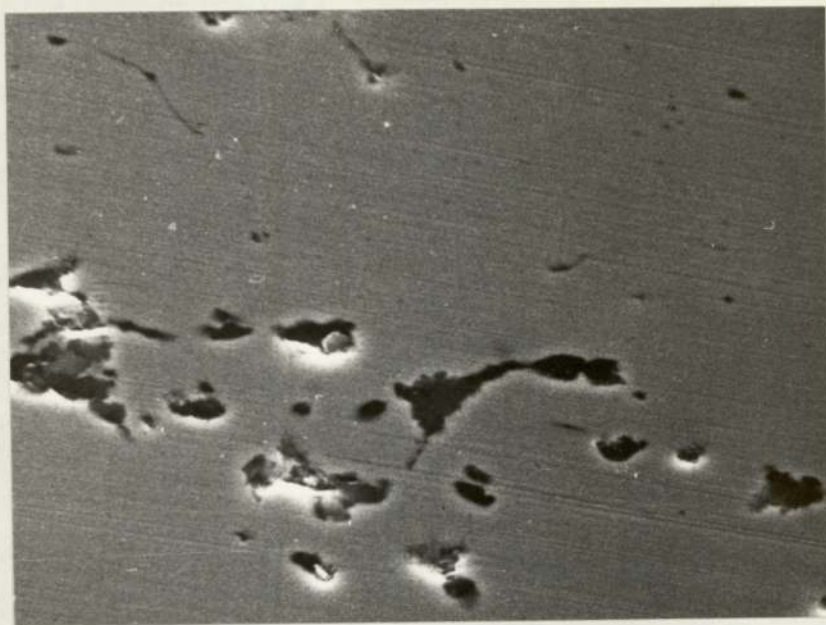


Fig.2A. Variation of Apparent Fracture Toughness with Notch Root Radii.

EXAMPLES OF PORES WITH VERY SHARP ROOT RADII IN
THE SINTERED MATERIALS TESTED.



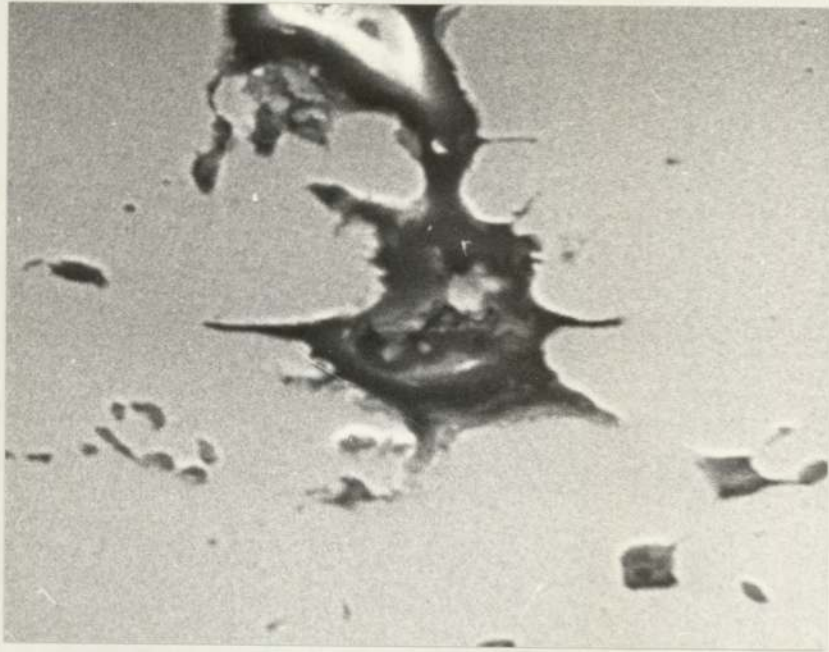
|1/50 P.S.|

Fig.1A1. M_{12} Sintered Compacts.
 $P_{min.} = 48.1 \times 10^3 \mu.$



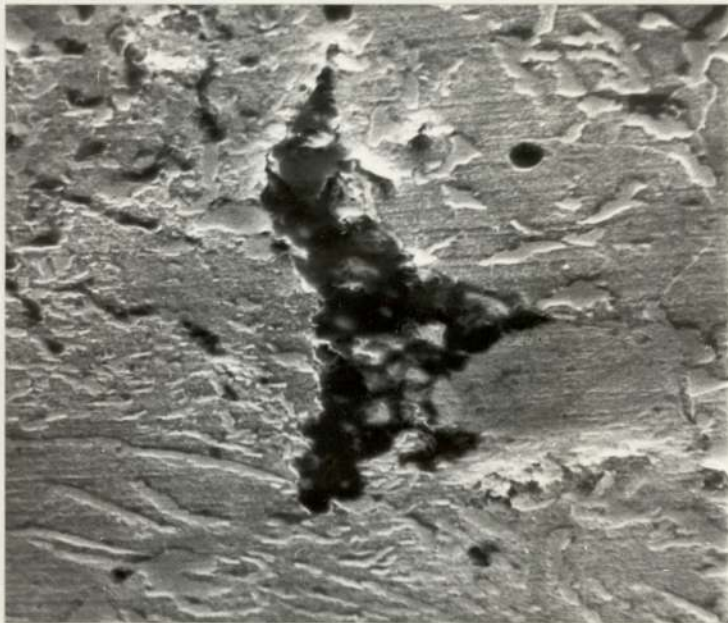
|1/10 P.S.|

Fig.1A2. M_{21} Sintered Compacts.
 $P_{min.} = 100 \times 10^3 \mu.$



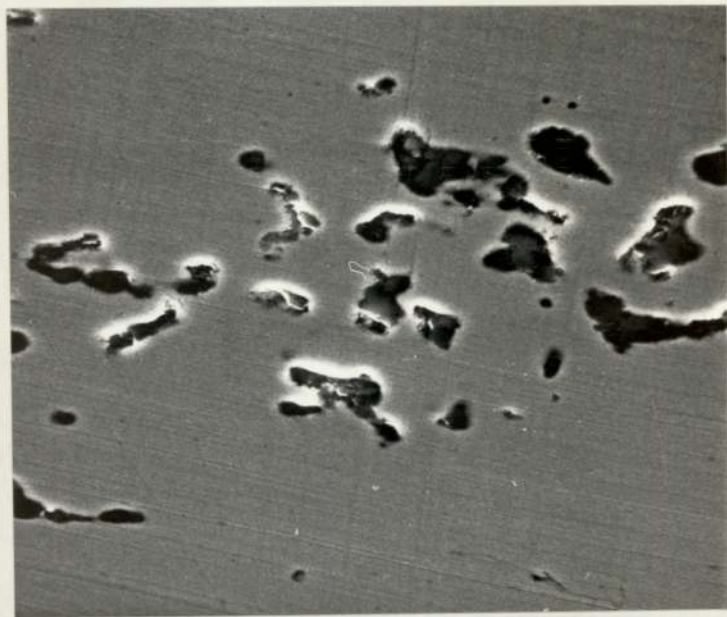
←1/10 P.S. →

Fig.1A3. M_{12} Sintered Compacts.
 $P_{\min.} = 64.5 \times 10^3 \mu.$



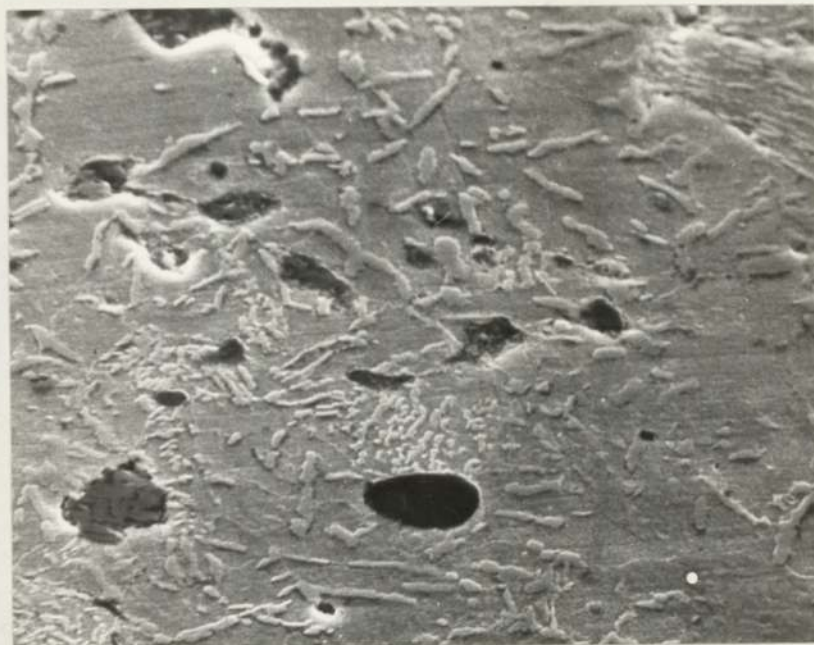
←1/50 P.S. →

Fig.2A1. ASA-S(1) Sintered Compacts.
 $P_{\min.} = 86.2 \times 10^3 \mu.$



←1/20 P.S.→

Fig.2A2. ASA-SQT(2) Sintered Compacts.
 $P_{\min.} = 76.9 \times 10^3 \mu.$



←1/50 P.S.→

Fig.2A3. ASA-S(2) Sintered Compacts.
 $P_{\min.} = 121.4 \times 10^3 \mu.$